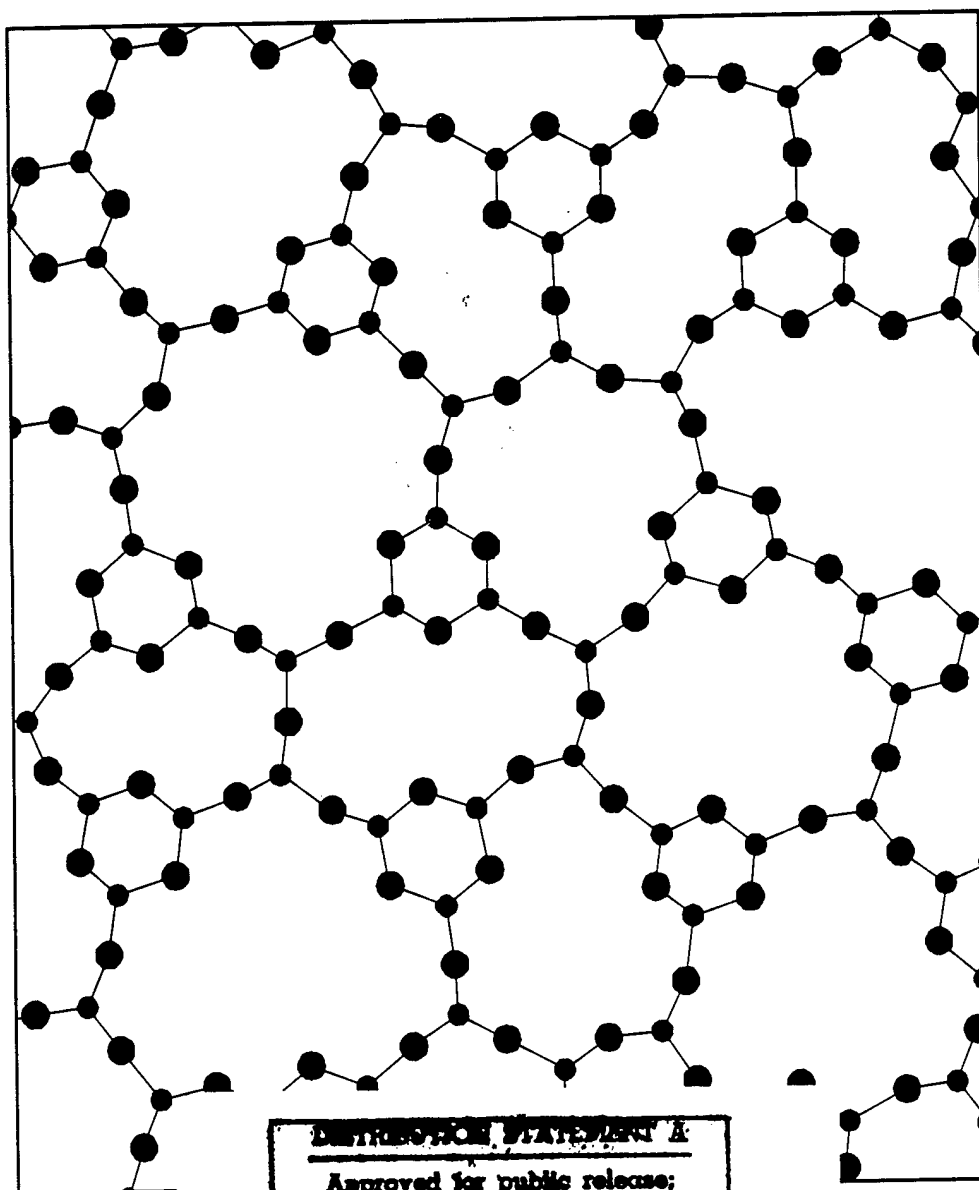


# BORATE GLASSES, CRYSTALS & MELTS



**DISTRIBUTION STATEMENT A**

**Approved for public release;  
Distribution Unlimited**

*Edited by:*

**Adrian C. WRIGHT, Steven A. FELLER  
and Alex C. HANNON**

REPORT DOCUMENTATION PAGE			Form Approved OMB No. 0704-0188	
Public reporting burden for this collection of information is estimated to average 1 hour per response, including the time for reviewing instructions, searching existing data sources, gathering and maintaining the data needed, and completing and reviewing the collection of information. Send comments regarding this burden estimate or any other aspect of this collection of information, including suggestions for reducing this burden to Washington Headquarters Services, Directorate for Information Operations and Reports, 1215 Jefferson Davis Highway, Suite 1204, Arlington, VA 22202-4302, and to the Office of Management and Budget, Paperwork Reduction Project (0704-0188), Washington, DC 20503.				
1. AGENCY USE ONLY (Leave blank)	2. REPORT DATE  2 December 1997	3. REPORT TYPE AND DATES COVERED  Conference Proceedings		
4. TITLE AND SUBTITLE  Borate Glasses, Crystals & Melts		5. FUNDING NUMBERS  F6170896W0102		
6. AUTHOR(S)  Conference Committee				
7. PERFORMING ORGANIZATION NAME(S) AND ADDRESS(ES)  Reading University Whiteknights Reading RG6 6AF United Kingdom		8. PERFORMING ORGANIZATION REPORT NUMBER  N/A		
9. SPONSORING/MONITORING AGENCY NAME(S) AND ADDRESS(ES)  EOARD PSC 802 BOX 14 FPO 09499-0200		10. SPONSORING/MONITORING AGENCY REPORT NUMBER  CSP 96-1013		
11. SUPPLEMENTARY NOTES				
12a. DISTRIBUTION/AVAILABILITY STATEMENT  Approved for public release; distribution is unlimited.		12b. DISTRIBUTION CODE  A		
13. ABSTRACT (Maximum 200 words)  The Final Proceedings for Borate, Glasses, Crystals and Melts, 22 July 1996 - 25 July 1996  This is an interdisciplinary conference. Topics include glass forming systems, triborate systems, structural studies, modeling and computer simulation, super-ionic conduction, ionic transport.				
14. SUBJECT TERMS  Nil		15. NUMBER OF PAGES  554		16. PRICE CODE  N/A
17. SECURITY CLASSIFICATION OF REPORT  UNCLASSIFIED	18. SECURITY CLASSIFICATION OF THIS PAGE  UNCLASSIFIED	19. SECURITY CLASSIFICATION OF ABSTRACT  UNCLASSIFIED	20. LIMITATION OF ABSTRACT  UL	

19980102 024

**BORATE GLASSES, CRYSTALS & MELTS**

Edited by:

Adrian C. WRIGHT, Steven A. FELLER and Alex C. HANNON



**The Society of Glass Technology  
Sheffield, 1997**

**DTIC QUALITY INSPECTED 4**

Borates glasses, crystals and melts

Proceedings of the Second International Conference on Borates Glasses, Crystals and Melt held at The Cosener's House, Abingdon, UK on 22–25 July 1996

The objects of the Society of Glass Technology are to encourage and advance the study of the history, art, science, design, manufacture, after treatment, distribution and end use of glass of any and every kind. These aims are furthered by meetings, publications, the maintenance of a library and the promotion of association with other interested persons and organisations.

Society of Glass Technology  
20 Hallam Gate Road  
Sheffield S10 5BT, UK  
Tel +44(0)114 2663168  
Fax +44(0)114 2665252  
Email [gt@glass.demon.co.uk](mailto:gt@glass.demon.co.uk)  
Web <http://www.sgt.org>

The Society of Glass Technology is a registered charity no. 237438.

© Society of Glass Technology 1997

ISBN 0-900682-23-X

Printed by Alden Press, Oxford, UK



---

**Professor Philip J. BRAY**



Professor Philip J. BRAY

Professor Philip J. Bray was born in Kansas City, Missouri in 1925 and is currently Hazard Professor of Physics (Emeritus) at Brown University. He was educated at Brown (Sc.B.) and Harvard (A.M. & Ph.D.) Universities and, in addition to his distinguished career in the Physics Department at Brown University, has served as Visiting Professor in the Department of Glass Technology, Sheffield University (U.K.; 1961-2 and 1968-9) and in the Department of Chemistry, Exeter University (U.K.; 1977). He is a recipient of both the Sir Neville Mott Award (Journal of Non-Crystalline Solids, 1991), for his "outstanding contributions to the field of glass science," and the George W. Morey Award (American Ceramic Society, 1970), for his "outstanding contributions to glass science and technology." He is a Fellow, not only of the Society of Glass Technology, but also of the American Academy of Arts and Sciences, the American Ceramic Society, the American Physical Society and Sigma Xi. The proceedings of the Second International Conference on Borate Glasses, Crystals & Melts are dedicated to Philip J. Bray, in recognition of his outstanding contributions to the science of borates.

## Foreword

The *Second International Conference on Borate Glasses, Crystals & Melts* was held during the period 22<sup>nd</sup> - 25<sup>th</sup> July, 1996 at The Cosener's House (the conference centre of the Rutherford Appleton Laboratory), Abingdon, U.K. This followed the first conference in the series, entitled *Boron in Glass and Glass Ceramics*, which was held at the New York State College of Ceramics in 1977.

For the present conference, 96 experimental and theoretical scientists from 18 countries (Austria, Brazil, Bulgaria, Egypt, France, Germany, Greece, Israel, Italy, Japan, Korea, Lichtenstein, Russia, Spain, Sweden, Turkey, the U.K. (England) and the U.S.A.) gathered to discuss all aspects of the science and technology of borate containing materials. In addition to the plenary lecture by Philip J. Bray, in whose honour the conference was held, there were 10 invited papers, by L. Börjesson, G.D. Chryssikos, R.A. Condrate, Sr., V.V. Golubkov, S.W. Martin, E.A. Porai-Koshits, B.A. Shakhmatkin, R.A. Smith, M. Teter and J.W. Zwanziger. A further 43 papers were presented orally and there was a single poster session with 12 posters. The conference sessions were chaired by R.J. Araujo, Y.B. Dimitriev, S.A. Feller, E.I. Kamitsos, A.J. Leadbetter, R. O'Connor, C. Rhee, L.M. Torell, N.M. Vedishcheva and A.C. Wright and comprised (1) NMR Spectroscopy, (2) Paradoxes of the Vitreous State, (3) Structure, Inhomogeneity & Phase Separation, (4) Spectroscopic Techniques, (5) Thermodynamics of Borate Systems, (6) Ternary Systems, (7) Non-Oxide & Mixed Glasses, (8) Superionic & Related Systems, (9) Industrial and Technological Applications, (10) Relaxation & the Glass Transition, (11) Optical Spectroscopy & Defects, (12) Modelling & Computer Simulation and (13) the Poster Session. At the conference dinner, the after dinner address, entitled *Three-fold, four-fold, rings and Bray*, was given by Robert A. Weeks and was preceded by various presentations to Philip J. Bray by his colleagues and former students.

The success of the Conference was due to the efforts and support of many people and institutions and we would like to extend our grateful thanks to them all. First, there are our sponsors, without whom the conference could not have been held:

- *Borax Consolidated Ltd.*
- *Corning Inc.*
- *International Science Foundation.*
- *Pilkington plc.*
- *Royal Society (London).*
- *U.S. Air Force European Office of Aerospace Research and Development.*
- *U.S. Borax, Inc.*
- *U.S./U.K. Fulbright Commission.*

We would also like to thank the members of the International Organising

Committee:

- Yanko B. Dimitriev (Bulgaria)
- Osama H. El-Bayoumi (U.S.A.)
- Alex C. Hannon (U.K.)
- Efstratios I. Kamitsos (Greece)
- Anna Musinu (Sardinia)
- L. David Pye (U.S.A.)
- Chunghi Rhee (Korea)
- Lena M. Torell (Sweden)
- Natalia M. Vedishcheva (Russia)
- Itaru Yasui (Japan)

for all their efforts on behalf of the conference.

Finally, our sincere thanks are extended to Jill Costello and the team at the Society of Glass Technology: Christine Brown, Jenny Lawless, Sara Lindley and David Moore, who did most of the real work, and to Barbara Feller, who organised the accompanying person's programme, parts of which were also enjoyed on occasion by some of the participants themselves!

Following discussions at the conference, Yanko B. Dimitriev (from the University of Chemical Technology & Metallurgy, Sofia) invited all those with an interest in borates to come to Bulgaria for the Third International Conference on Borate Glasses, Crystals & Melts, which will be held, probably on the Black Sea coast during 1999, under the joint chairmanship of himself and Adrian C. Wright.

Steven A. Feller  
Adrian C. Wright  
(Conference Co-Chairmen).



Conference Participants at The Cosener's House

## Contents

	Page
Professor Phillip J. Bray	iii
Foreword	iv
<b>1. NMR Spectroscopy</b>	
Session Chairs: S.A. FELLER (Coe College, Cedar Rapids, IA, USA) & A.C. WRIGHT (University of Reading, UK)	
NMR and NQR studies of borates and borides (Plenary Lecture) <b>P.J. BRAY</b> (Brown University, Providence, RI, USA)	1
High-resolution NMR studies of borate glass structure (Invited) <b>J.W. ZWANZIGER, R.E. YOUNGMAN &amp; M. BRAUN</b> (Indiana University, Bloomington, USA)	20
NMR studies of borate and borosilicate glass systems in Korea (Abstract Only) <b>C. RHEE</b> (Korea Research Institute of Standards and Science, Taejon, Korea)	33
Temperature effects on borate melt structure and dynamics: NMR studies <b>J.F. STEBBINS &amp; S. SEN</b> (Stanford University, CA, USA)	34
Studies of the structure of $\text{Li}_2\text{O-B}_2\text{O}_3\text{-Al}_2\text{O}_3$ glasses using $^{11}\text{B}$ NMR technique <b>H.-T. KIM, S.-J. CHUNG</b> (Chonnam National University, Kwang-ju, South Korea) & <b>M.-J. Park</b> (Korea University, Seoul, South Korea)	42
<b>2. Paradoxes of the Vitreous State</b>	
Session Chair: <b>N.M. VEDISHCHEVA</b> (Institute of Silicate Chemistry of the Russian Academy of Sciences, Sankt Petersburg, Russia)	
Some paradoxes of borate glasses and melts (Invited) <b>E.A. PORAI-KOSHITS</b> (Institute of Silicate Chemistry of	51

the Russian Academy of Sciences, Sankt Petersburg, Russia)  
& A.C. WRIGHT (University of Reading, UK)

The boron oxide "anomaly" revisited 63  
M.C. WEINBERG, D.R. UHLMANN & W.H. POISL  
(University of Arizona, Tucson, USA)

Low-Q features in diffraction data for borate glasses and crystals - 71  
an examination of similarities in medium-range structures  
P.H. GASKELL (University of Cambridge, UK)

The interrelationship between the structures of borate glasses and 80  
crystals  
A.C. WRIGHT (University of Reading, UK), N.M.  
VEDISHCHEVA & B.A. SHAKHMATKIN (Institute of  
Silicate Chemistry of the Russian Academy of Sciences,  
Sankt Petersburg, Russia)

### 3. Structure, Inhomogeneity & Phase Separation

Session Chair: N.M. VEDISHCHEVA (Institute of Silicate  
Chemistry of the Russian Academy of Sciences,  
Sankt Petersburg, Russia)

Structural and chemical inhomogeneities in borate glasses (Invited) 88  
V.V. GOLUBKOV (Institute of Silicate Chemistry of the  
Russian Academy of Sciences, Sankt Petersburg, Russia)

Cation and network structure in binary potassium borate glasses 99  
N. UMESAKI, D.A.H. CUNNINGHAM, N. KAMIJO  
(Osaka National Research Institute, Japan), K. HANDA  
(Ritsumeikan University, Siga, Japan) & Y. IWADATE  
(Chiba University, Japan)

Temperature dependence of the relaxation compressibility of boron 107  
oxide based on visible light scattering data  
N.A. BOKOV & N.S. ANDREEV (Institute of Silicate  
Chemistry of the Russian Academy of Sciences, Sankt  
Petersburg, Russia)

A structural study of  $\text{Bi}_2\text{O}_3\text{-B}_2\text{O}_3$  glasses 112  
E.M. GATTEF, V.V. DIMITROV, Y.B. DIMITRIEV  
(University of Chemical Technology & Metallurgy, Sofia,  
Bulgaria) & A.C. WRIGHT (University of Reading, UK)

Crystal structure and thermal behaviour of rubidium borates R.S. BUBNOVA, I.G. POLYAKOVA (Institute of Silicate Chemistry of the Russian Academy of Sciences, Sankt Petersburg, Russia), S.K. FILATOV & M.G. KRZHIZHANOVSKAYA (Sankt Petersburg University, Russia)	120
---	-----

#### 4. Spectroscopic Techniques

Session Chair: E.I. KAMITSOS (National Hellenic Research Foundation, Athens, Greece)	
Borate structures by vibrational spectroscopy (Invited) G.D. CHRYSSIKOS & E.I. KAMITSOS (National Hellenic Research Foundation, Athens, Greece)	128
Inelastic neutron scattering techniques for studying superstructural units in borate glasses R.N. SINCLAIR, A.C. WRIGHT, A.J. WANLESS (University of Reading, UK), A.C. HANNON (Rutherford Appleton Laboratory, Chilton, UK), S.A. FELLER, M.T. MEYHEW, B.M. MEYER, M.L. ROYLE, D.L. WILKERSON, R.B. WILLIAMS & B.C. JOHANSON (Coe College, Cedar Rapids, IA, USA)	140
n(=1,2,3)-dimensional Fourier transform electron paramagnetic resonance (FT-EPR) spectroscopy measurements in the B <sub>2</sub> O <sub>3</sub> -Li <sub>2</sub> O system and MO calculations G. KORDAS (National Center for Scientific Research "Demokritos", Athens, Greece)	148
Structural investigations of lead and strontium borate glasses T. HÜBERT, U. HARDER, G. MOSEL & K. WITKE (Bundesanstalt für Materialforschung und -prüfung, Berlin, Germany)	156
High-temperature Raman spectral studies of various borate- containing glasses (Invited) R.A. CONDRATE, Sr. & A.K. JILLAVENKATESA (New York State College of Ceramics, Alfred, USA)	164
X-ray photoelectron spectroscopy of borate glasses S. MATSUMOTO, Y. MIURA, C. MURAKAMI & T. NANBA (Okayama University, Japan)	173

Velocity of sound and elastic properties of alkali borate glasses <b>M. KODAMA</b> (Kumamoto Institute of Technology, Japan) & <b>S. KOJIMA</b> (University of Tsukuba, Japan)	181
--	-----

### 5. Thermodynamics of Borate Systems

Session Chair: **R.J. ARAUJO** (Corning Inc, NY, USA)

Thermodynamics of borate melts and glasses (Invited) <b>B.A. SHAKHMATKIN</b> , <b>N.M. VEDISHCHEVA</b> (Institute of Silicate Chemistry of the Russian Academy of Sciences, Sankt Petersburg, Russia) & <b>A.C. WRIGHT</b> (University of Reading, UK)	189
---	-----

Structure and properties of multi-component borate glasses based on Raman spectroscopy and the chemical equilibrium concept <b>R. OTA</b> , <b>J. FUKUNAGA</b> & <b>T. WAKASUGI</b> (Kyoto Institute of Technology, Japan)	199
---	-----

Thermodynamic, acoustic and elastic properties of $B_2O_3$ glasses <b>M.A. RAMOS</b> , <b>S. VIEIRA</b> (Universidad Autónoma de Madrid, Spain), <b>C. PRIETO</b> (Instituto de Ciencia de Materiales de Madrid, Spain) & <b>J.F. FERNANDEZ</b> (Universidad Autónoma de Madrid, Spain)	207
--	-----

Simulation of the structure of borate glasses and melts on the basis of thermodynamics <b>N.M. VEDISHCHEVA</b> , <b>B.A. SHAKHMATKIN</b> , <b>M.M. SHULTZ</b> (Institute of Silicate Chemistry of the Russian Academy of Sciences, Sankt Petersburg, Russia) & <b>A.C. WRIGHT</b> (University of Reading, UK)	215
--	-----

### 6. Ternary Systems

Session Chair: **R.J. ARAUJO** (Corning Inc, NY, USA)

Alkali borosilicate systems: phase diagrams and the structure of glass <b>I.G. POLYAKOVA</b> & <b>E.V. TOKAREVA</b> (Institute of Silicate Chemistry of the Russian Academy of Sciences, Sankt Petersburg, Russia)	223
---	-----

Effect of mode of formation on the structure of borosilicate glasses <b>Y.B. DIMITRIEV</b> , <b>E.P. KASHCHIEVA</b> , <b>M.A. BURSUKOVA</b> & <b>P.D. HINKOV</b> (University of Chemical Technology & Metallurgy, Sofia, Bulgaria)	231
---	-----



Surface studies of borate glasses <b>C.G. PANTANO, D.M. BEALL &amp; W. CERMIGNANI</b> (Pennsylvania State University, USA)	239
Physical properties of alkali borosilicate glasses <b>S.A. FELLER, J. KOTTKE, J. WELTER, S. NIJHAWAN, R. BOEKENHAUER, H. ZHANG, D. FEIL, C. PARAMESWAR, K. BUDHWANI, M. AFFATIGATO, A. BHATNAGAR, G. BHASIN, S. BHOWMIK, J. MACKENZIE, M. ROYLE, S. KAMBEYANDA, P. PANDIKUTHIRA &amp; M. SHARMA</b> (Coe College, Cedar Rapids, IA, USA)	246
Crystallization kinetics in Cd, Sr and Ba borophosphate systems <b>G.A. SYCHEVA</b> (Institute of Silicate Chemistry of the Russian Academy of Sciences, Sankt Petersburg, Russia) & <b>V.N. SIGAEV</b> (Mendeleev University of Chemical Engineering, Moscow, Russia)	254
<b>7. Non-Oxide &amp; Mixed Glasses</b>	
Session Chair: <b>A.J. LEADBETTER</b> (Institut Laue-Langevin, Grenoble, France)	
Structure and properties of alkali thioborate glasses: unique chemistries and unusual properties (Invited; Abstract Only) <b>S.W. MARTIN</b> (Iowa State University of Science & Technology, Ames, USA)	262
Analytical and molecular orbital modelling approach to the chemical bonding states of F <sup>-</sup> ions in oxyfluoroborate glasses <b>S. HAYAKAWA &amp; A. OSAKA</b> (Okayama University, Japan)	263
Preparation of lithium chloroboracite by the sol-gel method <b>T. NAGASE, K. SAKANE &amp; H. WADA</b> (Shikoku National Industrial Research Institute, Takamatsu, Japan)	271
Densities of the alkali thioborate glasses as a function of short range order <b>M. ROYLE, J. CHO &amp; S.W. MARTIN</b> (Iowa State University of Science and Technology, Ames, USA)	279

## 8. Superionic & Related Systems

Session Chair: L.M. TORELL (Chalmers University of Technology, Göteborg, Sweden)

An XPS study of the chemical structure of  $\text{AgI-Ag}_2\text{O-B}_2\text{O}_3$  glasses 287  
**H. JAIN**, A.C. MILLER (Lehigh University, Bethlehem, PA, USA), E.I. KAMITSOS & J.A. KAPOUTSIS (National Hellenic Research Foundation, Athens, Greece)

The role of silver in the structure of  $(\text{AgI})_x(\text{Ag}_2\text{O} \times n\text{B}_2\text{O}_3)_{1-x}$  borate glasses and their fast ion conducting properties 295  
**F. ROCCA** (Centro CNR-ITC di Fisica, Trento, Italy), G. DALBA, P. FORNASINI (Università di Trento, Italy) & F. MONTI (Università di Verona, Italy)

A structural study of silver borate glasses by infrared reflectance and Raman spectroscopies 303  
**J.A. KAPOUTSIS**, E.I. KAMITSOS & G.D. CHRYSSIKOS (National Hellenic Research Foundation, Athens, Greece)

## 9. Industrial & Technological Applications

Session Chair: R. O'CONNOR (Borax Europe Ltd, Guildford, UK)

History of the use of  $\text{B}_2\text{O}_3$  in commercial glass (Invited) 313  
**R.A. SMITH** (U.S. Borax Inc., Valencia, CA, USA)

Microfloat technology - a new challenge to the production of hightech borosilicate flat glasses (Abstract Only) 323  
**T. KLOSS**, K. SCHNEIDER, G. LAUTENSCHLÄGER (JENA<sup>er</sup> Glaswerk GmbH, Germany), P. KELLER, W. LINZ (Schott Glaswerke Mainz, Germany), T. KIMURA & Y. TAKAHASHI (Asahi Glass Corp, Tokyo, Japan)

The use of boron oxide in glass fiber formulations 324  
**F.L. HARDING**, J.F. BAUER, H.H. RUSSELL III & X. XU (Schuller International, Littleton, CO, USA)

Influence of small quantities of boron oxide additives on the microstructure and optical properties of dental glass-ceramics 332  
**W. HÖLAND**, M. FRANK & V. RHEINBERGER (IVOCLAR Ltd., Schaan, Liechtenstein)

Haloborate glass-ceramics as x-ray storage phosphors <b>K. PAPADOPOULOS &amp; K. SIEBER</b> (Eastman Kodak Co., Rochester, NY, USA)	340
---	-----

## 10. Relaxation & the Glass Transition

Session Chair: C. RHEE (Korea Research Institute of Standards and Science, Taejon, Korea)	
Liquid-glass transition in B <sub>2</sub> O <sub>3</sub> (Invited; Abstract Only) <b>L. BÖRJESSON</b> (Chalmers University of Technology, Göteborg, Sweden)	348
Relaxation processes in borate melts <b>B.J. REARDON, J. KIEFFER, J.E. MASNIK &amp; J.D. BASS</b> (University of Illinois, Urbana, USA)	349
High-pressure induced phenomena in glasses <b>M.I. KLINGER</b> (Bar Ilan University, Ramat Gan, Israel) & <b>S.N. TARASKIN</b> (Moscow Engineering-Physics Institute, Russia)	357
The Bray and the Landa-Patashinskii models, and polymorphism in borosilicate glasses and melts <b>L.M. LANDA &amp; K.A. LANDA</b> (Lancer Tech, Inc., Greensburg, PA, USA)	364

## 11. Optical Spectroscopy & Defects

Session Chair: Y.B. DIMITRIEV (University of Chemical Technology & Metallurgy, Sofia, Bulgaria)	
The structure of defects induced in silica glass by boron implantation <b>K. KAWAMURA, H. HOSONO, H. KAWAZOE</b> , (Tokyo Institute of Technology, Japan), <b>M. SETO &amp; S. FUJITSU</b> (Shonan Institute of Technology, Kanagawa, Japan)	370
Effect of the composition of some lead borate glasses containing uranium and tin ions on their optical absorption characteristics <b>M.M. MORSI &amp; N. ABD-ELSHAFI</b> (National Research Centre, Cairo, Egypt)	377

Hypersensitivity of neodymium ions in sodium borate, sodium silicate and sodium borosilicate glasses <b>K. GATTERER</b> (Graz University of Technology, Austria)	384
Luminescence quenching mechanisms for g-irradiated barium aluminoborate glasses doped with Fe <b>W.M. PONTUSCHKA, M.I.T. OLIVEIRA</b> (Instituto de Fisica da Universidade de São Paulo, Brazil) & <b>S.M. DEL NERY</b> (Universidade Estadual Paulista "Júlio Mesquita Filho", Guaratinguetá, Brazil)	392
Photostimulated luminescence of borate glasses doped with $Ce^{3+}$ and $Sm^{3+}$ ions <b>J. QIU, Y. SHIMIZUGAWA &amp; N. SUGIMOTO</b> (Hirao Active Glass Project, Kyoto, Japan) & <b>K. HIRAO</b> (Kyoto University, Japan)	399

## 12. Modelling & Computer Simulation

Session Chairs: <b>S.A. FELLER</b> (Coe College, Cedar Rapids, IA, USA) & <b>A.C. WRIGHT</b> (University of Reading, UK)	
Ab initio based studies of borate glasses (Invited) <b>M. TETER</b> (Corning Inc., NY, USA)	407
Ab initio molecular orbital calculations on the structure and the low-frequency vibrational modes in $B_2O_3$ and alkali borate glasses <b>T. UCHINO &amp; T. YOKO</b> (Kyoto University, Japan)	417
An investigation of the structure of vitreous boron trioxide by reverse Monte Carlo simulations <b>J. SWENSON &amp; L. BÖRJESSON</b> (Chalmers University of Technology, Göteborg, Sweden)	425

## 13. Poster Session

Molecular dynamics simulation of $PbO.xB_2O_3$ glasses with bond angle constraint <b>Y. AKASAKA</b> (Furukawa Electric Co. Ltd, Chiba, Japan) & <b>I. YASUI</b> (University of Tokyo, Japan)	435
---	-----

Molecular dynamics simulation of $B_2O_3$ glass using a coordination dependent potential <b>B. PARK &amp; A.N. CORMACK</b> (New York State College of Ceramics, Alfred, USA)	443
Surface crystallization of $CsLiB_6O_{10}$ glass P56 <b>Y. DING, Y. MIURA, S. NAKAOKA, T. NANBA &amp; A. OSAKA</b> (Okayama University, Japan)	453
Microstructure of low-melting $B_2O_3$ -containing glassy coatings for traditional ceramics <b>S.P. DJAMBAZOV, Y.Y. IVANOVA, E.P. KASHCHIEVA &amp; A.P. YOLEVA</b> (University of Chemical Technology & Metallurgy, Sofia, Bulgaria)	461
XAFS studies of the local structure of $CaO-K_2O-B_2O_3$ and $K_2O-B_2O_3$ glasses <b>K. HANDA</b> (Ritsumeikan University, Siga, Japan), <b>N. UMESAKI, D.A.H. CUNNINGHAM, N. KAMIJO</b> (Osaka National Research Institute, Japan) & <b>Y. IWADATE</b> (Chiba University, Japan)	468
Crystallization behaviour of some glasses in the systems $Li_2O-B_2O_3$ and $Li_2O-B_2O_3-Al_2O_3$ <b>F.A. KHALIFA &amp; H.A. EL BATAL</b> (National Research Centre, Cairo, Egypt)	474
Effect of $B_2O_3$ on boron-containing metallic glasses based on cobalt <b>M.A. KHUSAINOV</b> (Novgorod State University, Russia) & <b>A.C. WRIGHT</b> (University of Reading, UK)	484
Bioactivity of alkali and alkaline earth borosilicate glasses <b>A. OSAKA, S. HAYAKAWA, K. TSURU &amp; C. OHTSUKI</b> (Okayama University, Japan)	490
A comparison of the densities of lithium and sodium borate and silicate glasses with very high alkali contents <b>P. VENHUIZEN, A.M. PETERS, F. ALAMGIR, K. LOH, R.B. WILLIAMS &amp; S.A. FELLER</b> (Coe College, Cedar Rapids, IA, USA)	498
A proposed relationship between the position of the first neutron diffraction peak for alkali borate glasses and the separation between the modifying cations as found from density measurements	506

A.J. WANLESS, A.C. WRIGHT, R.N. SINCLAIR  
(University of Reading, UK), S.A. FELLER, **R.B.**  
**WILLIAMS**, B.C. JOHANSON & M.T. MAYHEW (Coe  
College, Cedar Rapids, IA, USA)

The abnormal properties of boron oxide in glass (Abstract Only) <b>J.J.L. YI</b> (Circon ACMI, Stamford, CT, USA)	513
A vibrational spectroscopic study of alkaline earth borate glasses <b>Y.D. YIANNPOULOS</b> , E.I. KAMITSOS, G.D. CHRYSSIKOS & J.A. KAPOUTSIS (National Hellenic Research Foundation, Athens, Greece)	514
Author index	523
Subject index	529
Participants	545

## NMR AND NQR STUDIES OF BORATES AND BORIDES

Philip J. BRAY

*Department of Physics, Box 1843, Brown University,  
Providence, RI 02912, USA*

A 1958 paper by Silver & Bray introduced the use of nuclear magnetic resonance (NMR) spectra for  $^{11}\text{B}$  to study structure and bonding in glasses. The NMR spectra clearly distinguished between 3-coordinated and 4-coordinated borons on the basis of the larger  $^{11}\text{B}$  quadrupole interactions for the  $\text{BO}_3$  configuration (2.4–2.9 MHz) and the smaller values for the  $\text{BO}_4$  (less than 0.90 MHz). Quantitative measurements of the area under the narrow resonance ( $\text{BO}_4$ ) and broad response ( $\text{BO}_3$ ) allowed the fraction,  $N_4$ , of 4-coordinated borons to be established. It was soon found that the "borate anomaly" in binary alkali borate glasses was not, as previously thought, due to the destruction of  $\text{BO}_4$  with added alkali oxide above 15–20 molar percent. Advances in experiment and theory then permitted clear distinctions between the NMR spectra for symmetric and asymmetric  $\text{BO}_3$  units (e.g. a  $\text{BO}_3$  with all bridging or all non-bridging oxygens (NBO) and one with 1 or 2 NBO.) The NMR data for many binary and ternary borate glass systems are consistent with the Krogh-Moe model in which the glasses consist of mixtures of structural groupings from the crystalline compounds of the glassforming oxides. More recent uses of zero-field NMR, or pure nuclear quadrupole resonance (NQR) spectroscopy, have yielded major improvement in the resolution of the  $^{11}\text{B}$  responses from the various boron–oxygen bonding configurations. (As an example: the NQR spectra clearly display responses from two boron sites in vitreous  $\text{B}_2\text{O}_3$ .) Extension of the NQR studies to the  $^{10}\text{B}$  isotope has yielded improvements by two or three significant figures in the parameters of the quadrupole interaction. These developments have greatly increased the ability to identify with high accuracy and relative certainty the type and amount of each boron site in a solid, and should allow clear identification of the structural groupings in glasses. The high accuracy in the quadrupolar parameters, and their sensitivity to minor changes in charge distribution and structure, make these parameters sensitive tools for comparison with calculated values and for monitoring compositional variations, radiation damage, stress, thermal histories, and other aspects of boron-containing solids.

### 1. INTRODUCTION

The first report of NMR studies of  $^{11}\text{B}$  in vitreous  $\text{B}_2\text{O}_3$  and sodium borate and borosilicate glasses was published by Silver & Bray in 1958 [1]. Studies of some polycrystalline borides and borates appeared soon thereafter [2,3]. The  $^{11}\text{B}$  NMR resonances exhibit characteristic effects from significant nuclear quadrupolar interactions, and can be analyzed to provide very useful

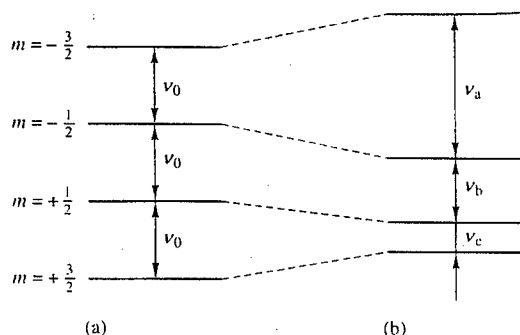


**Fig. 1.** Energy levels arising from the interaction of the nuclear magnetic dipole moment with a magnetic field: (a) no electrical quadrupolar interaction; (b) small quadrupolar interaction present (the levels shown are appropriate for the  $^{11}\text{B}$  nucleus).

information on structure and chemical bonding in the solids.

The work reviewed here was all carried out in the Magnetic Resonance Laboratory at Brown University. The excellent NMR studies of  $^{11}\text{B}$  in solids carried out in recent years in other laboratories are not included here, although directions to a number of those studies are given in the concluding remarks.

Since the nuclear electrical quadrupolar interaction is so important in the interpretation of NMR spectra for boron in solids, the theory for this interaction will be presented immediately along with spectra for several materials.

## 2. NMR WITH A QUADRUPOLEAR PERTURBATION

When a nucleus with a nuclear spin  $I$  is subjected to a magnetic field, the Zeeman interaction between the magnetic field and the nuclear magnetic dipole moment generates a set of energy levels. Transitions between those levels can be caused by an applied radiofrequency electromagnetic field of the correct resonance frequency  $\nu_0$ . The energy levels and resonance frequency are displayed in Fig. 1(a).

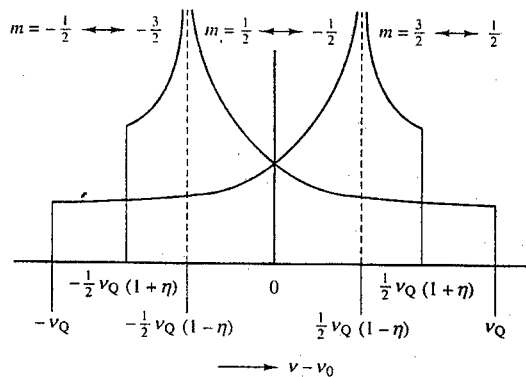


**Fig. 2.** First-order quadrupolar spectrum for  $I=3/2$  nuclei in a powder or glass. Here  $\nu_Q = 3Q\omega/2(2I-1)$



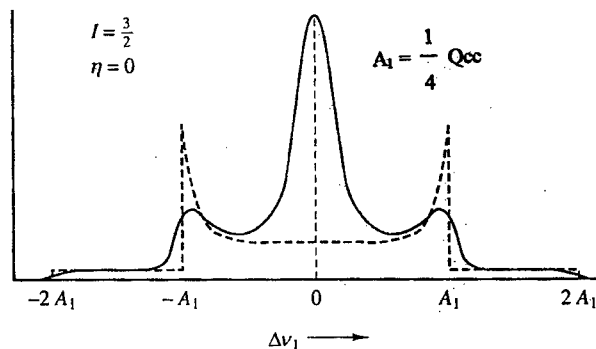


Fig. 3. Resonance lineshape (solid curve) predicted for a nucleus such as  $^{11}\text{B}$  with a small quadrupolar interaction in a glass or polycrystalline powder. This is the  $\eta = 0$  case.

But any nucleus for which  $I \geq 1$  also has an electrical quadrupole moment ( $eQ$ ) that interacts with the gradient of the electric field at the nuclear site. Figure 1(b) displays how the Zeeman energy levels are shifted when the nucleus under study experiences a small quadrupole interaction. (The shifts and the transition frequencies can be calculated [4] using the quadrupolar perturbation of the Zeeman interaction.) The shifts depend on the coupling of the nuclear electrical quadrupole moment  $eQ$  with the components of the electric field gradient (EFG) tensor at the nuclear site. These are  $V_{xx}$ ,  $V_{yy}$ , and  $V_{zz}$  in the system of principal axes for the EFG. Here  $V$  is the electrical potential at the nuclear site arising from charges outside the nucleus, and  $V_{xx} = \partial^2 V / \partial x^2$ , etc. The shifts also depend on the angles  $\theta$  and  $\phi$  that specify the orientation of the magnetic field with the principal axes of the EFG. Since all angles  $\theta$  and  $\phi$  are equally probable in a finely divided polycrystalline powder or a glass, the NMR

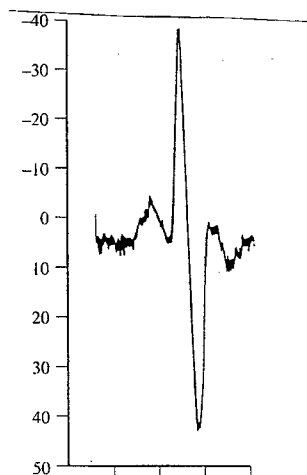


Fig. 4.  $^{11}\text{B}$  NMR spectrum in boron phosphate ( $\text{BPO}_4$ );  $\nu_0 = 7.177$  MHz.

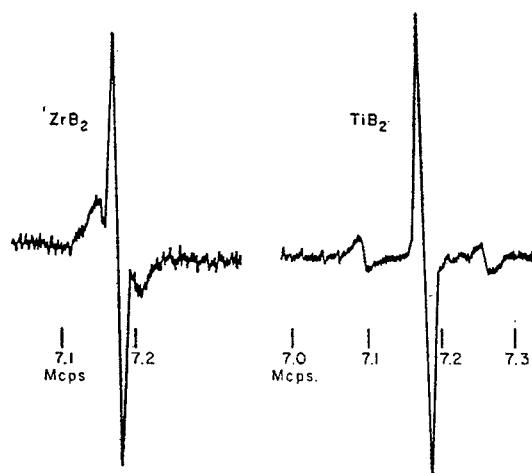


Fig. 5.  $B^{11}$  nuclear magnetic resonance in polycrystalline  $TiB_2$  and  $ZrB_2$ ,  $\nu_0 = 7.177$  MHz.

spectra for those cases will be the envelope of responses observed for a single crystal as it is placed in all possible orientations in the magnetic field. The resulting theoretical 'powder pattern' for a quadrupolar interaction that is sufficiently small to be treated with first-order perturbation theory is displayed in Fig. 2 for the case of a nuclear spin  $I = 3/2$ . (No dipolar or other broadening mechanisms have been taken into account.) Here  $Q_{cc} = e^2 V_{zz} Q$  is the quadrupole

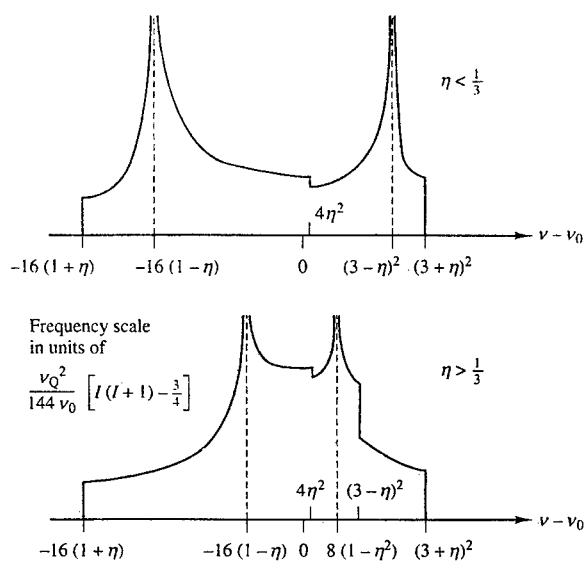
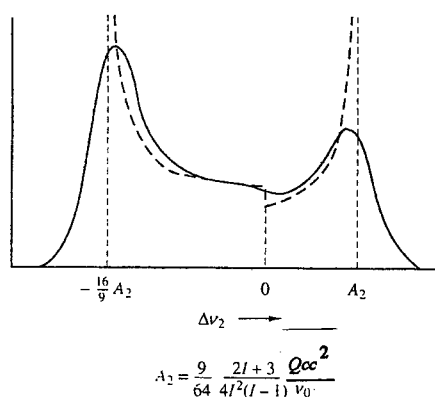


Fig. 6. Powder patterns for the central transition ( $m = -1/2 \leftrightarrow +1/2$ ) of half-integer spin nuclei in the presence of second-order quadrupolar interactions for two regimes:  $\eta < 1/3$  and  $\eta > 1/3$ . Here  $\nu_Q = 3Q_{cc}/2I(2I-1)$  and  $\nu_0$  is the Larmor frequency.



**Fig. 7.** Resonance lineshape (solid curve) for a nucleus with a large quadrupole interaction in a glass or polycrystalline powder. This is the  $\eta = 0$  case.

coupling constant that measures the strength of the quadrupolar interaction, and  $\eta = V_{xx} - V_{yy} / V_{zz}$  is the asymmetry parameter that measures the departure of the EFG from axial symmetry. (With  $|V_{zz}| \geq |V_{yy}| \geq |V_{xx}|$ , one finds that  $0 \leq \eta \leq 1$ ). Note that the 'central' transition ( $m = +1/2 \leftrightarrow -1/2$ ) is unaffected in first order and remains at the Larmor frequency  $\nu_0$ , while the 'satellite' transitions ( $m = +3/2 \leftrightarrow +1/2$  and  $m = -3/2 \leftrightarrow -1/2$ ) are spread out into the 'powder patterns'.

Broadening mechanisms (e.g. dipolar interactions, distributions in the EFG components) smooth the divergences in the theoretical powder pattern and give breadth to the central transition peak. This is exemplified in Fig. 3 for the particular case of  $\eta = 0$ . When use is made of older CW NMR spectrometers, the recorded resonance is usually the first derivative of the absorption curve. This is displayed in Fig. 4 for the  $^{11}\text{B}$  ( $I = 3/2$ ) response in polycrystalline boron phosphate ( $\text{BPO}_4$ ) for which the value of  $Q_{cc} = 50.4$  kHz if  $\eta$  is assumed to be zero[3]. (The boron atom is at the center of a  $\text{BO}_4$  tetrahedron that is only slightly distorted so the components of the EFG are quite small. The EFG vanishes for perfect tetrahedral and octahedral symmetry.) Additional exam-

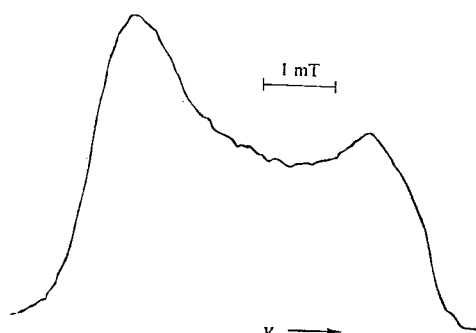


**Fig. 8.**  $^{11}\text{B}$  NMR spectrum of vitreous  $\text{B}_2\text{O}_3$  at 16 MHz [5].

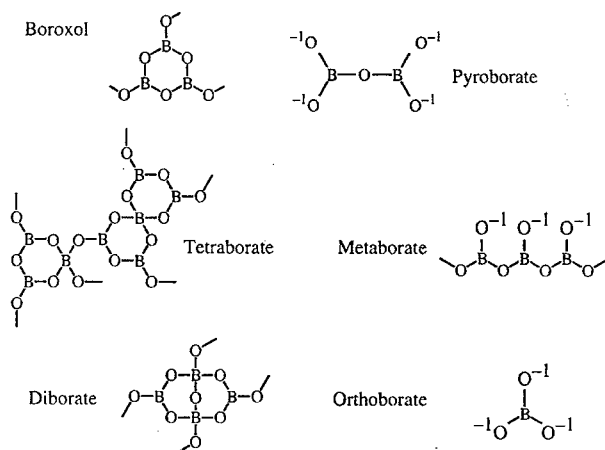


Fig. 9. Structural groupings found in alkali borate compounds and glasses.

ples [2] for this case of small  $Q_{cc}$  are shown in Fig. 5. Since the boron site in both  $ZrB_2$  and  $TiB_2$  has an axis of three-fold symmetry,  $\eta=0$  and this is the case depicted in Fig. 3. The measured values of  $Q_{cc}$  are 118 kHz for  $ZrB_2$  and 360 kHz for  $TiB_2$ .

When the quadrupole interaction is larger (but still treatable as a perturbation of the Zeeman interaction), the central ( $m=+1/2 \leftrightarrow -1/2$ ) transition is affected in second order. Figure 6 displays the theoretical pattern for this case, both for  $\eta < 1/3$  and  $\eta > 1/3$ . The particular case of small or zero  $\eta$  is illustrated in Fig. 7 where the dashed lines indicate the theoretical pattern without broadening and the solid line indicates the expected lineshape when broadening is included. This transition [5] for  $^{11}B$  in vitreous boron oxide ( $B_2O_3$ ) is displayed in Fig. 8.

In this case, in which all of the boron atoms are in the center of planar triangles of oxygens (i.e.  $BO_3$  units) and all of the oxygens are bridging (i.e. bonded to two borons), one finds  $Q_{cc}=2.76$  MHz and  $\eta=0.10$ . The departure from perfect trigonal symmetry about the axis perpendicular to the  $BO_3$  units and passing through the boron is small or moderate. One finds for such  $BO_3$  units that  $2.4 \text{ MHz} \leq Q_{cc} \leq 2.9 \text{ MHz}$  and  $0 \leq \eta \leq 0.2$ . (In the case of vitreous  $B_2O_3$ , the  $BO_3$  units are portions of the boroxol structural groupings depicted in Fig. 9, but they occur also in other borate structural groupings shown there.) See, however, further discussions of vitreous  $B_2O_3$  later in this paper.

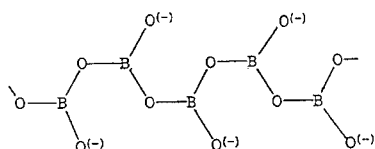
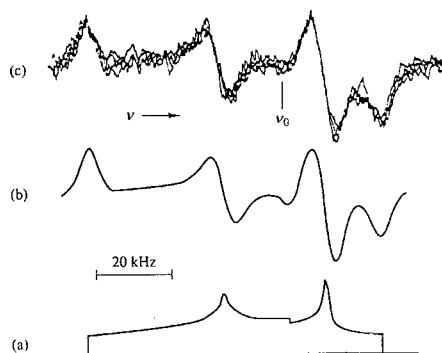
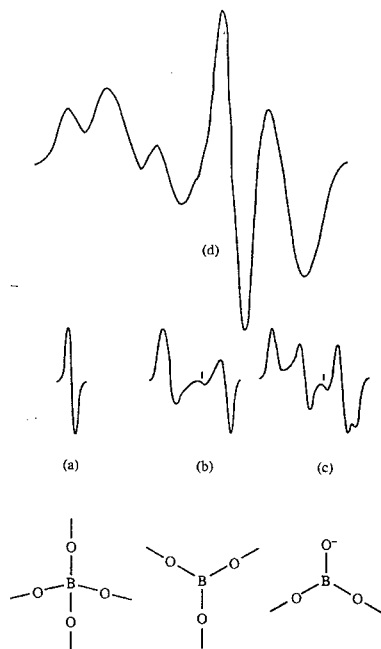


Fig. 10. A portion of the  $(BO_2)_h^{n-}$  chain in  $CaO \cdot B_2O_3$ ; non-bridging oxygen is negatively charged.



**Fig. 11.** (a) Theoretical powder pattern for the transition ( $m=+1/2 \leftrightarrow -1/2$ ), with  $I=3/2$ ,  $\nu_0=16$  MHz,  $Q_{cc}=2.56$  MHz, and  $\eta=0.54$ . (b) First derivative of the theoretical powder pattern after convolution with a Gaussian curve of linewidth  $2\sigma=5$  kHz. (c) Superposition of four experimental traces for  $^{11}\text{B}$  in polycrystalline calcium metaborate, at a resonant frequency of 16 MHz [5(a)].

In alkali borate compounds of 50 molar % or more of alkali oxide, one finds  $\text{BO}_3$  units that have one or more nonbridging oxygens (NBO). (That is, the oxygen is bonded to only one boron and is negatively charged.) If the  $\text{BO}_3$  unit has one or two of these, the trigonal symmetry noted above is lost and the asymmetry parameter has been found from NMR spectra to rise into the range



**Fig. 12.**  $^{11}\text{B}$  NMR spectrum of (a) a  $\text{BO}_4$  unit, (b) a  $\text{BO}_3$  unit, (c) a  $\text{BO}_3^-$  unit with one NBO, and (d) a sample containing all three units [5(a)]

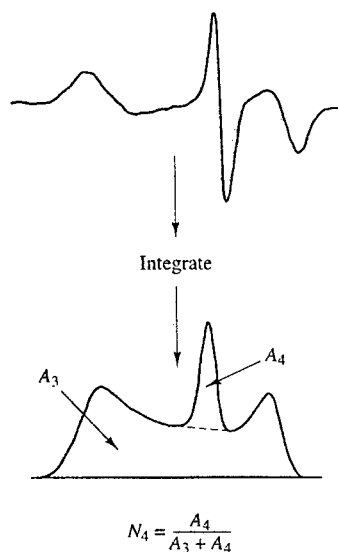


**Fig. 13.** Method for determining  $N_4$  in a  $^{11}\text{B}$  NMR spectrum. The experimental spectrum at the top is the first derivative of the absorption curve.

$0.4 \leq \eta \leq 0.9$ . An example is calcium metaborate ( $\text{CaO} \cdot \text{B}_2\text{O}_3$ ) whose chain structure is depicted in Fig. 10. The NMR spectrum [5(a)] for this material is displayed in Fig. 11. These asymmetric  $\text{BO}_3$  units, and the  $\text{BO}_4$  and symmetric  $\text{BO}_3$  units, are all present in many borate glasses. Responses from all three units are present in the  $^{11}\text{B}$  NMR spectrum [5(a)] displayed in Fig. 12, where

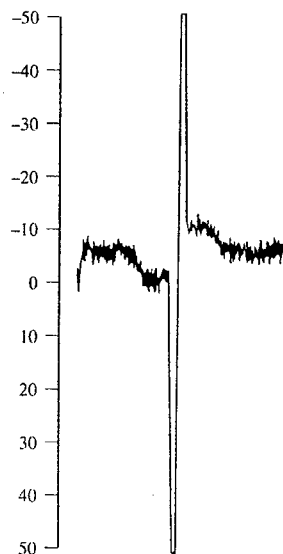


**Fig. 14.**  $^7\text{Li}$  NMR spectrum of glass of composition  $\text{Li}_2\text{O} \cdot 3\text{B}_2\text{O}_3$ .



Fig. 15. Composite of  $B^{11}$  nuclear magnetic resonances in lithium oxide-boron oxide glasses at  $\nu_0=16.130$  MHz. The mol% of  $Li_2O$  is given for each glass.

the narrow structureless line from  $BO_4$  units is in the center and the symmetric  $BO_3$  give rise to the middle positive peak on the left and part of one of the negative peaks on the right. The fraction of each type of unit present in the glass can be obtained from the intensity of the corresponding NMR responses, as illustrated in Fig. 13 for a low-alkali glass where  $N_4$  is the fraction of 4-coordinated borons (i.e. in  $BO_4$  tetrahedra).

A large number of spectra for 3-coordinated borons can be generated using ranges of  $Q_{cc}$ ,  $\eta$ , and the line broadening parameter  $s$ . (See, for example, Fig. 11). Comparison of the simulated and actual spectra permits determination of the values of  $Q_{cc}$  and  $\eta$ . Unfortunately, the satellite responses detected for 4-coordinated borons in crystalline materials (see Figs 4 and 5) are severely broadened in glasses (due to the disorder and consequent spread in the values of the EFG tensor components, and thus in  $Q_{cc}$  and  $\eta$ ) and concealed under the broad responses from the 3-coordinated borons. (Note that the effect of a spread of  $Q_{cc}$  and  $\eta$  values on the second-order quadrupolar effects in the central transition is much less than the effect on first-order quadrupolar effects, though it can be substantial [1]). It is rarely possible for  $Q_{cc}$  and  $\eta$  to be determined for 4-coordinated borons in glasses, though the satellite transitions have been obtained for other nuclei. Figure 14 displays the  $^7Li$  NMR spectrum for a lithium borate glass; the satellite transitions are certainly spread out, but are clearly visible.

The ability to distinguish and quantify by NMR the different types of bonding configurations in borates and borides can be used to study the structures of those materials. Several examples are given in the next sections of this paper.

## 2.1 Structure and bonding in alkali borate glasses.

Addition of an alkali oxide to boron oxide ( $B_2O_3$ ) initially converts 3-coordinated borons (i.e. in  $BO_3$  units) to 4-coordinated borons (i.e. in  $BO_4$  units). This is clearly displayed in the  $^{11}B$  NMR spectra (first derivative of the absorption line) in Fig. 15 where the narrow line ( $BO_4$ ) appears and grows at

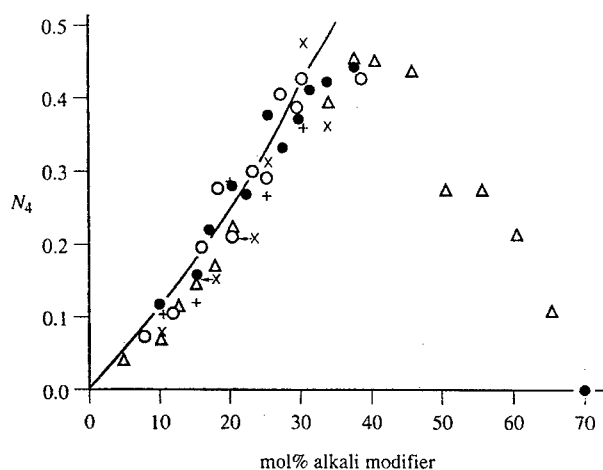


**Fig. 16.** The fraction  $N_4$  of boron atoms in  $\text{BO}_4$  configurations in alkali borate glasses plotted against the molar percentage of alkali oxide:  $\bullet$ ,  $\text{Na}_2\text{O}$ ;  $\circ$ ,  $\text{K}_2\text{O}$ ;  $\Delta$ ,  $\text{Li}_2\text{O}$ ;  $+$ ,  $\text{Rb}_2\text{O}$ ;  $\times$ ,  $\text{Cs}_2\text{O}$ .

the expense of the broad line ( $\text{BO}_3$ ). This was discovered by Warren [6] and Zachariasen [7] in the 1930s by analysis of x-ray spectra; but there had been disagreement for some 30 years or so over the behavior of  $N_4$ , the fraction of 4-coordinated borons, as the molar amount or fraction of the alkali oxide increased. This involved the so-called 'borate anomaly' so named because various physical properties of the glasses (e.g. density, coefficient of expansion) begin to change substantially at about 15–20 mol% alkali oxide. Several explanations were suggested [6,8] involving a leveling off or rapid reduction of

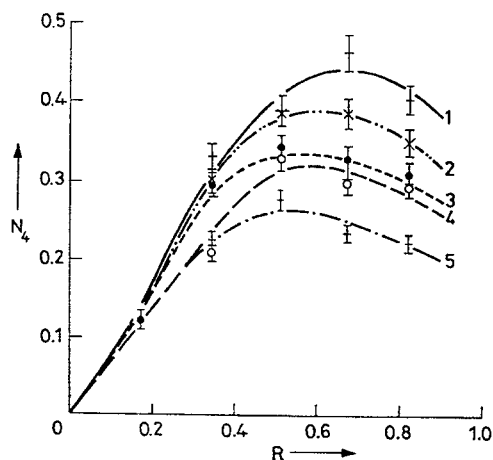


**Fig. 17.** The fraction  $N_4$  of boron atoms in  $\text{BO}_4$  configurations in alkali borate glasses plotted against the parameter  $R = x/(1-x)$ . This figure is compiled from recent data using signal averaging and rapid quenching to form some of the glasses: 1-lithiumborate; 2-sodium borate; 3-potassium borate; 4-rubidium borate; 5-cesium borate.



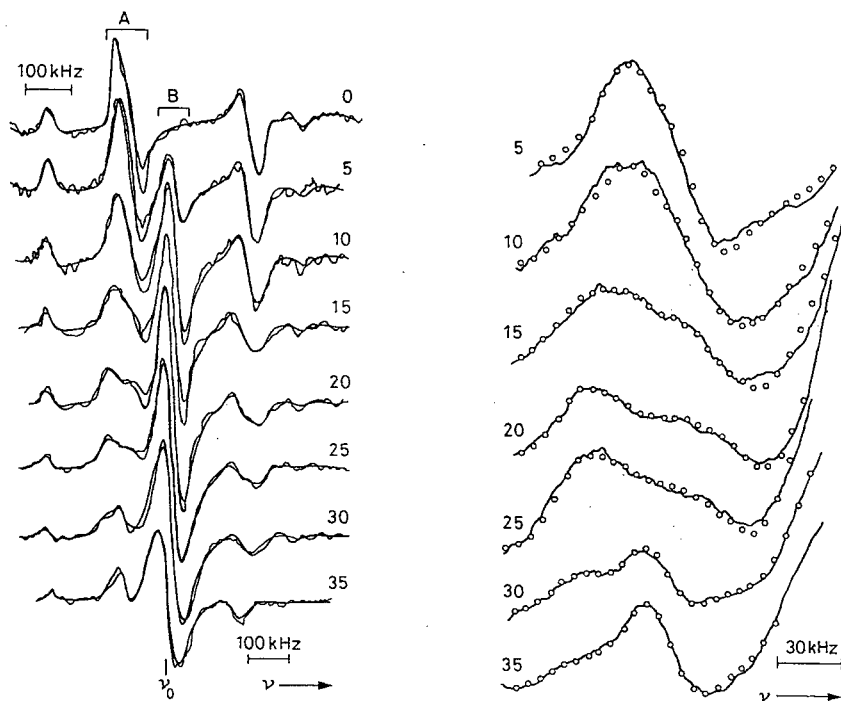


Fig. 18. (a)  $^{10}\text{B}$  NMR derivative spectra for eight  $\text{Na}_2\text{O}-\text{B}_2\text{O}_3$  glasses. Mol%  $\text{Na}_2\text{O}$  is indicated to the right of each trace, (b) Feature A of Fig. 18(a) on an expanded scale.

$N_4$  above 15–20 mol% alkali oxide. However, a plot (Fig. 16) of  $N_4$  values as a function of the mol% alkali modifier shows [9] no breaks at 15–20 mol% modifier, a maximum around 40 mol%, and a reduction to zero by 70 mol%. (The solid line in Fig. 15 is the function  $x/1-x$  where the composition of the glass is  $x\text{A}_2\text{O}(1-x)\text{B}_2\text{O}_3$  and  $\text{A}_2\text{O}$  is the alkali oxide. This is the expected behavior of  $N_4$  if each oxygen added to the glass melt as alkali oxide converts two  $\text{BO}_3$  triangles into two  $\text{BO}_4$  tetrahedra. It is clear that the ‘borate anomaly’ does not arise from any sudden change in the rate of formation of 4-coordinated borons in the vicinity of 15–20 mol% alkali oxide. A more probable explanation involves the appearance in the network of appreciable numbers of the large, awkward, space-filling tetraborate groups (see Fig. 9) that are expected to appear in this composition region in large numbers (according to the Krogh-Moe model).

More recent NMR studies [10], employing more sensitive instrumentation, have revealed the very interesting behavior shown in Fig. 17. Clearly, the value of  $N_4$  at a given value of  $R = x/1-x$  depends on the particular alkali ion, reflecting a competition between two processes: formation of  $\text{BO}_4$  tetrahedra; formation of NBO. Formation of 4-coordinated borons ( $\text{BO}_4$  units) at any specified composition (i.e. value of  $R$ ) is reduced as the size (and mass) of the alkali ion is increased.

The values of  $Q_{cc}$  and  $\eta$  for each type of  $BO_3$  unit in the glass, when combined with  $N_4$ , provide a basis for constructing a model of the borate glasses. This model is that of Jan Krogh-Moe [11] who postulated that borate glasses should consist of the structural groupings (See Fig. 9) found in the crystalline compounds of the particular glassforming system. (Gunnar Hagg [12] had suggested earlier that the structural units that appear in glasses should be those that rapidly form and break up in the liquid as one approaches the liquidus from higher temperatures). Having found  $Q_{cc}$ ,  $\eta$ , and  $N_4$  for the crystalline compounds, one can proceed to construct the NMR spectra for the glasses as superpositions of those for the compounds. (This procedure is aided by parameters obtained from the  $^{10}B$  NMR spectra for the glasses and crystalline compounds.  $^{10}B$  NMR is not discussed here, but typical spectra [13] are presented in Fig. 18. The circles in Fig. 18(b) indicate the ability to use computer simulation to obtain excellent fits of the computed spectra to features of the actual  $^{10}B$  spectra that are highly sensitive to the values of  $Q_{cc}$  and  $\eta$ .)

Figure 19 displays the fractions of each structural grouping found in a family of lithium borate glasses. (B=boroxol grouping, T=tetraborate, D=diborate, M=metaborate, P=pyroborate, O=orthoborate, L=unidentified. The superscripts denote 3 and 4 coordination of the borons.) Feller [14] and co-investigators have beautifully correlated the NMR-derived appearance and disappearance of borate structural groupings in glasses with changes in such physical properties as density.

## 2.2 Alkali borosilicate glasses.

The use of  $^{11}B$  (and  $^{10}B$ ) NMR to determine the structure of binary borate glasses can be extended to ternary and even more complex glasses. Figure 20

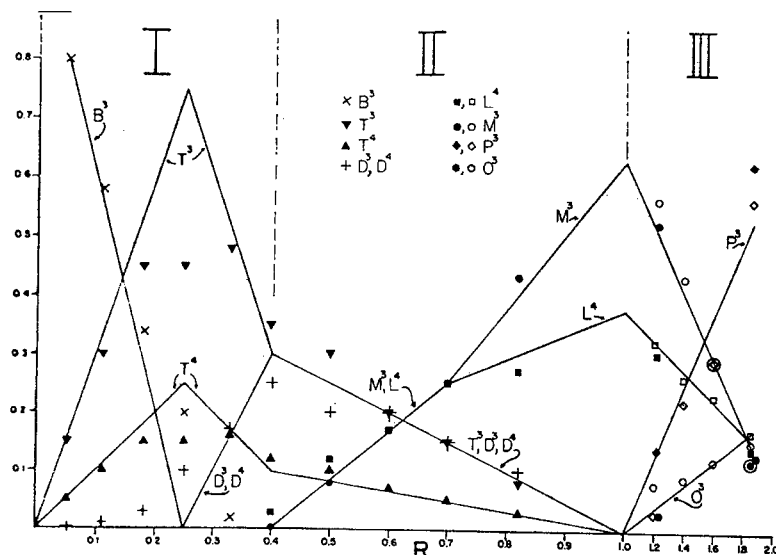


Fig. 19. Fractions of each borate grouping found in lithium borate glasses.

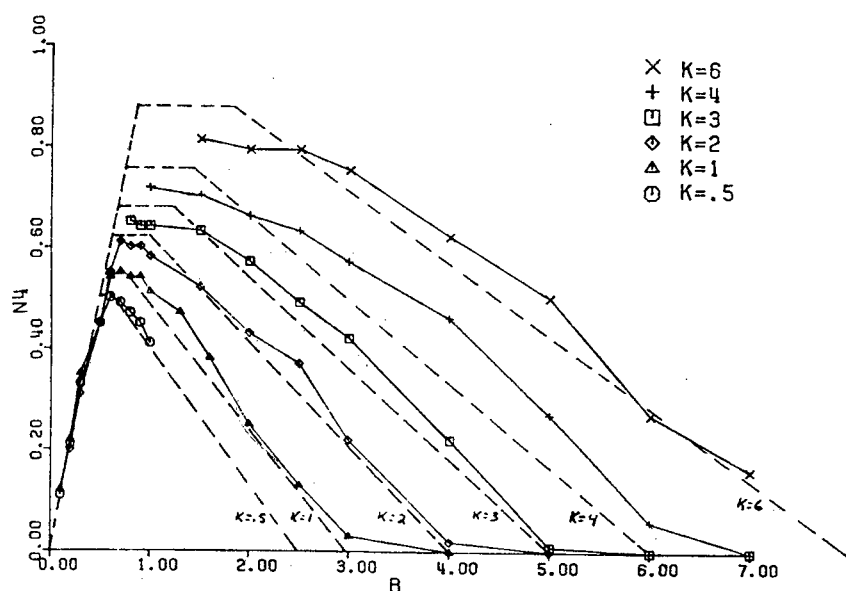


Fig. 20. Composite of  $N_4$  data for glasses in the system  $\text{Na}_2\text{O}-\text{B}_2\text{O}_3-\text{SiO}_2$ . The dashed lines are predictions based on the model presented in Refs [15,16].

displays the values [15, 16] of  $N_4$  for families of glasses in the system  $\text{RNa}_2\text{O} \cdot \text{B}_2\text{O}_3 \cdot \text{KSiO}_2$ . (This system is, of course, the basis for many glasses that are of great technological and commercial value, such as Pyrex and Vycor glasses). It is clearly useful to divide the glasses into families having specific values of  $K$  (the ratio of  $\text{SiO}_2$  to  $\text{B}_2\text{O}_3$ ) and plot the  $N_4$  data as a function of  $R$  (the ratio of  $\text{Na}_2\text{O}$  to  $\text{B}_2\text{O}_3$ ). The solid lines are predictions based on a very simple model [15, 16] of the Krogh-Moe type, employing only one configuration in addition to the borate groupings displayed in Fig. 9. That configuration is a  $\text{BO}_4$  unit whose four oxygens are all bonded to silicons in  $\text{SiO}_2$  tetrahedra; it is found in the mineral Reedmergnerite [15,16]. Similar plots can be constructed for the fractions of borons in symmetric and asymmetric  $\text{BO}_3$  units. Perhaps the most significant feature of Fig. 20 is the discovery that at low alkali content all, or virtually all, of the  $\text{Na}_2\text{O}$  is associated with the borate structures in the glass networks rather than being divided between the silicate and borate structures. The straight line of steep slope at the left of the figure and ascending from  $N_4 = 0$  at  $R = 0$  to  $N_4 = 1$  at  $R = 1$  is simply the  $N_4 = R = x/1-x$  relation displayed in Fig. 16 for the pure alkali borate ( $K = 0$ ) glasses. The  $N_4$  values for the sodium borosilicate glasses all fall on (or almost on) this line up to a value of  $R$  (depending on  $K$ ) at which the values depart from the line and eventually decrease. All of the  $\text{Na}_2\text{O}$  in the glass is being used to 4-coordinate borons up to that  $\text{Na}_2\text{O}$  content (value of  $R$ ) at which additional  $\text{Na}_2\text{O}$  begins to divide between the silicate and borate structures in the glass network. This is a wholly unexpected phenomenon.

### 3. PURE NUCLEAR QUADRUPOLE RESONANCE (NQR) STUDIES USING $^{11}\text{B}$ and $^{10}\text{B}$

#### 3.1 Introductory Comments

$^{11}\text{B}$  and  $^{10}\text{B}$  NMR can obviously yield much information about structure and chemical bonding in solids containing boron. However, the quadrupolar effects, that yield the information that is sought, are only perturbations on the Zeeman interaction, and the structures that they cause in the NMR spectra often overlap (even conceal) each other, and the values of  $Q_{cc}$  and  $\eta$  are limited to three or even two-figure accuracy (See, for example, Fig. 12(d).) One would like to have complete resolution of the structures, and be able to measure the parameters more accurately. The latter will facilitate identification of structural groupings, and can make it possible to detect and measure the effects of phase changes, very small compositional variations, heat treatments, doping, radiation, etc. Fortunately, this resolution and increased accuracy can be secured for borons with a sufficiently large quadrupole interaction (i.e. value of  $Q_{cc}$ ). The procedure involves pure nuclear quadrupole resonance (NQR) spectroscopy.

#### 3.2 History, Theory, and Experimental Results

Since the quadrupolar interaction generates a set of energy levels in the absence of a magnetic field, transitions between these levels will yield resonance spectra if the spectrometers employed are sufficiently sensitive in the relevant frequency regions. These zero-field NMR studies are labeled pure nuclear quadrupole resonance (NQR) spectroscopy.

Pure NQR spectra in solids were first detected by Dehmelt & Kruger in 1950 [17]. A large body of NQR studies of chemical bonding and atomic arrangements in crystalline solids, using quadrupolar nuclei, has followed from that discovery and continues to expand. (See, for example, the summaries by Lucken [18], Schempp & Bray [19], Semin *et al.* [20], and Rubenstein & Taylor [21].)

Analysis of the Hamiltonian [22] for the nuclear quadrupole interaction in the absence of a magnetic field and for a nuclear spin  $I=3/2$  (e.g.  $^{11}\text{B}$ ) yields only two energy levels and a single transition frequency between those levels:

$$\nu = \frac{Q_{cc}}{2} \sqrt{1 + \frac{\eta^2}{3}} \quad (1)$$

Since  $Q_{cc}$  for 3-coordinated borons has a range of values  $2.4 \leq Q_{cc} \leq 2.9$  MHz, the transition frequency predicted for  $^{11}\text{B}$  in those  $\text{BO}_3$  units is in the 1.2 to 1.7 MHz range. The signal-to-noise ratio for magnetic resonance transitions depends theoretically on the square of the resonance frequency, so detection of NQR in the 1 MHz region is clearly much more difficult than detection of responses at the decades or hundreds of MHz which is the common case in NMR (and in NQR for many nuclei such as Cl, Br, I, As, Sb, etc. in various bonding configurations.) But Fig. 21 displays the success obtained for  $^{11}\text{B}$  near 1.35 MHz in crystalline  $\text{B}_2\text{O}_3$  when the sample is at 77K. (Details of the

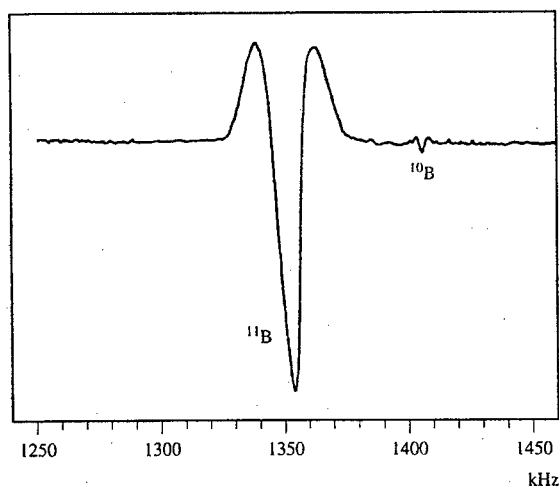


Fig. 21. Boron NQR spectrum of crystalline  $B_2O_3$ .

continuous wave (CW) spectrometer that employs a regenerative oscillator are given elsewhere [23,24].) The full width at half maximum (FWHM) is 15 kHz. Also present in Fig. 21 is a single response from the  $^{10}B$  isotope, which is shown in an expanded vertical scale in Fig. 22.

Nothing really new about crystalline  $B_2O_3$  can be deduced from the single  $^{11}B$  NQR frequency, which is in agreement with the value of  $Q_{cc}=2.69$  MHz and  $\eta=0.06$  deduced from the  $^{11}B$  NMR spectrum for this material [25]. Since Equation 1 contains both  $Q_{cc}$  and  $\eta$ , independent values of those parameters cannot be obtained from the single  $^{11}B$  resonance. But far more accurate values of  $Q_{cc}$  and  $\eta$  can be deduced from the 13  $^{10}B$  NQR responses predicted [26] from calculations of the transition frequencies for this case of a nucleus of

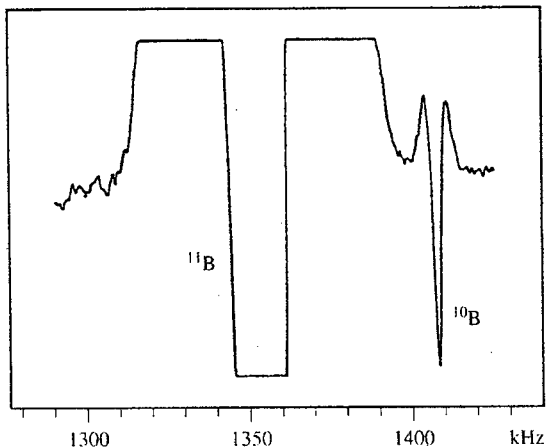


Fig. 22. The features of Figure 21 displayed with a greatly expanded vertical scale.

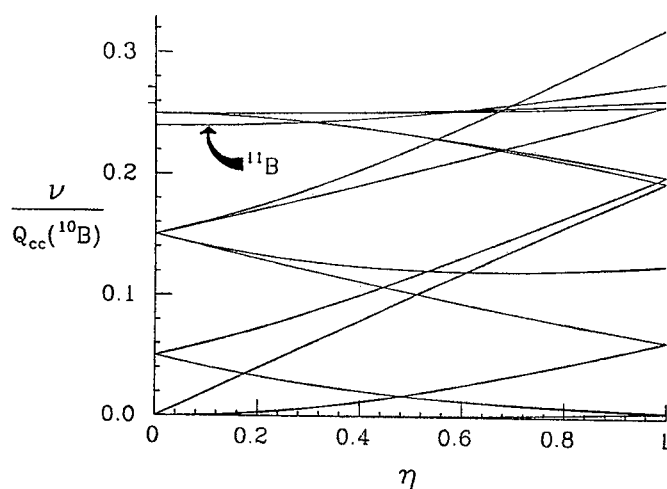


Fig. 23. NQR frequencies for the spin 3 nucleus  $^{10}\text{B}$  and the spin 3/2 nucleus  $^{11}\text{B}$ .

spin  $I=3$ . The allowed single-quantum transitions [26] are presented in Fig. 23 where the ratio  $\nu/Q_{cc}$  is plotted for each transition as a function of the asymmetry parameter  $\eta$ . A computer fit of the ratios of the observed  $^{10}\text{B}$  transition frequencies to those in Fig. 23 yields the correct value of  $\eta$ ; since  $\nu$  is known, the value of  $Q_{cc}$  is then obtained from  $\nu/Q_{cc}$ . (All of this can be done approximately by just using Fig. 23, but a computer program does the fitting quickly and yields very accurate values of  $Q_{cc}$  and  $\eta$ .) The  $^{10}\text{B}$  response shown in Figs. 21 and 22 is the highest frequency  $^{10}\text{B}$  resonance for crystalline  $\text{B}_2\text{O}_3$ . Use of additional  $^{10}\text{B}$  responses (see, for example, Fig. 24) detected at frequencies somewhat below the range used in Fig. 21 yields values of  $Q_{cc}(^{11}\text{B}) = 2701.1 \pm 0.2$  kHz and  $\eta = 0.0669 \pm 0.004$  for this material (at 77 K). These can be compared with the values  $Q_{cc} = 2690 \pm 30$  kHz and  $\eta = 0.06 \pm 0.02$  previously obtained [25] at 300 K from NMR spectra. Clearly, the values yielded by  $^{10}\text{B}$  NQR spectroscopy are of such accuracy that they can provide a very stringent test of various types of molecular orbital calculations from which  $Q_{cc}$  and  $\eta$  can be calculated, and also provide

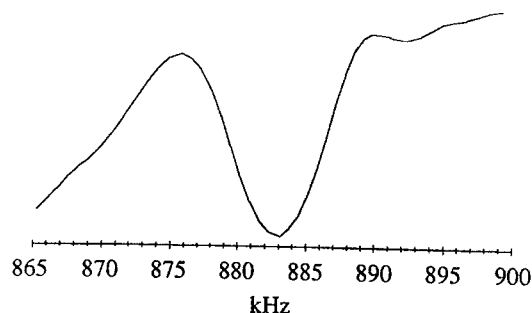
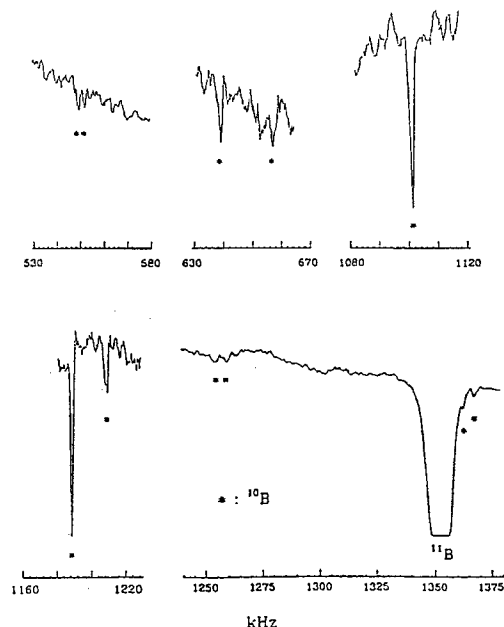


Fig. 24.  $^{10}\text{B}$  NMR resonance from the spectrum of crystalline  $\text{B}_2\text{O}_3$  at 77 K.



**Fig. 25.**  $^{11}\text{B}$  and  $^{10}\text{B}$  NQR spectra for  $\text{CaO} \cdot \text{B}_2\text{O}_3$  at 77 K; the  $^{11}\text{B}$  line is driven off scale in order to show the  $^{10}\text{B}$  lines.

the desired sensitivity to phase changes and the effects of doping, heat treatments, radiation, etc.

Another example of  $^{10}\text{B}$  and  $^{11}\text{B}$  NQR of borates is that for polycrystalline calcium metaborate ( $\text{CaO} \cdot \text{B}_2\text{O}_3$ ). Portions of the NQR spectrum for this material [27] are displayed in Fig. 25. The accumulation of many spectra validates the  $^{10}\text{B}$  responses that are weak in the figure. (It should be noted that, although it was not done in this case, enrichment of  $^{10}\text{B}$  from its normal isotopic abundance of about 18% to as much as 94% can be obtained at moderate cost when crystalline  $\text{H}_3\text{BO}_3$  is used in the preparation of boron-containing materials. This will increase the signal strength of the  $^{10}\text{B}$  response by a factor of five or so. It should also be noted that as few as two  $^{10}\text{B}$  responses are necessary for obtaining values of  $Q_{\infty}$  and  $\eta$ , if the responses have been correctly identified as to which of the 13 transitions they are.) Analysis of the responses in Fig. 25 yields  $Q_{\infty}(^{11}\text{B}) = 2594.3 \pm 0.5$  kHz and  $\eta = 0.515 \pm 0.001$ .

This discussion has so far considered only boron in  $\text{BO}_3$  units. Since the values of  $Q_{\infty}$  for  $^{11}\text{B}$  in  $\text{BO}_4$  units are less than 900 kHz, regions of frequency below about 500 kHz would have to be searched for the  $^{11}\text{B}$  and  $^{10}\text{B}$  responses for these 4-coordinated borons. Success [28] has been achieved (Fig. 26) for the single  $^{11}\text{B}$  response at about 275 kHz for 4-coordinated borons in polycrystalline lithium diborate ( $\text{Li}_2\text{O} \cdot 2\text{B}_2\text{O}_3$ ) at 77 K, but this is probably the lower frequency limit for the present NQR spectrometer. The  $^{11}\text{B}$  responses [24] for the

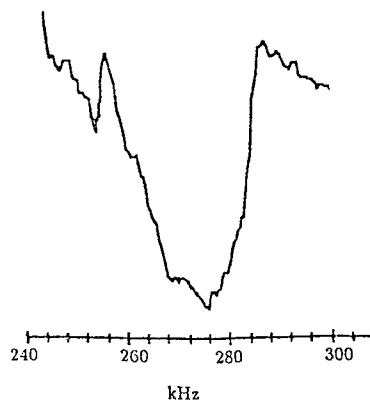


Fig. 26.  $^{11}\text{B}$  NQR spectrum for four-coordinated borons in crystalline  $\text{Li}_2\text{O} \cdot 2\text{B}_2\text{O}_3$ .

two 4-coordinated boron sites in crystalline lead diborate ( $\text{PbO} \cdot 2\text{B}_2\text{O}_3$ ) are displayed in Fig. 27. The frequencies and  $Q_{\infty}$  values are higher here because the presence of 3-coordinated oxygens 4-coordinates all of the borons in this material but distorts the  $\text{BO}_4$  tetrahedra.

Vitreous borates can also be studied by NQR. Figure 28 depicts the  $^{11}\text{B}$  NQR responses for a sample of  $\text{B}_2\text{O}_3$  glass. [29] The most interesting feature is the appearance of two responses reflecting the occurrence of two different boron sites in the glass. The responses from these two sites are not resolved in the NMR spectrum (see Fig. 8), but are very clearly resolved by NQR. The larger response at higher frequency apparently arises from borons in boroxol groups [30] (see Fig. 9), but the other site has not yet been identified. The major advantage of NQR over NMR in terms of resolving responses from various boron sites in solids is dramatically exemplified in this case of vitreous  $\text{B}_2\text{O}_3$ .

#### 4. CONCLUDING REMARKS

The  $^{10}\text{B}$  and  $^{11}\text{B}$  studies presented here of boron-containing solids have involved only NQR and standard NMR techniques. Other valuable NMR

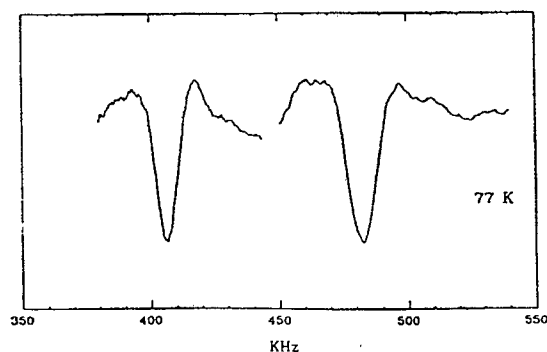


Fig. 27.  $^{11}\text{B}$  NQR responses for crystalline  $\text{PbO} \cdot 2\text{B}_2\text{O}_3$ .



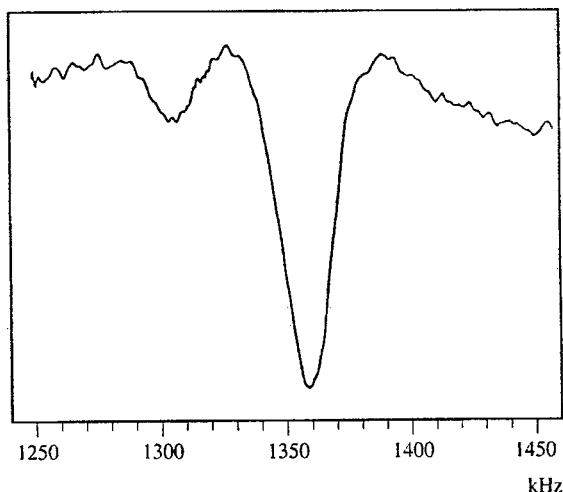


Fig. 28.  $^{11}\text{B}$  responses from vitreous  $\text{B}_2\text{O}_3$ .

studies of borates, principally involving glasses, have been conducted using newer NMR techniques. Examples include the pulsed NMR studies by Martin [31], magic angle sample spinning (MAS) NMR studies such as the work of Kirkpatrick & Oldfield [32], the very interesting work of Müller-Warmuth [33] using analysis of the spinning sidebands of MAS NMR (labeled SATRAS NMR), and the dynamic angle spinning (DAS) double rotation (DOR) and 2-dimensional (2D) NMR techniques employed by Zwanziger [34] and others. Clearly, there are now many ways to study boron in solids by magnetic resonance, and they will increasingly yield valuable information about composition, structure, chemical bonding, electron distribution, defects, strains, thermal histories, and other characteristics of borates and borides.

## REFERENCES

- [1] A.H. Silver & P.J. Bray, *J. Chem. Phys.* **29** (1958), 984.
- [2] A.H. Silver & P.J. Bray, *J. Chem. Phys.* **32** (1960), 288.
- [3] P.J. Bray, J.O. Edwards, J.G. O'Keefe, V.F. Ross, & I. Tatsuzaki, *J. Chem. Phys.* **35** (1961), 435.
- [4] M.H. Cohen & F. Reif, in '*Solid State Physics*', eds. F. Seitz and D. Turnbull, Academic Press, New York, 1958, Vol. 5, p. 321.
- [5] (a) P.J. Bray, in '*Interaction of Radiation with Solids*', ed. A. Bishay, Plenum Press, New York, 1970, p. 11; (b) S.G. Bishop, Ph.D. Thesis, Brown University, 1969.
- [6] B.E. Warren, H. Krutter & O. Morningstar, *J. Amer. Ceram. Soc.* **19** (1936), 202.
- [7] W.H. Zachariasen, *J. Amer. Chem. Soc.* **54** (1932), 3841.
- [8] T. Abe, *J. Amer. Ceram. Soc.* **40** (1957) 287; F.C. Eversteijn, J.M. Stevels, H.I. Watermann, *Phys. Chem. Glasses* **1** (1960), 123.
- [9] P.J. Bray & J.G. O'Keefe, *Phys. Chem. Glasses* **4** (1963), 37.
- [10] J. Zhong & P.J. Bray, *J. Non-Crystalline Solids* **111** (1989), 67.
- [11] J. Krogh-Moe, *Phys. Chem. Glasses* **6** (1965), 46.
- [12] G. Hagg, *J. Chem Phys.* **3** (1935) 42, 383.
- [13] G.E. Jellison, Jr., L.W. Panek, P.J. Bray, G. Rouse, *J. Chem Phys.* **66** (1978), 802.
- [14] (a) M. Shibata, C. Sanchez, H. Patel, S. Feller, J. Stark, G. Sumcad, & J. Kasper, *J. Non-*

- Cryst. Solids* **85** (1986), 29.
- (b) B. Chong, S. Choo, S. Feller, B. Teoh, O. Mathews, E. Khaw, D. Feil, K. Chong, M. Affatigato, D. Bain, K. Hazen & K. Farooqui, *J. Non-Cryst. Solids* **109** (1989) 105.
- (c) M. Affatigato, S. Feller, E. Khaw, B. Teoh & O. Mathews, *Phys. Chem. Glasses* **31**(1) (1990) 19.
- [15] Y.H. Yun, P.J. Bray, *J. Non-Cryst. Solids* **27** (1978), 363; Y.H. Yun; S.A. Feller; P.J. Bray, *J. Non-Cryst. Solids* **33** (1979), 273.
- [16] P.J. Bray, W.J. Dell, *J. de Phys.* **43** (1982) C9-131; W.J. Dell, P.J. Bray, X.Z. Xiao, *J. Non-Cryst. Solids* **58** (1983) 1.
- [17] H. G. Dehmelt & H. Kruger, *Naturwiss.* **37** (1950) 111; **38** (1951) 921.
- [18] E. A. C. Lucken, 'Nuclear Quadrupole Coupling Constants', Academic Press, New York (1969).
- [19] E. Schempp & P. J. Bray in *Physical Chemistry* Vol. 4, Academic Press, New York (1970) p. 521.
- [20] G. K. Semin, T. A. Babushkina & G. G. Yakobson, 'Nuclear Quadrupole Resonance in Chemistry', John Wiley and Sons, New York (1975).
- [21] (a) M. Rubenstein & P. C. Taylor, *Phys. Rev. Lett.*, **29**, 119; (b) M. Rubenstein & P. C. Taylor, *Phys. Rev* **B9**, 4258.
- [22] R. Bersohn, *J. Chem. Phys* **20** 1952, 1505.
- [23] S.J. Gravina, PhD thesis, Brown University (1989).
- [24] S.J. Gravina, P.J. Bray & G.L. Petersen, *J. Non-Crystalline Solids* **123** (1990), 165.
- [25] D. Kline, P.J. Bray & H.M. Kriz, *J. Chem. Phys.* **48** (1968), 5277; C. Rhee & P.J. Bray, *J. Chem. Phys.* **56** (1972), 2476.
- [26] R.B. Creel, *J. Magn. Reson.* **50**, (1982), 81.
- [27] D. Mao & P.J. Bray, *Solid State Nucl. Magn. Reson.* **1** (1992) 255.
- [28] D.H. Lee, D.G. Mao, G.L. Petersen, S. A. Feller, D.L. Bain, D.A. Feil, P. Pandikuthira, S. Nijhawan & P.J. Bray, *The Phys of Non-Cryst. Solids*, (Edited by L. David Pye, W.C. LaCourse & H.J. Stevens) Taylor & Francis (London and Washington, DC) (1992) 713-717.
- [29] D. Mao & P.J. Bray, *J. Non-Cryst. Solids* **144** (1992) 217.
- [30] (a) G.E. Jellison, L. W. Panek, P.J. Bray & G.B. Rouse, *J. Chem. Phys.* **66** (1977) 802.  
(b) A.C. Hannon, D.I. Grimley, R.A. Hulme, A.C. Wright & R.N. Sinclair, *J. Non-Cryst. Solids* **177** (1994), 299-316.  
(c) A.C. Wright, N.M. Vedishcheva & B.A. Shakhmatkin, *J. Non-Cryst. Solids*, **192 & 193** (1995), 92-97.
- [31] J.A. Sills, S.W. Martin & D.R. Torgeson, *J. Non-Cryst. Solids*, in press.
- [32] G. L. Turner, K.A. Smith, R. J. Kirkpatrick & E. Oldfield, *J. Magn. Reson.* **67** 1986, 544.
- [33] L. van Wüllen & W. Müller-Warmuth, *Solid State Nucl. Magn. Reson.*, **2** (1993), 279.
- [34] R.E. Youngman & J.W. Zwanziger, *J. Non-Cryst. Solids*, **168** (1994), 293; *J. Am. Chem. Soc.*, **117** (1995), 1397.

## HIGH RESOLUTION NMR STUDIES OF BORATE GLASS STRUCTURE

Josef W. ZWANZIGER, Randall E. YOUNGMAN  
& Marco BRAUN

*Department of Chemistry, Indiana University, Bloomington,  
IN 47405, USA*

A combination of nuclear magnetic resonance techniques are used to study the short and intermediate range structure of boron oxide glass and potassium borate glasses. It is inferred that intermediate range order in boron oxide glass arises from a propensity for boroxol rings to aggregate, making clusters with a typical size of 20-40 Å. As the glass is modified with potassium oxide it is shown that the modification occurs at both boroxol ring and non-ring sites, and a model is proposed that combines both NMR and Raman spectroscopic observations of the structural changes.

### 1. INTRODUCTION

The pioneering use of NMR by Bray as a probe of glass structure has established this technique as a key tool in glass science [1]. Nowhere has NMR been more effective than in application to borates, where the proportion of structural types and their dependence on the modification chemistry have been explored in detail [2]. The majority of what is known today on this subject is directly attributable to Bray and his research group, and so it is with great pleasure that we make the present contribution, at a meeting in his honor.

The complexity of borate glass structure stems, in our view, from the complexity of boron chemistry. While boron in oxides is always found in oxidation state III, it exists in both three-fold and four-fold coordinate forms. Also, in oxides it readily forms both chains and rings, and crystalline borates show a fascinating variety of linkages between these various forms.

Rings, in the form of boroxol groups ( $B_3O_3$ ) are present already in pure boron oxide glass, though to be sure their concentration is debated. The experimental evidence in favor of their existence is strong, however, and includes Raman spectroscopy [3], neutron scattering [4,5], NQR [6], and NMR [7-9]. There is a broad consensus among these techniques that the fraction of boron in rings is between 0.7-0.8, which is to say that the glass consists of roughly half boroxol rings, half non-ring  $BO_3$  units (because each boroxol ring itself contains three boron, to one for a  $BO_3$  unit). How these units are joined in  $B_2O_3$  is one of the subjects of this paper.

The other focus of the paper is the way that the linkages are changed when a modifier is added, in particular an alkali oxide,  $K_2O$ . It is well-known that metal oxide modifiers at low concentrations induce formation of four-coordinate  $(BO_4)^-$  groups [1,2,10,11]. For alkali oxides this persists up to about 33% added modifier, at which point non-bridging oxygen formation becomes significant [10,11]. Quantification of the fraction of four-coordinate boron has been one of the notable successes in the application of NMR to these materials. How these four-coordinate boron are incorporated in the structure, that is, how they are linked in rings and to non-ring boron, is a question about the intermediate-range order of the glass. Magnetic resonance has been used to study this question as well [6,12-15], but most results have been based on Raman spectra, which are known to be quite sensitive to the boroxol ring structures present in the pure glass [16-20]. Assignments of the spectra are made based on analogy with crystalline borates [3], which show a large variety of modified rings, including triborate, pentaborate, etc. These studies have focussed on the boroxol rings as the source of modifiable boron, and have not considered explicitly the incorporation of the non-ring  $BO_3$  into modified structures, and its possible direct modification to  $BO_4^-$ .

In this contribution we will present results of a study of potassium borate glasses, obtained using the Dynamic Angle Spinning NMR (DAS) experiment in conjunction with Raman spectroscopy. With DAS we can detect both the ring and non-ring  $BO_3$  groups, and the  $BO_4^-$  groups as they are formed [8,15]. We use DAS data taken on crystalline potassium borates to calibrate our results. Then, by combining the NMR data with Raman data on the same glasses, we arrive at a unified structural model of the modification in the glasses, which accounts for both modification in the rings and the non-ring groups, and estimates of how the proportions of these units change with added modifier.

In the following section of the paper we outline our experimental methods of sample preparation, NMR, and Raman spectroscopy. Then we list the results of the experiments, and turn to their interpretation. We end with conclusions and a summary of remaining problems.

## 2. EXPERIMENTAL METHODS

### 2.1 Sample Preparation

Glasses enriched to 90% in  $^{10}B$  were made by fusing together appropriate quantities of boric acid (Strem, 99.9995%), boric acid enriched to 97% in  $^{10}B$  (Aldrich), and potassium carbonate (Strem, 99.8%) at 1000°C. Depletion of the  $^{11}B$  isotope was necessary to alleviate spin diffusion in the DAS NMR experiments [8]. The melts were held at this temperature for one hour and quenched by removing the platinum crucible from the furnace and cooling in a dry nitrogen atmosphere. The clear, colorless glasses were broken into small pieces and stored under nitrogen to minimize absorption of water. After obtaining Raman data on the bulk samples, the glasses were powdered for NMR analysis. X-ray powder diffraction was used to verify the amorphous character of these samples. Final

compositions were checked by weight loss measurements.

Potassium borate glasses, enriched in  $^{17}\text{O}$ , were prepared by fusing together appropriate amounts of  $^{17}\text{O}$ -enriched boron oxide and potassium carbonate. The synthesis of  $^{17}\text{O}$ -enriched  $\text{B}_2\text{O}_3$  is described elsewhere [9]. After thoroughly mixing these two materials, they were melted at  $1000^\circ\text{C}$  for 15 minutes. The melts were quenched by cooling in a dry nitrogen environment.

## 2.2 NMR Spectroscopy

$^{11}\text{B}$  NMR spectra were acquired at both 115.6 MHz and 64.2 MHz, using a home-built spectrometer. Sample-spinning experiments were carried out with a commercial DAS probe (Doty Scientific), under the control of the spectrometer. Typical sample rotation frequencies were 6-7 kHz.

The DAS experiment was designed to remove anisotropic broadenings and yield high resolution NMR spectra of quadrupolar nuclei like  $^{11}\text{B}$  and  $^{17}\text{O}$  [21,22]. For these nuclei, at the magnetic field strengths used here, anisotropic terms of both first and second order are important. Conventional Magic Angle Spinning (MAS) removes the first order terms, but not the second order. Because the anisotropies depend on both  $P_2(\cos\theta)$  and  $P_4(\cos\theta)$ , where  $P_l$  is a Legendre polynomial and  $\theta$  is the angle between the rotor axis and the magnetic field, there is no single angle  $\theta$  about which sample spinning removes both sources of broadening. DAS exploits the fact that there are *pairs* of angles such that

$$P_2(\cos\theta_1) = -P_2(\cos\theta_2), P_4(\cos\theta_1) = -P_4(\cos\theta_2) \quad (1)$$

The experiment is executed with two time evolution periods, the first with the sample spinning about  $\theta_1$ , and the second about  $\theta_2$ . Because of the sign change in the anisotropy, a spin echo is formed in which all first and second order broadening is canceled out. Using this experiment, sites with 20 kHz line widths under static conditions and 5 kHz line widths under MAS yield spectra with 200 Hz wide lines.

For the DAS experiments discussed here, the rotor orientation angles used were  $\theta_1=37.38^\circ$  and  $\theta_2=79.19^\circ$ , with  $k=1$ . The time to reorient the probe and re-establish stable spinning between these angles was 40 ms. For the glass samples, the shifted-echo DAS sequence with hypercomplex data acquisition was used, while for the crystalline samples only shifted-echo DAS was employed [23]. Each data set consisted of typically 64-128 scans (256 complex points) at each of 80  $t_1$  points, with 15-60 seconds (for glasses) and 600 seconds (crystals) between scans to allow for full relaxation of all sites. Each such series of data was zero-filled to  $512 \times 512$  before transformation. No smoothing was used in either dimension. The time necessary to acquire each spectrum varied from about 24 hours for glass samples in the higher field, to as much as several weeks for the crystalline samples at the low field. The major difference is that the relaxation times in the glasses are typically an order of magnitude shorter than in corresponding crystals.

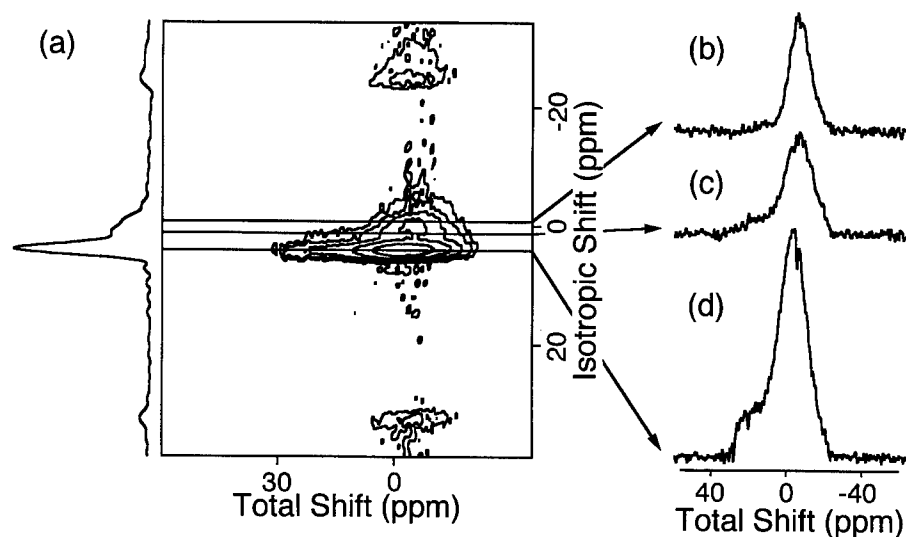


Fig. 1. (a) Two-dimensional DAS spectrum of  $^{11}\text{B}$  in  $(\text{K}_2\text{O})_{20}(\text{B}_2\text{O}_3)_{80}$  glass. The projection at the left is the high resolution dimension. Shifts are in ppm referenced to  $\text{Et}_2\text{OBF}_3$ . Slices through the data at three key isotropic shifts are shown to the right; (b)  $-0.3$  ppm, four fold coordinate boron; (c)  $1.0$  ppm, loose  $\text{BO}_3$  units; (d)  $4.7$  ppm,  $\text{BO}_3$  units in rings.

### 2.3 Raman Spectroscopy

Raman spectra were obtained on a commercial Raman spectrometer (Spectra-Code) at the Purdue University Chemistry Department Laser Facility. The excitation source was the  $632.8$  nm line of a  $30$  mW helium-neon laser and the spectral resolution was  $3\text{ cm}^{-1}$ . The instrument uses integral holographic filtering and a liquid nitrogen cooled CCD detector. Data was obtained using large pieces of glassy sample, sealed in a quartz sample cuvette. The scattering intensity was integrated over  $600$  s of detector exposure time. Spectra were acquired under ambient pressure and temperature conditions.

### 3. RESULTS

Figure 1 shows a typical two-dimensional DAS spectrum of a potassium borate glass. The powder patterns obtained at different isotropic shifts are shown on the right side of this figure; the total powder pattern is projected at the top of the contour plot. At left is the high resolution dimension. Figure 2 shows a series of high-resolution spectra as a function of potassium oxide content.

Raman spectra (not shown) of the potassium borate glasses show the same behavior seen in previous studies. The dominant feature is a sharp, strong peak at  $808\text{ cm}^{-1}$  in pure  $\text{B}_2\text{O}_3$  glass, which decreases in intensity with added modifier. In addition, a somewhat broader peak grows in at about  $770\text{ cm}^{-1}$ . By a modifier level of  $33\%$ , the  $808\text{ cm}^{-1}$  has vanished. Additionally, broad weak features in the  $300\text{--}800\text{ cm}^{-1}$  region were seen, which at low modifier content have been assigned to motions of the loose  $\text{BO}_3$  units [27].

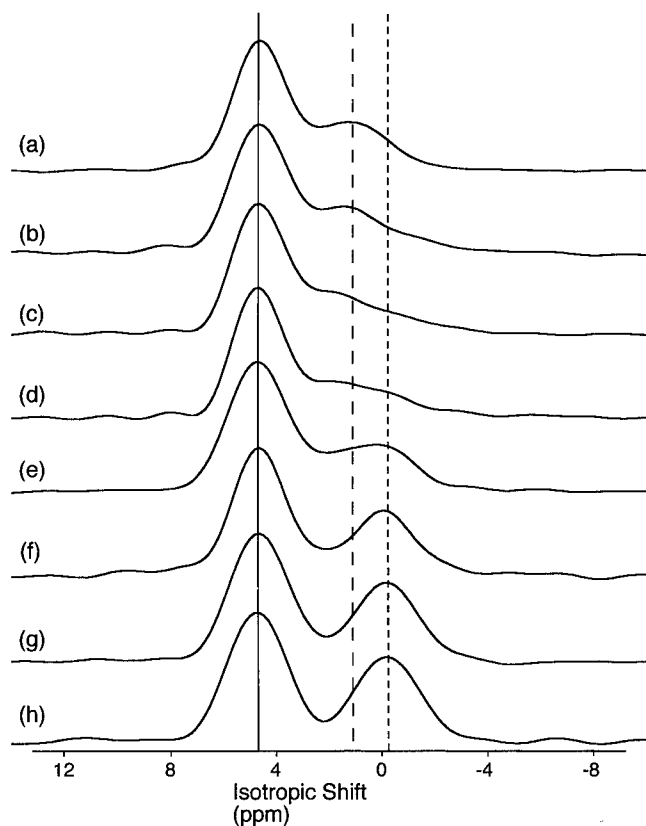


**Fig. 2.** Isotropic shift spectra of  $^{11}\text{B}$  in  $(\text{K}_2\text{O})_x(\text{B}_2\text{O}_3)_{1-x}$  glasses, from DAS NMR. (a)  $x=0.0$  ( $\text{B}_2\text{O}_3$ ); (b)  $x=0.08$ ; (c)  $x=0.13$ ; (d)  $x=0.18$ ; (e)  $x=0.23$ ; (f)  $x=0.28$ ; (g)  $x=0.33$ ; and (h)  $x=0.38$ . The vertical lines are drawn at the isotropic shifts of the three sites. Solid line: 4.7 ppm, the ring three coordinate boron shift; long dashed line: 1 ppm, boron in loose  $\text{BO}_3$  units; short dashed line: -0.3 ppm, four coordinate boron. Very weak features, for example those near 8 ppm, are truncation errors due to the finite data set size.

## 4. DISCUSSION

### 4.1 Intermediate Range Order and the Structure of Pure $\text{B}_2\text{O}_3$

Here we briefly review the structure of pure  $\text{B}_2\text{O}_3$  glass. As stated in the introduction, a wealth of experimental evidence supports the view that boroxol rings ( $\text{B}_3\text{O}_3$ ) are present in significant amounts in the pure glass, with estimates ranging up to 80% of the total boron being present in this form [3-9]. These units have a sharp Raman signature, where they give rise to a narrow band at  $808\text{ cm}^{-1}$  [3,16]. Moreover, Gravina & Bray, using NQR [6], and our lab, using NMR [8], obtained well resolved boron spectra that show two distinct sites, which are assignable to boron within boroxol rings and boron outside rings (see for example Figure 2a). Bray and co-workers have also obtained  $^{17}\text{O}$  NMR spectra that suggest the presence of multiple oxygen sites, again within and outside of boroxol rings [7].

The NMR spectra of potassium borate crystals provide strong evidence for the boroxol ring model. The crystal structures of a variety of such crystals are known, and so the boron resonances can be assigned unambiguously from their intensities. We found that boron in the metaborate ring (from  $K_3B_3O_6$ ),  $B_3O_6^{3-}$ , has an isotropic shift of 4.9 ppm, almost identical to the 4.7 ppm shift seen in the glass. The metaborate ring is a planar boroxol ring capped by non-bridging oxygen. Next, in the crystals, non-ring  $BO_3$  groups are found in the range 1.0-2.3 ppm, with the most down-field shift arising from a  $BO_3$  group with two  $BO_4^-$  neighbors.  $BO_3$  groups in modified boroxol rings have isotropic shifts within a ppm of the metaborate shift, never farther upfield than 3.8 ppm. These results on crystalline compounds are, in our opinion, only consistent with assignment of the 4.7 ppm shift in the glass to boroxol rings, and the 1.0 ppm shift to non-ring  $BO_3$  groups.

The glass structure is further probed through oxygen NMR. Recently, we obtained very high-resolution  $^{17}O$  NMR spectra, using the Double Rotation (DOR) NMR experiment, which showed three resolved oxygen sites [9]. This experiment removes both first and second-order quadrupole broadening, as does DAS. A difficulty in using this experiment, as compared to DAS and MAS, is the comparatively low spinning rates achievable ( $< 1$  kHz). This gives rise to spectra with a great many spinning sidebands, making accurate intensity determination problematic. To circumvent this problem we performed time-dependent simulations of the spectra, which account for the sidebands, and used the interaction parameters and intensities to simulate MAS spectra, which we could record with excellent signal to noise and little interference from sidebands. The results of these consistency checks were that the spectra arise from three sites with relative populations  $0.5 \pm 0.1$ ,  $0.3 \pm 0.1$  and  $0.2 \pm 0.1$ . The interaction parameters (chemical shift and quadrupole coupling) of the three sites are similar and all indicate oxygen in bridging configurations.

To assign these sites we constructed a model based on the assumption that four resolvable oxygen sites could be present: oxygen in boroxol rings, oxygen bridging boroxol rings, oxygen bridging rings and non-ring  $BO_3$ , and finally oxygen bridging two non-ring  $BO_3$  units. Two facts were used to constrain the concentrations of these four units: the ratio of oxygen to boron in the glass (3/2) and the fraction of boron present in rings (0.7, based on our NMR data on these samples) [8,9]. This is sufficient to constrain the oxygen site populations leaving only a single degree of freedom. For example, consider the ring oxygen. Call the number of ring boron atoms  $R$ ; then there are also  $R$  ring oxygen atoms, since the ring composition is  $B_3O_3$ . The fraction of ring oxygen is then  $R/N$ , where  $N$  is the total number of oxygen atoms. But  $N/M = 3/2$ , where  $M$  is the total number of boron atoms. Therefore  $R/N = 2R/3M = 0.7 \times 2/3 = 0.47$ , since the fraction of boron in rings  $R/M = 0.7$ . We thus assign the experimentally observed resonance with intensity 0.5 as the ring oxygen site (note that there are no adjustable parameters in this assignment). For the other three oxygen sites two independent equations may be derived, following reasoning



similar to the above. The solutions of these equations may be found in terms of one of the three unknowns, and they show that there is only one region of solution space that corresponds to the observed intensities of 0.5, 0.3, and 0.2: when the population of ring to non-ring bridging oxygen is small.

A small concentration of ring to non-ring connections suggests that the glass consists of regions rich in boroxol rings, and regions poor in rings. From the size of rings and the assumption that each ring on the surface of a ring-rich region makes a single connection to non-ring  $\text{BO}_3$  units, we estimated the size of the ring-rich regions to be about 20-40 Å. Interestingly, recent light-scattering measurements at the glass transition in  $\text{B}_2\text{O}_3$  [24,25], as well as an interpretation of the boson peak [26], are both consistent with structural inhomogeneities on this length scale. Indeed, intermediate range order is conjectured to be universal in glass formation. Our data suggests its structural origin in this particular material.

#### 4.2 Conversion from Three-fold to Four-fold Coordination

As stated in the introduction, there is considerable evidence showing that as modifiers are added to borate glass, the initial structural change is the conversion of three-fold coordinate boron to four-fold coordination. Because of the presence of both boroxol rings and non-ring  $\text{BO}_3$  units in the pure glass and melt [27], this modification could happen at either site or both. Considerable work using Raman spectroscopy indicates that the pure boroxol rings are modified in some way, as the sharp  $808\text{ cm}^{-1}$  peak indicative of the boroxol rings diminishes in intensity and is replaced by a broader feature at about  $770\text{ cm}^{-1}$ . This pattern is observed also in the present study, as mentioned above in Section 3.

The DAS NMR data presented in Fig. 2 also provides a way to follow the structural changes upon modification. In this figure it is clear that as more modifier is added, the less intense peak at 1.0 ppm decreases in intensity, while a new feature grows in at -0.3 ppm. The strong feature at 4.7 ppm decreases slightly. These three resonances are all well-fit by Gaussian lineshapes, and from such fits the relative intensities of the three resonances can be extracted. To make such a determination we fixed the isotropic shift of each resonance at its observed value in the 0% modification sample (for the 4.7 ppm and 1.0 ppm features) or the 30% modification (the -0.3 ppm feature). Then, the intensities and widths were allowed to vary freely in fitting the spectra for different modifier content. The results for the relative intensities are shown in Fig. 3. The widths do not change significantly with added modifier.

We verified that the DAS NMR experiment gives reliable relative intensities for this system by recording spectra of crystalline potassium borates, and comparing the boron site intensities against the populations derived from the crystal structures. This is a significant check because the three-fold and four-fold boron have quite different quadrupole interaction parameters, and hence different NMR nutation behavior. We found that by working at high pulse powers both the three-fold and four-fold site intensities are correctly reproduced. This strategy was used to acquire all the glass data presented here.

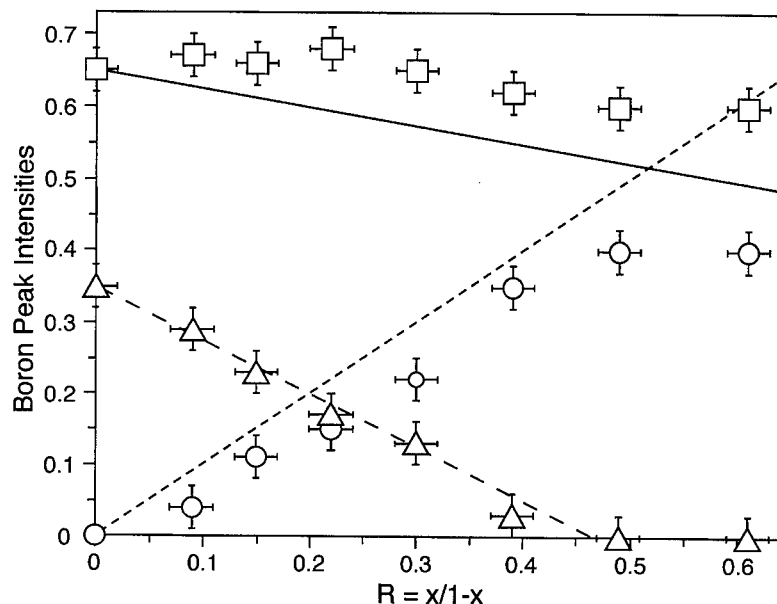


**Fig. 3.** Intensities obtained from spectral fits, of the three main features in the DAS NMR spectra of  $^{11}\text{B}$  in  $(\text{K}_2\text{O})_x(\text{B}_2\text{O}_3)_{1-x}$  glasses as a function of  $R=x/(1-x)$ , the ratio of modifier to boron oxide concentration. □: 4.7 ppm peak. Δ: 1.0 ppm peak. ○: -0.3 ppm peak. Solid lines are from model of Equations 2-4.

At 0% modifier (pure  $\text{B}_2\text{O}_3$  glass) the features in the NMR spectra have been assigned previously as boroxol ring boron (4.7 ppm) and non-ring  $\text{BO}_3$  units (1.0 ppm) [8]. [Note that these are isotropic shifts, not chemical shifts, and as such include both isotropic chemical shift and second-order quadrupole effects. The latter are field-dependent, so these shifts are specific to 8.4 T, the field at which the measurements were made.] This assignment is based on intensities, but agrees with recent *ab initio* calculations [28]. The feature at -0.3 ppm is due to four-coordinate boron. We studied this feature in detail with  $^{10}\text{B}$  NMR (chosen, due to its integer spin and lower gyromagnetic ratio, to accentuate quadrupole effects as much as possible) and found it to be remarkably insensitive not only to the modifier content in the glass, but even to the chemical nature of the modifier ( $\text{K}_2\text{O}$ ,  $\text{Rb}_2\text{O}$ ,  $\text{Na}_2\text{O}$ , etc.) and the physical structure (glass or crystal). The four-fold coordinate sites thus have a very robust structure and NMR shift signature. The three-fold sites are more difficult to assign in the modified glasses, and we turn to this problem in the next section.

#### 4.3 A Unified Model for Borate Modification Chemistry

As noted above, Raman spectra strongly indicate that the symmetric boroxol ring is modified, presumably being converted to triborate (two three-fold and one four-fold coordinate boron in a ring) and more complex ring structures. Earlier work from our laboratory, using DAS NMR, indicated that substantial

modification happens as well at the non-ring  $\text{BO}_3$  sites, which we observed in rubidium borate glasses to decrease markedly in intensity as modifier was added [15]. Moreover, the NMR resonance initially assigned to the boroxol ring boron in  $\text{B}_2\text{O}_3$  decreased only slightly in intensity with added modifier. These observations together suggested an interpretation in contradiction with Raman studies, namely that the ring sites are not modified to any great extent, while the non-ring  $\text{BO}_3$  groups are preferentially converted to  $(\text{BO}_4)^-$ .

Here we use our more complete data set, which includes both NMR and Raman spectra, to propose a unified model of modification. First, our NMR results (Figure 3) show that the resonance assigned to loose  $\text{BO}_3$  units decreases strongly with  $R$ ; a fit to the data yields

$$L^3 = 0.35 - 0.75R \quad (2)$$

where  $L^3$  is the fraction of boron in loose  $\text{BO}_3$  units. Likewise, the fraction of boron in all four-fold coordinate sites can be taken as

$$L^4 + Rg^4 = R \quad (3)$$

where  $L^4$  and  $Rg^4$  are the fractions of boron in loose and ring-bound four-fold sites, respectively. This estimation assumes that each modifier ion produces a single  $\text{BO}_4^-$  unit, and hence that no non-bridging oxygen are formed. At the modifier concentrations considered here this is a reasonably accurate assumption. Finally, the fraction of three-fold boron in rings of all kinds,  $Rg^3$ , follows from normalization, as

$$Rg^3 = 1 - L^3 - L^4 - Rg^4 = 0.65 - 0.25R \quad (4)$$

Lines corresponding to the above model are plotted on Fig. 3, along with the data, and show reasonable agreement. We assume in this plot that all three-fold coordinate boron in rings have equivalent isotropic shifts, and thus overlap in the resonance at 4.7 ppm. To check this assumption we have examined a variety of crystalline potassium borates, of known structure, and found that the three-fold ring sites are always within 1 ppm of the 4.7 ppm boroxol ring shift.

The above equations give a general model in agreement with our NMR data on the partitioning of the three-coordinate boron between rings and loose units. Our NMR data do not resolve individual modified ring structures, so there are a variety of ways to realize this model. We proceed by assuming that the modified rings include tetraborate and diborate groups, in accord with earlier analyses of alkali borate glasses. Then the glasses are taken to consist of 5 basic units: boroxol rings, tetraborate and diborate units, and loose  $\text{BO}_3$  and  $(\text{BO}_4)^-$ . To estimate the fractions of these building blocks we need 5 independent constraints. One is provided by normalization, and Equations 2 and 3 provide two more. Our Raman data give an estimate of the fraction of boroxol rings. In this data we see the  $808\text{ cm}^{-1}$  band decreasing roughly linearly, and vanishing by roughly the composition  $R = 0.5$  (this is in reasonable agreement with earlier  $^{10}\text{B}$  NMR studies [12,13]). From the NMR data on  $\text{B}_2\text{O}_3$  we find

$B^3$ , the fraction of boron in boroxol rings, to be 0.65, and so the fraction of boroxol rings themselves is 0.38. The boroxol ring fraction in the modified glass is thus taken as  $0.38 - 0.76R$ , that is, a linear function that vanishes at  $R=0.5$ . Finally, the diborate concentration is taken from Jellison & Bray's results [12], who found that the ratio of boron in diborate groups to boron in rings is roughly zero for  $R < 0.1$ , and then increases approximately linearly to about 0.68 by  $R=0.5$ . From Equations 2, 3, normalization, and the concentrations of boroxol rings and diborate rings, an estimate of the various units in the glasses can be made as a function of composition. Figure 4 shows the results, expressed in terms of the fraction of boron present in each type of site. The relative concentrations of boroxol, tetraborate, and diborate rings are quite similar to earlier determinations [12,13]. Here, however, account is taken explicitly of the loose units, so the concentrations of the ring species are reduced in absolute terms.

The agreement between the ring fractions exhibited in Figure 4 and those obtained in earlier works [12,13] is encouraging because here the only ingredient taken from those works is the diborate concentration. The boroxol ring fraction is set by our Raman results, and the loose 3- and 4-fold fractions by the DAS NMR results. Figure 4 thus represents a model that is consistent with our present high-resolution NMR results on the loose units, Raman spectra of the boroxol rings, and earlier  $^{10}\text{B}$  wide-line NMR results on the modified ring fractions.

## 5. CONCLUSIONS

We have presented results of several studies on borate glass structure, made primarily with high-resolution and multidimensional NMR methods. In pure  $\text{B}_2\text{O}_3$  glass we have used Double Rotation NMR to probe the oxygen environments, and found that three independent sites could be resolved. We constructed a model to interpret these sites, which suggests that the boroxol rings have a tendency to aggregate in the glass. This would explain the intermediate range order observed in scattering studies in this material.

In potassium borate glasses we were able to follow the modification using two-dimensional Dynamic Angle Spinning NMR. These experiments resolve three sites, assigned to ring, loose  $\text{BO}_3$ , and four-fold coordinate boron. The partitioning of the boron among these sites can be modeled in a simple way that is in reasonable agreement with the data. Then, by combining the intensities of these sites with Raman spectra and earlier estimations of the diborate concentration, a full model is developed which gives the concentrations of five structural units as a function of modifier: boroxol rings, tetraborate and diborate groups, and loose  $\text{BO}_3$  and  $\text{BO}_4^-$  groups. The model is consistent with the present DAS NMR data, Raman spectra, and the earlier studies of the modified rings. We believe it to be a significant result in this field, because for the first time the loose units are explicitly included in a structural model. While the majority of *boron atoms* are present in rings, at low modifier concentra-

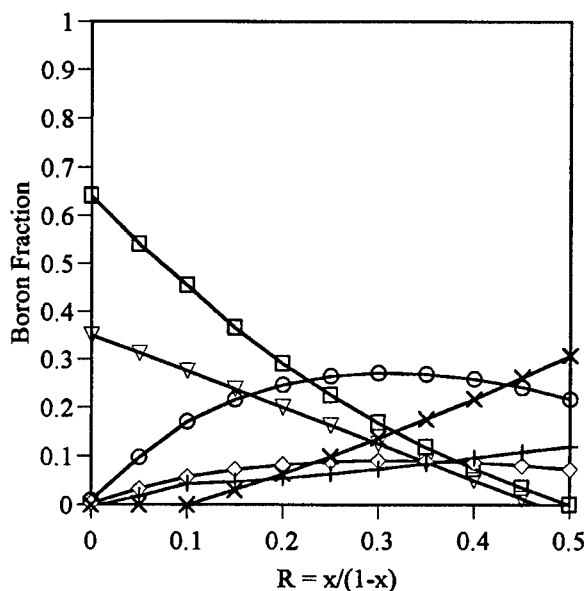


Fig. 4. Fraction of boron in each type of site for the model outlined in the text. □: boroxol rings ( $B^3$ ); ▽: loose  $BO_3$  groups ( $L^3$ ); ○: 3-coordinate boron in tetraborate groups ( $T^3$ ); ◇: 4-coordinate boron in tetraborate ( $T^4$ ); ×: three- and four-coordinate boron in diborate ( $D^3$ ,  $D^4$ ); +: loose  $BO_4$  groups ( $L^4$ )

tions the majority of *structural units* are loose  $BO_3$ . Thus taking them into account is important. Finally, the model provides a unified treatment of a variety of different experiments, each capable of probing different elements of the glass structure.

## ACKNOWLEDGMENTS

This research was supported by the National Science Foundation under Grants DMR-9115787 and DMR-9508625. M. Braun was supported by a fellowship from the Leopoldina.

## REFERENCES

- [1] A. Silver & P. J. Bray, *J. Chem. Phys.* **29** (1958), 984.
- [2] P. J. Bray, *J. Non-Cryst. Solids* **95 & 96** (1987), 45.
- [3] T. Bril, *Philips Res. Rep. Suppl.* **2** (1976), 1.
- [4] A. Hannon, A. Wright, J. Blackman & R. Sinclair, *J. Non-Cryst. Solids* **182** (1995), 78.
- [5] A. Hannon, D. Grimley, R. Hulme, A. Wright & R. Sinclair, *J. Non-Cryst. Solids* **177** (1994), 299.
- [6] S. Gravina & P. J. Bray, *J. Magn. Reson.* **89** (1990), 515.
- [7] G. E. Jellison, Jr., L. W. Panek, P. J. Bray & G. B. Rouse, Jr., *J. Chem. Phys.* **66** (1977), 802.
- [8] R. E. Youngman & J. W. Zwanziger, *J. Non-Cryst. Solids* **168** (1994), 293.
- [9] R. Youngman, S. Haubrich, J. Zwanziger, M. Janicke & B. Chmelka, *Science* **269** (1995), 1416.
- [10] Y. Yun & P. Bray, *J. Non-Cryst. Solids* **44** (1981), 227.
- [11] J. Zhong & P. Bray, *J. Non-Cryst. Solids* **111** (1989), 67.

- [12] G. Jellison, Jr. & P. Bray, *J. Non-Cryst. Solids* **29** (1978), 187.
- [13] S. Feller, W. Dell & P. Bray, *J. Non-Cryst. Solids* **51** (1982), 21.
- [14] P. Bray, J. Emerson, D. Lee, S. Feller, D. Bain & D. Feil, *J. Non-Cryst. Solids* **129** (1991), 240.
- [15] R. E. Youngman & J. W. Zwanziger, *J. Am. Chem. Soc.* **117** (1995), 1397.
- [16] B. Meera & J. Ramakrishna, *J. Non-Cryst. Solids* **159** (1993), 1.
- [17] W. Konijnendijk & J. Stevels, *J. Non-Cryst. Solids* **18** (1975), 307.
- [18] E. Kamitsos & M. Karakassides and G. Chryssikos, *Phys. Chem. Glasses* **30** (1989), 229.
- [19] G. Chryssikos, E. Kamitsos & M. Karakassides, *Phys. Chem. Glasses* **31** (1990), 109.
- [20] E. Kamitsos, G. Chryssikos & M. Karakassides, *J. Non-Cryst. Solids* **123** (1990), 283.
- [21] B. F. Chmelka, K. T. Mueller, A. Pines, J. Stebbins, Y. Wu & J. W. Zwanziger, *Nature* **339** (1989), 42.
- [22] K. T. Mueller, B. Sun, G. C. Chingas, J. W. Zwanziger, T. Terao & A. Pines, *J. Magn. Reson.* **86** (1990), 470.
- [23] P. Grandinetti, J. Baltisberger, A. Llor, Y. Lee, U. Werner, M. Eastman & A. Pines, *J. Magn. Reson. A* **103** (1993), 72.
- [24] N. A. Bokov, *J. Non-Cryst. Solids* **177** (1994), 74.
- [25] C. T. Moynihan & J. Schroeder, *J. Non-Cryst. Solids* **160** (1993), 52.
- [26] E. Duval, A. Boukenter & T. Achibat, *J. Phys.: Condensed Matter* **2** (1990), 10227.
- [27] G. E. Walrafen, S. R. Samanta & P. N. Krishnan, *J. Chem. Phys.* **72** (1980), 113.
- [28] J. A. Tossell, *J. Non-Cryst. Solids* **183** (1995), 307.

## NMR STUDIES OF BORATE AND BOROSILICATE GLASS SYSTEMS IN KOREA

Chunghi RHEE

*Korea Research Institute of Standards and Science,  
P.O. Box 102, Yusong, Taejeon 305-600, Korea*

In Korea NMR studies on borate and borosilicate glass systems have been carried out by Professor P. J. Bray's second and third generation physicists (NMR experts) for the last 25 years. It is Professor Bray's great contribution in this area. Borate glass systems studied by  $^{11}\text{B}$  NMR are  $\text{Na}_2\text{O}-\text{B}_2\text{O}_3$ ,  $\text{SrO}-\text{Al}_2\text{O}_3-\text{B}_2\text{O}_3$ ,  $\text{PbO}-\text{Al}_2\text{O}_3-\text{B}_2\text{O}_3$ ,  $\text{V}_2\text{O}_5-\text{B}_2\text{O}_3-\text{Al}_2\text{O}_3$ ,  $\text{Na}_2\text{O}-\text{Al}_2\text{O}_3-\text{B}_2\text{O}_3$ ,  $\text{MgO}-\text{Al}_2\text{O}_3-\text{B}_2\text{O}_3$ ,  $\text{BaO}-\text{B}_2\text{O}_3-\text{Al}_2\text{O}_3$ ,  $\text{Li}_2\text{O}-\text{B}_2\text{O}_3-\text{Al}_2\text{O}_3$  and  $\text{CdO}-\text{B}_2\text{O}_3-\text{GeO}_2$  systems. Borosilicate glass systems studied by  $^{11}\text{B}$  NMR are  $\text{CdO}-\text{B}_2\text{O}_3-\text{SiO}_2$ ,  $\text{Li}_2\text{O}-\text{B}_2\text{O}_3-\text{SiO}_2$ ,  $\text{K}_2\text{O}-\text{B}_2\text{O}_3-\text{SiO}_2$ ,  $\text{K}_2\text{O}-\text{B}_2\text{O}_3-\text{Al}_2\text{O}_3-\text{SiO}_2$  and  $\text{K}_2\text{O}-\text{B}_2\text{O}_3-\text{SiO}_2-\text{Fe}_2\text{O}_3$  systems. Structural studies of these glass systems by  $^{11}\text{B}$  NMR is reviewed in this paper.

## TEMPERATURE EFFECTS ON BORATE MELT STRUCTURE AND DYNAMICS: NMR STUDIES

Jonathan F. STEBBINS & Sabyasachi SEN  
Department of Geological and Environmental Sciences,  
Stanford University, Stanford CA 94305-2115, USA

Decades of NMR studies of borate glass structure have provided a rich background for NMR studies of the structure and dynamics of the corresponding melts. A number of studies of glasses with varying fictive temperatures have shown that the ratio of three coordinated to four coordinated boron increases with temperature, requiring a corresponding increase in the fraction of non-bridging oxygens. The corresponding effect on dynamics is to increase the rate of exchange among the boron sites, the frequency of which seems to accurately predict the shear correlation time. Dynamics of both network-former and network-modifier cations can also be assessed through spin-lattice relaxation time measurements. In  $\text{Na}_2\text{O}-\text{B}_2\text{O}_3$  melts, such data indicate that for low Na contents,  $\text{Na}^+$  diffusion is closely coupled with framework bond-breaking. For  $\text{Na}_2\text{O}$  contents greater than about 15 to 20 mole %, however,  $\text{Na}^+$  diffusion becomes decoupled from the network, suggesting long range percolative transport.

### 1. INTRODUCTION

The longest, and possibly the most fruitful, efforts at quantifying the distribution of short-range structural units in glasses have involved the application of solid state nuclear magnetic resonance (NMR) to borate and borosilicate glasses. A detailed picture has been developed of the effects of composition on the concentrations of trigonal  $\text{BO}_3$  and tetrahedral  $\text{BO}_4$  units, as well as of bridging and non-bridging oxygens (BO and NBO), aluminate and silicate species, first through extensive studies by low-resolution  $^{11}\text{B}$  NMR (primarily by Bray and colleagues, e.g. [1-3]), then through more recent application at high magnetic fields of magic angle spinning (MAS) NMR of this nuclide as well as  $^{17}\text{O}$ ,  $^{27}\text{Al}$ , and  $^{29}\text{Si}$  (e.g. [4-8]). The reader is referred to recent reviews for an overview of this impressive structural landscape [2,9,10].

This background also makes boron-containing oxide glasses an excellent choice for addressing some of the most fundamental of open questions concerning the nature of glass forming network liquids and of the process of glass formation itself. A liquid is distinguished by a progressive structural disordering with increasing temperature, which results in thermal expansivity, compressibility, and heat capacity usually being significantly larger than those of the solid-like glass.



An atomic-scale description of these changes is still far from complete for most systems, despite its potential importance in predictive theories of thermodynamics, viscous flow, diffusion, and structural relaxation.

In this report, we briefly review recent work on mechanisms of structural change with temperature in borate-rich liquids, and present new data on borate melts that makes important new connections between structure and dynamics.

### 1.1. Effects of Fictive Temperature on Structure

One useful approach to determining the effects of temperature ( $T$ ) on liquid structure is to vary the fictive temperature ( $T_f$ ) of the glass by cooling samples at different rates. In many cases, differences may be subtle because the range of  $T_f$  that can be sampled by this approach is usually only about 100-200°C. However, several early studies of borosilicates reported a decrease in the concentration of  $\text{BO}_4$  units ( $N_4$ ) relative to that of  $\text{BO}_3$  units as  $T_f$  was increased [11,12]. This was consistent with statistical thermodynamical models [13,14].

A more detailed recent study [15] presented  $^{11}\text{B}$  MAS NMR data on several borate and borosilicate compositions. In what seemed at first surprising, no detectable effect of quench rate and therefore of  $T_f$  on  $N_4$  was seen in binary borate glasses with 10 and 30 mole %  $\text{Na}_2\text{O}$ . However, a strong effect was noted in a composition with 20%  $\text{Na}_2\text{O}$ , 20%  $\text{B}_2\text{O}_3$ , and 60%  $\text{SiO}_2$  (Fig. 1a) and in commercial "e-glass," primarily a Ca boroaluminosilicate (the latter reproducing earlier results from "wideline" NMR [11]). These findings can be understood in light of existing theoretical models of the process by which  $\text{BO}_3$  groups are formed from  $\text{BO}_4$  groups with increasing  $T$ , which requires the production of non-bridging oxygens:



The apparent enthalpy change for this reaction can be estimated at a few tens of kJ/mole from data on the  $T_f$  effect on  $N_4$  and analysis of a simple apparent equilibrium constant  $K = X_{\text{NBO}}X_{\text{BO}_3}/X_{\text{BO}_4}$  [11,15]. In compositions where the mole fraction  $X$  of NBOs is small at  $T_g$  (e.g. where  $\text{Na}_2\text{O}/\text{B}_2\text{O}_3 < 0.5$ ), the required increase in  $K$  with  $T_f$  will lead to only small changes in  $N_4$ . However, when  $X_{\text{NBO}}$  is much larger (e.g. when the mole fraction of  $\text{Na}_2\text{O}$  is roughly equal to that of  $\text{B}_2\text{O}_3$ ), much larger  $T_f$  effects on  $N_4$  should be observable [13,15]. At much higher temperatures, greater changes in  $N_4$  with  $T$  are expected even in low-modifier compositions as the concentration of NBOs becomes significant. In such cases, the increase in disorder associated with mixing of tetrahedral and trigonal borate units may become a significant part of the total configurational heat capacity of the liquid [15].

### 1.2. In Situ, High Temperature NMR Studies

The relative ease of observing  $^{11}\text{B}$  NMR spectra makes this nuclide an obvious choice for technically challenging high temperature studies. Several early reports describe the narrowing of NMR peaks that occurs above the glass

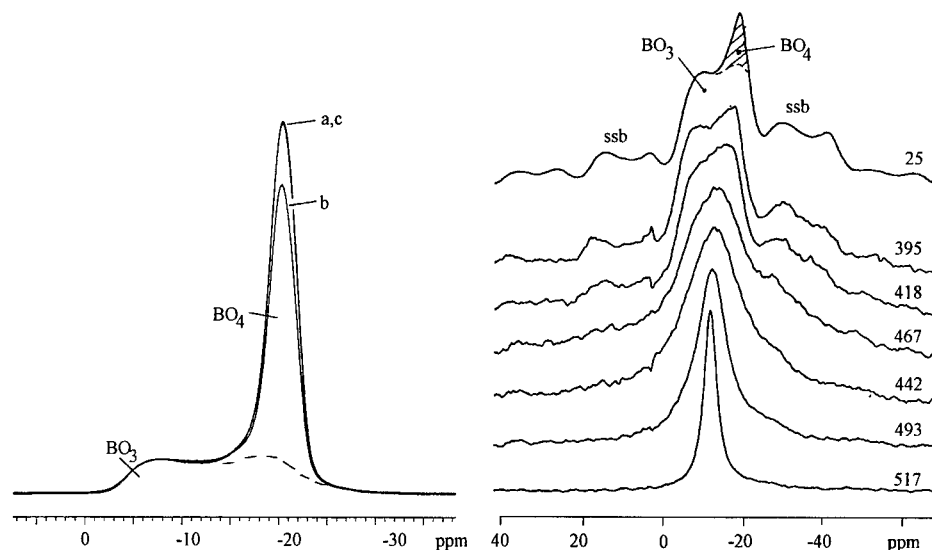


**Fig. 1a.** (Left)  $^{11}\text{B}$  MAS NMR spectrum of  $(\text{Na}_2\text{O})_{0.2}(\text{B}_2\text{O}_3)_{0.2}(\text{SiO}_2)_{0.6}$  glass. For spectrum (a), the quench rate was  $0.017^\circ\text{C/s}$ ; for (b) the rate was  $\sim 1000^\circ\text{C/s}$ ; for (c) sample a was reheated and cooled at  $0.017^\circ\text{C/s}$ . Frequency is referenced to aqueous  $\text{H}_3\text{BO}_3$ .

**Fig. 1b.** (Right) High temperature  $^{11}\text{B}$  MAS NMR spectra for  $(\text{Na}_2\text{O})_{0.1}(\text{B}_2\text{O}_3)_{0.9}$  glass and liquid collected at temperatures shown in  $^\circ\text{C}$ . "ssb" denotes spinning sidebands.

transition, and note that this requires the breaking of strong network bonds to allow isotropic motional averaging [16]. A more recent study of  $^{11}\text{B}$  spin-lattice relaxation times modeled data in terms of the isotropic reorientational diffusion of borate units [17]. It was later pointed out that as temperature is increased the motional correlation times calculated from fitting these data approach the shear correlation times estimated from viscosity data [18]. A close connection between B–O bond breaking rates and flow of the network species is clearly implied. This earlier study did not report data through the glass transition temperature, where the network dynamics and the NMR relaxation are expected to drastically change. This effect is demonstrated in new data reported below.

A more direct view of network dynamics can in some cases be obtained by high-resolution,  $^{11}\text{B}$  MAS NMR at high magnetic field, because this technique allows the isotropically averaged peak positions for  $\text{BO}_3$  and  $\text{BO}_4$  groups to be distinguished [15]. The motional averaging caused by exchange of borate species can thus also be detected, in addition to that due to reorientation. Because it is the latter which uniquely requires the breaking and reforming of B–O bonds, this approach has great potential for elucidating the mechanism of flow and network species diffusion. As shown in Fig. 1b, it is clear that exchange of different structural species can be observed and begins just above the glass transition (about  $350^\circ\text{C}$  for typical slow heating rates). In our previous report, a semi-quantitative analysis of these data suggested that the observed species

exchange rate was close to the inverse of the shear correlation time, at least at one temperature. As shown below, more detailed modeling of these spectra confirms this close connection.

## 2. EXPERIMENTAL METHODS

The  $^{11}\text{B}$  and  $^{23}\text{Na}$  spin-lattice relaxation time ( $T_1$ ) data described below were collected as described previously [19], on glass samples made from sodium carbonate and boric acid by standard melt-quench methods [15]. Relaxation times were measured by the saturation-recovery technique. Data were collected at Larmor frequencies of 128.3 MHz for  $^{11}\text{B}$  and 105.9 MHz for  $^{23}\text{Na}$  (9.4 T magnetic field) with a modified Varian VXR 400S spectrometer and a "home-built," resistively heated probe. Temperatures are accurate to about 10°C.

The high T MAS NMR data were collected with a Doty Scientific, Inc. probe with a sample spinning rate of 3.5-4 kHz. Previously reported spectra [15] have now been simulated by a multi-site exchange model in which a large number of narrow peaks, which map out the appropriate low-T quadrupolar MAS peak shapes, are allowed to randomly exchange at a single frequency at a given temperature. This approximation does not account for the effects of the partial averaging of quadrupolar satellite peaks, but this is expected to be of little consequence for the range of exchange rates observed here (Hz to kHz), which are much smaller than maximum quadrupolar splittings (MHz). The effects of magic angle spinning on the dynamic averaging of peak shapes were not modeled. The most important consequence of this approximation is simply that spinning sidebands do not appear in the simulations. The central part of the peak shapes is, however, largely unaffected by the sidebands, allowing motional effects to be estimated.

## 3. RESULTS

### 3.1. Modeling of $^{11}\text{B}$ Peak Shapes

Typical simulations of the  $^{11}\text{B}$  MAS high temperature peak shapes for a liquid with 10 mole %  $\text{Na}_2\text{O}$  and 90 %  $\text{B}_2\text{O}_3$  are shown in Fig. 2. At each temperature, the inverse of the modeled exchange frequency represents an average of the waiting time between exchange events for a given boron site. These exchange times are compared to shear correlation times ( $\tau_{\text{shear}}$ ) in Fig. 3. The latter are calculated from published viscosities  $\eta$  [20] using the Maxwell relation  $\tau_{\text{shear}} = \eta/G_{\infty}$ . The infinity frequency shear modulus ( $G_{\infty}$ ) is approximated as  $2.5 \times 10^{10}$  Pa [21]. The agreement is remarkably good given all of the approximations involved, further quantifying our earlier conclusion that B-O bond breaking (required for  $\text{BO}_3$ - $\text{BO}_4$  exchange) occurs at the correct time scale to be the fundamental control on the rate of viscous flow.

### 3.2. Spin-Lattice Relaxation Times for $^{11}\text{B}$ and $^{23}\text{Na}$

Spin-lattice relaxation time data are shown in Fig. 4 for  $\text{Na}_2\text{O}$ - $\text{B}_2\text{O}_3$  liquids and glasses with 5 and with 22 mole %  $\text{Na}_2\text{O}$ . In these and in all other observed

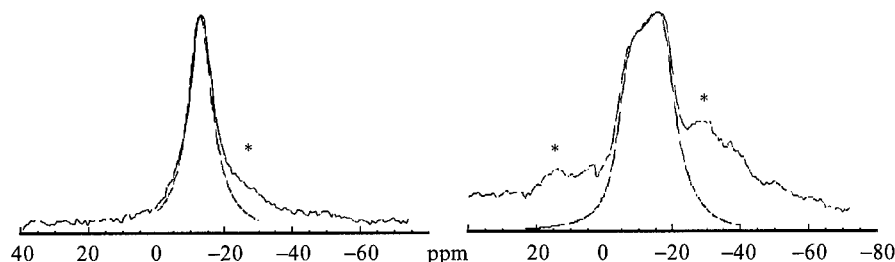


Fig. 2. Typical exchange model fits of spectra in figure 1b. (Left)  $T=493^{\circ}\text{C}$ , rate= $10^4$  Hz; (Right)  $T=418^{\circ}\text{C}$ , rate=250 Hz. Spinning sidebands are marked by \*.

compositions [22], the  $^{11}\text{B}$   $T_1$ 's decrease slowly as temperature increases in the glass, then decrease rapidly beginning just above the calorimetric glass transition temperature  $T_g$ . At higher temperature, the expected minimum in  $T_1$  is approached as the correlation time for the motion causing relaxation approaches the NMR resonant (Larmor) frequency. A similar pattern is observed for  $^{23}\text{Na}$  relaxation in the glasses with low  $\text{Na}_2\text{O}$  contents. However, in more Na-rich compositions, a qualitatively different behavior is seen with no change in slope or curvature near  $T_g$ .

In general, spin-lattice relaxation is caused either by fluctuations at the Larmor frequency in the local magnetic field "seen" by a nucleus, or, for a quadrupolar nuclide, by fluctuations in the gradient of the local electric field. For  $^{11}\text{B}$  and  $^{23}\text{Na}$  in glasses and liquids, the latter is expected to dominate because quadrupolar moments are large. These fluctuations can be caused either by low-frequency local oscillations, or, at higher temperature, by diffusive jumps from site to site. It is thus clear that a major change in the dynamics takes place at  $T_g$  for boron and for sodium in low-Na liquids. In contrast, for Na in high-

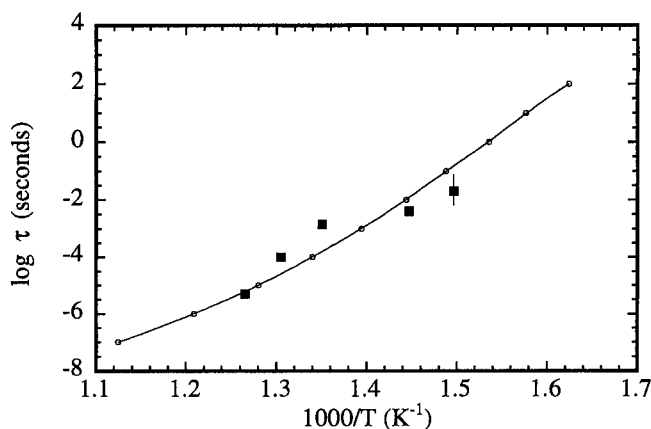
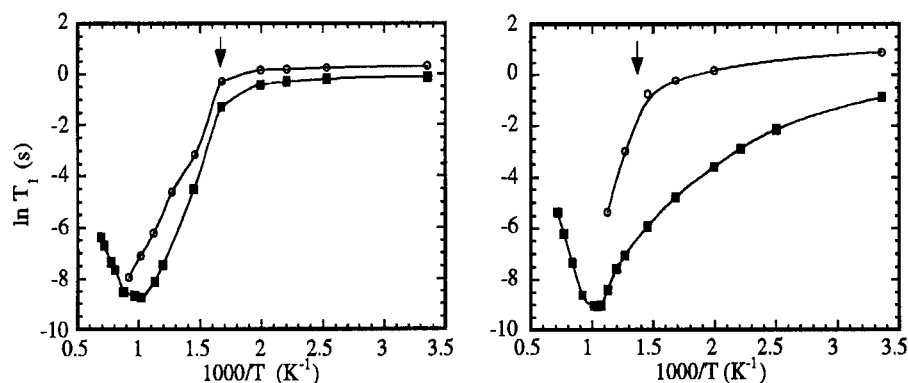


Fig. 3. Shear relaxation time (dots and fitted line) vs.  $1000/T$ , compared to borate species exchange frequencies from simulations of NMR peak shapes as in Fig. 2 (solid squares).



**Fig. 4a** (Left) and **4b** (Right)  $T_1$  data for  $^{23}\text{Na}$  (solid squares) and  $^{11}\text{B}$  (open circles) in sodium borate glasses and liquids. Arrows show calorimetric  $T_g$ . (Left) 5 mole%  $\text{Na}_2\text{O}$ ; (Right) 22 mole%  $\text{Na}_2\text{O}$ . Lines are to guide the eye only. Typical uncertainties are smaller than the symbols.

Na compositions, correlation times for the motions causing relaxation decrease monotonically through  $T_g$ .

#### 4. DISCUSSION

Measured average rates of borate species exchange, and the accompanying breaking and reforming of B–O bonds, successfully predict the time scale of macroscopic viscous flow in binary sodium borate liquids, at least in the range of about 10 to 30%  $\text{Na}_2\text{O}$ . For these compositions, this finding strongly suggests that such exchange is a fundamental step of the shear relaxation process. The freezing out of the latter in turn defines the transition from a liquid to a glass. Spin-lattice relaxation for boron should thus also change dramatically at  $T_g$ , because this process depends on large-amplitude fluctuations in the local bonding environment, such as coordination number and bond length. The breaks in slope of the temperature effect on  $^{11}\text{B}$   $T_1$ 's near to  $T_g$  provide additional information about the mechanism of the network rearrangement. Spin-lattice relaxation requires fluctuations with a frequency component ("spectral density") at the Larmor frequency ( $\sim 10^8$  Hz), which is many orders of magnitude faster than shear correlation frequencies (on the order of Hz or less near to  $T_g$ ). A likely connection between the two processes is that bond-breaking or species exchange has a "jump and wait" mechanism, rather than resembling a smooth oscillation or rotation. That is, even if the average exchange frequency is, say, 100 Hz, the exchange process itself is rapid enough to have a significant high frequency component.

In low-Na borate liquids, spin-lattice relaxation for  $^{23}\text{Na}$  is also strongly influenced by the network breaking and re-forming process: the plots for these data strongly resemble the  $^{11}\text{B}$  results (Fig. 4a). This in turn implies that diffusive motion of  $\text{Na}^+$  is greatly facilitated by the dynamical opening up of pathways through the structure caused by framework bond rearrangement above

$T_g$ . In other words, for an average  $\text{Na}^+$  cation in such a composition, the static structure does not define an unrestricted, low-energy preferred pathway for long-range alkali diffusion.

In contrast, in glasses with  $\text{Na}_2\text{O}$  contents greater than about 15 mole%,  $^{23}\text{Na}$  spin-lattice relaxation shows no obvious effect of the glass transition (Fig. 4b). Na motion apparently is unhindered by the borate network, and thus is not strongly affected by the beginning of anionic species exchange at  $T_g$ . In such compositions, the Na content must be high enough so that preferred Na diffusive pathways have formed, along which the cations can move without requiring B–O bond breaking. In this case, the recently developed picture of a strongly bonded network with a continuous “tissue” of modifier cation pathways seems most applicable [23].

#### 4.1. Comparison with Other Oxide Melts

We have previously found that exchange rates for anionic species in alkali silicate liquids are closely related to time scales for viscous flow, whether the latter are estimated from shear correlation times or from an Eyring model of network cation jumping [24–26]. In silicates also,  $^{29}\text{Si}$  spin-lattice relaxation is drastically affected by the calorimetric glass transition [27,28]. Collecting  $^{23}\text{Na}$   $T_1$  data for compositions that would mark the percolation threshold in silicates is made difficult by sub-liquidus phase separation. However, we have recently found that sodium dynamics in germanate liquids are in important respects similar to those for borates [22]. Thus the phenomena reported here seem to have some generality for network liquids.

#### 4.2. Future Questions

Here and elsewhere we have reported anionic species exchange rates that must, of course, be some kind of average over possibly wide ranges of real dynamics. The latter are exemplified by the distributions of frequencies typically derived from mechanical and dielectric relaxation measurements. Our present exchange rate data suggest only that on the average, all network sites are involved with viscous transport. The role of density or compositional heterogeneities remains unclear. However, our results imply that if flow is dominated by regions that are “weak,” i.e. concentrated planes of modifier cations and/or nonbridging oxygens, then these regions themselves must diffuse rapidly through the entire network. Wide ranges in dynamical frequencies may result from temporal complexity (e.g. non-exponential relaxation) or from spatial heterogeneity. New, multi-dimensional NMR techniques have recently shown great promise for clarifying such issues in organic glasses [29], and may eventually be applicable to oxide melts.

A second key question for the future is whether percolation pathways for modifier cation diffusion form at the volume fraction of predicted by random mixing, or whether actual chemically-induced clustering occurs. The latter should be more likely with higher field strength (smaller, higher charge) modi-

fiers. Further studies of spin-lattice relaxation in a wide variety of compositions may help to solve this problem.

## REFERENCES

- [1] P.J. Bray and J.G. O'Keefe, *Phys. Chem. Glasses* **4** (1963), 37.
- [2] P.J. Bray, *J. Non-Cryst. Solids* **73** (1985), 19.
- [3] P.J. Bray, *J. Non-Cryst. Solids* **75** (1985), 29.
- [4] P.J. Bray, *et al.*, In: *The Physics of Non-Crystalline Solids*, Eds L.D. Pye, W.C.L. Course and H.J. Stevens (Taylor and Francis, London, 1992), pp. 713-717.
- [5] B.C. Bunker, R.J. Kirkpatrick, R.K. Brow, G.L. Turner & C. Nelson, *J. Am. Ceram. Soc.* **74** (1991), 1430.
- [6] J. Zhong & P.J. Bray, *J. Non-Cryst. Solids* **111** (1989), 67.
- [7] R.E. Youngman & J.W. Zwanziger, *J. Non-Cryst Solids* **168** (1994), 293.
- [8] S.W. Martin, A. Bhatnagar, C. Parameswar, S. Feller & J. MacKenzie, *J. Am. Ceram. Soc.* **78** (1995), 952.
- [9] P.J. Bray, S.J. Gravina, P.E. Stallworth, S.P. Szu & J. Zhong, *Exp. Tech. Phys.* **36** (1988), 397.
- [10] H. Eckert, *Prog. Nucl. Mag. Reson.* **24** (1992), 159.
- [11] P.K. Gupta, M.L. Lui & P.J. Bray, *J. Am. Ceram. Soc.* **68** (1985), C82.
- [12] P.J. Bray, & Holupka, E.J., *J. Non-Cryst. Solids* **71** (1985), 411.
- [13] R. Araujo, In: *Structure and Bonding in Noncrystalline Solids*, Eds G.E. Walrafen and A.G. Revesz (Plenum Press, New York, 1986), pp. 13-28.
- [14] R.J. Araujo, *Phys. Chem. Glasses* **21** (1980), 193.
- [15] J.F. Stebbins & S.E. Ellsworth, *J. Am. Ceram. Soc.* **79** (1996), 2247.
- [16] S. Xu, L. Pan, F. Tian & X. Wu, *Act. Phys. Sin.* **37** (1988), 1866.
- [17] Y. Inagaki, H. Maekawa & T. Yokokawa, *Phys. Rev. B* **47** (1993), 674.
- [18] J.F. Stebbins, S. Sen & A.M. George, *J. Non-Cryst. Solids* **192&193** (1995), 298.
- [19] S. Sen, A.M. George & J.F. Stebbins, *J. Non-Crystal. Solids* **197** (1995), 53.
- [20] O.V. Mazurin, M.V. Streltsina & T.P. Shvaiko-Shvaikovskaya, *Handbook of Glass Data: Single-Component and Binary Non-Silicate oxide Glasses* (Elsevier, New York, 1983).
- [21] G.W. Scherer, *Relaxation in Glass and Composites* (Wiley, New York, 1986).
- [22] S. Sen & J.F. Stebbins, *Phys. Rev. B*, **55** (1997), 3512.
- [23] G.N. Greaves, S. J. Gurman, C. R. A. Catlow, A. V. Chadwick, S. Houde-Walter, C. M. B. Henderson & B. R. Dobson, *Phil. Mag. A* **64** (1991), 1059.
- [24] I. Farnan & J.F. Stebbins, *Science* **265** (1994), 1206.
- [25] J.F. Stebbins, S. Sen & I. Farnan, *Am. Mineral.* **80** (1995), 861.
- [26] I. Farnan & J.F. Stebbins, *J. Non-Cryst. Solids* **124** (1990), 207.
- [27] S.B. Liu, A. Pines, M. Brandriss & J.F. Stebbins, *Phys. Chem. Minerals* **15** (1987), 155.
- [28] I. Farnan & J.F. Stebbins, *J. Am. Chem. Soc.* **112** (1990), 32.
- [29] K. Schmidt-Rohr & H.W. Spiess, *Phys. Rev. Lett.* **66** (1991), 3020.

## STUDIES OF THE STRUCTURE OF $\text{Li}_2\text{O}-\text{B}_2\text{O}_3-\text{Al}_2\text{O}_3$ GLASSES USING $^{11}\text{B}$ NMR

Hyun-teh KIM

*Department of Physics Education, Chonnam National University,  
Kwang-ju, 500-757, South Korea.*

Suck-jong CHUNG

*Department of Physics, Chonnam National University,  
Kwang-ju, 500-757, South Korea*

and

Mann-jang PARK

*Department of Physics, Korea University, Seoul, 136-701,  
South Korea*

The  $^{11}\text{B}$  NMR technique has been employed to study the structure of glasses in the system  $\text{Li}_2\text{O}-\text{B}_2\text{O}_3-\text{Al}_2\text{O}_3$ . The values of  $N_4$ , the fraction of borons in tetrahedral coordination with oxygen, were measured and analyzed as a function of R and K (where,  $R=\text{mol}\% \text{Li}_2\text{O}/\text{mol}\% \text{B}_2\text{O}_3$ ,  $K=\text{mol}\% \text{Al}_2\text{O}_3/\text{mol}\% \text{B}_2\text{O}_3$ ). The results indicate that; (1) the formation of four coordinated borons and the formation of four coordinated aluminums associated with the network modifier lithium oxide are competing processes in the region  $R \leq R_{1st}$  (the point of the first transformation in  $N_4$ ), (2) in the region  $R < R_{1st}$ , there are both three and four coordinated aluminums in these glasses but in the region  $R \geq R_{1st}$ , only  $\text{AlO}_4$  units exist, (3) the  $R_{1st}$  glasses for all K families consist mainly of the lithium di-pentaborate units and the first modified lithium diborate units, (4) the  $R_{max}$  ( $N_4$  maximum point) glasses for all K families consist mainly of the lithium diborate units and the second modified lithium diborate units.

### 1. INTRODUCTION

It is well known that Nuclear Magnetic Resonance (NMR) is very useful for investigating the environments of boron atoms in several kinds of glasses [1,2]. In particular, NMR technique has been used to obtain the values of  $N_4$ , the fraction of borons in tetrahedral coordination with oxygen. Many authors proposed the well-defined structural models for the binary alkali and alkaline-earth borate glasses in a variety of experiments [1-8]. However, structural models for ternary borate glasses which contain other oxides were qualitative because of their structural complexity compared with the binary. Recent concerns have focused on developing quantitative models for analysis of the



ternary glasses as a function of composition [9-11]. Some clear structural models have been reported from studies of glasses in the systems  $\text{Na}_2\text{O}-\text{B}_2\text{O}_3-\text{SiO}_2$  [9],  $\text{PbO}-\text{B}_2\text{O}_3-\text{SiO}_2$  [10],  $\text{K}_2\text{O}-\text{B}_2\text{O}_3-\text{P}_2\text{O}_5$  [11] and  $\text{Li}_2\text{O}-\text{B}_2\text{O}_3-\text{SiO}_2$  [12].

On the other hand, the coordination relationship of aluminum with oxygen in ternary glasses has not yet been clearly identified. It was reported by Moore [13] and Owen [14] that all aluminum atoms in the glasses bind with four oxygens. From  $^{27}\text{Al}$  spectra of the crystals and glasses containing aluminum oxides, it is inferred by Bray [15] and Park [16] that the aluminate glasses do not have all four-coordinated aluminum atoms but can have six-coordinated aluminum.

In this paper, the values of  $N_4$  for ternary lithium boroaluminate glasses are measured and analyzed as a function of  $R$  ( $=\text{mol}\% \text{Li}_2\text{O}/\text{mol}\% \text{B}_2\text{O}_3$ ) and  $K$  ( $=\text{mol}\% \text{Al}_2\text{O}_3/\text{mol}\% \text{B}_2\text{O}_3$ ). The role of aluminum is discussed and structural models are proposed to explain these data.

## 2. EXPERIMENTAL

Thirty-one glass samples were made spanning the glass-forming region with various compositions. The compositions were chosen so that the glasses were grouped into families, each family having the same  $K$  value but different  $R$  values, as shown in Fig. 1 and Table 1. Reagent grade lithium carbonate ( $\text{Li}_2\text{CO}_3$ ), orthoboric acid ( $\text{H}_3\text{BO}_3$ ) and aluminum oxide ( $\text{Al}_2\text{O}_3$ ) were thoroughly mixed together. The mixtures were placed in a platinum crucible and fused at approximately  $1100^\circ\text{C}$  in an electric muffle furnace until all bubbles disappeared. The melts were agitated thoroughly to ensure homogeneity and then poured on a carbon mold and quickly covered with a brass block. Both mold and block were initially at room temperature. It was necessary to use rapid quenching techniques

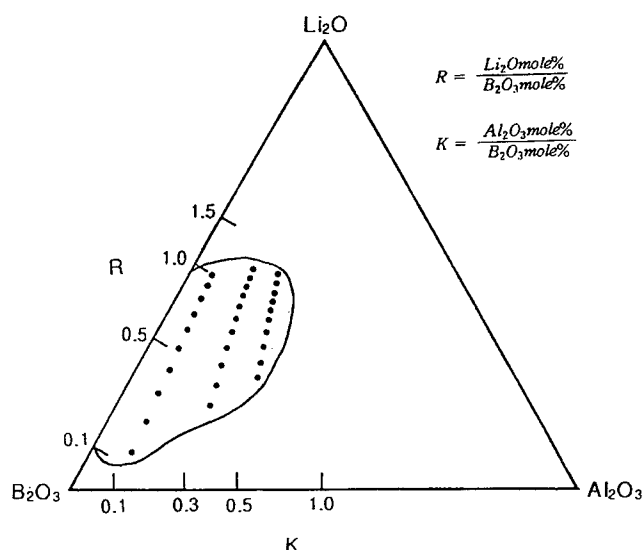


Fig. 1. Diagram of  $\text{Li}_2\text{O}-\text{B}_2\text{O}_3-\text{Al}_2\text{O}_3$  system, showing glass compositions.

**Table 1.**  
Experimentally obtained values of  $N_4$  for glasses in the system  $\text{Li}_2\text{O}-\text{B}_2\text{O}_3-\text{Al}_2\text{O}_3$ .

R	K	$\text{Li}_2\text{O}$ mol%	$\text{B}_2\text{O}_3$ mol%	$\text{Al}_2\text{O}_3$ mol%	$N_4$
0.1	0.1	8.33	83.33	8.33	0.09
	0.2	15.38	76.92	7.69	0.18
	0.3	21.42	71.42	7.14	0.26
	0.4	26.66	66.66	6.66	0.32
	0.5	31.25	62.50	6.25	0.38
	0.6	35.29	58.82	5.88	0.42
	0.7	38.88	55.55	5.55	0.45
	0.8	42.11	52.63	5.26	0.44
	0.9	45.00	50.00	5.00	0.40
	1.0	47.61	47.62	4.76	0.38
0.3	0.3	18.75	62.50	18.75	0.14
	0.4	23.53	58.82	17.65	0.19
	0.5	27.78	55.56	16.66	0.24
	0.6	31.58	52.63	16.66	0.24
	0.7	35.00	50.00	15.00	0.28
	0.8	38.10	47.62	14.29	0.29
	0.9	40.91	45.45	13.64	0.30
	1.0	43.48	43.48	13.04	0.31
	1.1	45.83	41.67	12.50	0.29
	1.2	48.00	40.00	12.00	0.27
0.5	1.3	50.00	38.46	11.54	0.24
	0.5	25.00	50.00	25.00	0.12
	0.6	28.57	47.62	23.81	0.14
	0.7	31.82	45.45	22.73	0.17
	0.8	34.78	43.48	21.74	0.19
	0.9	37.50	41.66	20.83	0.20
	1.0	40.00	40.00	20.00	0.20
	1.1	42.31	38.46	19.23	0.21
	1.2	44.44	37.04	18.52	0.22
	1.3	46.43	35.71	17.85	0.20
	1.4	48.28	34.48	17.24	0.17

in order to make these glasses. Glasses were transparent and showed no sign of devitrification when checked by X-ray diffraction techniques. All the glasses were crushed into powder and sealed in polystyrene vials for the  $^{11}\text{B}$  NMR study.

A Varian Associates Wide Line NMR spectrometer (V-4200B) was employed in connection with a Nicolet Signal Averager (Model 1072). The NMR spectra were obtained at a fixed frequency of 17 MHz by sweeping the magnetic field through the resonance condition. All measurements on the glass samples were performed at room temperature.

### 3. RESULTS AND DISCUSSION

The integral forms of the  $^{11}\text{B}$  NMR absorption spectra for all the glasses studied consist of two parts. Typical examples of experimental spectra are shown in Fig. 2. A central gaussian peak arises from boron atoms in oxygen tetrahedra

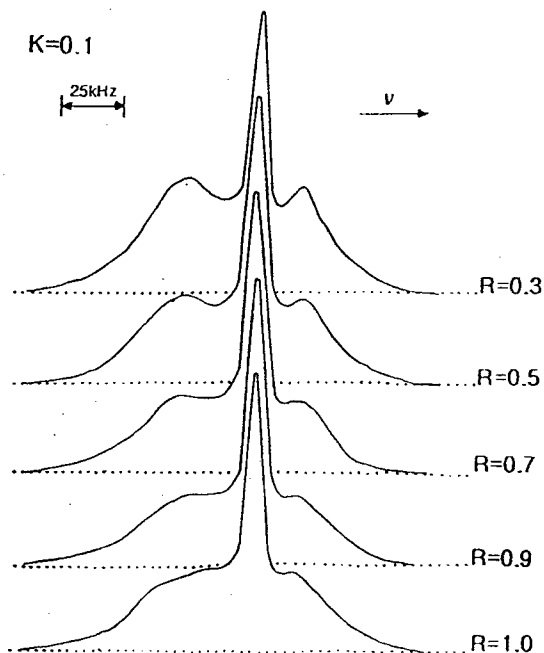


Fig. 2. Experimental  $^{11}\text{B}$  NMR spectra of the glasses of  $K=0.1$  family in the system  $\text{Li}_2\text{O}-\text{B}_2\text{O}_3-\text{Al}_2\text{O}_3$ .

$\text{BO}_4$  unit) while boron atoms at the center of oxygen triangles ( $\text{BO}_3$  units) yield a broad peak due to a larger interaction between the  $^{11}\text{B}$  nuclear quadrupole moment and the electric field gradient present at the boron site [2]. A direct measurement of the area under the central peak with respect to the total area gives the fraction of  $N_4$ . To obtain the values of the fraction  $N_4$  from these spectra, both the area method [17] and the computer simulation [18] have been employed. The two  $N_4$  values for a given sample agreed well within experimental error.

The measured values of  $N_4$  are listed in Table 1 and plotted as a function of  $R$  for fixed  $K$  in Fig. 3. The plots are separated into three families, each corresponding to one  $K$  value. In the figure, the dotted lines show the  $N_4$  values of binary ( $K=0$ ) glass system of  $\text{Li}_2\text{O}-\text{B}_2\text{O}_3$  [7] and the solid lines show the values resulting from least squares fits. The straight lines with arrows will be discussed later. It can be noticed that as  $K$  ( $=\text{mol}\% \text{Al}_2\text{O}_3/\text{mol}\% \text{B}_2\text{O}_3$ ) increases,  $N_4$  values show two transformation points. Up to the first transformation point, they steadily increase and then the slope changes after that point. At the second transformation point, they reach the maximum, and then decrease gradually. The term 'transformation' is used here as the slopes change. As can be seen in Fig. 3,  $N_4$  values decrease as  $K$  increases ( $\text{Al}_2\text{O}_3$  increases). Thus we can assume that  $\text{Al}_2\text{O}_3$  accepts  $\text{Li}_2\text{O}$  more preferentially than  $\text{B}_2\text{O}_3$ , and then forms  $\text{AlO}_4$  (*hypothesis 1*). This follows the assumption that  $\text{AlO}_4$  units are formed according to the amount of  $\text{Li}_2\text{O}$  ( $\text{mol}\%$ )

accepted by  $\text{Al}_2\text{O}_3$ , due to the electrical neutrality. And it is also based on the fact that all the amounts of  $\text{B}_2\text{O}_3$  accepting  $\text{Li}_2\text{O}$  change from  $\text{BO}_3$  unit to  $\text{BO}_4$  unit in binary glasses (remember:  $N_4=R$ ,  $R \leq R_{\max}$  in binary) [3]. Based on hypothesis, the amount (mol%) of  $\text{B}_2\text{O}_3$  change balanced by  $\text{Li}_2\text{O}$  is as follows:

$$\text{mol\% of } \text{B}_2\text{O}_3 \text{ change balanced by } \text{Li}_2\text{O} = \text{mol\% Li}_2\text{O} - \text{mol\% Al}_2\text{O}_3 \quad (1)$$

As mentioned above, all of the  $\text{B}_2\text{O}_3$  change is balanced by  $\text{Li}_2\text{O}$  changes from  $\text{BO}_3$  units to  $\text{BO}_4$  units. Therefore, at least in the region  $R \leq R_{\max}$ ,  $N_4$  can be calculated from the relation:

$$N_4 = \frac{(x)\text{mol\% Li}_2\text{O} - (z)\text{mol\% Al}_2\text{O}_3}{(y)\text{mol\% B}_2\text{O}_3} \quad (2a)$$

With the definition of  $K$  and  $R$ , the above formula can be rewritten as follows:

$$N_4 = R - K \quad (2b)$$

Thus,  $N_4$  values for  $K=0.1$ ,  $0.3$  and  $0.5$  should be as follows, respectively:

$$N_4 = R - 0.1 \text{ (for } K=0.1) \quad (3a)$$

$$N_4 = R - 0.3 \text{ (for } K=0.3) \quad (3b)$$

$$N_4 = R - 0.5 \text{ (for } K=0.5) \quad (3c)$$

These equations are plotted on Fig. 3. From the figure, the experimentally obtained data clearly do not follow Eqs. (3a-c). Therefore, the hypothesis 1 above that  $\text{Al}_2\text{O}_3$  accepts  $\text{Li}_2\text{O}$  in exclusive preference to  $\text{B}_2\text{O}_3$  forming  $\text{AlO}_4$

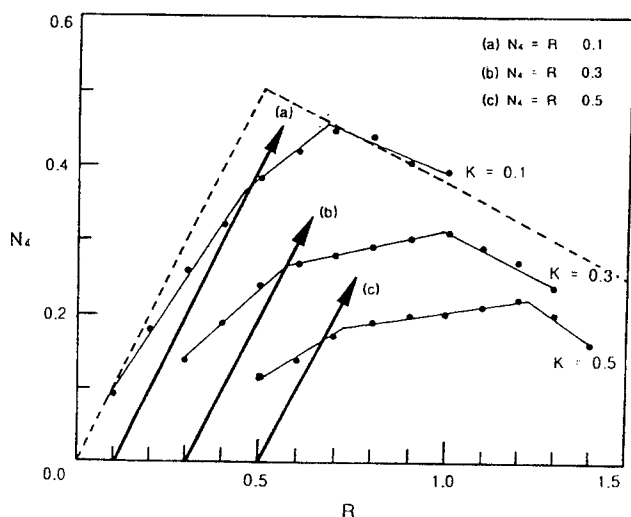


Fig. 3.  $N_4$  values of the glasses in the system  $\text{Li}_2\text{O}-\text{B}_2\text{O}_3-\text{Al}_2\text{O}_3$  as a function of  $R$ , containing postulation equations.

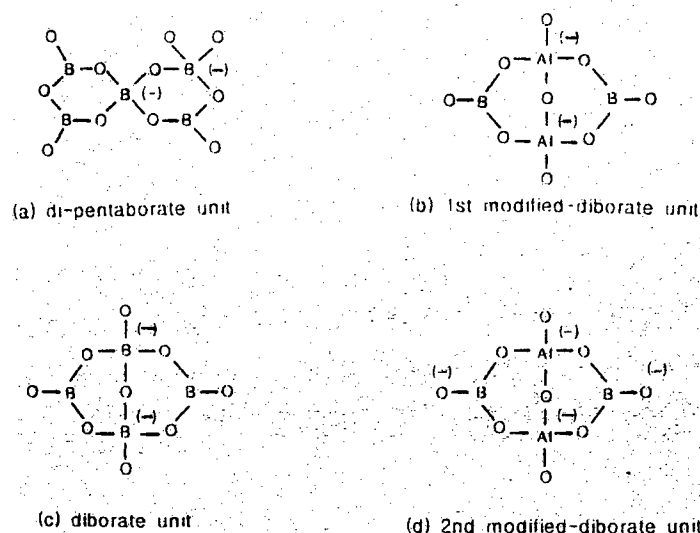


Fig. 4. Structural units related to the glasses in the system  $\text{Li}_2\text{O}-\text{B}_2\text{O}_3-\text{Al}_2\text{O}_3$ .

units is false. As shown in Fig. 3, the lines of the constraint equation (3a-c) pass the first transformation points with some deviations. According to hypothesis 1, the first transformation points indicate that  $\text{Al}_2\text{O}_3$  (mol.%) receives the same amount of  $\text{Li}_2\text{O}$  (mol.%) as its own mole fraction. This will be discussed below (when hypothesis 3 is discussed).

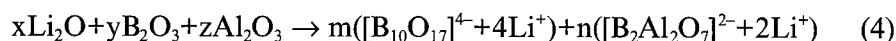
If Al (strictly speaking  $\text{Al}_2\text{O}_3$ ) does not interact with the boron structure of ternary glasses,  $N_4$  values of ternary glasses ought to be the same as those of binary glasses without being influenced by K value (the amount of  $\text{Al}_2\text{O}_3$ ) (hypothesis 2). As seen in Fig. 3, however, this is clearly not true. Therefore, it can be said that B (strictly speaking  $\text{B}_2\text{O}_3$ ) and Al (strictly speaking  $\text{Al}_2\text{O}_3$ ) compete with each other in attracting  $\text{Li}_2\text{O}$ .

As discussed above, hypothesis 1 was clearly false. Thus, up to the first transformation point,  $\text{Al}_2\text{O}_3$  receives  $\text{Li}_2\text{O}$  less than its own mole fraction. At the same time  $\text{B}_2\text{O}_3$  also receives  $\text{Li}_2\text{O}$  much less than its own mole fraction. These facts mean that  $\text{Al}_2\text{O}_3$  ( $\text{AlO}_3$  units) and  $\text{B}_2\text{O}_3$  ( $\text{BO}_3$  units) should form  $\text{AlO}_4$  (strictly twice mol% of  $\text{Li}_2\text{O}$ ) and  $\text{BO}_4$  (twice mol% of  $\text{Li}_2\text{O}$ ), respectively, so much as they receive  $\text{Li}_2\text{O}$  (mol%) to maintain electrical neutrality. Therefore, we consider that, below the first transformation point,  $\text{AlO}_3$  and  $\text{AlO}_4$  may coexist as  $\text{BO}_3$  and  $\text{BO}_4$ .

It is known that in binary alkali-borate glasses, the structure of the glasses with maximum  $N_4$  values,  $R_{\max}=0.5$ , consists primarily of diborate units [3,5,6]. This means that the diborate units are the structure which can hold the maximum  $\text{BO}_4$  units (incremental factor of  $N_4$ ). As shown in Fig. 3, the  $N_4$  values of ternary glasses with aluminum oxide are always less than those of binary lithium borate glasses. It can thus be inferred that added aluminum oxide af-

fects the structure of diborate units.

In addition, it is known that binary glasses with  $R=0.4$  consist primarily of dipentaborate units (Fig. 4) [3,5,6]. As shown in Fig. 3, the first transformation point of ternary glasses with the least aluminum ( $K=0.1$ ) is near to  $R=0.4$ . Therefore, we assume that the glasses at the first transformation points consist mainly of the dipentaborate units and the first modified diborate units (*hypothesis 3*). The dipentaborate units are formed by  $1/2(2\text{Li}_2\text{O} \bullet \text{B}_2\text{O}_3)$ , which has three  $\text{BO}_3$  units and two  $\text{BO}_4$  units. The first modified diborate units (cf. Fig. 4) are formed by  $\text{Li}_2\text{O} \bullet \text{B}_2\text{O}_3 \bullet \text{Al}_2\text{O}_3$  to have two  $\text{BO}_3$  units and two  $\text{AlO}_4$  units. The prefix 'first modified' means that original diborate structure has changed and then follows second modification. The reaction equation for the above hypothesis can be written as follows:



Considering the coefficients of Li, B, Al of the equation, one gets;

$$\text{Li,} \quad 2x = 4m + 2n \quad (5a)$$

$$\text{B,} \quad 2y = 10m + 2n \quad (5b)$$

$$\text{Al,} \quad 2z = 2n \quad (5c)$$

From the above equations and the definitions of  $R$  and  $K$ , one gets;

$$R_{1st} = \frac{2}{5} + \frac{3}{5}K \quad (6)$$

where the subscript '1st' in  $R_{1st}$  means the first transformation point. According to Eq. 6), when  $K$  is 0.1, 0.3 and 0.5,  $R_{1st}$  values should be 0.46, 0.58 and 0.70, respectively. As shown in Fig. 3, the experimental  $R_{1st}$  values corresponding to  $K=0.1$ , 0.3 and 0.5 are 0.45, 0.57 and 0.70, respectively. Both values are in good agreement within experimental error.

Considering Eq. (4),  $N_4$  can be written as;

$$N_{4,1st} = \frac{m \bullet \text{number of } \text{BO}_4 \text{ in first term} + n \bullet \text{number of } \text{BO}_4 \text{ in second term}}{m \bullet \text{number of B in first term} + n \bullet \text{number of B in second term}} \quad (7)$$

where  $N_{4,1st}$  means  $N_4$  values corresponding to  $R_{1st}$ . From Eqs (5a-c),  $m$  and  $n$  are

$$m = \frac{1}{5}(y - z) \quad (8a)$$

$$n = z \quad (8b)$$

Considering the Eq. (4), (8) and the definition of  $R$  and  $K$ ,  $N_{4,1st}$  in Eq (7) is:

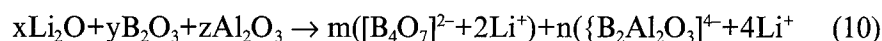
$$N_{4,1st} = \frac{2}{5}(1 - K) \quad (9)$$

From Eq. (9), when  $K$  is 0.1, 0.3 and 0.5, the  $N_{4,1st}$  values are 0.36, 0.28 and

0.20, respectively. As shown in Fig.3,  $N_{4,1st}$  values corresponding to  $K=0.1$ , 0.3 and 0.5 are 0.36, 0.27 and 0.18, respectively. Both values are in good agreement within experimental error.

These results support our choice of structure for the first modified diborate unit and suggest that the glasses at the first transformation point consist mainly of these units and the dipentaborate units. From the structures of the glasses at the first transformation point, we can recognize that all  $Al_2O_3$  forms only  $AlO_4$  units at that point and  $AlO_4$  units are formed by the amount of  $Li_2O$  accepted by  $Al_2O_3$  to maintain the electrical neutrality, as mentioned above.

It is well known that if  $R$  becomes more than 0.5, the metaborate units ( $BO_3^-$  unit) increases [6]. As can be seen in Fig. 3, the second transformation point ( $R=0.65$ ) with maximum  $N_4$  values in ternary glasses with the least aluminum added to binary  $Li_2O-B_2O_3$  glasses is close to  $R=0.5$ . In addition, aluminum oxide added to the ternary glass system affects the diborate unit structure, as mentioned above. From these explanations, we can guess that the glasses at the second transformation point with maximum  $N_4$  values consist mainly of diborate units and secondly modified diborate units (*hypothesis 4*). The diborate units (cf. Fig. 4) are formed with  $Li_2O \bullet 2B_2O_3$  and have two three-coordinated borons ( $BO_3$ ) and two four-coordinated borons ( $BO_4$ ). The second modified diborate units (cf. Fig. 4) are formed with  $2Li_2O \bullet B_2O_3 \bullet Al_2O_3$ , which have two  $BO_3^-$  units and two  $AlO_4$  units. The above hypothesis can be written with the reaction equation as follows:



Considering the coefficients of Li, B, Al, one gets:

$$Li: \quad 2x = 2m + 4n \quad (11a)$$

$$B: \quad 2y = 4m + 2n \quad (11b)$$

$$Al: \quad 2z = 2n \quad (11c)$$

From the above equations and the definition of  $K$  and  $R$ , one gets;

$$R_{max} = \frac{1}{2} + \frac{3}{2}K \quad (12)$$

where the subscript 'max' in  $R_{max}$  means that it corresponds to the maximum  $N_4$  values. According to Eq. (12),  $R_{max}$  values for  $K=0.1$ , 0.3 and 0.5 are to be 0.65, 0.95 and 1.25, respectively. As seen in Fig. 3, the experimentally obtained  $R_{max}$  values for  $K=0.1$ , 0.3 and 0.5 are 0.65, 0.98 and 1.24, respectively. It can be said that these values are in good agreement with each other within experimental error.

To obtain  $N_{4,max}$  values from the reaction equation (10), the same method is used as for  $N_{4,1st}$  values.  $N_{4,max}$  values found by the same method for  $K=0.1$ , 0.3 and 0.5 are 0.45, 0.35 and 0.25, respectively. As can be seen in Fig. 3, the experimentally obtained  $N_{4,max}$  values for  $K=0.1$ , 0.3 and 0.5 are 0.45, 0.32 and 0.24,

respectively. These values are in good agreement within experimental error.

The results support our assumption that the second modified diborate unit exists. Furthermore,  $\text{Al}_2\text{O}_3$  has maintained the  $\text{AlO}_4$  structure in spite of receiving twice its own amount of  $\text{Li}_2\text{O}$ . It can be inferred that the Al atoms remain in  $\text{AlO}_4$  units in the region beyond  $R_{\text{max}}$ .

In conclusion, we can say that  $R_{\text{max}}$  glasses consist mainly of diborate units and second modified diborate units, and that, although  $\text{AlO}_3$  units coexist with  $\text{AlO}_4$  units in the region below  $R_{\text{1st}}$ , there are only  $\text{AlO}_4$  units in the region above  $R_{\text{1st}}$ .

## REFERENCES

- [1] A.H. Silver & P.J. Bray, *J. Chem. Phys.* **29** (1958), 984.
- [2] P.J. Bray & J.G. O'Keefe, *Phys. Chem. Glasses* **4** (1963), 37.
- [3] J. Krogh-Moe, *Phys. Chem. Glasses* **6** (1965), 46.
- [4] C. Rhee & P.J. Bray, *Phys. Chem. Glasses* **12** (1971), 165.
- [5] M.J. Park & P.J. Bray, *Phys. Chem. Glasses* **13** (1972), 50.
- [6] G.E. Jellison & P.J. Bray, *Solid State Comm.* **19** (1976), 517.
- [7] Y.H. Yun & P.J. Bray, *J. Non-Cryst. Solids* **44** (1981), 227.
- [8] I.A. Harris & P.J. Bray, *Phys. Chem. Glasses* **25** (1984), 69.
- [9] Y.H. Yun & P.J. Bray, *J. Non-Cryst. Solids* **27** (1978), 363.
- [10] K.S. Kim, P.J. Bray & S. Merrin, *J. Chem. Phys.* **64** (1976), 4459.
- [11] Y.H. Yun & P.J. Bray, *J. Non-Cryst. Solids* **30** (1978), 45.
- [12] T. Kim *et al.*, *New Physics* (Korean Phys. Soc.) **27** (1987), 257.
- [13] H. Moore & H. Winkelmann, *J. Soc. Glass Technol.* **43** (1955), 254.
- [14] A.E. Owen, *Phys. Chem. Glasses* **2** (1961), 87.
- [15] S.G. Bishop & P.J. Bray, *Phys. Chem. Glasses* **7** (1966), 41.
- [16] S.J. Chung & M.J. Park, *et al.*, *J. Korean Phys. Soc.* **14** (1980), 59.
- [17] M.E. Milberg, I.G. O'Keefe, *et al.*, *Phys. Chem. Glasses* **13** (1972), 79.
- [18] P.C. Taylor & P.J. Bray, *J. Non-Cryst. Solids* **2** (1970), 305.



## SOME PARADOXES OF BORATE GLASSES AND MELTS

Evgenii A. PORAI-KOSHITS

*I. V. Grebenshchikov Institute of Silicate Chemistry of the  
Russian Academy of Sciences, Ul. Odoevskogo, 24, Korp. 2,  
Sankt Petersburg, 199155, Russia*

and

Adrian C. WRIGHT

*J.J. Thomson Physical Laboratory, University of Reading,  
Whiteknights, Reading, RG6 6AF, UK*

An account is given of some of the paradoxes of borate glasses and melts and their possible explanations. These concern the inhomogeneous structure of borate glasses on the nanometre scale and include the nature of the regions of inhomogeneity in glasses such as  $B_2O_3$ - $SiO_2$ . The latter are termed *pseudophases*, since they are not regions of metastable immiscibility, which are absent in all of the alkali borate glass systems except  $Li_2O$ - $B_2O_3$ . Breaks in the temperature dependence of the X-ray scattering from thermal density fluctuations in borate melts, at the liquidus temperature or above, are explained in terms of rearrangements of the superstructural units present as a function of temperature.

### 1. INTRODUCTION

There are various paradoxes associated with borate glasses, some of which arise because borate glasses do not conform to the conventional interpretation of the Zachariasen [1] and Warren [2,3] random network theory while others are common to a much wider range of glass-forming systems. Some of these paradoxes are the subject of the present paper, which will primarily address the use of small angle X-ray scattering (SAXS) techniques to study what has been termed the range IV order [4] (i.e. density fluctuations on the scale  $1\text{ nm}=10\text{ \AA}$  or larger).

Clearly, the range IV order is a consequence of the basic structural units that form the vitreous network and it is in this range I order that borate glasses first deviate from the conventional random network picture. First, the addition of a conventional network modifier to vitreous  $B_2O_3$  leads initially to the conversion of  $BO_3$  triangles into  $BO_4$  tetrahedra, rather than the formation of non-bridging oxygen atoms; i.e. network modifiers act as *network strengtheners* rather than *network breakers* and lead to more compact regions in the network with increased rigidity/connectivity.

The second major way in which borate glasses differ concerns the important structural role played by **superstructural units**, which comprise well-defined and effectively rigid arrangements of the basic  $\text{BO}_3$  and  $\text{BO}_4$  structural units with no internal degrees of freedom in the form of variable bond or torsion angles, as shown in Fig. 1 of the accompanying paper by Sinclair *et al.* [5]. The idea that well-defined groupings, larger than the basic structural units, exist in glasses was first postulated by Hägg [6], following the publication of Zachariasen's original paper in 1932 [1]. Although dismissed by Zachariasen [7], Hägg's ideas were later adopted and extended by Krogh-Moe [8], who was particularly interested in borate glasses and stressed the identity between the larger groupings (superstructural units) in these glasses and those in the corresponding crystalline materials. Support for this hypothesis is provided by the extensive nuclear magnetic resonance (NMR) studies of Bray and co-workers [9,10], who propose a structural model comprising a modified Warren-Zachariasen network in which the superstructural units, rather than the basic  $\text{BO}_3$  and  $\text{BO}_4$  structural units, are connected randomly to each other [11].

The fact that borate glasses are formed from these larger units may be expected to have important consequences for the density and composition fluctuations occurring in the resulting vitreous network, i.e. the range IV order. In any random network constructed from essentially rigid units with a well-defined connectivity and stereochemistry, the characteristic dimension and magnitude of the local fluctuations in the network density, and in the composition for glasses with more than one component, will depend on the size and stereochemistry of the units in question. Such density fluctuations may be seen, for example, in the well-known random network schematic of Zachariasen [1]. It might therefore be expected that the presence of the much larger superstructural units in borate glasses will result in an increase in the characteristic length of the contribution to the fluctuations arising from the borate **network** component.

In the following sections, the nature of the range IV order in borate glasses will be discussed and, in particular, the mystery of the so-called **pseudophases** in some two-component borate glass systems (e.g.  $\text{B}_2\text{O}_3\text{-SiO}_2$ ). To date, this mystery has not been solved, although SAXS measurements prove that they are not regions of metastable immiscibility. A second paradox, which will be considered, concerns the breaks in the temperature dependence of the general **magnitude** of both the conventional SAXS intensity and the X-ray scattering immediately below the first diffraction peak (here designated intermediate angle X-ray scattering, IAXS, rather than medium angle X-ray scattering, MAXS, as initially used by Porai-Koshits) for alkali borate **melts**, at and sometimes above the liquidus temperature,  $T_L$ .

## 2. FIRST PARADOX (ALKALI BORATE GLASSES)

The method of additivity was applied to various binary glass systems by Porai-Koshits in 1943 [12] and examples of its use for borate glasses are given in Figs 1 and 2. From Fig. 1, it can be seen that the X-ray diffraction intensity

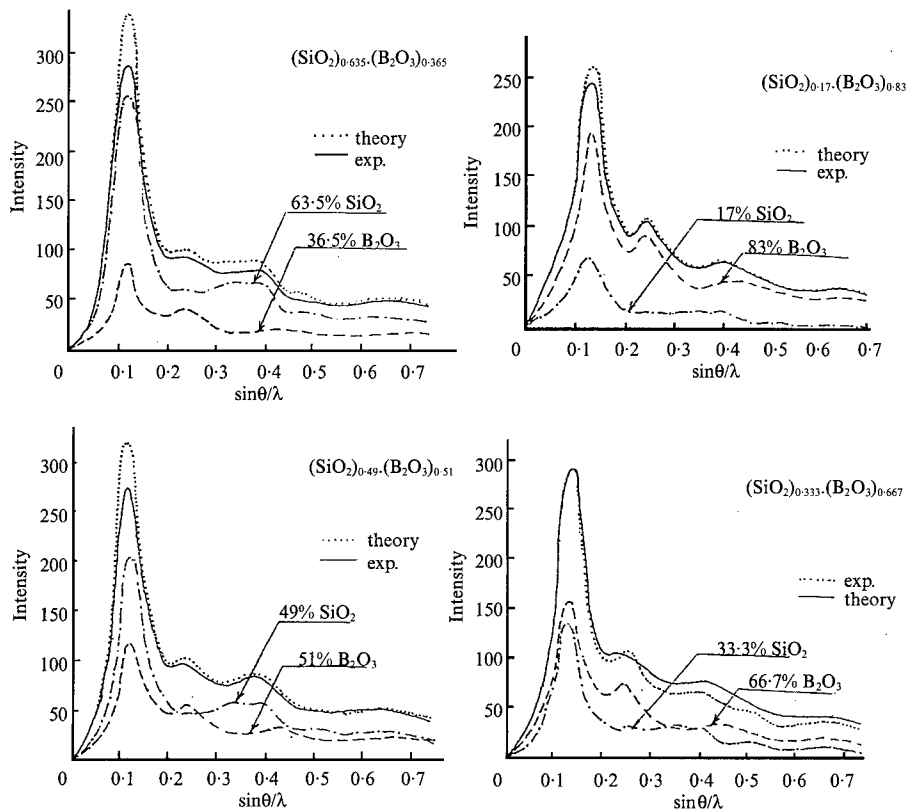


Fig. 1. Application, by Porai-Koshits [12], of the method of additivity to the diffraction pattern for vitreous  $B_2O_3$ - $SiO_2$  obtained by Warren *et al* [13].

for vitreous  $B_2O_3$ - $SiO_2$  at large angles (in absolute electron units, e.u.) is a simple sum of the curves for pure boron oxide and silica in proportion to their molecular content. A similar result was obtained for sodium borate glasses, which were modelled by a combination of the patterns for  $B_2O_3$  and  $NaBO_2$ . The small differences in the region of the first diffraction peak were attributed to inaccuracies in the photographic measurement of the diffracted X-ray intensities. However, the first diffraction peak reflects the periodicity resulting from the network cages [15] and hence is associated with larger distances than those within the units/groupings from which the network is built and which dominate the diffraction pattern at higher scattering vector magnitudes,  $Q$ . Thus it might be expected that discrepancies would occur on this length scale.

The above results demonstrate the independence of the scattering from the constituents of complex glasses with respect to their composition, for length scales shorter than those characteristic of the first diffraction peak. For example, it means that, in two-component glasses, the vitreous silica and boron oxide form some homogeneous regions, but not a random disordered network.

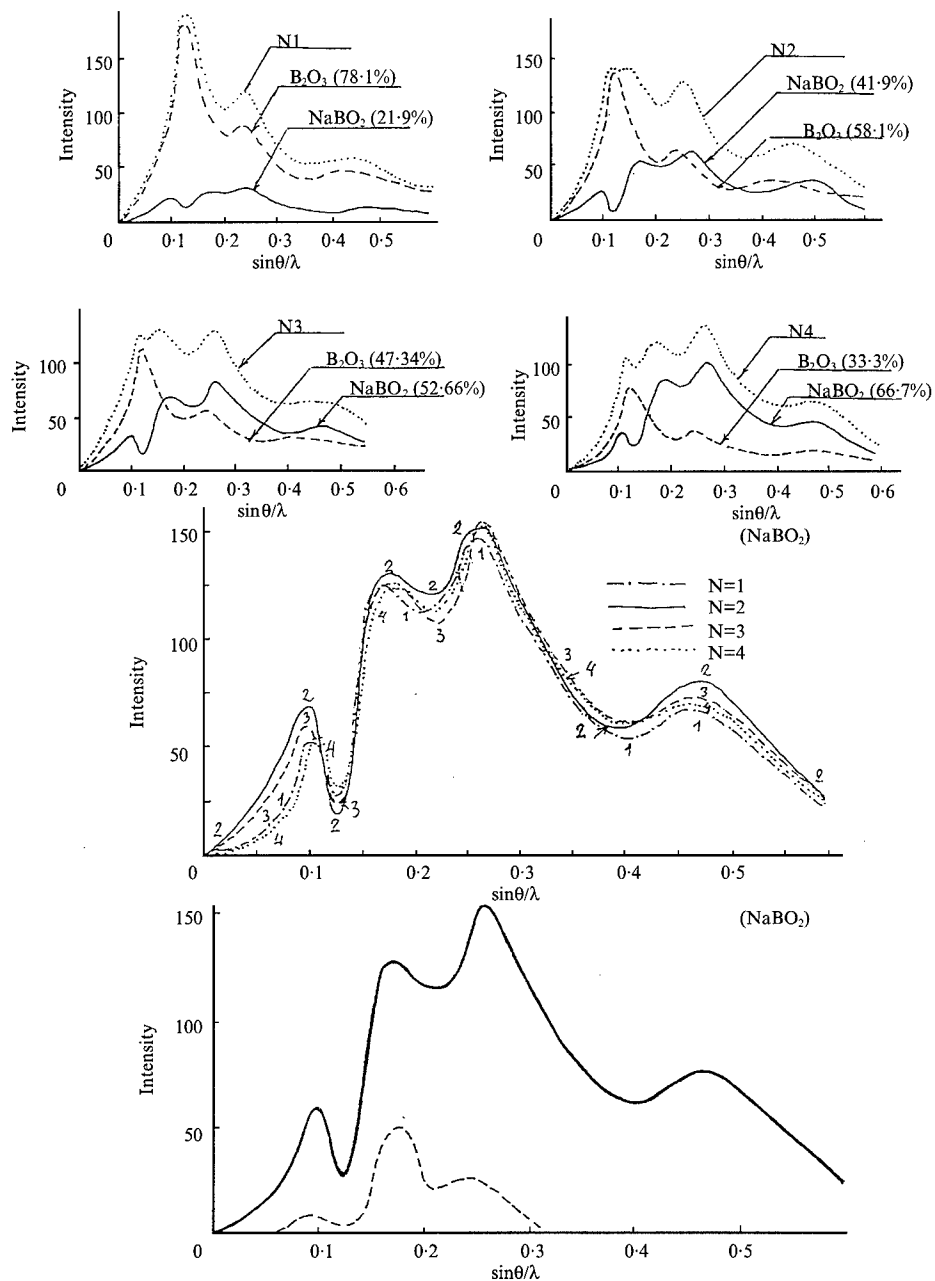


Fig. 2. Application, by Porai-Koshits [12], of the method of additivity to the diffraction pattern for vitreous  $\text{Na}_2\text{O}-\text{B}_2\text{O}_3$  obtained by Warren *et al* [14].

The same additivity is present in some other two-component glasses, including the sodium silicate system.

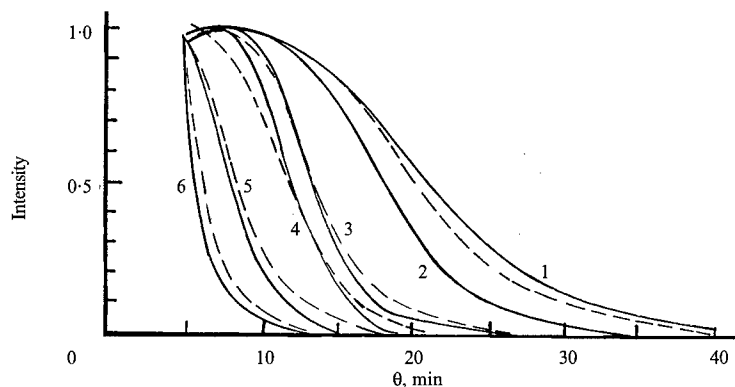


Fig. 3. SAXS intensity for initial glasses (solid lines) and the porous glasses obtained from them by leaching (dashed lines) [16,17]. Heat treatments: (1), 530°C, 5 h; (2), 600°C, 1 h; (3), 600°C, 4 h; (4), 600°C, 8 h; (5), 650°C, 1 h and (6), 650°C, 6 h.

Fifteen years later, in 1958, Andreev [16,17] first applied the SAXS technique to the investigation of phase separated glasses, as shown in Fig. 3. Later, this technique was employed to study many different types of glasses. It was as a result of these SAXS experiments that the first paradox of alkali borate glasses appeared, as discussed at the conference in honour of N.J. Kreidl in Vienna in 1985 [18].

A decade earlier, Shaw & Uhlmann [19], using electron microscopy, found a metastable region of immiscibility in all five alkali borate glass systems (Li, Na, K, Rb and Cs) and constructed the corresponding immiscibility domes shown in Fig. 4. The same year a similar result was obtained for the  $B_2O_3$ - $SiO_2$

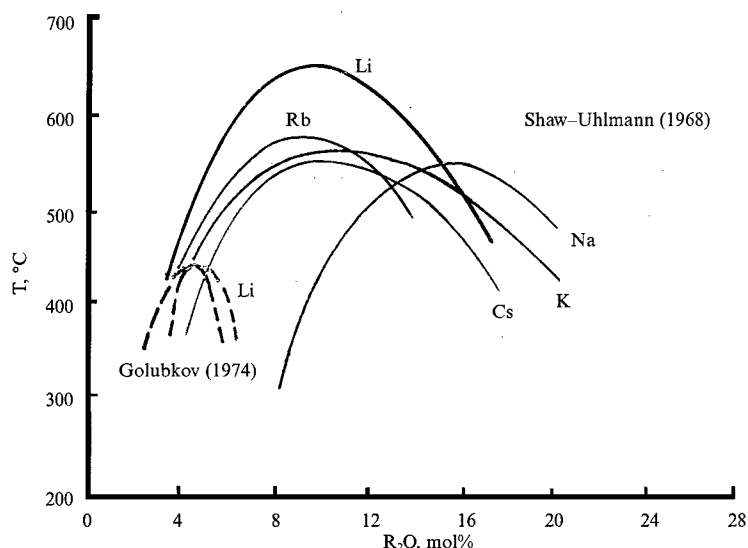


Fig. 4. Immiscibility dome for alkali borate glasses according to electron microscopy data [19] and to SAXS data for  $Li_2O$ - $B_2O_3$  glasses [18] (lower left curve).

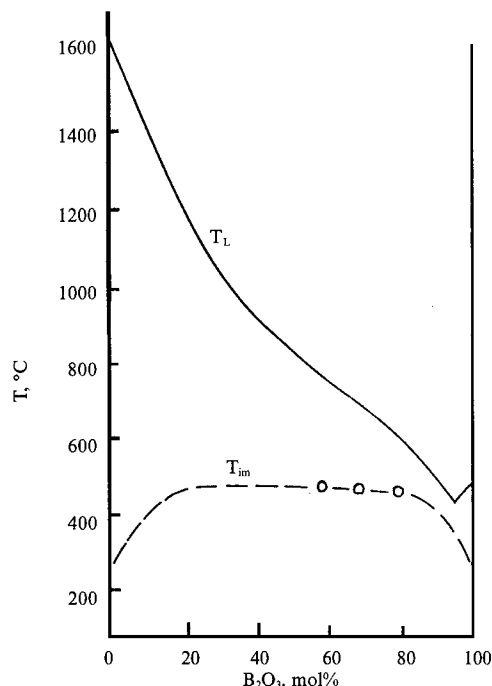
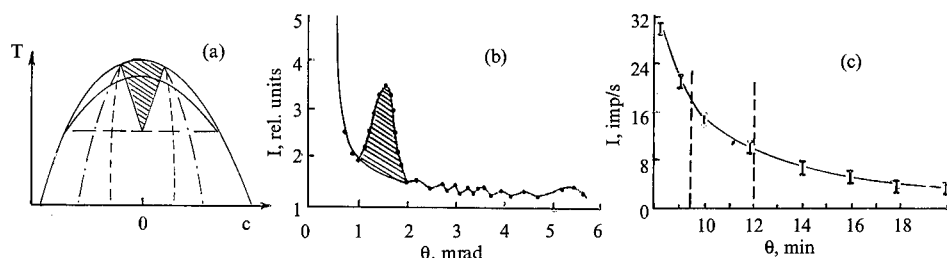


Fig. 5. Immiscibility dome for  $B_2O_3$ - $SiO_2$  glasses according to electron microscopy data [20].

system by Charles & Wagstaff [20]. As may be seen from Fig. 5, this dome was constructed using only three points!

Later, at the International Congresses on Glass in Kyoto (1974) and Prague (1977), Golubkov *et al.* [21,22] presented SAXS and IAXS results which make it quite clear that **phase separation is absent in all of the above systems, except  $Li_2O$ - $B_2O_3$** . This follows from the clearly established independence of the structure on isothermal annealing of any duration at any temperature below  $T_L$ . In the lithium borate system, a metastable immiscibility region was discovered, but the dome is located at quite a different place than that determined by Shaw & Uhlmann [19] (cf. Fig. 4).

In 1984, Döpkins and co-workers [23,24] tried to reconcile these contradictions in terms of the **modulated** structure peak (Fig. 6) which they had found by the SAXS method. However, Porai-Koshits *et al.* [18] failed to reproduce the results of Döpkins *et al.*, as demonstrated in Fig. 6, which shows (b) the modulated structure peak obtained by Döpkins *et al.* for a potassium borate glass at 600°C (Mo  $K_\alpha$  radiation) and (c) the SAXS curve obtained by Porai-Koshits *et al.* for a potassium borate glass heated at 500°C for 60 h (Cu  $K_\alpha$  radiation). For the latter, the vertical dashed lines delineate the composition region where the modulated structure peak should have been detected. It is possible that the modulated structure peak in Fig. 6(b) arises from small crys-



**Fig. 6.** Comparison of the results obtained by Döpkens *et al* [23,24] and Porai-Koshits *et al* [18]. (a), Stable region of modulated structure; (b), modulated structure peak for  $9\cdot8\text{K}_2\text{O}\cdot90\cdot2\text{B}_2\text{O}_3$  glass at  $600^\circ\text{C}$  (Mo  $\text{K}_\alpha$  radiation) and (c), SAXS curve obtained by Porai-Koshits *et al* for  $8\cdot5\text{K}_2\text{O}\cdot91\cdot5\text{B}_2\text{O}_3$  glass after heating at  $500^\circ\text{C}$  for 60 h (Cu  $\text{K}_\alpha$  radiation). The vertical dashed lines in (c) delineate the composition region where the modulated structure peak should have been detected.

talline particles, but this needs to be further investigated.

While the results of Charles & Wagstaff [20] can be rejected as artifacts [25,26], this is not unambiguously the case for those of Shaw & Uhlmann [19], as indicated by more recent results [27-29] suggesting the presence of regions of inhomogeneity in borate glasses, which have been termed *pseudophases*. A pseudophase may be defined as a stable microscopic region which has no phase boundaries and is characterised in terms of its electron density and size, as obtained from SAXS measurements. This pseudophase structure turns out to be a common feature of all of the two-component glasses studied by Porai-Koshits and co-workers, including both those containing alkali ions and those formed from two glass-forming oxides. Attention is drawn to the similar sizes of the regions of inhomogeneity in these glasses: in alkali borate glasses, the radii of these regions are 10-15 Å, in alkali silicate glasses 20-30 Å and in  $\text{B}_2\text{O}_3$ - $\text{SiO}_2$  and  $\text{B}_2\text{O}_3$ - $\text{GeO}_2$  glasses 10-20 Å; i.e. of the order of a nanometre. It is also very interesting to note that, above the glass transition temperature,  $T_g$ , the size and geometry of the pseudophase structure in borate glasses remains unchanged with increasing temperature up to 100-200 degrees in excess of  $T_g$ ; i.e. these are preserved in the (supercooled) melt. In a new book entitled *Two-Phase Glasses: Structure, Properties, Applications*, Mazurin *et al.* [30] write that phase separation is not usually observed in borate glasses and melts at temperatures higher than that of the glass transition region, except for a narrow region in the lithium borate system. Contrary to the opinion of the authors of this book, the term *pseudophases* is preferred for the regions of inhomogeneity in borate glasses, rather than the verbose expression *regions of inhomogeneity not of the phase-separated type*.

The above results are consistent with the existence of superstructural units in borate glasses and also suggest the possibility of studying them by small and intermediate angle scattering using both X-rays and neutrons. They do not, however, reveal the *nature* of the superstructural units nor do they explain the structural rearrangements comprising the submicroscopic pseudophases.

To understand this, further investigations are needed. Nevertheless, the existence of submicroheterogeneous pseudophases (and fluctuation structures) in borate glasses and melts seems to have been established, although this was not accepted by Uhlmann at the time of the N.J. Kreidl anniversary conference in Vienna [18]. Hence the question of the existence of pseudophases is repeated in the context of the present conference, specifically devoted to borate glasses.

### 3. SECOND PARADOX (ALKALI BORATE GLASSES AND MELTS)

In his well-known paper, Zachariasen [1] asserted that to find the structure of glass it is necessary to proceed from the structure of the corresponding crystalline modification and not from the liquid structure, which is even less understood. However, inorganic oxide glasses are the result of quenching the (supercooled) melt to a temperature below  $T_g$ . Hence, they inherit the structural characteristics of the latter, although in a modified form as a result of passing through the glass transition. Indeed, Zachariasen admitted the possibility of the existence of some structural order on a nanometre scale, but he supposed this to be experimentally hard to discover.

Warren [31] focussed Zachariasen's ideas further and wrote "the absence of SAXS by glasses proves their homogeneity on a scale larger than the interatomic distances." However, as indicated above, the SAXS technique demonstrated the existence of inhomogeneity in glasses, in the form of frozen-in density and composition fluctuations of different dimensions which, in the liquid above  $T_g$ , may be either static or dynamic in character. In practice, the

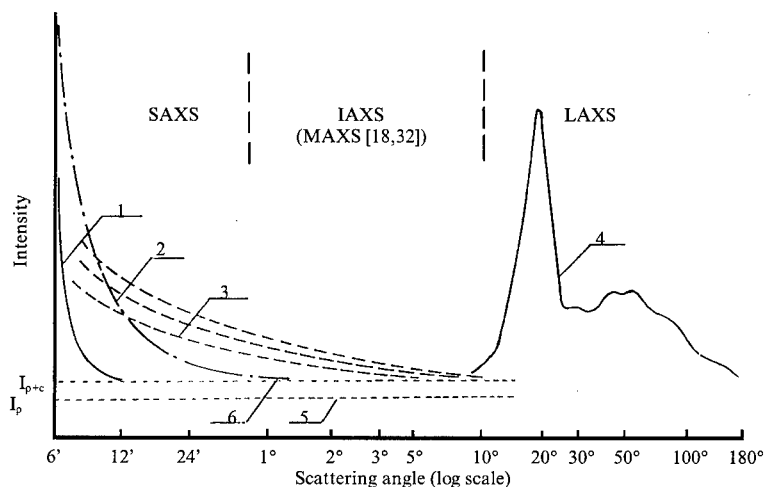


Fig. 7. Schematic representation of the combined SAXS, IAXS and conventional (LAXS) X-ray diffraction intensities for a glass and the different types of inhomogeneity responsible for this scattering [32]. (1), "technological inhomogeneity (approximate scattering region size 500-1000 Å); (2), metastable phase separation (20-1000 Å); (3), clusters, atomic groupings, submicroinhomogeneous structure of single phase glasses, etc. (5-20 Å) and (4), short range order (1-7 Å).  $I_p$  and  $I_{p+c}$  are the contributions from the thermal density and concentration fluctuations.



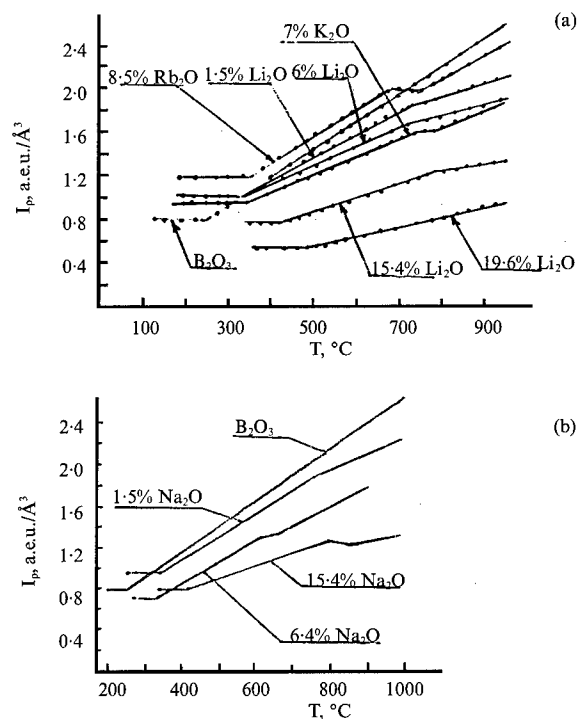


Fig. 8. The temperature dependence of  $I_p$  (in absolute units) for vitreous  $B_2O_3$  and some alkali borate glasses.

scattered X-ray intensity from a glass is a continuous function of angle, and hence  $Q$ , from the small angle region through the conventional diffraction range and hence it is difficult to isolate the contribution from each length scale.

Figure 7 presents a schematic representation of the combined SAXS, IAXS and conventional X-ray diffraction intensities for a glass and the different types/ranges of order responsible for this scattering [32]. These comprise (1) "technological" inhomogeneity (approximate scattering region size 500-1000 Å), (2) metastable phase separation (20-1000 Å), (3) clusters, atomic groupings, submicroinhomogeneous structure of single phase glasses, etc. (5-20 Å) and (4) short range order (1-7 Å).  $I_p$  and  $I_c$  are the contributions from the thermal density and concentration fluctuations. An analogous real-space analysis [4] is based on four ranges (cf. Section 1) but, at the present time, the interpretation of particularly ranges II {the interconnection of adjacent (super)structural units} and III (the network topology) is only possible with the help of computer modelling.

In the light of the above, it is necessary to discuss the results of investigations of the temperature dependence of the magnitude of the SAXS and IAXS arising from thermal fluctuations ( $I_{p+e}$ ) in both glasses and melts for the various alkali borate systems (Li, Na, K, Rb and Cs). From thermodynamics, it can be shown that, if the isothermal compressibility,  $\beta_T$ , is effectively inde-

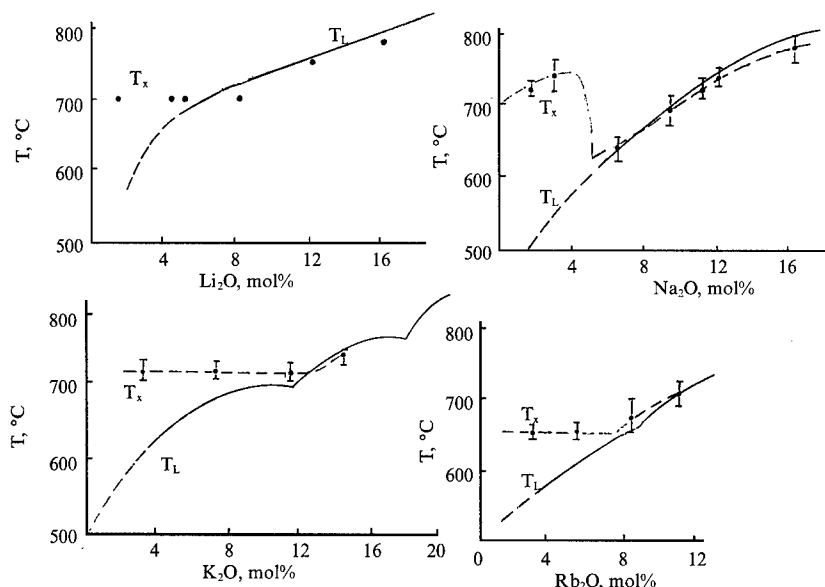


Fig. 9. A comparison of the liquidus temperature,  $T_L$ , and the temperature,  $T_x$ , of the break in the temperature dependence of  $I_p$ .

pendent of temperature,  $T$ ,  $I_p$  is directly proportional to  $T$ :

$$I_p = \langle \rho \rangle^2 k_B \beta_T V T \quad (1)$$

where  $\langle \rho \rangle$  is the mean electron density,  $k_B$  Boltzman's constant and  $V$  the scattering volume. An important result is the violation of this direct proportionality at the liquidus temperature in the case of both alkali borate and alkali silicate glasses with low alkali contents.

An example is given in Fig. 8, but similar results have been obtained many times and for many different melt compositions. The coincidence of the temperature,  $T_x$ , at which the break occurs, with  $T_L$  for all of the melts with more than 6-9 mol% alkali oxide is very interesting. These melts are very sensitive to the crossing of the liquidus temperature. Figure 9 includes both  $T_L$  and  $T_x$  and it can be seen that an exception from the above rule are the melts with less than 4-5 mol% alkali oxide. In this case,  $T_x$  is larger than  $T_L$  and coincides with  $T_L$  for the melts containing 12-14 mol% alkali oxide.

It has been suggested [33] that these regions of inhomogeneity are built up from superstructural units, which are temperature sensitive and change on passing through the liquidus temperature. This is supported by the NMR studies of Bray and co-workers [9,10], as shown in Fig. 10 [34] and the thermodynamic modelling studies of Shakhmatkin and co-workers [35]. Recently, Golubkov [36] has found a similar break in his data for pure  $B_2O_3$ . This is consistent with the fact that the boroxol groups in vitreous  $B_2O_3$  start to break up in the (supercooled) melt above  $T_g$ , as demonstrated by the Raman data of Walrafen *et al.* [37].

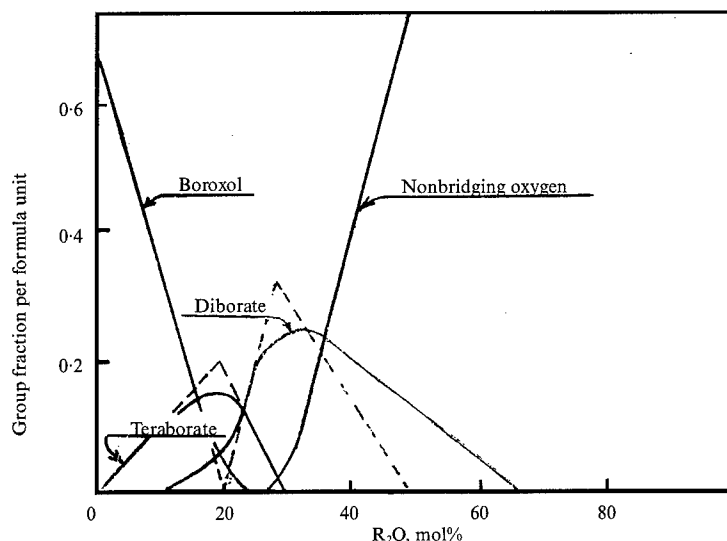


Fig. 10. A simple structural model for alkali borate glasses based on the work of Krogh-Moe & Bray [34].

#### 4. CONCLUDING REMARKS

The paradoxes discussed above are of course not the only unresolved mysteries connected with borate glasses and there are further extraordinary paradoxes or secrets of alkali borate glasses waiting to be resolved. Among these is the explanation of the transient effects in the SAXS intensity, from not only vitreous  $B_2O_3$  but also a sodium borate glass with 10 mol%  $Na_2O$ , on stepping the temperature through  $T_g$ , as discussed by Golubkov elsewhere in these proceedings [38], and similar light scattering studies of Bokov & Andreev [39]. The present paper has, however, summarised some of the long established peculiarities (paradoxes) of borate glasses. The progress of science in general lies in explaining paradoxes and of course in finding new ones. Such are the ways of fundamental science!

#### REFERENCES

- [1] W.H. Zachariasen, *J. Am. Chem. Soc.* **54** (1932), 3841.
- [2] B.E. Warren & J. Bischof, *J. Am. Ceram. Soc.* **21** (1938), 259.
- [3] B.E. Warren, *Chem. Rev.* **26** (1940), 237.
- [4] A.C. Wright, *J. Non-Cryst. Solids* **106** (1988), 1.
- [5] R.N. Sinclair, A.C. Wright, A.J. Wanless, A.C. Hannon, S.A. Feller, M.T. Mayhew, B.M. Meyer, M.L. Royle, D.L. Wilkerson, R.B. Willaims & B.C. Johanson, *Proc. Second Int. Conf. on Borates Glasses, Crystals and Melts*, 140.
- [6] G. Hägg, *J. Chem. Phys.* **3** (1935), 42.
- [7] W.H. Zachariasen, *J. Chem. Phys.* **3** (1935), 162.
- [8] J. Krogh-Moe, *Phys. Chem. Glasses* **6** (1965), 46.
- [9] G.E. Jellison Jr. & P.J. Bray, *J. Non-Cryst. Solids* **29** (1978), 187.

- [10] S.A. Feller, W.J. Dell & P.J. Bray, *J. Non-Cryst. Solids* **51** (1982), 21.
- [11] P.J. Bray, *J. Non-Cryst. Solids* **75** (1985), 29.
- [12] E.A. Porai-Koshits, *Ph.D. Thesis* (Physical Institute of the Academy of Sciences, Kazan', 1943).
- [13] J. Bischoe, C.S. Robinson, Jr. & B.E. Warren, *J. Am. Ceram. Soc.* **22** (1939), 180.
- [14] J. Bischoe & B.E. Warren, *J. Am. Ceram. Soc.* **21** (1938), 287.
- [15] A.C. Wright, A.G. Clare, B. Bachra, R.N. Sinclair, A.C. Hannon & B. Vessal, *Trans. A.C.A.* **27** (1991), 239.
- [16] N.S. Andreev & E.A. Porai-Koshits, *Dokl. Akad. Nauk. SSSR* **118** (1958), 735.
- [17] E.A. Porai-Koshits & N.S. Andreev, *Nature* **182** (1958), 335.
- [18] E.A. Porai-Koshits, *J. Non-Cryst. Solids* **73** (1985), 79.
- [19] R.R. Shaw & D.R. Uhlmann, *J. Am. Ceram. Soc.* **51** (1968), 377.
- [20] R.J. Charles & F.E. Wagstaff, *J. Am. Ceram. Soc.* **51** (1968), 16.
- [21] E.A. Porai-Koshits, V.V. Golubkov & A.P. Titov, In: *Proc. 10th Int. Cong. on Glass* (Ceram. Soc. Japan, Kyoto, 1974), pp. 12-1 - 12-8.
- [22] V.V. Golubkov, A.P. Titov & E.A. Porai-Koshits, In: *Proc. 11th Int. Cong. on Glass* (CVTS-Dum Techniky Prague, 1977), pp. 93-102.
- [23] S.-K. Chan, J. Döpkens & U. Wurz, *J. Non-Cryst. Solids* **64** (1984), 363.
- [24] J. Döpkens, U. Wurz and G.H. Frischat, *J. Non-Cryst. Solids* **64** (1984), 377.
- [25] T.N. Vasilevskaya, V.V. Golubkov & E.A. Porai-Koshits, *Fiz. Khim. Stekla* **6** (1980), 51.
- [26] V.V. Golubkov, T.N. Vasilevskaya & E.A. Porai-Koshits, *J. Non-Cryst. Solids* **38-39** (1980), 99.
- [27] R. Jeanloz & Q. Williams, *Nature* **350** (1991), 659.
- [28] I. Amato, *Science* **252** (1991), 1377.
- [29] P.H. Gaskell, M.C. Eckersley, A.C. Barnes & P. Chieux, *Nature* **350** (1991), 675.
- [30] O.V. Mazurin, G.P. Roskova, V.I. Averianov & T.V. Antropova, *Two-Phase Glasses: Structure, Properties, Applications*, Ed. B.G. Varshal (Nauka, Leningrad, 1991), pp. 114-117.
- [31] B.E. Warren & J. Bischoe, *J. Am. Ceram. Soc.* **21** (1938), 49.
- [32] E.A. Porai-Koshits, *Fiz. Khim. Stekla* **3** (1977), 292.
- [33] E.A. Porai-Koshits, V.V. Golubkov, A.P. Titov & T.N. Vasilevskaya, *J. Non-Cryst. Solids* **49** (1982), 143.
- [34] J.E. Shelby, *J. Am. Ceram. Soc.* **66** (1983), 225.
- [35] N.M. Vedishcheva, B.A. Shakhmatkin, M.M. Shultz & A.C. Wright, this proceedings, paper P25.
- [36] V.V. Golubkov, *Fiz. Khim. Stekla* **18** (1992), 14.
- [37] G.E. Walrafen, S.R. Samanta & P.N. Krishnan, *J. Chem. Phys.* **72** (1980), 113.
- [38] V.V. Golubkov, *Proc. Second Int. Conf. on Borates Glasses, Crystals and Melts*, 88.
- [39] N.A. Bokov & N.S. Andreev, *Proc. Second Int. Conf. on Borates Glasses, Crystals and Melts*, 107.

## THE BORON OXIDE "ANOMALY" REVISITED

M. C. WEINBERG, D. R. UHLMANN  
& W. H. POISL

*Department of Materials Science & Engineering,  
Arizona Materials Laboratory, University of Arizona,  
Tucson, Arizona 85721, USA*

Reconsideration is given to the allegedly anomalous thermal expansion of alkali borate glasses, and to explanations for this behavior which have been advanced. Several issues (e.g. differences in the thermal expansion data found by different investigators, theoretical expressions for the thermal expansion, borate glass structural information) are addressed, which have a direct bearing upon this phenomenon. Explanations for the borate glass anomaly offered by previous investigators have been in terms of the changes in structural features of binary borate glasses as the alkali concentration is increased. It may be observed, however, that much ambiguity and contradictory evidence exists regarding these structural changes. It is concluded that the thermal expansion behavior of alkali borate glasses will not be fully understood until a quantitative relationship between thermal expansion and structural features is derived.

### 1. PERSONAL INTRODUCTION

It is a pleasure for us to join in this festive occasion honoring Professor Philip Bray. We have known Phil for more than a quarter-century and have never failed to be impressed by the breadth of his knowledge, his outstanding insight and physical intuition, and his remarkable ability to communicate ideas with such clarity that even non-specialists gain valuable new understanding. Phil, without doubt, occupies a special place in the scientific pantheon as the father of NMR studies of glass structure. These studies have provided new insight and perspective of such fundamental importance that no work which discusses the structure and properties of glasses is complete without liberal citation of the gospel according to St. Philip. For those of us who teach new generations of students, our classes are replete with references to Phil's opus, and his name is a household word for all our students.

Beyond his contributions as a scientist, which have been legion and weighty, mention should be made of Phil's role as the Sage of Providence. He has served for years as a mentor to the field—both to his own students and the students

of others, as well as to colleagues throughout the world. His counsel and perspective, which are widely sought-after, have had important influence upon directions which the field has taken—and have helped us through numerous ‘sticky situations’. Many of us recall how, during the turmoil of the late 1960’s–early 1970’s, Phil managed to maintain a sense of greatly-needed balance and judgment.

Perhaps, most important of all, is Phil Bray, our friend. Phil is a warm and caring individual, whose enthusiasm is downright contagious and whose love of life provides an example for all. Even when one may not see eye-to-eye with him on issues Phil never loses his cool and never lets disagreements compromise friendship. We salute you, Phil, on this special occasion; and we look forward to joining you in celebrating your 80th birthday.

## 2. BORON OXIDE ANOMALY

The ‘boron oxide anomaly’ refers to the appearance of extrema in various property vs. composition relations for borate glasses, particularly alkali borate glasses. Perhaps the best-known extrema are the minima observed in the curves of thermal expansion coefficient vs.  $R_2O$  concentration. There is, however, no consensus as to the detailed forms of these relations, nor the locations of the minima (see, e.g., Fig. 2 in Ref. [1] for sodium borate glasses). The most extreme differences in the data are represented by the results reported by Uhlmann & Shaw [1] and by Shelby [2].

When all alkali borate systems are considered, the data of Shelby [2] indicate minima at about 20 mol%  $R_2O$  independent of alkali type, with the minima being quite steep for  $Li_2O$ , reasonably steep for  $Na_2O$ , notably more shallow for  $K_2O$ , and more shallow still for  $Rb_2O$ . In contrast, the data of Uhlmann & Shaw [1] indicate broad minima in all five systems, with the location of the minima depending on the type of alkali.

There is, however, general agreement that the depth of the minimum follows the order  $Li > Na > K > Rb > Cs$ . This likely reflects the larger cations being less bonded in the borate framework, producing less coherent structures and higher thermal expansion coefficients.

Some of the variations in the reported data may reflect issues such as the water content, thermal history of the glasses, and the temperature range over which measurements are made. As examples of the last, the data of Shelby represent the average over the range 100 to 200°C; while those of Uhlmann & Shaw are the average over the range -196 to 25°C. This difference in the temperature range of the data may well be important in light of the observations of Ahmed *et al.* [3], who reported significant variations in  $\alpha$  with temperature, over the temperature range between 100 and 300°C.

Thus, in summary, although certain features of the thermal expansion anomaly are common to all previous results, the actual shapes of the thermal expansion curves vary markedly for different investigations.

### 3. EXPLANATIONS FOR THE ANOMALY

Several explanations have been advanced to explain the anomaly. These include:

#### 3.1. Warren *et al.* [4,5]:

These authors associated the minimum in  $\alpha$  with a competition between the formation of four-coordinated borons (4CB's) (which they suggested would lower  $\alpha$ ) and the formation of nonbridging oxygens (NBO's) (which they suggested would raise  $\alpha$ ). At small concentrations of  $R_2O$ , the formation of 4-coordinated borons was suggested to dominate.

This explanation was called into question by the NMR data of Bray *et al.* [6,7], which suggested that insignificant numbers of NBO's were formed until the alkali oxide content of the glass reached about 30 mol% (well beyond the range of the minima as seen in nearly all data). Further, this explanation would not account for the observed dependence of the minima on the alkali oxide species.

#### 3.2. Uhlmann & Shaw [1]:

These authors associated the minima with a competition between the formation of 4CB's (which were taken as decreasing  $\alpha$ ) and the introduction of modifying cations as well as NBO's (which were taken as increasing  $\alpha$ ). This explanation can account qualitatively for the dependence of  $\alpha$  on the type of alkali for glasses having the same concentration of 4-CB's (at small content of  $R_2O$ ). It neglects, however, any influence of the structural units in the glasses (save for the 4CB's and NBO's); and ignores complicated cation effects (see below).

#### 3.3. Shelby [2]:

This author associated the minima with the disappearance of boroxol groups, maxima in tetraborate and appearance of diborate groups, and hence directs attention to the types of structural units in the glass. This explanation does not account for the dependence of  $\alpha$  and the steepness of the minima on the type of alkali; nor does it allow for differences in the distributions of the various structural units depending on the type of cation (as indicated by recent structural studies).

#### 3.4. Chryssikos *et al.* [8]:

These authors cite the data of Shelby and associate the steepness of the minima with NBO's, which they suggest are formed at lower  $R_2O$  contents, and whose concentration increases more rapidly with  $R_2O$  content, as the size of the alkali ion increases. This explanation effectively combines the view of Warren *et al.* with newer NMR results of Zhong & Bray [9] which show a dependence of NBO concentration on the type of alkali.

This explanation also has difficulties. For example, the data of Shelby on

lithium borate glasses show a pronounced minimum in  $\alpha$  at about 20 mol%  $\text{Li}_2\text{O}$ , while the NMR results of Zhong & Bray indicate the absence of significant quantities of NBO's until at least 23 mol%  $\text{Li}_2\text{O}$ . Further, NBO's are formed in the largest quantities in  $\text{Cs}_2\text{O}-\text{B}_2\text{O}_3$  glasses, where the minimum is shallow at best, and in the smallest quantities in  $\text{Li}_2\text{O}-\text{B}_2\text{O}_3$  glasses, where the minimum is the most pronounced.

Taken as a whole, the above explanations are qualitative, rather than quantitative. One must consider such explanations somewhat inadequate since they cannot account for the positions, depths, or breadths of the minima, nor can they explain in detail the differences in thermal expansion behavior exhibited as a function of alkali type.

#### 4. THERMAL EXPANSION FORMULA

One can express  $\alpha$  in terms of the Gruneisen constant [10],  $\gamma$ , as shown in Eq. (1).

$$\alpha = \gamma \beta C_v / V_m \quad (1)$$

Here,  $V_m$  is the molar volume,  $C_v$  is the constant volume molar specific heat, and  $\beta$  is the isothermal compressibility. Several points regarding this formula and its relationship to the thermal expansion minima are worth mentioning.

In order to find the compositional dependence of  $\alpha$ , one must utilize the compositional dependence of the Gruneisen constants for the different systems, which are not known. However, one can use thermal expansion data and the measured compositional dependences of the other thermodynamic parameters to infer the behavior of  $\gamma$  as a function of alkali content. This procedure has been carried out for lithium, sodium, and potassium borate glass compositions (using the thermal expansion data of Ref. [1]). Using Eq. (1), one can compute the composition dependence of the Gruneisen constant as shown in Eq. (2).

$$\frac{d \ln \gamma}{dx} = \frac{d \ln \alpha}{dx} - \left\{ \frac{d \ln \beta}{dx} + \frac{d \ln C_v}{dx} + \frac{d \ln V_m}{dx} \right\} \quad (2)$$

Figure 1 illustrates the results for lithium borate glasses. The open squares give the composition derivative of the logarithm of the thermal expansion coefficient, the circles give the term in the curly brackets, and the difference between these curves (as seen from Eq. (2)) gives the change in the logarithm of the Gruneisen constant with composition. One observes that the Gruneisen constant has a minimum value at about 17 mol%  $\text{Li}_2\text{O}$  and that the thermal expansion minimum occurs at about 23 mol%  $\text{Li}_2\text{O}$ . By inspecting similar plots for sodium and potassium borate glasses the following observations can be made:

1. All Gruneisen constants exhibit minima when plotted vs. composition.
2. The minima in  $\gamma$  occur at smaller concentrations of alkali than the minima in  $\alpha$ , for all  $\text{R}_2\text{O}$ .



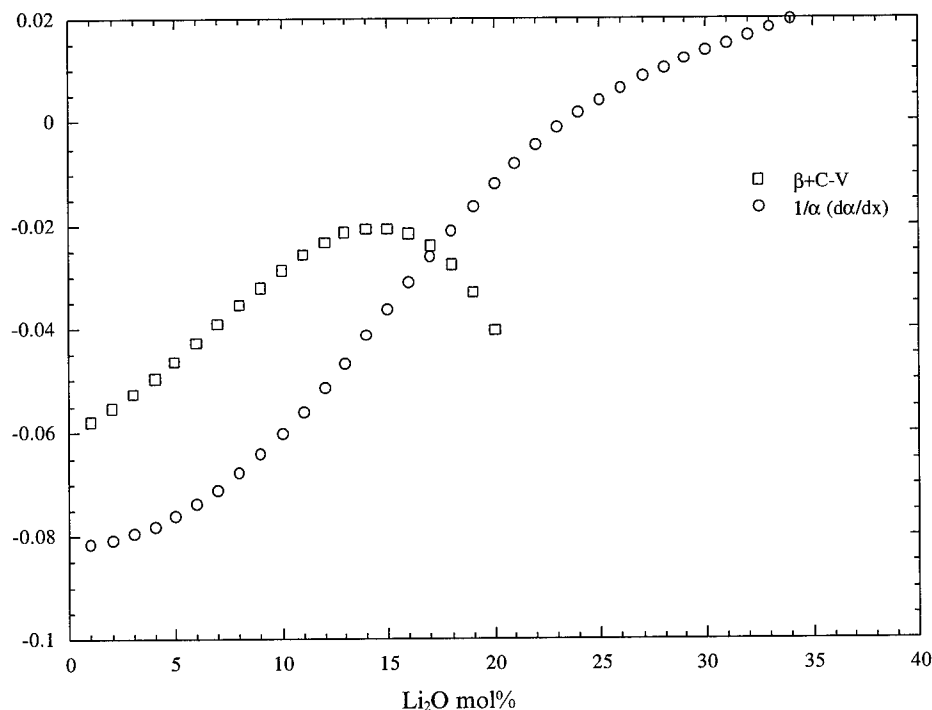


**Fig. 1.** Composition derivatives of the logarithms of thermodynamic quantities. The circles are  $d\ln\alpha/dx$  and the squares are the values of the term in curly brackets in Eq. (2).

3. The depth in the thermal expansion minimum appears to be related to the value of  $d\ln\gamma/dx$  at  $x=0$  (where  $x$  is the mole %  $R_2O$ ), with larger values of this derivative being associated with deeper minima. Thus, the characteristics of the thermal expansion minima appear to be intimately related to the composition dependences of  $\gamma$ .

On the other hand, the quantitative relationship between glass structure and the thermodynamic quantities which appear in Eq. (1) are not known.

## 5. STRUCTURE OF ALKALI BORATE GLASSES

### 5.1. Fraction of 4CB's

Since all previous explanations of the anomalous thermal expansion behavior of alkali borate glasses have been presented in terms of changes in glass structure with increasing  $R_2O$ , it is important to assess the current state of knowledge of the structure of such glasses. In particular, two aspects of glass structure are particularly germane; the fraction of 4CB's or NBO's as a function of  $x$  (i.e.  $R_2O$  concentration) and the borate structural units which form with increasing  $x$ . These two features are considered in turn.

If no NBO's are formed, the fraction of 4CB's for  $x\text{R}_2\text{O} \cdot (1-x)\text{B}_2\text{O}_3$  is given by  $N_4 = x/(1-x)$ . The classic NMR studies of Bray *et al.* [6,7] suggested that this relationship was followed closely by the experimental data for all alkali borate systems up to about  $x=0.33$ ; and hence the formation of NBO's would be insignificant up to at least this range of composition.

In more recent work, using modern instrumentation, Zhong & Bray [9] report that  $N_4$  deviates significantly below  $x/(1-x)$  in the range below  $x=0.3$ , and that this deviation increases in the order:  $\text{Li} < \text{Na} < \text{K} < \text{Rb} < \text{Cs}$ . Also, in contrast to previous results, the data of Zhong & Bray indicate major deviations between  $N_4$  and  $x/(1-x)$  by  $x=0.33$ , and that the deviation of  $N_4$  from  $x/(1-x)$  decreases (at least for some systems) between  $x=0.17$  and  $0.23$ , and then increases between  $x=0.23$  and  $0.33$ , a curious result. The authors point out that the errors in previous determinations of  $N_4$  were as large as  $\pm 0.05$ , but do not provide an estimate of the error in the new data: However, Chryssikos *et al.* [8] suggest an error of  $\pm 0.02$  in the new determinations of  $N_4$ .

## 5.2. Borate Structural Units

Raman spectroscopy has been the principal experimental tool used to obtain information about the borate structural units in alkali borate glasses, e.g. [11-15]. The data of Lorosch *et al.* [12] indicate that different  $0.25\text{R}_2\text{O} \cdot 0.75\text{B}_2\text{O}_3$  glasses have quite different structures. For Cs, the  $806\text{ cm}^{-1}$  band due to boroxol rings has almost completely disappeared; while, for Li, the  $806\text{ cm}^{-1}$  band is comparable in intensity to the other strong band at about  $770\text{ cm}^{-1}$ .

With respect to the specific borate structural units present, as a function of composition, in different alkali borate systems, there are major disagreements in the literature, resulting from differences in the band assignments. All studies indicate the gradual disappearance of boroxol units and the appearance of 6-membered rings containing  $\text{BO}_4$  tetrahedra over the range about 0 to 25 mol%  $\text{R}_2\text{O}$ , but here the agreement ceases. Konijnendijk & Stevels [11] suggest the presence of loose  $\text{BO}_3$  triangles and  $\text{BO}_4$  tetrahedra and tetraborate groups, others [8,14] also suggest tetraborate units, but also metaborate chains containing NBO's, while Meera & Ramakrishna [15] suggest that all alkali borate glasses in this composition range, with the exception of Cs borates, contain only pentaborate units.

Lorosch *et al.* [12] and others [8,14] argue in favor of a strong cation effect, with boroxols being destroyed more rapidly with the addition of larger cations, while Meera & Ramakrishna suggest that different alkali ions have the same effect on the borate network.

Thus, it appears that there is uncertainty regarding changes in glass structure with increasing  $\text{R}_2\text{O}$  in alkali borate glasses. Namely, there is contradictory evidence from Raman studies relating to the rate of boroxol destruction as well as triborate and pentaborate formation with increasing  $\text{R}_2\text{O}$ . Furthermore, the most recent NMR results for  $N_4$  display unusual behavior in the region between  $x=0$  and 23 mol%.

## 6. CONCLUDING REMARKS

We meet today, more than six decades after Gooding & Turner [16] reported a minimum in  $\alpha$  in the  $\text{Na}_2\text{O}-\text{B}_2\text{O}_3$  system and after outstanding advances using NMR, XRD and Raman spectroscopy to elucidate the structural features of borate glasses. There is, however, no agreement about the forms of such minima in various alkali borate systems, or the detailed structural features (particularly the borate groupings) in such glasses; and the prospects for *a priori*, quantitative predictions of a behavior remain bleak.

One major issue is the marked variations reported in the thermal expansion behavior, as well the different ranges of temperature covered by the different sets of data. In order to assess the thermal expansion anomaly in a rational manner, one first needs an agreed upon set of data to interpret. Thus, it would seem highly desirable to perform a round-robin investigation of the thermal expansion in alkali borate glasses. The temperature range should span room temperature in order to produce data in the temperature region where most structural studies are executed.

Qualitative explanations for the observed behavior of  $\alpha$  have suggested that the fraction of  $\text{BO}_4$  units, the numbers of NBO's, the nature of the borate groupings formed and the cation species are all important. However, ambiguities in the interpretation of structural measurements prevent one from assessing the relative significance of the above factors. Hence, more investigations aimed at obtaining quantitative information regarding structural features are needed.

Finally, one may argue that even if there were consistency in the sets of thermal expansion data and if the alkali borate glass structures were known precisely, the thermal expansion anomaly could not be explained at a fundamental level. This stems from the fact that we are totally ignorant of the required structure-property relationship for thermal expansion. One observes from Eq. (1) that the thermal expansion depends upon several thermodynamic parameters, each of which has a complex relationship with structural features. Thus, much work needs to be done to provide a quantitative relationship between thermal expansion behavior and structural modifications.

One could hope to explain the thermal expansion anomaly (in a less physical manner) by examining the concentration dependencies of the thermodynamic quantities in Eq. (1). However, as mentioned previously, this procedure calls for knowledge of the composition dependencies of the Gruneisen constants. If one could calculate these composition dependencies theoretically, then one might develop a viable theory of the thermal expansion anomaly.

The authors are reminded of the comments of Adlai Bishay at the 1984 Kreidl Symposium [17]: "After having been out of the field of glass science for more than a decade, it is delightful to be reunited with so many old friends discussing so many of the same old problems using so many of the same old models". We would not be surprised if these comments apply when Phil Bray joins us on his centennial birthday.

## ACKNOWLEDGMENTS

Financial support for the present work was provided by the National Science Foundation and by the Air Force Office of Scientific Research. This support is gratefully acknowledged.

## REFERENCES

- [1] D.R. Uhlmann & R.R. Shaw, *J. Non-Cryst. Solids* **1** (1969), 347.
- [2] J.E. Shelby, *J. Am. Ceram. Soc.* **66** (1983), 225.
- [3] A.A. Ahmed, A.F. Abbas & S.M. Salman, *Phys. Chem. Glasses* **26** (1985), 17.
- [4] J. Biscoe & B.E. Warren, *J. Am. Ceram. Soc.* **21** (1938), 287.
- [5] B.E. Warren, *J. Appl. Phys.* **13** (1942), 602.
- [6] A.H. Silver & P.J. Bray, *J. Chem. Phys.* **29** (1958), 984.
- [7] P.J. Bray & J.G. O'Keefe, *Phys. Chem. Glasses* **4** (1963), 37.
- [8] G.D. Chryssikos, E.I. Kamitsos & M.A. Karakassides, *Phys. Chem. Glasses* **31** (1990), 109.
- [9] J. Zhong & P.J. Bray, *J. Non-Cryst. Solids* **11** (1989), 67.
- [10] J.C. Slater, *Introduction to Chemical Physics* (McGraw-Hill, New York, 1959).
- [11] W.L. Konijnendijk & J.M. Stevels, *J. Non-Cryst. Solids* **18** (1975), 307.
- [12] J. Lorosch, M. Couzi, J. Pelous, R. Vacher & A. Levasseur, *J. Non-Cryst. Solids* **69** (1984), 1.
- [13] B.P. Dwivedi, M.H. Rahman, Y. Kumar & B.N. Khanna, *J. Phys. Chem. Solids* **54** (1993), 621.
- [14] E.I. Kamitsos, M.A. Karakassides & G.D. Chryssikos, *Phys. Chem. Glasses* **30** (1989), 229.
- [15] B.N. Meera & J. Ramakrishna, *J. Non-Cryst. Solids* **159** (1993), 1.
- [16] E.J. Gooding & W.E.S. Turner, *J. Soc. Glass Technol.* **18** (1934), 32.
- [17] A.M. Bishay: remarks at the Conference in honor of the 80th birthday of Professor Norbert Kreidl, Vienna, July, 1984.

## LOW-Q FEATURES IN DIFFRACTION DATA FOR BORATE GLASSES AND CRYSTALS - AN EXAMINATION OF SIMILARITIES IN MEDIUM-RANGE STRUCTURES

Philip H. GASKELL

*Cavendish Laboratory, University of Cambridge, Madingley Road,  
Cambridge CB3 0HE, UK*

Features in X-ray and neutron scattering data for amorphous solids at low values of the scattering vector,  $Q$ , are related to the medium-range structure of the glass. In many glasses (and some melts and simple liquids) the positions of low- $Q$  peaks are related to features in equivalent crystalline phases. In silica, recent work has shown that low- $Q$  peaks are associated with "quasi-Bragg" planes in the glass with a distinct similarity to those found in cristobalite and tridymite. X-ray and neutron scattering data for borate glasses containing cations like  $\text{Ag}^+$ ,  $\text{Cs}^+$  and  $\text{Li}^+$  are compared with simulated diffraction patterns for equivalent crystals. Comparison is close and supports the conclusion that large polyanionic "super-structural" units are *intrinsic* features of the vitreous phase. The packing of such groups and the interstitial cations is likely to reflect that of the crystals too.

### 1. SHARP FIRST DIFFRACTION PEAKS IN OXIDE GLASSES.

Vitreous boron oxide, like silica, exhibits a sharp first diffraction peak but, unlike silica, the position in the glass differs from that of a strong Bragg peak in corresponding crystals. The peak in  $\alpha\text{-SiO}_2$  corresponds to a similar feature in cristobalite and tridymite, whereas the peak in  $\alpha\text{-B}_2\text{O}_3$  is distinctly different in the glass and crystal. The reason almost certainly lies in the *similarity* of the medium-range structures of glass and crystal for  $\text{SiO}_2$  and the essential *dissimilarity* for  $\text{B}_2\text{O}_3$ . Questions arise also over the variations in the low- $Q$  features as a function of additions of the so-called network-modifying oxides. Recent neutron scattering data by Swenson, Börjesson & Howells [1] have added to earlier x-ray results so that there is now adequate experimental data to base a more general explanation of the origin of low- $Q$  diffraction peaks in borate glasses.

The essence of the argument for the occurrence of First Sharp Diffraction Peaks (FSDPs) in glasses is that the medium-range structure may be qualitatively similar to one or more equivalent crystalline phases. If so, it is reasonable to interpret FSDPs in glasses and crystals in the same language [2]. For crystals, we consider Bragg planes, planes in real space with a separation  $d_{hkl}$ : atoms lying on these planes scatter in phase, and with a phase difference  $\exp(i\mathbf{Q}\cdot\mathbf{r})$  for atoms lying between planes ( $\mathbf{Q}$  is the scattering vector:  $|\mathbf{Q}|=Q=4\pi\sin\theta/\lambda$ ; where  $2\theta$  is the scattering angle,  $\lambda$  the wave-

length;  $\mathbf{r}$  is an atomic position vector with origin on a Bragg plane). For glasses we argue that small contiguous or interlocking regions of a macroscopic specimen will have distorted but essentially planar atomic density fluctuations, with a spacing characteristic of  $\{hkl\}$  Bragg planes in the corresponding crystal. Although it is natural to extrapolate the model and brand it a "microcrystallite model", the temptation should be resisted. Current evidence suggests similarity between lattice planes in crystals and microscopic regions in glasses with (randomly-orientated) "quasi-lattice" planes but we have no real evidence of their spatial extent: perfection, parallelism etc, or the degree to which they are (flat) planes at all - as distinct from "alliacious" (onion-like) structures with parallel "skins" separated by  $d_{hkl}$ .

The suggestion that the structures of glasses are comparable to those of equivalent crystals is not confined to FSDPs - nor is it new. It is generally accepted that the *local structures* of glasses and crystals are similar: the suggestion is only really contentious for correlations extending into the medium-range of structure from 0.5-1.5 nm, say. Krogh-Moe argued consistently, thirty years ago, for similarity of the polyanionic structure of crystalline and vitreous borates, and he also pioneered x-ray determinations of the structure of many crystalline borates and thus laid the foundations for a more general understanding of the structures of amorphous and crystalline phases.

## 2. INVESTIGATION

In this paper, I compare the x-ray and neutron scattering data for several glasses with calculated diffraction data for (where possible) compositionally-equivalent crystalline phases. The test of this approach is quality of the fit and the degree of insight offered by the crystal structure into the medium-range structure of the glass. Where there is a good fit then I argue that it is reasonable to suppose that *structure-forming operations* (SFOs) are similar in each case. The result is not so much a *theory* of medium-range structure in these glasses or of glasses in general - more an observation which may turn into a theory once we understand how SFOs in the glass and crystal are related.

Analysis is restricted to two heavy-atom glasses - containing Cs and Ag, and a glass containing Li, a typical light alkali metal. X-ray scattering in the first series is dominated by the metal cation whereas the Li atoms effectively disappear in x-ray data. An advantage of studying the Li and Ag borates is that isotopes exist with different scattering lengths so that the contribution of the metal atoms can be emphasized. Scattering data were produced using the Cerius package [3] and results are given for microcrystallites with an (arbitrary) edge length of 3 nm. This provides more representative graphical data but does not imply a microcrystallite model of course.

## 3. RESULTS

### 3.1. Caesium Borates

Krogh-Moe [4] has published (early) x-ray data for a series of glasses containing up to 20.9%  $\text{Cs}_2\text{O}$  - Fig. 1, and crystal structures for the enneaborate,

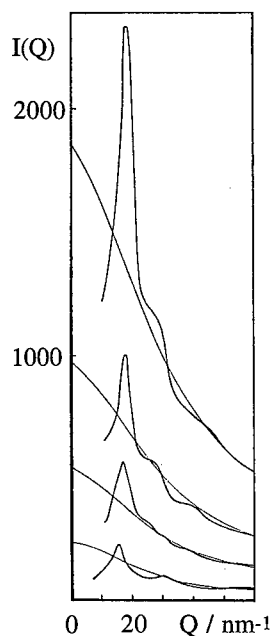


Fig. 1. X-ray scattering from  $B_2O_3$  and caesium borate glasses with 4.6, 10.7 and 20.9%  $Cs_2O$ . [4].

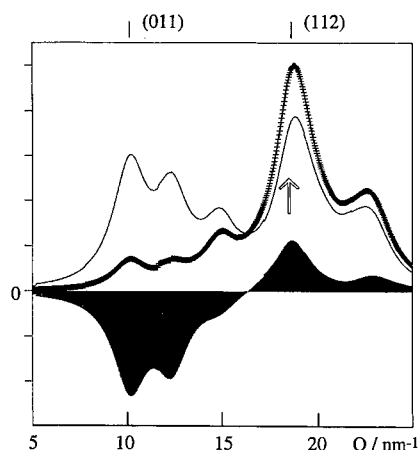
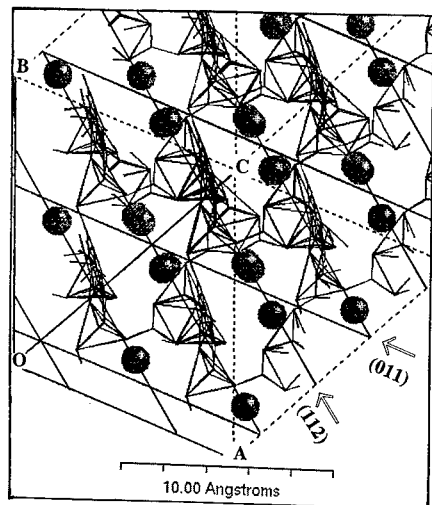


Fig. 2. Simulated x-ray diffracted intensity data for  $Cs_2O \cdot 3B_2O_3$ . Points show data for the crystal, broadened to represent 3 nm microcrystals. The full line is for a lattice with Cs atoms only, the hatched plot, the difference. The ordinate scale for the scattered intensity is arbitrary. The arrow marks the position of the FSDP.

$Cs_2O \cdot 9B_2O_3$  and triborate [5,6]. Data for the glasses show a shift of the first peak from about  $15.9 \text{ nm}^{-1}$  in  $B_2O_3$  to  $17.1 \text{ nm}^{-1}$  with even a minor (4.7%) addition of  $Cs_2O$ . Krogh-Moe points out that this is due to overlap of the contribution of a " $B_2O_3$ " peak and a higher  $Q$  peak at  $18.4 \text{ nm}^{-1}$ , the position of which remains constant on further addition of caesium.

The first strong x-ray peak for  $c\text{-}Cs_2O \cdot 3B_2O_3$  (Fig. 2) occurs at  $Q = 18.8 \text{ nm}^{-1}$  - about 2% higher than the value of  $18.4 \text{ nm}^{-1}$  for the glass containing about 21%  $Cs_2O$ . (A likely increase in specific volume of about 5% is reflected in a decrease of *inverse* distances in glasses of about 2% compared to crystals.) This peak corresponds to (112) and (121) reflections in the ratio of about 2:1 and is clearly dominated by scattering from the Cs atoms. The scattered intensity for the Cs-Cs pairs alone contributes over 75% of the total (Fig. 2). It is therefore reasonable to treat the scattering as principally due to Cs and then consider the modifications imposed by the B-O network. The lattice containing only Cs atoms has three strong reflections at low values of  $Q$ , the lowest at  $Q \sim 10 \text{ nm}^{-1}$ . It is interesting to see why these appear as only insignificant shoulders in the full structure and, I suggest, thus make little or no contribution to the FSDP in glasses. Considering the (011) planes at  $Q = 10.1 \text{ nm}^{-1}$  (Fig. 3): these pass close to the Cs positions and contribute a high scattered ampli-



**Fig. 3.** Projection of  $\text{Cs}_2\text{O} \cdot 3\text{B}_2\text{O}_3$  along  $\langle 111 \rangle$  showing the borate network and Cs atoms (circles). (001) planes ( $Q = 10.1 \text{ nm}^{-1}$ ) pass close to the Cs atoms with the "borate" network between. The Cs atoms and most of the B and O atoms lie close to the (112) planes at a higher value of  $Q$  ( $18.8 \text{ nm}^{-1}$ ). A, B, C are the axes of a  $2 \times 2 \times 2$  supercell.

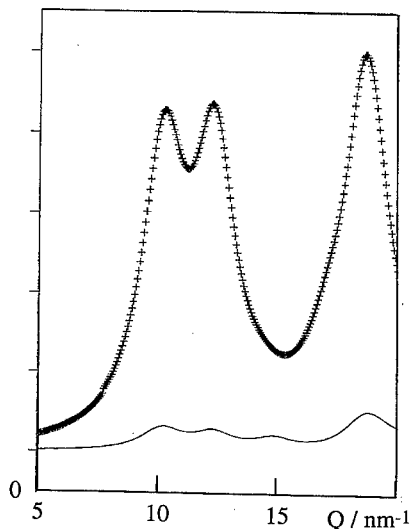


**Fig. 4.** Simulated neutron scattering data for  $\text{Cs}_2\text{O} \cdot 3\text{B}_2\text{O}_3$  (points) and for the lattice containing only Cs (line).

tude. But the B and O atoms that populate the space *between* the Bragg planes give *out-of-phase* contributions so that the intensity of the (011) peak falls to about a quarter of that of the (112) peak at  $Q = 18.8 \text{ nm}^{-1}$ .

The effect of the "borate" network on the (112) peak at  $Q = 18.8 \text{ nm}^{-1}$  is quite different. Fig. 3 shows that most B and O atoms lie close to the (112) Bragg planes and therefore make an *in-phase* contribution to the scattered amplitude and *increase* the intensity. This is a general effect for heavy atom glasses - although the resultant intensities depend rather crucially on the atomic scattering amplitudes.

Neutron scattering amplitudes for the three atoms are more equal (b values for  $^{11}\text{B}$ , O and Cs are 6.7, 5.8 and 5.4 fm). The contribution of the B-O network now dominates the scattering: Cs-Cs pairs contribute only 8% to the intensity of the (112) peak for instance. The first strong neutron peak in the triborate lies at  $Q = 10.1 \text{ nm}^{-1}$  (Fig. 4). The Cs atoms between the B and O atoms near the Bragg planes give out-of-phase contributions to the scattered amplitude but the Cs concentration is insufficient to reduce the intensity significantly. I am not aware of neutron scattering data for Cs borate glasses but it seems reasonable to predict an FSDP at about  $11 \text{ nm}^{-1}$ . (But see note [12])



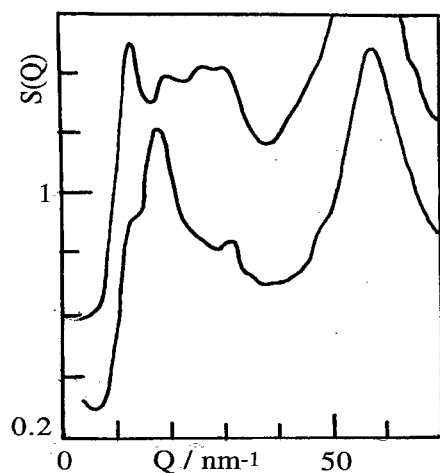


Fig. 5. Neutron scattering data for Ag tetraborate (lower) and diborate glasses. Curves displaced vertically by 0.4 [1].

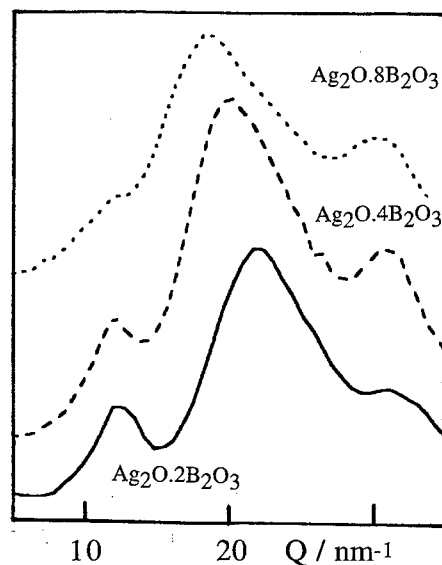


Fig. 6. X-ray scattering data for several silver borate glasses [7].

### 3.2. Silver borates

Swenson *et al* [1] show neutron scattering data for a number of  $\text{Ag}_2\text{O}-\text{B}_2\text{O}_3$  glasses. The single peak in  $\text{a-B}_2\text{O}_3$  decreases in intensity in  $\text{a-Ag}_2\text{O.8B}_2\text{O}_3$  and splits into two obvious components - a shoulder near  $13.5 \text{ nm}^{-1}$  and the main peak at  $19 \text{ nm}^{-1}$  for  $\text{a-Ag}_2\text{O.4B}_2\text{O}_3$  (Fig. 5). In  $\text{a-Ag}_2\text{O.2B}_2\text{O}_3$ , the first peak at  $13.2 \text{ nm}^{-1}$  is the most prominent (but with low intensity). A third peak appears at  $27 \text{ nm}^{-1}$  - the growth of this feature being obvious in  $\text{Ag}_2\text{O.4B}_2\text{O}_3$  as a shoulder.

X-ray data for Ag borate glasses (Fig. 6) has been published by Cervinka & Rocca [7], supplementing earlier work by Kamiya *et al* [8]. The main feature moves from  $18.9 \text{ nm}^{-1}$  in the octaborate to  $22.2 \text{ nm}^{-1}$  in the diborate with a feature at  $12.3 \text{ nm}^{-1}$  increasing from a shoulder in the octaborate to a distinct peak in tetraborate and diborate glasses but without any shift in position. The difference between the x-ray peak at  $12.3 \text{ nm}^{-1}$  and the neutron peak ( $13.2\text{-}13.5 \text{ nm}^{-1}$ ), although small, appears to be significant.

Simulated x-ray diffraction data for the tetraborate,  $\text{Ag}_2\text{O.4B}_2\text{O}_3$  [9] are shown in Fig. 7. Two strong features appear: a first peak at about  $12.5 \text{ nm}^{-1}$  and a broad feature at  $20.6 \text{ nm}^{-1}$  - in reasonable agreement with the peaks in the x-ray data for the glass. Again scattering from high atomic number atoms ( $Z_{\text{Ag}}=47$ ) dominates: the contribution from Ag-Ag pairs is shown in Fig. 7. Again the intensity of the first peak at  $12.5 \text{ nm}^{-1}$  is reduced (by a factor of about 2) as a result of destructive interference from the network, whereas the second peak intensity increases by fourfold due to constructive interference.

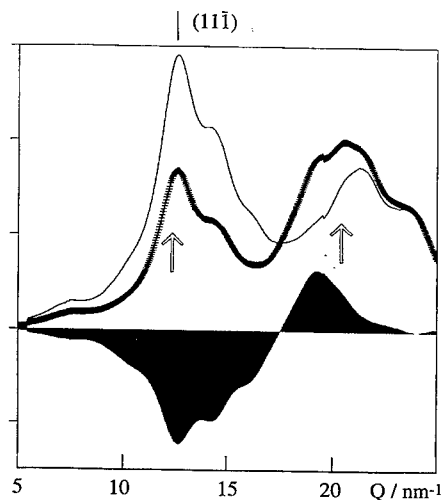


Fig. 7. Simulated x-ray scattering data for  $\text{Ag}_2\text{O} \cdot 4\text{B}_2\text{O}_3$  (points). The full line gives the scattered intensity for a lattice containing only Ag and the hatched curve is the difference. The "glitch" at  $19 \text{ nm}^{-1}$  is an artefact.

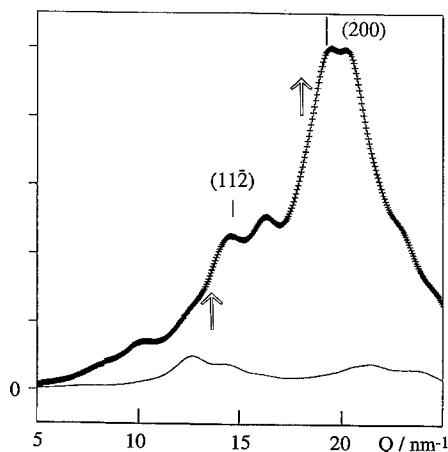


Fig. 8. Simulated neutron scattering data for  $\text{Ag}_2\text{O} \cdot 4\text{B}_2\text{O}_3$  (points). Curves labelled as in Fig. 7.

Neutron scattering is different. The neutron scattering lengths of Ag,  $^{11}\text{B}$  and O are similar, but the concentration of Ag is less than 0.1. Consequently the periodicities in the *borate* sub-structure produce the prominent features. The strongest,  $Q=19.2 \text{ nm}^{-1}$ , is due to (200) Bragg planes that pass through obvious *layers* in the borate sub-structure and also close to Ag positions, although the contribution of the latter is only small. The strongest diffraction features that come principally from the Ag network are the  $(11\bar{1})$  and  $(111)$  peaks at  $Q = 12.6 \text{ nm}^{-1}$  which produce the strong FSDP in the x-ray data: these contribute only about 12% of the intensity of the strong peak at  $Q=19.2 \text{ nm}^{-1}$ . The most prominent low- $Q$  feature at  $Q \sim 14.2\text{--}14.4 \text{ nm}^{-1}$  arises from overlap of several Bragg peaks, the strongest being the  $(11\bar{2})$  at  $14.0 \text{ nm}^{-1}$ .

The crystal structure data therefore reproduces (semi-quantitatively) the different positions of the first component of the FSDP in x-ray and neutron data ( $12.5$  and  $14.2\text{--}14.4 \text{ nm}^{-1}$ ) compared to the shift from  $12.3 \text{ nm}^{-1}$  to  $13.2\text{--}13.5 \text{ nm}^{-1}$  seen in experiments.

### 3.3. Lithium borates

Little change occurs in the FSDP as the Li content increases [1] except that the peak moves from  $16.1$  to  $15.3 \text{ nm}^{-1}$  in the diborate. The intensity changes only a little but the peak becomes about 15% narrower. There is no indication of any shoulder on the low- $Q$  side of the peak although a shoulder near  $20 \text{ nm}^{-1}$  appears in the diborate glass. X-ray data of Paschina *et al* [10]

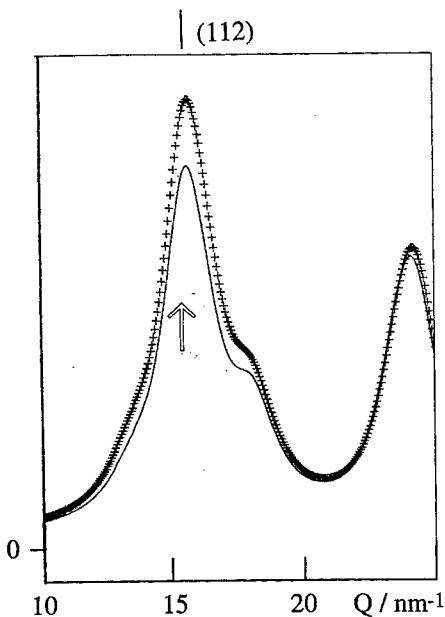


Fig. 9. Simulated neutron scattering data for  $\text{Li}_2\text{O} \cdot 2\text{B}_2\text{O}_3$ . Points are for the glass containing natural Li, the full line gives approximate data for the glass with a zero scattering mixture of isotopes,  $^0\text{Li}$ . For details, see text.

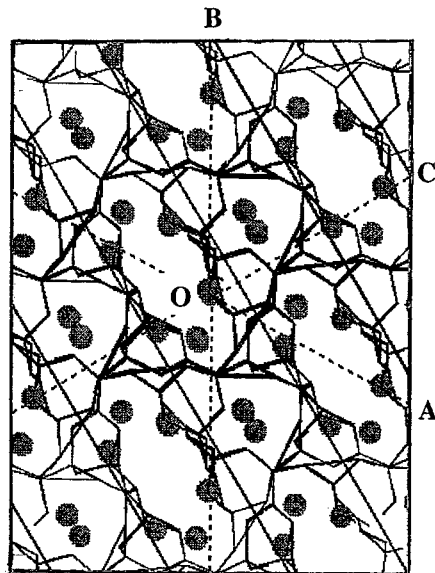


Fig. 10. Projection of the  $\text{Li}_2\text{O} \cdot 2\text{B}_2\text{O}_3$  structure along  $\langle 111 \rangle$  showing (112) planes.

for glasses containing up to about 25%  $\text{Li}_2\text{O}$ , show one of these features: the FSDP moves to about  $15.7 \text{ nm}^{-1}$  in the high Li glass but the peak intensity is much lower than in  $\alpha\text{-B}_2\text{O}_3$  and the width is larger.

Calculated neutron scattering data for  $\text{c-Li}_2\text{O} \cdot 2\text{B}_2\text{O}_3$  [11] are shown in Fig. 9. The strongest peak, (112), is at  $Q = 15.4 \text{ nm}^{-1}$ , compared with the FSDP at  $15.3 \text{ nm}^{-1}$  in the glass.  $^{\text{nat}}\text{Li}$  has a negative scattering length - the amplitude of the neutron wave scattered by Li atoms is in *anti-phase* with respect to waves scattered by B and O. Thus Li atoms, that lie mostly between the (112) B-O network planes (Fig. 10) add *in-phase* contributions to the total scattered amplitude and thus *increase* the scattered intensity. Swenson *et al* [1] have observed a decrease in scattered intensity following substitution of  $^{\text{nat}}\text{Li}$  by  $^0\text{Li}$  - a mixture of  $^6\text{Li}$  and  $^7\text{Li}$  with zero coherent scattering length. The effect can be simulated semi-quantitatively by "substituting" Li in the  $\text{Li}_2\text{O} \cdot 2\text{B}_2\text{O}_3$  structure with the scattering length for V. Vanadium scatters almost incoherently - that is interference between M and the other atoms is reduced to almost zero. Fig. 9 shows qualitative agreement with experiment although the change is about twice as large as measured, which probably reflects positional disorder of the Li atoms in the glass.

#### 4. DISCUSSION AND CONCLUSIONS

The examples above suggest that real progress has been made in understanding FSDPs and the medium-range structures of borate glasses through examination of low-Q peaks in the scattering data for equivalent crystals. The first peak in the glass and features for the crystal show a pleasing agreement in positions and although one would not expect quantitative agreement of the intensity distributions, the results are not too un-representative either. Moreover, some of the detailed effects noted in experiments - differences between glasses with different isotopic composition, differences between the positions of peaks in neutron and x-ray data, are also reproduced by these simulations.

There are of course questions raised by this work: the problem raised by lack of agreement between positions of the FSDPs of amorphous and crystalline  $B_2O_3$ , for example. But perhaps the most difficult to understand is the origin of the fluctuations in atom and electron density in the glasses. Two factors (SFOs) seem important: packing efficiency and local charge balancing. In glasses containing big cations, Cs and Ag, with coordination numbers between 7 and 10, the boron-oxygen network must, to a degree, fold around the cation sites. In some structures - like the Li and Ag borates considered here - the boron-oxygen network is in fact plural - two independent nets intertwining and interweaving each other and the cations, which in some senses link the two networks. The reason for this plurality is the low packing efficiency of the n-membered B-O ring structures that characterise the structure of the borate polyanions. Associated with this will be the difficulties in maintaining local charge balance around the cation and the negative charge located in the vicinity of tetrahedrally-coordinated B. It seems reasonable to argue therefore that these constraints will lead to a limited set of low energy local configurations - the global minimum being the crystal, of course. These constraints thus favour medium-range structures, related - perhaps quite closely - to the energetically-favoured medium-range structure exhibited by the crystal.

The likelihood is that the ordering of the metal cations will resemble that of the crystal - thus explaining the x-ray data for the Cs and Ag borates. It is equally possible to argue (more conventionally) that strong, partially covalent B-O bonds need to be satisfied by low energy configurations, and that some degree of local ordering (certainly) and medium-range ordering (possibly) like that of the crystal is the only way this can be achieved. The glasses therefore have the *chemical* order of the polyanionic structures of the crystals - pentaborate, triborate and diborate rings, for example with cations occupying the intervening spaces. This would explain the neutron data for the Li and Ag borates.

*But the most plausible assumption is that order in the cationic and in the anionic sub-structures are inextricably linked - the one being only possible providing the other is satisfied. If so, equivalence of the FSDPs implies equivalence of local and medium-range order in both substructures.*

One further feature needs emphasis, perhaps. There are (many) alternative

structural explanations for the origin of FSDPs in glasses - void-network interference; preferred distances across n-membered rings; oscillations in atomic density on several scales; layer structures. The choice between these may to a degree be seen as purely a matter of preference or even a question of semantics. What this work demonstrates is that whatever language is chosen to describe the structure - arrangement of voids, say - the arrangement that fits the experimental data will most likely have a close similarity to that of an equivalent crystalline phase. But I believe that the notion of "quasi-Bragg" planes gives by far the clearest representation and interpretation of the experimental facts.

## REFERENCES

- [1]. J. Swenson, L. Börjesson & W.S. Howells, *Phys. Rev. B* **52** (1995), 9310.
- [2]. P.H. Gaskell & D.J. Wallis, *Phys. Rev. Lett.* **76** (1996), 66.
- [3]. Cerius<sup>2</sup> BIOSYM/ Molecular Simulations, San Diego, California, USA.
- [4]. J. Krogh-Moe, *Arkiv Kemi* **14** (1959), 451.
- [5]. J. Krogh-Moe, *Acta Cryst.* **23** (1967), 427.
- [6]. J. Krogh-Moe, *Acta Cryst.* **13** (1960), 889.
- [7]. L. Cervinka & F. Rocca, *J. Non-Cryst. Solids* **192&193** (1995), 12.
- [8]. K. Kamiya, S. Sakka, K. Matusita & Y. Yoshinaga, *ibid* **38&39** (1980), 147.
- [9]. J. Krogh-Moe, *Acta Cryst.* **18** (1965), 77.
- [10]. G. Paschina, G. Piccaluga & M. Magini, *J. Chem. Phys.* **81** (1984), 6201.
- [11]. J. Krogh-Moe, *Acta Cryst.* **15** (1962), 190.
- [12]. Neutron scattering data reported for the first time at this conference and published in the paper by Wanless *et al.* (A. J. Wanless, A. C. Wright, R. N. Sinclair, S. A. Feller, R. B. Williams, B. C. Johanson & M. T. Mayhew, *Proc. Second Int. Conf. on Borates Glasses, Crystals and Melts*, pp 506–512, show a prominent first peak at about  $11 \text{ nm}^{-1}$  in glassy  $\text{Cs}_2\text{O} \cdot 2 \cdot 5\text{B}_2\text{O}_3$ .

## THE INTERRELATIONSHIP BETWEEN THE STRUCTURES OF BORATE GLASSES AND CRYSTALS

Adrian C. WRIGHT,  
*J.J. Thomson Physical Laboratory, Reading University,  
Whiteknights, Reading, RG6 6AF, UK*

Natalia M. VEDISHCHEVA & Boris A. SHAKHMATKIN  
*Institute of Silicate Chemistry of the Russian Academy of Sciences,  
Ul. Odoevskogo, 24, Korp. 2, Sankt Petersburg, 199155, Russia*

A summary is presented of structural data for the crystalline polymorphs existing in a wide range of binary borate glass-forming systems and is used as a basis to propose a set of topological criteria for the formation of vitreous borate networks. It is shown that this yields considerable insight concerning the structural criteria for the formation of such networks, but that the information which can be obtained is limited by the fact that many of the relevant crystalline structures have not been determined.

### 1. INTRODUCTION

In any structural study of melt-quenched glasses, much useful information can be derived by considering the structures of related crystalline polymorphs. Thus, the traditional random network theory was first proposed by Zachariasen [1], using structural principles elucidated from crystallography, taking due regard of the additional degrees of topological freedom required by a disordered network appropriate to the vitreous state. The present survey of the crystalline polymorphs,  $mM_xO_y \cdot nB_2O_3$  (abbreviated  $mM.nB$ ), occurring in binary borate glass-forming systems [2,3], is being carried out in conjunction with neutron scattering and thermodynamic modelling studies of related glasses.

### 2. GLASS-FORMING REGIONS

The conventional single-phase glass-forming regions for the binary alkali borate and related systems are shown as a function of the mole fraction,  $x_M$ , of the modifying oxide in Fig. 1(A), together with the crystalline polymorphs occurring in each system which, in addition to those listed in the Gmelin Handbook [4], include  $3Li.7B$  [5] and  $3Rb.7B$  [6]. With the exception of the  $Ag_2O-B_2O_3$  [7],  $Rb_2O-B_2O_3$  and  $Cs_2O-B_2O_3$  [8] systems, the glass-forming regions are taken from Rawson [9] and the handbooks compiled by Mazurin and co-work-

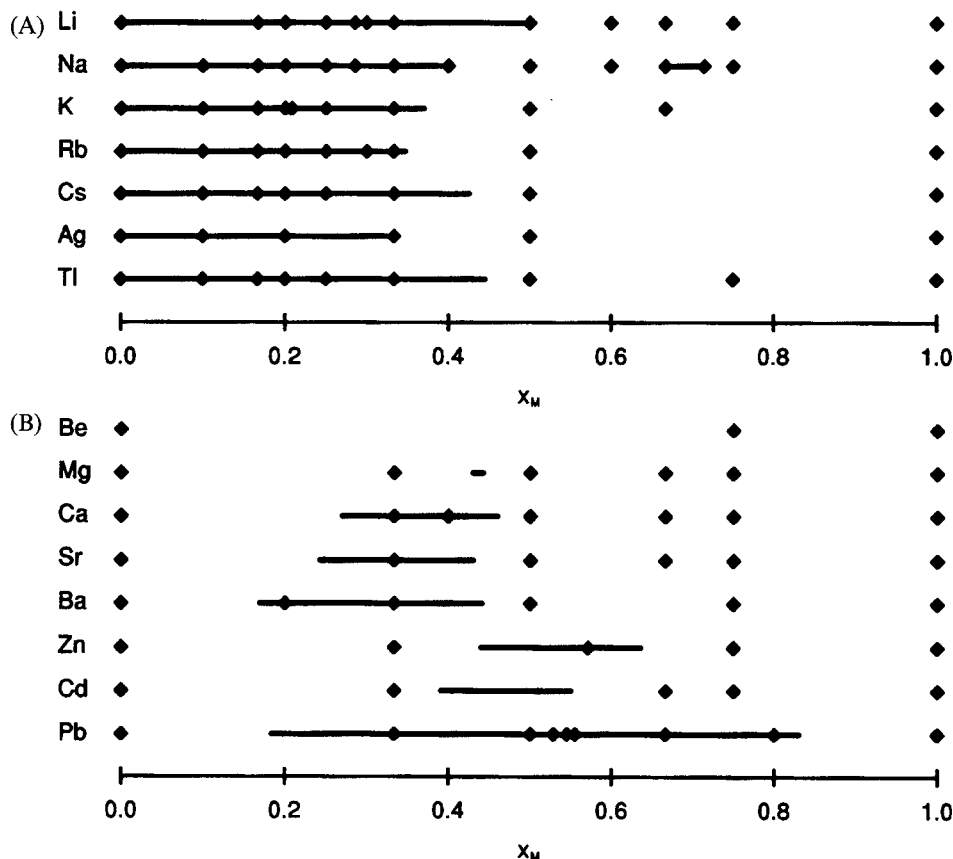


Fig. 1. Conventional glass-forming regions (—) for binary borate systems, together with the corresponding crystalline polymorphs (◆). (A),  $M_2O-B_2O_3$  and (B),  $MO-B_2O_3$ .

ers [10]. For all of the binary systems in Fig. 1(A), the single-phase glass-forming region commences at zero  $x_M$ , whereas, for all of the  $MO-B_2O_3$  systems {Fig. 1(B)}, single phase glasses do not form at low modifier contents. Any glass formation in this region results in phase-separated glasses. For example, Shelby [11] records two glass transition temperatures for  $PbO-B_2O_3$  glasses in the region  $0.005 < x_M < 0.195$ , corresponding to those for the two limiting compositions. Before discussing the relationship between the glass-forming regions and crystalline polymorphs in Fig. 1, however, it is first necessary to summarise the structural model of borate glasses which has evolved from early studies of Krogh-Moe and Bray [12].

### 3. BRAY MODEL

Borate glasses are an enigma in that there is now increasing evidence that, for  $x_M < 0.5$ , an important aspect of their structures is that they contain *superstructural units*, which comprise well defined arrangements of the basic

**Table 1**  
Superstructural Units Occurring in Crystalline Borates

	Superstructural Unit	Formula	BO <sub>3</sub>	BO <sub>4</sub>	Connectivity			Examples	
					B <sup>[3]</sup>	B <sup>[4]</sup>	Total	Sole unit	Multi-unit
A	Boroxol	B <sub>3</sub> O <sub>6</sub>	3	-	3	-	3	-	Cs.9B
B	Triborate	B <sub>3</sub> O <sub>7</sub>	2	1	2	2	4	Li.3B	β-Na.3B
C	Di-triborate	B <sub>3</sub> O <sub>8</sub>	1	2	1	4	5	Ba.2B	K.2B
D	Metaborate	B <sub>3</sub> O <sub>9</sub>	-	3	-	6	6	Ca.B-IV	Ca.B-III
E	Diborate	B <sub>4</sub> O <sub>9</sub>	2	2	2	2	4	Li.2B	α-Na.3B
F	Pentaborate	B <sub>5</sub> O <sub>10</sub>	1	4	4	-	4	K.B	α-Na.4B
G	Di-pentaborate	B <sub>5</sub> O <sub>11</sub>	2	3	3	2	5	-	α-Na.2B
H	Tri-pentaborate	B <sub>5</sub> O <sub>12</sub>	3	2	2	4	6	-	2Ca.3B

structural units (BO<sub>3</sub> and BO<sub>4</sub>), with no internal degrees of freedom in the form of variable bond or torsion angles, as summarised in Table 1 (above) and in Fig. 1 of the accompanying paper by Sinclair *et al.* [13]. The much lower incidence of superstructural units in molecular dynamics simulations suggests that they are present in significantly greater numbers, as a result of a favourable formation energy, than might be expected on statistical grounds, given an equilibrium B-Ö-B bond angle of ~120-130°. The currently accepted model of borate glasses, therefore, comprises a modified Zachariasen-Warren network in which the superstructural units are connected randomly to each other [12], together with the basic BO<sub>3</sub> and BO<sub>4</sub> structural units. The question thus arises as to how such units can be connected together topologically to achieve a disordered glass network with no broken bonds, except for non-bridging oxygen atoms, and what are the criteria for their interconnection. As will be demonstrated, much useful information concerning this question can be obtained by studying related crystalline structures.

#### 4. M<sub>2</sub>O-B<sub>2</sub>O<sub>3</sub> SYSTEMS

The lack of crystallographic information for binary borate systems can be seen from the Na<sub>2</sub>O-B<sub>2</sub>O<sub>3</sub> system, where a full crystal structure determination has only been performed for 7 out of a total of 22 polymorphs listed in the Gmelin Handbook [4]. The superstructural units or borate anions occurring in these 7 polymorphs are summarised in Table 2, which shows the complexity of the crystalline borates in that the first four polymorphs all have structures that include more than one superstructural unit. Similarly, the various diborate structures also exhibit a wide range of superstructural units, as may be seen from Table 3. Note that, unlike many diborates, α-Na.2B does not contain the diborate group [14], although this is found in α-Na.3B [15] which conversely does not have any triborate groups. Of the crystalline diborates included in Fig. 1, structures have not been reported for Cs, Ag and Tl.

Another consequence of the lack of crystallographic data is that, in most cases, the nature of the transitions between polymorphs of the same stoichi-



**Table 2**  
Superstructural Units in Crystalline Na<sub>2</sub>O–B<sub>2</sub>O<sub>3</sub> Polymorphs [2]

Crystal	B <sub>5</sub> O <sub>10</sub>	B <sub>3</sub> O <sub>7</sub>	B <sub>5</sub> O <sub>11</sub>	B <sub>4</sub> O <sub>9</sub>	BO <sub>4</sub>	B <sub>3</sub> O <sub>6</sub> <sup>3-</sup>	B <sub>2</sub> O <sub>3</sub> <sup>4-</sup>	BO <sub>3</sub> <sup>3-</sup>
α-Na.4B	0.5	0.5	-	-	-	-	-	-
α-Na.3B	0.5	-	-	0.5	-	-	-	-
β-Na.3B	0.33	0.33	-	-	0.33	-	-	-
α-Na.2B	-	0.5*	0.5	-	-	-	-	-
α-Na.B	-	-	-	-	-	1.0	-	-
2Na.B	-	-	-	-	-	-	1.0	-
3Na.B	-	-	-	-	-	-	-	1.0

\* Has non-bridging oxygen atom on one B<sup>[3]</sup>

ometry with increasing temperature is also unknown. Basically, these can be of three main types: displacive (superstructural units and network topology unchanged), reconstructive (superstructural units unchanged, network topology changed) and super-reconstructive (superstructural units changed). In the case of Na.3B, the α–β transition is super-reconstructive.

Where only BO<sub>4</sub> tetrahedra and no non-bridging oxygen atoms are formed, the fraction of 4-fold co-ordinated boron atoms,  $x_4$ , is given by [16]

$$x_4 = x_M / (1 - x_M) = m/n \quad (1)$$

in which m and n refer to the crystalline compound with the general formula given in Section 1. The fact that almost all crystalline structures with  $x_M < 0.5$  have this value of  $x_4$  (α-Na.2B [14] is a notable exception) indicates that the conversion of BO<sub>3</sub> triangles into BO<sub>4</sub> tetrahedra is energetically more favourable than the formation of non-bridging oxygen atoms. The rich variety of borate structural chemistry, however, is due to the proximity of these two formation energies and in the glass extra degrees of freedom can be generated by the formation of non-bridging oxygen atoms at higher modifier contents, as shown for a number of systems elsewhere in these proceedings. The degrees of freedom required for glass formation also mean that superstructural units with the higher connectivities (e.g. di-pentaborate, cf. Table 1) are less likely to be present in

**Table 3**  
Superstructural Units in Crystalline Diborates

Diborate	B <sub>3</sub> O <sub>7</sub>	B <sub>5</sub> O <sub>11</sub>	B <sub>4</sub> O <sub>9</sub>	B <sub>3</sub> O <sub>8</sub>	BO <sub>3</sub>	BO <sub>4</sub>
Li,Mg,Zn,Cd	-	-	1.0	-	-	-
Na	0.5*	0.5	-	-	-	-
K,Rb	-	-	0.33	0.33	0.33	-
Ca	0.33	-	0.33	-	-	0.33
Sr,Pb	-	-	-	-	-	1.0**
Ba	-	0.5	-	0.5	-	-

\* Has non-bridging oxygen atom on one B<sup>[3]</sup>

\*\* Has 3-co-ordinated O atoms

the vitreous state, in line with Zachariasen's second rule [1] which effectively defines the connectivity of the (super)structural units.

Many crystalline polymorphs containing superstructural units exist as two independent, interpenetrating networks suggesting that, in the presence of significant numbers of superstructural units, the corresponding glasses are locally similar, in order to achieve a sufficiently high borate network density. As pointed out by Krogh-Moe [17], the bond angles and superstructural units of a single borate network do not in general permit efficient atom packing. Instead, a double network is formed so as to avoid a very open, low density structure. Alternatively, as in 5K.19B [18], a normal borate network density can be obtained by the incorporation of larger numbers of independent  $\text{BO}_3$  triangles and  $\text{BO}_4$  tetrahedra.

An important stereochemical parameter is the effective radius of the network modifying cations, which determines the size of the cavities in the borate network in which these ions reside and hence influences the borate network density. It is characteristic of borate crystal structures that the co-ordination number,  $n_{\text{M(O)}}$ , of a given network modifying cation varies for different crystalline polymorphs and frequently between different sites in the same structure. Similarly, the oxygen polyhedra surrounding the network modifying cations are often considerably distorted, with a wide range of M-O distances. Krogh-Moe [19] ascribes this to the effect of the rigid superstructural units and hence similar distorted network modifying cation polyhedra will exist in the vitreous state with considerable variation in both distortion and co-ordination number.

The repulsion between negatively charged  $\text{BO}_4$  tetrahedra means that  $\text{B}^{[4]}\text{O}-\text{B}^{[4]}$  bridges not within a superstructural unit are energetically unfavourable. Hence, only  $\text{B}^{[3]}\text{O}-\text{B}^{[3]}$  and  $\text{B}^{[3]}\text{O}-\text{B}^{[4]}$  bridges are found outside superstructural units in the crystalline state until  $\text{B}^{[4]}\text{O}-\text{B}^{[4]}$  bridges are unavoidable, which occurs at  $x_{\text{M}}=0.3$  if there are also none within superstructural units. If the number of  $\text{B}^{[4]}\text{O}-\text{B}^{[4]}$  bridges is the minimum required by the stoichiometry, the average co-ordination number,  $n_{4(4)}$ , of  $\text{BO}_4$  tetrahedra around a central  $\text{BO}_4$  tetrahedron in the range  $0.3 \leq x_{\text{M}} \leq 0.5$  is given by [20]

$$n_{4(4)} = (10x_{\text{M}} - 3)/x_{\text{M}} \quad (2)$$

and it is interesting to note that, at the diborate composition,  $n_{4(4)}=1$ , which is consistent with a network of diborate groups linked only by  $\text{B}^{[3]}\text{O}-\text{B}^{[4]}$  bridges. In the vitreous state,  $\text{B}^{[3]}\text{O}-\text{B}^{[3]}$  and  $\text{B}^{[3]}\text{O}-\text{B}^{[4]}$  bridges will be formed together with the minimum number of  $\text{B}^{[4]}\text{O}-\text{B}^{[4]}$  bridges outside superstructural units necessary to attain the required degrees of topological freedom. As discussed elsewhere [20], the variation of  $x_4$  with composition can be modelled by assuming that  $\text{B}^{[4]}\text{O}-\text{B}^{[4]}$  bridges are not present in the vitreous state. When compared to NMR data for the  $\text{Li}_2\text{O}-\text{B}_2\text{O}_3$  system, this model does, however, underestimate  $x_4$  in the region ( $0.35 \leq x_{\text{M}} \leq 0.55$ ) due to the presence of  $\text{B}^{[4]}\text{O}-\text{B}^{[4]}$  bridges within superstructural units, such as the diborate group.

## 5. VITREOUS BORON OXIDE

The structure of vitreous  $B_2O_3$  is the subject of considerable controversy in the literature, with regard to the structural role played by the  $B_3O_6$  boroxol group {Fig 1(A) of ref. [13]}, and, as may be seen from papers elsewhere in this proceedings, there are currently two main models of the structure of vitreous  $B_2O_3$ , the boroxol ring model, where the fraction,  $f$ , of boron atoms in boroxol groups is  $\sim 0.8$  [21], and the  $BO_3$  triangle model with  $f \leq 0.1$  [22]. The ambient pressure crystalline polymorph,  $B_2O_3$ -I [23], does not contain boroxol groups, but is formed from planar ribbons of  $BO_3$  triangles. However, there are a number of indications that the structure of vitreous  $B_2O_3$  is very different from that of  $B_2O_3$ -I. For example, the density of  $B_2O_3$ -I is very much higher (41%) than that of the glass and, in addition, a crystal of  $B_2O_3$ -I seeded into the anhydrous supercooled melt does not grow, even over a period of several months [24], indicating an extremely high activation energy for crystallisation. Neither of these facts is explained by the  $BO_3$  triangle model which, in addition, fails to predict the sharp peak at  $3.6 \text{ \AA}$  in the real space correlation function,  $T(r)$ . This would require a large fraction of the  $BO_3$  triangles to be constrained to be approximately coplanar and there is no mechanism for this in the vitreous state in the absence of boroxol groups. Note that, with inadequate numbers of boroxol groups, the reverse Monte Carlo technique [22] is likely to constrain adjacent  $BO_3$  triangles to be coplanar in order to reproduce the sharpness of this peak, although the resulting structures will almost certainly be unstable to relaxation with a realistic potential or else occupy too small a region of configuration space to be accessible by conventional melt quenching.

Evidence for the boroxol ring model, which explains both the anomalously low density of vitreous  $B_2O_3$  and the extremely high activation energy for crystallisation from the melt, has been summarised elsewhere [21] and will not be repeated here. One of the main objections to the boroxol ring model has been that it is extremely difficult to construct a random network model with a sufficiently high number density,  $\rho^\circ$ . However, the problem with all of the random network models of vitreous  $B_2O_3$  to date is that they have been constructed with the preconceived notion that the structure comprises a *single* network, rather than locally independent interpenetrating networks as discussed in Section 4. An extremely interesting question is why there are no crystalline form of  $B_2O_3$  containing only boroxol groups. Clearly crystallisation from the melt would similarly require a similar substantial degree of boroxol ring breaking and network rearrangement, as for the formation of  $B_2O_3$ -I, but the fascinating possibility exists of the formation of such a crystalline polymorph by the appropriate chemical synthesis.

## 6. MO- $B_2O_3$ SYSTEMS

The lack of single phase glass formation for the MO- $B_2O_3$  systems at low modifier contents is extremely interesting and may be connected with the fact that two  $BO_4$  tetrahedra are required in close proximity to balance the charge on a  $M^{2+}$  ion. This is supported by the lack (Be) or very small range (Mg) of

glass formation for the smallest modifying cations. Conversely, glasses are formed at the lowest modifier contents for the largest and most easily polarised cations (Ba and Pb), the lowest of all being for Ba, which is the only system for which a crystalline tetraborate has been reported.

The situation where the second oxide has considerable intermediate character and can behave as a network forming oxide, at least at high concentrations, is more complicated, as may be seen from the crystal structure of 6Pb.5B [25] ( $x_M = 0.545$ ), which has the largest isolated borate anion found to date, consisting of two diborate groups connected together by a chain of two  $\text{BO}_3$  triangles. This includes a terminating  $\text{B}^{(4)}\text{-O}$  on each diborate group, but examination of the Pb-O bonding reveals the presence of considerable covalent character. It is therefore likely that similar groupings or superstructural units also occur in lead borate glasses and are responsible for the survival of the 3.6 Å superstructural unit peak in  $T(r)$  to high PbO contents [26].

## 7. CONCLUSIONS

From the preceding sections, it is apparent that a study of the appropriate crystal structures can yield considerable insight into the structures of borate glasses, provided suitable allowance is made for the extra degrees of network freedom necessary for glass formation. However, the information which can be inferred is limited by the fact that many crystalline borate polymorphs either have unknown structures or have merely been established to be isostructural with another compound, without detailed structural parameters such as bond lengths and angles being determined. Hence there is a great need for further crystallographic studies of borate systems.

## Acknowledgement

The authors would like to thank R.L. Snyder for his help in searching various crystallographic databases and G.D. Chryssikos for helpful discussions concerning the structures of the crystalline diborates.

## REFERENCES

- [1] W.H. Zachariasen, *J. Amer. Chem. Soc.* **54** (1932), 3841.
- [2] A.C. Wright, N.M. Vedishcheva & B.A. Shakhmatkin, *J. Non-Cryst. Solids* **192&193** (1995), 92.
- [3] A.C. Wright, N.M. Vedishcheva & B.A. Shakhmatkin, *Adv. X-Ray Anal.* **39** (1996), in press.
- [4] G. Heller, *Gmelin Handbuch der Anorganischen Chemie*, Vol. 28, *Borverbindungen Part 7* (Springer-Verlag, Berlin, 1975).
- [5] J. Aidong, L. Shirong, H. Qingzhen, C. Tianbin & K. Deming *Acta Crystallogr.* **C46** (1990), 1999.
- [6] R.S. Bubnova, I.G. Polyakova, S.K. Filatov & M.G. Krzhizhanovskaya, *Proc. Second Int. Conf. on Borates Glasses, Crystals and Melts*, 223.
- [7] J.A. Kapoutsis, E.I. Kamitsos & G.D. Chryssikos, *Proc. Second Int. Conf. on Borates Glasses, Crystals and Melts*, 303.
- [8] M.M. Shultz, N.M. Vedishcheva, B.A. Shakhmatkin & A.M. Starodubtsev, *Fiz. Khim.*

*Stekla* **11** (1985), 472.

- [9] H. Rawson, *Inorganic glass-forming systems* (Academic Press, London, 1967).
- [10] O.V. Mazurin, M.V. Streltsina & T.P. Shvaiko-Shvaikovskaya, *The properties of Glasses and Glass-Forming Systems*, Vol. 2 (Nauka, Leningrad, 1975) and Vol. 4, Part 1 (1980).
- [11] J.E. Shelby, *J. Non-Cryst. Solids* **49** (1982), 287.
- [12] P.J. Bray, *J. Non-Cryst. Solids* **75** (1985), 29.
- [13] R.N. Sinclair, A.C. Wright, A.J. Wanless, A.C. Hannon, S.A. Feller, M.T. Mayhew, B.M. Meyer, M.L. Royle, D.L. Wilkerson, R.B. Willaims & B.C. Johanson, *Proc. Second Int. Conf. on Borates Glasses, Crystals and Melts*, 140.
- [14] J. Krogh-Moe, *Acta Crystallogr.* **B30** (1974), 578.
- [15] J. Krogh-Moe, *Acta Crystallogr.* **B30** (1974), 747.
- [16] J. Krogh-Moe, *Phys. Chem. Glasses* **3** (1962), 1.
- [17] J. Krogh-Moe, *Acta Crystallogr.* **18** (1965), 77.
- [18] J. Krogh-Moe, *Acta Crystallogr.* **B30** (1974), 1827.
- [19] J. Krogh-Moe, *Acta Crystallogr.* **B28** (1972), 168.
- [20] A.C. Wright, N.M. Vedishcheva & B.A. Shakhmatkin, *M.R.S. Symp. Proc.* **455** (1997), in press.
- [21] A.C. Hannon, D.I. Grimley, R.A. Hulme, A.C. Wright & R.N. Sinclair, *J. Non-Cryst. Solids* **177** (1994), 299.
- [22] J. Swenson & L. Börjesson, *Proc. Second Int. Conf. on Borates Glasses, Crystals and Melts*, 425.
- [23] G.E. Gurr, P.W. Montgomery, C.D. Knutson & B.T. Gorres, *Acta Crystallogr.* **B26** (1970), 906.
- [24] F.C. Kracek, G.W. Morey & H.E. Merwin, *Am. J. Sci.* **35A** (1938), 143.
- [25] J. Krogh-Moe & P.S. Wold-Hansen, *Acta Crystallogr.* **B29** (1973), 2242.
- [26] N.M. Vedishcheva, B.A. Shakhmatkin, A.C. Wright, D.I. Grimley, G. Etherington & R.N. Sinclair, In: *Fundamentals of Glass Science and Technology* (ESG, Venice, 1993) p. 459.

## STRUCTURAL AND CHEMICAL INHOMOGENEITIES IN BORATE GLASSES

V. V. GOLUBKOV

*Institute of Silicate Chemistry, Odоеvskogo 24/2,  
St. Petersburg, 199155, Russia*

The structure of  $B_2O_3$  and alkali borate glasses has been investigated using the SAXS technique. The radii of the regions of structural inhomogeneity observed in  $B_2O_3$  in the equilibrium state are predominantly 6-7 Å. A change in the water content has no effect on the structural inhomogeneity, which depends only on the temperature. After rapid changes of temperature, this structure develops independently of the changes in the thermal density fluctuations. The development of the structural inhomogeneity that proceeds after abrupt increases in temperature is primarily associated with the formation of regions of inhomogeneity with radii as large as 30-35 Å. An abrupt decrease in temperature leads to the appearance of regularity in the distribution of the regions of structural inhomogeneity. The inhomogeneity regions in low alkali borate glasses are chain branched clusters. A certain regularity in the distribution of the chemical inhomogeneity regions is revealed at low temperatures. The degree of regularity increases with decreasing temperature and becomes a maximum at a temperature close to the temperature of the transition to a disordered solid state,  $T_s$ . After abrupt changes in temperature, the development of structural inhomogeneity brings about a change in the distribution of chemical inhomogeneity. The redistribution of the inhomogeneity regions throughout the bulk of the glass proceeds further, even if the structure of the matrix attains its equilibrium state. Therefore, the structural relaxation in alkali borate glasses involves changes in the short and medium range order, due to thermal density fluctuations and the development of structural inhomogeneity, and also the redistribution of regions of chemical inhomogeneity.

### 1. INTRODUCTION

The small angle X-ray scattering (SAXS) technique has been used previously to study the structure of  $B_2O_3$  and alkali borate glasses [1,2]. It was further used to investigate the temperature and concentration dependences of the SAXS intensity for  $B_2O_3$  and alkali borate melts [3] and the kinetics of structural relaxation in  $B_2O_3$  over a wide range of temperatures below the glass transition temperature ( $T_g$ ) [4]. It was found, on the basis of the SAXS data, that a metastable phase separation region exists in the lithium borate system and that there are no phase separation regions in the other alkali borate systems [5].

Two types of inhomogeneity can be considered. In one-component liquids and glasses the inhomogeneities responsible for small angle x-ray scattering

are mainly caused by thermal density fluctuations. Such objects can be regarded as homogeneous.

The term microheterogeneous structure indicates the presence of regions of inhomogeneity, RI, i.e. the occurrence of regions whose electron density differs from the mean electron density of the surrounding matrix. This difference in the electron density may be due to changes in the short range order structure and, it so, is denoted structural inhomogeneity. Chemical inhomogeneity arises due to the appearance of RI whose composition differs from that of the surrounding matrix.

It seems reasonable to assume that inhomogeneities in (single-component) vitreous  $B_2O_3$  have to arise only from thermal density fluctuations. Nevertheless, the presence of RI was observed for  $B_2O_3$ , both in the vitreous state and in the metastable equilibrium supercooled liquid state.

It was shown [2,3] that there is a temperature (temperature range) at which structural inhomogeneity disappears and a sample can be considered as homogeneous, i.e. the sample does not contain RI. At this temperature, a supercooled liquid transforms into a new state: a noncrystalline solid. Hence, in what follows, this temperature will be designated as  $T_s$ . Abrupt changes in temperatures give rise to the transitional structural states and, primarily, the structural inhomogeneity undergoes substantial changes.

A clearly expressed microheterogeneous structure was revealed in studies of glasses and melts in all alkali borate systems [3]. The radii of the RI in these materials were equal to 10-15 Å. The sizes of the RI decreased with increasing content of the alkali metal oxide and in passing from the sodium borate to the cesium borate system. The RI are regions with a higher content of alkali ions. The concentration of alkali metal oxide at which the degree of inhomogeneity reached a maximum also decreased in passing from the lithium borate to the cesium borate system (from 4-5%  $Na_2O$  for the sodium borate system to 2%  $Cs_2O$  for the cesium borate system). It should be noted that, in single phase lithium borate glasses, containing up to 10 mol%  $Li_2O$ , the development of supercritical fluctuations proceeded independently of the changes in the chemical inhomogeneity inherent to glasses of all of the alkali borate systems.

This paper reports some of the new results obtained in a SAXS study of the structure of and structural relaxation processes in both  $B_2O_3$  and alkali borate glasses.

## 2. THEORY AND EXPERIMENTAL MEASUREMENTS.

The SAXS intensity,  $I_{SAXS}$ , for single component homogeneous liquids,  $I_r$ , is due to the inhomogeneity related to their thermal density fluctuations (TDF) at scattering angles close to zero

$$I_p(0) = \rho^2 k T \chi_T V \quad (1)$$

where  $\rho$  is the mean electron density,  $k$  is Boltzmann's constant,  $\chi_T$  is the isothermal compressibility,  $T$  is the absolute temperature and  $V$  is the volume.

This intensity is independent of the scattering angle. Usually, however, due to the influence of large angle X-ray scattering, an increase in  $I_p$  is observed with increasing scattering angle

$$I_p = I_p(0) \exp(Ks^2) \quad (2)$$

where  $s = (4\pi \sin \varphi/2)/\lambda$ ,  $\varphi$  is the scattering angle,  $\lambda$  is the wavelength of the X-radiation and  $K$  is a constant which, in the case of molecular liquids, depends on the molecular volume [6].

Molecular liquids can be regarded as ultimately homogeneous media. For all one-component molecular liquids so far investigated, Eq. (2) holds at all attainable scattering angles. Hence, satisfying Eq. (2) can be regarded as a criterion for the homogeneity of the sample.

In the presence of RI of nanometre size, a characteristic scattering occurs whose intensity,  $I_{RI}$ , may be represented by

$$I_{RI} = I_{RI}(0) \exp(-s^2 R_g^2/3) \quad (sR_g \ll 1) \quad (3)$$

and

$$I_{RI} = 2\pi(\rho_1 - \rho_2)S/s^4 \quad (sR_g \gg 1) \quad (4)$$

where  $\rho_1$  and  $\rho_2$  are the electron densities of the RI and the surrounding matrix,  $S$  is the interfacial surface and  $R_g$  is the radius of gyration of the RI.

It should be noted that, in the case of scattering by a fractal structure, a range of scattering angles has to exist at which the  $I_{SAXS}$  can be represented by

$$I(s) \sim s^{-n} \quad (5)$$

In the general case,  $n$  depends on the type of fractal structure. For scattering by chain branched structures,  $n=2$  [7].

Given a certain regularity in the distribution of the RI throughout the bulk of a sample, the SAXS curve exhibits a maximum associated with interference effects. The location of this maximum provides a way of determining the spacing (mean or repetitive) between the centers of the RI.

The mean square value of the electron density difference,  $\langle(\Delta\rho)^2\rangle$ , can be determined from  $I_{SAXS}$ . The value of  $\langle(\Delta\rho)^2\rangle$  is the most general characteristic of the degree of inhomogeneity. In the case of a two-phase sample

$$\langle(\Delta\rho)^2\rangle = (\rho_1 - \rho_2)^2 W_1 W_2 \quad (6)$$

where  $W_1$  and  $W_2$  are the respective volumes of the phases.

The glass and melt structures were investigated, using a SAXS instrument with a high temperature attachment [8], at temperatures up to 1200°C. Cu  $K_{\alpha}$  radiation was used and  $I_{SAXS}$  was measured at scattering angles from 6 to 550'. Note that, from the known temperature dependence of  $I_{SAXS}$  for a sample in an equilibrium state, it is very easy to determine the fictive temperature,  $T_f$ , and glass transition temperature,  $T_g$ , or the standard  $T_g$ ,  $T_g^{st}$  [9]. Since the influence of water content on the  $T_g$  of  $B_2O_3$  has been well studied [10], the water content in a  $B_2O_3$  sample can be checked from the measured  $T_g$ .



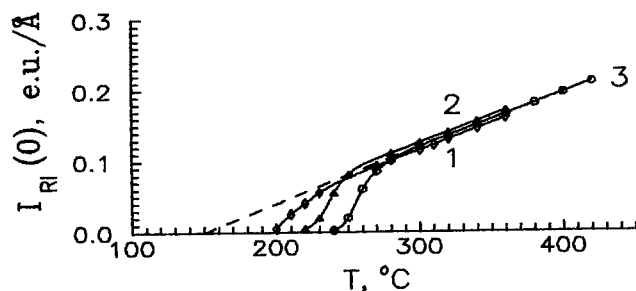


**Fig.1.** Temperature dependences of the SAXS due to structural inhomogeneity,  $I_{RI}(0)$ , for  $B_2O_3$  in the equilibrium state at different water contents. Content of  $H_2O$  in mol%:(1), 1; (2), 0.5 and (3), 0. The lines are drawn as a guide to the eye and the errors are within the size of the data points.

### 3. RESULTS

#### 3.1. The Structure of $B_2O_3$

The glasses were synthesized by melting boric acid in a platinum crucible. Within the limits of the experimental errors in the  $I_{SAXS}$  measurements, the impurities contained in the reagent did not affect the magnitude and angular dependence of the  $I_{SAXS}$ . The water content of the vitreous  $B_2O_3$  was controlled by changes in the synthesis conditions. The sample was prepared from the melt, which was allowed to stand under atmospheric conditions at  $1000^\circ C$  for 0.5 h and further heat-treated at  $1250^\circ C$  for 3 h, and also from the same melt held under vacuum at  $1000^\circ C$  for 1 h. It was shown [9] that a change in the water content does not affect the angular dependence of  $I_{SAXS}$ . Therefore, it can be concluded that the presence of water does not affect the structural inhomogeneity of  $B_2O_3$ .

The temperature dependence of the SAXS due to regions of structural inhomogeneity,  $I_{RI}(0)$ , for samples with different water contents are shown in Fig. 1. All of the curves exhibit a sharp decrease in  $I_{RI}(0)$  in the range  $T_s \pm 10^\circ C$ , which is associated with the disappearance of these regions. It is evident from Fig. 1 that, at high temperatures (above  $\sim 275^\circ C$ ),  $I_{RI}(0)$  is independent of the water content and depends only on temperature.

The sizes of the RI (radii obtained from Eq. 3 on the assumption that the regions have a spherical shape and constant electron density) depend weakly on temperature and increase from 6 Å at  $300^\circ C$  to 7 Å at  $400^\circ C$ . As noted above, sharp increases or decreases of temperature give rise to transitional states of the structure.

Figure 2 shows the SAXS curves for a  $B_2O_3$  sample heat-treated for different times at  $270^\circ C$ , after abruptly increasing the temperature from  $245$  to  $270^\circ C$ . As may be seen, when the temperature was abruptly raised, the  $I_{SAXS}$  in the small angle region increased to values exceeding the equilibrium value and then decreased back to it.

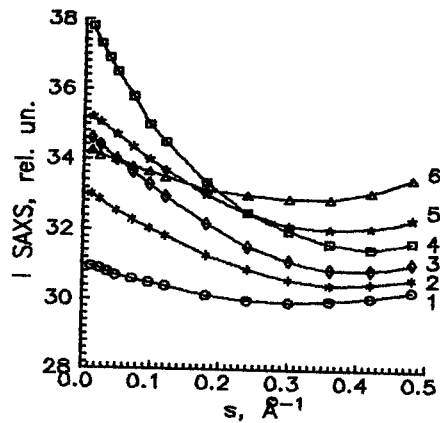


Fig. 2. Angular dependence of the SAXS intensity for a  $B_2O_3$  sample in the equilibrium state at (1) 245 and (6) 270°C and following different times of heat treatment at 270°C after abrupt heating from 245 to 270°C. Time of heat treatment at 270°C: (2), 10; (3), 20; (4), 40; (5), 80 and (6), 180 min. The lines are drawn as a guide to the eye and the errors are within the size of the data points.

It can be concluded from the angular dependence of the SAXS that the size of the RI in the  $B_2O_3$  sample in the transitional state increases with development of structural inhomogeneity. The maximum size of the RI under these heat treatment conditions is equal to 30-35 Å. Thus, the regions with sizes (radii) from 6 to 30-35 Å exist in the samples passing through the transition state.

After a sharp decrease in temperature, the SAXS intensity in the small scattering angle region decreases to lower than the equilibrium value and a maximum appears in the SAXS curve [2]. The angular dependence of  $I_{SAXS}$  from

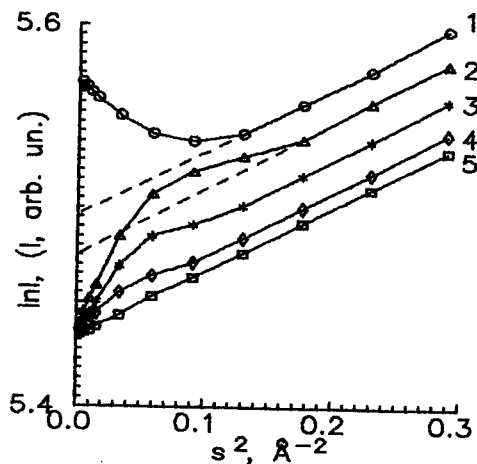


Fig. 3. Dependence of  $\ln I_{SAXS}$  on  $s^2$  for  $B_2O_3$ : (1), Equilibrium state at 220°C; (2-5), A sample cooled from 350°C at 10 K/min and then heat treated at 200°C for 17, 40, 70 and 170 h, respectively. The lines are drawn as a guide to the eye and the errors are within the size of the data points.

$B_2O_3$ , heat-treated for different times at  $T < T_s$ , are shown in Fig. 3. These changes in the angular dependence of  $I_{SAXS}$  result from interference effects caused by the appearance of regularity in the electron density. The mean distance between the centers of the regions, determined from the position of the maximum in the SAXS curve, is equal to 15-20 Å. It is seen from Fig. 3 that, with increasing heat treatment time, the interference effects decrease and, in the final stage,  $I_{SAXS}$  corresponds to scattering by TDF only. At temperatures above  $T_s$ , an increase in the heating time leads to the decay of the regular structure. When the equilibrium structural state is attained, it can be concluded from the angular dependence of  $I_{SAXS}$  that the RI are distributed randomly throughout the sample volume.

### 3.2. Alkali Borate Glasses

Figure 4 shows graphs of  $\log I_{RI}$  vs  $s$  for samples of sodium borate glasses containing 1.0 and 4.0 mol%  $Na_2O$  (curves 1 and 2, respectively) and for rubidium and cesium borate glasses containing 1.0 mol%  $Rb_2O$  or  $Cs_2O$  (curves 3 and 4, respectively). The precision measurements of  $I_{SAXS}$  enable a linear portion to be obtained with a slope equal to  $-1$  (taking into account the collimation conditions, this slope corresponds to a value of  $n$  in Eq. (5) equal to 2) in the curve of  $\log I_{RI}$  vs  $\log s$  at scattering angles of  $100-200'$ . Similar linear portions are clearly seen in the angular dependence of  $I_{RI}$  for glasses in all of the alkali borate systems, when the concentration of alkali metal oxides are below the concentrations at which the degree of inhomogeneity reaches a maximum. The presence of these portions in the SAXS curves can be considered fairly reliable evidence for a fractal structure.

At higher concentrations, similar linear portions are less pronounced. How-

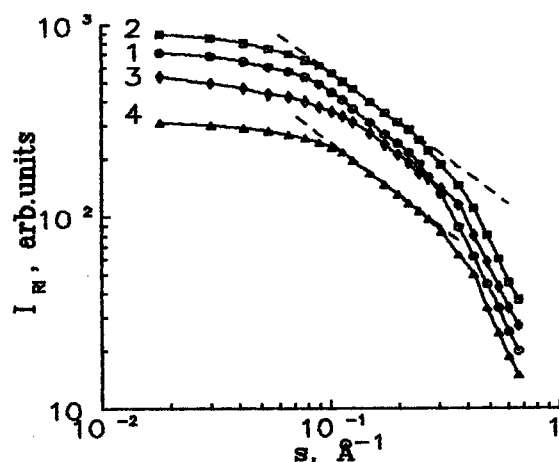


Fig.4. Graphs of  $\log I_{RI}$  vs  $\log s$  for alkali borate glass samples. Content of alkali oxide: (1), 1.5 mol%  $Na_2O$ ; (2), 4.0 mol%  $Na_2O$ ; (3), 1.0 mol%  $Rb_2O$  and (4), 1.0 mol%  $Cs_2O$ . The lines are drawn as a guide to the eye and the errors are within the size of the data points.

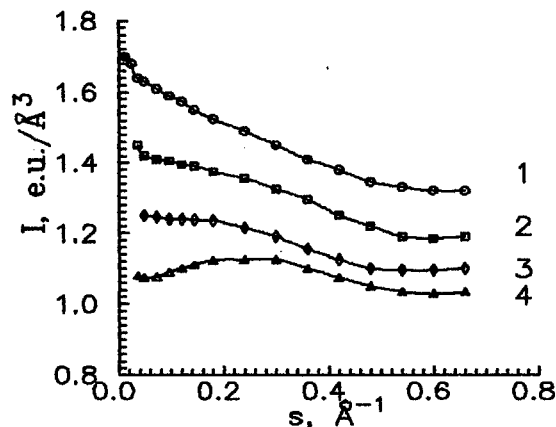


Fig.5. Angular dependence of  $I_{\text{SAXS}}$  for a sodium borate glass, containing 8.0 mol%  $\text{Na}_2\text{O}$ , in the equilibrium state at different temperatures. Temperature T: (1), 320; (2), 350; (3), 400 and (4), 460°C. The lines are drawn as a guide to the eye and the errors are within the size of the data points.

ever, as shown below, this is mainly associated with a new specific behaviour of the structure rather than with a change in its nature.

As mentioned above, chemical inhomogeneity was observed at temperatures up to 1200°C. In the case of low-alkali sodium borate glasses (containing up to 4-5 mol%  $\text{Na}_2\text{O}$ ), structural rearrangements of the chemical inhomogeneity cease in the temperature range 420-450°C. At higher concentrations of alkali metal oxide, a specific behaviour of the chemically inhomogeneous structure was observed at temperatures lower than  $T_g$ .

The SAXS curves for a sample of sodium borate glass, containing 8.0 mol%  $\text{Na}_2\text{O}$ , in the equilibrium state at different temperatures are displayed in Fig. 5.  $T_g$  for this sample is equal to 350°C. A clearly defined maximum is observed at 320°C. At 350°C, the SAXS curve shows a substantial portion in the small angle range, in which  $I_{\text{SAXS}}$  is almost independent of the scattering angle. This portion is the result of interference effects - a decrease in  $I_{\text{SAXS}}$ , caused by the RI, is compensated for by an increase due to interference effects. It should be noted that the sizes of the RI determined from the slope of the  $\log I_{\text{RI}}$  vs  $s^2$  plot, will depend on the magnitude of the interference effects and, in the general case, the role of interference phenomena cannot be elucidated solely from SAXS data. At temperatures lower than  $T_g$ , a regularity in the distribution of the regions of chemical inhomogeneity was observed for glasses in all of the alkali borate systems, when the concentration of the alkali oxide was above the concentrations at which the degree of inhomogeneity reaches a maximum.

The development of structural inhomogeneity in alkali borate glasses was investigated after a sharp increase in the temperature of a sample initially in an equilibrium state. In all cases, the temperature jump was equal to 50°C. The stabilization temperatures were chosen close to  $T_g$ , while the observation tem-

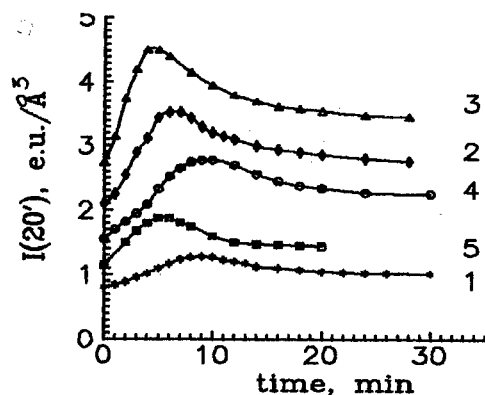


**Fig.6.** The dependence of  $I(20)$  on the duration of heat treating after a sharp increase in temperature for (1)  $B_2O_3$  and for sodium borate glasses containing (2), 1.5; (3), 4.0; (4), 6.0 and (5), 8.0 mol%  $Na_2O$ , respectively. The lines are drawn as a guide to the eye and the errors are within the size of the data points.

peratures were around  $T_g$ . Figure 6 shows the dependence of  $I_{SAXS}$  at a scattering angle of  $20^\circ$ ,  $I(20)$ , on the heat treatment time for samples of sodium borate glass, containing 1.5, 4.0, 6.0 and 8.0 mol%  $Na_2O$  (curves 2-5), after an increase in temperature at a rate of  $120^\circ C/min$ . The curve obtained for a pure  $B_2O_3$  sample under the same conditions (curve 1) is shown for comparison.

As in the case of  $B_2O_3$ , the increase in temperature initially causes  $I_{SAXS}$  for sodium borate glasses to increase, to a point where its value exceeds that in the equilibrium state at a given temperature, and then, to decrease. It can be seen from Fig. 6 that, in general, the dependence of  $I(20)$  on the heat treatment time is similar to that observed for  $B_2O_3$ . Therefore, it can be concluded that the increase in  $I_{SAXS}$ , on raising the sample temperature, is due to the appearance of new inhomogeneities; i.e. to the development of structural inhomogeneity. However, the difference between  $I(20)$  at the maximum degree of structural inhomogeneity and for the structure in the equilibrium state at given temperature,  $\Delta I_{max}$ , depends on the  $Na_2O$  content. This indicates that the structure arising from the chemical inhomogeneity exhibits changes in the transition state.

#### 4. DISCUSSION

As mentioned above, the presence of water or other impurities does not affect the structural inhomogeneity in  $B_2O_3$ . At present, the nature of this structure is not completely clear. It is possible that the RI observed by means of SAXS are "hot spots", the existence of which was assumed in Ref. [14]. An increase in the SAXS intensity and, correspondingly, in the light scattering intensity, is caused by the formation of larger-sized inhomogeneities. It should be noted that large-sized regions can be formed in small amounts. Unfortunately, it is not possible to estimate independently the number of RI and their electron density. In Ref. [15], an explanation is suggested for the increase in the scattering

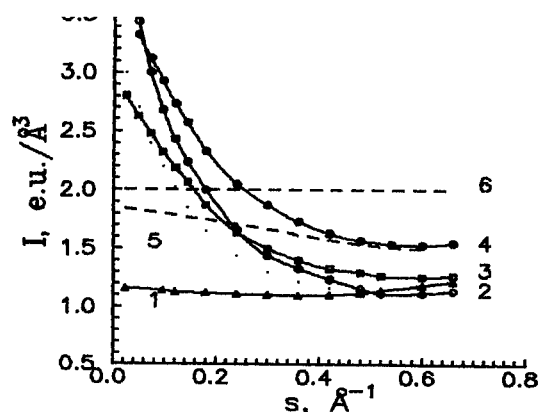


Fig.7. Angular dependence of  $I_{\text{saxs}}$  at 350°C for (1)  $\text{B}_2\text{O}_3$  and for alkali borate glasses containing (2) 4.0 mol%  $\text{Na}_2\text{O}$ , (3) 1.0 mol%  $\text{Rb}_2\text{O}$ , and (4) 1.0 mol%  $\text{Cs}_2\text{O}$  and the calculated SAXS curves for a statistically random distribution of the alkali ions in glasses with (5) 4.0 mol%  $\text{Na}_2\text{O}$  and (6) 1.0 mol%  $\text{Cs}_2\text{O}$ . The lines are drawn as a guide to the eye and the errors are within the size of the data points.

intensity after an increase of temperature. However, as it follows from Ref. [2] these regions cannot be interpreted as purely fluctuation regions, as they were in Ref. [15].

An important characteristic of the chemical inhomogeneity is the ratio of the number of ions distributed in the matrix to those incorporated into the RI. From the value of  $\langle(\Delta\rho)^2\rangle$ , it was found that the RI in sodium borate glasses contain not less than 25%  $\text{Na}_2\text{O}$  [3]. However, it is possible to specify quite reasonable values for the electron densities of the matrix and RI for which the experimental  $\langle(\Delta\rho)^2\rangle$  values will coincide with those calculated assuming that all of the sodium oxide introduced into the glass is contained in the RI.

Figure 7 shows the angular dependence of  $I_{\text{saxs}}$  for sodium (curve 5) and cesium (curve 6) borate glasses containing 4 mol%  $\text{Na}_2\text{O}$  and 1 mol%  $\text{Cs}_2\text{O}$ , respectively. These curves are calculated assuming a statistically random distribution of the alkali ions in the bulk of the glass at a temperature of 350°C. In the case of the cesium borate glass, the cesium ion was considered a scattering center. Based on the Krogh-Moe model [11] and on thermodynamic data [12], it can be assumed that, in range of  $\text{Na}_2\text{O}$  concentration investigated, the main structural elements in the glasses are tetraborate groups and boroxol rings. The sodium tetraborate structural grouping was regarded as the scattering center. Figure 7 also displays the measured SAXS curves for sodium borate glass containing 4 mol%  $\text{Na}_2\text{O}$  (curve 2), rubidium borate glass with 1 mol%  $\text{Rb}_2\text{O}$  (curve 3), cesium borate glass with 1 mol%  $\text{Cs}_2\text{O}$  (curve 4) and  $\text{B}_2\text{O}_3$  (curve 1), at a sample temperature of 350°C. It can be seen from Fig. 7 that the SAXS intensity for cesium borate glass at  $s=0.5\text{--}0.7\text{ \AA}^{-1}$  is greater than that for the  $\text{B}_2\text{O}_3$  sample but less than the SAXS intensity calculated assuming a statistically random distribution of cesium ions. However, the SAXS intensity for

the sodium borate glass at the same scattering angle is found to be less than that for the  $B_2O_3$  sample whereas, assuming a statistically random distribution of tetraborate groupings, the SAXS intensity should exceed  $I_{SAXS}$  for the  $B_2O_3$  sample by  $0.36 \text{ e.u./\AA}^3$ . The experimental errors in measurements of  $I_{SAXS}$  did not exceed  $0.01\text{--}0.02 \text{ e.u./\AA}^3$ . Therefore, it can be concluded that randomly distributed tetraborate groups are virtually absent in sodium borate glasses and, thus, all structural groupings form chain structures.

Using sodium borate glasses as an example, the pattern of structural changes occurring with increasing alkali oxide content or with temperature can be traced. In glasses containing as little as 3–4 mol%  $Na_2O$ , individual clusters consisting of branched chains are distributed randomly throughout the  $B_2O_3$  matrix. A change in the  $Na_2O$  contents causes the number of these clusters to change. The formation of a continuous cluster is observed at a content of 4–5 mol%  $Na_2O$ . A further increase in the  $Na_2O$  content brings about an increase in the degree of branching. In glasses with about 10–12 mol%  $Na_2O$ , the state is attained where essentially all of the  $BO_{3/2}$  triangles are involved in the coordination of alkali ions and the glass structure can be treated as being composed of identical structural elements. Beginning at this concentration of  $Na_2O$ , the glasses can be considered as homogeneous [2,3].

In molten glasses containing up to 4–5 mol%  $Na_2O$ , there are individual chains or small-sized clusters. As the temperature decreases, these groupings are joined into larger clusters, which leads to an increase in the size of the RI detectable by the SAXS technique. This process ceases at 420–450°C and, at lower temperatures, the structure remains virtually unaltered.

At low temperatures, glasses containing more than 4–5 mol%  $Na_2O$  exhibit a regular structure. The structural regularity can be attributed to the stresses arising in transition layers due to the "coherent" conjugation of the structural elements of the chemical inhomogeneities and the matrix, i.e. without breaking B–O bonds. In the case of closely spaced inhomogeneities (chains), the stresses are superimposed and cause the elastic strain energy to increase. It can be assumed that the additional energy related to these stresses reaches a minimum when the RI are about equally spaced.

As mentioned above, the chemical inhomogeneity exhibits changes in the transitional state. It was observed in Ref. [13] that, in the case of transitional states arising after a decrease in temperature, the relaxation time for the chemical inhomogeneities was more than an order of magnitude longer than that for the TDF of the matrix. This means that, in two-component glasses, the structural relaxation of the chemical inhomogeneity proceeds even if the TDF have achieved their equilibrium state.

## 5. CONCLUSION

The radii of the regions of structural inhomogeneity observed in  $B_2O_3$  in the equilibrium state are predominantly 6–7 Å. The development of structural inhomogeneity in the transitional states following a sharp increase in temperature

is primarily related to the appearance of RI with radii as large as 30-35 Å.

The chemical inhomogeneity in low alkali borate glasses exhibits a fractal nature. A certain regularity in the distribution of the chemical inhomogeneities is revealed at temperatures lower than  $T_g$ . The degree of regularity increases with decreasing in temperature and becomes maximum at temperatures close to  $T_g$ . After sharp changes in temperature, the development of structural inhomogeneity brings about changes in the distribution of chemical inhomogeneities. The redistribution of RI throughout the bulk of a glass continues, even if the structure of the matrix attains its equilibrium state. Therefore, structural relaxation in alkali borate glasses involves changes in the short and medium range order due to thermal density fluctuations and the development of structural inhomogeneity and also the redistribution processes occurring in the regions of chemical inhomogeneity.

#### ACKNOWLEDGEMENT

This work was supported by the Russian Foundation for Basic Research, project no. 95-02-05165

#### REFERENCES

- [1] E. A. Porai-Koshits, V.V. Golubkov, A.P. Titov & T.N. Vasilevskaij, *J. Non-Cryst. Solids* **49** (1982), 143.
- [2] V.V. Golubkov, *J. Non-Cryst. Solids* **192-193** (1995), 463.
- [3] V.V. Golubkov, *Sov. J. Glass Phys. Chem.* **18** (1992), 14.
- [4] V.V. Golubkov, *Fiz. Khim. Stekla* **15** (1989), 467.
- [5] V.V. Golubkov & E.A. Porai-Koshits, *Sov. J. Glass Phys. Chem.* **18** (1992), 46.
- [6] V.V. Golubkov, *Sov. J. Glass Phys. Chem.* **18** (1992), 57.
- [7] D.W. Schaefer & K.D. Keefer, In: Proc. 6th Symp. Internat. on *Fractals in Physics*, Trieste, Italy, July 9-12, 1985, Eds. L. Pietronero, E. Tosatti (North-Holland, Amsterdam, 1986), pp.62-71.
- [8] V.V. Golubkov, A.P. Titov & E.A. Porai-Koshits, *Prib. Tekhnika Eksper.* (1975), 215.
- [9] V.V. Golubkov, *Sov. J. Glass Phys. Chem.* **22** (1996), 178.
- [10] T.J.M. Visser, J.M. Stevels, *J. Non-Crystal. Solids* **7** (1972), 394.
- [11] J. Krogh-Moe, *Phys. Chem. Glasses* **1** (1960), 26.
- [12] N.M. Vedischeva, B.A. Shakmatkin & M.M. Shultz *J. Therm. Anal.* **33** (1988), 923.
- [13] V.V. Golubkov, *Sov. J. Glass Phys. Chem.* **22** (1996), 186.
- [14] C.A. Angell, *J. Am. Ceram. Soc.* **51** (1968), 117.
- [15] C.T. Moynihan & J. Schroeder, *J. Non-Crys. Solids* **160** (1993), 52.



## CATION AND NETWORK STRUCTURE IN BINARY POTASSIUM BORATE GLASSES

Norimasa UMESAKI, Derek A. H. CUNNIGHAM,  
Nagao KAMIJO  
*Osaka National Research Institute (ONRI), AIST,  
1-8-31, Midoriga-oka, Ikeda, Osaka 563, Japan.*

Katsumi HANDA  
*Faculty of Science and Engineering, Ritsumeikan University,  
1916, Noji-cho, Kusatsu, Siga 525-77, Japan.*

and

Yasuhiro IWADATE  
*Department of Materials Science, Chiba University,  
1-33, Yayo-cho, Inage-ku, Chiba 263, Japan.*

XAFS studies of network modifying cations in alkali borate glasses have made an important contribution to our understanding of the structure of glass. Using a laboratory XAFS facility, the local structure in  $K_2O-B_2O_3$  glasses has been determined in order to elucidate the environment of network modifying  $K^+$  ions. The average coordination number,  $N_{K-O}$ , of oxygen around  $K^+$  cations and the mean distance,  $r_{K-O}$ , for K-O correlations are found to be approximately 6 and 2.83-2.86 Å, respectively. The XAFS results are in good agreement with X-ray diffraction and MD simulation results.

### 1. INTRODUCTION

The structures of alkali borate glasses have been extensively studied by X-ray/neutron diffraction [1-4], NMR [5] and Raman [6] measurements. In borate glasses, modifying cations, such as alkali ions, break the B-O network structure. Unfortunately, the detailed features of the local structural environments of the modifying cations, such as alkali ions, are still unknown.

X-ray absorption fine structure (XAFS) spectroscopy has been used extensively as an aid to understanding local coordination characteristics, and the pair correlation functions for specific elements can be obtained. However, XAFS experiments in the soft X-ray domain (700-4000 eV), for elements such as potassium (K-edge: 3607 eV), appear less developed than those in the hard X-ray or VW regions: the reasons for this may lie in some intrinsic experimental difficulties, such as the few available monochromators, difficulties in sample preparation and weak theoretical background, etc.

In the present study, the structural features of the potassium coordination environments in  $K_2O-B_2O_3$  glasses are discussed, mainly based on experiments at the potassium K-edge using a laboratory XAFS facility. Furthermore, the B-O network structure of  $K_2O-B_2O_3$  glasses is analysed by X-ray diffraction, molecular dynamics (MD) simulation and Raman spectroscopy.

## 2. EXPERIMENTAL

### 2.1 Sample Preparation

The samples studied in this work were as follows;  $K_2O.2B_2O_3$ ,  $K_2O.4B_2O_3$ ,  $K_2O.3B_2O_3$ ,  $K_2O.5B_2O_3$  and  $B_2O_3$  glasses. They were prepared from analytical reagent grade powders of  $H_3BO_3$  and  $K_2CO_3$ . About 5-10 g batches were mixed and then melted at the temperatures about above  $100^\circ\text{C}$  above their melting points. The melts were cooled to room temperature to obtain the glass samples.

### 2.2 XAFS Measurement

Transmission experiments were performed at the potassium K-edge (3607 eV) of the above-mentioned sample films using a Technos EXAC800 laboratory XAFS facility, which consists of a rotating anode X-ray generator with a thin Be window (25 pm), curved-crystal monochromator and Si(Li) solid state detector (SSD). In the present study, a copper rotating-anode was employed as the X-ray source, which was operated at 12.5 kV and 70 mA. A Johan-type LiF(200) ( $2d=4.026$  Å) monochromator was used for the K K-edge measurement. Due to the soft nature of the K-K X-rays, a conventional vacuum system was used, the vacuum being maintained inside the X-ray path during XAFS measurement by means of a thin beryllium window (25 pm) at the front of the rotating anode X-ray generator.

The EXAFS data obtained were analyzed using the standard procedure, which has been described in detail in a previous paper [7]. Theoretical phase and amplitude functions of Rehr *et al.* [8] were employed for the  $k^3\chi(k)$  fitting procedure.

### 2.3 X-ray Diffraction

The scattered intensities were measured with a Rigaku RINT-TTR X-ray diffractometer having  $\theta/\theta$  type reflection geometry and a Ge detector (Canberra GL0210R). Mo  $K\alpha$  radiation was used with a continuous output of 60 kV and 300 mA. Measurements were made using a step-scanning technique, with a fixed time of 10 s at every  $\Delta\theta=0.25^\circ$  in the range  $3^\circ$ - $15^\circ$  and 60 s in the range  $13^\circ$ - $60^\circ$ , covering the range from 0.925 to  $15.31\text{ \AA}^{-1}$  in  $Q=4\pi\sin\theta/\lambda$ . Details of the X-ray data treatment are given elsewhere [9].

### 2.4 MD Simulation

Molecular dynamics (MD) simulations have been carried out on pure  $B_2O_3$ ,  $K_2O.4B_2O_3$  and  $K_2O.2B_2O_3$  glasses at 298 K, in order to investigate the detailed three-dimensional configuration of the atoms in these glasses. The MD calculations were performed in a way similar to that described previously by one of

**Table 1**  
Interatomic Potential Parameters

Ion	w	z	a (Å)	b (Å)	c (kJ <sup>1/2</sup> Å <sup>3</sup> mol <sup>-1/2</sup> )
K	39.10	+1	1.595	0.080	30.0
B	10.81	+3	0.720	0.080	-
O	16.00	-2	1.626	0.085	20.0

the authors [4].

In this study, the pair potential functions are assumed to consist of simplified Coulombic, repulsive and Van der Waals attraction terms:

$$U_{ij}(r_{ij}) = \frac{z_i z_j e^2}{r_{ij}} + f_0 (b_i + b_j) \exp\left(\frac{a_i + a_j - r_{ij}}{b_i + b_j}\right) - \frac{c_i c_j}{r_{ij}^6} \quad (1)$$

where  $z_i$  is the formal charge number of ion  $i$  (e.g. +3 for the  $B^{3+}$  ion),  $e$  is the electronic charge,  $r_{ij}$  is the distance between ions  $i$  and  $j$ ,  $f_0$  is a force constant, arbitrarily taken here to be 1 kcal/mol Å ( $=6.948 \times 10^{-6}$  dyne), and  $a_i$ ,  $b_i$  and  $c_i$  are the crystal radii and compressibility of ion  $i$ , respectively. All of the parameters are shown in Table 1.

The edge length of the basic cell was calculated from the number of simulated atoms and the observed density of the relevant  $K_2O-B_2O_3$  glass [10]. The number of particles (atoms) within the basic cell was 800 (320 B, 480 O) for  $B_2O_3$ , 690 (60 K, 240 B, 360 O) for  $K_2O.4B_2O_3$  and 650 (100 K, 200 B, 350 O) for  $K_2O.2B_2O_3$ . The time increment,  $\Delta t$ , was chosen to be  $2.5 \times 10^{-15}$  s.

### 2.3 Raman Scattering

The Raman spectra of the glass samples were measured using a Jobin Yvon T64000 triple-grating spectrometer at a scattering angle of  $90^\circ$ . Sample excitation was achieved with the 5145 Å line of a Coherent Innova 300 model  $Ar^+$  ion laser at a power level of 600 mW.

## 3. RESULTS AND DISCUSSION

### 3.1 Potassium Environments in $K_2O-B_2O_3$ Glasses

Figure 1 shows normalized XAFS spectra at the K  $K$ -edge of the  $K_2O.xB_2O_3$  ( $x=2, 3, 4$  and  $5$ ) glasses. As shown by this figure, the K  $K$ -XAFS spectra obtained for all of the glass samples are of good enough quality to extract structural information concerning the K ion environments. The potassium borate glasses exhibit a strong white fine centered at 3618 eV and two broad oscillations in the energy range from 3630 to 3720 eV. The fine-structure of the K-edge XANES in the energy range below 30 eV were well reproduced by the results of a first-principle molecular orbital calculation using a discrete-variational, DV-X $\alpha$ , method and  $(KO_6)^{11-}$  and  $(K_{13}O_{14})^{15-}$  model clusters [11].

The Fourier transform of the EXAFS function  $k^3\chi(k)$  for the  $K_2O-B_2O_3$

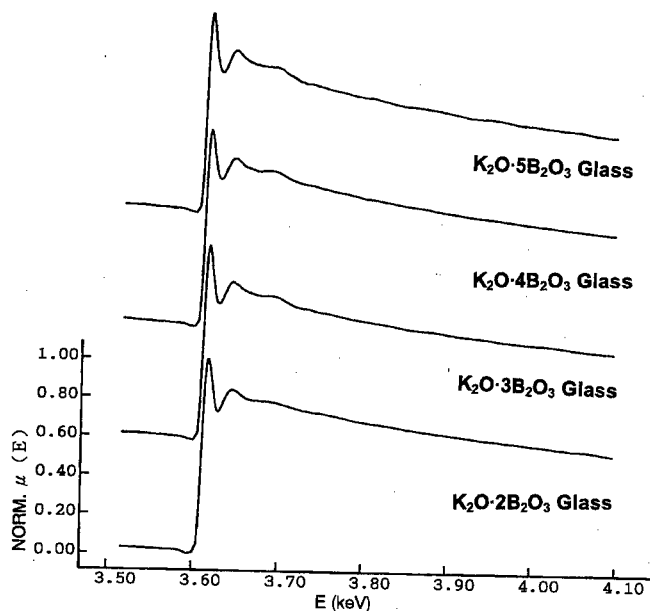


Fig. 1. Normalized K K-XAFS spectra for the  $K_2O \cdot xB_2O_3$  ( $x=2, 3, 4$  and  $5$ ) glasses.

glasses is shown in Fig. 2. The main peaks of the first oxygen shell, due to the nearest-neighbor K–O pair, are well defined for all of the spectra. More recently, Gaskell suggested that the network-modifying elements such as Li, Na, Mg, Ca and some of the divalent transition metals form a disordered cationic

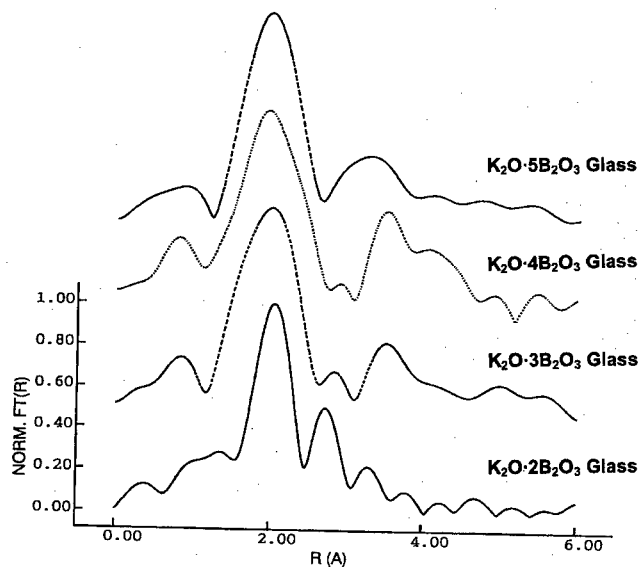


Fig. 2. Fourier transform of the K K-edge  $k^3\chi(k)$  for the  $K_2O \cdot xB_2O_3$  ( $x=2, 3, 4$  and  $5$ ) glasses

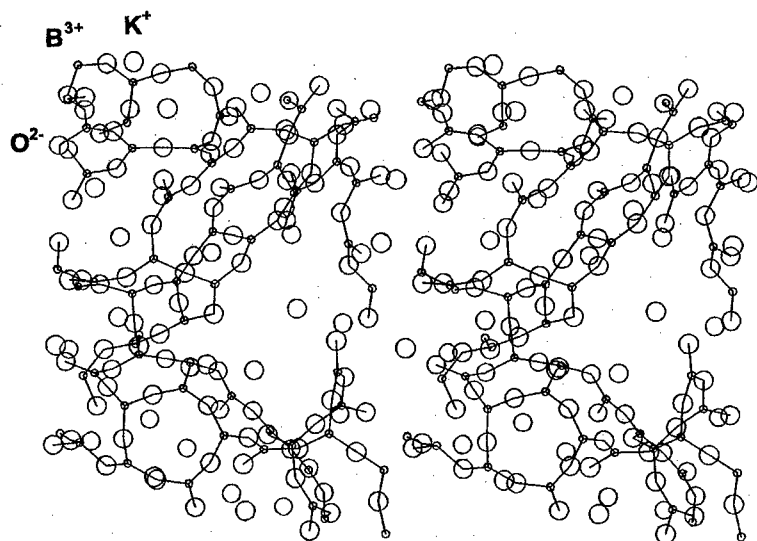


Fig. 3. Stereoscopic snapshot of the ions in  $K_2O \cdot 2B_2O_3$  glass at 298 K.

sublattice in oxide glasses [12,13]. However, no evidence of any K–K correlation due to  $K^+$  ion clustering in these potassium borate glasses is seen in the present EXAFS results. The short range order structural parameters for the  $K_2O$ – $B_2O_3$  glasses have been obtained from a best-fit routine, as summarized

**Table 2**  
Short Range Order Parameters for  $K_2O$ – $B_2O_3$  Glasses Obtained From EXAFS, X-ray diffraction (XRD) and MD Results.

Glass	i-j	r <sub>i-j</sub> (Å)	N <sub>i-j</sub> (atoms)	(s <sub>i-j</sub> <sup>2</sup> ) <sup>1/2</sup> (Å)	Method
[B <sub>2</sub> O <sub>3</sub> ]	B-O	1.36	3.0	-	MD
	O-O	2.38	4.0	-	
	B-B	2.64	3.0	-	
∠O-B-O=119.32°±4.34°		∠B-O-B=151.07°±13.52°			
[K <sub>2</sub> O.4B <sub>2</sub> O <sub>3</sub> ]	B-O	1.37±0.01	3.0±0.2	0.143±0.01	XRD
		1.48±0.01	4.0±0.2	0.155±0.01	
		1.38	3.2	-	
∠O-B-O=118.92°±5.07°		∠B-O-B=150.15°±14.47°			
	O-O	2.36±0.02	4.0±0.3	0.150±0.01	XRD
		2.40	4.2	-	MD
	K-O	2.86±0.02	6.8±0.5	0.153±0.02	EXAFS
		2.83±0.02	6.0±0.3	0.182±0.01	XRD
		2.74	6.1	-	MD
[K <sub>2</sub> O.2B <sub>2</sub> O <sub>3</sub> ]	B-O	1.38	3.3	-	MD
	O-O	2.40	4.6	-	
	∠O-B-O=115.23°±6.41°		∠B-O-B=148.70°±14.52°		
	K-O	2.83±0.04	5.9±0.4	0.100±0.02	EXAFS
		2.74	6.6	-	MD

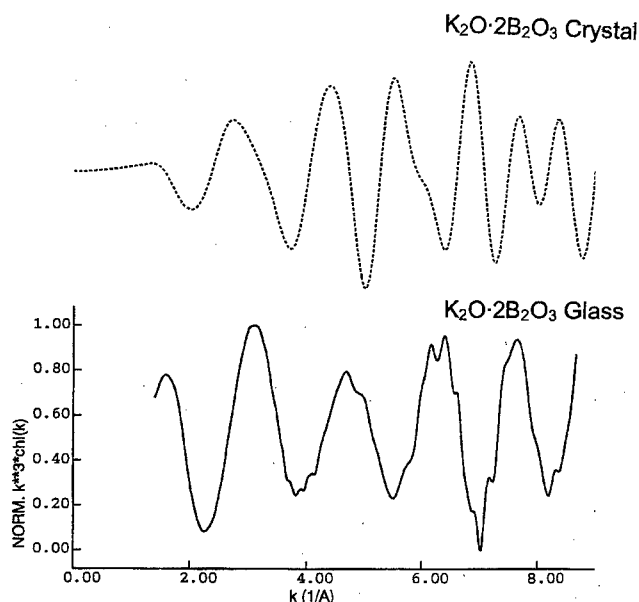


Fig. 4.  $k^3\chi(k)$  spectrum from experimental data of  $K_2O \cdot 2B_2O_3$  glass and that calculated using FEFF program for  $K_2O \cdot 2B_2O_3$  crystal.

in Table 2. This table also includes the X-ray diffraction results and the MD calculations for comparison with the EXAFS data. The mean bond distances,  $r_{ij}$  for the K–O correlations in the  $K_2O$ – $B_2O_3$  glasses are 2.74–2.86 Å, and are approximately equal to the sum of the ionic radii  $K^+$  and  $O^{2-}$  (=2.73 Å). These K–O distances are also similar to those in potassium silicate glasses, as obtained from XAFS [7,14,15] and X-ray diffraction [17] results. The average coordination numbers,  $N_{ij}$ , found are approximately 6. These results indicate that the potassium ions are surrounded by six oxygen ions, i.e. disordered octahedral geometry, and that the  $K^+$  ions have a strong preference to reside in the vicinity of negatively charged non-bridging oxygens (NBOs) and bridging oxygens (BOs) in the large cages of the B–O network structure, to provide local charge neutrality, as shown in Fig. 3. Table 2 also shows that the coordination numbers,  $N_{K-O}$ , for  $K_2O$ – $B_2O_3$  glasses are almost constant, at around 6, independent of the  $K_2O$  content. The root mean-square bond length deviations,  $(\sigma_{ij}^2)^{1/2}$ , lie between 0.1 and 0.2 Å.

Figure 4 compares the experimental  $k^3\chi(k)$  curve for the  $K_2O \cdot 2B_2O_3$  glass with a  $k^3\chi(k)$  curve calculated for crystalline  $K_2O \cdot 2B_2O_3$  [17] using the *ab-initio* XAFS computer code, FEFF [8]. In crystalline  $K_2O \cdot 2B_2O_3$ , the  $K^+$  cations are coordinated in an unsymmetrical fashion by six or eight oxygen atoms at distances ranging from 2.631 to 3.106 Å. As shown by Fig. 4, the oscillations of the two  $k^3\chi(k)$  curves are significantly different, due to the different  $K^+$  ion environment in the  $K_2O \cdot 2B_2O_3$  glass and crystal; i.e. the  $K^+$  ions in the  $K_2O$ – $B_2O_3$  glasses are symmetrically coordinated to about six oxygen atoms at dis-

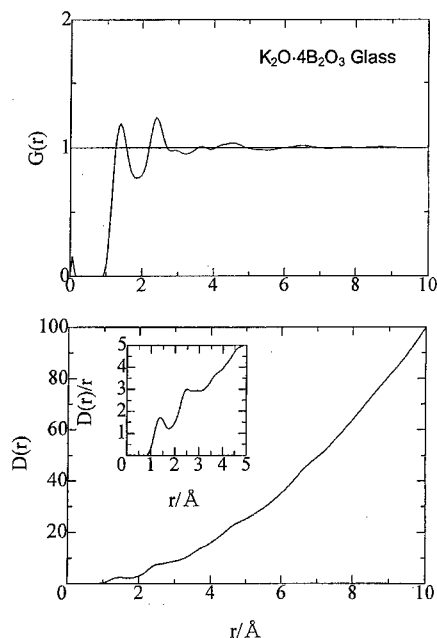


Fig. 5. Reduced radial density function,  $G(r)$ , and radial distribution function,  $D(r)$ , and the function  $D(r)/r$  for  $\text{K}_2\text{O} \cdot 4\text{B}_2\text{O}_3$  glass.

tances of 2.74–2.86 Å and are randomly distributed in the large cages of the B–O network structure, as shown in Fig. 3.

### 3.2 Network Structure of $\text{K}_2\text{O} \cdot \text{B}_2\text{O}_3$ Glasses

The experimental radial distribution function,  $D(r)$ , and the reduced radial density function,  $G(r)$ , for  $\text{K}_2\text{O} \cdot 4\text{B}_2\text{O}_3$  glass are shown in Fig. 5. The values of the structural parameters for  $\text{K}_2\text{O} \cdot 4\text{B}_2\text{O}_3$  glass, optimized using the Debye's equation [18] are given in Table 2. As can be seen from Fig. 5, the first peak at 1.40 Å is attributed to the nearest-neighbor B–O pairs for the  $\text{BO}_3$  ( $r_{\text{B-O}} = 1.37$  Å) and  $\text{BO}_4$  ( $r_{\text{B-O}} = 1.48$  Å) units in the  $\text{K}_2\text{O} \cdot 4\text{B}_2\text{O}_3$  glass.

As regards the structure of alkali borate glasses,  $\text{M}_2\text{O} \cdot \text{B}_2\text{O}_3$ , it has been established that the  $\text{BO}_3$  structural units, which form the network structure of  $\text{B}_2\text{O}_3$  glass, are converted into tetrahedral  $\text{BO}_4$  units by the addition of  $\text{M}_2\text{O}$  to  $\text{B}_2\text{O}_3$  up to 33 mol%. According to Raman [19,20] and NMR [21,22] studies, on the addition of one molecule of  $\text{Na}_2\text{O}$  to  $\text{B}_2\text{O}_3$  glass, two  $\text{BO}_3$  units are converted into two  $\text{BO}_4$  units [20]. Zhong & Bray [22] indicate, from their NMR results, that the fraction  $N_4$  of  $\text{BO}_4$  units in alkali borate glasses decreases in the order  $\text{Li} > \text{Na} > \text{K} > \text{Rb} > \text{Cs}$ ; also, the value of  $N_4$  exhibits a maximum, which decreases in magnitude with increasing cation size. The NMR value (0.31 [22]) of  $N_4$  agrees very closely with that (0.31) for the  $\text{K}_2\text{O} \cdot 2\text{B}_2\text{O}_3$  glass obtained from the present MD results.

#### 4. CONCLUSION

This paper has discussed the information concerning the  $K^+$  ion environment in  $K_2O-B_2O_3$  glasses, obtained from XAFS measurements. The average coordination number,  $N_{K-O}$ , of oxygen around  $K^+$  cations, and the mean distance,  $r_{K-O}$ , for K-O correlations, are found to be approximately 6 and 2.83-2.86 Å, respectively. The XAFS results are in poor agreement with our X-ray diffraction and MD simulation results.

#### REFERENCES

- [1] G. Paschina, G. Piccaluga & M. Magini, *J. Chem. Phys.* **81** (1984), 6201
- [2] G. Herm, M. Derno & H. Stiel, *J. Non-Cryst. Solids* **88** (1986), 381.
- [3] Y. Iwadate, K. Igarashi, T. Hattori, S. Nishiyama & J. Mochinaga, *J. Chem. Phys.* **99** (1993), 6890.
- [4] N. Umesaki, Y. Kita, T. Kiriara, T. Iida, T. Fukunaga & M. Misawa, *J. Non-Cryst. Solids* **177** (1994), 200.
- [5] P. J. Bray, *J. Non-Cryst. Solids* **95&96** (1987), 45.
- [6] B. N. Meera & J. Ramakrishna, *J. Non-Cryst. Solids* **159** (1993), 1.
- [7] N. Kamijo, K. Handa & N. Umesaki, *Mater. Trans. JIM* **37** (1996), 927.
- [8] J. J. Rehr, J. Mustre de Leon, S. I. Zabinsky & R. C. Albers, *J. Am. Chem. Soc.* **113** (1991), 5136.
- [9] H. Ohno, K. Igarashi, N. Umesaki & K. Furukawa, *X-Ray Diffraction Analysis of Ionic Liquids, Molten Salt Forum* Vol. 3 (Trans Tech Publications, Switzerland, (1994), pp 1-14.
- [10] L. Shartis, W. Capps & S. Spinner, *J. Am. Ceram. Soc.* (1953), 35.
- [11] I. Tanaka & N. Umesaki, Unpublished data.
- [12] P. H. Gaskell, In: *The Physics of Non-Crystalline Solids*, Eds L. D. Pye, W. C. LaCourse and H. J. Stevens (Taylor and Francis, London, 1992), pp 15-21.
- [13] P. H. Gaskell, In: *Proc. XI7 International Congress on Glass*, (Vol. 1, Madrid, Spain, 1992) pp 25-44.
- [14] G. N. Greaves, In: *Glass Science and Technology*, Vol. 4B, Eds D. R. Uhlmann and N. J. Kreidl (Academic Press, Boston, 1990), Chap. 1.
- [15] G. N. Greaves, In: *The Physics of Non-Crystalline Solids*, Eds L. D. Pye, W. C. LaCourse and H. J. Stevens (Taylor and Francis, London, 1992), pp 453-459.
- [16] Y. Waseda & H. Suito, *Trans. Iron Steel Inst. Jpn.* **62** (1976), 19.
- [17] J. Krogh-Moe, *Acta Cryst.* **B28** (1972), 3089.
- [18] H. A. Levy, M. D. Danford & A. H. Narten, *ONRL Report* No. 3960 (1966).
- [19] W. L. Konijnendijk & J. M. Stevels, *J. Non-Cryst. Solids* **18** (1975), 307.
- [20] W. L. Konijnendijk & J. M. Stevels, In: *Borate Glasses (Proc. Conf. Boron in Glasses and Glass Ceramics)*, Eds. L. D. Pye, V. D. Frechette and N. J. Kreidl (Plenum, New York, 1978), p 259.
- [21] P. J. Bray & J. G. O'Keefe, *Phys. Chem. Glasses* **4** (1963), 37.
- [22] J. Zohng & P. J. Bray, *J. Non-Cryst Solids* **111** (1989), 67.



## TEMPERATURE DEPENDENCE OF THE RELAXATION COMPRESSIBILITY OF BORON OXIDE BASED ON VISIBLE LIGHT SCATTERING DATA

Nikolai A. BOKOV & Nikolai S. ANDREEV

*Institute of Silicate Chemistry Russian Academy of Sciences,  
ul. Odoevskogo 24, korp.2, St. Petersburg, 199155, Russia*

Using data obtained from Rayleigh scattering of visible light in  $B_2O_3$ , a change in the isothermal compressibility with temperature was calculated for the temperature range 180 to 600°C. Data for the relaxation compressibility were compared to those calculated from the degenerate excited state model. It was shown that the calculated data, for temperatures above 260°C, are in a good agreement with those obtained experimentally. As the temperature was reduced below 260°C, an increasing disagreement was noted between the calculated and the measured data. A possible reason for the disagreement is discussed.

### 1. INTRODUCTION

Leideker *et al.* [1] assumed the occurrence of a degenerate excited state in the boron oxide structure. This model describes well the temperature variation of the relaxational parts of the thermal expansion coefficient, specific volume, and specific heat in the 350 to 1400°C range. According to this model, the occurrence of the degenerate excited state is the reason for the large magnitude of the relaxational part of the compressibility,  $\beta_{T,rel}$ , for molten boron oxide. As follows from the model,  $\beta_{T,rel}$  can be calculated using the following equation:

$$\beta_{T,rel} = [(\delta V)^2 / vRT](r + x)(1 - x) \quad (1)$$

x being given by relation

$$x = \{1 + \exp[(\Delta U - T\Delta S)/RT]\}^{-1}$$

Here, R is the gas constant, T is the absolute temperature, v is the specific volume,  $\Delta U$  and  $\Delta S$  are the energy and entropy differences, respectively, between the ground and excited states and  $\delta V$  and r are the volume difference and population ratio between two degenerate states. Numerical values of  $\Delta U$ ,  $\Delta S$ ,  $\delta V$ , and r can, according to Ref. [1], be taken as -5.07 kcal/mol, -6.75 cal/molK, 0.117 cm<sup>3</sup>/g, and 3.8, respectively.

According to Eq. (1), the magnitude of  $\beta_{T,rel}$  should, in the low-temperature range, rapidly decrease with decreasing temperature, due to the fact that the

excited states become sparsely populated. Such a decrease in  $\beta_{T,rel}$  was confirmed by the data of Bucaro & Dardy [2] from Brillouin light scattering in boron oxide over the range 284 to 516°C. According to the conclusions of Ref. [2], the small disagreement between the experimental and calculated data in this range can be entirely eliminated by insignificant changes in the parameters of Eq. (1).

The present investigation is aimed of obtaining data on  $\beta_{T,rel}$  for boron oxide using Rayleigh scattering of visible light over a broad temperature range, including the glass transition region, and comparing these data with the predictions of the model proposed in Ref. [1].

## 2. EXPERIMENTAL PROCEDURE

As follows from the thermodynamic theory [3], the static isothermal compressibility,  $\beta_{T,o}$ , can be obtained from the scattered light intensity through the relationship:

$$\beta_{T,o} = R_d / (\pi^2 / \lambda^4) k T [\rho (\delta \epsilon / \delta \rho)]^2 \quad (2)$$

where  $R_d$  is the scattered intensity measured at a scattering angle of 90° ( $R_d$  being due to the density fluctuations),  $\lambda$  is the wavelength,  $\epsilon$  is the dielectric constant,  $\rho$  is the density,  $k$  is the Boltzmann constant, and  $T$  is the absolute temperature.

Thus, experimental data on the temperature variation of the scattered light intensity allow the calculation the equilibrium compressibility,  $\beta_{T,o}$ , which is connected to  $\beta_{T,rel}$  by the relationship  $\beta_{T,rel} = \beta_{T,o} - \beta_{T,\infty}$ , where  $\beta_{T,\infty}$  is the high-frequency compressibility.  $\beta_{T,\infty}$  values were obtained from ultrasonic measurements [4] and Brillouin scattering experiments conducted by Japanese investigators [5], the data of Refs. [4] and [5] being in good agreement.

When conducting measurements of the scattered light intensity from boron oxide, a major problem is the fact that the material is a highly hygroscopic. This results in a progressive worsening of the optical quality of sample surface and, correspondingly, in an increase in the scattered light intensity.

When conducting high-temperature measurements, the boron oxide melt was contained in a cell made of fused quartz. This protected the melt surface from the effect of atmospheric moisture and provided reliable values of the scattered light intensity. It was shown that the scattered intensity continuously decreases with sample cooling through the glass transition range. However, this conclusion is not unambiguous because macroscopic stresses arose in the sample under study, which finally resulted in the destruction of the sample.

Therefore, the low-temperature measurements were conducted using solid glass samples prepared beforehand by quenching the boron oxide melt. In preliminary experiments, it was shown that even a short contact of the sample surface with the atmosphere in the course of sample polishing results in the formation of a film at the surface and in an overestimation for light intensity scattered from the sample. A short heating of the sample up to 300–350°C removed the

film from the surface. This was confirmed by the fact that the magnitudes of the scattered light intensity measured using the solid glass sample and the sample obtained by cooling the glass melt in a cell were in a good agreement.

Such a method for the reconstruction of the sample surface was used in the present work. To avoid the repeated formation of a film, all of the low-temperature measurements were conducted under a dry nitrogen atmosphere. This was sufficient to keep the sample surface intact for the period required to conduct the measurements.

### 3. RESULTS

To determine  $\beta_{T,0}$  using Eq. (2), the magnitude of  $\rho(\delta\epsilon/\delta\rho)$  should be known. However, there are no reliable methods for calculating  $\rho(\delta\epsilon/\delta\rho)$  and so a relationship proposed by Oster [6], was employed

$$\rho(\delta\epsilon/\delta\rho) = [n^2(n^2-1)(2n^2+1)]/(2n^4+1) \quad (3)$$

where  $n$  is the refractive index. Notably, the  $\rho(\delta\epsilon/\delta\rho)$  magnitudes estimated for  $B_2O_3$  with Eq. (3) are in agreement with those calculated from Pockels coefficients [7]. For calculating  $\rho(\delta\epsilon/\delta\rho)$  with Eq. (3), the temperature dependence of the refractive index for  $B_2O_3$  [8] was used.

Figure 1 shows the dependence of  $\beta_{T,rel}$  on temperature according to (1) our experimental data, (2) the data of Bucaro & Dardy [2], and (3) data obtained from calculations using Eq. (1).

As follows from the Figure 1, the present experimental data for  $\beta_{T,rel}$  and those of Ref. [2] using Brillouin scattering are in a good agreement. This supports the reliability of our experimental method and also the method chosen for calculating  $\rho(\delta\epsilon/\delta\rho)$  with Eq. (3) ( $\beta_{T,rel}$  being obtained in Ref. [2] with no  $\rho(\delta\epsilon/\delta\rho)$  factor).

Moreover, as can be seen from the Figure 1  $\beta_{T,rel}(T)$  substantially decreases as the boron oxide sample is cooled to relatively low temperatures. This is in qualitative agreement with the conclusions based on the degenerate excited state model [1].

At the same time, the present data demonstrate a quantitative difference between the  $\beta_{T,rel}$  values calculated with Eq. (1) and those obtained experimentally, and the difference increases progressively with decreasing temperature. An attempt aimed at bringing the calculated  $\beta_{T,rel}$  values into correspondence with the experimental ones over the entire temperature range studied by introducing small variations in the parameters of Eq. (1) did not allow a complete elimination of the differences.

The results of such calculations are included in the Figure 1 (curve 4). The magnitudes of the parameters  $\Delta U$ ,  $\Delta S$ ,  $\delta V$ , and  $r$  in Eq. (1) were taken, in this calculation, to be  $-5.85$  kcal/mol,  $-7.82$  cal/mol K,  $0.113$  cm<sup>3</sup>/g, and  $3.8$ , respectively. As may be seen from the Figure 1, an increase in  $\Delta U$  and  $\Delta S$  by about 15%, as compared to those chosen in Ref. [1], results in a good agreement between the calculated and experimental  $\beta_{T,rel}$  values down to  $260^\circ\text{C}$ . At

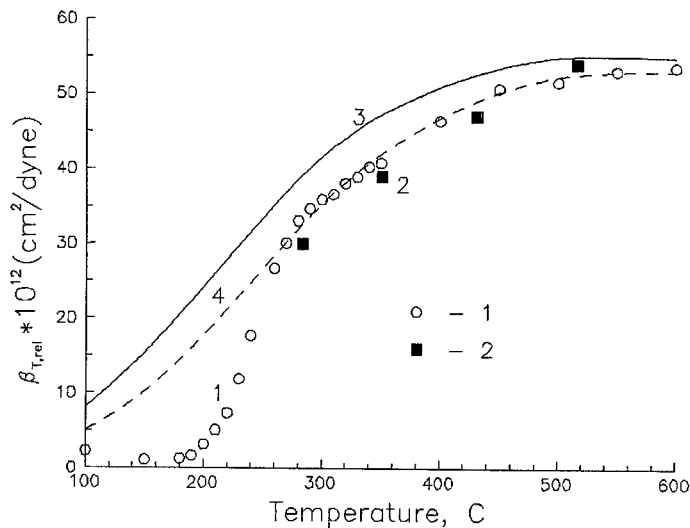


**Fig.1.** The relaxation part of the isothermal compressibility vs temperature.  
 1, light scattering results from the present work; 2, results of Ref. [2];  
 3, from the degenerate excited state model {Eq. (1)} and  
 4, from the degenerate excited state model with new parameters.

lower temperatures, however, variations in the parameters of Eq. (1) alone do not allow a coincidence between the calculated and experimental  $\beta_{T,rel}$  values.

It should be noted that so crucial a decrease in the scattered light intensity in the course of the glass transition for boron oxide as revealed in this research, was observed using a sample that was multiply subjected to heating and cooling through the glass transition range. This sample was selected because it had the minimum scattering coefficient among the series of samples synthesized under approximately the same conditions. Qualitatively, the temperature dependence of the scattered light intensity obtained for all the samples was similar to that shown above; i.e. it was characterized by a substantial decrease in the scattered light intensity when cooling through the glass transition range. However, the final intensity magnitudes reached at temperatures lower than 250°C, for other samples of the same series, were greater than that for the selected sample. This may be due to the worse optical quality of these samples, but reasons for this difference remains unclear.

#### 4. DISCUSSION

As is well known [9], the time required for structural transformations progressively increases with decreasing temperature and, finally, a frozen state is reached. As a result, the structural contributions to the specific heat, thermal expansion coefficient, and compressibility are small for the vitreous state and the magnitudes of the above quantities are in most cases close to those characteristic of the crystalline state.

Such a reasoning which, in general, well represents the pattern of the glass transition process, cannot explain the substantial intensity of the light scattered by glasses. The solution to this problem was found in terms of the hypothesis that assumes the fluctuational structure of a melt is frozen-in during the glass transition.

The present data on boron oxide show that, at temperatures higher than 260°C, the  $\beta_{T,rel}$  magnitudes are in a good agreement with the predictions of the degenerate excited state model [1] and with the data of Ref. [2].

On the contrary, below 260°C a rapid decrease in the scattered light intensity occurs which not only contradicts the qualitative expectation following the hypothesis of the frozen-in fluctuational structure but also results in a large difference between  $\beta_{T,rel}$  values calculated from Eq. (1) and those found experimentally.

A possible explanation for this effect can be derived from the work of Golubkov [10]. Based on SAXS data, Golubkov concluded that a decrease in the intensity of the scattered electromagnetic radiation for boron oxide may be due to interference effects.

## 5. CONCLUSIONS

It is shown experimentally that cooling a boron oxide melt through the glass transition range is accompanied by a sharp decrease in the intensity of the isotropic light scattering, down to a level close to that determined by the high-frequency magnitude of the compressibility. A possible reason for this effect may be some regularity in the spacial distribution of the regions of inhomogeneity throughout the bulk of the sample. This specific feature of the inhomogeneous structure may result in the interference effects causing a decrease in both the SAXS intensity and the intensity of scattered light.

## ACKNOWLEDGEMENT

This work was supported by Russian Foundation for Basic Research, project no. 95-02-05165.

## REFERENCES

- [1] W. Leidecker, J.H. Simmons, T.A. Litovitz & P.B. Macedo, *J. Chem. Phys.* **55** (1971), 2028.
- [2] J.A. Bucaro & H.D. Dardy, *J. Chem. Phys.* **60** (1974), 2559.
- [3] I.L. Fabelinskii, *Molecular Scattering of Light* (Plenum, New York, 1968).
- [4] W. Capps, P.B. Macedo, B. O'Mera & T.A. Litovitz, *J. Chem. Phys.* **45** (1966), 3431.
- [5] M. Cho, M. Kodama & T. Yagi, *J. Phys. Soc. Jpn.* **55** (1986), 981.
- [6] G. Oster, *Chem. Rev.* **43** (1948), 319.
- [7] J. Schroeder, *J. Non-Cryst. Solids* **40** (1980), 549.
- [8] L. Prod'homme, *Verres Refr.* **5** (1956), 267.
- [9] T. Litovitz & C. Davis, In: *Physical Acoustics*, Ed. W.P. Mason (Academic Press, New York, 1965), p.p. 298-370.
- [10] V.V. Golubkov, *Fiz. Khim. Stekla* **18** (1992), 14.

## A STRUCTURAL STUDY OF $\text{Bi}_2\text{O}_3$ - $\text{B}_2\text{O}_3$ GLASSES

Emil M. GATTEF, Vesselin V. DIMITROV, Yanko B. DIMITRIEV  
*University of Chemical Technology & Metallurgy, Sofia-1756, Bulgaria*

and

Adrian C. WRIGHT  
*J. J. Thomson Physical Laboratory, Reading University,  
Whiteknights, Reading RG6 6AF, UK*

The structure of glasses in the system  $\text{Bi}_2\text{O}_3$ - $\text{B}_2\text{O}_3$  is studied by X-ray diffraction and IR spectroscopy in the concentration range 30–92.3 mol%  $\text{Bi}_2\text{O}_3$ . It is found that, together with the appearance of  $\text{BO}_4$  groups, a part of the borate network is retained up to 66.6 mol% bismuth oxide. In the same concentration region, short and long Bi-O bonds exist but for the 3:5 and 2:1 stoichiometric compounds only one Bi-O distance is found. Above this concentration limit, the borate network vanishes and the structure becomes selenite-like consisting of isolated  $\text{BO}_4$  groups and deformed  $\text{BiO}_6$  groups.

### 1. INTRODUCTION

Boron oxide belongs to the family of the classical glass-formers and is also the basic component of a large number of two- and multi-component oxide glass forming systems [1]. The structure of pure  $\text{B}_2\text{O}_3$  glass has been the subject of various studies, some of which are summarized in [2,3]. Based on neutron diffraction data, Hannon *et al.* [3] have suggested that in the structure of vitreous  $\text{B}_2\text{O}_3$  about 80 % of the boron atoms are present in boroxol rings, which are linked by independent  $\text{BO}_3$  groups.

During recent years, there has been an increasing interest in the synthesis and in the investigation of the structure and the properties of heavy metal oxide glasses containing bismuth oxide [4-11]. These possess a high refractive index and a high IR transparency, together with an increased third order non-linear optical susceptibility [12] which makes them possible materials for use in both linear and non-linear optics. Moreover, bismuthate glasses are excellent precursors for the fabrication of ceramic superconductors [13-15] and, in this connection, the structure of several bismuthate glasses was studied by Dimitriev *et al.* [15-17] by neutron and X-ray diffraction.

In view of the results cited above, concerning the synthesis and properties of bismuthate glasses, it is of fundamental interest to study the structural changes occurring as a function of composition for the binary system  $\text{Bi}_2\text{O}_3$ -

$\text{B}_2\text{O}_3$ . The phase diagram of this system has been investigated [18] and, with increasing  $\text{Bi}_2\text{O}_3$  content, the formation of four congruently melting (1:4, 1:3, 3:5, 2:1) and one incongruently melting compound (12:1) has been established. In the  $\text{B}_2\text{O}_3$ -rich region there also exists a region of obvious phase separation, while relatively low liquidus temperatures make it easy to obtain stable glasses. The crystalline structures of the compounds  $3\text{Bi}_2\text{O}_3 \cdot 5\text{B}_2\text{O}_3$  and  $2\text{Bi}_2\text{O}_3 \cdot \text{B}_2\text{O}_3$  have been determined [19,20]. The basic structural unit for the (3:5) composition is the pentaborate ion  $(\text{B}_5\text{O}_{11})^{7-}$ , formed from two  $\text{BO}_4$  and three  $\text{BO}_3$  groups, whereas the structure of  $2\text{Bi}_2\text{O}_3 \cdot \text{B}_2\text{O}_3$  only contains isolated  $\text{BO}_3$  groups. Glass formation in the  $\text{Bi}_2\text{O}_3$ – $\text{B}_2\text{O}_3$  system has been investigated by many authors and glasses are obtained in the region 9.4–85 mol%  $\text{Bi}_2\text{O}_3$  [1]. The purpose of the present study is to obtain information on the basic structural polyhedra which form the glass network in the binary  $\text{B}_2\text{O}_3$ – $\text{Bi}_2\text{O}_3$  system using X-ray diffraction and IR spectroscopy.

## 2. EXPERIMENTAL

The glasses were obtained by melting chemically pure  $\text{Bi}_2\text{O}_3$  and  $\text{H}_3\text{BO}_3$  in porcelain crucibles in the temperature range 850–1000°C. Vittrification was achieved by pouring the melt onto a metal plate. Well defined glasses were produced in the range 30–92.3 mol%  $\text{Bi}_2\text{O}_3$ .

For the structural investigation of the bismuth borate glasses, X-ray diffraction patterns were obtained using a DRON-UM 1 powder diffractometer with a goniometer radius of 195 mm. The goniometer was equipped with 1.5° Soller slits for the incident and for the diffracted beams, a curved crystal monochromator at an angle of 13.37° (0.21 bandpass) and a NJ(Tl) scintillation counter connected to a pulse height analyzer. Measurements were made in reflection geometry over the  $2\theta$  range from 10 to 120° using  $\text{CuK}_\alpha$  radiation. (Scattering vector,  $Q=4\pi(\sin\theta)/\lambda$ , range 0.71–7.06  $\text{\AA}^{-1}$ , where  $2\theta$  is the scattering angle and  $\lambda$  the incident wavelength.) After data reduction to give the structure factor  $F(Q)$ , the reduced correlation function  $G(r) = 4\pi r[\rho(r)-\rho_0]$  was determined. Interatomic distances were found from the total pair correlation function  $T(r) = 4\pi r\rho_0 + G(r)$ .

The IR spectra for the glasses were recorded with a two-beam spectrophotometer (SPECORD-M80, Carl Zeiss, Jena) in the range 1300–300  $\text{cm}^{-1}$ . The wavenumber accuracy was  $\pm 3 \text{ cm}^{-1}$ .

## 3. RESULTS

The IR spectra of the glasses in the  $\text{Bi}_2\text{O}_3$ – $\text{B}_2\text{O}_3$  system are shown in Fig. 1 and exhibit a systematic variation with increasing  $\text{Bi}_2\text{O}_3$  content. The glass containing the minimum amount of  $\text{Bi}_2\text{O}_3$  (30 mol%) is characterized by a complicated high-frequency maximum at 940  $\text{cm}^{-1}$  and a shoulder at 1060  $\text{cm}^{-1}$ . In addition two low-frequency maxima are registered at 680  $\text{cm}^{-1}$  and 490  $\text{cm}^{-1}$ . The intensity of the high-frequency shoulder becomes comparable to that of the band at 940–930  $\text{cm}^{-1}$  in the spectrum for the 50 mol%  $\text{Bi}_2\text{O}_3$  glass. A fur-

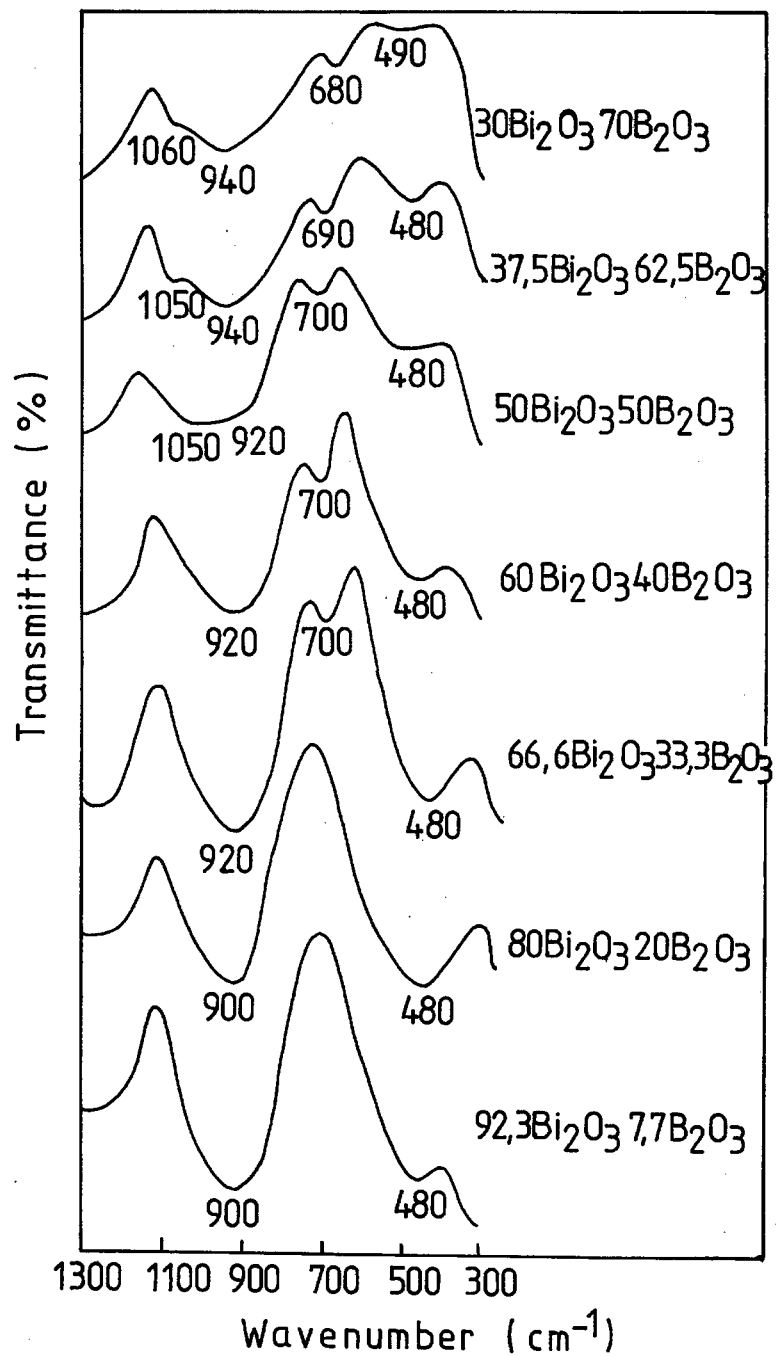


Fig. 1. IR spectra of glasses in the system  $\text{Bi}_2\text{O}_3\text{-B}_2\text{O}_3$ .



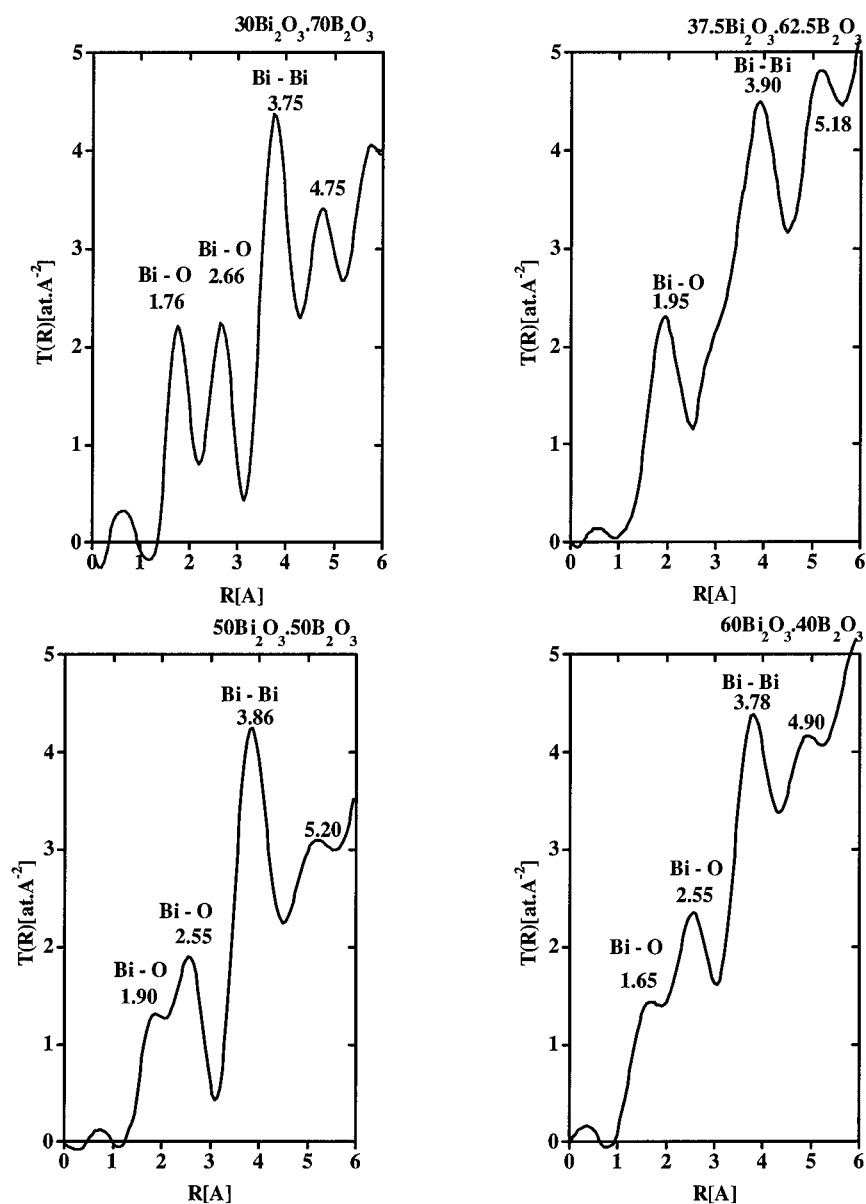


Fig. 2A. X-ray correlation functions for bismuth borate glasses.

ther variation of the composition leads to the vanishing of the band at  $1060\text{ cm}^{-1}$  and, at the same time, the initial band at  $940\text{ cm}^{-1}$  shifts to  $900\text{ cm}^{-1}$ . Beyond the 2:1 composition, the maximum at  $700\text{ cm}^{-1}$  also vanishes. All these changes are accompanied by a remarkable increase in the intensity of the peak at  $480\text{ cm}^{-1}$ .

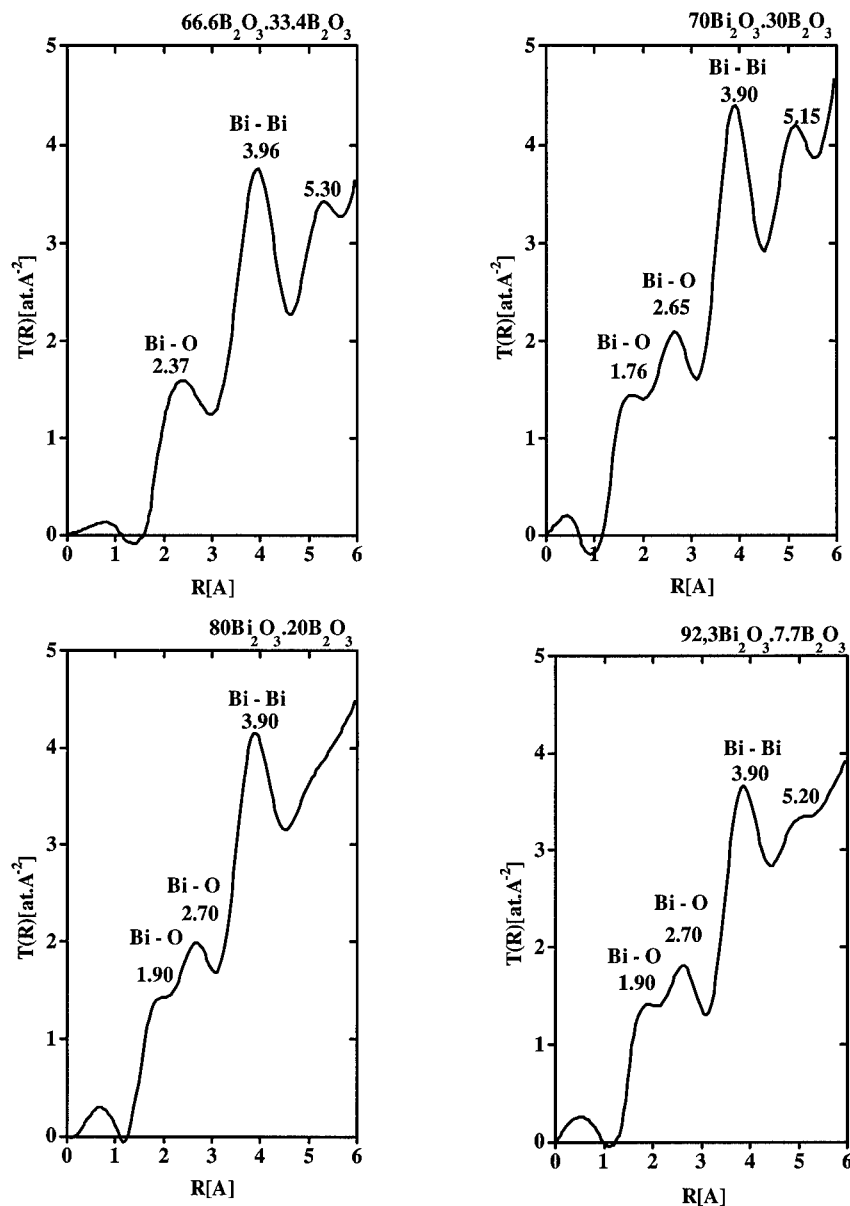


Fig. 2B. X-ray correlation functions for bismuth borate glasses.

As may be seen from Figs 2A and 2B, at low  $r$ , two maxima are resolved in the correlation functions,  $T(r)$ , for almost all of the glasses studied. On adding  $\text{Bi}_2\text{O}_3$ , the peak positions shift in the range  $1.65$ – $1.90$   $\text{\AA}$  for the first peak and  $2.55$ – $2.70$   $\text{\AA}$  for the second. Only for the  $30\text{Bi}_2\text{O}_3.70\text{B}_2\text{O}_3$  glass are these two peaks well resolved, while for the other compositions the first peak is eventu-

ally a shoulder. In this  $r$  range, instead of the usual two maxima, a single peak is found at 1.95 Å and at 2.37 Å respectively, for the  $37.5\text{Bi}_2\text{O}_3 \cdot 62.5\text{B}_2\text{O}_3$  and  $66.6\text{Bi}_2\text{O}_3 \cdot 34.4\text{B}_2\text{O}_3$  glasses, which correspond to the stoichiometric crystalline 3:5 and 2:1 compositions [19,20]. A well resolved maximum is situated in the interval 3.75–3.96 Å for all of the glass compositions.

#### 4. DISCUSSION

The structure of pure vitreous  $\text{B}_2\text{O}_3$  has been discussed at length by a variety of authors [2,3] and, according to the most commonly accepted model [3], about 80% of the boron atoms are contained in boroxol groups, the remainder being present as independent  $\text{BO}_3$  triangles. The addition of  $\text{Bi}_2\text{O}_3$  transforms this structure. As can be seen from Fig. 1, the appearance of the shoulder at  $1060\text{ cm}^{-1}$  and the basic maximum at  $940\text{ cm}^{-1}$  in the spectrum of the 30 mol%  $\text{Bi}_2\text{O}_3$  glass is probably due to the vibration of  $\text{BO}_4$  tetrahedra which are present in tetraborate and diborate groups [21–25]. The band at  $700\text{--}680\text{ cm}^{-1}$  suggests that at least some superstructural units are retained in the structure. The existence of both  $\text{BO}_3$  and  $\text{BO}_4$  groups in the glass structure, over the 30–50 mol%  $\text{Bi}_2\text{O}_3$  concentration range, is in good accord with the crystalline 3:5 structure [19] which built from these units. The results are also consistent with previous studies of borate glasses containing heavy metal ions which establish the appearance of  $\text{BO}_4$  tetrahedra [26–28]. The disappearance of the band at  $700\text{ cm}^{-1}$  in the spectra of the glasses with higher  $\text{Bi}_2\text{O}_3$ -concentration (80–92.3 mol%) indicates the destruction of the superstructural units and the disappearance of the  $\text{BO}_3$  triangles. The spectrum of the 92.3 mol%  $\text{Bi}_2\text{O}_3$  glass, which corresponds to the stoichiometric composition 12:1, is quite similar to the spectra of selenite structure [29,30]. This gives grounds to relate the vibration at  $900\text{ cm}^{-1}$  to isolated  $\text{BO}_4$  tetrahedra, since isolated  $\text{MeO}_4$  tetrahedra ( $\text{Me} = \text{Si}, \text{Ti}, \text{Ge}$ ) are typically found for selenite structures [31,32]. The low-frequency band at  $490\text{--}480\text{ cm}^{-1}$ , which rises gradually over the whole glass-forming range with increasing  $\text{Bi}_2\text{O}_3$  content, may be related to the Bi–O valence vibrations of very deformed  $\text{BiO}_6$  groups [15, 29].

The spectral results discussed above mainly comprise a description of the boron environment in the glasses. Further information may be obtained by X-ray diffraction in respect of the structural peculiarities of the bismuthate complexes, on the basis of the known crystalline structures of the 3:5, 2:1 [19,20] and selenite-like compounds [29,30] and from the authors former studies of bismuthate glasses [15–17]. The first maximum at 1.65–1.90 Å in  $T(r)$  curves can be interpreted as indicating the presence of a relatively short Bi–O distance. Obviously, there should be some contribution to the low- $r$  side of this peak from the B–O distance, but this is not apparent because of the very much lower scattering ability of the boron atom. The next maximum at 2.55–2.70 Å arises from the longer Bi–O bonds of deformed  $\text{BiO}_6$  octahedra. Bi–B bonds also have some influence on the position of this peak. The third peak at 3.76–3.90 Å is in good accordance with the Bi–Bi bond lengths in the crystalline

polymorphs. The shoulderless peaks at 1.95 Å and at 2.37 Å, for the compositions 37.5Bi<sub>2</sub>O<sub>3</sub>.62.5B<sub>2</sub>O<sub>3</sub> and 66.6Bi<sub>2</sub>O<sub>3</sub>.34.4B<sub>2</sub>O<sub>3</sub> are probably due to the overlapping of the peaks for the short and long Bi–O bonds. In the corresponding crystalline structures, the difference between these distances is small and the resulting peak will not be greatly influenced by the B–O and Bi–B bonds.

## 5. CONCLUSION

In the binary system Bi<sub>2</sub>O<sub>3</sub>–B<sub>2</sub>O<sub>3</sub>, glasses may be investigated over the concentration range 30–92.3 mol% bismuth oxide and their structure has been studied by means of IR spectroscopy and X-ray diffraction. Up to 66.6 mol% Bi<sub>2</sub>O<sub>3</sub> BO<sub>4</sub> groups have been found to exist together with the superstructural units. Over the whole concentration region short and long Bi–O bonds are present, except for the stoichiometric compositions 3:5 and 2:1 where there is only one Bi–O distance. For the glasses with higher concentration of Bi<sub>2</sub>O<sub>3</sub> (66.6–92.3 mol%), the structure becomes selenite-like, consisting of isolated BO<sub>4</sub> groups and distorted BiO<sub>6</sub> groups.

## REFERENCES

- [1] *Handbook of Glass Data*, Ed. O. V. Mazurin, M. Streltsina and T. P. Shvaiko-Shvaikovskaya, Physical Sciences Data 15, Part A and B, Elsevier, Amsterdam, 1983)
- [2] *First Borate Conf. Borate glasses: Structure, Properties, Applications*, Mat. Sci. Res. Vol. 12, Eds L. D. Pye, V. D. Frechette and N. J. Kreidl, (Plenum, New York, 1978).
- [3] A. C. Hanon, D. I. Grimley, R. A. Hulme, A. C. Wright & R. Sinclair, *J. Non-Cryst. Solids* **177** (1994), 299.
- [4] W. Dumbaugh, *Phys. Chem. Glasses* **27** (1986), 119.
- [5] R. Brown, *J. Non-Cryst. Solids* **92** (1987), 89.
- [6] J. Ruller & J. Shelby, *Phys. Chem. Glasses* **33** (1992), 177.
- [7] W. Dumbaugh & J. Lapp, *J. Am. Ceram. Soc.* **75** (1992), 2315.
- [8] O. El-Bayoumi, A. Said, R. Andrews, M. Suscavage, T. Swiler, J. Simmons & E. van Stryland, *Proc. Int. Congress on Glass, Madrid*, Vol. 3, p. 91.
- [9] F. Miyaji, S. Fujimine, T. Yoko & S. Sakka, *Bull. Inst. Chem. Res. Kyoto Univ.* **72** (1994), 134.
- [10] J. Fu & H. Yatsuda, *Phys. Chem. Glasses* **36** (1995), 211.
- [11] W. Dumbaugh, *Phys. Chem. Glasses* **19** (1978), 121.
- [12] D. Hall, N. Newhouse, N. Barrelli, W. Dumbough & D. Weidman, *J. Appl. Phys. Lett.* **54** (1989), 1293.
- [13] Y. Dimitriev & V. Michailova, *J. Mat. Sci. Lett.* **9** (1990), 1251.
- [14] Y. Dimitriev, B. Samuneva, Y. Ivanova, E. Gattef, V. Michailova & A. Staneva, *Supercond. Sci. Technol.* **3** (1990) 606.
- [15] Y. Dimitriev & V. Michailova, *Proc XVI Int. Congress on Glass, Madrid*, Vol. 3, 1992, p. 293.
- [16] Y. Dimitriev, E. Gattef, V. Michailova, C. A. Guy, A. C. Wright, R. N. Sinclair, J. D. Mackenzie & H. Zheng, In: *Fundamentals of Glass Science and Technology 1993* (Staz. Sper. Vetro, Venice, 1993), p. 471.
- [17] Y. Dimitriev, A. C. Wright, V. Michailova, E. Gattef & C. Guy, *J. Mater. Sci. Lett.* **14** (1995), 347.
- [18] E. Levin & C. McDaniel, *J. Am. Ceram. Soc.* **45** (1962), 355.
- [19] A. Vegas, F. Cano & S. Garcia-Blanco, *J. Solid State Chem.* **17** (1976), 151.
- [20] A. Hyman & A. Perloff, *Acta. Cryst.* **B 28** (1972), 2007.
- [21] A. Efimov & N. Rogova, *Glass Phys. Chem.* **2** (1976), 21.
- [22] N. Kishore, K. Aggarwal, R. Kamal & R. Mendiratta, *Phys. Chem. Glasses* **23** (1982), 202.

- [23] V. Kolesova, *Phys. Chem. Glasses* **12** (1986), 4.
- [24] E.I. Kamitsos, A. Patsis & G.D. Chryssikos, *J. Non-Cryst. Solids* **152** (1993), 246.
- [25] J. Parsons & M. Milberg, *J. Am. Ceram. Soc.* **43** (1960), 326.
- [26] N. Mochida & K. Takahashi, *J. Ceram. Soc. Jap.* **973** (1976), 413.
- [27] A. Lu & R. Lu, *Proc. XVIII Int. Congr. on Glass*, Chinese Cer. Soc., Beijing, Vol. 2, (1995), p 533.
- [28] N.M. Vedishcheva, B.A. Shakhmatkin, A.C. Wright, D.I. Grimley, G. Etherington & R.N. Sinclair, *In: Fundamentals of Glass Science and Technology 1993* (Staz. Sper. Vetro, Venice, 1993), p. 459.
- [29] R. Betsch & W. White, *Spectrochim Acta* **34A** (1977), 505.
- [30] U. Kargin, N. Neljapina, A. Marin & V. Skorikov, *Inorg. Mater.* **19** (1983), 278.
- [31] V. Batog, V. Pahomov, G. Safronov & P. Fedorov, *Inorg. Mater.* **9** (1973), 1576.
- [32] S. Abrahams, P. Jamieson & J. Brenstein, *J. Chem. Phys.* **47** (1967), 4034.

## CRYSTAL STRUCTURE AND THERMAL BEHAVIOUR OF RUBIDIUM BORATES

Rimma S. BUBNOVA, Irina G. POLYAKOVA

*Institute of Silicate Chemistry of the Russian Academy of Sciences,  
Ul. Odoevskogo, 24, korp. 2, St. Petersburg, 199155, Russia*

Stanislav K. FILATOV & Maria G. KRZHIZHANOVSKAYA

*St. Petersburg University, Dept. of Crystallography,  
University Emb. 7/9, St. Petersburg, 199034, Russia*

The paper presents new data on the crystal structures, thermal expansion and phase transitions of anhydrous rubidium borates. The extremely high magnitude and the sharply anisotropic character of the thermal expansion of crystalline network borates within the glass forming region have been revealed. Phase equilibria in the  $\text{Rb}_2\text{O}-\text{B}_2\text{O}_3$  system have been studied by high-temperature X-ray diffraction (HTXRD). New compounds,  $\text{Rb}_3\text{BO}_3$  and  $\text{Rb}_3\text{B}_7\text{O}_{12}$ , and new modifications,  $\alpha$ - and  $\beta$ - $\text{RbB}_3\text{O}_5$ , have been discovered.  $\text{Rb}_3\text{B}_7\text{O}_{12}$  is formed in the course of a solid-state reaction above  $620^\circ\text{C}$  and melts via a peritectic reaction. The new low-temperature modification,  $\alpha$ - $\text{RbB}_3\text{O}_5$ , crystallises in the orthorhombic space group  $P2_12_12_1$  and is isostructural with  $\text{CsB}_3\text{O}_5$ . The framework of the structure consists of triborate groups. This modification transforms to  $\beta$ - $\text{RbB}_3\text{O}_5$  on heating at about  $675^\circ\text{C}$ . The crystal structure of  $\text{Rb}_2\text{B}_4\text{O}_7$  is determined with  $R=0.053$  and is triclinic with space group  $P\bar{1}$ . It is isostructural with  $\text{K}_2\text{B}_4\text{O}_7$ . The borate anion forms a single three-dimensional framework built up from diborate groups, di-triborate groups and single triangles.

### 1. INTRODUCTION

Anhydrous alkali borate systems are rich in chemical compounds, especially in the region 5–35 mol% alkali oxide. Within this region, some glass properties have extrema and the boron atoms have three- and fourfold co-ordination. Tetrahedra and triangles, by sharing corners with each other, condense to rigid arrangements (diborate, triborate groups and others). These groups form (sometimes interlocking) frameworks in melts, glasses and crystals [1,2,3]. The behaviour of such groups in borate crystal structures is a factor of major significance for an understanding of the structure of melts and glasses. Thus, studying crystal structures and their thermal expansion is of special interest. Up to now, no systematic high-temperature crystal chemistry study of rubidium borates has been performed and no mention has been made of the crystalline thermal expansion.

## 2. EXPERIMENTAL

Samples were prepared by solid state reaction as well as by the crystallisation of glasses. Investigations show that, in the latter case, high-temperature metastable phases crystallise first, and it takes several months to reach phase equilibria.

Crystallographic data were obtained by X-ray analysis and the optical and immersion methods [4]. Three-dimensional X-ray intensity data for the determination of crystal structure were measured with a  $P2_1$  diffractometer. The thermal expansion, phase transitions and melting processes for the various crystalline borates were investigated by powder HTXRD and DTA.

## 3. CRYSTAL DATA AND PHASE EQUILIBRIA

The phase equilibria in the  $\text{Rb}_2\text{O}-\text{B}_2\text{O}_3$  system were first studied in Ref. [5]. The phase diagram of the system has been refined by HTXRD and DTA (Fig. 1). New compounds,  $\text{Rb}_3\text{BO}_3$  and  $\text{Rb}_3\text{B}_7\text{O}_{12}$ , and new polymorphic modifications,  $\alpha$ - and  $\beta$ - $\text{RbB}_3\text{O}_5$ , have been found [6,7].

Rubidium orthoborate,  $\text{Rb}_3\text{BO}_3$ , was prepared by solid-state reaction at  $600^\circ\text{C}$  and melts at  $760^\circ\text{C}$ . Under atmospheric conditions,  $\text{Rb}_3\text{BO}_3$  is hydrated within a few minutes.

Rubidium heptaborate,  $\text{Rb}_3\text{B}_7\text{O}_{12}$ , is formed above  $620^\circ\text{C}$  during the course of the solid-state reaction  $\text{Rb}_2\text{B}_4\text{O}_7 + \alpha\text{-RbB}_3\text{O}_5 \rightarrow \text{Rb}_3\text{B}_7\text{O}_{12}$  and melts at about  $700^\circ\text{C}$  according to the peritectic reaction  $\text{Rb}_3\text{B}_7\text{O}_{12} \rightarrow \beta\text{-RbB}_3\text{O}_5 + \text{Liquid}$ . The crystals are biaxial, with a negative sign and the following parameters:  $2V=45^\circ$ ,  $n_g=1.550$ ,  $n_m=1.546$  and  $n_p=1.511$ .

The crystal structure of rubidium diborate,  $\text{Rb}_2\text{B}_4\text{O}_7$ , has been determined. It is triclinic with space group  $P\bar{1}$  and following parameters:  $a=9.860(4)$ ,  $b=10.653(6)$ ,  $c=6.649(4)$  Å,  $\alpha=103.4(1)$ ,  $\beta=101.4(1)$ ,  $\gamma=89.1(1)^\circ$ ,  $Z=4$ , and  $R=0.053$  [8]. The crystal optic constants are: sign '+',  $2V=80^\circ$ ,  $n_g=1.562$ ,

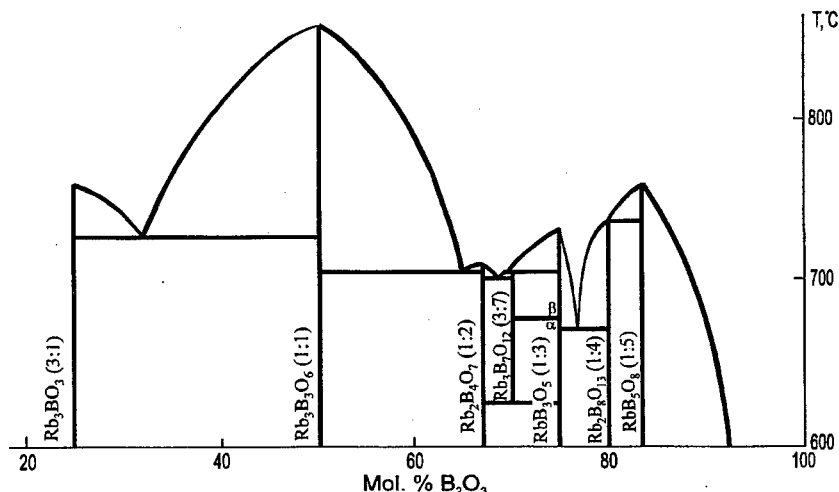


Fig. 1. Phase diagram of the  $\text{Rb}_2\text{O}-\text{B}_2\text{O}_3$  system.

$n_m=1.550$  and  $n_p=1.542$ . It is isostructural with  $K_2B_4O_7$  [9]. Diborate groups,  $[B_2^{IV}B_2^{III}O_7]^{2-}$ , di-triborate groups,  $[B_2^{IV}B^{III}O_{5.5}]^{2-}$ , and single triangles,  $[B^{III}O_{1.5}]^0$ , are the basic units of the single three-dimensional anion framework of  $Rb_2B_4O_7$  (Fig. 2). Di-triborate groups and single triangles, by sharing corners, form  $[B_2^{IV}B_2^{III}O_7]^{2-}$  chains along the  $c$  axis {Fig. 2 (e)}.

The new low-temperature modification of rubidium triborate,  $\alpha$ - $RbB_3O_5$ , was obtained by solid-state reaction. It crystallises in the orthorhombic space group  $P2_12_12_1$ , with  $a=8.217(3)$ ,  $b=10.095(3)$ ,  $c=5.391(2)$  Å and  $Z=2$ . It is isostructural with  $CsB_3O_5$  [10]. The framework of the structure consists of triborate groups,  $[B^{IV}B_2^{III}O_5]^-$ . This modification transforms to  $\beta$ - $RbB_3O_5$ , on heating at about 675°C, which melts at 735°C.

Rubidium pentaborate,  $RbB_5O_8$ , crystallises in the orthorhombic space group  $Pcab$ , with  $Z=2$  [11]. Its unit cell parameters,  $a=11.835(7)$ ,  $b=14.81(1)$  and  $c=7.527(5)$  Å, have been refined. It is isostructural with  $KB_5O_8$  [12], but the polymorphic transition of  $RbB_5O_8$ , mentioned in Ref. [5], has not been observed in HTXRD patterns. The compounds  $2Rb_2O \cdot 5B_2O_3$  [13] and  $Rb_2O \cdot 9B_2O_3$  [5] have also not been found. The fraction of the boron atoms in fourfold coordination,  $N_{BO_4}$ , for each of the crystalline polymorphs, is presented in Fig. 3.

#### 4. SOME FEATURES OF THE HIGH-TEMPERATURE CRYSTAL CHEMISTRY OF RUBIDIUM BORATES

The thermal behaviour of three anhydrous framework borates has been studied:

##### 4.1. Average Thermal Expansion

The average linear coefficient of thermal expansion  $\bar{\alpha}=\alpha_v/3$  ( $\alpha_v$ =coefficient of volume expansion) is equal to  $25 \times 10^{-6}$  for  $\alpha$ - $RbB_3O_5$ ,  $30 \times 10^{-6}$  for  $RbB_5O_8$

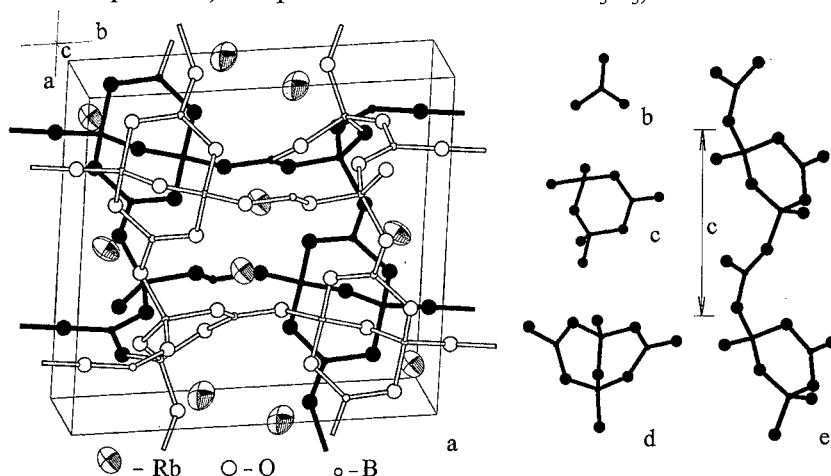


Fig. 2. Representation of the  $Rb_2B_4O_7$  crystal structure (a) and its basic units (b-e): (b), single triangle,  $[B^{III}O_{1.5}]^0$ ; (c), di-triborate group,  $[B_2^{IV}B^{III}O_{5.5}]^{2-}$ ; (d), diborate group,  $[B_2^{IV}B_2^{III}O_7]^{2-}$  and (e), infinite  $[B_2^{IV}B_2^{III}O_7]^{2-}$  chains.



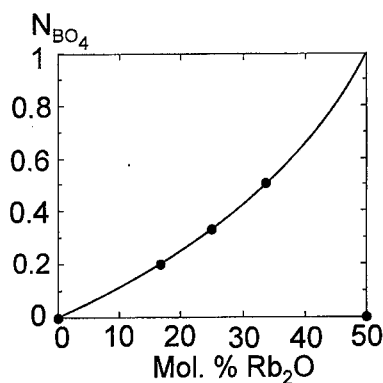


Fig. 3. The fraction of boron atoms in fourfold co-ordination as a function of composition in the  $\text{Rb}_2\text{O}-\text{B}_2\text{O}_3$  system. Closed circles, experimental data and solid line, theoretical curve [10].

and  $17 \times 10^{-6} \text{C}^{-1}$  for  $\text{Rb}_2\text{B}_4\text{O}_7$  (Fig. 4). The last is close to the coefficient for glasses ( $\alpha = 14 \times 10^{-6} \text{C}^{-1}$  [14]), hydrous chain borates, hydroboracite ( $\text{CaMgB}_6\text{O}_{18}(\text{OH})_6 \cdot 3\text{H}_2\text{O}$ ,  $\alpha = 15 \times 10^{-6} \text{C}^{-1}$ ) and colemanite ( $\text{Ca}_2\text{B}_6\text{O}_{11} \cdot 5\text{H}_2\text{O}$ ,  $\alpha = 17 \times 10^{-6} \text{C}^{-1}$  in the linear approximation) [15]. However, the other two coefficients ( $\sim 30 \times 10^{-6} \text{C}^{-1}$ ) are unusually high for borates and it is interesting to note that the both borates are located in the glass forming region.

#### 4.2. $\alpha\text{-RbB}_3\text{O}_5$

The temperature dependence of the unit cell parameters for  $\alpha\text{-RbB}_3\text{O}_5$  {Fig. 5 (a)} has a sharply anisotropic character: the thermal expansion along the  $a$  axis,  $\alpha_a = 29 \times 10^{-6} \text{C}^{-1}$ , is close to the average (cf. Section 4.1), but  $\alpha_c = 74 \times 10^{-6} \text{C}^{-1}$  is much higher and  $\alpha_b = -27 \times 10^{-6} \text{C}^{-1}$  is negative. Thus the  $bc$  plane has the most anisotropic expansion.

The crystal structure of  $\alpha\text{-RbB}_3\text{O}_5$  (Fig. 6) contains a single borate framework. It is obvious that borate rhombuses may be distinguished in the  $bc$  plane.

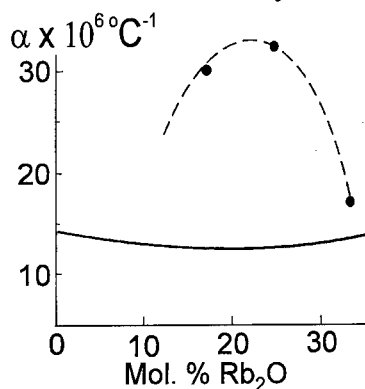
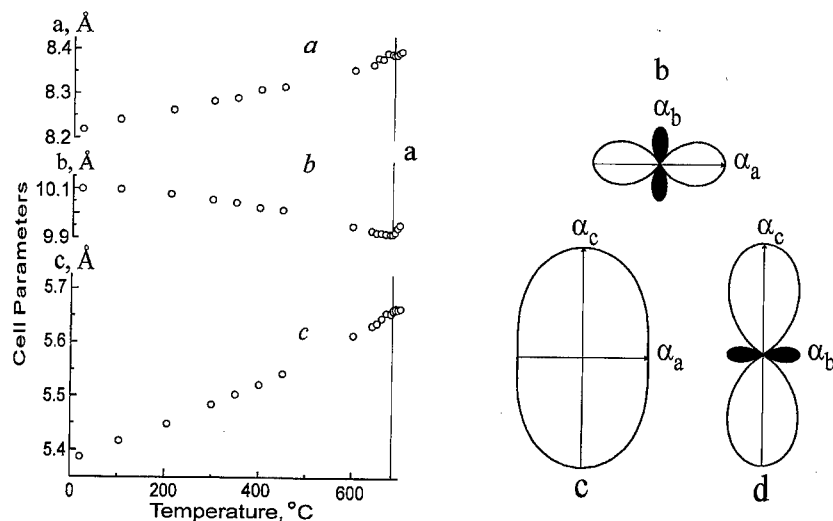
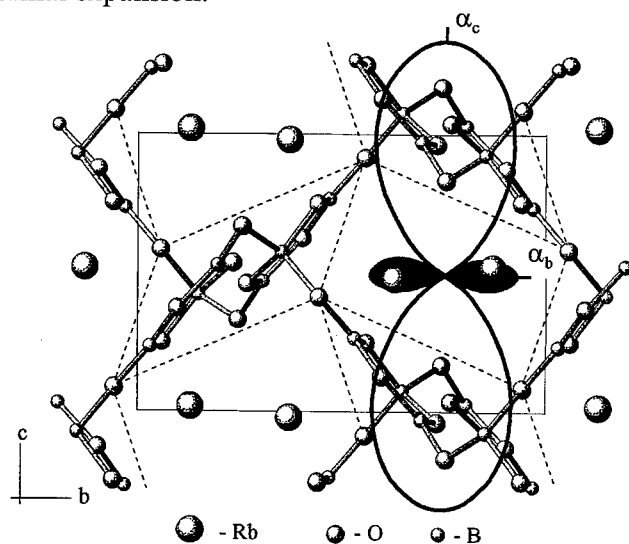


Fig. 4. Linear coefficient of thermal expansion as a function of composition in the  $\text{Rb}_2\text{O}-\text{B}_2\text{O}_3$  system. Solid line, data for glasses [14] and closed circles, data for crystals (present work).



**Fig. 5.** Temperature dependence of the orthorhombic cell parameters (a) and pole figures for the coefficients of thermal expansion in the  $ab$  (b),  $ac$  (c) and  $bc$  (d) planes for  $\alpha$ -RbB<sub>3</sub>O<sub>5</sub>. The mean square deviation for the cell parameters is comparable with the size of the data points. Darkened parts in the thermal expansion diagrams indicate directions of negative expansion.

Hence if the rhombus is extended along one of its diagonal lines it has to be compressed along the other, as demonstrated by the pole figure for the coefficients of thermal expansion.



**Fig. 6.** The correlation between pole figure for the coefficients of thermal expansion and the crystal structure in the  $bc$  plane for  $\alpha$ -RbB<sub>3</sub>O<sub>5</sub>. The dashed lines denote infinite chains of triborate groups along the  $a$  axis. The atomic co-ordinates are taken from Ref. [10] for CsB<sub>3</sub>O<sub>5</sub>.

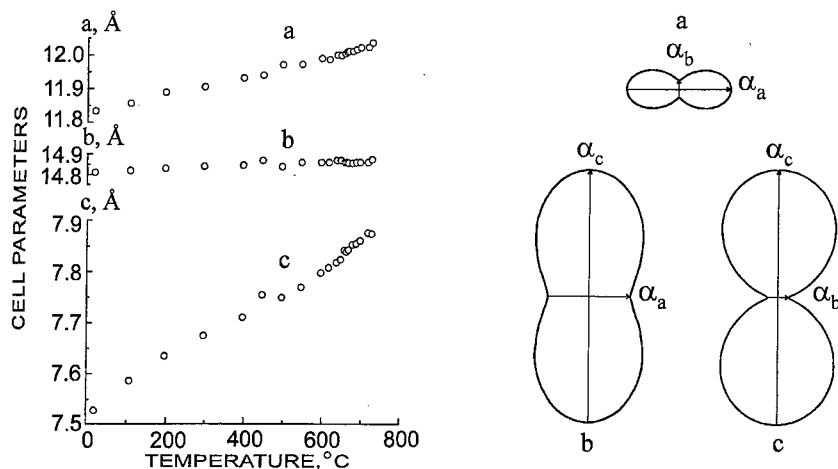


Fig. 7. The temperature dependence of the orthorhombic cell parameters (a) and pole figures for the coefficients of thermal expansion in the  $ab$  (b),  $ac$  (c) and  $bc$  (d) planes for  $\text{RbB}_5\text{O}_8$ . Mean square deviation for the cell parameters is comparable with the size of the data points.

Thus the anisotropy of the thermal expansion of  $\alpha\text{-RbB}_3\text{O}_5$  is correlated to the thermal reconstruction of its structure. The framework of the structure consists of triborate groups,  $[\text{B}^{\text{IV}}\text{B}_2^{\text{III}}\text{O}_5]^-$ , which form infinite spiral chains around the twofold screw axes along the  $a$  axis. In Fig. 6, the chains appear as pairs of triborate groups and are marked by dashed lines. It may be predicted that the principal feature of the thermal reconstruction of the structure is the rotation of such chains around the oxygen atoms which are common for two chains.

#### 4.3. $\text{RbB}_5\text{O}_8$

The temperature dependence of the unit cell parameters (Fig. 7) has approximately the same anisotropic character as for  $\alpha\text{-RbB}_3\text{O}_5$  ( $\alpha_a=23$ ,  $\alpha_b=4.7$ ,  $\alpha_c=61 \times 10^{-6} \text{C}^{-1}$ ), except for the absence of the negative thermal expansion in the case of  $\text{RbB}_5\text{O}_8$ .

The crystal structure of  $\text{RbB}_5\text{O}_8$  is composed of two interlocking frameworks consisting of pentaborate groups,  $[\text{B}^{\text{IV}}\text{B}_4^{\text{III}}\text{O}_{8.5}]^{2-}$  (Fig. 8). As in the case of  $\alpha\text{-RbB}_3\text{O}_5$ , rhombuses may be defined which consist of infinite chains of pentaborate groups along the  $a$  axis. It is believed that the structure is reconstructed on heating so that the chains rotate around the bridging oxygen atoms connecting two such chains.

#### 4.4. $\text{Rb}_2\text{B}_4\text{O}_7$

On heating, the linear parameters of the triclinic unit cell of rubidium diborate change by about the same amount as the angular parameters. The thermal expansion of the structure has a weakly anisotropic character. The

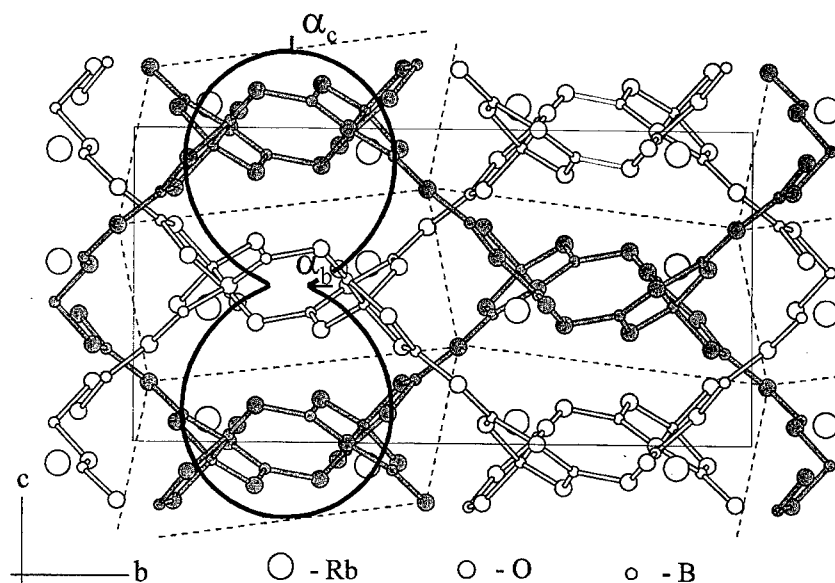


Fig. 8. The correlation between the pole figure for the coefficients of thermal expansion and the crystal structure in the  $bc$  plane for  $\text{RbB}_5\text{O}_8$ . The darkened framework denotes one of two which interlock. Atomic co-ordinates are taken from Ref. [12] for  $\text{KB}_5\text{O}_8$ .

principal coefficients of thermal expansion are  $\alpha_{11}=23$ ,  $\alpha_{22}=14$ ,  $\alpha_{33}=13$  and  $\alpha_v=50 \times 10^{-6} \text{ } ^\circ\text{C}^{-1}$ .

## 5. DISCUSSION

Three important features emerge from the present study:

1. The linear coefficient of thermal expansion for rubidium borate glasses has a weak minimum within the glass forming region (cf. Fig. 4, solid line). In contrast, the crystals demonstrate a large maximum (Fig. 4, dots and dashed line). This difference may be caused by the open nature of the crystalline network, with widely-spaced chemical bonds.
2. The average index of refraction for the crystals (1.551 for  $\text{Rb}_2\text{B}_4\text{O}_7$  and 1.536 for  $\text{Rb}_3\text{B}_7\text{O}_{12}$ ) is greater than for the glasses (1.49 [14]). This may be correlated with the fact that the density for the crystals (2.73 [11], 3.0 and 3.26  $\text{g/cm}^3$  for  $\text{RbB}_5\text{O}_8$ ,  $\alpha\text{-RbB}_3\text{O}_5$  and  $\text{Rb}_2\text{B}_4\text{O}_7$ , respectively) is greater than that for the glasses (2.465, 2.778 and 2.978  $\text{g/cm}^3$  for 16.9, 26.1 and 33.3 mol%  $\text{Rb}_2\text{O}$  [16]).
3. It was possible to expect that the crystalline framework borates would show practically isotropic thermal expansion [17], but it appears that two out of three borates have highly anisotropic deformations.

The anisotropy of the crystal lattice expansion may be caused by anisotropic thermal vibrations of such heavy atoms as rubidium. The crystal structure of  $\alpha\text{-RbB}_3\text{O}_5$  contains infinite channels along the  $a$  axis (see Fig. 6) in which the Rb atoms are located. Two neighbouring Rb atoms are very close to

each other along the  $b$  axis. On heating the atoms are restricted in certain directions and so the diagonals of the 'rhombuses' of the borate network increase along the  $c$  axis and decrease along the  $b$  axis. This kind of deformation is known as shear and has by nature a highly anisotropic character [17].

The same type of shear deformation occurs for  $\text{RbB}_5\text{O}_8$ . The two interlocking frameworks form cavities (see Fig. 8) occupied by pairs of Rb atoms. Two kinds of Rb pairs are oriented approximately along the  $b$  axis, which makes it difficult for the thermal vibration of the Rb atoms in this direction and is favourable for their vibration in a perpendicular plane.

The opposite situation exists for  $\text{Rb}_2\text{B}_4\text{O}_7$ . In the cavities of its structure four kinds of Rb pairs are located (see Fig. 2). The Rb-Rb axes of the pairs have different orientations and, for this reason, the lengthening of the thermal vibration ellipsoids of the Rb atoms also have different orientations. As a result the crystal lattice deformation is only slightly anisotropic.

## 6. CONCLUSION

Thus in all of the cases under review the crystal lattice thermal expansion depends mainly on the thermal behaviour of the Rb atoms. This is in agreement with the statement that the deformation of the crystal lattice is controlled by the transformations of the 'softest' (largest and most irregular) co-ordination polyhedra [17].

## REFERENCES

- [1] J.Krogh-Moe, *Phys. Chem. Glasses* **3** (1962), 101.
- [2] J.Krogh-Moe, *Phys. Chem. Glasses* **6** (1965), 46.
- [3] A.C.Wright, N.M.Vedishcheva & B.A.Shakmatkin, *Advances in X-Ray Analysis* **39** (1996), in press.
- [4] V.B.Tatarskii, *Optical and immersion methods*, (Nedra, Moscow, 1965) (Russ. Edition).
- [5] A.P.Rollet & J.Kocher, *C. R. Acad. Sci.* **259** (1964), 4692.
- [6] R.S.Bubnova, I.G.Polyakova, M.G.Krzhizhanovskaya & S.K.Filatov, Abstracts of Intern. Conf. 'Powder Diffraction and Crystal Chemistry', St.Petersburg, Russia, June 20-23, 1994, p. 80.
- [7] R.S.Bubnova, M.G.Krzhizhanovskaya, V.B.Trofimov, I.G.Polyakova & S.K.Filatov, Abstracts of VII Conf. on Crystal Chemistry of Inorganic and Co-ordination Compounds, St.Petersburg, Russia, June 27-30, 1995, p. 97.
- [8] M.G.Krzhizhanovskaya, R.S.Bubnova, I.I.Bannova & S.K.Filatov, *Crystallogr. Reports* **42**, **2** (1997), 264.
- [9] J.Krogh-Moe, *Acta Crystallogr.* **B30** (1974), 578.
- [10] J.Krogh-Moe, *Acta Crystallogr.* **13** (1960), 889.
- [11] J.Krogh-Moe, *Arkiv Kemi* **14** (1959), 439.
- [12] J.Krogh-Moe, *Acta Crystallogr.* **B30** (1965), 1088.
- [13] P.Toledano, *Bull. Soc. Chim. France* **7** (1966), 2302.
- [14] O.V.Mazurin, M.V.Streltsina & T.P.Shvaiko-Shvaikovskaya, *Handbook of Glass Data V* (Nauka, Leningrad, 1987) (Russ. Edition).
- [15] S.K.Filatov, *High-Temperature Crystal Chemistry* (Nedra, Leningrad, 1990) (Russ. Edition).
- [16] O.V.Mazurin, M.V.Streltsina & T.P.Shvaiko-Shvaikovskaya, *Handbook of Glass Data II* (Nauka, Leningrad, 1975) (Russ. Edition).
- [17] S.K.Filatov & R.M.Hazen, In: *Advanced Mineralogy* **1**, Ed. A.S.Marfunin (Springer-Verlag, Berlin, Heidelberg, 1994), pp. 76-90.

## BORATE STRUCTURES BY VIBRATIONAL SPECTROSCOPY

Georgios D. CHRYSSIKOS & Efstratios I. KAMITSOS

*Theoretical and Physical Chemistry Institute,  
National Hellenic Research Foundation,  
48 Vass. Constantinou Ave., Athens 11635, Greece*

This paper deals with some recent contributions of infrared and Raman spectroscopies to the structural description of borate systems. It demonstrates how the vibrational spectra can assist the decoding of local and intermediate range structure of crystals and glasses. Spectroscopic tools have been developed to tackle thermodynamic and kinetic aspects of chemical reactions relevant to the vitrification of borates. Case studies of alkali and alkaline earth borate glasses and crystals highlight the cation and composition dependence of borate networks. The interactions between the network sites and the modifying cations are monitored by the characteristic cation motion bands in the far-infrared. Some structural aspects of the mixed-alkali effect are discussed.

### 1. INTRODUCTION

Borates with the general formula  $xM_{2/n}O \cdot (1-x)B_2O_3$  result commonly from the fusion of boric anhydride,  $B_2O_3$ , with metal oxides  $M_{2/n}O$  provided by the thermal decomposition of carbonate or nitrate salts. The structural chemistry of borates is very rich, and their phase diagrams include broad glass-forming ranges. There is an extensive research effort aiming at the elucidation, classification, and prediction of borate structures, much of which relies on vibrational spectroscopic techniques.

The purpose of this report is to highlight contributions of vibrational spectroscopy to the systematic structural mapping of borate crystals and glasses by presenting selective spectroscopic tools and structural concepts employed in the authors' laboratory over the last decade. The principles and instrumentation of infrared and Raman spectroscopies can be found in books and monographs. Technical details, spectral analysis and band assignments should be sought in the original references.

### 2. THE LOCAL STRUCTURE OF BORATE NETWORKS

Boron has an  $s^2p^1$  electronic configuration. In borates it adopts  $sp^2$  or  $sp^3$  hybridizations, therefore acquiring trigonal or tetrahedral coordination. In the former case boron affords an empty  $p_z$  orbital perpendicular to the borate plane. The planarity of the borate triangle is enhanced by the  $\pi$ -bonding between this

**Table 1**  
Schematic structural classification of borate polyhedra as a function of stoichiometry

$xM_{2/n}O \cdot (1-x)B_2O_3$		Average stoichiometry	Local structure		4-coordinated	
			3-coordinated			
0		$BO_{1.5}^0$	$B\emptyset_3^0$	Ref. [2]		
0.5	meta	$BO_2^{1-}$	$B\emptyset_2O^{1-}$	Ref. [3]	$B\emptyset_4^{1-}$	Ref. [4]
0.67	pyro	$BO_{2.5}^{2-}$	$B\emptyset O_2^{2-}$	Ref. [5]		
0.75	ortho	$BO_3^{3-}$	$BO_3^{3-}$	Ref. [6]	$B\emptyset_2O_2^{3-}$	Ref. [9]
0.83	5:1	$BO_4^{3-}$			$BO_4^{3-}$	Ref. [7]

empty  $p_z$  orbital and the filled  $p$  orbitals of the (bridging and non-bridging) oxide ligands [1]. Alternatively, the  $\sigma$  nucleophilic attack of oxygens lying above or below the plane, leads to the formation of 4-coordinated borate species.

Table 1 comprises a list of the network polyhedra found in borate compounds as a function of stoichiometry. Oxygen atoms are shown either bridging two boron centers ( $\emptyset$ ), or as non-bridging or terminal (O). There is direct crystallographic evidence for all species [2-7], except for the 4-coordinated orthoborate ( $B\emptyset_2O_2^{3-}$ ), analogous to  $Al\emptyset_2O_2^{3-}$  [8], for which the only evidence comes from the interpretation of the Raman spectrum of some alkali orthoborate glasses [9]. Polyhedra with oxygen coordinated to three boron centers [10] are not included in Table 1.

To a good approximation, the polyhedra of Table 1 can be considered as the primary building blocks for every borate structure, either glassy or crystalline. For example, diborate crystals and glasses, with average stoichiometry ( $x=0.33$ ) not corresponding to that of a primary polyhedron, ought to consist of formally neutral  $B\emptyset_3^0$  triangles and metaborate polyhedra ( $B\emptyset_2O^{1-}$  triangles and/or  $B\emptyset_4^{1-}$  tetrahedra) in equal proportions. There are two chemical processes leading to structural diversification at the local level. The first is the *isomerization* between 3- and 4-coordinated species of the same stoichiometry (e.g.  $B\emptyset_2O^{1-} \rightleftharpoons B\emptyset_4^{1-}$ ), the second is the *disproportionation* of a species into polyhedra of higher and lower stoichiometry (e.g.  $2B\emptyset O_2^{2-} \rightleftharpoons B\emptyset_2O^{1-} + BO_3^{3-}$ ). Both depend on the nature of the  $M^{n+}$  cation [9,11].

The species of Table 1 have distinct vibrational signatures due to differences in symmetry and bonding. Despite the fact that these signatures can be obscured by the coupling between different groups, crystal field effects, or merely by the coexistence of many groups with overlapping spectra, the spectroscopic identification of the local structural species is in many cases possible [12, 13]. As an example, Fig. 1 compiles the infrared absorption spectra of representative  $xLi_2O \cdot (1-x)B_2O_3$  glasses with compositions spanning the glass forming range. The spectra are collected in the specular reflectance mode which ensures continuous spectral acquisition over broad frequency ranges (30-4000  $cm^{-1}$ ) and yields quantitative spectra free of hydrolysis and optical dispersion effects [14]. While detailed assignments are provided in [14], we note here that the stretching vibrations of metaborate tetrahedra,  $B\emptyset_4^{1-}$ , are observed at fre-

quencies ( $800\text{--}1100\text{ cm}^{-1}$ ) lower than the corresponding modes of borate triangles ( $1100\text{--}1600\text{ cm}^{-1}$ ). Analysis of the spectra and appropriate ratioing of integrated intensities, (Fig. 2a), demonstrates the non-monotonic dependence of the fraction of four-coordinated boron centers in the glass ( $N_4$ ) on  $x$  [14], already familiar from the NMR work of P. J. Bray [15], as well as the composition dependence of meta-, pyro- and orthoborate triangles. The same spectral features allow the determination and quantification of a pronounced cation dependence of  $N_4$  [16], where for a fixed stoichiometry below the metaborate, the larger alkalis induce the formation of fewer tetrahedral species and, consequently, favor increased fractions of  $\text{BO}_2\text{O}^{1-}$  triangles [13, 16, 17] (Figure 2b). Incidentally, this trend appears reversed for  $x > 0.50$  [9].

### 3. DANGLING BONDS ON BORATE TRIANGLES: A RAMAN PROBE OF INTERMEDIATE ORDER

Let us now focus on the distribution of  $\pi$ -bonding over the three B–O bonds of a borate triangle. The three oxygen atoms will compete for the empty boron  $p_z$  orbital and their ability to neutralize boron will depend on their charge (basicity) and on how much of this charge is involved in bonding outside the triangle, i.e. towards the neighboring boron centers and/or towards the charge balancing cations  $\text{M}^{n+}$ . Therefore, in the general case, the three B–O bonds of the triangle will be of unequal length and strength, (i.e. of unequal force constant), and would result in different B–O stretching frequencies. All of these are valid strictly

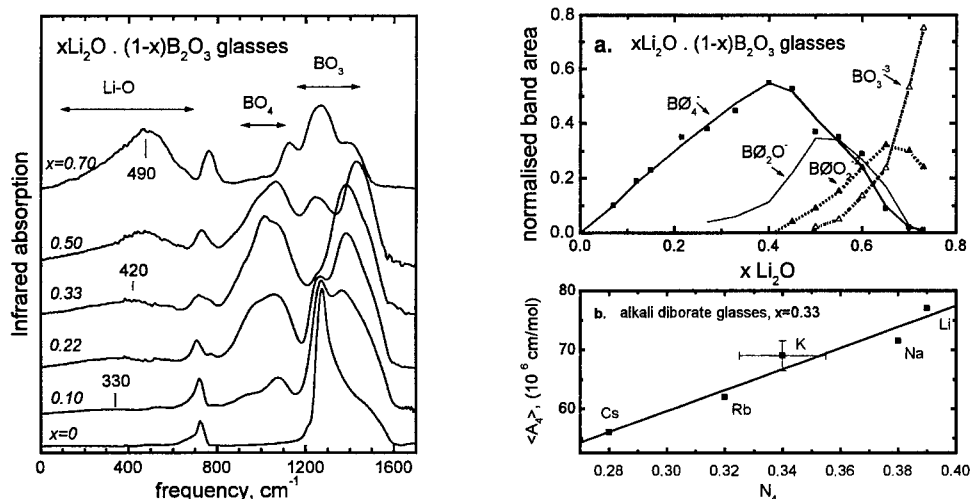


**Fig.1.** (left) Infrared absorption spectra of selected  $x\text{Li}_2\text{O} \cdot (1-x)\text{B}_2\text{O}_3$  glasses [14]  
**Fig. 2.** (right) (a) Compositional dependence of the integrated intensities of infrared bands due to metaborate tetrahedra and meta-, pyro- and orthoborate triangles in lithium borate glasses. Lines are guiding the eye [14]. (b) Cation dependence of the integrated intensity of the infrared envelope due to  $\text{BO}_4^{1-}$  units in alkali diborate glasses. The line is a linear least squares fit [16].



in the dipole approximation. The structural entity that most closely fulfills the requirement for vibrational decoupling from the rest of the network is the B-O<sup>-</sup> dangling bond, especially when the charge balancing M-O interactions are fully ionic and, therefore, weak. Due to its large force constant, the stretching vibration of these B-O<sup>-</sup> bonds is observed in the highest frequency part of the Raman spectrum with very little interference from other vibrations. By the same token, it is often possible to locate at lower frequencies a strong feature that could be assigned to a stretching vibration of B-O bonds [18 and Refs. therein].

Based on the Raman spectra of nine meta-, pyro- and orthoborate crystals consisting solely of triangular units, a simple linear correlation has been developed between the boron-oxygen bond length, ( $r$ ), and the corresponding stretching frequency  $\nu$  in cm<sup>-1</sup>,  $\nu = 16900 - 11600r$ , ( $1.31 \leq r \leq 1.40$  Å). Since  $r$  has been empirically correlated with the valence of the B-O bond,  $s$ , the latter can be correlated also with  $\nu$ :  $s = 0.8 + 2 \times 10^{-4}\nu$ . The implications (and limitations) of the two equations have been presented elsewhere [18]. We only note here that spectral acquisition at  $\pm 2$  cm<sup>-1</sup> accuracy in reading band maxima allows Raman spectroscopy to monitor minute changes of  $r$  or  $s$  in borate triangles. Such changes often result from second neighbor effects (i.e. from intermediate range order).

Representative Raman signatures of metaborate B-O<sup>-</sup> triangles in crystals and glasses are shown in Fig. 3. Crystalline NaBO<sub>2</sub> and  $\alpha$ -LiBO<sub>2</sub> consist solely of metaborate triangles. The large frequency difference of their B-O<sup>-</sup> stretches (ca. 1560 cm<sup>-1</sup> vs. 1485 cm<sup>-1</sup>) reflects their different intermediate range order: rings vs. chains [19]. The presence of two basic B $\ddot{O}_4^-$  units adjacent to the B $\ddot{O}_2O^-$  "probe" in Ba<sub>2</sub>LiB<sub>5</sub>O<sub>10</sub> strengthens the B-O bonds of the triangle and shifts the B-O<sup>-</sup> stretch to ca. 1400 cm<sup>-1</sup> [18]. Even lower frequencies (ca. 1360 cm<sup>-1</sup>) are measured in crystalline Li<sub>2</sub>BAlO<sub>4</sub>, where even more basic Al $\ddot{O}_4^-$  tetrahedra are neighboring the B $\ddot{O}_2O^-$  triangle [20]. Overall, the ca. 200 cm<sup>-1</sup> frequency span of the metaborate B-O<sup>-</sup> stretch corresponds approximately to a 0.02 Å variation in bond length and a 0.04 change in bond valence [18].

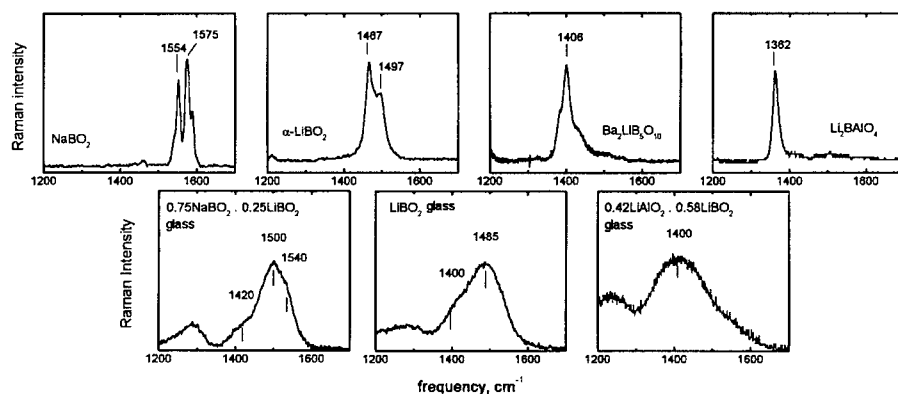


Fig.3. Raman spectra of B-O<sup>-</sup> stretches in crystalline (top) and glassy (bottom) metaborates [18-20].

Based on this "calibration", we can now reveal the structural richness of metaborate glasses. For example,  $\text{B}\text{O}_2\text{O}^-$  participates in (and probes) two distinct environments in glassy  $\text{LiBO}_2$ , [18] (see Fig. 3), a result confirmed by NQR [21]. These environments change systematically upon partial substitution of Li by Na, and of B by Al, and provide a structural fingerprint of the mixed alkali and mixed network effects [20,22]. Even more so, due to isomerization and disproportionation, the formation of metaborate triangles is not restricted to the metaborate stoichiometry. Thus, the  $\text{B}-\text{O}^-$  stretch of  $\text{B}\text{O}_2\text{O}^-$  units can be used to monitor the sequence of network polyhedra in every borate glass family, and over practically the whole glass forming range.

#### 4. BORATE STRUCTURE AT INTERMEDIATE RANGES: RINGS, CONDENSED RINGS AND CHAINS

The primary polyhedra of Table 1 are not randomly connected in forming borate networks. Crystalline borate structures offer a variety of examples where these polyhedra are stabilized (mostly due to charge delocalization) in well-defined six-membered rings, condensed rings and chains [2,3,23-30].

Figure 4 compiles such structures built of  $\text{B}\text{O}_3^0$ ,  $\text{B}\text{O}_2\text{O}^-$ , as well as  $\text{B}\text{O}_4^-$  polyhedra. Isomerism is evident, especially for  $x=0.50$ , while the structural similarity between arrangements of different stoichiometry warrants easy disproportionations. Taking into account the charge balancing cations  $\text{M}^{n+}$ , the intermediate spatial order of these units is in the range of 5-10 Å. We also note that pyro- and orthoborate triangles which would lead to the cleavage of the arrangements of Fig. 4, can also form ring structures where the charge balancing cation  $\text{M}^{n+}$  occupies the place of a boron center [31].

As a rule of thumb, triangular borate network rings like the boroxol and the metaborate (see Fig. 4) have aromatic character. They tend to be planar and are stacked parallel to each other. This planarity is interrupted by four-coordinated boron atoms. Some crystalline compounds offer examples of intermediate cases where small deviations from planarity are due to weak  $\text{B}-\text{O}$  interplanar interac-

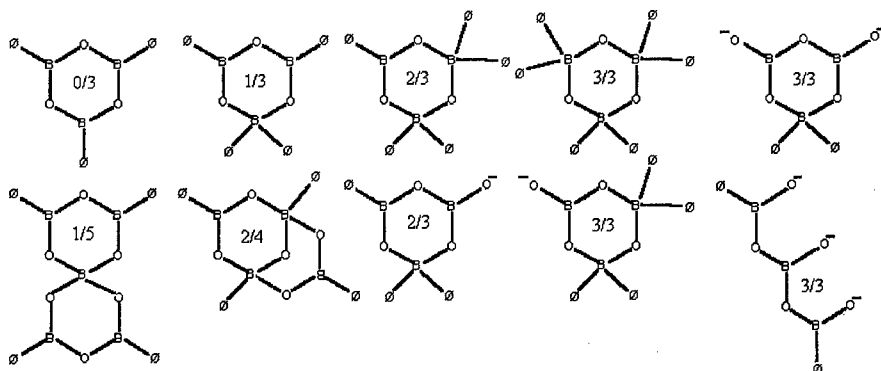


Fig. 4. Six-membered rings, condensed rings and chains found in crystalline borates. The labels denote their average formal negative charge per boron center,  $x/(1-x)$ .

tions, precursing the isomerization of metaborate triangles into tetrahedra.

Due to differences in symmetry and bonding, the structures in Fig. 4 have discrete vibrational signatures which in many cases compare favorably with the predictions of group theory. Most structures of Fig. 4 exhibit breathing modes of the oxygen atoms which, due to the large polarisability changes involved, have strong Raman activity. It is on the basis of such a Raman band at  $806\text{ cm}^{-1}$  that boroxol rings have been unambiguously identified as a major constituent of glassy  $\text{B}_2\text{O}_3$  [32].

A more recent example of the extreme sensitivity of Raman spectroscopy to probe subtle structural differences of intermediate range order in borates is shown in Fig. 5. High temperature  $\text{NaBO}_2$ ,  $\text{BaB}_2\text{O}_4$  and  $\text{CaB}_2\text{O}_4$  compounds are representative of three classes of metaborates which consist solely of  $\text{BO}_2\text{O}^{1-}$  triangles but differ in their intermediate range ordering ( $\text{D}_{3h}$  aromatic rings with degenerate annular bonds,  $\text{C}_{3h}$  Kékulé rings and infinite chains, respectively) [19]. The Raman spectra probe the subtle cation-dependent structural difference between the ring structures which has occasionally remained unnoticed by crystallographers. Even more so, a correlation between spectroscopic parameters and the field strength of the charge balancing  $\text{M}^{n+}$  ion has guided the discovery of a hitherto unknown strontium metaborate compound with the  $\text{C}_{3h}$  ring structure [19].

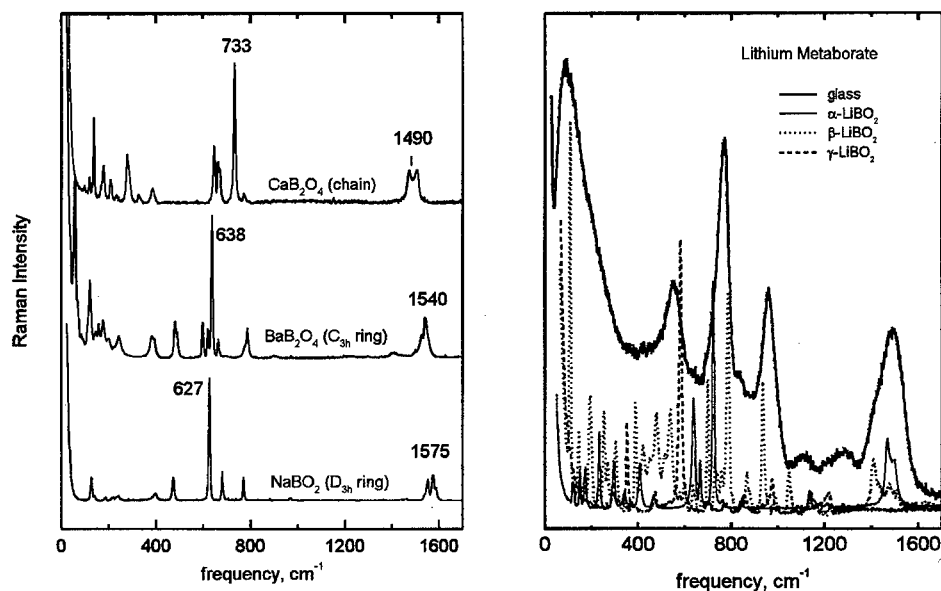


Fig. 5. (left) Raman spectra of  $\text{CaB}_2\text{O}_4$ ,  $\text{BaB}_2\text{O}_4$ , and  $\text{NaBO}_2$  crystals which consist of metaborate triangles [19].

Fig. 6. (left) Raman spectra of glassy lithium metaborate (thick solid line) as well as  $\alpha$ - (thin solid line),  $\beta$ - (dotted) and  $\gamma$ - $\text{LiBO}_2$  (dashed) polymorphs [35].

## 5. POLYMORPHISM AND GLASS FORMATION: LONGER RANGE STRUCTURE

Since Krogh-Moe [33] and Konijnendijk [34] conducted their studies, the comparative analysis of the vibrational spectra of glasses and compounds of crystallographically known structure has become a very useful method in assessing the structure of the former. A practical problem arises concerning the criterion in selecting those crystalline compounds that are of relevance to the composition of the glass under investigation. The available data basis of borate crystals favors high temperature congruent phases. Yet, forming a glass by melt cooling, involves the activation of temperature dependent chemical equilibria and their freezing close to the glass transition temperature.

It has been demonstrated that our knowledge of low temperature or incongruent phases can be enlarged by subjecting the glass to systematic low-temperature devitrification treatments [22,35]. In those cases where low temperature nucleation and crystallization occurs homogeneously, a relevance between the structure of the glass and those of the crystalline polymorphs is implied, and confirmed by spectral comparisons. Figure 6 provides an example of this comparison depicting the Raman spectrum of lithium metaborate glass together with the spectra of the three corresponding crystalline polymorphs. More interestingly, apart from the well known high temperature chain polymorph ( $\alpha$ -LiBO<sub>2</sub>), two tetrahedra-containing low-temperature polymorphs ( $\beta'$ -, and  $\gamma$ -LiBO<sub>2</sub>), previously considered as high pressure phases, have been isolated by sub- $T_g$  devitrification. Spectral comparison demonstrates that the glass exhibits structural similarities with its devitrification products, which extend beyond local and intermediate ranges [35].

It is tempting to interpret such data as suggesting that the structure of borate glasses can be inhomogeneous, in the sense that, relatively denser (tetrahedra containing low-temperature-like) domains seem to coexist with less dense (structurally metastable but kinetically arrested) liquid-like regions [35]. The sudden formation of the former upon quenching would cause a positive deviation of viscosity from Arrhenian behavior [36], and would therefore signal "fragility" in Angell's classification of glassforming liquids [37].

## 6. M-O INTERACTIONS IN BORATE GLASSES: GLASS MODIFIERS OR CONDITIONAL FORMERS?

B-O bonding yields only one part of the structural landscape of borate systems, the other being the M-O interactions. In fact, M and B coexist in the structure and compete for the negative charge of the oxide ions in a manner that depends on their relative concentration (i.e. on the composition of the system), and on the nature of  $M^{n+}$ . Obviously, M-O bonding as a structure determining factor becomes more important as the  $M_{2n}O$  fraction in the binary system increases. But is this only due to the fact that the  $M^{n+}$  cations outnumber the  $B^{3+}$  centers, or is there a manifestation for a qualitative change of M-O bonding with increasing  $M_{2n}O$  content?

The infrared spectra of  $x\text{Li}_2\text{O} \cdot (1-x)\text{B}_2\text{O}_3$  glasses shown in Fig. 1 can provide an answer to this question [14]. The absorption envelope of the spectra, dominating the far-infrared range below  $550\text{ cm}^{-1}$ , has been shown to involve "rattling" vibrations of the  $\text{Li}^+$  ion in the sites provided by the network. Such vibrations are observed in all modified glasses, with characteristic frequencies, widths and intensities depending on the mass of the cation  $\text{M}^{n+}$ , the nature of the glass former, and the composition [38]. While the details of the far-infrared spectroscopic study of glasses are beyond the scope of this report, we note in Fig. 1 that increasing  $x$  causes, apart from the expected increase of the band intensity, a systematic upward frequency shift of the Li-O vibrational mode. This latter trend is a direct manifestation of the enhancement of Li-O bond strength in glass [14], and therefore of increased Li-O covalency [39]. Indeed, the term "ionic modifier" describing the structural role of  $\text{Li}_2\text{O}$  in borate glasses ought to be used with caution for compositions of very high  $x$ .

Extending this thought to other  $\text{M}^{n+}$  cations, we show in Fig. 7 the  $x$  dependence of  $T_g$  in alkali and alkaline earth borates with  $x < 0.50$  [40]. The bell shaped trend in all systems is associated with the non monotonic variation of the number of B-O bonds [16], due to the formation and the disappearance of  $\text{BO}_4^-$  species. Among alkali borates with  $x < 0.50$ , the Li-system has the highest  $T_g$  because it has the highest  $N_4$ . The glassy network of alkali borates is set mainly by freezing the boron-oxygen bonding;  $\text{M}_2\text{O}$  is therefore a modifier. In alkaline earth borates, increasing cationic field strength induces the increase of  $T_g$ , despite the decrease of  $N_4$  [40,41]. Due to the high cross-linking efficiency of the  $\text{M}^{2+}$  ions, it is M-O bonding that freezes the glass structure before the formation of  $\text{BO}_4^-$  units, the low temperature choice of the B-O system, can be sufficiently activated. The oxides of the lighter alkaline earths act more as conditional glass formers [40,41].

A closer look at the far-infrared spectra reveals that they are asymmetric in a way that suggests a bimodal gaussian distribution of oscillators (Fig. 8) [16]. This is a general property of ionically modified glasses, although the relative intensity of the two components is cation- and, to some extent, composition-dependent. This bimodal nature of the far-infrared envelope has been associated with the existence of two distributions of cation-hosting environments in glass [41,42]. The high frequency component, is attributed to cation-site interactions bearing a higher degree of covalency, similar to those encountered in the relevant crystals. Cations that upon quenching do not succeed in achieving such environments assume more ionic (i.e. less basic) sites in the network [39]. Obviously, this interpretation is compatible with the concept of a microheterogeneous glass structure [35,43].

## 7. ON THE STRUCTURAL ASPECTS OF THE MIXED ALKALI EFFECT

The simultaneous presence of two modifying oxides induces a non-linear variation of dynamic glass properties on composition, which is known as the mixed mobile ion or mixed alkali effect (MAE) [44]. Most of the earlier theo-

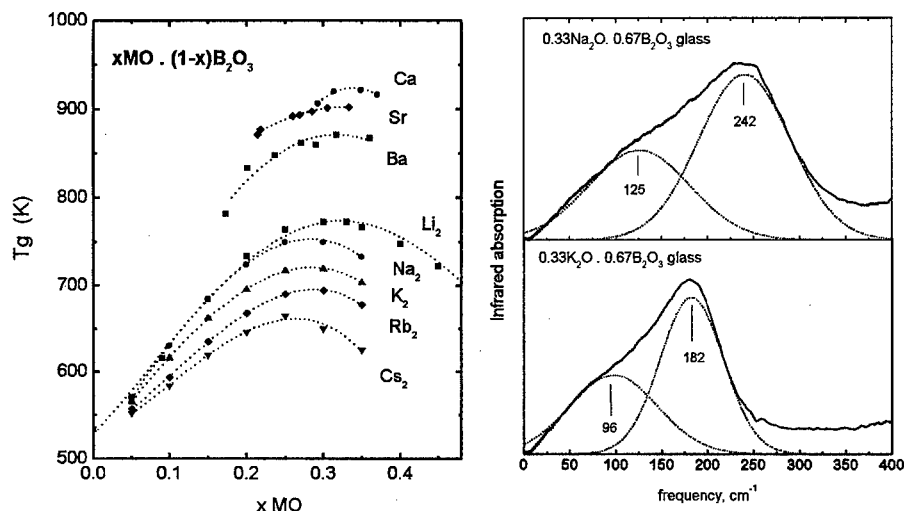


Fig. 7. (right) Glass transition temperatures of alkali and alkaline earth borate glasses [40].

Fig. 8. (left) Far-infrared spectra of Na-, and K-diborate glasses. Dotted lines show their deconvolution into Gaussian components [16,38].

ries accounting for the MAE were not concerned with the possibility of non-linear variations of the network structure upon alkali mixing.

It is quite evident from the vibrational [22,45-47] (as well as from the  $^{11}\text{B}$  NMR [17]) spectra of mixed alkali borates below the metaborate composition, that alkali mixing causes the partial destruction of  $\text{BO}_4^-$  groups and favors the formation of their triangular  $\text{BO}_2\text{O}^-$  isomers (see Fig. 9). Also, in the presence of two alkalis, the crystallization and devitrification chemistry of borates is affected in a non-linear way [19,22]. Thus, alkali mixing affects the local and intermediate range network order in glass, and, presumably alters its (longer range) morphology. Altogether, these findings imply that alkali mixing induces a chemical smoothening of vitrification [22], termed "strengthening" in Angell's classification of liquids [37].

At the same time, alkali mixing results in the non-additivity of the M-O interactions in glass [45-48]. Figure 10 compares the far-infrared spectra of typical mixed alkali glasses [48] with the linear combination of the corresponding end-member spectra. Such comparisons demonstrate that the high field strength cations in a mixed-alkali glass occupy more covalent sites than those occupied by the same cation in the single alkali glass. The opposite is observed for the low field strength cation [45,48]. The following structural picture emerges: In single alkali glasses, one kind of cation needs to compensate the structure by compromising its own bonding requirements with the constraints imposed by the network. It does that by occupying two distinct distributions of sites [41,42]. In mixed alkali glasses, the cation with the highest field strength can be more selective and assume mostly the high basicity sites, because the lower basicity sites can now be compensated by its weaker field strength counterpart.

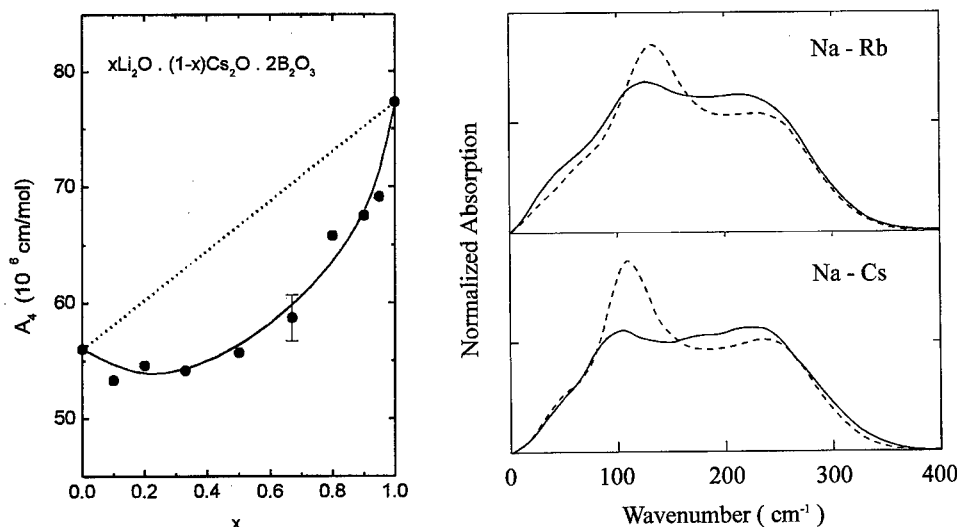


Fig. 9. (left) Integrated intensity of the infrared envelope due to  $\text{BO}_4^-$  units in Li-Cs diborate glasses as a function of alkali mixing. Solid line is for guiding the eye, and the dotted line between end-members indicates additivity [45-47].

Fig. 10. (right) Far infrared spectra of Na-Rb and Na-Cs diborate glasses (solid line) compared to the weighted averages of their corresponding end-member spectra [45,48].

## 8. PERSPECTIVES

There is one conclusion that should be evident from the above discussion. The chemical richness of borates can provide the keys to decode, on a structural basis, the complex and widespread phenomenon of vitrification. Everytime we study the structure of one particular glass composition, we ought to aim at unfolding the memory of those high-temperature processes that lead to its formation. The better we understand the potential energy hypersurface of a glass forming system, the easier we will discover how this system "flows" in it upon cooling. We need to map isomerizations, disproportionations and polymorphic transitions. Thus, we need to know more about crystalline borates. It is challenging to realize that most of the lithium borate compounds of a 1958 phase diagram [49] remain structurally unidentified. We also need to acquire more and direct evidence of the structure of borate melts, and on how this structure is affected by additives. We should understand the specific in order to be able to tackle the general. Once we adopt this perspective, new experimental techniques and theoretical approaches will develop. Among them, vibrational spectroscopy will keep playing an important role.

## Acknowledgments

Data included in this report are due to the careful experimental work of M. A. Karakassides, A. P. Patsis, J. A. Kapoutsis, M. S. Bitsis and Y. D. Yannopoulos (NHRF). Several of the ideas presented have benefited from discussions with J.

A. Duffy, M. D. Ingram, J. M. Hutchinson (Aberdeen), S. A. Feller (Coe), and H. Jain (Lehigh). We thank them all. Funding was provided by NHRF and occasionally through European and international programmes.

## REFERENCES

- [1] C. A. Coulson & T. W. Dingle, *Acta. Cryst.* **B24** (1968), 153.
- [2] J. Krogh-Moe, M. Ihara, *Acta Cryst.* **23** (1967), 27.
- [3] A. Kirfel, G. Will & R. F. Stewart, *Acta Cryst.* **B39** (1983), 175.
- [4] M. Marezio & J. P. Remeika, *J. Chem. Phys.* **44** (1966), 3348.
- [5] H. Koenig, R. Hoppe & M. Jansen, *Z. anorg. allg. chem.* **449** (1979), 91.
- [6] F. Stewner, *Acta Cryst.* **B27** (1971), 904.
- [7] A. M. Heyns, K. J. Range & M. Wildenauer, *Spectrochim. Acta* **46A** (1990), 1621.
- [8] P. Mondal & J. W. Jeffery, *Acta Cryst.* **B31** (1975), 689.
- [9] G. D. Chryssikos, E. I. Kamitsos, A. P. Patsis & M. A. Karakassides, *Mater. Sci. Eng.* **B7** (1990), 1.
- [10] C. T. Prewitt & R. D. Shannon, *Acta Cryst.* **B24** (1968), 869; A. Perloff & S. Block, *Ibid* **20** (1966), 274; D. L. Corker & A. M. Glazer, *Ibid* **B52** (1996), 260.
- [11] E. I. Kamitsos & G. D. Chryssikos, *J. Molec. Struct.* **247** (1990), 1.
- [12] E. I. Kamitsos, M. A. Karakassides & G. D. Chryssikos, *Phys. Chem. Glasses* **28** (1987), 203.
- [13] G. D. Chryssikos, E. I. Kamitsos & M. A. Karakassides, *Phys. Chem. Glasses* **31** (1990), 109.
- [14] E. I. Kamitsos, A. P. Patsis, M. A. Karakassides & G. D. Chryssikos, *J. Non-Cryst. Solids* **126** (1990), 52.
- [15] G. E. Jellison, Jr., S. A. Feller & P. J. Bray, *Phys. Chem. Glasses* **19** (1978), 52.
- [16] E. I. Kamitsos, A. P. Patsis & G. D. Chryssikos, *J. Non-Cryst. Solids* **152** (1993), 246.
- [17] J. Zhong & P. J. Bray, *J. Non-Cryst. Solids* **111** (1989), 67.
- [18] G. D. Chryssikos, *J. Raman Spectr.* **22** (1991), 645.
- [19] G. D. Chryssikos, J. A. Kapoutsis, A. P. Patsis & E. I. Kamitsos, *Spectrochim. Acta* **47A** (1991), 1117.
- [20] G. D. Chryssikos, J. A. Kapoutsis, M. S. Bitsis, E. I. Kamitsos, A. P. Patsis & A. J. Pappin, *Bol. Soc. Esp. Ceram. Vid.* **31-C2** (1992), 27.
- [21] P. J. Bray, J. F. Emerson, Donghoon Lee, S. A. Feller, D. L. Bain & D. A. Feil, *J. Non-Cryst. Solids* **129** (1990), 283.
- [22] G. D. Chryssikos, J. A. Kapoutsis, E. I. Kamitsos, A. P. Patsis & A. J. Pappin, *J. Non-Cryst. Solids* **167** (1994), 92.
- [23] J. Krogh-Moe, *Acta Cryst.* **B30** (1974), 1178.
- [24] S. Block & A. Perloff, *Acta Cryst.* **19** (1965), 297.
- [25] J. Krogh-Moe, *Acta Cryst.* **B30** (1974), 578.
- [26] N. L. Ross & R. J. Angell, *J. Solid State Chem.* **90** (1991), 27.
- [27] R. W. Smith & D. A. Keszler, *Mater. Res. Bull.* **24** (1989), 725.
- [28] J. Fayos, R. A. Howie & F. P. Glasser, *Acta Cryst.* **C41** (1985), 1396.
- [29] W. Schneider & G. B. Carpenter, *Acta Cryst.* **B26** (1990), 1189.
- [30] S. F. Radaev, L. A. Muradyan, L. F. Malakhova, Y. V. Burak & V. I. Simonov, *Sov. Phys. Crystallogr.* **34** (1989), 842.
- [31] P. D. Thomson, J. Huang, R. W. Smith & D. A. Keszler, *J. Solid State Chem.* **95** (1991), 126.
- [32] C. F. Windisch, Jr. & W. M. Risen, Jr., *J. Non-Cryst. Solids* **48** (1982), 307.
- [33] J. Krogh-Moe, *Phys. Chem Glasses* **3** (1962), 101.
- [34] W. L. Konijnendijk, *Philips Res. Rep. Suppl.* **1**, (1975), 1.
- [35] G. D. Chryssikos, E. I. Kamitsos, A. P. Patsis, M. S. Bitsis & M. A. Karakassides, *J. Non-Cryst. Solids* **126** (1990), 42.
- [36] G. D. Chryssikos, J. A. Duffy, J. M. Hutchinson, M. D. Ingram, E. I. Kamitsos & A. J. Pappin, *J. Non-Cryst. Solids* **172-174** (1994), 378.



- 
- [37] C. A. Angell, *J. Non-Cryst. Solids* **131-133** (1991), 13, and refs therein.
- [38] E. I. Kamitsos, *J. Phys. Chem.* **93** (1989), 1604.
- [39] J. A. Duffy, G. D. Chryssikos & E. I. Kamitsos, *Phys. Chem. Glasses* **36** (1995), 53.
- [40] G. D. Chryssikos, E. I. Kamitsos & Y. D. Yiannopoulos, *J. Non-Cryst. Solids* **196** (1996), 244.
- [41] Y. D. Yiannopoulos, E. I. Kamitsos, G. D. Chryssikos & J. A. Kapoutsis, *Proc. Second Int. Conf. on Borates Glasses, Crystals and Melts*, 514.
- [42] E. I. Kamitsos, M. A. Karakassides & G. D. Chryssikos, *Solid State Ionics* **28-30**, (1988) 687.
- [43] E. I. Kamitsos, G. D. Chryssikos, A. P. Patsis & M. A. Karakassides, *J. Non-Cryst. Solids* **131-133** (1991), 1092.
- [44] M. D. Ingram, *Phys. Chem. Glasses* **28** (1987), 215.
- [45] E. I. Kamitsos, A. P. Patsis & G. D. Chryssikos, in *The Physics of Non-Crystalline Solids*, (L. D. Pye, W. C. LaCourse, H. J. Stevens, Eds), Taylor & Francis, London (1992), p. 460.
- [46] E. I. Kamitsos, A. P. Patsis, G. D. Chryssikos & J. A. Kapoutsis, *Bol. Soc. esp. Ceram. Vid.* **31-C3** (1992), 287.
- [47] E. I. Kamitsos, *J. Physique IV (Colloque)* **C4** (1992), 87.
- [48] E. I. Kamitsos, A. P. Patsis & G. D. Chryssikos, *Phys. Chem. Glasses* **32** (1991), 219.
- [49] B. S. R. Sastry & F. A. Hummel, *J. Am. Ceram. Soc.* **41** (1958), 7, and **42** (1959), 216.

## INELASTIC NEUTRON SCATTERING TECHNIQUES FOR STUDYING SUPERSTRUCTURAL UNITS IN BORATE GLASSES

Roger N. SINCLAIR, Adrian C. WRIGHT,  
Andrew J. WANLESS  
*J.J. Thomson Physical Laboratory, Reading University,  
Whiteknights, Reading, RG6 6AF, UK*

Alex C. HANNON  
*ISIS Facility, Rutherford Appleton Laboratory, Chilton,  
OX11 0QX, UK*

Steven A. FELLER, Mark.T. MAYHEW, Benjamin M.  
MEYER, Michael L. ROYLE, Douglas L. WILKERSON,  
Richard B. WILLIAMS & Bruce C. JOHANSON  
*Department of Physics, Coe College, Cedar Rapids, IA  
52402-5092, USA*

There is now increasing evidence that the structures of many borate glasses are dominated by superstructural units. Spectroscopic data are invaluable for testing models of glass structure and the inelastic neutron scattering technique is now able to supplement information gained from optical measurements, due to improvements in instrumentation and source strength which have led to an energy transfer resolution comparable to that available optically. The use of inelastic neutron scattering techniques for investigating the role of superstructural units in borate glass structures is discussed, using vitreous  $B_2O_3$  and a binary glass in the  $Rb_2O-B_2O_3$  system as examples. The inelastic scattering results for vitreous  $B_2O_3$  strongly support a model for the structure in which the majority of the boron atoms are in boroxol groups. The neutron weighted vibrational density of states has a significant feature at the energy of the boroxol ring breathing mode, the natural width of which is very small due to the localised nature of the breathing mode of these highly planar rings. The inelastic neutron scattering data for a  $0.6Rb_2O.B_2O_3$  glass show no evidence for boroxol groups and are entirely consistent with Raman data, but clearly demonstrate the important role of matrix element effects in determining the relative intensities of the modes in the Raman spectrum.

### 1. INTRODUCTION

Binary borate glasses up to the metaborate composition have been studied by a variety of techniques due to the relative ease of glass formation and knowledge of the corresponding crystalline phases. A particular point of interest is the fact that the addition of network modifiers to vitreous  $B_2O_3$  initially leads

mainly to an increase in the co-ordination number of the boron atoms from 3 to 4 rather than to the formation of non-bridging oxygen atoms; i.e. the conversion of the  $\text{BO}_3$  triangular structural units into  $\text{BO}_4$  tetrahedra [1].

The classic structural work on borate glasses dates back to Zachariasen [2] and Warren *et al.* [3,4]. However, controversy immediately arose with the paper of Hägg [5] which challenged Zachariasen's hypothesis and postulated the existence in glasses of groupings larger than the basic structural units. More recently support for Hägg's ideas has come first from the work of Krogh-Moe [6] and then that of Bray and co-workers [7,8], who both confirm the existence of larger structural groupings, such as those in Fig. 1, which comprise well defined arrangements of the basic  $\text{BO}_3$  and  $\text{BO}_4$  structural units with no inter-

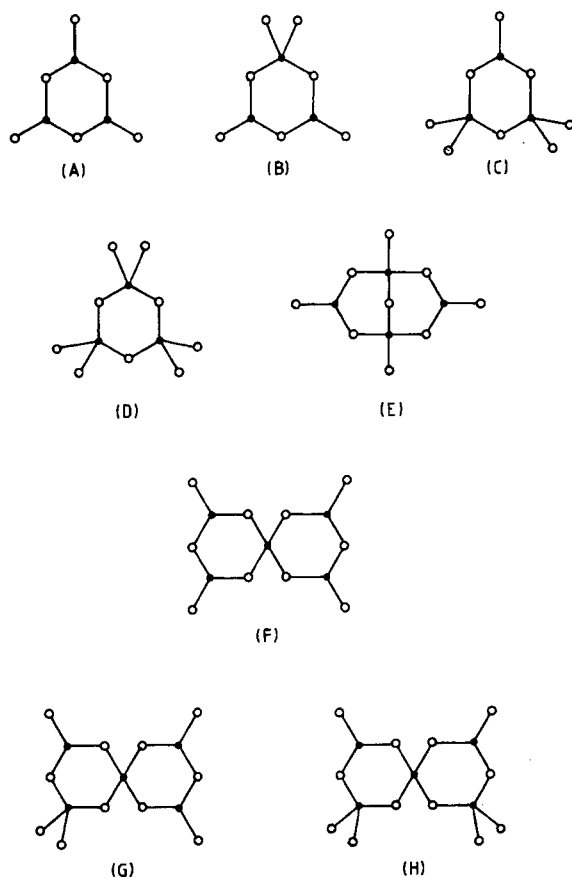


**Fig. 1.** Superstructural units occurring in anhydrous binary crystalline borates. (A) boroxol group,  $\text{B}_3\text{O}_6$ ; (B) triborate group,  $\text{B}_3\text{O}_7$ ; (C) di-triborate group,  $\text{B}_3\text{O}_8$ ; (D) metaborate group,  $\text{B}_3\text{O}_9$ ; (E) diborate group,  $\text{B}_4\text{O}_9$ ; (F) pentaborate group,  $\text{B}_5\text{O}_{10}$ ; (G) di-pentaborate group,  $\text{B}_5\text{O}_{11}$ ; and (H) tri-pentaborate group,  $\text{B}_5\text{O}_{12}$ . Note that the di-triborate group corresponds to the composition  $2\text{M}.\text{3B}$ , etc.

nal degrees of freedom in the form of variable bond or torsion angles. The existence of large numbers of these "superstructural units" in certain borate glasses is still a matter of considerable controversy, even in the case of pure vitreous  $B_2O_3$ .

As the composition is varied, Raman spectroscopy studies [9] of alkali borate glasses indicate the presence of various 3-membered rings, both boroxol and those containing a combination of  $BO_3$  triangles and  $BO_4$  tetrahedra (e.g. triborate,  $B_3O_7$ , and di-triborate,  $B_3O_8$ ), which give rise to sharp lines at  $808\text{ cm}^{-1}$  (100 meV) and  $\sim 760\text{--}770\text{ cm}^{-1}$  ( $\sim 95$  meV) respectively, together with other larger superstructural units such as diborate and pentaborate groups. The latter involve two 3-membered rings and lead to broad peaks in the Raman spectrum in addition to that at  $\sim 95$  meV. As demonstrated by previous inelastic neutron scattering measurements on vitreous  $B_2O_3$  [10], the problem with the Raman technique is that unknown matrix element effects make it extremely difficult to determine the absolute numbers of each unit for a given glass.

In the present paper, the application of the inelastic neutron scattering technique to the investigation of the role of superstructural units in the structure of borate glasses is discussed, using vitreous  $B_2O_3$  and a binary  $Rb_2O\text{--}B_2O_3$  glass as examples. This particular binary system is of interest in that glasses can be formed over a wide range of composition such that, at the lowest  $B_2O_3$  contents, a continuous borate network is not possible [11].

## 2. THE INELASTIC NEUTRON SCATTERING TECHNIQUE

Spectroscopic information is invaluable for testing models of the structure of amorphous materials. The energies of the relevant excitations vary from a fraction of a meV up to several hundred meV and so it is clear that a variety of spectroscopic methods is needed to characterise and assign the atomic motions. The inelastic neutron scattering technique [12] has recently become able to supplement information gained from optical measurements, due to improvements in instrumentation and source strength which have lead to an energy transfer resolution comparable to that available optically. A wide range of instrumentation is now able to measure the dynamical structure factor,  $S(Q, E)$ , with the optimum resolution in scattering vector and energy transfer for a variety of problems. The main area of application for the borate glasses to be considered here is the investigation of an effective vibrational density of states (VDOS) so as to confirm the important local atomic configurations in the short range order.

In an inelastic neutron scattering experiment, the measured quantity is the double differential cross-section [13]

$$\frac{d^2\sigma}{d\Omega dE} = \frac{k'}{k_0} \frac{\sigma}{4\pi} S(Q, E) = \frac{k'}{k_0} \frac{\sigma}{4\pi} (S^S(Q, E) + S^D(Q, E)) \quad (1)$$

in which  $\sigma = \langle 4\pi b^2 \rangle$  is the average total scattering cross-section per atom,  $k_0$

and  $k'$  are the magnitudes of the initial and final neutron wavevectors,  $Q$  is the magnitude of the scattering vector,  $Q=k_0-k'$ , and  $E$  is the energy transfer ( $E=E_0-E'$ , where  $E_0$  and  $E'$  are the initial and final neutron energies).  $S(Q,E)$ ,  $S^D(Q,E)$  and  $S^S(Q,E)$  are the total, distinct and self scattering functions respectively. For a multicomponent sample these are themselves weighted sums of partial scattering functions. The relationship between the one phonon creation self scattering function and the VDOS is of the form [13]

$$S^{S+1}(Q, E) = \frac{1}{\langle b^2 \rangle} \langle n+1 \rangle \frac{g(E)}{2E} \sum_l 3\hbar b_l^2 \left( \frac{|\mathbf{Q} \cdot \mathbf{e}_l|^2}{M_l} \right) \exp\left( \frac{-Q^2 \langle u_l^2 \rangle}{3} \right) \quad (2)$$

where the  $l$  summation is over the elements in the sample,  $n = \{\exp(E/kT) - 1\}^{-1}$  is a thermal population factor,  $g(E)$  is the VDOS (defined here to integrate to a total area of unity),  $\langle u_l^2 \rangle^{1/2}$  is the isotropic root mean square (RMS) displacement from equilibrium for the atoms of element  $l$  and  $M_l$  is the atomic mass for element  $l$ . The factor  $|\mathbf{Q} \cdot \mathbf{e}_l|^2$  represents the average of  $|\mathbf{Q} \cdot \mathbf{e}_j^s|^2$  over atoms of element  $l$  and modes of energy  $E$  where  $\mathbf{e}_j^s$  is the vibrational displacement vector of atom  $j$  for the normal mode  $s$ .

### 3. EXPERIMENTAL DETAILS

#### 3.1. Sample Preparation

The boron in the samples used for the experiments discussed here was enriched to greater than 99.57%  $^{11}\text{B}$  to minimise the absorption of neutrons by  $^{10}\text{B}$ . The vitreous  $\text{B}_2\text{O}_3$  inelastic neutron scattering sample was cast as a plate and subsequently crushed to a coarse powder form and placed in an aluminium sample can while in a dry box. Since alkali borate glasses are extremely water-sensitive, especially at high alkali contents, the rubidium borate sample was prepared and the resulting crushed glass sealed into the sample can in a dry box. It was prepared from rubidium oxide and boric acid, enriched in  $^{11}\text{B}$ . Rubidium oxide was used instead of the more conventional rubidium carbonate, since this avoids carbon dioxide retention by the melt and allows the formation of high alkali content glasses. The melt was heated for a period of 15 to 20 minutes at 900°C. The glass composition was confirmed to be very close to the nominal value ( $0.6\text{Rb}_2\text{O} \cdot \text{B}_2\text{O}_3$ ) of 37.5mol%  $\text{Rb}_2\text{O}$  by determining the weight loss. For both the inelastic scattering measurements, the sample was in the form of a hollow cylinder to increase the amount of material in the beam while maintaining multiple scattering at a reasonably low level.

#### 3.2. Inelastic Neutron Scattering

Inelastic neutron scattering experiments have been performed using the MARI spectrometer at ISIS. For the experiment on vitreous  $\text{B}_2\text{O}_3$ , the sample was maintained at a temperature of 24 K to minimise multiphonon scattering. For a given mode to be observed by neutron energy loss, the incident neutron

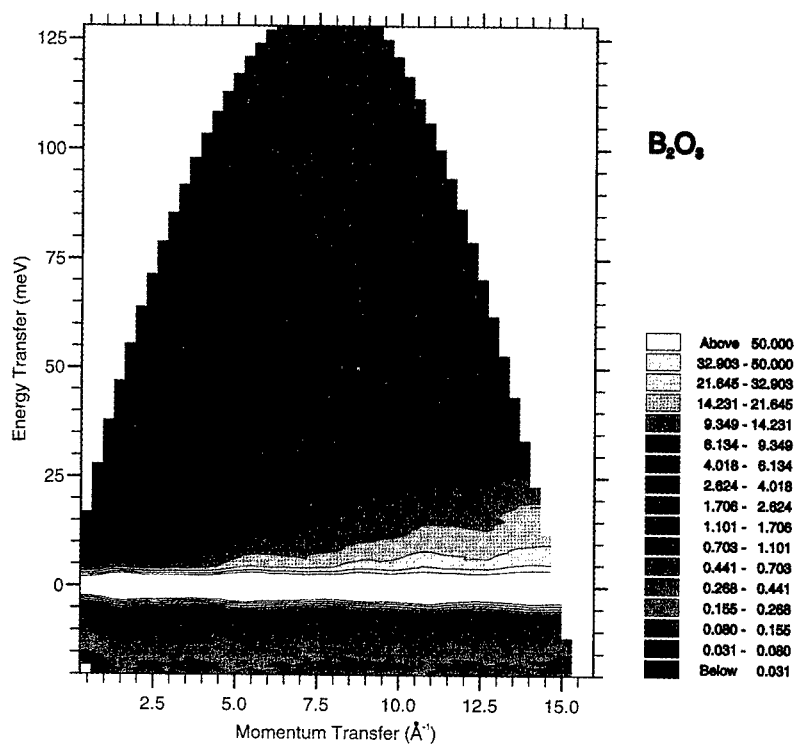


Fig. 2. A contour diagram of the neutron scattering law,  $S(Q,E)$ , for vitreous  $B_2O_3$  at 24K energy,  $E_0$ , must be greater than the energy of the mode. A value for  $E_0$  of 135 meV was chosen, close to the energy of the boroxol ring breathing mode to maximise the resolution at this energy transfer. For this  $E_0$ , the elastic scattering, recorded by the detectors used here, covers a range in momentum transfer from  $0.4$  to  $14.7 \text{ \AA}^{-1}$ . The energy resolution function with an incident energy of 135 meV was calculated using parameter values which correctly predict the elastic resolution (3.8 meV FWHM). The calculated energy resolution (FWHM) at the energy transfer for the boroxol ring breathing mode is 1.6 meV.

The data for vitreous  $B_2O_3$  were reduced to yield  $S(Q,E)$  at constant scattering angles (Fig. 2), detector internormalisation factors being calculated from the fitted elastic peak area for a run at the same incident energy on a vanadium tube. The result obtained from averaging the data [13,14] over the range  $2.5 < Q < 12.5 \text{ \AA}^{-1}$  is shown in Fig. 3. A multiphonon correction was not performed, but, since the multiphonon scattering scales as  $Q^{2n}$  ( $n=2,3,4,\dots$ ) [13], this should not significantly modify the data.

For the measurements on the  $Rb_2O-B_2O_3$  glass at 14 K, the incident energy (135 meV) was similarly optimised for the 90-105 meV energy transfer region. The data analysis followed similar lines to that for vitreous  $B_2O_3$  and the averaged scattering law,  $S(Q,E)$ , over the range  $5.0 < Q < 12.0 \text{ \AA}^{-1}$ , is shown in Fig. 3.

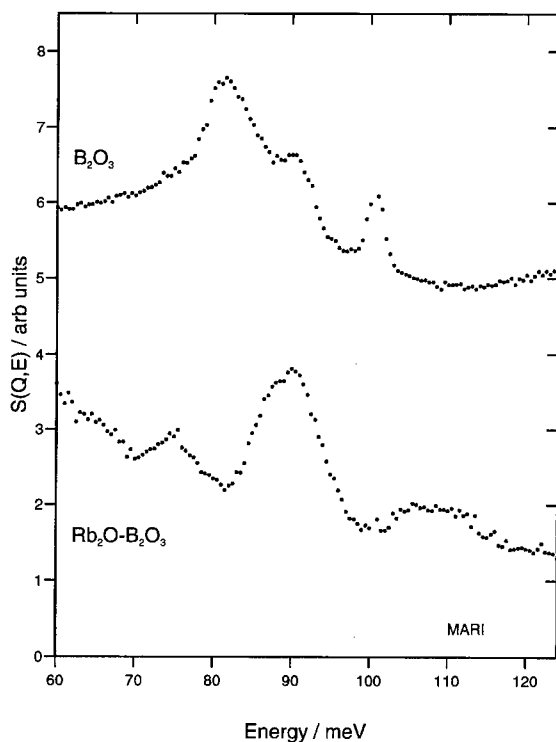


Fig. 3. The neutron scattering law,  $S(Q, E)$ , for vitreous  $B_2O_3$  and a  $Rb_2O-B_2O_3$  glass of nominal composition 37.5 mol%  $Rb_2O$ .

#### 4. VITREOUS BORON OXIDE

The presence of boroxol groups {Fig 1(A)}, in vitreous  $B_2O_3$  was first suggested by Goubeau & Keller [15] and further evidence is summarised by Krogh-Moe [16] and Johnson *et al.* [17]. However, the role played by boroxol groups in the structure of vitreous  $B_2O_3$  is still the subject of considerable controversy in the literature and, in particular, the fraction,  $f$ , of the boron atoms involved in boroxol groups [14]. It has been suggested [18] that the value of  $f$  is very much smaller than indicated by NMR [19] and the value  $f=0.80\pm0.05$  from neutron diffraction data [20].

The data for vitreous  $B_2O_3$  in the region of the boroxol ring breathing mode (Fig. 3) exhibit a relatively broad band of modes at approximately 82 meV with two narrower peaks at approximately 90 and 100 meV. These features correspond to peaks 4, 5 and 6 in the numbering scheme used by Galeener & Thorpe [21] for the Raman spectrum. The modes in this region of the VDOS arise from the symmetric stretch and out-of-plane deformation of the  $BO_3$  triangle. Clearly the 100 meV peak can be identified as being due to the breathing mode of the boroxol ring. The mode is seen here much more clearly than in the previous inelastic neutron scattering measurement [10], due to the improved

energy resolution. The statement in the literature that the neutron data show no significant feature at  $808\text{ cm}^{-1}$  [22] is clearly contradicted by the present result. A fit to the data in the region of the boroxol ring breathing mode, by a linear background plus a Gaussian function, yields a peak position of  $100.68\text{ meV}$  and a FWHM of  $2.37 \pm 0.01\text{ meV}$ .

The fitted width of the Gaussian function for the inelastic neutron scattering data is only slightly greater than the calculated energy resolution. If the widths add in quadrature then the natural width of the boroxol ring breathing mode may be estimated to be  $\sim 1.75\text{ meV}$  ( $\sim 14\text{ cm}^{-1}$ ), in agreement with the published Raman value [23]. From the narrowness of this width, it may be concluded that the lifetime of the mode is long, arising from its high spatial localisation (i.e. it is localised on a single boroxol ring [24]) which is due to the high degree of planarity of the boroxol group. In contrast to the reputation of amorphous solids for yielding experimental results which are "broad and ill-defined", the boroxol ring breathing mode is actually an extremely sharp feature.

## 5. A BINARY BORATE GLASS : $\text{Rb}_2\text{O}-\text{B}_2\text{O}_3$

In the inelastic neutron scattering data for vitreous  $0.6\text{Rb}_2\text{O} \cdot \text{B}_2\text{O}_3$  (Fig. 3, lower curve), there is no indication of the boroxol ring breathing mode at  $100\text{ meV}$ , in accord with the Raman data of Kamitsos *et al.* [25]. Three broad bands are observed, centred at  $\sim 75\text{ meV}$  ( $605\text{ cm}^{-1}$ ),  $\sim 90\text{ meV}$  ( $726\text{ cm}^{-1}$ ) and  $\sim 108\text{ meV}$  ( $871\text{ cm}^{-1}$ ), the second of which appears to comprise at least two components. The total extent of each of these bands is in good agreement with the Raman data, the composition of the present glass being between the values of 35 and 40 mol%  $\text{Rb}_2\text{O}$ , for which spectra are given in Fig. 6 of Ref. [25].

At 35 mol%  $\text{Rb}_2\text{O}$ , the Raman spectrum exhibits a broad band at  $610\text{ cm}^{-1}$  ( $75.6\text{ meV}$ ), while at 40 mol%  $\text{Rb}_2\text{O}$ , this has a sharp line superimposed on top of it, due to the presence of  $\text{B}_3\text{O}_6^{3-}$  cyclic metaborate ions [25]. As demonstrated by the relative intensity of the peak arising from the boroxol group breathing mode at  $100\text{ meV}$ , relative to that in the Raman spectrum for vitreous  $\text{B}_2\text{O}_3$ , the matrix element enhancement of this mode in the Raman spectrum is very large and hence a similar enhancement may be expected for the equivalent mode for the metaborate ring. For this reason, the small feature, which by interpolation would be expected at  $610\text{ cm}^{-1}$  in the Raman spectrum at 37.5 mol%  $\text{Rb}_2\text{O}$ , is not visible in the neutron data.

Although the total width of the broad peak at  $\sim 90\text{ meV}$  ( $726\text{ cm}^{-1}$ ) is very similar to that in the equivalent Raman spectrum, the detailed shape is not the same, due to different relative weightings of the constituent bands. In the case of the Raman spectrum, the band at  $\sim 756\text{ cm}^{-1}$  ( $93.7\text{ meV}$ ), due to the breathing mode of the di-triborate unit {Fig. 1(C)} or the same ring involved in larger pentaborate groups {Figs 1(G) and (H)} [9,25], is dominant. This is presumably due to matrix element enhancement effects, whereas in the neutron data the contribution from metaborate chains ( $\sim 91\text{ meV}$  or  $735\text{ cm}^{-1}$  [9,25]) is very much greater, thus shifting the position of the maximum to lower energy.



## 6. CONCLUSIONS

It may thus be concluded that the neutron inelastic scattering technique can provide considerable insight into the structures of borate glasses by assignment and characterisation of features in the effective density of vibrational states.

The neutron inelastic scattering results for vitreous  $B_2O_3$  strongly support a model for the structure in which the majority of boron atoms are in boroxol groups since the neutron weighted vibrational density of states has a significant feature at the energy of the boroxol ring breathing mode, the natural width of which is very small due to the very localised nature of the breathing mode of these highly planar rings.

The inelastic neutron scattering data for the  $Rb_2O-B_2O_3$  glass are entirely consistent with the Raman data of Kamitsos *et al.* [25], but clearly demonstrate the important role of matrix element effects in determining the relative intensities of the various modes in the Raman spectrum.

## REFERENCES

- [1] G.E. Jellison Jr., S.A. Feller & P.J. Bray, *Phys. Chem. Glasses* **19** (1978), 52.
- [2] W.H. Zachariasen, *J. Amer. Chem. Soc.* **54** (1932), 3841.
- [3] B.E. Warren, H. Krutter & O. Morningstar, *J. Amer. Ceram. Soc.* **19** (1936), 202.
- [4] J. Bischoe & B.E. Warren, *J. Amer. Ceram. Soc.* **21** (1938), 287.
- [5] G. Hägg, *J. Chem. Phys.* **3** (1935), 42.
- [6] J. Krogh-Moe, *Phys. Chem. Glasses* **6** (1965), 46.
- [7] G.E. Jellison Jr. & P.J. Bray, *J. Non-Cryst. Solids* **29** (1978), 187.
- [8] S.A. Feller, W.J. Dell & P.J. Bray, *J. Non-Cryst. Solids*, **51** (1982), 21.
- [9] B.N. Meera & J. Ramakrishna, *J. Non-Cryst. Solids* **159** (1993), 1.
- [10] A.C. Hannon, R. N. Sinclair, J. A. Blackman, A.C. Wright & F.L. Galeener, *J. Non-Cryst. Solids* **106** (1988), 116.
- [11] M. Royle, J. MacKenzie, J. Taylor, M. Sharma & S. Feller, *J. Non-Cryst. Solids* **177** (1999), 242.
- [12] R.N. Sinclair, *J. Non-Cryst. Solids* **76** (1985), 61.
- [13] D.L. Price & J.M. Carpenter, *J. Non-Cryst. Solids* **92** (1987), 153.
- [14] A.C. Hannon, D.I. Grimley, R.A. Hulme, A.C. Wright & R.N. Sinclair, *J. Non-Cryst. Solids* **177** (1994), 299.
- [15] J. Goubeau & H. Keller, *Z. Anorg. Allg. Chem.* **272** (1953), 303.
- [16] J. Krogh-Moe, *J. Non-Cryst. Solids* **1** (1969), 269.
- [17] P.A.V. Johnson, A.C. Wright & R.N. Sinclair, *J. Non-Cryst. Solids* **50** (1982), 281.
- [18] S.R. Elliott, *Nature* **354** (1991), 445.
- [19] G.E. Jellison Jr., L.W. Panek, P.J. Bray & G.B. Rouse Jr., *J. Chem. Phys.* **66** (1977), 802.
- [20] A.C. Wright, R.N. Sinclair, D.I. Grimley, R.A. Hulme, N.M. Vedishcheva, B.A. Shakmatin, A.C. Hannon, S.A. Feller, B.M. Meyer, M.L. Royle & D.L. Wilkerson, *Fiz. Khim. Stekla* **22** (1996), 364 [tr. *Glass Phys. Chem.* **22** (1996), 268].
- [21] F.L. Galeener & M.F. Thorpe, *Phys. Rev.* **B28** (1983), 5802.
- [22] S.R. Elliott, In: *Physics of Amorphous Materials*, 2<sup>nd</sup> edn, (Longman, London, 1990), p. 142.
- [23] M.A. Ramos, S. Viera & J.M. Colleja, *Solid State Commun.* **62** (1987), 455.
- [24] F.L. Galeener, R.A. Barrio, E. Martinez & R.J. Elliott, *Phys. Rev. Lett.* **53** (1984), 2429.
- [25] E.I. Kamitsos, M.A. Karakassides & G.D. Chrysikos, *Phys. Chem. Glasses* **30** (1989), 229.

# **n(=1,2,3)-DIMENSIONAL FOURIER TRANSFORM ELECTRON PARAMAGNETIC RESONANCE (FT-EPR) SPECTROSCOPY MEASUREMENTS IN THE B<sub>2</sub>O<sub>3</sub>-Li<sub>2</sub>O SYSTEM AND MO CALCULATIONS**

George KORDAS

*National Center for Scientific Research "Demokritos",  
Institute of Materials Science, 153 10 Ag. Paraskevi Attikis,  
Athens, Greece*

(100-x)B<sub>2</sub>O<sub>3</sub>.xLi<sub>2</sub>O (mol%) glasses with x=0-50 were prepared by conventional melting techniques and exposed to γ-ray irradiation. The CW-EPR (Continuous Wave Electron Paramagnetic) spectra were recorded at room temperature and show a strong dependence on x. The spectrum of the glass with x=0 was simulated to obtain the spectroscopic parameters. SCF HF (Self Consistent Field Hatree Fock) and MNDO (Molecular Neglect Differential Overlap) calculations were done for the interpretation of the spectra. The echo induced EPR spectrum of the B<sub>2</sub>O<sub>3</sub> glass is different from the CW-EPR spectrum showing better resolution. The echo induced EPR spectra of the Li<sub>2</sub>O.4B<sub>2</sub>O<sub>3</sub> glass recorded at 20 K depend on the distance between the two pulses, τ. The FID (Free Induction Decay) spectrum of the defects obtained in the Li<sub>2</sub>O.4B<sub>2</sub>O<sub>3</sub> glass was recorded using a two and three pulse sequence. The Fourier transformation exhibits frequencies of <sup>11</sup>B(4·782043 MHz), <sup>10</sup>B(1·60133 MHz), and <sup>7</sup>Li(5·791950 MHz). The ESEEM (Electron Spin Echo Envelope Modulation) spectra contain valuable information regarding the defect structure.

## **1. INTRODUCTION**

The CW EPR spectroscopy has widely been used to investigate the structure of borate glasses [1-11]. Basically, two centres were identified accounting for EPR signal of the borate glasses [8-11].

Recently, new developments in instrumentation and theory have made possible pulsed EPR spectroscopy, greatly enhancing the CW EPR resolution and sensitivity to atomic arrangements, bond angles, and a variety of time-dependent phenomena. The new more powerful techniques open up new opportunities for the precise determination of defect structures in glasses, where CW

**Table 1.**  
Spectroscopic parameters of defect centers detected in borate glasses.

Glass composition	g <sub>1</sub>	g <sub>2</sub>	g <sub>3</sub>	A <sub>1</sub> (G)	A <sub>2</sub> (G)	A <sub>3</sub> (G)
25 mol% Li <sub>2</sub> O	2·0020	2·0103	2·0350	12·1	14·2	10·0
25 mol% Li <sub>2</sub> O	2·0049	2·0092	2·0250	11·2	12·9	8·0

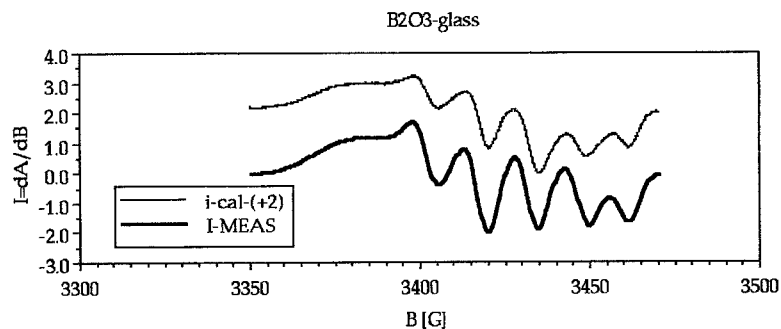


Fig. 1. Measured and calculated cw-EPR spectrum of  $B_2O_3$  glass.

Table 2.

Spectroscopic parameters of spectrum of the  $B_2O_3$  glass derived from simulation.

CW EPR	$g_1$	$g_2$	$g_3$	$A_1$ [MHz]	$A_2$ [MHz]	$A_3$ [MHz]	LW(G)
$B_2O_3$	2.0025	2.0118	2.0370	39.44	43.45	22.00	10.0

EPR suffers from limited energy or time resolution.

This paper presents ESEEM (Electron Spin Echo Envelope Modulation) experiments based on two- and three-pulse sequence and ECHO Field Sweep (fs) experiments based on a two-pulse sequence. The paper presents CW EPR spectra to contrast the new findings. SCF HF and MNDO calculations were carried out to obtain some indication about the Molecular Orbitals (MOs) of the defect structures.

## 2. EXPERIMENTAL

$(100-x) B_2O_3 \cdot x Li_2O$  (mol%) glasses with  $x=0-50$  have been prepared by the melting technique in a platinum crucible. The paramagnetic centres were induced using a  $^{60}Co$  gamma-ray source. The EPR spectra were recorded using a BRUKER ESP 300 E spectrometer with an ESP 380 FT-EPR apparatus. The ECHO fs sequence was  $\pi/2-\tau-\pi/2$ . The ESEEM spectra  $V(\tau, T)$  were recorded

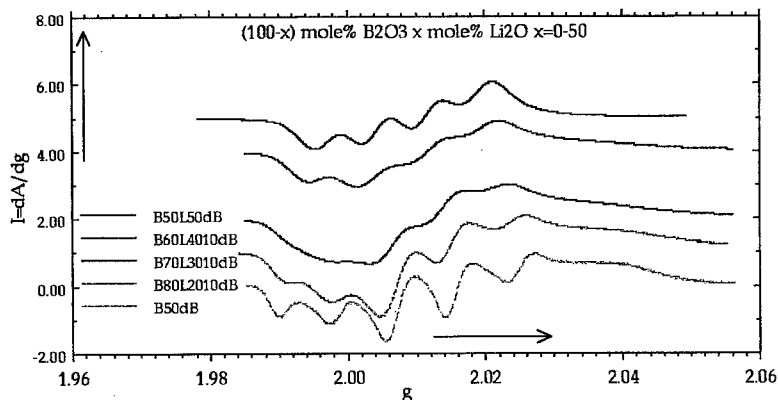


Fig. 2. CW-EPR spectra of the  $(100-x)$  mol%  $B_2O_3 \cdot x$  mol%  $Li_2O$  glasses with  $x=0-50$ .

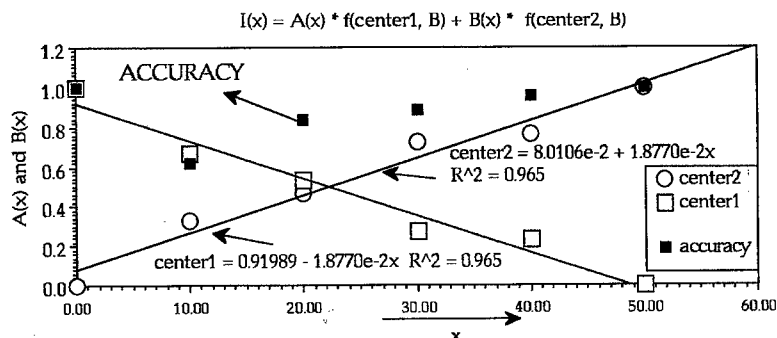


Fig. 3. Coefficients A(x) and B(x) of reproduction of the I(x) spectra using the I(x=0) and I(x=50) spectra

using two-pulse  $\pi/2-\tau-\pi/2$  and three-pulse sequences  $\pi/2-\tau-\pi/2-T-\pi/2$ .

MNDO (Molecular Neglect Differential Overlap, VAMP 4.4 Erlangen convex computer version) and Gaussian 92 (SCF HF, with STO6-311G data set) program were used to calculate the spin densities and structures of the boron-oxygen related units. The two programs are explained in other papers [12-14].

### 3. RESULTS

#### 3.1 CW-EPR Studies

Figure 1 shows the measured (bottom) and calculated (top) EPR spectrum of the  $B_2O_3$  glass. The line shape of this spectrum was independent of the microwave power. Table 2 gives the values of the simulation.

Figure 2 shows the EPR spectra of the (100-x) mol%  $B_2O_3$ , x mol%  $Li_2O$  glasses with x=0-50. We first assume that two centres contribute to the intermediate glass compositions ( $0 < x < 50$  mol%). The first center dominates for  $x < 25$  mol% and the second for  $x > 25$  mol%. Thus, the signals (I(x=0) and I(x=50) of the x=0 and x=50 glasses were taken to generate the intermediate compositions ( $I(x) = A(x) * I(x=0) + B(x) * I(x=50)$ ). Figure 3 shows the coefficients (A(x) and B(x)) resulting

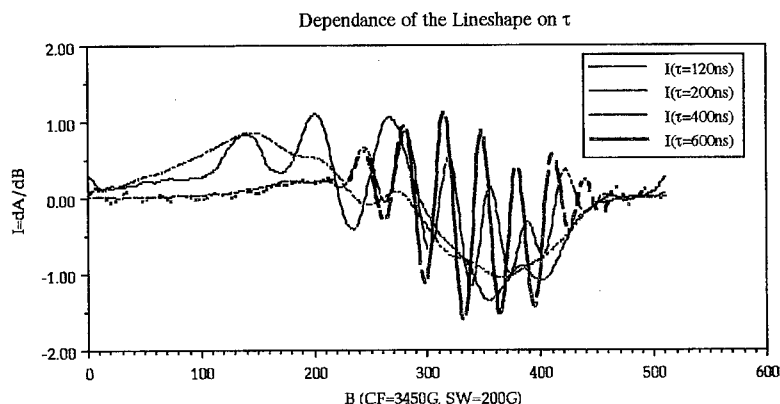


Fig. 4. Echo fs spectra of the  $Li_2O.4B_2O_3$  glass.

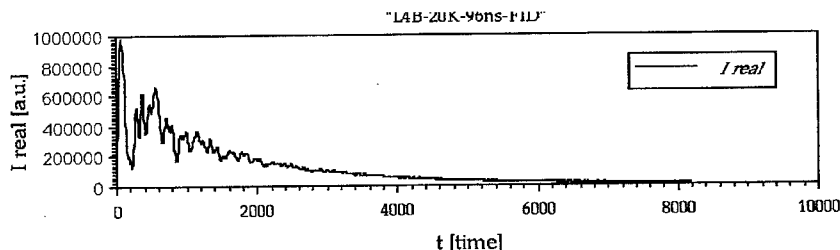


Fig. 5. Two pulse FID spectrum of the  $\text{Li}_2\text{O} \cdot 4\text{B}_2\text{O}_3$  glass.

from a least square fit with the basic spectra of the  $x=0$  (center 1) and  $x=50$  (center 2) glasses. The squares in this figure give the accuracy of the least squares fit.

### 3.2 Pulse EPR Studies

Figure 4 shows the pulse EPR spectrum of the  $\text{Li}_2\text{O} \cdot 4\text{B}_2\text{O}_3$  glass recorded with a sequence  $\pi/2-\tau-\pi/2$  for  $\tau = 120, 200, 400$ , and  $600$  ns. Figure 5 shows the FID (Free Induction Decay) of this glass exhibiting strong modulation. Figure 6 shows the Fourier transformation of this spectrum demonstrating the peaks of  $^{10}\text{B}$ ,  $^{11}\text{B}$ , and  $^7\text{Li}$ . Figure 7 shows the ESEEM spectrum of this glass recorded using three-pulse sequence  $\pi/2-\tau-\pi/2-T-\pi/2$ .

## 4. DISCUSSION

The spectrum of the  $\text{B}_2\text{O}_3$  glass is nearly independent of the microwave power (Fig. 1). This "five line plus shoulder" spectrum exhibits  $g$ -values that are close to those reported for non-bridging oxygens in a number of glasses [8].

The unpaired state trapped at a non-bridging oxygen exhibits a localisation of more than 0.95 [7-11]. This oxygen can be bonded to a boron that is three-fold co-ordinated or between two boron atoms, the one four-fold and the other three-fold co-ordinated. The MNDO and SCF-HF calculations have shown that the unpaired electron localised at a non-bridging oxygen bonded to a three-fold co-ordinated boron exhibits a high localisation on this site. The unpaired electron trapped by a bridging oxygen between a four-fold and three-fold co-ordination is distributed over several atomic orbitals of oxygens. The degree of delocalization depends on the cross linking of the four-fold and three-fold co-ordination structural arrangement. The results of Table 4 can only be considered as a rough approximation of the reality. This finding suggests that the signal of  $\text{B}_2\text{O}_3$  glass is due to an unpaired electron localised at a non-bridging oxygen.

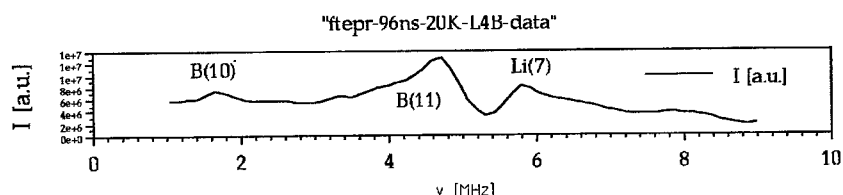


Fig. 6. FT-EPR spectrum of the two pulse FID spectrum of the  $\text{Li}_2\text{O} \cdot 4\text{B}_2\text{O}_3$  glass.

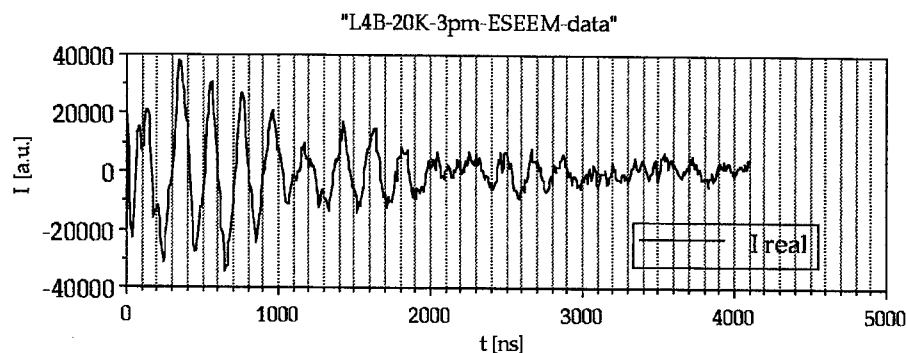


Fig. 7. Three pulse ESEEM spectrum of the  $\text{Li}_2\text{O} \cdot 4\text{B}_2\text{O}_3$  glass.

Table 3.  
MNDO calculation of the  $\text{BO}_3\text{H}_2$  unit.

Atom	BL	BA	TA				S	PX	PY	PZ	Total
H							0.002				0.002
O	0.95			1			0.001	0.001	0.034	0.000	0.036
B	1.36	116.5		1	2		0.000	0.000	0.003	0.000	0.003
O	1.36	119.0	179.8	3	2	1	0.000	0.001	0.919	0.003	0.923
O	1.41	120.2	359.7	3	2	1	0.001	0.000	0.033	0.000	0.035
H	0.95	120.0	359.0	5	2	1	0.002				0.002
BL	Bond Length (Å)			BA	Bond Angle (degrees)		TA	TwistAngle (degrees)			

In  $\text{B}_2\text{O}_3$  glasses, boron is only three-fold co-ordinated. Thus, an oxygen dangling bond can only be attached to a three-fold co-ordinated boron unit.

It is evident from Fig. 2 that the line shape of the EPR signals of the borate glasses are a function of the alkali metal concentration. The spectra of intermediate compositions ( $0 < x < 50$  mol%) may be composed of the spectra of the

Table 4.  
MNDO calculation of the  $\text{H}_2\text{--O}_2\text{B--O--BO}_3\text{H}_3$  unit.

	S	PX	PY	PZ	TOTAL	X	Y	Z
O	0.000	0.000	0.379	0.001	0.381	0.00	0.00	0.00
B	0.000	0.000	0.000	0.000	0.000	0.39	0.00	0.00
O	0.000	0.011	0.003	0.000	0.014	0.20	1.10	0.00
O	0.000	0.020	0.006	0.000	0.026	2.03	-1.21	0.04
H	0.000	0.000	0.000	0.000	0.000	1.78	1.95	0.04
H	0.000	0.000	0.000	0.000	0.000	1.48	-1.97	0.04
B	0.000	0.000	0.005	0.000	0.005	-1.15	0.88	-0.38
O	0.000	0.065	0.062	0.006	0.132	-1.10	1.18	-1.77
O	0.000	0.017	0.185	0.000	0.202	-2.33	0.17	-0.02
O	0.001	0.004	0.232	0.003	0.240	-0.98	2.05	0.47
H	0.000	0.000	0.000	0.000	0.000	-0.43	1.78	-2.04
H	0.000	0.000	0.000	0.000	0.000	-2.94	0.01	-0.72
H	0.000	0.000	0.000	0.000	0.000	-1.42	2.03	1.31

**Table 5.**  
g-values of oxygen related centers.

Material	Nucleus	$g_1$	$g_2$	$g_3$	$\langle A \rangle / A_s$
Borate glass	$^{11}\text{B}$	2.002	2.010	2.035	0.013
Silicate glass	$^{29}\text{Si}$	2.003	2.009	2.019	0.010
Titanate glass	$^{47,49}\text{Ti}$	2.003	2.010	2.022	
Germanate glass	$^{37}\text{Ge}$	2.002	2.008	2.051	
Phosphate glass	$^{31}\text{P}$		2.010		0.009
Aluminate glass	$^{27}\text{Al}$		2.009		0.005
Niobate glass	$^{93}\text{Nb}$		2.010		0.002

$x=0$  and  $x=50$  mol% glasses. Such a description can be realised as a linear combination of the  $I(x=0)$  and  $I(x=50)$  spectra:

$$I(x) = A(x) \cdot I(x=0) + B(x) \cdot I(x=50) \quad (1)$$

The coefficients  $A(x)$  and  $B(x)$  were determined by a least squares fit and are given in Fig. 3. The coefficient  $A(x)$  shows a variation  $0.92 - 0.021x$  with  $x$ . Thus, the concentration of the defect generating exclusively the spectrum of the  $x=0$  glass decreases with increasing  $x$ . This may be due to the reduction of the boroxol units with the increase of the alkali concentration. The  $B(x)$  coefficient depends on  $x$  as  $0.08 + 0.019x$ . The increase of this new center at the expense of the first center can be due to the formation of four-fold co-ordinated boron. This statement is partially correct. The squares in this figure present the accuracy of the lsq fit for given  $x$ . These numbers are less than one in all intermediate compositions. For  $x=10$ , the deviation is maximum. For  $x=10$ , the accuracy of the fit is about 0.6. This proves that the  $I(x=0)$  and  $I(x=50)$  signals are not the only data set that can describe the spectra in the entire region of compositions. The CW-EPR spectra may be composed of several other signals due to other defects that contribute to the spectra. The isolation of these defects is very laborious. It would require the combination of experiments such as annealing of the defects and measurements of the signals at different temperatures and microwave power levels.

The echo of a spin system,  $V(\tau, B)$ , can be measured as a function of the distance between the two-pulses,  $\tau$ , and the external magnetic field,  $B$ . The observation of the echo  $V(\tau=\text{constant}, B)$  for  $\tau=\text{constant}$  results in a signal corresponding to a CW-EPR spectrum. Assuming that  $\tau$  is equal to the spin lattice relaxation  $T_1$  of a defect, this center is saturated and cannot be observed. The centres with  $T_1 \neq \tau$  contribute to the echo fs spectrum with given  $\tau$  values. Fig. 4 shows the echo fs spectrum of the  $\text{Li}_2\text{O} \cdot 4\text{B}_2\text{O}_3$  glass recorded for  $\tau = 120, 200, 400$ , and 600 ns. The spectra are different for different  $\tau$  up to 400 ns. For this glass and temperature of measurements, the echo fs signals are not significantly affected by  $\tau$  greater than 400 ns. The variation of the echo fs spectrum of the  $\text{Li}_2\text{O} \cdot 4\text{B}_2\text{O}_3$  glass with  $\tau$  is due to the elimination of some defects that saturate or decay faster than  $\tau$ . This finding is very important for EPR spectroscopy. The isolation of the signals due to different centres may give a unique opportunity to

better describe the local structure of the glasses. The echo fs signals of Fig. 4 may be attributed to the different ring structures that are present in the glass. The assignment of the echo fs signals to a defect needs extensive theoretical work that is under way and will be reported in a future publication. Goldfarb & Kevan [16] suggested that the field swept spectra expressed can be as follows:

$$E(\tau, B) = I(B) V(\tau, B) \quad (2)$$

assuming that the phase memory time and spin relaxation times are field independent. An expression was given by Siderer & Luz [17] with which the the EPR powder pattern intensity  $I(B)$  can be deduced from the echo-field swept spectra. This expression includes the  $g$ -values of the defect and the line width of its EPR signal.

The echo  $V(\tau, T)$  at constant  $B$  can be measured as a function of  $\tau$  in a two-pulse sequence or  $T$  in a three-pulse sequence. Due to the presence of nuclei with non-zero nuclear spins, the echo decay is modulated with the frequency corresponding to the Larmour frequency of the nuclei at a certain external magnetic field  $B$ . The equations that describe the ESEEM signals for  $I \geq 1$  and for random system are the following [15]:

$$\langle V(\tau) \rangle = 1 - \frac{2}{5} I(I+1) \frac{g_e^2 \beta_e^2}{H_0^2 r^2} [2 - 4 \cos 2\pi \nu_I \tau F(T_c, \tau) + \cos 2\pi (2\nu_I \tau) + F(T_c, \tau)] \quad (3)$$

$$V(\tau, T) = 1 - \frac{1}{3} I(I+1) \frac{B^2}{\nu_I^2} \left\{ \begin{aligned} &2 + 2 \cos 2\pi \nu_I \frac{A}{2} \tau G(\gamma \tau) \\ &+ \cos 2\pi \nu_I T \left[ \begin{aligned} &2 \cos 2\pi \frac{A}{2} (\tau + T) G(\gamma(\tau + T)) \\ &+ \cos 2\pi \frac{A}{2} T G \left( \begin{aligned} &\gamma(2\tau + T) \\ &+ \cos 2\pi \frac{A}{2} (\tau + T) G(\gamma T) \end{aligned} \right) \end{aligned} \right] \end{aligned} \right\} \quad (4)$$

where  $T_c = g_e \beta_e g_I \beta_I / h r^3$ ,  $A = T_c (1 - 3 \cos^2 \theta) + a$ ,  $B = 3 T_c \sin \theta \cos \theta$ , and  $\nu_I$  is the Larmour frequency of the nucleus  $I$ .

The  $F$  and  $G$  functions of the above equations have the form:

$$F(T_c t) = \frac{15}{4} \int_0^\pi \sin^2 \theta \cos^2 \theta \cos [\pi T_c t (1 - 3 \cos^2 \theta)] \sin \theta d\theta \quad (5)$$

$$\gamma = \frac{3eQV_{zz}}{4hI(2I-1)} \quad (6)$$

$$G(x) = \frac{3}{2I(I+1)(2I+1)} \sum_{m=-I}^{I-1} [I(I+1) - m(m+1)] \cos 2\pi(2m+1)x \quad (7)$$

The simulation of the two (Fig. 4) and three (Fig. 7) pulse ESEEM can deliver the various parameters, e.g. distance,  $r$ , of the nuclei from the electron spin



contributing to the modulation, the RDF of the atoms around the site, the quadrupole moment of the site, etc. This simulation is time-consuming for borate glasses due to the contribution of several nuclei to the ESEEM spectrum. The kind of nuclei contributing to the ESEEM spectrum can be determined by the FT-EPR spectra. The Fourier transformation of the two pulse (Fig. 4) and three (Fig. 7) pulse ESEEM signals in the  $\text{Li}_2\text{O} \cdot 4 \text{B}_2\text{O}_3$  glass gives peaks corresponding to frequencies of  $^{11}\text{B}$ ,  $^{10}\text{B}$ , and  $^7\text{Li}$ . Thus, the ESEEM spectra contain significant information that could reveal in detail the local structure of the center.

## SUMMARY

The CW-EPR spectrum of the  $x=0$  glass may be due to a non-bridging oxygen attached to a three-fold co-ordinated boron member of a boroxol-ring. As  $x$  increases, the four line plus shoulder spectrum decreases due to the reduction of those units. The formation of other ring structures affect the CW-EPR spectra. Some of the signals of these structures were indicated in the echo fs spectra of the  $\text{Li}_2\text{O} \cdot 4 \text{B}_2\text{O}_3$  glass recorded with different pulse separation. The two and three pulse modulation spectra contain significant information about the local environment of the defects.

## ACKNOWLEDGEMENTS

This work was supported by EPIET II 296 grant. Since this conference is dedicated to Professor Philip Bray, I use this opportunity to thank him once more for his support during my stay at Vanderbilt University and University of Illinois at Urbana-Champaign. I also thank A. Kokkinos for his assistance in making the glasses and irradiation.

## REFERENCES

- [1] E.L. Yasaitis & B. Smaller, *Phys. Rev.* **92** (1953), 1068.
- [2] K. Nakai, *Phys. Chem. Glasses* **4** (1963), 13A.
- [3] S. Lee & P.J. Bray, *Bull. Am. Phys. Soc.* **6** (1961), 246.
- [4] S. Lee & P.J. Bray, *Bull. Am. Phys. Soc.* **7** (1962), 306.
- [5] G.O. Karapetayan & D.M. Yudin, *Sov. Phys. Solid State* **4** (1963), 1943.
- [6] G. M. Muha, *J. Phys. Chem.* **70** (1966), 1930.
- [7] M.C.R. Symons, *J. Chem. Phys.* **53** (1970), 468.
- [8] D.L. Griscom, P.C. Taylor & P.J. Bray, *J. Chem. Phys.* **53** (1970), 469.
- [9] P.C. Taylor, D.L. Griscom & P.J. Bray, *J. Chem. Phys.* **54** (1971), 748.
- [10] D.L. Griscom, P.C. Taylor, D.A. Ware & P.J. Bray, *J. Chem. Phys.* **48** (1968), 5158.
- [11] D.L. Griscom, *J. Chem. Phys.* **53** (1971), 1113.
- [12] M.J.S. Dewar & M.L. McKee, *J. Am. Chem. Soc.* **99** (1977), 5231.
- [13] M.J.S. Dewar & W. Thiel, *J. Am. Chem. Soc.* **99** (1977), 4899.
- [14] Gaussian 92, Revision B, M. J. Frisch, G. W. Trucks, M. Head-Gordon, P. M. W. Gill, M. W. Wong, J. B. Foresman, B. G. Johnson, H. B. Schlegel, M. A. Robb, E. S. Replogle, R. Gomperts, J. L. Andres, K. Raghavachari, J. S. Binkley, C. Gonzalez, R. L. Martin, D. J. Fox, D. J. Defrees, J. Baker, J. J. P. Stewart, & J. A. Pople, Gaussian, Inc., Pittsburgh PA, 1992.
- [15] S.A. Dikanov & Y.D. Tsvetkov, *ESEEM Spectroscopy*, CRC Press, London, 1992, p 91.
- [16] D. Goldfarb & L. Kevan, *J. Magn. Reson.* **76** (1998) 276.
- [17] Y. Siderer & Z. Luz, *J. Magn. Reson.* **37** (1980) 449.

## STRUCTURAL INVESTIGATIONS OF LEAD AND STRONTIUM BORATE GLASSES

Thomas HÜBERT, Ulrike HARDER, Günter MOSEL  
& Klaus WITKE

*Bundesanstalt für Materialforschung und -prüfung (BAM),  
Unter den Eichen 87, 12200 Berlin, Germany*

Raman, IR and EXAFS spectroscopic methods were used for structural investigations of strontium and lead borate glasses of three composition series  $x\text{SrO} \cdot (93-x)\text{B}_2\text{O}_3 \cdot 7\text{Al}_2\text{O}_3$  ( $10 < x < 68$  mol%),  $x\text{PbO} \cdot (100-x)\text{B}_2\text{O}_3$  ( $0 < x < 75$  mol%) and  $x\text{PbO} \cdot (95-x)\text{B}_2\text{O}_3 \cdot 5\text{Al}_2\text{O}_3$  ( $5 < x < 80$  mol%). Strontium ions should act only as network modifiers also in the range of invert glass composition because EXAFS experiments give a coordination number of 6, hardly affected by the composition of the glasses. The incorporation of lead ions in the glass structure is discussed from the low frequency part of the Raman and IR spectra. Confirming NMR results, fourfold coordinated lead ions can be observed. The  $\text{PbO}_4$  units are similar to those in tetragonal lead oxide. The assignment of IR and Raman vibrations yields boroxol rings, borate groupings containing one or two  $\text{BO}_4$ , meta-, pyro- and orthoborate units. To obtain quantitative results Kramers-Kronig analysis was applied on IR reflectance spectra. The complex dielectric function and the absorption coefficient spectra were calculated. Band integrals were determined by band separation. The differences of the quantitative results due to the different acting cations are shown.

### 1. INTRODUCTION

Amorphous lead and strontium borates are basic components of special glasses, which are applied in modern technology because of their interesting rheological, electrical and optical properties. For tailoring the properties of such high-tech materials structural information is needed.

First investigations of the structure of lead and strontium borate glasses were performed using  $^{11}\text{B}$  NMR spectroscopy by Bray and co-workers [1-4] and recently by Moon *et al.* [5]. IR and Raman investigations were performed by Tarte & Portier [6], Konijnendijk [7], Meera *et al.* [8] and others [9-12]. Further, neutron diffraction [13] and ESR spectroscopy were applied [14,15]. The results support the model of Krogh-Moe, that in borate glasses structural groupings exist as in crystalline borates of corresponding composition.

Although strontium and lead have different positions in the periodic table, their two-valent ions can be compared with regard to ionic radii (1.32 and 1.27 Å), the high polarizability, and field strengths (0.34 and 0.27). Lead contain-

ing glasses are available in a great composition range due to the ability of lead ions to act as network modifiers in a  $\text{PbO}_6$  coordination, as well as network formers in  $\text{PbO}_4$  coordination, depending on composition. Such a behaviour is unknown for strontium ions, but borate glasses can be prepared also in a large composition range. Thus, the aim of this paper is to compare the results of structural investigations concerning the short range order, i.e. the oxygen coordination of the cations and the borate groupings in the glasses.

We used Raman, IR and EXAFS spectroscopic methods for structural investigations of compositions enclosing the whole glass forming range. Some alumina was added to extend the glass forming range and suppress phase separation or crystallization.

## 2. EXPERIMENTAL

### 2.1. Glass Preparation

Glasses were melted from chemically pure reagents,  $\text{H}_3\text{BO}_3$ ,  $\text{Al}_2\text{O}_3$ ,  $\text{Pb}_3\text{O}_4$  or  $\text{SrCO}_3$ , in a platinum crucible for 30 min at 800 to 1200°C depending on chemical composition. The melt was pressed between steel plates and, after annealing, cooled down to room temperature. Crystalline strontium and lead borates were prepared for references by sintering of the components or crystallization from the melt.

### 2.2. Spectroscopic Methods

Raman spectra were recorded using a RGS2 Raman Gitterspektrograph or a DILOR XY spectrometer, equipped with a nitrogen-cooled CCD camera as a detector. Samples were excited using the 488.0 nm or the 514.5 nm line from a Carl Zeiss ILA 120 argon ion laser. The infrared measurements were carried out on the BRUKER IFS66v spectrometer, equipped with the far infrared option. Kramers–Kronig transformation and band separation were performed for quantitative analysis to obtain absorption coefficient spectra and band integral intensities. EXAFS room temperature measurements were performed at the Sr-*K* edge in transmission mode at the storage ring VEPP-3 (INP Novosibirsk) and HASYLAB at DESY (Hamburg). EXAFS modulations  $k^3\chi(k)$  were extracted from the spectra by standard procedures and were Fourier transformed ( $2.0 \text{ \AA}^{-1} < k < 12.0 \text{ \AA}^{-1}$ ) into *r* space.

## 3. RESULTS

### 3.1. Short Range Order of Strontium and Lead Ions

The short range order of strontium atoms was examined by EXAFS experiments which give information about the first coordination shell of the absorber atom. Thus, data for the mean Sr–O distance,  $R_{\text{Sr-O}}$ , the coordination number, *N*, and the Debye–Waller factor,  $\exp(-2\sigma^2k^2)$ , characterising the structural disorder, were determined [16]. Sr-*K* EXAFS modulations and the Fourier transforms of the investigated glasses are given in Fig. 1.

Whereas from the Sr/O atomic radii ratio a coordination number of 8 would be expected, Sr ions in crystalline borates can be coordinated by 6 to 11 oxygen

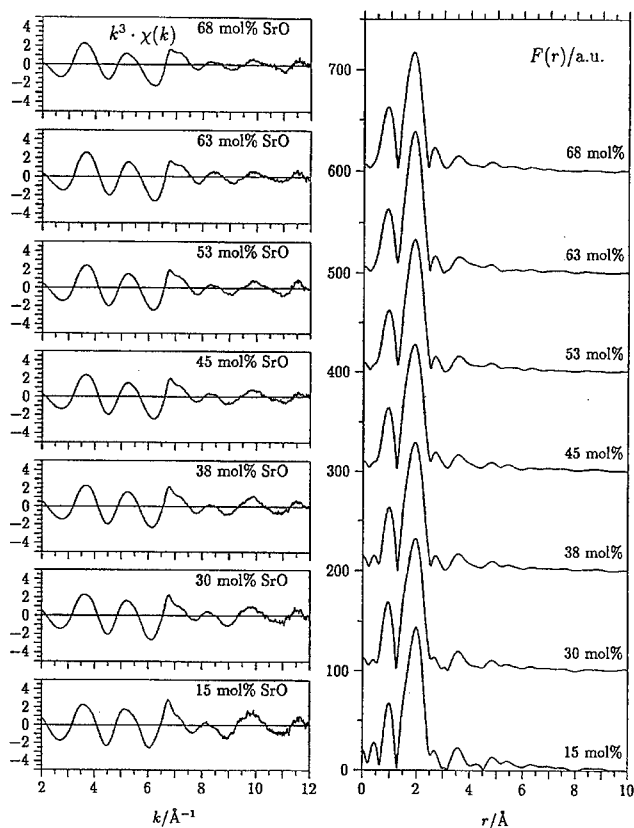
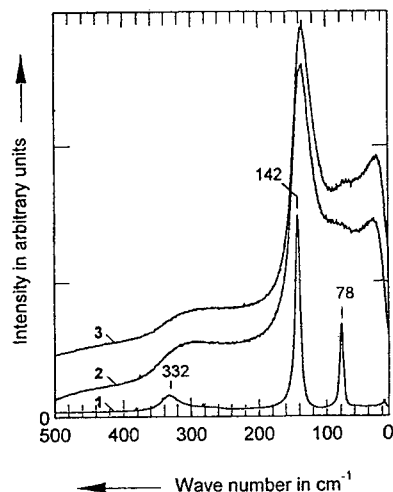


Fig. 1. Sr-K EXAFS modulations and Fourier transforms of strontium borate glasses (SBA).

atoms. In crystalline  $\text{Sr}_2\text{B}_2\text{O}_5$  the Sr ions occupy two positions surrounded by 6 and 7 oxygens, respectively [17]. Quantitative structural parameters for the SBA glasses were obtained by parameter fitting of the Sr-K EXAFS modulations. To derive starting parameters for the fit, the two Sr positions in the  $\text{Sr}_2\text{B}_2\text{O}_5$  structure were averaged. Since the radial distribution of the oxygen atoms in the Sr environment is expected to be asymmetric, a modified EXAFS formula was used (the convolution of a Gaussian distribution, characterised by the mean square deviation,  $\sigma^2$ , with an exponential distribution, characterised by the asymmetry parameter,  $a$ ). Only slight changes were observed with increasing SrO content ( $x = 15\text{...}63 \text{ mol}\%$ ):  $R_{\text{Sr-O}}$  decreases from 2.60 to 2.57 Å ( $\Delta R_{\text{Sr-O}} = 0.02 \text{ Å}$ ),  $N$  remains nearly unchanged ( $6.1 \pm 0.5$ ) and  $(a^2 + \sigma^2)^{1/2}$ , which is a measure for the width of the first coordination shell, increases from 0.12 to 0.14 Å. The parameters for the glass with  $x = 68 \text{ mol}\%$  are significantly different:  $R_{\text{Sr-O}} = 2.61 \text{ Å}$ ,  $N = 6.3$  and  $(a^2 + \sigma^2)^{1/2} = 0.17 \text{ Å}$ . It was concluded from these results that Sr ions are in sixfold coordination in all glasses. With increasing SrO content the disorder of the Sr environment is enhanced.

Information on the short range structure of the lead ions was extracted



**Fig. 2.** vv-polarized Raman spectra. Curve 1: tetragonal crystalline PbO, Curve 2: 75 mol% PbO (PB), Curve 3: 80 mol% PbO (PBA).

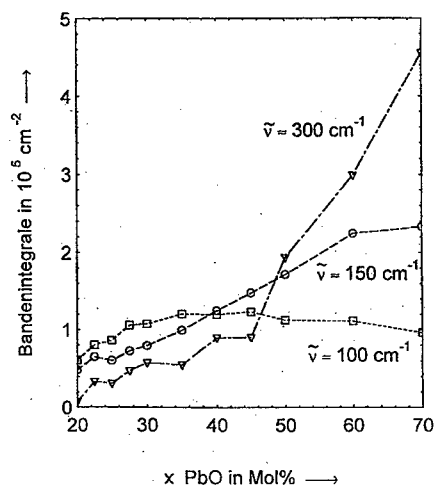


**Fig. 3.** IR band integrals of far infrared bands versus lead oxide concentration (PB).

from the low frequency range of Raman and IR spectra. Fig. 2 shows an intensity increase with growing PbO content of the glasses. The spectra become comparable with the spectra of tetragonal crystalline PbO. The formation of  $\text{PbO}_4$  pyramids in lead borate glasses containing high PbO contents is known from NMR investigations by Bray [1], but these results are not able to distinguish between tetragonal and orthorhombic symmetry.

Fig. 3 presents the integral band intensities of the Pb–O vibrational bands in the far infrared. The bands between 100 and 200  $\text{cm}^{-1}$  are assigned to ionic Pb–O bonds and  $\text{Pb}^{2+}$  motions in the borate network, whereas the band near 300  $\text{cm}^{-1}$  due to covalent Pb–O bonds corresponds to the band at 290  $\text{cm}^{-1}$  of tetragonal PbO. With increasing PbO content the band at 150  $\text{cm}^{-1}$  continuously increases and the band at 100  $\text{cm}^{-1}$  decreases above 50 mol% PbO. The intensity of the band at 300  $\text{cm}^{-1}$  distinctly increases above 45 mol% PbO. This confirms that, for low PbO content, lead oxide predominantly acts as modifier (ionic Pb–O bond) and with increasing PbO content it acts as a glass former (covalent Pb–O bond) [18] as well.

### 3.2. Borate Groupings in Strontium and Lead Borate Glasses

**3.2.1. Raman investigations** - Fig. 4 shows the Raman review spectra of the glasses. The spectra of low modifier content are similar. The Raman spectra of lead borate glasses have more intensive absorption bands in the 1100 to 1500  $\text{cm}^{-1}$  region. High strontium borate glasses show in contrast to lead borate glasses more structured spectra. An assignment of the Raman peaks in the glasses was performed by comparing with the spectra of prepared crystalline reference substances and with the results of other authors, showing slight

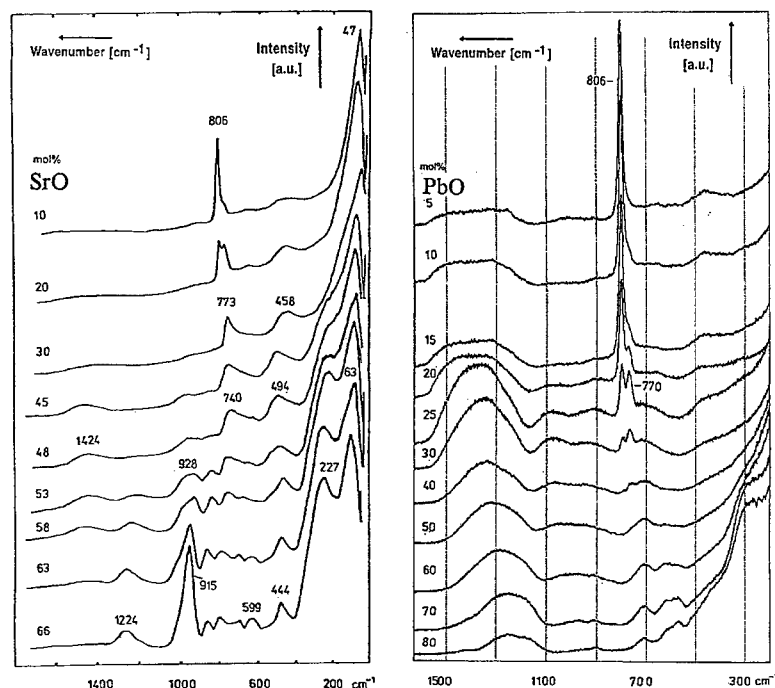


Fig. 4. Raman spectra of strontium (SBA) [19] and lead (PBA) borate glasses.

differences in the peak positions of alkali borate glasses [8, 20] (see Table 1). The glasses of low modifier content were dominated by peaks in the 740...810  $\text{cm}^{-1}$  region due to boroxol rings and borate ring groupings. The determination of the intensity ratios of the 770 and 805  $\text{cm}^{-1}$  bands give the quantitative results demonstrated in Ref. [21]. With increasing oxide content the intensities of these bands decrease whereas the intensities of new bands rise in the 1100...1500  $\text{cm}^{-1}$  range, near 900  $\text{cm}^{-1}$  and below 300  $\text{cm}^{-1}$ . According to the

Table 1  
Assignment of Raman Bands in the Spectra of Strontium and Lead Borate Glasses

Band No.	Frequency range ( $\text{cm}^{-1}$ )		Assignment
	Strontium borate	Lead borate	
1	1390...1430	1150...1500	metaborate, $\text{B-O}^-$
2	1210...1230	1260	ortho-, pyroborate units
3		1050	diborate units
4	950...960	950	diborate units
5	915	900...930	orthoborate units
6		900	pentaborate units
7	806	806	boroxol rings
8	740...770	770	tri-, tetra-, pentaborate units
9	600...670	620...710	metaborate units
10	430...500	550	isolated $\text{BO}_4$ units

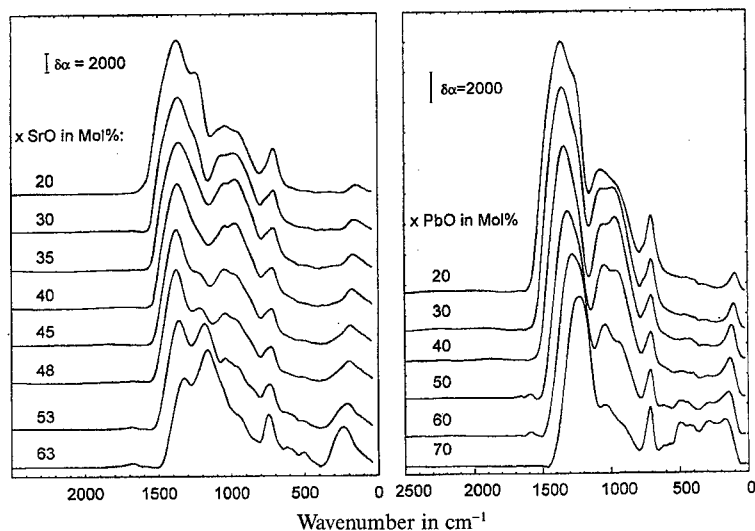


Fig. 5 IR absorption coefficient spectra of strontium and lead borate glasses (series SBA, PBA).

assignment given in Table 1 the large amounts of metaborate groupings are characteristic of lead borate glasses. Strontium borate glasses of high modifier content exhibit intense peaks due to ortho- and pyroborates. The spectra below  $300\text{ cm}^{-1}$  are dominated by Me-O bending vibrations and the so-called Boson peak which is characteristic for the glassy state. It was used for determination of structural correlation lengths (SCL) varying from 3.5 to 7 Å (see Ref. [22]).

**3.2.2. IR investigations** - The absorption coefficient spectra obtained and an assignment of the separated IR bands are given in Fig. 5 and Table 2, respectively. Most of the separated bands are caused by several borate groupings depending on metal oxide concentration. In comparison to strontium borate glasses the bands 1 and 2 in the spectra of the lead containing glasses appear at lower frequencies whilst the band 3 appears at higher frequencies. The dependence of the band intensities on metal oxide content are given in Fig. 6 and show differences concerning bands 3, 4 and 5 [23]. The high intensity of

**Table 2**  
Assignment of the infrared bands in the spectra of strontium and lead borate glasses.

Band No.	Frequency range ( $\text{cm}^{-1}$ )		Assignment
	Strontium borate	Lead borate	
1	1450...1480	1410...1475	penta-, meta- and pyroborate units
2	1345...1365	1290...1360	penta-, tri-, di-, pyro- and orthoborate units
3	1170...1225	1190...1240	boroxol rings, penta- and triborate units, metaborate chains, (pyro-) and orthoborate units
4	1060...1080	1040...1100	penta-, tri-, and pyroborate units
5	955...975	920...975	di- and triborate units (pentaborate)

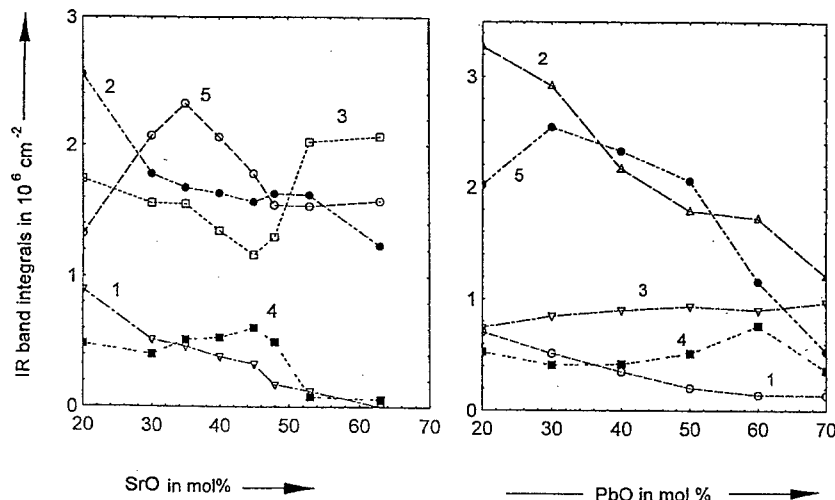


Fig. 6. IR band integrals of borate structural units versus strontium and lead oxide content (series SBA, PBA).

band 3 (curve 3) assigned to ortho-, pyro- and chain metaborate units of glasses containing more than 50 mol% SrO is evident. Bands in the region of 690...770  $\text{cm}^{-1}$  and 550...630  $\text{cm}^{-1}$  are due to bending vibrations of various borates and isolated  $\text{BO}_3^{3-}$ .

#### 4. CONCLUSIONS

From EXAFS experiments it was concluded that strontium is incorporated over the whole glass forming range in  $\text{SrO}_6$  octrahedra and acts as a network modifier. Low frequency Raman and IR measurements of high lead oxide containing glasses indicate  $\text{PbO}_4$  tetrahedra and confirm their network former function. Raman and IR investigations show that glasses of low metal oxide content contain mainly boroxol rings and borate rings with one or two  $\text{BO}_4$  units. The structure of strontium borate glasses of high metal oxide concentration is dominated by pyro- and orthoborates, whereas lead borate glasses include various and larger groupings.

#### REFERENCES

- [1] P.J. Bray, M. Leventhal & H.O. Hooper, *Phys. Chem. Glasses* **4** (1963), 47.
- [2] P.J. Bray & M. Leventhal, *Phys. Chem. Glasses* **6** (1965), 113.
- [3] D. Mao & P.J. Bray, *J. Non-Cryst. Solids* **144** (1992), 217.
- [4] M.J. Park & P.J. Bray, *Phys. Chem. Glasses* **13** (1972), 50.
- [5] S.-J. Moon, M.-S. Kim & S.-J. Chung, *J. Korean. Phys. Soc.* **29** (1996), 213.
- [6] P. Tarte & M.J. Portier, In: *The Structure of Non-Crystalline Solids*, Ed. P.H. Gaskell (Taylor and Francis, London, 1976), 227.
- [7] W.L. Konijnendijk, Philips Res. Rep. Suppl. 1975, 1.
- [8] B.N. Meera, A.K. Sood, N. Chandrabhas & J. Ramakrishna, *J. Non-Cryst. Solids* **126** (1990), 224.
- [9] S.M. Brekhovskikh & V.P. Cheremisinov, *The Structure of Glass*, Vol.2 (New York 1960), 191.
- [10] V.G. Tchehovski, Y.I. Keich, Y.A. Petrov, S.N. Yarkova & P.G. Paukch, *Fiz. Khim. Stekla*



- 14 (1988), 150.
- [11] S. Ram & K. Ram, *J. Mater Sci.* **23** (1988), 4546.
  - [12] A.-M. Zahra, C.Y. Zahra & B. Piriou, *J. Non-Cryst. Solids* **155** (1993), 45.
  - [13] N.M. Vendishcheva, B. A. Shakhmatkin, A.C. Wright, R. Sinclair & D.I. Grimley, *Bol. Soc. Esp. Ceram. Vid.* **31-C** (1992), 41.
  - [14] H. Hosono, H. Kawazoe & T. Kanazawa, *Yogyo-Kyokai-Shi* **90** (1982), 544.
  - [15] Y. Otha, M. Shimada & M. Koizumi, *J. Non-Cryst. Solids* **51** (1982), 161.
  - [16] G. Mosel, Thesis (Rostock University, 1995).
  - [17] H. Bartl, W. Schuckmann, *Neues Jb. Miner. Mh.* (1966), 253.
  - [18] K. Witke, U. Harder, M. Willfahrt, T. Hüberr & P. Reich, *Glastechn. Ber.* **69** (1996), 143.
  - [19] T. Hüberr, U. Banach, K. Witke & P. Reich, *Phys. Chem. Glasses* **32** (1991), 58.
  - [20] E.I. Kamitsos, M.A. Karakassides & G.D. Chryssikos, *J. Phys. Chem.* **91** (1987), 1073.
  - [21] K. Witke, T. Hüberr, P. Reich & C. Splett, *J. Raman Spectr.* **24** (1993), 407.
  - [22] K. Witke, M. Willfahrt, T. Hüberr & P. Reich, *J. Mol. Str.* **349** (1995), 373.
  - [23] U. Harder, Thesis, (Technical University Berlin, 1996).

## HIGH-TEMPERATURE RAMAN SPECTRAL STUDIES OF VARIOUS BORATE-CONTAINING GLASSES

Robert A. CONDRATE, Sr. & Ajit K. JILLAVENKATESA  
*Institute of Glass Engineering and Science, NYS College of  
Ceramics at Alfred University, Alfred, NY 14802, USA*

Raman spectroscopy provides a powerful tool for investigating the network of borate-containing glasses, particularly in the borate portion of the glasses. This paper will deal with the structural information that can be obtained *in-situ* from Raman spectra of borate-containing glasses at high temperatures and specifically considers Raman spectral information that was obtained for  $B_2O_3$ , borosilicate, borogermanate and borosilicogermanate glasses possessing larger concentrations of boron oxide, along with sodium borate and borosilicate glasses. At room temperature, such glasses which possess a high concentration of  $B_2O_3$  contain a large number of superstructural units with tri-coordinated and/or tetra-coordinated boron atoms whose amounts depend upon the metal oxide content. Raman spectra clearly indicate that such boroxol-type rings break up as the temperature increases, forming probably chains or isolated groups.

### 1. INTRODUCTION

Variations in the network structure of glasses can alter their physical and chemical properties. Borate-containing systems provide glass compositions which can undergo glass structural changes with changes in temperature. This paper will investigate the structural changes that can occur for various borate-containing glasses (particularly in the borate network) with respect to changes in heat treatment temperature as indicated by changes in their Raman spectra.

### 2. EXPERIMENTAL CONSIDERATIONS

The nature of the cells that were used for measuring the Raman spectra of glass specimens at high temperatures was critical. Two types of cells that have been used for measuring the spectra were the wire wound furnace cell and the platinum resistance strip cell. A schematic diagram illustrating the wire wound furnace cell is shown in Fig. 1. A fused silica tube (1.5 cm diameter and 7.0 cm height) was wrapped with kanthal wire with approximately 10 winds per inch. The silica tube was insulated with a layer of refractory cement and glass wool. The sample was placed on an aluminum platform in the furnace, and the scattered radiation was collected through the window. The cell was precalibrated, and the current was controlled by a variac. The temperature could be controlled

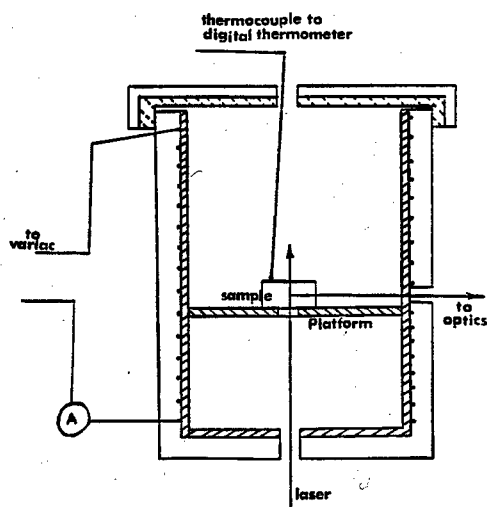


Figure 1. Schematic diagram of wire wound furnace cell.

within 3°C. The temperature during the spectral measurements was monitored by a thermocouple which was placed on the glass surface. The platinum resistance strip cell is illustrated in Fig. 2. The cell consisted of a brass jacket with an internal water channel for cooling the jacket. Openings were made in the walls of the jacket at 90° to each other so that the incident laser radiation could enter the cell, and the scattered radiation can come out. Samples were placed on a platinum strip ~10 cm wide and 30 mm long. The platinum strip was heated directly by passing electrical current through it. Electrical current controlling the temperature was supplied through a variastat. Insulated copper bases were used to couple the power leads to the platinum strip. Sample temperatures were monitored using two S-type thermocouples, with one being placed at the platinum strip and the other being placed on top of the glass sample.

### 3. RAMAN SPECTRA OF $B_2O_3$ GLASS AT HIGH TEMPERATURE

The structure of vitreous and molten  $B_2O_3$  have been a subject of controversy since Zacharisen's classic paper [1]. However, the x-ray work of Mozzi & Warren [2] has virtually established that the glass contains  $BO_3$  triangles which share apical oxygen atoms to form boroxol rings ( $B_3O_6$  units containing  $B_3O_3$  rings). The structural changes that occur in molten  $B_2O_3$  have been uncertain [3] and questioned. However, it has been known from the study of Young & Westerdahl [4] that the integrated Raman band intensity at  $\sim 801\text{ cm}^{-1}$  decreases with heat treatment temperature rise to 800°C and beyond. These spectral data indicate that a breakdown of boroxol rings occurs at elevated temperatures, in agreement with Strong's high-temperature x-ray data [5]. Walrafen *et al.* investigated the high-temperature Raman spectra of vitreous and molten  $B_2O_3$  [6,7] in order to obtain information concerning this boroxol ring breakdown with

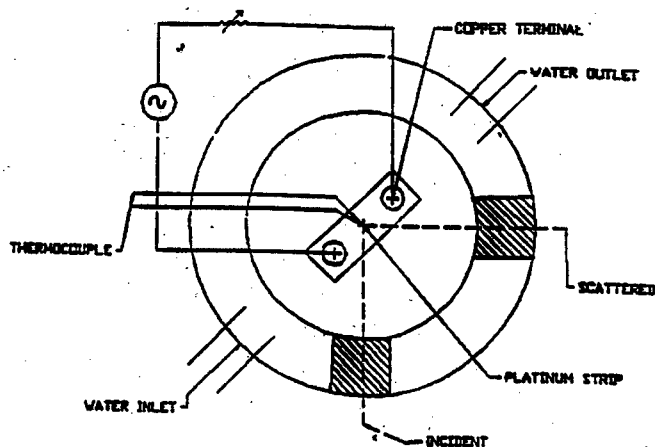


Figure 2. Schematic diagram of platinum resistance strip cell.

increasing temperature, and to determine the energy involved in the breakdown. They measured the intensity ratio between the bands associated with the boroxol breathing mode at  $801\text{ cm}^{-1}$  with respect to treatment temperature. These data were plotted as an Arrhenius type equation that was developed by Young & Westerdahl [4]. From this equation, the calculated enthalpy of ring rupture was  $6.4 \pm 0.4\text{ kcal/mol}$  boroxol ring [6]. A later study by Walrafen *et al.* [7], using also a Bose-Einstein correction and neutron data, improved the calculated value to  $5.0\text{ kcal/mol}$  boroxol ring. The latter paper also investigated the nature of the low-wavenumber Raman bands observed for  $\text{B}_2\text{O}_3$ . Hassan *et al.* [8] have conducted a similar, related Raman spectral study of  $\text{B}_2\text{O}_3$  glass at high temperatures (upto  $1273\text{ K}$ ). They related changing Raman bands in the  $1000\text{--}1600\text{ cm}^{-1}$  range with temperature change to the disruption of the borate rings. They [9] also noted that the low-wavenumber boson peak showed different temperature behavior which mirrored that of the sound velocity.

#### 4. RAMAN SPECTRA OF BOROSILICATE GLASSES AT HIGH TEMPERATURES.

Furukawa & White investigated  $\text{B}_2\text{O}_3\text{--SiO}_2$  glasses which were heat treated at different temperatures and for different periods in time [10]. The intensity ratio of the boroxol ring mode at  $810\text{ cm}^{-1}$  with respect to the silicate bending mode at  $\sim 475\text{ cm}^{-1}$  depended upon the thermal history and composition of the glass. The intensity ratio versus heat-treatment temperature curve exhibited a maximum in the glass-transition temperature range. Raman spectra were measured at high temperatures for  $50\text{B}_2\text{O}_3\cdot 50\text{SiO}_2$  glass during both the heating and cooling cycle (between room temperature and  $600^\circ\text{C}$ ). Above  $\sim 300^\circ\text{C}$ , with increasing temperature, the relative intensity of the band at  $810\text{ cm}^{-1}$  decreased. This change reversed with decreasing temperature. The reversible change of intensity for the breathing mode was interpreted as a reversible for-

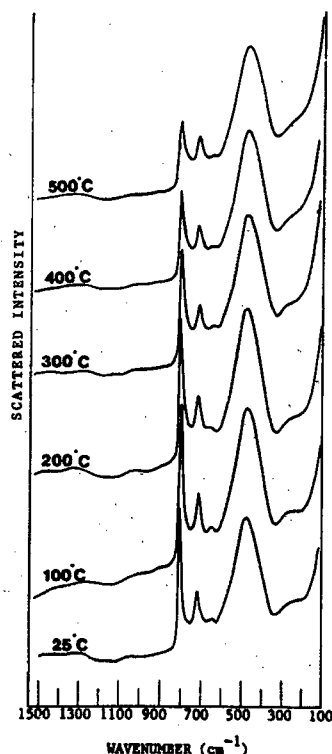


Figure 3. Raman spectra of air-quenched  $35\text{GeO}_2.65\text{B}_2\text{O}_3$  glass at various temperatures during the heating cycle.

mation and decomposition of boroxol rings with temperature. Such a reaction becomes very sluggish below the glass transition so that the intensity ratio stayed constant below  $300^\circ\text{C}$ .

##### 5. RAMAN SPECTRA OF BOROGERMANATE AND BOROSILICOGERMANATE GLASSES AT HIGH TEMPERATURES.

Chakraborty & Condrate [11,12] investigated the Raman spectra of various glass compositions in the  $\text{B}_2\text{O}_3\text{--GeO}_2$  and  $\text{B}_2\text{O}_3\text{--GeO}_2\text{--SiO}_2$  systems at high temperatures. Fig. 3 illustrates the Raman spectra of air quenched  $35\text{GeO}_2.65\text{B}_2\text{O}_3$  at different elevated temperatures. The intensity of the boroxol breathing mode at  $808\text{ cm}^{-1}$  dramatically decreases relative to the band at  $\sim 450\text{ cm}^{-1}$  (primarily due to Ge–O motion) with increase of the temperature above  $300^\circ\text{C}$ . The half-width of the band at  $808\text{ cm}^{-1}$  increases with increasing temperature. The latter effect is due to an increase in thermal disorder of the structural units with increasing temperature. The Raman band also shifts to lower wavenumbers with increase in temperature due to network expansion. Reverse spectral effects have been observed during the cooling cycle of the sample.

As noted earlier, the decrease in intensity of the Raman band in the region

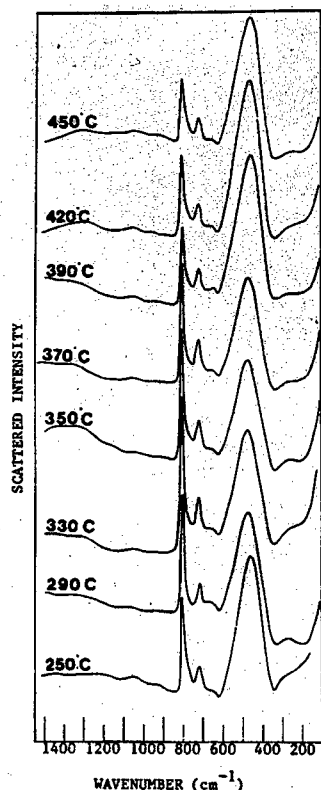


**Figure 4.** Room-temperature Raman spectra of air-quenched  $40\text{B}_2\text{O}_3.60\text{GeO}_2$  glass treated at different elevated temperatures for 24 h before re-quenching.

of  $808\text{ cm}^{-1}$  with increasing temperature can be associated with a decrease in the boroxol ring concentration. The enthalpy for rupture of such rings can be determined using an equation similar to the one that Walrafen *et al.* used in calculations for  $\text{B}_2\text{O}_3$  glass [6]. Using the  $I_{808}/I_{450}$  integrated intensity ratio as the variable parameter, one obtains an enthalpy of  $7.7\text{ kcal/mol}$  which is comparable to the value observed for  $\text{B}_2\text{O}_3$  glass ( $6.4 \pm 0.4\text{ kcal/mol}$ ) [6]. The former value is probably higher due to the higher viscosity of the borogermanate glass and the narrower temperature range used for the calculation.

Due to variations of the borate network structure with heat treatment temperature, the structure of an air-quenched borogermanate glass at room temperature can vary depending upon the temperature from which the resulting glass is quenched. Fig. 4. illustrates the Raman spectra of an air quenched  $40\text{GeO}_2.60\text{B}_2\text{O}_3$  glass composition which has been retreated at different elevated temperatures for 24 h before it was re-quenched. No noticeable changes were observed in relative intensity of the band at  $808\text{ cm}^{-1}$  below  $250^\circ\text{C}$ . However, an increase in intensity of this band is observed for the glass treated above  $330^\circ\text{C}$ . The relative intensity of the band at  $808\text{ cm}^{-1}$  decreases dramatically compared

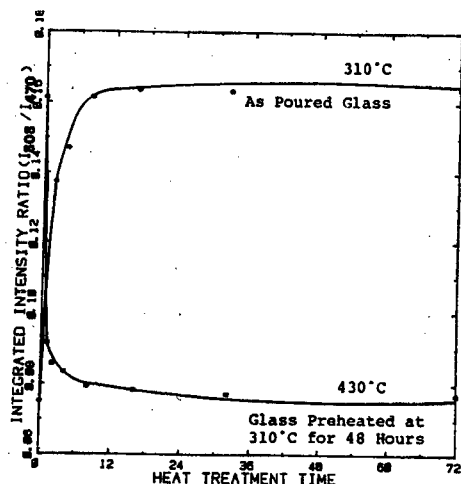


Figure 5. The  $I_{808}/I_{450}$  ratio for 40  $\text{GeO}_2$ .60  $\text{B}_2\text{O}_3$  glass heat treated at different temperatures for different periods of time.

to the germanate band at  $\sim 430\text{ cm}^{-1}$ . This indicates that the boroxol ring concentration in the resulting quenched glasses goes through a maximum at approximately  $T_g$  for these glasses under the given conditions of heat treatment.

Raman spectra were measured at room temperature for 40 $\text{GeO}_2$ .60 $\text{B}_2\text{O}_3$  glasses after the air-quenched glasses were treated at  $310^\circ\text{C}$  for different periods of time. The relative intensity of the band at  $808\text{ cm}^{-1}$  increases dramatically with treatment time (see Fig. 5). The rapid increase in intensity indicates an increase in the boroxol ring concentration. However, after approximately 12 h of heat treatment, the increase in intensity ceases, indicating the approximate attainment of an equilibrium involving the boroxol rings. The effect of heat treatment at  $430^\circ\text{C}$  was also investigated. The glass samples in this experiment were preheated at a temperature close to  $T_g$  ( $430^\circ\text{C}$ ) for 48 h to obtain the initial boroxol concentration. In this experiment, the boroxol ring concentration attains approximate equilibrium in 8 h. As would be expected, the equilibrium concentration at  $430^\circ\text{C}$  is much lower than at  $310^\circ\text{C}$ .

Similar Raman spectra studies were conducted for borosilicogermanate glass compositions [12]. The concentrations of the boroxol rings also decreased in these glass compositions with increasing heat treatment temperature. Their enthalpies of ring rupture calculated from Raman spectral intensities possessed a similar magnitude to those of the other investigated boron-oxide containing glass compositions.

## 6. RAMAN SPECTRA OF SODIUM BORATE AND BOROSILICATE GLASSES AT HIGH TEMPERATURES

Furukawa & White [13] investigated the high-temperature Raman spectra of alkali borate glasses. The spectra varied with temperature but no abrupt changes were observed at any temperature. The wavenumber shifts, band broad-

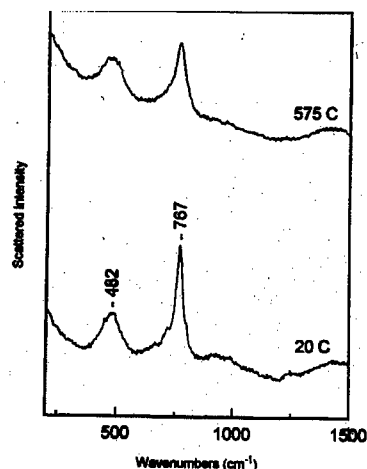
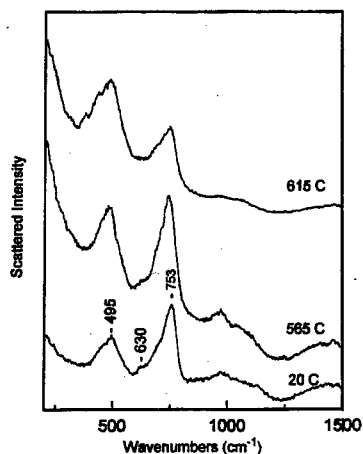


Figure 6. Raman spectra of a sodium borosilicate glass composition (20-65-15, 20 mol%  $\text{Na}_2\text{O}$ -65 mol%  $\text{B}_2\text{O}_3$ -15 mol%  $\text{SiO}_2$ ) with  $T_g$  of 480°C at different temperatures.

ening and changes of the intensity ratio of the 805 and 770  $\text{cm}^{-1}$  bands that are associated with the breathing modes of boroxol and triborate rings respectively, were interpreted in terms of the thermal expansion of boron-oxygen bonds as well as configurational rearrangements of the boron oxide network. They noted that the triborate rings were more persistent with increasing temperature than boroxol rings. Some rearrangement of the borate groups may occur above the glass transition temperature.

Raman spectra which were obtained for selected sodium borosilicate glass compositions[14] will be discussed on the basis of the glass structure. Band feature changes can be noted during in-situ spectra measurements, with changes in heat treatment temperature for the Raman bands at  $\sim 740$ – $780 \text{ cm}^{-1}$  that are associated with 3-membered rings possessing one or more four-coordinated boron atoms. Fig. 6 illustrates the Raman spectra for a glass composition which involves a boron oxide network containing mainly triborate rings possessing only one four-coordinated boron atom. The room-temperature Raman spectrum possesses a band in the 480–490  $\text{cm}^{-1}$  region that is associated with the bending vibrations of silicate tetrahedra along with a band at  $\sim 767 \text{ cm}^{-1}$  that is associated with the breathing vibration of the borate rings. The Raman spectral data clearly indicate that the concentration of the borate rings decreases on passing through the melting temperature. The rings probably breakdown into chains or isolated  $\text{BO}_3$  units. This ring breakdown is reversible. Upon cooling this glass composition through the softening point, the concentration of the ring species again increases. Fig. 7 illustrates the Raman spectra for a sodium borosilicate glass composition (30-55-15) also containing mainly diborate rings. Its borate ring breathing mode is located at 753  $\text{cm}^{-1}$ . This difference in wavenumber location is due to another three-coordinated boron atom being replaced by a four-coordinated boron atom in the boron-oxide ring with  $\text{Na}_2\text{O}$  addition. The intensity of





**Figure 7.** Raman spectra of a 30-55-15 sodium borosilicate glass composition with  $T_g$  of 491°C at different temperatures.

this Raman band (associated with a ring breathing mode) with respect to that for the silicate bending mode decreases with increasing heat treatment temperature, indicating a decrease in the concentration of the latter-mentioned borate rings. It is also interesting to note that the wavenumbers of the boron-oxide ring breathing modes decrease as the heat treatment temperature increases. This shift in wavenumber is due to an expansion of the borate portion of the network with increasing temperature. Fig. 8 illustrates the Raman spectra for a glass composition (40-35-25) containing a smaller amount of  $B_2O_3$ . As noted for other glass compositions, the intensity of the ring breathing mode decreases with respect to the silicate bending mode, indicating a decrease in the concentration of the borate ring species. For this composition, the increase in intensity of the Raman

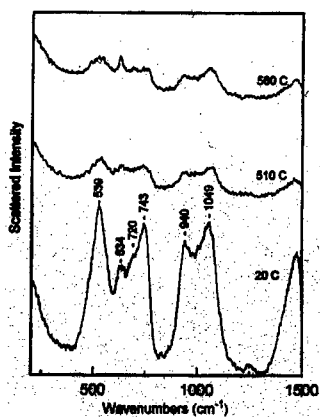


**Figure 8.** Raman spectra of a 40-35-25 sodium borosilicate glass composition with  $T_g$  of 437°C at different temperatures.

bands at  $\sim 634$  and  $720\text{ cm}^{-1}$  may also be noted with increasing treatment temperature. Such Raman bands appear for metaborate chains. Apparently at this glass composition, a sufficient number of such types of chain species are formed so that they are detectable in the Raman spectra.

## 7. CONCLUSIONS

The following conclusions can be made on the basis of the spectral studies considered in this presentation:

- (1) Structural changes can be determined for borate-containing glasses from Raman spectra with changes in temperature.
- (2) A decrease in concentration of 3-membered rings can be seen with increasing temperature for  $\text{B}_2\text{O}_3$ , borosilicate, borogermanate and borosilicogermanate glasses. Current literature [6-14] suggests that this is due to formation of isolated trigonal borate units or borate chains. An alternate interpretation involves the boroxol-type rings breaking and forming larger rings. A distant alternative is that the structure of the rings is being distorted with increasing temperatures. However, in this case, very strong structural distortions have to occur for the observed spectral changes.
- (3) The enthalpies of ring rupture of boroxol rings in all of the investigated boron-oxide containing glass compositions are comparable to those for  $\text{B}_2\text{O}_3$  glass. Slight differences might be due to differences in their structural environment.
- (4) A decrease in the concentration of 3-membered rings involving one or more four-coordinated boron atoms can be seen with increase in temperature for sodium borate and borosilicate glasses containing higher concentrations of  $\text{B}_2\text{O}_3$ .
- (5) Other changes in borate network structure can be seen with changes in temperature for sodium borosilicate glasses with lower concentrations of  $\text{B}_2\text{O}_3$ .

## REFERENCES

- [1] W. H. Zachariasen, *J. Amer. Chem. Soc.* **54** (1932), 3841.
- [2] R. L. Mozzi & B. E. Warren, *J. Appl. Cryst.* **3** (1970), 351.
- [3] J. Krogh-Moe, *J. Non-Cryst. Solids* **1** (1969), 269.
- [4] T. F. Young & R. P. Westerdahl, ARL 135, Office of Aerospace Research, U. S. Air Force (1961).
- [5] S. L. Strong, *Ph.D. Thesis* (M. I. T., 1965-66).
- [6] G. E. Walrafen, S. R. Samanta & P. N. Krishnan, *J. Chem. Phys.* **72** (1980), 113.
- [7] G. E. Walrafen, M. S. Hokambadi, P. N. Krishnan, S. Guha & R. G. Munro, *J. Chem. Phys.* **79** (1983), 3609.
- [8] A. K. Hassan, L. M. Torell and L. Borjesson & H. Doweidar, *Phys. Rev.* **45B** (1992), 12797.
- [9] A. K. Hassan, L. M. Torell & L. Borjesson, *J. Phys.* **IV** (1992) C2-265.
- [10] T. Furukawa & W. B. White, *J. Am. Ceram. Soc.* **54** (1981), 443.
- [11] I. N. Chakraborty & R. A. Condrate, Sr., *J. Non-Cryst. Solids* **81** (1986), 271.
- [12] I. N. Chakraborty & R. A. Condrate, Sr., *J. Mater. Sci. Letters* **5** (1986), 361.
- [13] T. Furukawa & W. B. White, *Phys. and Chem. of Glasses* **21** (1980), 85.
- [14] A. K. Jilavenkatesa & R. A. Condrate, Sr., *J. Can. Ceram. Soc.* **63** (1994) 215.

## X-RAY PHOTOELECTRON SPECTROSCOPY OF BORATE GLASSES

Syuji MATSUMOTO, Yoshinari MIURA, Chiaki MURAKAMI  
& Tokuro NANBA

*Department of Environmental Chemistry and Materials,  
Faculty of Environmental Science and Technology, Okayama  
University, 2-1-1, Tsushima-naka, Okayama-shi, 700, Japan*

The O1s photoelectron spectra in binary borate glasses show lower binding energy shift with increasing alkali or alkaline earth oxide content. For  $x\text{Li}_2\text{O}(100-x)\text{B}_2\text{O}_3$  the O1s peaks consist of only one component up to  $x=51.9$  mol%  $\text{Li}_2\text{O}$ . For  $x\text{Cs}_2\text{O}(100-x)\text{B}_2\text{O}_3$ , on the other hand, the O1s peak is separated into bridging oxygen (BO) and non-bridging oxygen (NBO) contributions above  $x=36.8$  mol%. The formation of tetrahedral  $[\text{BO}_4]^-$  units becomes more favourable compared with the formation of NBOs as the alkali ion size decrease. The O1s chemical shifts of core-level electrons were roughly interpreted by an empirical expression for the optical basicity of oxides, in which a linear correlation was found between the O1s chemical shift and the basicity. Clear photoelectron spectra near the valence level were obtained and compared with a molecular orbital calculation.

### 1. INTRODUCTION

It is well known that the introduction of alkali oxide into  $\text{B}_2\text{O}_3$  glass initially results in the presence in the glass structure of some tetrahedral  $\text{BO}_4$  units containing only bridging oxygens (BOs). The  $^{11}\text{B}$  nuclear magnetic resonance (NMR) studies by Bray *et al.* [1-3] have revealed the environments of boron atoms in several glasses as a function of composition. Their earlier studies suggested that non-bridging oxygens (NBOs) do not occur for alkali oxide concentration (or alkaline earth oxide concentration) less than about 33 mol%. However, later results from infrared reflection spectra and Raman studies [4-6], as well as NMR [7], show that as the alkali ionic radius increases there is a corresponding increase in the effective charge on the alkali cation. Thus, as the alkali ionic radius increases, there is a corresponding decrease in the minimum alkali concentration for which there is a significant number of NBOs.

X-ray photoelectron spectroscopy (XPS) is one of the most effective techniques for the characterization of the electronic structures of materials. Since the pioneering study by Brückner *et al.* [8], XPS has often been used to investigate glass structure. Kaneko *et al.* [9] have measured the O1s photoelectron spectra for binary alkali borate glasses by using a non-monochromatic  $\text{Mg-K}\alpha$  X-ray

source. They report that the O1s binding energies of alkali borate glasses decrease with increasing alkali oxide content. The determination of the NBO/BO ratio, however, was not performed successfully. In recent years, XPS devices equipped with a monochromatic Al-K $\alpha$  X-ray source were developed to obtain high resolution spectra without satellite peaks and background noises for conducting materials, such as metals and semiconductors. In the case of insulating materials like glasses, however, the charge-up problem is unavoidable even when a conventional neutralization method, such as a flood gun, is applied. The authors have discovered that a new charge control method using not only the flood gun but also a metal mesh screen gives clear spectra for non-conducting glasses [10]. For SiO<sub>2</sub> glass (Corning #7940), a sharp O1s peak with 1.4 eV full width at half maximum (FWHM) was observed. This novel charge control method has been applied to the XPS measurements for binary alkali and alkaline earth borate glasses reported here.

The variations in O1s photoelectron spectra with the content of alkali and alkaline earth oxides, such as chemical shift and peak splitting, are discussed based on an optical basicity concept proposed by Duffy & Ingram [11] and on glass structures.

## 2. EXPERIMENTAL

### 2.1. Glass Preparation

The samples used were the binary alkali and alkaline earth borate glasses in the systems R<sub>2</sub>O-B<sub>2</sub>O<sub>3</sub> (R=Li, Na, K, Rb and Cs) and MO-B<sub>2</sub>O<sub>3</sub> (M=Mg, Ca, Sr and Ba). The glasses were prepared from the mixtures of reagent grade alkali or alkaline earth carbonates and B<sub>2</sub>O<sub>3</sub>. Each batch was melted in a platinum crucible for 30 minutes in air at 1100–1200°C and quenched between two stainless steel plates. In this paper, the chemical analyzed compositions were used for the discussions.

### 2.2. XPS Measurement

A Fisons Instruments "S-Probe ESCA" (SSX100S) was employed for the XPS measurements. Glass samples were broken under ultra high vacuum ( $\approx 7 \times 10^{-8}$  Pa) and the fresh surface was irradiated by a monochromatic Al-K $\alpha$  X-ray (1486.6 eV) beam. The surface charge up was controlled by the combined use of a low energy electron flux and an electrically grounded Ni mesh screen positioned about 1mm above the sample surface [10, 12]. The photoelectron spectrometer was calibrated by using the Au4f<sub>7/2</sub> binding energy (83.96 eV) for the etched surface of an Au-metal reference sample; The measured C1s binding energy for hydrocarbon impurities accumulated on the Au-metal surface in the vacuum was calibrated as 284.6 eV. Since the C1s peak was hardly detected for the fresh glass surface just after being fractured in a vacuum, the correction of the binding energies of various ions in the glass were made by referencing the measured C1s binding energy for hydrocarbon impurities accumulated on the glass surface after a few hours in a vacuum as 284.6 eV.

### 2.3. Optical Basicity

Macroscopic optical basicity,  $\Lambda$ , was calculated from the following equation [11], which represents the mean (bulk) basicity of a matrix

$$\Lambda = \sum_i \frac{z_i r_i}{2\gamma_i} \quad (1)$$

where  $z_i$  is the oxidation number of the  $i$ th cation,  $r_i$  is the ionic ratio of the  $i$ th cation with respect to the total number of oxide ions and  $\gamma_i$  is the basicity moderating parameter,  $\gamma_i = 1.36(c_i - 0.26)$ , where  $\chi_i$  is the Pauling electronegativity.

Microscopic optical basicity,  $\lambda$  [11], which gives the basicity of an individual oxide in an oxyanion group, was also calculated from the equation

$$\lambda_j = 1 - \frac{z_j}{2} r'_j \left( 1 - \frac{1}{\gamma_j} \right) \quad (2)$$

where  $r'_j$  is the ionic ratio in an oxyanion group.

## 3. RESULTS AND DISCUSSION

### 3.1. The O1s Core-level Photoelectron Spectra

Fig. 1 shows the O1s photoelectron spectra of  $x\text{Li}_2\text{O}(100-x)\text{B}_2\text{O}_3$ ,  $x\text{Cs}_2\text{O}(100-x)\text{B}_2\text{O}_3$  and  $x\text{BaO}(100-x)\text{B}_2\text{O}_3$  glasses obtained by XPS measurements. No satellite peaks appear in any of the spectra. For the  $x\text{Li}_2\text{O}(100-x)\text{B}_2\text{O}_3$  system, the O1s spectra consist of only one component up to  $x=51.9$  mol%. For  $x\text{Cs}_2\text{O}(100-x)\text{B}_2\text{O}_3$  and  $x\text{BaO}(100-x)\text{B}_2\text{O}_3$  system, on the other hand, the O1s spectra were successfully separated into two components attributed to bridging oxygens (BOs) and non-bridging oxygens (NBOs) above  $x \geq 36.8$  and  $x \geq 42.7$  mol%, respectively. Table 1 shows the NBO/BO ratio calculated by O1s

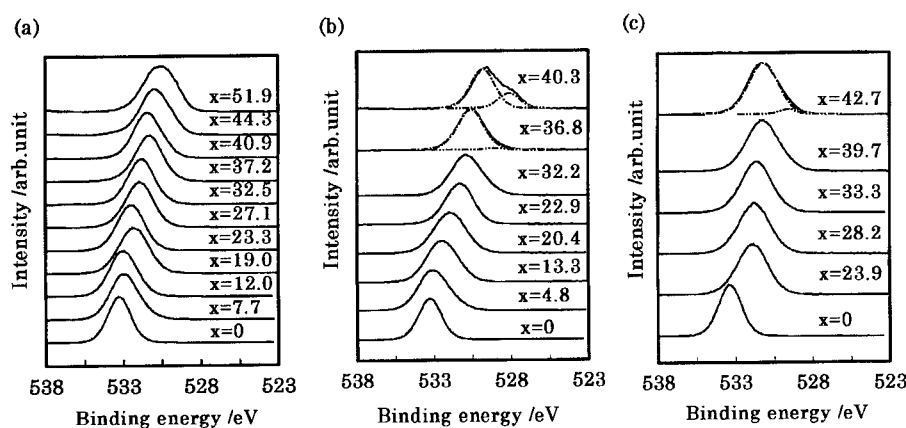


Fig. 1. O1s photoelectron spectra for the glasses, (a)  $x\text{Li}_2\text{O}(100-x)\text{B}_2\text{O}_3$ , (b)  $x\text{Cs}_2\text{O}(100-x)\text{B}_2\text{O}_3$  and (c)  $x\text{BaO}(100-x)\text{B}_2\text{O}_3$ .

**Table 1**  
NBO/BO Ratio of Na<sub>2</sub>O-, K<sub>2</sub>O-, Rb<sub>2</sub>O-, Cs<sub>2</sub>O- and BaO-B<sub>2</sub>O<sub>3</sub>.

Glass	Peak Area of BO/% (± 2 %)	Peak Area of NBO/% (± 2 %)
41.3Na <sub>2</sub> O58.7B <sub>2</sub> O <sub>3</sub>	85	15
34.3K <sub>2</sub> O65.7B <sub>2</sub> O <sub>3</sub>	92	8
32.8Rb <sub>2</sub> O67.2B <sub>2</sub> O <sub>3</sub>	96	4
37.7Rb <sub>2</sub> O62.3B <sub>2</sub> O <sub>3</sub>	94	6
39.5Rb <sub>2</sub> O60.5B <sub>2</sub> O <sub>3</sub>	88	12
36.7Cs <sub>2</sub> O63.3B <sub>2</sub> O <sub>3</sub>	97	3
38.2Cs <sub>2</sub> O61.8B <sub>2</sub> O <sub>3</sub>	91	9
40.1Cs <sub>2</sub> O59.9B <sub>2</sub> O <sub>3</sub>	75	25
42.7BaO57.3B <sub>2</sub> O <sub>3</sub>	93	7

peak deconvolution for some binary alkali and alkaline earth borate glasses with higher modifier oxide concentration. The small variation in glass composition leads to large change in the NBO ratio because of the steep generation in NBOs in the region of high modifier oxide concentration. It is well known that the addition of modifier oxide to B<sub>2</sub>O<sub>3</sub> glass produces the tetrahedral [BO<sub>4/2</sub>]<sup>-</sup> unit and/or NBO. Thus, it is expected that there are three types of BOs: O<sub>2/2</sub>B<sup>(3)</sup>-O-B<sup>(3)</sup>O<sub>2/2</sub>, O<sub>2/2</sub>B<sup>(3)</sup>-O-B<sup>(4)</sup>O<sub>3/2</sub> and O<sub>3/2</sub>B<sup>(4)</sup>-O-B<sup>(4)</sup>O<sub>3/2</sub>. However, it is not appropriate to separate the BOIs (OIs of bridging oxygen) spectra into the components attributed to them because a single Gaussian-Lorentzian function completely describes each observed BOIs peak.

Fig. 2 shows the OIs spectra for 40R<sub>2</sub>O60B<sub>2</sub>O<sub>3</sub> (R=Li, Na, Rb and Cs) and 40MO60B<sub>2</sub>O<sub>3</sub> (M=Mg, Ca, Sr and Ba) glasses (in batch composition). For Cs<sub>2</sub>O-, Rb<sub>2</sub>O-, Na<sub>2</sub>O- and BaO-B<sub>2</sub>O<sub>3</sub>, the spectra were separated into two components attributed to BOs and NBOs. On the other hand, for Li<sub>2</sub>O-, MgO-, CaO- and SrO-B<sub>2</sub>O<sub>3</sub> glasses, each OIs spectrum consisted of only one component. For 40R<sub>2</sub>O(or MO)60B<sub>2</sub>O<sub>3</sub> glasses the ratio of NBO/BO decreased as the modifier cation size decreased. This indicates that the formation of [BO<sub>4/2</sub>]<sup>-</sup> tetrahedral units becomes more significant compared to the formation of NBOs as the cation field strength of the modifier ion increases. Chrysikos *et al.* [5] have discussed how the nature of the alkali cation influences the equilibrium between the formation of [BO<sub>4/2</sub>]<sup>-</sup> and of NBO. The competition between the [BO<sub>4/2</sub>]<sup>-</sup> tetrahedron and the BO<sub>2/2</sub>O<sup>-</sup> triangle depends on the acidity of the counter cation [5]. With decreasing cation field strength, the cation becomes a softer Lewis acid. Thus, with increasing content of soft-acid cation such as Cs<sup>+</sup>, the soft cation favours the formation of BO<sub>2/2</sub>O<sup>-</sup> which is a soft-base, and hence the NBO peak appeared in the OIs spectrum for Cs<sub>2</sub>O-B<sub>2</sub>O<sub>3</sub> glass at the composition with Cs<sub>2</sub>O≈40mol%. However, a hard-acid cation such as Li<sup>+</sup> induces the formation of the [BO<sub>4/2</sub>]<sup>-</sup> tetrahedron which is a harder-base than the BO<sub>2/2</sub>O<sup>-</sup> triangle, and hence the OIs spectrum consists of only one component for Li<sub>2</sub>O-B<sub>2</sub>O<sub>3</sub> glasses.

It is well known that the OIs chemical shift toward lower binding energy implies an increase in the electron charge density of the oxide ions. Therefore, it is

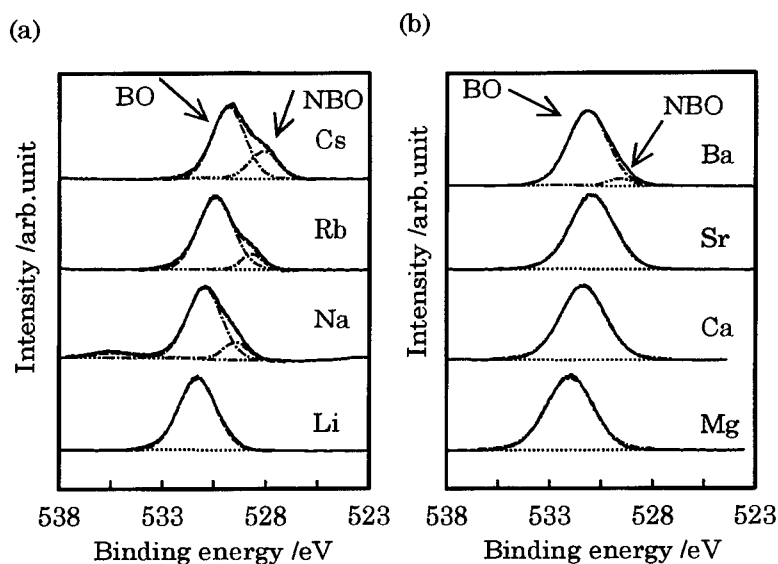


Fig. 2. O1s photoelectron spectra for the glasses, (a)  $40R_2O60B_2O_3$  ( $R=Li, Na, Rb$  and  $Cs$ ), (b)  $40MO60B_2O_3$  ( $M=Mg, Ca, Sr$  and  $Ba$ ) in batch compositions.

expected that a quantitative relationship between the degree of Lewis basicity of the oxide ions and the O1s chemical shift of the ligand oxide ions can be found. Kawazoe [13] has successfully applied the basicity concept of oxides to explain chemical shifts in X-ray emission in various oxide glasses, in which an empirical expression of optical basicity proposed by Duffy & Ingram [11] was used.

Variations in O1s photo-electron spectra with the content of the alkali and alkaline earth oxides, such as chemical shift, were also estimated based on optical basicity. Fig. 3 shows the correlation between the O1s binding energy

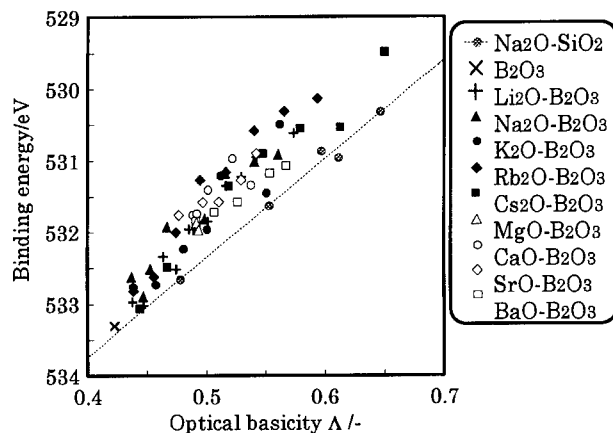


Fig. 3. Relation between O1s binding energy and macroscopic optical basicity  $\Lambda$  for binary alkali and alkaline earth borate glasses. O1s values for sodium silicate glasses are also plotted.

**Table 2**  
Microscopic Optical Basicity  $\lambda$  Given by Eq. 2 for Individual Oxides in  
Borate Glass Networks.

Structural unit	b1 B(3)*-O-B(3)	b2 B(3)-O-B(4)	b3 B(4)-O-B(4)	b4 B(3)-O	b5 B(4)-O
$f$	2/3	1/3+1/4	2/4	1/3	1/4
$\lambda$	0.42	0.50	0.57	0.71	0.78

\* Numbers in parentheses represent coordination numbers

of the binary alkali and alkaline earth borate glasses and the calculated macroscopic optical basicity  $\Lambda$ . In this figure, O1s values for sodium silicate glasses [10] were also plotted for reference. The O1s binding energy decreases with increasing  $\Lambda$ . The shift shows a linear correlation of O1s binding energy with  $\Lambda$  in sodium silicate glasses, but binary alkali and alkaline earth borate glasses show a non-linear correlation, in which a large decrease in the O1s binding energy can be seen at  $\Lambda \approx 0.5$ .

The non-linear chemical shift for borate glasses cannot be explained by the macroscopic optical basicity  $\Lambda$ . Since  $\Lambda$  is directly calculated from the glass composition, it does not reflect the local structure in the matrix. Duffy & Ingram [11] have given a convenient concept of microscopic optical basicity,  $\lambda$ , which gives the basicity of individual oxide ions (eq. 2). Thus  $\lambda$  was calculated for some typical structural units in borate glasses (Table 2). Mean microscopic optical basicity,  $\lambda_m$ , was calculated using the following equation

$$\lambda_m = \sum_j c_j \lambda_j \quad (3)$$

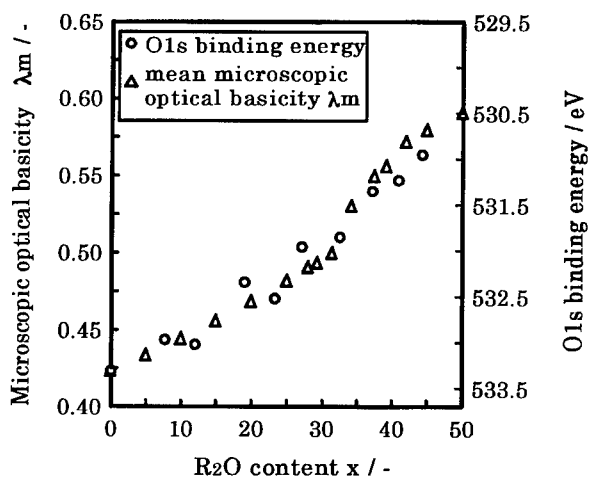


**Fig. 4.** Variation in the microscopic optical basicity,  $\lambda_m$ , and experimental O1s binding energy against alkali oxide content  $x$  for  $x\text{Li}_2\text{O} \cdot (100-x)\text{B}_2\text{O}_3$  glasses.



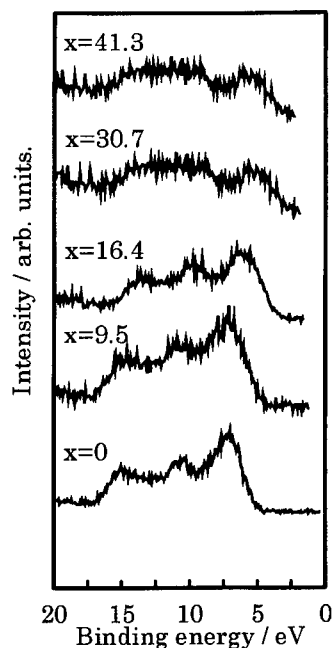


Fig. 5. Near valence level photo-electron spectra for  $x\text{Na}_2\text{O}(100-x)\text{B}_2\text{O}_3$  glasses.

where  $c_j$  and  $\lambda_j$  are the concentration and the microscopic optical basicity of the  $j$ th oxygen, respectively. In this calculation, the structural units, b1, b2 and b4 in Table 2, were assumed to be present in borate glass. The concentrations of the structural units were determined from Ref. [1]. Figure 4 shows the variation in the calculated optical basicity  $\lambda_m$  with the experimental O1s binding energy.  $\lambda_m$  shows a good correlation with the O1s binding energy. An improvement in the best fit above  $x > 30$  in the  $x\text{Li}_2\text{O} \cdot (100-x)\text{B}_2\text{O}_3$  glass would be achieved by considering the presence of the b3 unit in the diborate group. The concentration of such unit, however, could not be estimated. This result suggests that the microscopic optical basicity, which is given as a function of the glass structure, is better suited to express the chemical shift in the O1s binding energy.

### 3.2. The Valence Level Photoelectron Spectra

Clear photoelectron spectra near the valence level were obtained. Fig. 5 shows the valence level photoelectron spectra for  $x\text{Na}_2\text{O}(100-x)\text{B}_2\text{O}_3$  glasses. For  $\text{B}_2\text{O}_3$  glass, the distinguishable three peaks near 6, 11 and 15 eV are observed. With increasing  $\text{Na}_2\text{O}$  content the peaks become gradually obscure, eventually, the peaks around 11 and 15 eV change to a broad plateau above  $x \geq 30.7$ . A molecular orbital calculation was applied for  $\text{B}_2\text{O}_3$  glass by using the model cluster composed of only boroxol ring. The peaks near 6, 11 and 15 eV were assigned to O2p lone pair electrons, O2p–B2p p-bonding and O2p–B2s (or B2p) s-bonding electrons, respectively, from the DV- $X\alpha$  cluster method [14] which gives a reasonable explana-

tion for the measured valence band photoemission. However, the computer simulation of the valence level photoelectron spectra for other alkali containing glasses could not succeed for the model cluster composed of only boroxol ring. It is necessary that the molecular orbital calculation is applied by using the new model cluster containing both several  $\text{BO}_3$  and  $\text{BO}_4$  units. The identification of electronic structure in the valence level of borate glass is still open for discussion. The highest occupied molecular orbital (HOMO) of borate glass, in general, is made up of O2p lone pair electrons. Therefore an analysis of their binding energies will give important hints for the characterization of optical properties.

#### 4. CONCLUSIONS

XPS spectra were measured for binary alkali and alkaline earth borate glasses. The charge control method using an Ni-metal mesh screen gave clear spectra with no satellite peaks. With increasing alkali and alkaline earth oxide content, the O1s photoelectron spectra in binary borate glasses show a lower binding energy shift. The O1s peaks were successfully separated into two components assigned to bridging and non-bridging oxygens for glasses with either a high concentration of network-modifier or with a "soft" cationic acid as the network-modifier. The formation of  $[\text{BO}_{4/2}]^-$  tetrahedral units becomes more favourable compared to the formation of NBOs as the modifier cation size decreases. An empirical expression for optical basicity given by Duffy and Ingram was applied to explain the experimental results. It was found that the optical basicity concept was able to describe the XPS chemical shifts. Clear photoelectron spectra near the valence level were obtained and compared with a molecular orbital calculation. The calculation gives a reasonable explanation for the measured valence band of  $\text{B}_2\text{O}_3$  glass.

#### ACKNOWLEDGEMENT

The authors would like to thank Mr. K.Nishida in the graduate school of Okayama University for the XPS measurement and helpful assistance.

#### REFERENCES

- [1] P.J. Bray, *Phys. Chem. Glasses* **19** (1978), 52.
- [2] G.E. Jellison & P.J. Bray, *J. Non-Cryst. Solids* **29** (1978), 187.
- [3] P.J. Bray, *J. Non-Cryst. Solids* **95 & 96** (1987), 45.
- [4] E.I. Kamitsos, M.A. Karakassides & G.D. Chryssikos, *Phys. Chem. Glasses* **30** (1989), 229.
- [5] G.D. Chryssikos, E.I. Kamitsos & M.A. Karakassides, *Phys. Chem. Glasses* **31** (1990), 109.
- [6] E.I. Kamitsos, A.T. Patsis & G.D. Chryssikos, *J. Non-Cryst. Solids* **152** (1993), 246.
- [7] J. Zhong & P.J. Bray, *J. Non-Cryst. Solids* **111** (1989), 67.
- [8] R. Brückner, H.U. Chun & H. Goretzki, *Glastechn. Ber.* **51** (1978), 1.
- [9] Y. Kaneko, H. Nakamura, M. Yamane & Y. Suginoara, *Yogyo-Kyokai-Shi* **90** (1982), 9.
- [10] S. Matsumoto, Y. Miura, T. Nanba & A. Osaka, *Proc. XVII International Congress on Glass* **3** (1995), 72.
- [11] J.A. Duffy & M.D. Ingram, *J. Non-Cryst. Solids* **21** (1976), 373.
- [12] C.E. Bryson III, *Surface Science* **189&190** (1987), 50.
- [13] H. Kawazoe, *J. Non-Cryst. Solids* **42** (1980), 281.
- [14] H. Adachi, M. Tsukada & C. Satoko, *J. Phys.Soc. Jpn.* **45** (1978), 875.

## VELOCITY OF SOUND AND ELASTIC PROPERTIES OF ALKALI BORATE GLASSES

Masao KODAMA

*Department of Industrial Chemistry, Kumamoto Institute of  
Technology, Ikeda, Kumamoto 860, Japan*

and

Seiji KOJIMA

*Institute of Applied Physics, University of Tsukuba, Tsukuba,  
Ibaraki 305, Japan*

Ultrasonic velocities of both longitudinal and transverse waves in alkali borate glasses have been measured by the pulse-echo overlap method at a frequency of 10 MHz and a temperature of 298 K over the bulk-glass formation range of each binary system  $x_2\text{M}_2\text{O} \cdot (1-x_2)\text{B}_2\text{O}_3$ , where M stands for Li, Na, K, Rb and Cs, and  $x_2$  denotes the mole fraction of  $\text{M}_2\text{O}$ . Each of the longitudinal and transverse velocities plotted against  $x_2$  shows the following characteristics: the velocity in lithium borate glasses increases monotonously with increasing  $x_2$ ; the velocity in sodium and potassium borate glasses shows a single maximum; the velocity in rubidium and caesium borate glasses shows a maximum, a minimum and another maximum in succession. Elastic properties for the extremes of lithium borate glasses and caesium borate glasses are analysed in terms of the elastic constants of the three structural units defined as  $\text{B}\text{O}_3$ ,  $\text{M}^+\text{B}\text{O}_2\text{O}^-$  and  $\text{M}^+\text{B}\text{O}_4^-$ , where  $\text{O}$  represents a bridging oxygen and  $\text{O}^-$  a nonbridging oxygen. The way in which these structural units change as a function of composition is discussed.

### 1. INTRODUCTION

The structure and properties of alkali borate glasses are of special interest, since their properties plotted against their respective compositions often exhibit maxima or minima termed "borate anomalies" [1]. The structure of alkali borate glasses is dependent not only upon the content of alkali metal ions but also upon the difference in the alkali metal ions themselves [2,3]. Since ultrasonic velocity is sensitive to many types of structural changes, it would be of great interest to study the velocity of sound in alkali borate glasses. The velocity of sound in every binary system of lithium, sodium, potassium, rubidium and caesium borate glasses has been measured [4-8]: (i) the velocity in lithium borate glasses increases monotonously with an increase in the content of lithium oxide, (ii) the velocity in sodium and potassium borate glasses shows

a single maximum, (iii) the velocity in rubidium and caesium borate glasses exhibits a maximum, a minimum and another maximum in succession. Thus, the velocity of sound is dependent upon the content and the kind of alkali metal ions. The relationship between the velocity of sound and the structure is analysed in terms of the elastic constants of three structural units with special reference to lithium borate glasses and caesium borate glasses. From the elastic constants of the structural units, the fraction,  $N_4$ , of boron atoms in tetrahedral coordination has been calculated as a function of composition to conclude that the change in the amount of each structural unit causes the anomalous behaviour of ultrasonic velocity in caesium borate glasses.

## 2. EXPERIMENTAL

A series of glasses was prepared at regular intervals of 0.02 mole fraction through the bulk-glass formation range of each binary system  $x_2M_2O \cdot (1-x_2)B_2O_3$ , where M represents Li, Na, K, Rb and Cs, and  $x_2$  denotes the mole fraction of  $M_2O$ . All the glasses were prepared with high homogeneity and without strains or bubbles in order that they might transmit ultrasound satisfactorily.

Alkali metal hydroxide MOH and boric acid  $H_3BO_3$  were used as the starting materials for  $M_2O$  and for  $B_2O_3$ , respectively. With the aim of preparing glasses with high homogeneity, the starting materials were initially made to react in an aqueous solution. Amounts of the starting materials calculated to yield 20 to 34 g in the melts were dissolved in a beaker made of polytetrafluoroethylene by adding distilled water. The water of the solution was evaporated in a dry box to obtain a chemically reacted powder.

The powder was fused in a 20 cm<sup>3</sup> platinum crucible at temperatures from 900 to 1300°C for about 4 h by heating with an SiC resistance electric furnace. The liquid was then poured into a cylindrical graphite mould, 15 mm in diameter and 30 mm deep, which had been preheated at 300°C in an electric muffle furnace. Subsequently, the cast glass in the mould was held at 300°C for 1 h, then cooled at a rate of 1 K/min to room temperature while passing dry nitrogen through the muffle furnace. The residual liquid was poured onto an aluminium plate and later used for chemical analysis and for differential thermal analysis (DTA). Each cast glass was annealed at the glass transition temperature determined by DTA [8]. The actual compositions of all of the prepared alkali borate glasses were determined by a potentiometric titration by means of the mannitol method [9]. The density of each annealed glass was measured at 298 K by a hydrostatic weighing method using a silicon single crystal as the density standard [10].

Each annealed glass was ground and polished to give a pair of end faces that were flat and parallel. Inspection with a strain viewer showed that all specimens were transparent and free from strain. The ultrasonic travel time was measured at a frequency of 10 MHz and at a temperature of 298 K by means of the pulse-echo overlap method [11]. The apparatus used was constructed by one of the present authors and the electric circuit was described in a previous paper [12]. X-cut and Y-cut quartz transducers resonating at a fun-

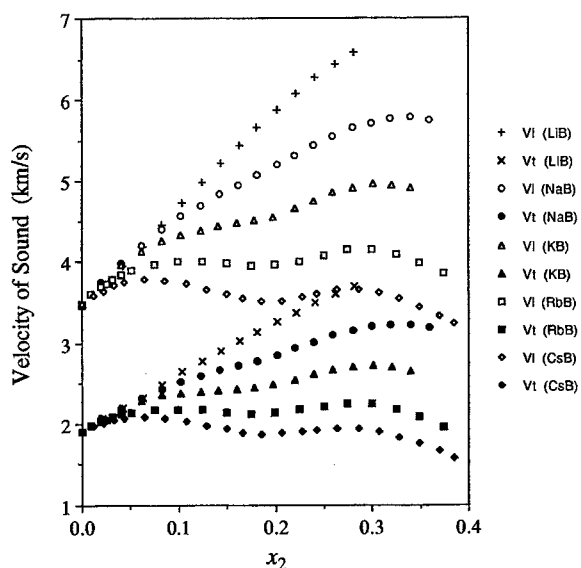


Fig. 1. Velocity of sound in alkali borate glasses plotted against  $x_2$ . The upper five curves and the lower five curves represent the longitudinal waves and the transverse waves, respectively. The meanings of the symbols and the abbreviations are, for example, + Vl (LiB) denotes the velocity of longitudinal wave in lithium borate glasses, ♦ Vt (CsB) denotes the velocity of transverse wave in caesium borate glasses.

damental frequency of 10 MHz were used for the longitudinal wave and for the transverse wave, respectively. The transducer was bonded to the specimen on one of the two parallel faces with phenyl benzoate [13] and used for both generation and detection of ultrasound. In order to measure the ultrasonic travel time within an error of 0.02% for round trips greater than 5  $\mu$ s, adjacent two echoes were overlapped according to the McSkimin criterion [14,15].

### 3. RESULTS AND DISCUSSION

Figure 1 shows the longitudinal velocity,  $V_l$ , and the transverse velocity,  $V_t$ , of alkali borate glasses plotted against  $x_2$ . The relationship between the elasticity and the structure of alkali borate glasses is analysed in the following in terms of the three structural units defined as  $B\text{O}_3$ ,  $M^+B\text{O}_2\text{O}^-$  and  $M^+B\text{O}_4^-$ , where  $\text{O}$  represents a bridging oxygen and  $\text{O}^-$  a nonbridging oxygen, on the assumption that these structural units exhibit their inherent elastic properties and hence have their respective elastic constants. The elastic constants of the structural units in alkali borate glasses have been defined in previous papers [6-8] on the basis of a thermodynamic equation of a deformed body so that only the final formulations are given in the following.

For simplicity, we write the three structural units as  $B\text{O}_3 \equiv a$ ,  $M^+B\text{O}_2\text{O}^- \equiv b$  and  $M^+B\text{O}_4^- \equiv c$ . Let  $M_{M_2O}$  and  $M_{B_2O_3}$  be the molar masses of the component  $M_2O$  and the component  $B_2O_3$ , respectively. Then the molar mass,  $M_s$ , which

always contains unit amount of the structural units  $a$ ,  $b$  and  $c$  is defined as

$$M_s = \frac{1}{2(1-x_2)} \{x_2 M_{M_2O} + (1-x_2) M_{B_2O_3}\} \\ = \left(1 - \frac{x_2}{1-x_2}\right) M_a + \left(\frac{x_2}{1-x_2} - N_4\right) M_b + N_4 M_c \quad (1)$$

where  $M_a$ ,  $M_b$  and  $M_c$  are the molar masses of the structural units  $a$ ,  $b$  and  $c$ , respectively, and  $N_4$  is the fraction of boron atoms in tetrahedral coordination. The elastic constants  $E_a$ ,  $E_b$  and  $E_c$  of the structural units  $a$ ,  $b$  and  $c$  are defined, respectively, as the second order derivatives of the molar internal energies of these units with respect to the Lagrangian strain. Finally, the required equation is written as

$$M_s V^2 = \left(1 - \frac{x_2}{1-x_2}\right) E_a + \left(\frac{x_2}{1-x_2} - N_4\right) E_b + N_4 E_c \quad (2)$$

where  $V$  is the velocity of sound.

The elastic property of alkali borate glasses has been analysed on the basis of Eq. (2). In the following, the analyses for the extremes of lithium borate glasses and caesium borate glasses are shown.

### 3.1. Lithium Borate Glasses

An NMR study on lithium borate glasses by Jellison, Feller & Bray [16] showed that  $N_4 = x_2/(1-x_2)$  for  $0 \leq x_2 < 0.28$  and  $N_4 < x_2/(1-x_2)$  for  $x_2 > 0.28$ . These findings were also ascertained by Kamitsos & Chryssikos from infrared spectroscopy [2]. We can therefore assume that the relation of  $N_4 = x_2/(1-x_2)$  holds in the composition range  $0 \leq x_2 < 0.28$  and thus in the range  $0 \leq x_2/(1-x_2) < 0.39$ . Substitution of  $N_4 = x_2/(1-x_2)$  into Eq. (2) give

$$M_s V^2 = \left(1 - \frac{x_2}{1-x_2}\right) E_a + \frac{x_2}{1-x_2} E_c \quad (3)$$

so that a plot of  $M_s V^2$  against  $x_2/(1-x_2)$  should be a single straight line in the composition range  $0 \leq x_2/(1-x_2) < 0.39$ .

**Table 1**  
Elastic Constants of Three Structural Units

	Lithium borate glasses		Caesium borate glasses	
	Longitudinal	Shear	Longitudinal	Shear
$E_a$ (MJ/mol)	0.415	0.125	0.43	0.13
$E_b$ (MJ/mol)	—	—	-0.04	-0.27
$E_c$ (MJ/mol)	3.96	1.25	3.9	1.2

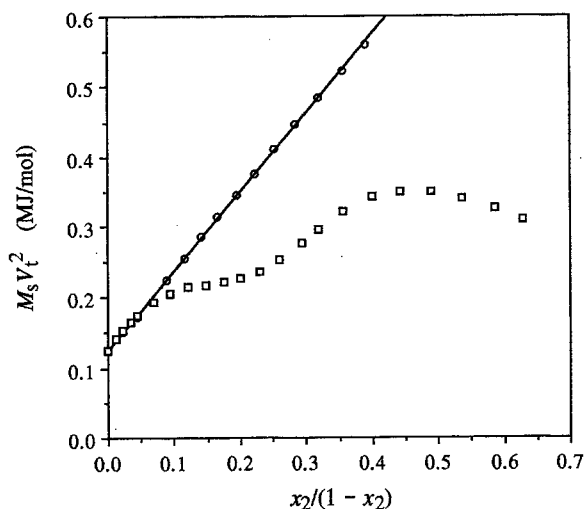
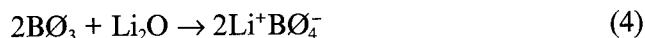


Fig. 2. The plots of  $M_s V_t^2$  against  $x_2/(1-x_2)$  for lithium borate glasses (O) and for caesium borate glasses (□). The least-squares line through the lithium borate glass data points is also shown.

Figure 2 shows a plot of the shear elastic constant,  $M_s V_t^2$ , against  $x_2/(1-x_2)$  for lithium borate glasses. The plot can be represented by a straight line, indicating that the relation of  $N_4 = x_2/(1-x_2)$  holds. A plot of the longitudinal elastic constant,  $M_s V_l^2$ , against  $x_2/(1-x_2)$  shows almost the same behaviour. Thus, it can be ascertained from the present analysis too that the structural unit  $a$  is converted only into the structural unit  $c$  in the composition range  $0 \leq x_2 < 0.28$  by the reaction



Such a simple reaction occurs only in lithium borate glasses. The values of  $E_a$  and  $E_c$  calculated from Eq. (3) are listed in Table 1.

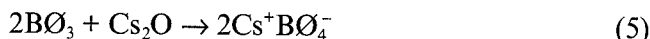
### 3.2. Caesium Borate Glasses

Figure 2 also shows a plot of the shear elastic constant,  $M_s V_t^2$ , against  $x_2/(1-x_2)$  for caesium borate glasses; a plot of the longitudinal elastic constant,  $M_s V_l^2$ , against  $x_2/(1-x_2)$  has almost the same characteristic. The plot of  $M_s V^2$  against  $x_2/(1-x_2)$  is analysed by dividing it into the following four ranges:

- (i) The first composition range  $0 < x_2 < 0.065$  or  $0 < x_2/(1-x_2) < 0.070$  in which the velocity of sound increases with increasing  $x_2$ .
- (ii) The second composition range  $0.065 < x_2 < 0.19$  or  $0.070 < x_2/(1-x_2) < 0.235$  in which the velocity of sound decreases with increasing  $x_2$ .
- (iii) The third composition range  $0.19 < x_2 < 0.275$  or  $0.235 < x_2/(1-x_2) < 0.38$  in which the velocity of sound again increases with increasing  $x_2$ .
- (iv) The fourth composition range  $0.275 < x_2 < 0.39$  or  $0.38 < x_2/(1-x_2) < 0.64$  in which the velocity of sound again decreases with increasing  $x_2$ .

The initial slope of  $M_s V^2$  against  $x_2/(1-x_2)$  for caesium borate glasses is in

close agreement with the slope for lithium borate glasses. This coincidence in the slopes indicates that the structural change in the first composition range is identical to that for lithium borate glasses and thus this initial slope for caesium borate glasses can be analysed on the basis of Eq. (3). Table 1 shows that the values of  $E_a$  and  $E_c$  calculated in this way for caesium borate glasses are in close agreement with the values for lithium borate glasses both for longitudinal and transverse waves. Thus, in the first composition range, the structural unit  $a$  is converted only into the structural unit  $c$  by the reaction



For  $x_2 > 0.065$  and hence  $x_2/(1-x_2) > 0.070$ , the plot of  $M_s V^2$  against  $x_2/(1-x_2)$  for caesium borate glasses deviates from the plot for lithium borate glasses. If the structural unit  $b$  forms, then the slope of the plot of  $M_s V^2$  against  $x_2/(1-x_2)$  should decrease since the structural unit  $b$  destroys the glass network to decrease the rigidity of the glass. The decrease in slope above the composition of  $x_2/(1-x_2) = 0.070$  indicates that the structural unit  $b$  now forms so that the relation of  $M_s V^2$  as a function of  $x_2/(1-x_2)$  should be analysed on the basis of Eq. (2). In order to calculate the value of  $E_b$ , it is necessary to use one known value of  $N_4$  at a given composition. For this purpose, we use the value of  $N_4 = 0.28$  at a composition of  $x_2/(1-x_2) = 0.50$  determined from NMR spectroscopy by Zhong & Bray [17]. The value of  $M_s V^2$  at this composition can be calculated by fitting a least squares parabola to nearby points. In Table 1, the value of  $E_b$  calculated from Eq. (2) at the point of  $x_2/(1-x_2) = 0.50$  is shown. It seems unusual that  $E_b$  takes a negative value. However, the negative value is permissible since the structural unit  $b$  does not arise alone but coexists always with the structural unit  $c$ . Since  $E_b$  is negative, we conclude that the structural unit  $b$  decreases the rigidity of the glass, which can be attributed to the fact that the structural unit  $b$  acts to break down the covalent bonds of the glass network.

By rewriting Eq. (2) in the form

$$N_4 = \frac{1}{E_c - E_b} \left\{ M_s V^2 - \left( 1 - \frac{x_2}{1-x_2} \right) E_a - \frac{x_2}{1-x_2} E_b \right\} \quad (6)$$

we can calculate  $N_4$  as a function of  $x_2/(1-x_2)$  from the values of  $E_a$ ,  $E_b$  and  $E_c$  given in Table 1. Figure 3 shows the plot of  $N_4$  as a function of  $x_2/(1-x_2)$  calculated from the values of transverse sound velocities. Three points of  $N_4$  determined from the area under the NMR absorption curves by Zhong & Bray [17] are also shown in Fig. 3, where the point at  $x_2/(1-x_2) = 0.50$  is used for the calculation of  $E_b$ . We see that the trend of  $N_4$  calculated from the ultrasonic velocity is consistent, at least qualitatively, with the trend of  $N_4$  measured by NMR spectroscopy. Since the quantity,  $x_2/(1-x_2) - N_4$ , indicates the fraction of the structural unit  $b$  with one nonbridging oxygen, the calculated behaviour of  $N_4$  as a function of  $x_2/(1-x_2)$  can be summarized in terms of the three structural units as follows:

(i) In the first composition range, the structural change can be described by



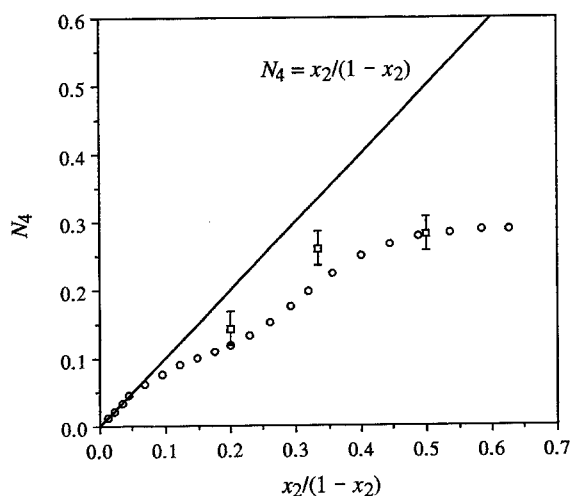
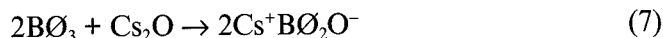


Fig. 3. The plot of  $N_4$  against  $x_2/(1-x_2)$  for caesium borate glasses. O denotes  $N_4$  calculated from Eq. (6) with values for the transverse wave; □ denotes  $N_4$  determined from NMR spectroscopy by Zhong & Bray [17]. The line  $N_4 = x_2/(1-x_2)$  is also shown.

Eq. (5) and no nonbridging oxygen forms.

(ii) In the second composition range, the formation of the structural unit  $b$  expressed by



is predominant over the formation of the structural unit  $c$  expressed by Eq. (5).

(iii) In the third composition range, the formation of the structural unit  $c$  expressed by Eq. (5) is predominant over the formation of the structural unit  $b$  expressed by Eq. (7).

(iv) In the fourth composition range, the formation of the structural unit  $b$  expressed by Eq. (7) becomes gradually predominant over the formation of the structural unit  $c$  expressed by Eq. (5) and further the isomerization



takes place.

A Raman study by Kamitsos *et al* [18,19] on caesium borate glasses has shown, first, that nonbridging oxygens begin to form at a composition less than  $x_2=0.10$  and, second, that the chain type metaborate group forms for compositions of  $x_2=0.10, 0.14$  and  $0.17$  while the ring type metaborate group forms for compositions of  $x_2 \geq 0.30$ . The present study has revealed that nonbridging oxygens begin to form at  $x_2=0.065$ , which is in agreement with the findings of Kamitsos *et al*. We see also from the study by Kamitsos *et al* that nonbridging oxygens in the second composition range are present in the form of the chain type metaborate group while nonbridging oxygens in the fourth composition range are present in the form of the ring type metaborate group.

We see from Table 1 that the value of  $E_c$  is about ten times the value of  $E_a$  for both the longitudinal and transverse waves. This difference is caused partly by the fact that structural unit  $c$  forms four covalent bonds whereas structural unit  $a$  forms three covalent bonds. The effect of the difference in the number of these covalent bonds on the ratio  $E_c/E_a$  can be evaluated from the Phillips–Thorpe rigidity percolation theory [20–22]. On the basis of this percolation theory, He and Thorpe [23] performed numerical simulations for the elastic stiffness constants  $c_{11}$  and  $c_{44}$  as a function of the average number,  $\langle r \rangle$ , of covalent bonds per atom and found that the dependences of  $c_{11}$  and  $c_{44}$  on  $\langle r \rangle$  could both be represented approximately by  $(\langle r \rangle - r_p)^{1.5}$ ,  $r_p = 2.4$  being the percolation threshold; the values of  $c_{11}$  and  $c_{44}$  at  $\langle r \rangle = 4.0$  were both five times those at  $\langle r \rangle = 3.0$ . Thus we can estimate the value of  $E_c/E_a$  to be five if the effect of the covalent bonds alone is taken into account, which is however insufficient to explain the fact that the actual value of  $E_c/E_a$  is about ten. Since the structural unit  $c$  ( $\equiv M^+B\bar{O}_4^-$ ,  $M$  stands for the respective alkali) forms both covalent bonds and ionic bonds, the effect of ionic bonds on  $E_c$  should also be included. We may attribute the residual value of  $E_c/E_a \approx 5$  to the effect of ionic bonds. However, the exact calculation is difficult at present, since the long-range interaction caused by Coulomb's force should be evaluated.

We see also from the study by He & Thorpe that the rigidity arises only if  $\langle r \rangle$  is greater than 2.4. Since the structural unit  $b$  forms two covalent bonds, the presence of the structural unit  $b$  acts negatively on the rigidity, leading to a negative value of  $E_b$ .

## REFERENCES

- [1] J. E. Shelby, *J. Am. Ceram. Soc.* **66** (1983), 225.
- [2] E. I. Kamitsos & G. D. Chryssikos, *J. Molec. Struct.* **247** (1991), 1.
- [3] S. Kojima & M. Kodama, *Jpn. J. Appl. Phys.* **33** (1994), 2886.
- [4] M. Kodama, T. Matsushita & S. Kojima, *Jpn. J. Appl. Phys.* **34** (1995), 2570.
- [5] M. Kodama, *J. Mater. Sci.* **26** (1991), 4048.
- [6] M. Kodama, *J. Non-Cryst. Solids* **127** (1991), 65.
- [7] M. Kodama, *J. Am. Ceram. Soc.* **74** (1991), 2603.
- [8] M. Kodama, T. Hirashima & T. Matsushita, *Phys. Chem. Glasses* **34** (1993), 129.
- [9] J. J. Kankare, *Analyt. Chem.* **45** (1973), 2050.
- [10] H. A. Bowman, R. M. Schoonover & C. L. Carroll, *Metrologia* **10** (1974), 117.
- [11] E. P. Papadakis, In: *Physical Acoustics*, Vol. 12, Eds. W. P. Mason and R. N. Thurston (Academic Press, New York, 1976), pp. 277–374.
- [12] M. Kodama & S. Hayashi, *Bull. Kumamoto Inst. Technol.* **3** (1978), 121.
- [13] M. Kodama, *Jpn. J. Appl. Phys.* **21** (1982), 1247.
- [14] H. J. McSkimin, *J. Acoust. Soc. Am.* **33** (1961), 12.
- [15] M. Kodama, *Phys. Chem. Glasses* **26** (1985), 105.
- [16] G. E. Jellison, S. A. Feller & P. J. Bray, *Phys. Chem. Glasses* **19** (1978), 52.
- [17] J. Zhong & P. J. Bray, *J. Non-Cryst. Solids* **111** (1989), 67.
- [18] E. I. Kamitsos, M. A. Karakassides & G. D. Chryssikos, *Phys. Chem. Glasses* **30** (1989), 229.
- [19] G. D. Chryssikos, E. I. Kamitsos & M. A. Karakassides, *Phys. Chem. Glasses* **31** (1990), 109.
- [20] J. C. Phillips, *J. Non-Cryst. Solids* **34** (1979), 153.
- [21] J. C. Phillips, *J. Non-Cryst. Solids* **43** (1981), 37.
- [22] M. F. Thorpe, *J. Non-Cryst. Solids* **57** (1983), 355.
- [23] H. He & M. F. Thorpe, *Phys. Rev. Lett.* **54** (1985), 2107.

## THERMODYNAMICS OF BORATE MELTS AND GLASSES

Boris A. SHAKHMATKIN, Natalia M. VEDISHCHEVA  
*Institute of Silicate Chemistry of the Russian Academy of Sciences,  
Odoevskogo Str., 24, korp. 2, St. Petersburg, 199155, Russia.*

and

Adrian C. WRIGHT  
*J.J. Thomson Physical Laboratory, University of Reading,  
Whiteknights, Reading, RG6 6AF, UK*

This paper considers the relationship between the thermodynamic potentials and other physical properties of borate glasses and melts. The validity of the model of associated solutions, for an adequate prediction of a variety of properties, is illustrated by a number of examples, which include the modelling on a unified basis of the thermodynamic potentials, the densities, the refractive indices and the electrical conductivity of glasses.

### 1. INTRODUCTION

In the present paper, the thermodynamic investigation of glasses and melts is considered to be closely connected to the modelling of their properties. This is due to the fact that a detailed experimental study of multi-component systems requires the performance of numerous time-consuming experiments, whereas a model, based on the data available for various binary systems, allows an adequate description of systems formed from any number of components. Also, the model enables the thermodynamic potentials to be related to specific atomic interactions and to the distribution of various structural units. Hence, a specific physical meaning is assigned to the thermodynamic functions. Moreover, since a wide range of physical properties of glasses and melts are the derivatives of the Gibbs free energy, with respect to the variables of state, an adequate thermodynamic model can provide the possibility of calculating these properties, as will be shown in this paper.

### 2. THERMODYNAMICS AS A BASIS FOR MODELLING PROPERTIES

#### 2.1. Thermodynamic Potentials

Figure 1 shows the concentration dependence of the Gibbs free energy of mixing,  $\Delta G^M$ , for alkali borate melts at 1000°C. As is seen,  $\Delta G^M$  is large and negative. This indicates that the oxides forming these systems strongly in-

teract with each other. To illustrate the scale of this interaction, the values of  $\Delta G^M$  for an ideal solution are also shown in Fig. 1, together with those for sodium oxide, water and sodium chloride. It is known that the processes of formation of  $\text{Na}_2\text{O}$ ,  $\text{H}_2\text{O}$  and  $\text{NaCl}$  are highly exothermic. As seen from Fig. 1, their Gibbs free energies are comparable to those for the mixing of oxides in alkali borate systems. It is obvious that, in the latter, the highly exothermic processes lead to the formation of very stable products (borates). As in the case of  $\text{Na}_2\text{O}$ ,  $\text{H}_2\text{O}$  and  $\text{NaCl}$ , the structures of these salt-like products are determined by strictly specific spatial arrangements of atoms, and each arrangement is characterized by its own energy.

The fact of the formation of salt-like products in borate melts is confirmed by the character of the concentration dependence of the partial entropies of the alkali oxides,  $\Delta \bar{S}_{\text{M}_2\text{O}}$ . Thus, Fig. 2 shows this dependence for sodium oxide in sodium borate melts at 800–900°C, together with the dependence for an ideal solution and the data reported in Refs. [1,2]. The complex shape of this

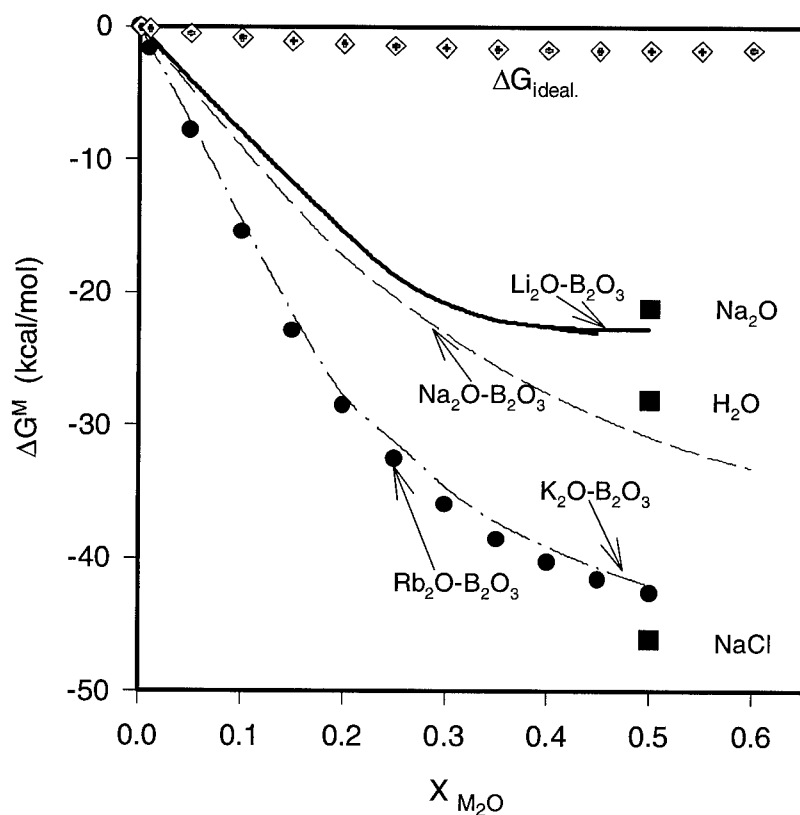


**Fig. 1.** The Gibbs free energies of mixing for oxides in alkali borate melts and the Gibbs free energies of formation of  $\text{Na}_2\text{O}$ ,  $\text{H}_2\text{O}$  and  $\text{NaCl}$  at 1000°C. The symbol  $\Delta G_{\text{ideal}}$  denote the Gibbs free energy of mixing for the components in an ideal solution.

dependence, which differs very much from that for the ideal system, as well as the negative values of the partial entropy indicate that, firstly, a significant ordering occurs in the course of the interaction between the oxides in the systems discussed and, secondly, the contribution to the values of  $\Delta\bar{S}_{M_2O}$  from the vibrational components is considerable.

The above indicates that the most logical approach to the description of the glasses and melts formed from oxides with different chemical natures is the use of the model of associated solutions. Using the formalism described in Ref. [3], it is possible to obtain an equation for the Gibbs free energy of mixing, where this potential is a known function of the composition, temperature and pressure, so that this relationship is the equation of state for a given system. Hence, it allows the calculation of a wide variety of properties of glasses and melts, using well-known differential relationships between the potential  $\Delta G^M$  and different properties. The primary quantities are the thermodynamic potentials (the chemical potentials of the oxides, their partial entropies, etc.), which may be calculated with satisfactory accuracy, as illustrated in Figs. 3 and 4.

To illustrate the possibilities provided by the model of associated solutions, the examples given in Fig. 3 and later not only involve borate glasses (melts) but also other systems and, in particular, silicates and phosphates. This is due

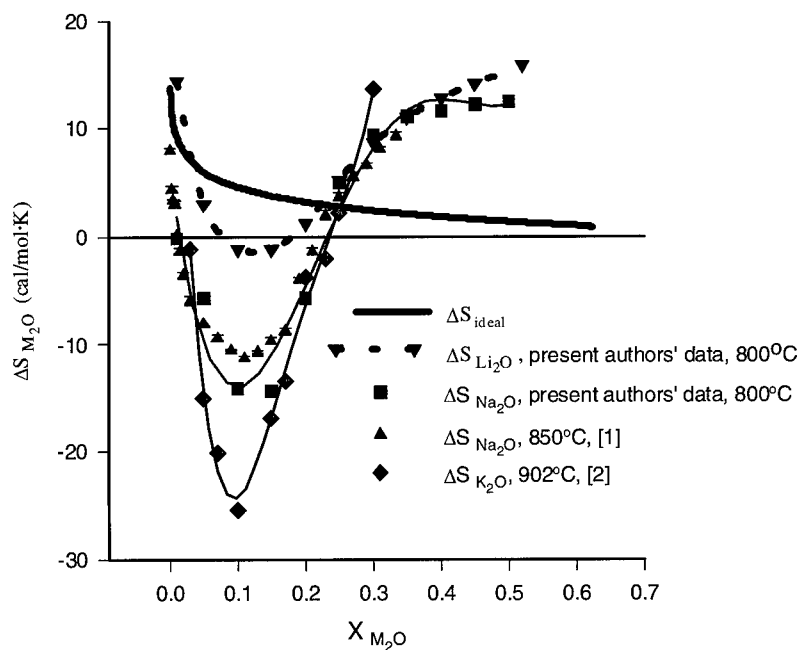


**Fig. 2.** Partial entropies of alkali oxides in alkali borate melts at different temperatures. The symbol  $\Delta S_{ideal}$  denotes the partial entropy of a component of an ideal solution.

to the fact that many properties of borate glasses cannot be calculated in practice (although, in theory, the present approach enables them to be modelled [3]) because of the lack of necessary information on the relevant properties of the crystals existing in borate systems.

## 2.2. Physical Properties

As indicated in Ref. [3], from the formalism of the model it follows that a wide range of the properties of glasses, such as the molar volume, the refractivity, the heat capacity, the isothermal compressibility, the coefficient of thermal expansion, etc. (represented below by  $V_{\text{glass}}$ ), are the additive functions of the relevant properties of the species present in a given glass ( $V_j^0$ ); i. e.

$$V_{\text{glass}} = \sum n_j V_j^0 \quad (1)$$

Here,  $n_j$  represent the number of moles of species  $j$  present in the glass considered. The index  $j$  refers both to the salt-like groupings and to the unreacted oxides. Note that, as follows from the formalism of the model, the properties of the salt like groupings refer to the crystalline state, while those of the unreacted oxides refer to the molten state.

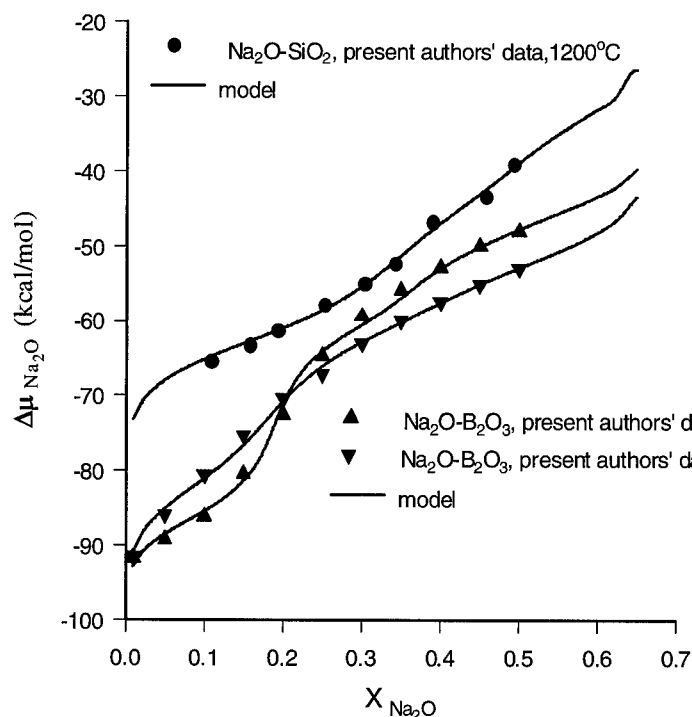
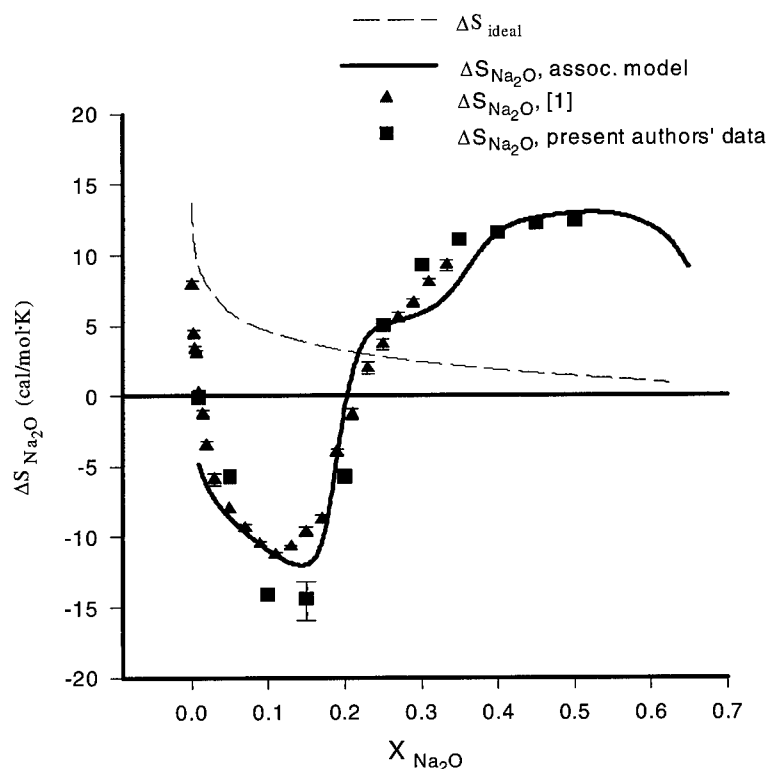


Fig. 3. The experimental and model chemical potentials for sodium oxide in sodium borate and sodium silicate melts.

Examples of calculations made with Eq. (1) are given in Fig. 5 (the densities of sodium borate and sodium silicate glasses) and Fig. 6 (the refractive indices of sodium silicate and zinc phosphate glasses). As follows from both figures, the properties of glasses can indeed be considered with a satisfactory degree of accuracy as a superposition of the relevant properties of the compounds which form in each system. This indicates that Eq. (1) yields a rigorous theoretical confirmation of the validity of known semi-empirical methods of calculating the properties of glasses [4] and determines the limits of their applicability. Moreover, from the above, it follows that, to obtain information on the properties of glasses (melts), it is first necessary to study the structure and relevant properties of crystals which form in the system in question.

Special attention should be paid to the presence of the extrema in curves for the concentration dependence of the properties of glasses, such as those observed for the refractive index in the zinc phosphate system (Fig. 6). Traditionally, the presence of specific features, i.e. maxima and minima, or points of inflection, has been associated with the occurrence of some structural rearrangements in glasses. However, as is shown in Fig. 7, the concentration de-



**Fig. 4.** The experimental and model partial entropies for sodium oxide in sodium borate melts at 800°C. The curve for an ideal solution is shown for comparison.

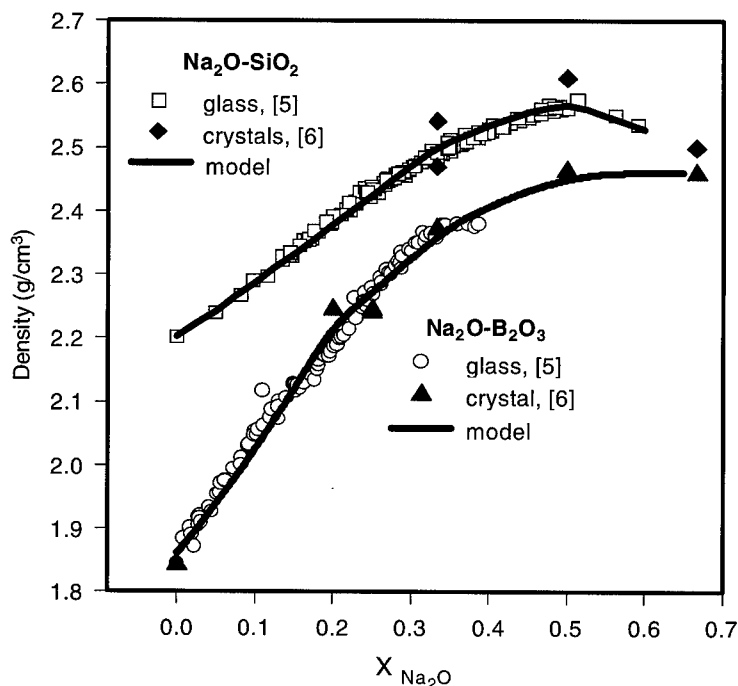


Fig. 5. The experimental and model density for glasses and the experimental density of crystalline polymorphs in sodium borate and sodium silicate systems.

pendence of the molar volume ( $V^M$ ) and molar refractivity ( $R^M$ ) of zinc phosphate glasses are monotonic and almost linear. Since both dependences have been determined as a function of the chemical structure of these glasses\* and used for the calculation of the refractive index, a complex shape of the curve for the latter shown in Fig. 6 is only due to the interplay between the monotonic dependences for  $V^M$  and  $R^M$  in the expression for the refractive index,

$$n = [(V^M + 2R^M)/(V^M - R^M)]^{1/2} \quad (2)$$

and not because of any structural changes. The absence of any specific features in the curves for the refractive index of sodium silicate glasses, also shown in Fig. 6, is due to a considerably smaller difference in the slope of the curves for  $V^M$  and  $R^M$  than that observed for zinc phosphate glasses.

The above means that any judgment concerning changes in the structure of glasses made on the basis of information on changes in their properties is valid only if a specific relationship is known to exist between a given property and a specific structure. However, in the majority of publications on structural changes in glasses, the authors' judgements are not sufficiently justified.

\* The concept of the chemical structure is explained in Ref. [7].



### 2.3. Transport Properties

According to the current literature, there are many theories of the electrical conductivity of glasses. However, none of them can provide a quantitative or indeed even a qualitative description of a more or less wide variety of systems. All of the theories are based on either a complete or a partial dissociation of the alkali oxide which corresponds, respectively, to the case of a strong or a weak electrolyte. Ravaine *et al.* [8] are the first and the only authors who have investigated the correlation between the electrical conductivity of glasses and their thermodynamic properties. They have also pointed out the necessity of taking into account the activity of the oxide  $M_2O$  in glasses, instead of its analytical concentration, when the equation of mass action is written for the dissociation of  $M_2O$ . This is very important because the activity of  $M_2O$  in glasses differs from its concentration by several orders of magnitude.

The most general and rigorous equation for the specific electroconductivity (denoted  $\sigma$ ) is

$$\sigma = (F/N_A) Z_+ n_+ (U_+ + U_-) \quad (3)$$

where  $F$  and  $N_A$  are, respectively, the Faraday constant and Avogadro's number.  $Z_+$  is the ionic charge (equal to unity in the case of alkali ions),  $U_+$  is the ionic mobility and  $n_+$  is the number of ions in unit volume. It is first necessary to

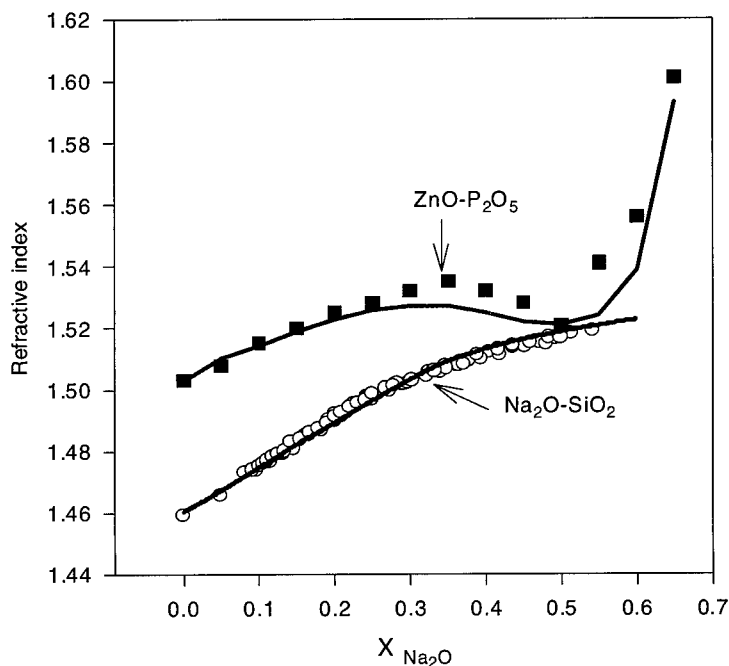


**Fig. 6.** The refractive index of sodium silicate and zinc phosphate glasses. Solid line (model), glasses in both systems; Solid squares and open circles (experiment [5]), glasses in the zinc phosphate and sodium silicate systems, respectively.

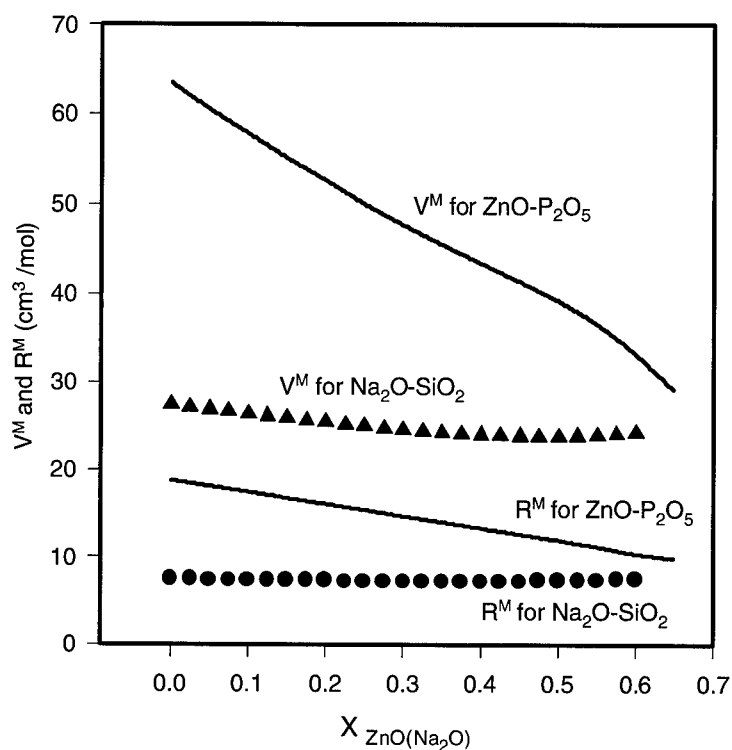


Fig. 7 The model molar volume and molar refractivity for zinc phosphate glasses (solid lines), together with the molar volume (triangles) and molar refractivity (circles) for sodium silicate glasses.

determine the concentration of the ions. According to Ref. [8], the process of dissociation of  $M_2O$  is written as



The equilibrium constant,  $K_{dis}$ , of reaction (4) is

$$K_{dis} = (X_{M^+} X_{OM^-}) / a_{M_2O} \quad (5)$$

where  $X_{M^+}$  and  $X_{OM^-}$  are the mole fractions of the corresponding ions. (As a first approximation, the activity coefficients of the ions are neglected because of their low concentrations in a given glass.) According to reaction (4),

$$X_{M^+} = X_{OM^-} \quad (6)$$

Hence, from Eqs. (5) and (6), it follows that

$$X_{M^+} = (K_{dis} a_{M_2O})^{1/2} \quad (7)$$

From the definition of the mole fraction, the number of moles of the ions  $M^+$

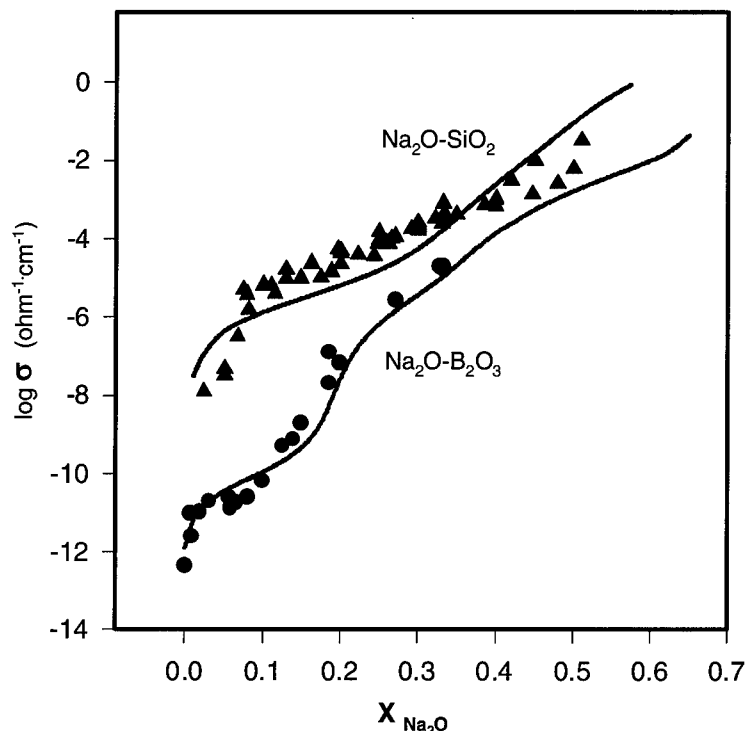


Fig. 8. The model (solid lines) and experimental (triangles and circles [5]) electrical conductivity for sodium borate and sodium silicate glasses at 300° C.

(denoted as  $n_{M^+}$ ) in a given glass is equal to

$$n_{M^+} = X_M + \sum n_i = \sum n_i (K_{\text{dis}} a_{M_2O})^{1/2} \quad (8)$$

where  $\sum n_i$  is the sum of the numbers of moles of all ions and neutral species (the salt-like groupings and the unreacted oxides) present in the glass considered.

Substituting Eq. (8) into Eq. (3) and changing the notation from the numbers of ions used in Eq. (3) to the numbers of moles of ions used in Eq. (8), the following logarithmic relationship can be obtained

$$\log \sigma = \log(F \sum n_i / V^M) + \log U_{\pm} + (\Delta \mu_{M_2O} - \Delta G_{\text{dis}}^{\circ}) / 4 \cdot 606 RT \quad (9)$$

where  $V^M$  is the molar volume of a given glass,  $U_{\pm} = (U_+ + U_-)$ ,  $\Delta G_{\text{dis}}^{\circ}$  is the standard Gibbs free energy of dissociation and  $\Delta \mu_{M_2O}$  is the chemical potential of  $M_2O$ . In this equation, the potentials  $\Delta G_{\text{dis}}^{\circ}$  and  $U_{\pm}$  are the unknown values.

However, the former does not depend at all on the composition of the glass, while the latter depends on the composition insignificantly, which follows from the data available in literature for various salt systems. Thus, Eq. (9) describes the values of  $\log \sigma$  with an accuracy determined by the constant term  $(\log U_{\pm} - \Delta G_{\text{dis}}^{\circ})$ .

Figure 8 shows the calculated dependence and the experimental values of  $\log \sigma$  for the systems  $\text{Na}_2\text{O}-\text{B}_2\text{O}_3$  and  $\text{Na}_2\text{O}-\text{SiO}_2$  at  $300^\circ\text{C}$ . The original position of the calculated curves for both systems differed systematically from that for the corresponding experimental data by a constant value of 3 units. Since this discrepancy was due to the term  $(\log U_{\pm} - \Delta G_{\text{dis}}^\circ)$ , it was eliminated by the corresponding displacement of the calculated curves relative to the experimental data. The result of this procedure is presented in Fig. 8, which shows a satisfactory agreement between the experimental data and the model. This indicates that the electrical conductivity is mainly determined by the chemical potential of  $\text{M}_2\text{O}$  and confirms the above statement concerning the insignificant dependence of the mobility of the  $\text{M}^+$  ion (i.e.  $U_{\pm}$ ) on the glass composition.

### 3. CONCLUSIONS

A systematic study of borate and other oxide glasses and melts has revealed a dominating influence of various chemical processes, which proceed in systems formed from components with different chemical natures, on a large variety of properties of such glasses. It has been shown that the model of associated solutions enables a wide range of properties to be adequately described on a unified basis over extended concentration regions. In addition to the entire set of the thermodynamic potentials for a given glasses, this also refers to such physical properties as the density, refractive index, etc. It has also been shown that the thermodynamic properties of glasses are closely related to their transport properties, such as the electrical conductivity.

### REFERENCES

- [1] M. Itoh, S. Sato & T. Yokokawa, *J. Chem. Thermodynamics* **8** (1976), 339.
- [2] M. Itoh, S. Sasahira, T. Maekawa & T. Yokokawa, *J. Chem. Soc., Faraday Trans.* **80** (1984), 473.
- [3] B.A. Shakhmatkin, N.M. Vedishcheva, M.M. Shultz & A.C. Wright, *J. Non-Cryst. Solids* **177** (1994), 249.
- [4] A.A. Appen, *The Chemistry of Glass* (Khimiya, Leningrad, 1974).
- [5] O.V. Mazurin, M.V. Streltsina & T.P. Shvaiko-Shvaikovskaya, *Properties of Glasses and Glass-Forming Liquids (Handbook)*, Eds. V.K. Leko & S.V. Nemilov **1** (Nauka, Leningrad, 1973); Ed. S.V. Nemilov **2** (Nauka, Leningrad, 1975).
- [6] N.A. Toropov, V.P. Barzakovskii, V.V. Lapin & N.N. Kurtseva, *Phase Diagrams of Silicate systems (Handbook)*, Ed. N.A. Toropov **1** (Nauka, Leningrad, 1969).
- [7] N.M. Vedishcheva, B.A. Shakhmatkin, M.M. Shultz & A.C. Wright, *Proc. Second Int. Conf. on Borates Glasses, Crystals and Melts*, 215.
- [8] D. Ravaine, E. Azandegle & J.L. Souquet, *Silicat. Ind.* **40** (1975), 333.

# STRUCTURE AND PROPERTIES OF MULTI-COMPONENT BORATE GLASSES BASED ON RAMAN SPECTROSCOPY AND THE CHEMICAL EQUILIBRIUM CONCEPT

Rikuo OTA, Jiro FUKUNAGA & Takashi WAKASUGI

*Department of Chemistry and Materials Technology, Kyoto  
Institute of Technology, Matsugasaki, Sakyo-ku, Kyoto 606, Japan*

Ota *et al.* [1] determined a set of equilibrium constants which govern the number density of the structural units in the alkali borate glass. Based on this result molar volumes of the alkali borate system were computed from the molar volumes allocated to each of the structural units. In the present study a second glass-forming component  $\text{GeO}_2$  was added to the  $\text{Na}_2\text{O}-\text{B}_2\text{O}_3$  system and the change of coordination state of borons was examined by Raman spectroscopy. It was shown that the intensity ratio of  $770\text{ cm}^{-1}$  peak due to boroxol rings with  $\text{BO}_4$  units over that of  $803\text{ cm}^{-1}$  due to boroxol rings of  $\text{BO}_3$  units increased with the replacement of  $\text{B}_2\text{O}_3$  for  $\text{GeO}_2$ . This indicates that  $\text{Na}_2\text{O}$  affinity for  $\text{B}_2\text{O}_3$  is stronger than that for  $\text{GeO}_2$ . Assuming the relative magnitude of activity coefficient  $\gamma$  of  $\text{Na}_2\text{O}$  for  $\text{GeO}_2$  and  $\text{B}_2\text{O}_3$  to be tentatively 1:2, distributions of alkali oxide among  $\text{B}_2\text{O}_3$  and  $\text{GeO}_2$  were determined according to the principle that  $\text{Na}_2\text{O}$  activity in  $\text{Na}_2\text{O}-\text{B}_2\text{O}_3$  system is equal to that in  $\text{Na}_2\text{O}-\text{GeO}_2$  system. Molar volumes  $V_m$  of the  $\text{Na}_2\text{O}-\text{B}_2\text{O}_3-\text{GeO}_2$  system were computed from the partial molar volumes,  $V_1$  and  $V_2$ , allocated to the respective sub-systems in good agreement with the observed molar volumes.

## 1. INTRODUCTION

In the alkali borate systems, boron ions change their coordination number from 3 to 4 with alkali content  $\text{M}_2\text{O}$  up to about 40 mol% and from 4 to 3 with more than 40 mol%  $\text{M}_2\text{O}$ . Ota, Yasuda & Fukunaga [1] proposed a set of equations which govern the equilibriums among the structural units in the alkali borate systems. They determined a set of equilibrium constants to calculate the number density of the structural units so that computed fractions of structural units may reproduce the NMR data [2,3];  $N_4$ , the fraction of boron ions combined to four oxygens, and  $N_{3s}$ ,  $N_{3a1}$  and  $N_{3a2}$ , the fraction combined to three oxygens. Using the equilibrium constants and using the partial molar volumes and partial molar refractivities allocated to each of the structural units, Ota and co-authors computed the molar volume and molar refraction of alkali borate systems [4]. The molar volumes and molar refractions thus calculated were in excellent agreement with the observed ones. On the other hand in alkali germanate system [5], germanium ions assume four-fold as well as six-fold coordination at alkali compositions less than 40 mol%  $\text{M}_2\text{O}$

and four-fold coordination at alkali rich compositions more than 40 mol%  $M_2O$ . Another set of cations whose coordination state is changeable with alkali content are aluminum ions and gallium ions. Combined with alkali ions they assume a four-fold coordinated structure, forming  $AlO_4M$  and  $GaO_4M$  tetrahedral complexes. From the Raman spectroscopic observations of glasses in the  $Na_2O-B_2O_3-GeO_2$  system [6],  $MgO-B_2O_3-Al_2O_3$  system [7] and  $CaO-B_2O_3-Ga_2O_3$  system [8], formation of  $AlO_4M$  and  $GaO_4M$  complexes was suggested together with  $BO_4M$  complexes. Sakka [9] measured the fluorescence X-ray spectra of aluminum ions in  $CaO-Al_2O_3-B_2O_3$  glasses and showed that the coordination state of aluminum ions is effectively in four-fold coordinated and tend to shift to six-fold coordination with increasing  $B_2O_3$  content. However, the coordination state of aluminum ions is not affected substantially by the  $Al_2O_3/CaO$  ratio. There have been no theories so far to explain this phenomenon. The structures and properties of the multi-component systems such as  $Na_2O-B_2O_3-GeO_2$ , and  $Na_2O-B_2O_3-Al_2O_3$  have not been computed because there has been no method to estimate the distribution of sodium ions among the glass-forming cations such as boron, germanium and aluminum ions and to compute the glass properties from the alkali distribution.

## 2. OBJECTIVE

When germanium, aluminum and gallium ions are introduced to an alkali borate glass the properties of the system will feature a complex compositional dependence, since the concentrations of the  $BO_4M$ ,  $AlO_4M$  and  $GaO_4M$  complexes can not be estimated directly as a function of composition and yet these concentrations will certainly determine the properties of the system. The primary objective of the present study is to explore a method to determine the alkali distribution among the glass-forming cations and based on this result to describe quantitatively the compositional dependence of properties of multi-component borate systems. In the present study  $Na_2O-B_2O_3-GeO_2$  system is chosen and density (volume) is computed according to the new method and is compared with the observed values.

## 3. METHOD

### 3.1. Sample Preparation

Glass samples for measurements of Raman spectroscopy and density were prepared by melting mixtures of reagent grade chemicals,  $Na_2CO_3$ ,  $B_2O_3$  and  $GeO_2$  powders in a platinum crucible in an electric furnace at temperatures 1000–1600°C for 20–30 min. Fused liquids were cast onto a stainless steel plate to obtain glasses. The glass compositions were  $xNa_2O \cdot (1-x)(B_2O_3 + GeO_2)$ , where  $x=0.05-0.35$ , and  $B_2O_3$  was substituted for  $GeO_2$  with  $GeO_2/B_2O_3$  ratio=1/4, 1 and 4.

### 3.2. Raman Spectroscopy Measurements

Raman spectroscopy was employed to deduce with which cations, boron or germanium ions, alkali ions would react more preferentially. Laser Raman spectroscopy measurements were conducted in the wave number range between 200

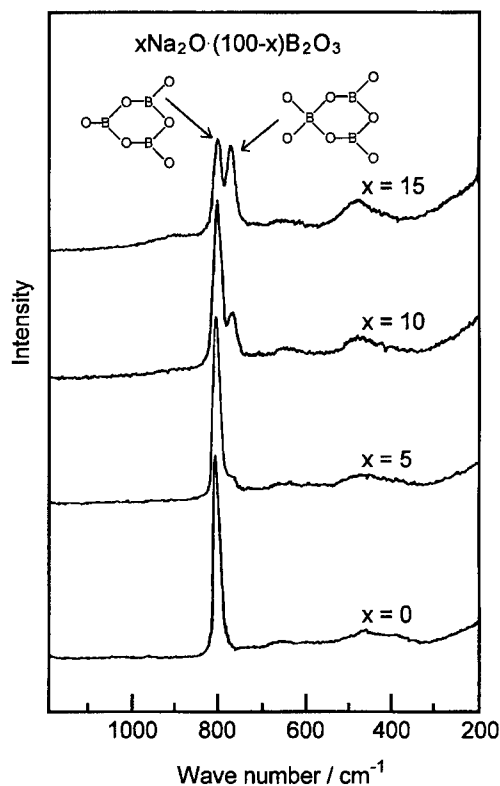


Fig.1 Raman spectra of  $x\text{Na}_2\text{O} \cdot (100-x)\text{B}_2\text{O}_3$  glasses, where  $x$  is  $\text{Na}_2\text{O}$  molar percentage.

and  $1600\text{ cm}^{-1}$  at room temperature. Raman spectra were measured on  $\text{Na}_2\text{O}-\text{B}_2\text{O}_3$  system in the  $\text{Na}_2\text{O}$  range  $\text{Na}_2\text{O}=0-40\text{ mol}\%$ . The Raman peak at  $803\text{ cm}^{-1}$  of alkali borate glass is ascribed to boroxol ring group in which boron ions are exclusively in three-fold coordination, while the  $770\text{ cm}^{-1}$  peak is ascribed to triborate, di-triborate and diborate groups in which four-fold coordinated boron ions are incorporated. By observing the relative change of Raman scattering intensity of  $770\text{ cm}^{-1}$  peak over that of the  $803\text{ cm}^{-1}$  peak, it was observed that  $I(770)/I(803)$  increases with increasing  $\text{Na}_2\text{O}$  content. From the Raman spectra of  $\text{Na}_2\text{O}-\text{B}_2\text{O}_3-\text{GeO}_2$  glass one can judge the relative strength of affinity of alkali ions for respective cations. From the relative strength of affinity, the relative magnitude of the activity and the activity coefficient of  $\text{Na}_2\text{O}$  was deduced.

### 3.3. Measurements of Density(Volume)

Density was chosen among glass properties because molar volume should be additive with respect to the partial molar volumes allocated to the subsystems. Density was measured by Archimedeian method using kerosene as medium. Observed molar volume  $V_{\text{ob}}$  was calculated as  $V_{\text{ob}}=M/d$ , where  $d$  is density and  $M$  is the molecular weight of the system.

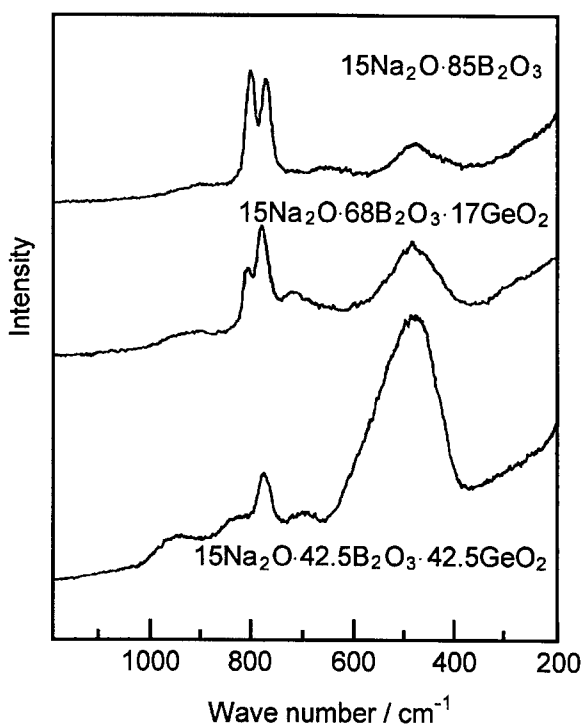


Fig.2 Raman spectra of  $15\text{Na}_2\text{O} \cdot 85(\text{B}_2\text{O}_3 + \text{GeO}_2)$  glasses.

## 4. RESULTS AND DISCUSSION

### 4.1. Raman Spectra of $\text{Na}_2\text{O}-\text{B}_2\text{O}_3-\text{GeO}_2$ System

Raman spectra of the  $\text{Na}_2\text{O}-\text{B}_2\text{O}_3$  system (Fig.1) show that in the range 0–15 mol%  $\text{Na}_2\text{O}$  the relative intensity of the  $770\text{ cm}^{-1}$  peak over that of the  $803\text{ cm}^{-1}$  peak increases with  $\text{Na}_2\text{O}$  content. Figure 2 shows the Raman spectra of  $\text{Na}_2\text{O}-\text{B}_2\text{O}_3-\text{GeO}_2$  system at 15 mol%  $\text{Na}_2\text{O}$  and  $\text{B}_2\text{O}_3$  is partially substituted for  $\text{GeO}_2$ . It is seen that  $I(770)/I(803)$  increases with  $\text{B}_2\text{O}_3$  substitution for  $\text{GeO}_2$ . This situation occurs when  $\text{B}_2\text{O}_3$  is substituted iso-cationically for  $2\text{GeO}_2$  or  $\text{Ge}_2\text{O}_4$ , as confirmed for the 15 mol%  $\text{Na}_2\text{O}$  composition. The above result implies that  $\text{Na}_2\text{O}$  affinity for  $\text{B}_2\text{O}_3$  is stronger than that for  $\text{GeO}_2$ . This means therefore that  $\text{Na}_2\text{O}$  concentration in the  $\text{Na}_2\text{O}-\text{B}_2\text{O}_3$  sub-systems should be higher than that in the  $\text{Na}_2\text{O}-\text{GeO}_2$  sub-system when  $\text{B}_2\text{O}_3$  is coexistent with  $\text{GeO}_2$ .

### 4.2. Activity Coefficients of $\text{Na}_2\text{O}$ in $\text{Na}_2\text{O}-\text{B}_2\text{O}_3$ and $\text{Na}_2\text{O}-\text{GeO}_2$

From the foregoing results, it follows that the relative magnitude of activity of  $\text{Na}_2\text{O}$ ,  $a$ , in the sub-systems should be  $a(\text{Na}_2\text{O}-\text{B}_2\text{O}_3) < a(\text{Na}_2\text{O}-\text{GeO}_2)$ . In terms of activity coefficient,  $\gamma$ , it should be  $\gamma(\text{B}_2\text{O}_3) < \gamma(\text{GeO}_2)$ . The activity coefficient of  $\text{Na}_2\text{O}$  may vary depending on the  $\text{Na}_2\text{O}$  concentration. However,



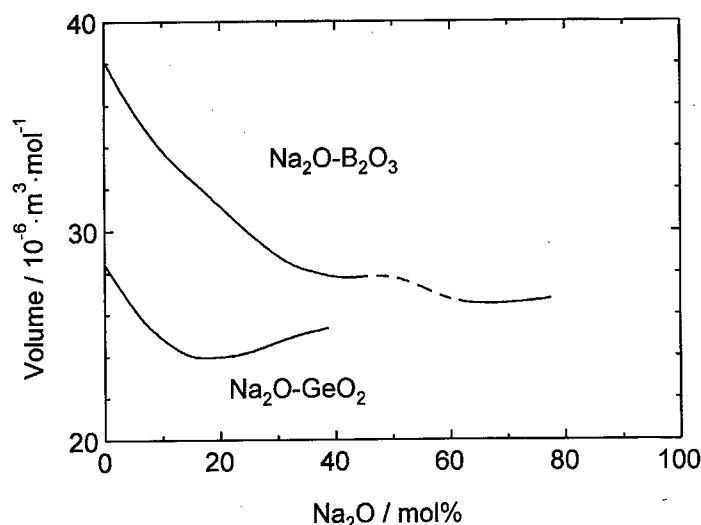


Fig.3  $V_1$  and  $V_2$  of  $\text{Na}_2\text{O}-\text{B}_2\text{O}_3$  and  $\text{Na}_2\text{O}-\text{GeO}_2$  glasses.

to the first approximation, one can assume that relative magnitude of activity coefficient among the sub-systems should be invariable despite the  $\text{Na}_2\text{O}$  concentration in the range concerned.  $r$  defined as  $\gamma_2(\text{GeO}_2)/\gamma_1(\text{B}_2\text{O}_3)$  was set equal to 2, arbitrarily.

#### 4.3. Theoretical Calculations of Molar Volume of the $\text{Na}_2\text{O}-\text{B}_2\text{O}_3-\text{GeO}_2$ System

Theoretical molar volumes were calculated according to the proposed method (see Appendix). Assume that the  $\text{Na}_2\text{O}-\text{B}_2\text{O}_3-\text{GeO}_2$  system is composed of  $\text{Na}_2\text{O}-\text{B}_2\text{O}_3$  and  $\text{Na}_2\text{O}-\text{GeO}_2$  sub-systems.  $\text{Na}_2\text{O}-\text{B}_2\text{O}_3$  system [10,11] and  $\text{Na}_2\text{O}-\text{GeO}_2$  systems are obtained as glasses in the range of 0–45 and 59–79 mol%  $\text{Na}_2\text{O}$ , and 0–40 mol%  $\text{Na}_2\text{O}$ , respectively. Molar volume of glasses with 46–59 mol% and more than 80 mol%  $\text{Na}_2\text{O}$  compositions must be estimated by the method proposed by Ota, Yasuda & Fukunga [4]. Partial molar volumes  $V_1$ , defined as the molar volume of the  $\text{Na}_2\text{O}-\text{B}_2\text{O}_3$  sub-system, and  $V_2$ , defined as the molar volume of the  $\text{Na}_2\text{O}-\text{GeO}_2$  sub-system, are shown in Fig. 3. Alkali distribution,  $s_1$  and  $s_2$ , among  $\text{B}_2\text{O}_3$  and  $\text{GeO}_2$  was estimated from eqs.(5) and (6) described in the Appendix with tentatively assumed  $r=2$ . The theoretical molar volume  $V_{th}$  was constructed from partial molar volumes  $V_1$  and  $V_2$ . Observed and theoretical molar volumes of the  $\text{Na}_2\text{O}-\text{B}_2\text{O}_3-\text{Ga}_2\text{O}_3$  system are shown in Fig. 4 (a)–(d) as a function of  $\text{Na}_2\text{O}$  content. It is seen that  $V_{ob}$  of at 5–10 mol%  $\text{Na}_2\text{O}$  compositions (Fig. 4 (a), (b)) exhibits an almost linear decrease as  $\text{B}_2\text{O}_3$  is progressively substituted for  $\text{GeO}_2$ . However a different situation occurs in the composition range of 20–30 mol%  $\text{Na}_2\text{O}$  (Fig. 4 (c), (d)).  $V_m$  deviates negatively from the additive values. It is obvious that overall agreement between the  $V_{th}$  and  $V_{ob}$  is excellent.

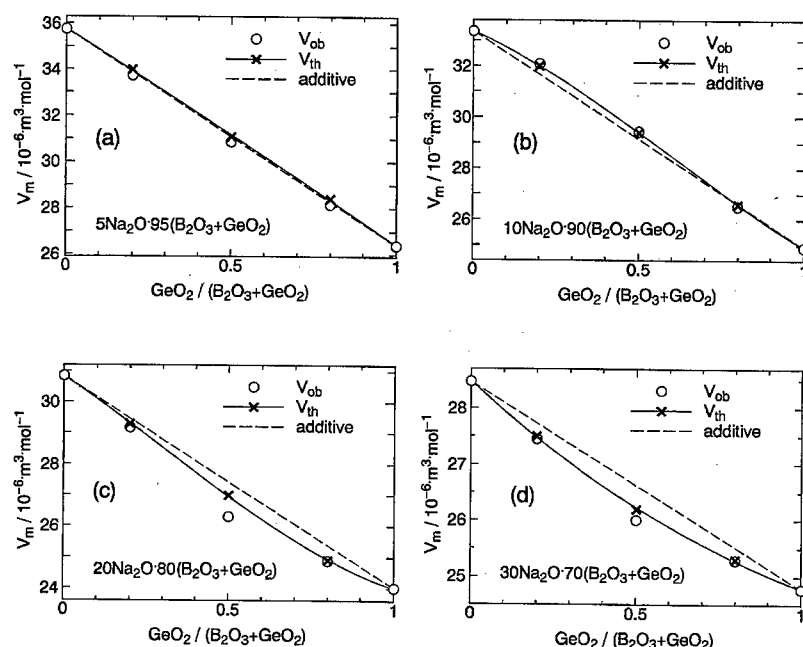


Fig.4  $V_m$  of  $\text{Na}_2\text{O}-\text{B}_2\text{O}_3-\text{GeO}_2$  glass, theoretical  $V_{th}$  (solid line) and observed  $V_{ob}$  (open circle). Dotted line indicates additive values. Glass compositions are 5 mol%  $\text{Na}_2\text{O}$  (a), 10 mol%  $\text{Na}_2\text{O}$  (b), 20 mol%  $\text{Na}_2\text{O}$  (c), 30 mol%  $\text{Na}_2\text{O}$  (d).

#### 4.4. Choice of Activity Coefficient Ratio $r$

The foregoing calculations were made assuming  $r=2$ . Here the choice of  $r$  values was inspected. The  $V_{th}$  values were computed for different values of  $r$  in the range  $r=1, 2, 3$  and  $4$  for the glass compositions with 10 and 30 mol%  $\text{Na}_2\text{O}$  and with  $\text{GeO}_2/\text{B}_2\text{O}_3=1/4, 1$  and  $4$ . It was found that  $V_{th}$  values with  $r=2$  agree most closely with the observed molar volumes  $V_{ob}$ . This means that  $r=2$  selection was most correct.

#### 5. CONCLUSION

The results of the present study are summarized as follow. In the  $\text{Na}_2\text{O}-\text{B}_2\text{O}_3-\text{GeO}_2$  system the relative intensity of the Raman spectra implies that the  $\text{Na}_2\text{O}$  affinity for  $\text{B}_2\text{O}_3$  is stronger than that for  $\text{GeO}_2$ . Assuming the relative magnitude of activity coefficient of  $\text{Na}_2\text{O}$  for  $\text{B}_2\text{O}_3$  against that for  $\text{GeO}_2$  to be tentatively 1:2, the distribution of  $\text{Na}_2\text{O}$  between  $\text{B}_2\text{O}_3$  and  $\text{GeO}_2$  was estimated. Using this result the molar volumes  $V_m$  of the  $\text{Na}_2\text{O}-\text{B}_2\text{O}_3-\text{GeO}_2$  system were computed from the partial molar volumes  $V_1$  of the  $\text{Na}_2\text{O}-\text{B}_2\text{O}_3$  sub-system and  $V_2$  of the  $\text{Na}_2\text{O}-\text{GeO}_2$  sub-system in good agreement with the observed ones. It is expected that the same procedure could be applied to the multi-component alkali borate systems including glass-forming oxides such as  $\text{Al}_2\text{O}_3$ , or  $\text{Ga}_2\text{O}_3$ .

## APPENDIX

A new method which enables one to estimate the distribution of alkali ions among glass-forming cations is described. Consider a ternary system of the chemical formula:  $s\text{Na}_2\text{O}-m_1\text{B}_2\text{O}_3-m_2\text{GeO}_2$  where  $s$ ,  $m_1$  and  $m_2$  are the molar compositions of  $\text{Na}_2\text{O}$  and  $\text{B}_2\text{O}_3$  and  $\text{GeO}_2$  oxides, respectively. Assume that out of  $s$  moles of  $\text{Na}_2\text{O}$   $s_1$  moles are allocated to  $m_1$  moles of  $\text{B}_2\text{O}_3$ , and  $s_2$  moles are allocated to  $m_2$  moles of  $\text{GeO}_2$ . When equilibrium is reached the  $\text{Na}_2\text{O}$  activity in the  $\text{Na}_2\text{O}-\text{B}_2\text{O}_3$  sub-system,  $a_1$ , must be equal to that in the  $\text{Na}_2\text{O}-\text{GeO}_2$  sub-system,  $a_2$ .

$$a_1 = \gamma_1 s_1 / (s_1 + m_1) \quad (1)$$

$$a_2 = \gamma_2 s_2 / (s_2 + m_2) \quad (2)$$

$$\gamma_1 s_1 / (s_1 + m_1) = \gamma_2 s_2 / (s_2 + m_2) \quad (3)$$

$\gamma_1$  and  $\gamma_2$  denote the activity coefficient of  $\text{Na}_2\text{O}$  in the sub-system,  $\text{Na}_2\text{O}-\text{B}_2\text{O}_3$  and  $\text{Na}_2\text{O}-\text{GeO}_2$ , respectively. Of course

$$s_1 + s_2 = s \text{ and } s + m_1 + m_2 = 1 \quad (4)$$

From eqs. (3) and (4) one can obtain  $s_1$  and  $s_2$  as follows:

$$s_1 = [-1 - (r-1)m_1 + sr + \{(1 + (r-1)m_1 - sr)^2 + 4r(r-1)sm_1\}^{1/2}] / 2(r-1) \quad (5)$$

$$s_2 = s - s_1 \quad (6)$$

where  $r = \gamma_2(\text{GeO}_2) / \gamma_1(\text{B}_2\text{O}_3)$ . The chemical formula of the  $\text{Na}_2\text{O}-\text{B}_2\text{O}_3-\text{GeO}_2$  system is rewritten as

$$s\text{Na}_2\text{O}-m_1\text{B}_2\text{O}_3-m_2\text{GeO}_2 = (s_1 + m_1) \{ s_1 / (s_1 + m_1) \text{Na}_2\text{O} + m_1 / (s_1 + m_1) \text{B}_2\text{O}_3 \} + (s_2 + m_2) \{ s_2 / (s_2 + m_2) \text{Na}_2\text{O} + m_2 / (s_2 + m_2) \text{GeO}_2 \} \quad (7)$$

The partial molar fractions of the  $\text{Na}_2\text{O}-\text{B}_2\text{O}_3$  and  $\text{Na}_2\text{O}-\text{GeO}_2$  sub-systems are  $s_1 + m_1$  and  $s_2 + m_2$ , and the  $\text{Na}_2\text{O}$  concentrations in the respective sub-systems are  $s_1 / (s_1 + m_1)$  and  $s_2 / (s_2 + m_2)$ , respectively.

Assuming additivity for the partial molar volumes,  $V_1$  of the  $\text{Na}_2\text{O}-\text{B}_2\text{O}_3$  sub-system at the  $\text{Na}_2\text{O}$  concentration  $s_1 / (s_1 + m_1)$  and  $V_2$  of the  $\text{Na}_2\text{O}-\text{GeO}_2$  sub-system at the  $\text{Na}_2\text{O}$  concentration  $s_2 / (s_2 + m_2)$ , the molar volume  $V_m$  of the  $s\text{Na}_2\text{O}-m_1\text{B}_2\text{O}_3-m_2\text{GeO}_2$  system may be calculated as

$$V_m = (s_1 + m_1)V_1 + (s_2 + m_2)V_2 \quad (8)$$

## REFERENCES

- [1] R. Ota, T. Yasuda & J. Fukunaga, *J. Non-Cryst. Solids* **116** (1990), 46.
- [2] G.E. Jellison Jr., S.A. Feller & P.J. Bray, *Phys. Chem Glasses* **19** (1978), 52.
- [3] Y.H. Yun & P.J. Bray, *J. Non-Cryst. Solids* **44** (1981), 227.
- [4] R. Ota, T. Yasuda & J. Fukunaga, *J. Non-Cryst. Solids* **139** (1992), 93.
- [5] K. Kamiya & S. Sakka, *Phys. Chem. Glasses* **20** (1979), 60.
- [6] J. Fukunaga, R. Bando, R. Ota & N. Yoshida, *J. Ceram. Soc. Japan* **96** (1988), 634.
- [7] J. Fukuanga, R. Ota, M. Shiroyama & N. Yoshida, *J. Chem. Soc. Japan* No.12, (1988) 1971.

- [8] J. Fukunaga, Xiu-Jian Zhao, M. Ihara, R. Ota & Y. Onoda, *Zairyo* **37** (1988), 87.
- [9] S. Sakka, *J.Ceram.Soc.Japan*, **85**(1977), 299.
- [10] A. Karki, S. Feller, H.P. Lim, J. Stork, C. Sanchez & M. Shibata, *J. Non-Cryst. Solids* **92** (1987), 11.
- [11] R.I. Bresker & K.S. Evstropiev, *Zh. Prikl. Khim.* **35** (1952), 905.

## THERMODYNAMIC, ACOUSTIC AND ELASTIC PROPERTIES OF $B_2O_3$ GLASSES

Miguel A. RAMOS, Sebastián VIEIRA  
*Laboratorio de Bajas Temperaturas, Depto. de Física de la  
Materia Condensada, C-III, Universidad Autónoma de  
Madrid, Cantoblanco, E-28049 Madrid, Spain.*

Carlos PRIETO  
*Instituto de Ciencia de Materiales de Madrid  
Consejo Superior de Investigaciones Científicas Cantoblanco,  
E-28049 Madrid, Spain*

and

J. Francisco FERNANDEZ  
*Departamento de Física de Materiales, C-IV  
Universidad Autónoma de Madrid, Cantoblanco,  
E-28049 Madrid, Spain.*

Since some basic properties of vitreous  $B_2O_3$  depend very strongly on the stabilization temperature and the water content of the glass, one can exploit this fact to work with pure  $B_2O_3$  as a model glass, studying how the glass-transition parameters and the physical properties of glasses vary with basic material parameters of the same substance. We have prepared, characterized and studied several glass samples of pure  $B_2O_3$ . The glass transition of each glass has been investigated through differential scanning calorimetry, obtaining the glass-transition temperature  $T_g$  from the specific-heat measurements, and the fictive temperature  $T_f$  from the corresponding enthalpy variations. Brillouin-scattering measurements have shown a remarkable variation of sound velocities, elastic constants and Debye temperature of  $B_2O_3$  glasses with previous thermal treatments. Correlation of these acoustic and elastic properties with the mass density and the fictive temperature  $T_f$  are presented and briefly discussed.

### 1. INTRODUCTION

$B_2O_3$  is a very good glass-former, which has been widely studied as a model glass for many years. Nevertheless, many of its physical properties depend strongly on the thermal history. Besides, boron oxide is a very hygroscopic material. Eversteijn *et al.* [1] have shown how some basic properties of vitreous  $B_2O_3$  depend on the *stabilization* temperature and the water content of the glass, finding a relation between the mass density and the method of prepara-

tion and later annealing of the glasses.

We have prepared, characterized and studied several different samples of pure glassy  $B_2O_3$ , with the aim of investigating for the same substance how some physical properties vary with or correlate to others. They have been characterized by measuring their mass density and the concentration of hydroxyl ions  $OH^-$ . Differential Scanning Calorimetry (DSC) has been used to obtain the glass-transition temperature  $T_g$ . The fictive temperature  $T_f$  was also determined from the corresponding enthalpy variations. Brillouin scattering measurements have also been carried out for all the  $B_2O_3$  glasses in order to study how the sound velocities and the elastic constants depend on the thermal treatment.

## 2. EXPERIMENTAL DETAILS

Different  $B_2O_3$  glass samples were made from boron oxide pellets (Aldrich, 99.999% purity), melted in a platinum crucible. Two *wet* samples were prepared by simply pouring the melt into a brass mold. In order to obtain (*dry*) samples with a much lower water content, the melt was slowly heated in vacuum up to 1050°C, and kept for 24 h at that temperature before pouring the melt. Glass samples were cut and carefully polished without using water. Several pieces were obtained from the same batch to provide appropriate samples for every experimental technique. After this, glasses were subjected to a range of thermal treatments: annealing for hours or days at temperatures below  $T_g$  (sub- $T_g$  relaxations) produces structural changes, as evidenced by the noticeable variations observed in the mass density, measured by the Archimedes flotation method at 25°C using a mineral oil as fluid, in agreement with the experiments of Eversteijn *et al.* [1].

The concentration of hydroxyl ions  $OH^-$  was determined from infrared transmission spectra around the hydroxyl absorption band at 2.8  $\mu m$ , by using the extinction coefficient found by Franz [2]. Thermal treatments and characterization parameters of the different glasses prepared and studied are shown in Table 1.

Specific-heat measurements around the glass-transition temperature were carried out by Differential Scanning Calorimetry (DSC) in a commercial calorimeter, Perkin-Elmer DSC-4. The samples were heated at a constant rate of 10 K/min.

Right-angle scattering Brillouin experiments were conducted in order to obtain both longitudinal and transverse sound velocities. Spectra were recorded at room temperature, using a (3+3) tandem Sandercock interferometer with a free spectral range of 25 GHz. Experimental work and data analysis are described in much more detail elsewhere [3].

## 3. RESULTS

As can be observed in Table 1, both sub- $T_g$  structural relaxations produced by annealing and the presence of hydroxyl ions in the network tend to increase mass density significantly [1,3]. The results of DSC experiments are also shown in Table 1. The calorimetric glass-transition temperature  $T_g$  has been determined as the temperature where the experimental curve reaches the midpoint of the specific-heat jump to the liquid-state value well above  $T_g$ . All *dry*  $B_2O_3$

**Table 1**  
Basic characterization data of the different B<sub>2</sub>O<sub>3</sub> glasses studied.

Sample	Thermal treatment	[OH <sup>-</sup> ] (mol%)	ρ (g/cm <sup>3</sup> )	T <sub>g</sub> (°C)	T <sub>f</sub> (°C)
W-1	as quenched	3.4	1.818	282	285
W-2	217°C, 100 h	5.8	1.866	264	224
D-1a	as quenched	0.27	1.804	297	288
D-1b	as quenched	—	1.804	299	296
D-2	312°C, 48 h	—	1.806	292	279
D-3	255°C, 50 h	0.27	1.826	297	277
D-4	250°C, 92 h	0.32	1.823	296	261
D-5	205°C, 170 h	0.40	1.834	295	257

samples exhibit a very similar value about  $T_g \approx 300^\circ\text{C}$ , in good agreement with other previous reports [4,5] of  $T_g = 570\text{--}580\text{ K}$ . Nevertheless, values of  $T_g$  as low as 530 K are also found here and there in the literature. In these cases, no mention of any care in order to avoid a significant water concentration is to be found. The explanation for these discrepancies in the literature can be seen in Table 1:  $T_g$  decreases appreciably with increasing water content and moreover with further annealing [3], an effect not observed in *dry* B<sub>2</sub>O<sub>3</sub> glasses. Therefore, reported glass-transition temperatures typically in the range 250–280°C or around 530 K must be attributed to B<sub>2</sub>O<sub>3</sub> glasses with a high OH<sup>-</sup> concentration.

The so-called fictive temperature  $T_f$  has also been determined from the enthalpy variation with temperature, obtained from the corresponding specific-heat measurements.  $T_f$  is defined as the temperature at which the supercooled-liquid configurational enthalpy (in metastable equilibrium) intersects the glass enthalpy curve. It can be observed in Table 1 that fictive temperature  $T_f$  decreases clearly with increasing mass density [3]. This effect seems independent of the cause of the density increase, either annealing below  $T_g$  or the presence of water in the glassy network.

Brillouin-scattering spectra recorded in right-angle geometry enabled us to obtain longitudinal ( $v_L$ ) and transverse ( $v_T$ ) sound velocities of our *wet* and *dry* B<sub>2</sub>O<sub>3</sub> glasses. It may be seen in Fig. 1 that sound velocities exhibit a remarkably wide variation as a function of mass density  $\rho$ , but do not depend on whether they are *dry* or *wet* glasses. Other sound-velocity measurements taken from the literature [6–8] are included as well in Fig. 1, but only those few which also report the density of the samples.

With the measured values of the corresponding mass densities, elastic constants were also determined through the well-known relations [9]:

$$C_{11} = \rho v_L^2; \quad C_{44} = \rho v_T^2 \quad (1)$$

Elastic constants  $C_{11}$  and  $C_{44}$  of our *wet* and *dry* B<sub>2</sub>O<sub>3</sub> glass samples are shown in Fig. 2. They are plotted as a function of enthalpic fictive temperature  $T_f$ . Since there is a clear correlation between sound velocities and mass density (see Fig. 1), and there is another one between the latter and fictive

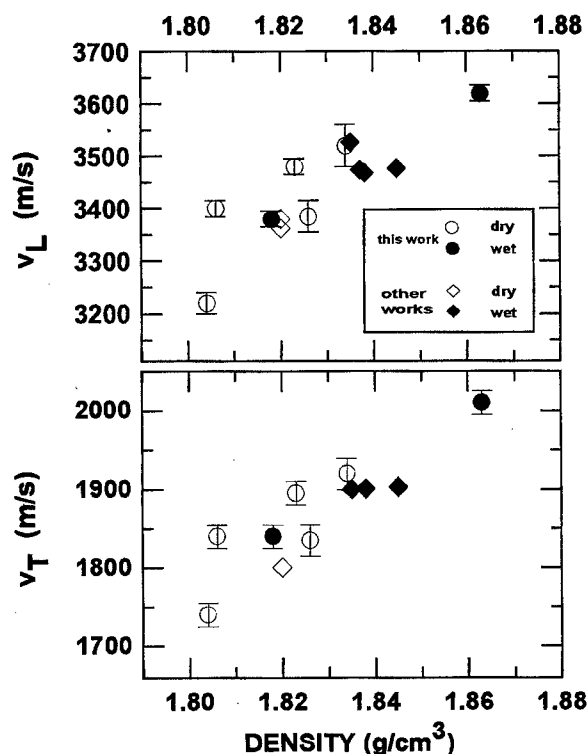


Fig. 1. Longitudinal ( $v_L$ ) and transverse ( $v_T$ ) sound velocities of *wet* (full symbols) and *dry* (open symbols)  $B_2O_3$  glasses, plotted as a function of mass density. Measurements taken from the literature [6-8], for which density is known, are also included.

temperature  $T_f$  (see Table 1), it is not surprising to find the monotonic decrease of elastic constants with increasing  $T_f$  shown in Fig. 2. It is to be stressed that we are obtaining a range of variation of the elastic constants as wide as about 30% for the same material: pure glassy  $B_2O_3$ .

#### 4. DISCUSSION

In order to shed some light on the physical origin of such a noticeable variation in the elastic constants of vitreous  $B_2O_3$  from glass to glass, we have added in Fig. 2 data for longitudinal ( $M_\infty$ ) and shear ( $G_\infty$ ) compressibility moduli, taken from ultrasonic [10] and Brillouin-scattering [11] measurements in the literature, for the metastable equilibrium fluid at the corresponding temperature. In the relevant temperature range,  $M_\infty$  and  $G_\infty$  are equal to  $C_{11}$  and  $C_{44}$ , respectively. As a matter of fact,  $B_2O_3$  has been found to support transverse sound waves well above its melting temperature [12]. Compressibility moduli determined from hypersonic Brillouin-scattering measurements [11] appear somewhat higher than those determined from ultrasonic measurements [10]. One reason may be the considerably higher frequencies used in the former



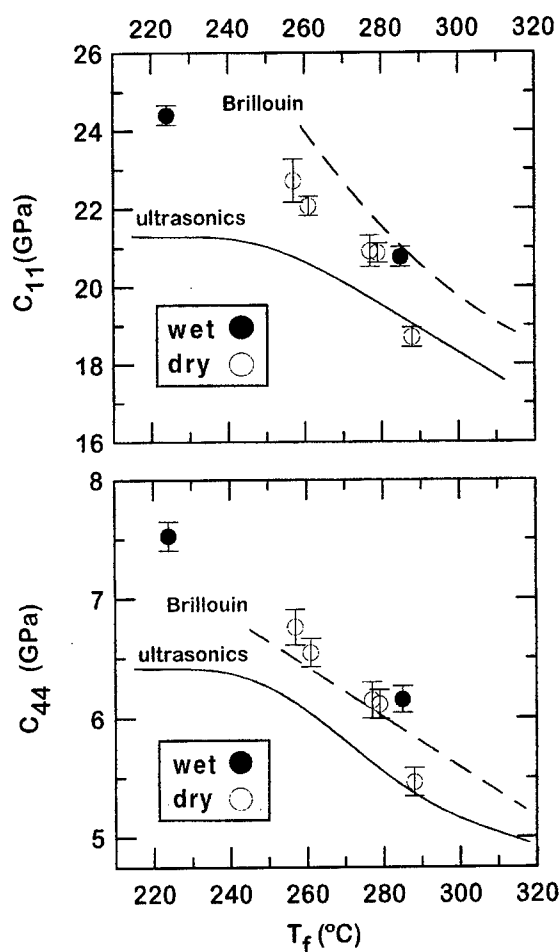


**Fig. 2.** Elastic constants  $C_{11}$  and  $C_{44}$  of our *wet* and *dry*  $B_2O_3$  glasses, plotted versus fictive temperature  $T_f$  obtained from enthalpy measurements. Longitudinal ( $M_\infty$ ) and shear ( $G_\infty$ ) compressibility moduli, taken from reports of ultrasonic [10] and Brillouin-scattering [11] measurements for the metastable equilibrium fluid at the corresponding temperature, are also shown

(~5 GHz) compared to the latter (~5 MHz). The water content in liquid  $B_2O_3$  may also play a role. In the ultrasonic measurements of Capps *et al.* [10] shown in Fig. 2, special experimental techniques were used in order to reduce water content as much as possible. Since a higher water content tends to shift  $T_f$  and  $T_g$  towards lower temperatures, this could explain why the change of slope is still not observed at the lowest temperatures investigated in the Brillouin experiments of Grimsditch & Torell [11]. This should then also be the reason for the very high elastic constants achieved by the annealed *wet* glass. In any case, the data collection of Fig. 2 shows, at least qualitatively, that the wide varia-

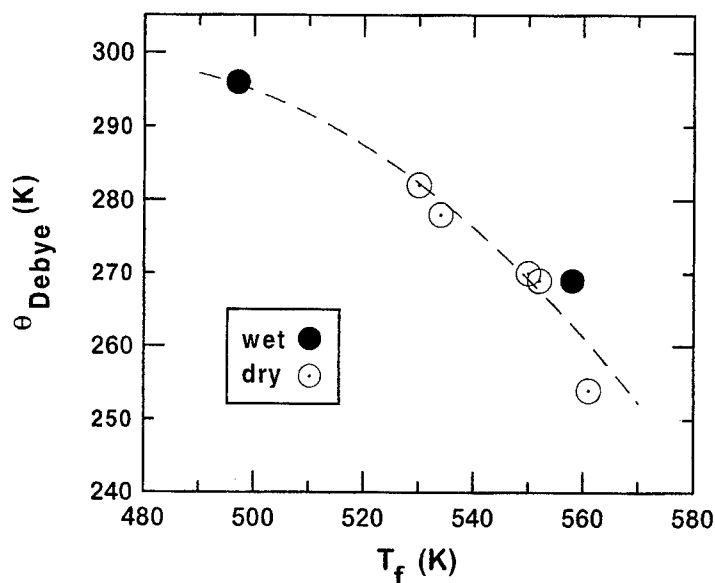


Fig. 3. Debye temperature  $\theta_D$  of our wet and dry  $B_2O_3$  samples, plotted versus the fictive temperature  $T_f$  obtained from enthalpy measurements. The dashed line is a guide for the eye.

tion of elastic constants (and of sound velocities) with different thermal treatments is simply following the same trend in its transformation range that the supercooled liquid does at the corresponding equilibrium temperatures. It is a remarkable fact that glassy  $B_2O_3$  can be modified over such a wide transformation range, due to the conspiring effects of its *flexibility* for appreciable structural relaxations around and below  $T_g$  (which is likely to be related to the peculiar two-dimensional character conferred by its planar structural units, including *boroxol* rings) and of the influence of the variable water content on the network rigidity.

As mentioned above, one can exploit the possibilities of variation in glassy  $B_2O_3$  material parameters to use it as a model glass to investigate other physical properties, such as the universal low-temperature *anomalies* of glasses and the related low-frequency vibrational excitations. In order to tackle this task, it is crucial to determine the contribution of ordinary lattice-vibrational modes. Most relevant physical properties of solids at low temperatures are related to the Debye temperature  $\theta_D$ , defined through:

$$k_B \theta_D = (h/2\pi) v_D (6\pi^2 n)^{1/3} \quad (2)$$

where  $k_B$  is Boltzmann constant,  $h$  is Planck's constant,  $n$  is atomic number density, and Debye sound velocity  $v_D$  is given by  $v_D^{-3} = 1/3 (v_L^{-3} + 2v_T^{-3})$ .

The values of the Debye temperatures  $\theta_D$  for our wet and dry  $B_2O_3$  samples, calculated via eq. (2), are shown in Fig. 3. As may be anticipated, there is a noticeable variation from glass to glass. This variation is particularly relevant,

since the Debye contribution to the specific heat at low temperature is proportional to  $\theta_D^{-3}$ . Once again, a correlation is found between the studied physical property and the fictive temperature  $T_f$  or the mass density  $\rho$ :  $\theta_D$  decreases monotonically with  $T_f$  increase, as shown in Fig. 3. Accordingly, the Debye temperature  $\theta_D$  increases with density.

We have recently measured [13] the low-temperature specific heats of the same  $B_2O_3$  glass samples used in the present study. An appreciable dependence of the low-temperature specific-heat excess on annealing processes was found for *dry* glasses. However, this variation can be well accounted for by the different Debye contributions discussed above. On the contrary, *wet*  $B_2O_3$  glasses seem to behave in a different way [13], probably indicating that changes introduced in the glassy network by water are indeed influencing the low-energy dynamics of  $B_2O_3$  glasses.

## 5. CONCLUSIONS

Several different *wet* and *dry*  $B_2O_3$  glasses have been prepared and studied. Both sub- $T_g$  structural relaxations and the water content present in this hygroscopic material affect noticeably its physical properties. Mass density  $\rho$  shows up as a simple useful parameter to characterize the glassy state of a given  $B_2O_3$  sample. DSC measurements have allowed us to determine the fictive temperature  $T_f$  from enthalpy variation around the glass-transition temperature, and to relate it to different methods of preparation and thermal treatments applied to glass samples.

Enthalpic  $T_f$  (much more than calorimetric  $T_g$ ) serves as a thermodynamic link, which helps to correlate and parameterize the remarkably wide variation range of acoustic and elastic properties of  $B_2O_3$  glasses, obtained from Brillouin-scattering measurements. This simply reflects the fact that *solid* glasses have frozen out the structure and hence the physical properties of the *supercooled liquid* which would be in thermal equilibrium at the temperature  $T_f$  of the corresponding glass. Owing to its specific physico-chemical properties,  $B_2O_3$  exhibits a transformation range much wider than usual, this being the reason for the large spread of physical constants from  $B_2O_3$  glass to  $B_2O_3$  glass.

## Acknowledgements

We wish to thank Prof. Dr. U. Buchenau for stimulating discussions and helpful suggestions. We are also grateful to Prof. F. J. Piqueras for conducting infrared measurements, and to A. Buendía and J. A. Moreno for their assistance in sample preparation. This work has been supported in part by INTAS project No. 93-3230.

## REFERENCES

- [1] F. C. Eversteijn, J. M. Stevels & H. I. Waterman, *Phys. Chem. Glasses* **1** (1960), 123.
- [2] H. Franz, *J. Am. Ceram. Soc.* **49** (1966), 473.
- [3] M. A. Ramos, J. A. Moreno, S. Vieira, C. Prieto & J. F. Fernández, *J. Non-Cryst. Solids* (submitted).
- [4] M. A. DeBolt, A. J. Easteal, P. B. Macedo & C. T. Moynihan, *J. Am. Ceram. Soc.* **59** (1976), 16.

- [5] H. S. Chen & C. R. Kurkjian, *J. Am. Ceram. Soc.* **66** (1983), 613.
- [6] J. T. Krause & C. R. Kurkjian, In: *Borate Glasses*, Eds. L. D. Pye, V. D. Fréchet and N. J. Kreidl (Plenum Press, New York, 1978), pp. 577-585.
- [7] W. M. MacDonald, A. C. Anderson & J. Schroeder, *Phys. Rev. B* **32** (1985), 1208.
- [8] M. Kodama, *J. Non-Cryst. Solids* **127** (1991), 65; M. Kodama, *J. Mater. Sci. Lett.* **11** (1992), 1406.
- [9] F. C. Brown, *The Physics of Solids* (Benjamin, 1967), Chapter 5.
- [10] W. Capps, P. B. Macedo, B. O'Meara & T. A. Litovitz, *J. Chem. Phys.* **45** (1966), 3431.
- [11] M. Grimsditch & L. M. Torell, In: *Dynamics of Disordered Materials*, Eds. D. Richter, A. J. Dianoux, W. Petry and J. Teixeira (Springer, Berlin, 1989), pp. 196- 210.
- [12] M. Grimsditch, R. Bhadra & L. M. Torell, *Phys. Rev. Lett.* **62** (1989), 2616.
- [13] E. Pérez-Enciso, M. A. Ramos & S. Vieira, *Phys. Rev. B* **56** (1997).

## SIMULATION OF THE STRUCTURE OF BORATE GLASSES AND MELTS ON THE BASIS OF THERMODYNAMICS

Natalia M. VEDISHCHEVA, Boris A. SHAKHMATKIN,  
Mikhail M. SHULTZ

*Institute of Silicate Chemistry of the Russian Academy of Sciences,  
Odoevskogo Str., 24, korp. 2, St. Petersburg, 199155, Russia.*

and

Adrian C. WRIGHT

*J.J. Thomson Physical Laboratory, University of Reading,  
Whiteknights, Reading, RG6 6AF, UK*

This work is a continuation of the series of papers on the model of ideal associated solutions as applied to the distribution of the various structural units in borate glasses and melts. It is shown that this approach yields an adequate description of the medium-range order of these glasses (melts). Also, it predicts the influence of temperature on the distribution of the structural units which are characteristic of both the short-range and medium-range order.

### 1. INTRODUCTION

As has previously been shown [1-4], the model of ideal associated solutions, when applied to systems formed from components with different chemical natures, enables reliable information to be obtained on the distribution of the basic structural units determining the short-range order in glasses and melts. These units characterize the first co-ordination sphere of the glass-forming atoms and include  $\text{BO}_3$  triangles and  $\text{BO}_4$  tetrahedra in borate glasses (melts). A good agreement between the calculated fractions of 3-fold and 4-fold co-ordinated boron atoms in alkali borate glasses and melts [1-3] and the corresponding experimental data is evidence for the validity of the thermodynamic model as a description of the structure of glasses and melts, in terms of their short-range order. This is due to the possibility to transfer easily from the notions used in the model to the traditional view of the structure of glasses and melts. In general, the suggested approach is in agreement with Hägg's concept of the existence in glasses of groupings larger than the basic structural units [5], which has been supported later by Krogh-Moe [6] and then developed by Bray and co-workers [7,8]. It should be noted that the latter have made a quantitative estimate of the content of superstructural units in a number of binary and ternary systems. Taking this into account, the present paper aims to determine whether the model of ideal

associated solutions can describe the medium-range order in glasses (melts) and predict the influence of temperature on their structure.

## 2. THE MODEL OF ASSOCIATED SOLUTIONS

The model of associated solutions [2], based on the rigorous approach of De Donder, is valid for systems formed from any number of components with different chemical natures. This model, which has no adjustable parameters, considers glasses and melts as solutions formed from (unreacted) oxide components and the salt-like products of their interaction, the latter being similar in their stoichiometry to the crystalline compounds which exist in the phase diagram of the system in question. Their structural similarity may also be assumed.

Single-phase systems can be described using the ideal approximation of the model. This implies that the salt-like products and the unreacted oxides form an ideal solution. As shown in Ref. [9], this approximation is valid for a large variety of the systems that form the basis of many industrial glasses (alkali borates, silicates, germanates, phosphates, etc.).

A full derivation of the formalism of the model of associated solutions has been given elsewhere [2]. Briefly, it consists of solving the system of equations for the mass balance of the components and the equations for the law of mass action for all reactions proceeding in the system. The solution of these equations provides information on the chemical structure of a given glass (melt), which implies the relative content of the salt-like products (groupings) and the

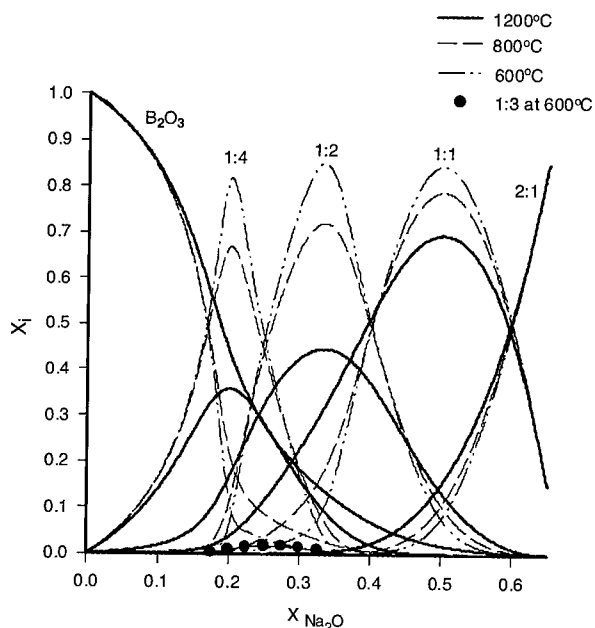
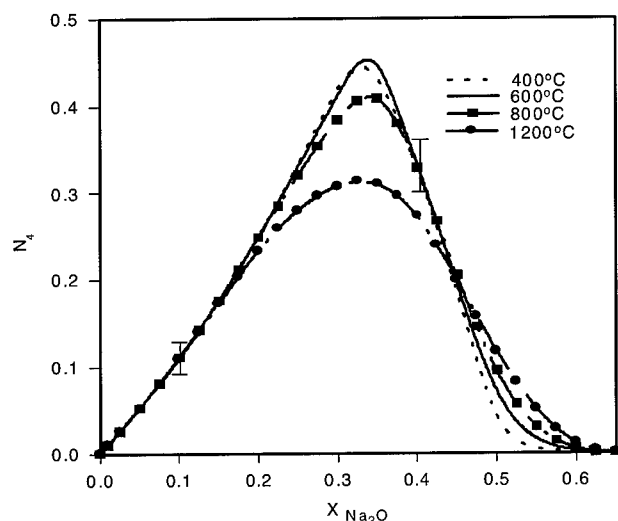


Fig.1. The chemical structure of sodium borate melts at 600, 800 and 1200°C. The sodium borate species are denoted  $m:n$  (i.e.  $m\text{Na}_2\text{O} \cdot n\text{B}_2\text{O}_3$ ).



**Fig. 2.** The concentration and temperature dependences of the fraction of 4-fold co-ordinated boron atoms ( $N_4$ ) in sodium borate melts.

unreacted oxides. The relative content is represented by the number of moles or the mole fractions,  $X_i$ , of each species. Fig. 1 shows the chemical structure of sodium borate melts at different temperatures. The species denoted  $m:n$  are the salt-like groupings of the same stoichiometry ( $m\text{Na}_2\text{O} \cdot n\text{B}_2\text{O}_3$ ) as the crystalline compounds which form in the  $\text{Na}_2\text{O}-\text{B}_2\text{O}_3$  system. The standard Gibbs free energies of formation of the compounds  $m\text{Na}_2\text{O} \cdot n\text{B}_2\text{O}_3$ , necessary for the calculation of the values  $X_i$  have been taken from Refs. [10,11].

### 3. INFLUENCE OF TEMPERATURE ON GLASS (MELT) STRUCTURE

As shown in Refs [1-4], a knowledge of the chemical structure enables a reliable description to be made of the distribution of the various structural parameters which characterize the short-range order in borate glasses and melts, provided that all of the crystal structures in a given system are known. Now it will be determined whether the model can predict the influence of temperature on the structure, when the latter is considered at two levels (short and medium-range order).

#### 3.1. Short-Range Order

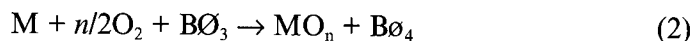
Figure 2 shows the temperature dependence of the distribution of 4-fold co-ordinated boron atoms ( $N_4$ ) in sodium borate melts at 400-1200°C over the composition region 0-65 mol%  $\text{Na}_2\text{O}$ . This has been calculated using information on the chemical structure of these melts. As is seen, in the region up to 15-18 mol%  $\text{Na}_2\text{O}$ , the temperature dependence of  $N_4$  is insignificant (the discrepancy between the curves corresponding to different temperatures is less than the sensitivity of direct structural methods), although the chemical structure of the melts

over this composition region changes considerably (see Fig. 1). As the content of  $\text{Na}_2\text{O}$  increases, the temperature dependence becomes more pronounced and reaches its maximum ( $\Delta_{\text{max}} N_4 \sim 0.1$ ) in the region corresponding to the stoichiometric composition  $\text{Na}_2\text{O} \cdot 2\text{B}_2\text{O}_3$ . Note that the uncertainty in the calculations of  $N_4$  as shown by the error bars, is  $\pm 0.02$  in the region up to 33 mol%  $\text{Na}_2\text{O}$  and  $\pm 0.03$  at higher sodium oxide contents, which is due to the fact that the literature data on the thermodynamic potentials of the ortho- and pyroborates used in modelling the high-alkali region are not sufficiently reliable.

As is seen from Fig. 2, an increase in temperature leads to a decrease in the fraction of 4-fold coordinated boron atoms in sodium borate melts. This might be interpreted as evidence for the exothermic nature of the conversion of 3-fold coordinated boron atoms to 4-fold coordinated atoms:



where  $\text{O}$  represents a bridging oxygen atom. However, calculations made on the basis of reliable thermochemical data [10,12-14] indicate that reaction (1) is a weakly endothermic process ( $\Delta H^0 = +4.5$  kcal/mol). This discrepancy is explained by the fact that here as in any other borate system, reaction (1) cannot be considered alone, since its progress is associated with another process, viz. with the formation of  $\text{MO}_n$  polyhedra, where  $n$  is the coordination number of the network modifying cations with respect to oxygen. Since this is a highly exothermic reaction, the overall process



is exothermic, which is in agreement with the temperature dependence of the value  $N_4$  shown in Fig. 2.

The above example indicates that great care is required concerning so-called polymer models [15,16], since they are based solely on a consideration of reactions of type (1). Thus, these models are inadequate in that they only include a subset of the processes proceeding in systems which are formed from components with different chemical natures and, as a result, erroneous values are ascribed to the equilibrium constants of these reactions.

Figure 3 presents the change in the value of  $N_4$  for cuts of constant  $\text{Na}_2\text{O}$  content, equal to 20 and 33.3 mol%, when sodium borate melts are cooled from 1200° C to a temperature close to  $T_g$ . It is seen that, in both cuts, the temperature dependence is nonlinear, the nonlinearity becoming more pronounced with increasing temperature.

### 3.2. Medium-Range Order

A consideration of the structure in terms of the short-range order enables some properties of melts and glasses to be described qualitatively, provided that these properties are not too sensitive to the structural peculiarities of a given system (e.g. the viscosity of silicate glasses, the density of glasses in various systems, etc.). However, it is impossible to explain such properties as the



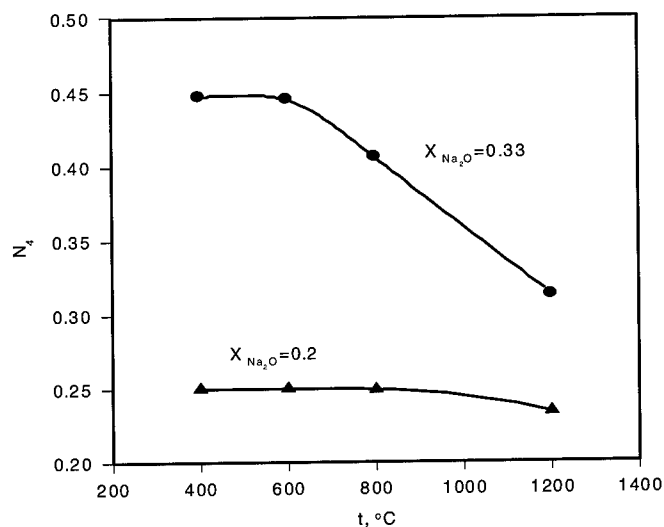


Fig.3. The temperature dependence of the fraction of 4-fold co-ordinated boron atoms ( $N_4$ ) in sodium borate melts at constant  $\text{Na}_2\text{O}$  contents of 20 and 33 mol%.

viscosity of borate glasses and the coefficient of thermal expansion, isothermal compressibility, optical and thermodynamic properties of glasses in different systems, in terms of the statistical distribution of the basic structural units. This leads to the idea of a non-statistical distribution of the basic structural units and, in particular, of  $\text{BO}_3$  triangles and  $\text{BO}_4$  tetrahedra in borate glasses, which implies the formation of "superstructural units" in which the basic units are connected together in a strictly determined way. The concept of superstructural units results in a more detailed approach to the structure of glasses (melts) at the level of the medium-range order.

Superstructural units can be defined as specifically arranged groups of atoms, each group being characterized by the unique value of the standard Gibbs free energy. The formation of superstructural units is the basis on which the model of associated solutions is used to consider the medium-range order in glasses (melts). This approach allows an adequate description of a wider range of physical properties and structural peculiarities of various glasses and melts than can be obtained from the short-range order alone.

Judging from the literature data on the structures of borate crystals, the average dimensions of superstructural units are in the range of 5-10 Å, for different borate groups (boroxol rings, diborate and triborate groups, etc.), which makes the experimental identification of superstructural units difficult. Hence the present thermodynamic approach is of particular interest, because the primary purpose of the model of associated solutions is to calculate the relative content of various superstructural units in melts and glasses which, in terms of the model, corresponds to the concept of the chemical structure.

In respect of the terminological analogies, special attention should be paid

to the relationship between the notion of a superstructural unit, used in structural studies, and that of a salt-like grouping, as introduced in the model. In a number of cases, both imply one and the same thing. This is true for diborate, triborate and pentaborate units. However, some groupings consist of several superstructural units, e.g. the tetraborate grouping is a combination of pentaborate and triborate superstructural units. The current development of experimental methods used in structural studies does not enable a distinction to be made between triborate units incorporated into tetraborate groupings and "free" triborate units (in other words, triborate groupings). However, the present calculations unambiguously indicate that in some glasses (e.g. in the sodium borate system) pentaborate and triborate superstructural units are distributed not randomly but in an orderly way, viz. they form tetraborate groupings. As is clear, this leads to ordering at the level next in complexity with respect to the formation of superstructural units. Having no effect on the scattering of X-rays and neutrons, this ordering reveals itself in the thermodynamic properties of glasses and melts. Thus, in each particular case, it is necessary to find out whether a given grouping is an individual superstructural unit in itself or whether it is formed from several other units. However, the notions of groupings and superstructural units should not be contrasted, since both terms imply products of the ordered distribution of the basic structural units; i.e.  $\text{BO}_3$  and  $\text{BO}_4$ .

As shown in Ref. [3], a knowledge of the chemical structure of melts and glasses enables the distribution of their basic structural units to be calculated from different groupings present. This means that the combination of the two structural levels is intrinsic to the model of associated solutions, i.e. it includes both the short-range and medium-range order. Of special importance is the fact that no structural notions are originally introduced in the formalism of the model. On the contrary, these notions follow from its very basis, viz. from the chemical nature of the components forming a given system. As an illustration, consider the temperature dependence of the above distribution for the sodium borate system, as shown in Fig. 4, where  $B^3$  is the fraction of 3-fold coordinated boron atoms incorporated into the unreacted  $\text{B}_2\text{O}_3$ ,  $T^3$  and  $T^4$  are, respectively, the fractions of 3-fold and 4-fold coordinated borons distributed among tetraborate groupings and  $D^3$  and  $D^4$  are, correspondingly, the fractions of boron atoms in 3-fold and 4-fold coordination included into diborate groupings. The distribution of these structural parameters, modelled for melts at 800 and 1200°C, are compared in Fig. 4 with the relevant NMR data for the corresponding glasses from Ref. [7], where the authors suggest the presence of diborate and tetraborate groupings in the region 0-35 mol%  $\text{Na}_2\text{O}$ .

As seen from the figure, an increase in temperature leads to a widening of the peaks for all of the structural parameters shown. This is evidence for the redistribution of 3-fold and 4-fold coordinated boron atoms among the various groupings in glasses as the temperature changes. Note that the NMR data for the glasses are in better agreement with the model at 1200°C rather than at 800°C, as might be expected. This may be due to the combined uncertainty in the present

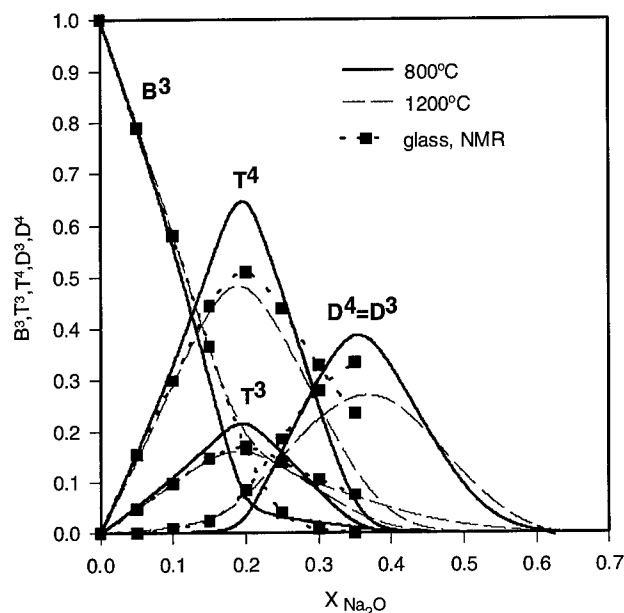


**Fig. 4.** The distribution of 3-fold and 4-fold co-ordinated boron atoms among various groupings in sodium borate melts at 800 and 1200°C (model) and glasses (NMR data from Ref. [7]). The notations used are explained in the text.

calculations and those of Ref. [7]. However, it is the general trends of the changes in the distribution of  $B^3$ ,  $T^3$ ,  $T^4$ ,  $D^3$  and  $D^4$  with temperature that is of primary interest in this figure, rather than the absolute values of these parameters.

### 3.3. Structural Motifs

After considering the structure of glasses in terms of the distribution of their basic structural units, the next-commonest approach to this problem is that based on the notion of structural motifs (chains, layers or networks) in glasses. This approach is in complete agreement with the concept of the chemical structure of glasses. This is illustrated by Fig. 1, where the intersection points of the curves showing distributions of the various salt-like groupings correspond to the compositions at which a change in the dominating structural motif occurs. Note that, although the chemical structure of the sodium borate system has been calculated allowing for the presence of  $Na_2O \cdot 3B_2O_3$  in the phase diagram, the number of triborate groupings in the melt is negligibly small at 1200 and 800°C and becomes barely noticeable (less than 1%) at 600°C. This is in agreement with the fact that  $Na_2O \cdot 3B_2O_3$  melts incongruently and hence is thermodynamically unstable with respect to decomposition into the neighbouring (in the phase diagram) compounds,  $Na_2O \cdot 2B_2O_3$  and  $Na_2O \cdot 4B_2O_3$ .

A similar situation exists with respect to the presence in lithium silicate melts of the disilicate grouping, which does not exceed 6% at 727°C and whose crys-

talline analogue,  $\text{Li}_2\text{O} \cdot 2\text{SiO}_2$ , also melts incongruently. These examples are not exceptional and indicate that there is no single set of species which is common for all glass-forming systems of a given type. In each particular case, this set has to be determined on the basis of information from the phase diagram of the given system, followed by an analysis of thermodynamic stability of the relevant compounds. The idea of a certain set of species, which is unique for a range of borate, silicate or other systems, can lead to serious mistakes such as the misinterpretation of structural data obtained by various experimental techniques, a misjudgement of the tendency of glasses towards crystallization, etc.

#### 4. CONCLUSIONS

It has been shown that the concept of the chemical structure of glasses and melts, which follows from the model of associated solutions, enables a description of their structure to be made not only in terms of the short-range order, as has recently been reported [2-4], but also at the level of the medium-range order. In addition, this concept provides an adequate prediction of the temperature dependence of the distribution in glasses (melts) of the basic structural units which represent the short-range order as well as that of the superstructural units characterizing the medium range order. It has also been found that each glass-forming system has its own characteristic set of species present in the glasses (melts), which has to be determined on the basis of information on the thermodynamic stability of the compounds shown in the phase diagram of the system in question.

#### REFERENCES

- [1] N.M. Vedishcheva, B.A. Shakhmatkin, A.C. Wright, D.I. Grimley, G. Etherington & R.N. Sinclair, In: *Fundamentals of Glass Science and Technology 1993*, [Suppl. to Riv. Staz. Sper. Vetro **23** (1993)] (Staz. Sper. Vetro, Venice, 1993), pp. 459-462.
- [2] B.A. Shakhmatkin, N.M. Vedishcheva, M.M. Shultz & A.C. Wright, *J. Non-Cryst. Solids* **177** (1994), 249.
- [3] B.A. Shakhmatkin, N.M. Vedishcheva, M.M. Shultz & A.C. Wright, *Glastechn. Ber.* **67C** (1994), 191.
- [4] N.M. Vedishcheva, B.A. Shakhmatkin, M.M. Shultz & A.C. Wright, *J. Non-Cryst. Solids* **196** (1996), 239.
- [5] G. Hagg, *J. Chem. Phys.* **3** (1935), 42.
- [6] J. Krogh-Moe, *Phys. Chem. Glasses* **6** (1965), 46.
- [7] G.E. Jellison & P.J. Bray, *J. Non-Cryst. Solids* **29** (1978), 187.
- [8] S.A. Feller, W.J. Dell & P.J. Bray, *J. Non-Cryst. Solids* **51** (1982), 21.
- [9] B.A. Shakhmatkin & N.M. Vedishcheva, *J. Non-Cryst. Solids* **171** (1994), 1.
- [10] I. Barin & O. Knacke, *Thermodynamic Properties of Inorganic Substances* (Springer, Berlin, 1973).
- [11] M.W. Chase, C.A. Davies, J.R. Downey, D.J. Frurip, R.A. McDonald & A.N. Sywerud, *JANAF Thermochemical Tables*, 3rd Ed. (Amer. Chem. Soc., Amer. Inst. Phys., Nat. Bur. Stand., 1985).
- [12] W.H. Zachariasen, *Acta Cryst.* **16** (1963), 385.
- [13] J. Krogh-Moe, *Acta Chem. Scand.* **17** (1963), 843.
- [14] C.T. Prewitt & R.D. Shannon, *Acta Cryst.* **B24** (1968), 869.
- [15] C.W. Toop & C.S. Samis, *Trans. TMS-AIME* **224** (1962), 878.
- [16] C.R. Masson, *Proc. Roy. Soc.* **A287** (1965), 201.

## ALKALI BOROSILICATE SYSTEMS: PHASE DIAGRAMS AND THE STRUCTURE OF GLASS

Irina G. POLYAKOVA & Ekaterina V. TOKAREVA

*Institute of Silicate Chemistry of the Russian Academy of Sciences,  
24/2 Odoevskogo St., St. Petersburg, 199155, Russia*

The paper summarises the results of a systematic investigation of glass properties (glass transition temperature, tendency for crystallisation and liquid immiscibility) and phase equilibria for alkali borosilicate systems and presents phase diagrams for the  $K_2O-B_2O_3-SiO_2$  and  $Rb_2O-B_2O_3-SiO_2$  systems. Several new stable and metastable compounds have been found and X-ray powder diffraction data are given for some of them. The comparison of plots of glass property vs. composition with the corresponding phase diagrams demonstrates that the structure of all of the alkali borosilicate glasses contains boroleucite-type groups over wide composition ranges. The concept of the "boroleucite anomaly" makes it possible to explain the presence of extrema in many of the properties of alkali borosilicate glasses over a wide region in the neighbourhood of the boroleucite composition.

### 1. INTRODUCTION

It is well known that the addition of cations to boron oxide glass results in the strengthening of its network, because the cations transform a fraction of the boron atoms into a tetrahedrally-coordinated state. In all alkali borate glasses, the maximum content of tetrahedral boron occurs at 25–30 mol% alkali oxide and does not exceed one-half of the total quantity of boron atoms. In this region (the borate anomaly maximum), the structure-sensitive properties such as the glass transition temperature and chemical durability have maxima.

In sodium borosilicate glasses a similar effect is observed. There are maxima in the concentration variation of the above properties and of some other properties (e.g. density and refractive index), but their locations are far from the borate anomaly and are displaced to the silica corner of each diagram. In the neighbourhood of the maxima, according to NMR data [1], nearly all of the boron atoms are in tetrahedral co-ordination. From the physical chemistry point of view, a new type of structure forms in these regions, but there are no ternary compounds in the sodium borosilicate system with which this structure may be connected. Similar tendencies occur in other alkali borosilicate systems, but their glass properties are relatively poorly studied and their phase diagrams remain unknown (except for the sodium system). This paper presents a comparative physico-chemical investigation of the sodium, potassium, rubidium and, to a lesser extent, the lithium and

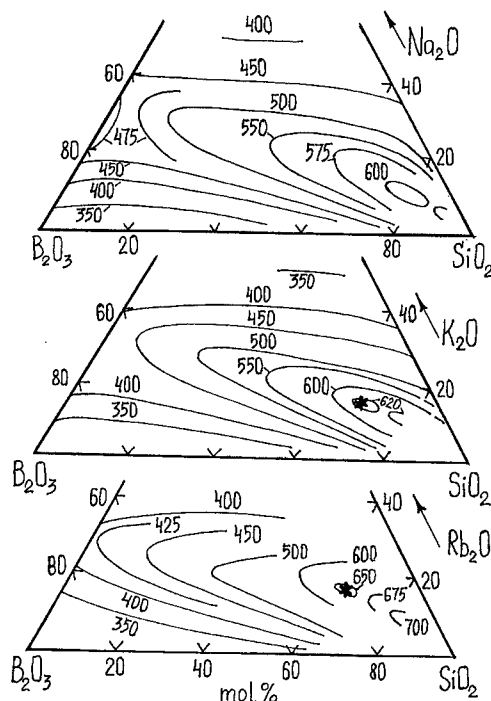


**Fig. 1.**  $T_g$  surfaces for the NBS, KBS and RBS systems. The numbers near the curves are the temperature in  $^{\circ}\text{C}$ .

cesium borosilicate systems (NBS, KBS, RBS, LBS and CBS, respectively), in order to reveal the nature of the alkali borosilicate (ABS) anomaly.

## 2. EXPERIMENTAL

More than 350 NBS, KBS and RBS and nearly 20 LBS and CBS compositions were prepared in the form of glasses and, where necessary, in the form of polycrystalline materials by using solid state reactions (SSR). The glasses were synthesised in platinum crucibles at temperatures of  $900\text{--}1600^{\circ}\text{C}$ , depending on the composition. The SSR samples, and glasses crystallised at certain temperatures, were used for the phase equilibria study. The glass transition temperatures ( $T_g$ ) and the melting points ( $T_L$ ) were determined by differential thermal analysis, to an error of  $\pm 5^{\circ}\text{C}$ . X-ray powder diffractometry (XRPD) has been used for crystal phase identification. The details of the liquid immiscibility investigation were reported in Ref. [2].

## 3. GLASS TRANSITION TEMPERATURES FOR ALKALI BOROSILICATE SYSTEMS

Figure 1 shows " $T_g$  vs. composition" diagrams for the NBS, KBS and RBS systems, based on the present data. All of the diagrams depict similar surfaces of intricate topology, with maxima near the silica corner of each diagram. The

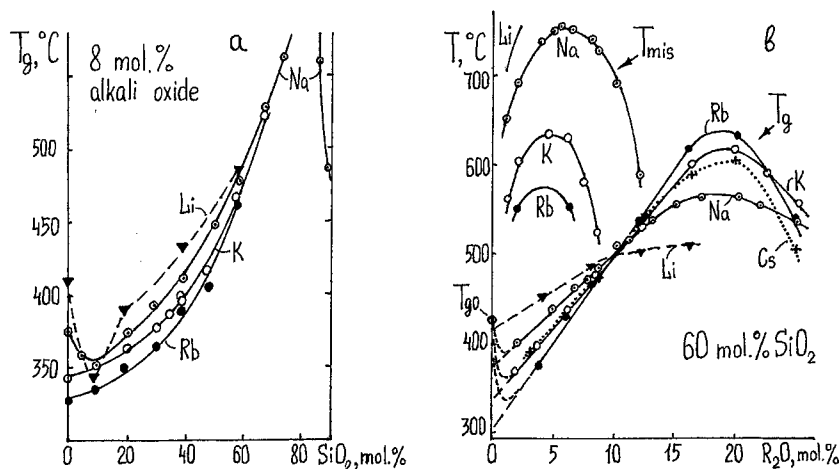


Fig. 2. Polythermal sections of  $T_g$  surfaces: (a) with 8 mol% alkali oxide and (b) with 60 mol%  $\text{SiO}_2$ . The  $T_{\text{mis}}$  curves represent the immiscibility boundaries.

data for the LBS and CBS systems show that their  $T_g$  diagrams have a similar shape. For the NBS system, it is clear that there is a saddle point separating the borosilicate maximum region from the borate anomaly maximum. Figure 2(a) demonstrates that such saddle points are present in other systems and that their depth diminishes with increasing cation atomic number. This means that the nature of this new structure is not connected with the borate anomaly. Another saddle point separates each borosilicate maximum from  $\text{SiO}_2$  in all of the diagrams. The new structure type, therefore, also differs from the silica glass structure. The composition dependencies of ABS  $T_g$  surfaces along the 60 mol%  $\text{SiO}_2$  line are compared in Fig. 2(b). Each of the dependencies have a maximum at approximately 20 mol% alkali oxide. As the alkali oxide content decreases, the glass transition temperatures diminish too and the heavier the cation, the greater the rate of diminution. The only exception is the CBS system, whose glass transition temperatures are close to those of KBS system. At approximately 10 mol%, the composition dependencies of  $T_g$  in all of the systems intersect and their extrapolation to zero alkali oxide content leads to different values of  $T_g$  for the alkali-free borosilicate system ( $T_{g0}$ ). Because the dependencies must in reality terminate at the same point, it is evident that they must all pass through minima, and the heavier the cation, the deeper the minimum (except for the CBS system). The cation atomic number dependence of  $T_{g0}$  is smooth in the series  $\text{Li} \rightarrow \text{Rb}$  and its extrapolation to zero atomic number gives a  $T_g$  value for the alkali-free system close to that known from the literature. On the  $T_g$  surfaces (Fig. 1), these minima must be located along the  $\text{B}_2\text{O}_3$ - $\text{SiO}_2$  axis and lie very close to it. They separate the structure connected with the alkali borosilicate system maxima from that of the alkali-free borosilicate glasses.

The  $T_g$  surfaces comparison discloses that this new structure is common for all of the ABS systems and covers a wide composition region. There are no ternary

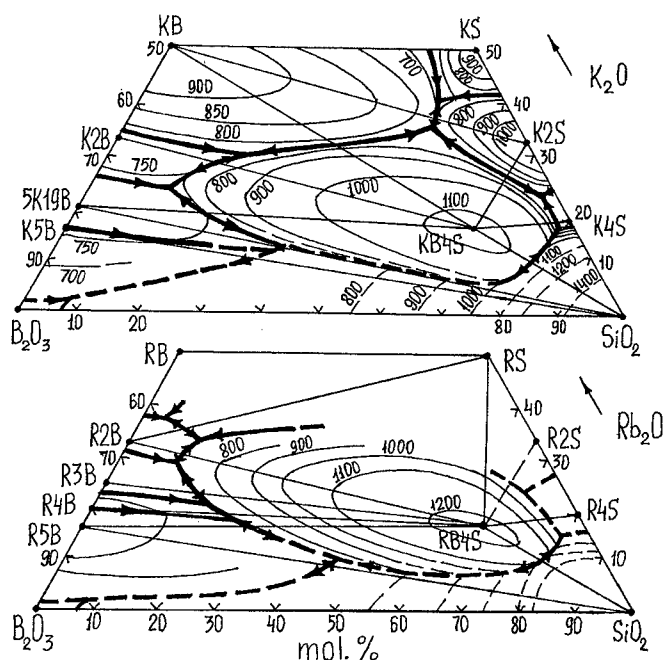


Fig. 3. Fragments of the liquidus surfaces for the potassium and rubidium borosilicate systems.

compounds in the LBS and NBS systems to explain this phenomenon. The required ternary compounds do, however, exist in the KBS, RBS and CBS systems.

#### 4. PHASE DIAGRAMS FOR THE KBS AND RBS SYSTEMS

The ternary compounds  $\text{K}_2\text{O} \cdot \text{B}_2\text{O}_3 \cdot 4\text{SiO}_2$  and  $\text{Rb}_2\text{O} \cdot \text{B}_2\text{O}_3 \cdot 4\text{SiO}_2$  were first found by Voldan [3,4], while  $\text{Cs}_2\text{O} \cdot \text{B}_2\text{O}_3 \cdot 4\text{SiO}_2$  was described in Ref. [5]. They are isostructural with each other and with the high temperature cubic form of leucite  $\text{K}_2\text{O} \cdot \text{Al}_2\text{O}_3 \cdot 4\text{SiO}_2$ . The structure of the potassium compound named "boroleucite" by Voldan was investigated independently in Ref. [6]. According to Ref. [6], all of the boron atoms in the boroleucite structure are in fourfold co-ordination and statistically replace silicate tetrahedra in the three-dimensional anionic network. The cations are situated in large framework cavities. The unit cell parameters and the melting temperatures for all three boroleucites are given in Ref. [7] but a  $T_L$  value of about  $1150^\circ\text{C}$  is now suggested for the cesium compound.

The first versions of the KBS and RBS phase diagrams were presented previously [7,8], while their improved and expanded variants are shown in Fig. 3.

For the description of phase diagrams, the following designations will be used:  $\text{K}_2\text{O}$  - K,  $\text{Rb}_2\text{O}$  - R,  $\text{Cs}_2\text{O}$  - C,  $\text{B}_2\text{O}_3$  - B,  $\text{SiO}_2$  - S; for example,  $\text{K}_2\text{O} \cdot \text{B}_2\text{O}_3 \cdot 4\text{SiO}_2$  will be denoted KB4S. A number of new ternary compounds have been found in the KBS system. XRPD data for some of these were given



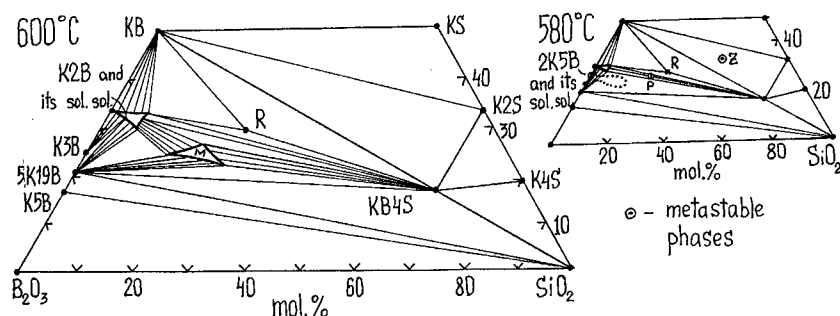


Fig. 4. Stable and metastable phase equilibria in the KBS system at (a) 600°C and (b) 580°C.

**Table 1**  
XRPD data for the P-phase, cubic, unit cell  
parameter  $a=8.779(2) \text{ \AA}$

d/n, Å	I/I <sub>0</sub>	hkl
5.08	5	111
3.106	100	220
2.648	45	311
2.196	15	400
2.015	20	331
1.791	5	422
1.689	3	511

**Table 2**  
XRPD data for the M-phase

d/n, Å	I/I <sub>0</sub>	d/n, Å	I/I
5.61	15	2.670	10
4.87	20	2.611	10
3.91	15	2.522	10
3.87	100	2.153	20
3.74	75	2.110	30
3.01	50	2.101	30
2.800	35	2.043	20

in Ref. [7,8], but now their compositions can be refined: the R-phase 3K4B3S (not 5K7B6S), decomposing in the solid state above 650°C, and two metastable phases, 2K5B (not 3K8B) and the Z-phase 3K2B4S (not 6K5B7S). Table 1 presents XRPD data for a new metastable P-phase, 5K8B4S, named pseudo-boroleucite because of the similarity of its pattern to that of KB4S. In the ternary system, a solid solution region exists, on the basis of the M-phase, 5K11B4S (stable only in the interval 600-640°C; XRPD data are given in Table 2). Two ternary solid solutions occur, based on binary compounds: one stable, based on K2B, and the other metastable, based on 2K5B. Figure 4 shows triangulation variants for the KBS system at 600 and 580°C.

In the RBS system solid solutions have been recorded, based on the binary compounds R5B and 3R7B, and two new ternary compounds the compositions of which must be refined.

## 5. BOROLEUCITE ANOMALY IN THE STRUCTURE OF ALKALI BOROSILICATE GLASSES

The central regions of the liquidus surfaces of the KBS and RBS systems are occupied by the primary crystallisation fields of the boroleucites (Fig. 3). The general view of the  $T_g$  surfaces (Fig. 1) for the ABS systems shows that their shapes are similar to those of the KBS and RBS liquidus surfaces. For these systems, the  $T_g$  surface maxima are located at the boroleucite composition (marked

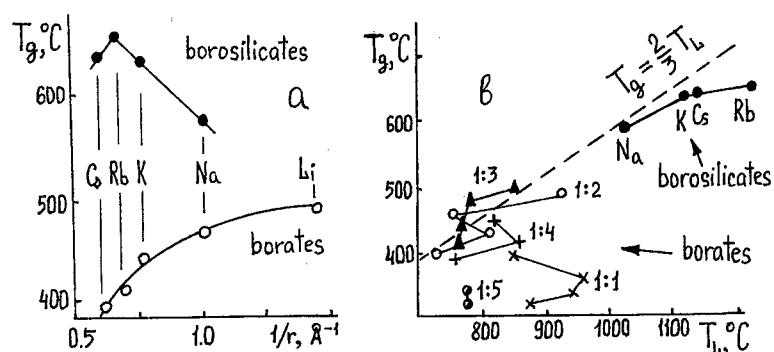


Fig. 5. A comparison of alkali borate and borosilicate systems:  $T_g$  for (a) glasses located at the maxima of the borate and boroleucite anomalies versus reciprocal atomic radius and (b)  $T_g$  for glasses with compositions corresponding to different stoichiometries: 1:5, pentaborates; 1:4, tetraborates; 1:3, triborates; 1:2, diborates and 1:1, extrapolation for metaborates.

with an asterisk in Fig. 1). The thermal stability of the glasses in this region corresponds to that of the respective crystals. Indeed, rubidium is the most thermally stable crystal among the boroleucites; the potassium cation is too small and the cesium cation is too large for the anion framework cavity and hence their crystals melt at lower temperatures. The sodium and lithium cations are so small that they cannot conform to the anion network and therefore cannot form any crystalline compounds. During the discussion of Fig. 2(b) the same relationship was noted between the  $T_g$  of glasses: the better the steric matching of the cation size to the framework cavity, the higher the glass transition temperature. As a result, RBS glass has the highest  $T_g$  value in the maximum region. For the other systems,  $T_g$  decreases as the boroleucite structures become weaker. The composition dependence of  $T_g$  (Figs. 1 and 2) is determined by the boroleucite group content; the greater this content, the larger the connectivity of the anion network and the higher the glass transition temperature. The difference between borates and borosilicates is also apparent from Fig. 5(a). For alkali borate glasses in the borate anomaly region, the normal cation field strength dependence of  $T_g$  can be seen: the greater the field strength, the more rigid the glass structure and the larger the  $T_g$  value. For the boroleucite anomaly, the rigidity of the glass structure is not sensitive to the cation field strength, but is governed by the above steric matching of the cation and cavity size. Moreover, in Kauzmann's co-ordinates (Fig. 5(b)), the points for systems having a boroleucite type compound lie on a straight line. For alkali borate systems, nothing of this kind is observed. The boroleucite anomaly, in boroleucite crystal containing systems, produces so-called "regular" maxima on "property-composition" diagrams because, in these cases, the structure of the glass is directly related to the crystalline structure. The borate anomaly causes "irregular" property maxima, because the structure of the glasses does not correspond to any particular crystalline structure but generates a great variety of compounds. Another fact is apparent from Fig. 5(b). Only if compositions are located in either anomaly maximum region

(boroleucites, di-, tri- and tetraborates), do their points lie close to the Kauzmann rule straight line. Pentaborate and metaborate (extrapolated data for  $T_g$ ) points depart from Kauzmann's line.

## 6. THE NATURE OF LIQUID PHASE SEPARATION IN ALKALI BOROSILICATE SYSTEMS

Alkali borosilicate systems are the only non-organic ones having ternary immiscibility gaps which are not connected with phase separation in corresponding binary systems. This phenomenon may appear only if the very factor responsible for phase separation is intrinsic to the ternary system itself. The refined versions of the boundary locations for the NBS, KBS and RBS immiscibility gaps are presented in Ref. [9,10]. The comparison of these data with literature data for the LBS system shows that the cation change does not affect composition limits of the immiscibility gap along the major axes or the tie-line directions, which are approximately the same for all of the systems, far from the upper critical points. These phase separation properties are determined by the anion framework common to ABS systems. The cation atomic number affects the temperatures of the upper critical points and the extent of the gaps along minor axes. The upper critical points for all of the systems lie along a straight line, and the minor axes for all systems coincide with each other and with this line [9], which passes through the boroleucite composition (the critical point for the LBS system practically coincides with it). The tendency for separation is greatest at the critical point and, in ABS systems, it is greatest in the vicinity of boroleucite. Figure 2(b) depicts the immiscibility boundaries for ABS systems along the 60 mol%  $\text{SiO}_2$  line. The low-alkali boundary locations coincide with the minimum on the composition dependence of  $T_g$ , i.e. phase separation develops with increasing alkali oxide content only if a sufficient quantity of boroleucite groups is present, resulting in an increase in the glass transition temperature. When the boroleucite groups begin to form a three-dimensional network, the miscibility of separated phases occurs. Weak boroleucite groups are present in the lithium system, but they are not able to form a network and thus the immiscibility covers a large composition region, including the boroleucite anomaly maximum. In other systems, the temperature and composition ranges of the immiscibility gap decrease as the strength of the boroleucite groups increases. It may therefore be suggested that, because the boroleucite groups in the CBS system are weaker than those in the RBS system, the immiscibility gap in the CBS system will not be less than in the RBS system.

## 7. CONCLUSIONS

The comparative physico-chemical analysis carried out above cannot provide information about the form of boroleucite groups in alkali borosilicate glasses. This is for structure-sensitive methods to determine. It may only be said that: (1) the existence of a maximum on the property-composition dia-

grams for alkali borosilicate systems is connected with the presence of boroleucite groups in the glass structure; (2) boroleucite groups are present in the structure of all alkali borosilicate glasses, regardless of whether the corresponding crystalline compound exists in the system (KBS, RBS and CBS) or not (LBS and NBS); (3) the fact that the boroleucite crystal structure contains only four-coordinated boron is the reason why, in the glass, nearly all of the boron atoms are in the tetrahedral state in this region; (4) the flat tops of the liquidus surfaces for the boroleucite primary crystallisation fields point to a high degree of dissociation for these congruently melting compounds; (5) large fragments of the boroleucite structure, including large cavities, remain in the melts; (6) boroleucite groups are joined to one another and form a strong three-dimensional anion framework that explains the high density, high chemical stability and some other properties of the glasses in this anomalous region and (7) liquid immiscibility may be used as an indicator of structural transformations in the boroleucite anomaly region of alkali borosilicate systems.

## REFERENCES

- [1] B.C. Bunker, D.R. Tallant, R.I. Kirkpatrick & G.L. Turner, *Phys. Chem. Glasses* **31** (1990), 30.
- [2] I.G. Polyakova, *Glass Phys. Chem.* **20** (1994), 386.
- [3] J. Voldan, *Silikaty* **23** (1979), 133.
- [4] J. Voldan, *Silikaty* **25** (1981), 165.
- [5] Powder Diffraction File, Card No 37-1347, International Center for Diffraction Data.
- [6] M. Ihara & F. Kamei, *J. Ceram. Soc. Japan* **88** (1980), 32.
- [7] I.G. Polyakova, E.V. Tokareva & T.V. Popova, In: *Proc. 17th Congr. on Glass*, Beijing, China, Nov. 1995, **2**, pp. 381-386.
- [8] E.V. Tokareva & I.G. Polyakova, In: *Proc. 17th Congr. on Glass*, Beijing, China, Nov. 1995, **2**, pp. 279-284.
- [9] I.G. Polyakova, In: *Proc. 17th Congr. on Glass*, Beijing, China, Nov. 1995, **2**, pp. 414-419.
- [10] I.G. Polyakova, *Glass Phys. Chem.* **23** (1997), 45.

## EFFECT OF MODE OF FORMATION ON THE STRUCTURE OF BOROSILICATE GLASSES

Yanko B. DIMITRIEV, Elena P. KASHCHIEVA,  
Maria A. BURSUKOVA & Plamen D. HINKOV  
*University of Chemical Technology and Metallurgy,  
Sofia - 1756, Bulgaria*

Borate glasses containing  $\text{SiO}_2$  and  $\text{TeO}_2$  have been synthesised both by traditional melting technology and by the sol-gel method. The influence of the method of preparation on the short and medium range order as well as on the formation of microheterogeneities is examined by transmission electron microscopy and electron diffraction. The structural evolution is established both in the gels and in the glasses after thermal treatment.

### INTRODUCTION

The role of vitreous boron oxide as a basic glass-former has been intensively investigated using various different complementary techniques. Recently a review has been presented [1], on the basis of a neutron diffraction study, and conclusions are drawn concerning the main structural units. The fraction of boron atoms involved in boroxol groups ( $\text{B}_3\text{O}_6$ ) is found to be 0.8, which is in agreement with earlier results [2-4]. The structure of glasses containing boron oxide is very complicated and its study involves the solving of several structural problems: first, the participation of  $\text{BO}_3$  and  $\text{B}_3\text{O}_6$  units in the network depends on the method of synthesis and second, the appearance of  $\text{BO}_4$  and other more complex superstructural units follows the introduction of  $\text{M}_2\text{O}$  or  $\text{MO}$  into the glass composition. Finally, further structural complications arise from the ability of  $\text{B}_2\text{O}_3$  to form heterogeneous structures in multicomponent systems, which may result from liquid phase separation, metastable immiscibility, etc.

In previous studies by the present authors, the boundaries between the homogeneous and heterogeneous amorphous compositions have been established for various  $\text{B}_2\text{O}_3\text{-TeO}_2\text{-M}_m\text{O}_n$  systems [5,6]. Different oxides were used as the third component, in appropriate concentrations: (i) modifying oxides -  $\text{Ag}_2\text{O}$ ,  $\text{CaO}$ ,  $\text{SrO}$  and  $\text{BaO}$ ; (ii) transitional metal oxides -  $\text{TiO}_2$ ,  $\text{Cr}_2\text{O}_3$ ,  $\text{CoO}$ ,  $\text{NiO}$ ,  $\text{MnO}$ ,  $\text{WO}_3$ ,  $\text{Fe}_2\text{O}_3$  and  $\text{CuO}$  and (iii) oxide glass formers -  $\text{GeO}_2$ ,  $\text{Sb}_2\text{O}_3$  and  $\text{SiO}_2$ . Recently special attention has been paid to the systems  $\text{B}_2\text{O}_3\text{-TeO}_2$  and  $\text{B}_2\text{O}_3\text{-SiO}_2\text{-TeO}_2$ , which only contain glass formers, due to the possibility of obtaining specific microstructures with a wide variety of dimensions, depending on the thermal treatment regime and the composition [7,8].

The precursors and the mode of preparation also influence the formation of different glass structures and, in this connection, sol-gel technology is of special interest, since it can be employed for the production of fibres, coatings and bulk materials. By this method, it is possible to create new glass compositions with a high concentration of non-traditional components, to prevent the appearance of micro- and macrophase separation and to improve the homogeneity of the glasses. Borosilicate compositions have been prepared by the sol-gel method [9,10] and the structural evolution has been studied, following heat treatment of the gels, by IR and NMR spectroscopy. Conclusions are drawn concerning the co-ordination number of the boron atoms with respect to oxygen and the formation of B-O-Si bonds [11-16].

In the present study, the structure of melt-quenched amorphous samples from  $B_2O_3$ ,  $B_2O_3$ - $TeO_2$  and  $B_2O_3$ - $SiO_2$  systems are compared and the structural evolution from the gel to the gel-glass is examined using electron diffraction (ED) and transmission electron microscopy (TEM). The purpose is to determine the basic structural units composing the glass network in the system  $B_2O_3$ - $SiO_2$ - $TeO_2$  and to obtain new information concerning the tendency for microaggregation, as a function of the composition and the mode of formation.

## EXPERIMENTAL

$H_3BO_3$ ,  $SiO_2$  and  $TeO_2$  were used as the starting materials for the preparation of the melt quenched glasses. The batches were heated in platinum crucibles in an electrical furnace and melted at a temperature of  $\sim 1200^\circ C$ . Different cooling rates were employed to obtain melt-quenched glasses: slow cooling in the crucibles ( $10$ – $100^\circ C/s$ ) and roller quenching techniques ( $10^4^\circ C/s$ ). Tetraethylorthosilicate (TEOS) and triethylborate (TEB) were used as precursors for the synthesis of the gels, using the techniques explained in ref. [9]. The gels were thermally treated at  $200$  and  $600^\circ C$ .

A Philips EM400 electron microscope was employed to examine powder specimens by transmission electron microscopy (TEM) and electron diffraction (ED).  $TeO_2$  was used to nucleate the formation of microheterogeneities, in accordance with the phase diagram for  $B_2O_3$ - $TeO_2$  [17]. It also enhances the contrast in the TEM observations.

The main advantage of ED is the possibility of determining the short range order (SRO) in microvolumes, from small quantities of sample and thin films, and also for materials containing both light and heavy elements. Another advantage is that, with the same equipment, it is possible to carrying out experiments to determine the morphology and electron scattering for one and the same region of the sample. The method is not very popular because of various experimental difficulties, which are connected with incoherent scattering of the electrons. This problem may be solved directly, by electrostatic filtering of the incoherently scattered electrons [18,19], or indirectly, following methods based on the comparison of the background scattering from the same substance in the amorphous and crystalline state [20-22]. These methods were



**Fig. 1.** (Left) TEM micrograph of the  $55\text{B}_2\text{O}_3.45\text{SiO}_2$  gel sample, after heating at  $600^\circ\text{C}$ , and (Right) TEM micrograph of the  $50\text{TeO}_2.10\text{B}_2\text{O}_3.40\text{SiO}_2$  glass sample.

verified for pure  $\text{TeO}_2$ , which may be crystallised under the influence of electron-beam irradiation, in that they yielded identical results.

The primary electron diffraction data were measured photometrically, with a Carl-Zeiss (Jena) microphotometer, to yield the intensity curves. Corrections for the incoherent scattering and background intensity were made according to ref. [20] and the data were normalised using the procedure described by Vainstein [23]. The atomic Radial Distribution Function (RDF) was obtained by Fourier transformation of the coherently scattered intensity. The first peak positions were determined by fitting with Gaussian functions.

## RESULTS AND DISCUSSION

Figure 1(a) is a TEM micrograph of the  $55\text{B}_2\text{O}_3.45\text{SiO}_2$  gel sample after heating at  $600^\circ\text{C}$ . It demonstrates that the gel has a homogeneous structure. The structure of the melt-quenched glass with the same composition is identical.

In comparison, pure vitreous  $\text{B}_2\text{O}_3$  and binary compositions containing a small amount of  $\text{TeO}_2$  (<4%) develop different types of microheterogeneity, which are well resolved by TEM [8]. The first, here referred to as the “background structure”, consists of ultrafine nanometer-sized inhomogeneities (1–3 nm). As pointed out elsewhere [8] such a structure is typical for  $\text{B}_2\text{O}_3$  glass (slow cooled samples), but is not found in other glass formers. The second type of microheterogeneity is well-shaped spherical formations, ranging in size from 10 to 20 nm. These exist

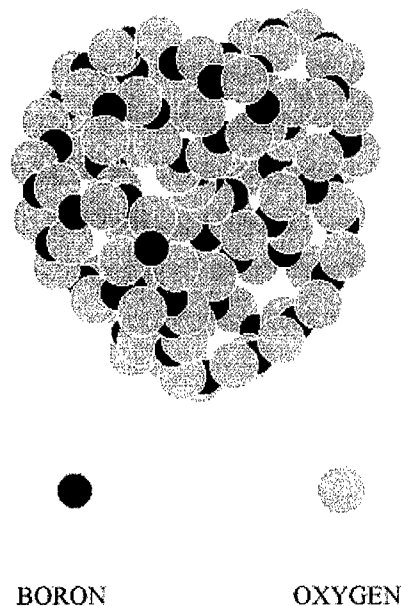


Fig. 2. Computer model of a cluster without free bonds, containing 66 B atoms and 99 O atoms, with 46% of the B atoms in  $B_3O_6$  groups.

either separately or as conglomerates. Finally, different types of large scale droplet are formed. The latest two microstructures are due to metastable phase separation. A comparison of  $B_2O_3$ - $SiO_2$  gels and glasses with more complicated compositions from the  $B_2O_3$ - $SiO_2$ - $TeO_2$  system shows (Fig. 1(b)) that  $TeO_2$  nucleates the formation of microheterogeneities embedded in the amorphous matrix.

In the authors' opinion, the different types of inhomogeneity and microaggregation in borate compositions are directly influenced by the specific building units simultaneously participating in the more complex borate melts. One qualitative explanation may be given on the basis of the SRO parameters for the structural polyhedra [24]. In fact, the problem of the inhomogeneous structure of glass-formers was discussed a long time ago. For example, in the papers of Zarzycki [25], the problem of the atomic domain structure is described. The most precise classification of the microheterogeneities is developed by Porai-Koshits *et al.* [26], for both one component and different binary systems, on the basis of SAXS measurements and includes thermal density fluctuations, structural inhomogeneities, supercritical fluctuations and heterogeneous structures resulting from the interconnection of similar structural complexes. Following this classification and the results obtained by Golubkov [27], the background structure observed in our TEM experiments may be considered as a more complicated structure also including thermal density fluctuations. Recently, on the basis of NMR results, it has been proposed that boron oxide glass consists of domains with a variable content of boroxol rings [28].



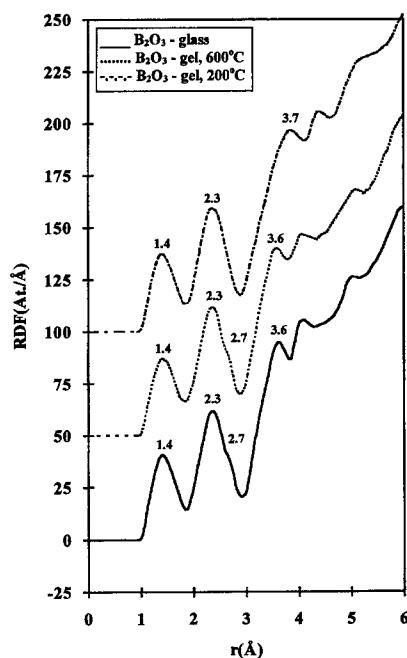


Fig. 3. RDF curves for  $B_2O_3$  gel and glass samples.

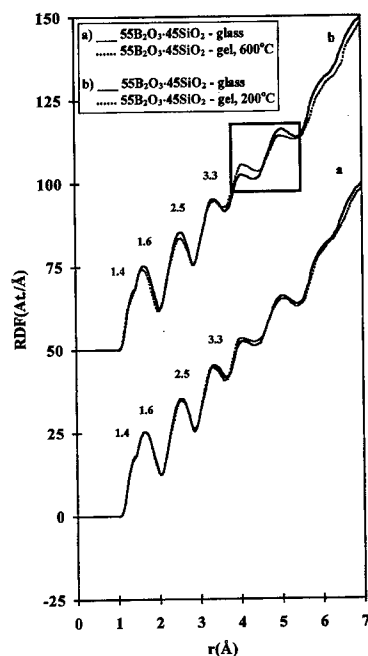


Fig. 4. RDF curves for  $55B_2O_3.45SiO_2$  gel and glass samples.

Using molecular mechanics techniques (MMT), an attempt has been made to simulate the formation of nanoscale clusters in vitreous  $B_2O_3$  [8]. When  $B_{10}O_{15}$  units (the molecule of Gerber [29]) are used as a superstructural unit, together with  $B_3O_6$  and  $BO_3$  groups in appropriate ratios, an energetically and geometrically minimised model cluster may be constructed (Fig. 2), which contains 66 boron atoms and 99 oxygen atoms without free bonds. The resulting model density is  $1.79 \text{ g cm}^{-3}$  following the calculating procedure recommended in ref. [30]. The first B–O distances and O–B–O angles for both the  $BO_3$  and  $B_3O_6$  groups in the cluster are  $1.36 \text{ Å}$  and  $120^\circ$  respectively. The dimension of the cluster is about  $15 \text{ Å}$ . These computer modelling studies show that, by using an appropriate combination of structural units, it is possible to obtain borate glass network fragments with different degrees of microheterogeneity, and this is why information about the SRO and the main building units of the glass-network is important in the generation of more realistic structures. Figure 3 shows the RDF curves for amorphous  $B_2O_3$  samples obtained under different conditions. The (B–O) distances between the atoms in the first co-ordination shell are identical ( $r_1 \sim 1.4 \text{ Å}$ ), while the maximum at  $2.33 \text{ Å}$  is well resolved and corresponds to O–O pairs ( $r_2$ ) and to the B–B distances ( $r_3$ ) within the boroxol group as discussed in ref. [2]. The shoulder at approximately  $2.7 \text{ Å}$ , which may be attributed to the next B–O distance in the  $B_3O_6$  group ( $r_4$ ), is absent in the gel and appears in the RDF curve only after thermal treatment of the sample

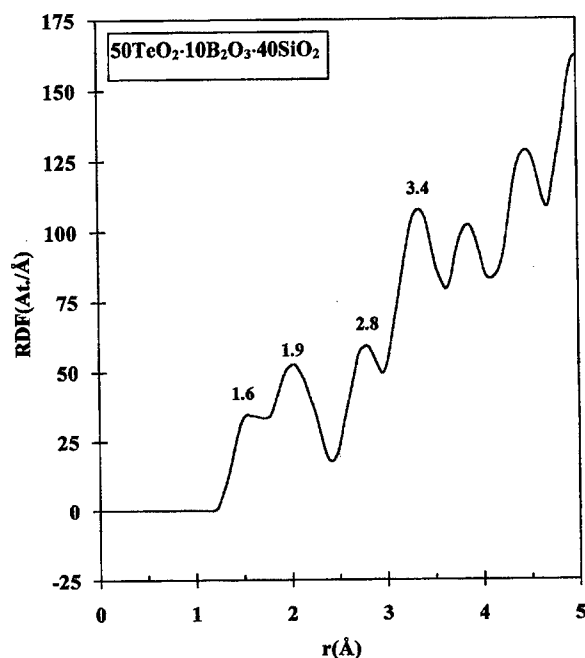


Fig. 5. RDF curve for 50TeO<sub>2</sub>·10B<sub>2</sub>O<sub>3</sub>·40SiO<sub>2</sub> glass.

up to 600°C. The other point of note is that, after heating, the distance  $r_5$ , corresponding to the third B–O distance in the B<sub>3</sub>O<sub>6</sub> unit, is shifted from 3.7 Å to 3.6 Å as found in the melt-quenched sample.

The RDF curves for the binary compositions (Fig. 4) are similar to that for amorphous SiO<sub>2</sub>. The diffraction data for the thermally-treated gel and the melt-quenched glass are almost the same. There is a shoulder at ~1.4 Å and peaks at ~1.6 Å and ~2.5 Å. Some differences appear in the curves in the region above 3 Å, consisting of a change in the peak heights at 4 and 5 Å. According to a model developed by Kamyia *et al.* [31], this may be explained in terms of the presence of 4-fold siloxane rings in the gel. Only after heating are these destroyed and the structure is transformed and becomes similar to that of the melt-quenched glasses containing only 6-fold rings.

In the RDF of the three-component glass, 50TeO<sub>2</sub>·10B<sub>2</sub>O<sub>3</sub>·40SiO<sub>2</sub> (Fig. 5), peaks are observed associated with the Si–O atomic pairs at ~1.6 Å and the Te–O pairs at ~1.9 Å. The maximum at 3.38 Å may possibly be due to Si–Si pairs from adjacent SiO<sub>4</sub> tetrahedra. The displacement of this maximum to higher  $r$ , in comparison with pure SiO<sub>2</sub>, may result from overlapping distances from the B<sub>3</sub>O<sub>6</sub> group, while Te–Te pairs are responsible for the maximum at 3.9 Å, which is also shifted to higher  $r$  in comparison with pure TeO<sub>2</sub>. According

to earlier results of Dimitriev [24], the addition of a second component leads to a change in the  $\text{TeO}_4$  polyhedra as a result of the inclusion of other structural units into the vitreous network. Hence, the angles between the polyhedra are altered and the Te-Te distances also are changed. This result indicates that the structure of such a complex  $\text{TeO}_2\text{-B}_2\text{O}_3\text{-SiO}_2$  glass comprises independent polyhedra participating simultaneously in one and the same network.

## CONCLUSION

Using TEM and ED it has been shown that the mode of formation and the cooling rate influence both the type of basic structural unit (short range order) and the manner of their interconnection in the glassy network (medium range order). They also determine the tendency for the formation of microheterogeneities in these glasses. The medium range order structure of the gels is different but, after thermal treatment, it is transformed into the glass structure.

## ACKNOWLEDGEMENT

This investigation is supported financially by the Bulgarian National Foundation for Science, under Contract No. X-527/1995.

## REFERENCES

- [1] A.C. Wright, *J. Non-Cryst. Solids* **192&193** (1995), 92.
- [2] P.A.V. Johnson, A.C. Wright & R.N. Sinclair, *J. Non-Cryst. Solids* **50** (1982), 281.
- [3] A.C. Hannon, D.I. Grimley, R.A. Hulme, A.C. Wright & R.N. Sinclair, *J. Non-Cryst. Solids* **177** (1994), 299.
- [4] G.E. Jellison Jr. & P.J. Bray, *J. Non-Cryst. Solids* **29** (1978), 187.
- [5] E. Kashchieva, *Ph.D. Thesis* (VHTI, Sofia, 1984).
- [6] Y. Dimitriev, E. Kashchieva & M. Koleva, *J. Mat. Sci.* **16** (1981), 3045.
- [7] E. Kashchieva & Y. Dimitriev, *J. Mat. Sci. Lett.* **14** (1995), 732.
- [8] E. Kashchieva, P. Hinkov, Y. Dimitriev & S. Miloshev, *J. Mat. Sci. Lett.* **13** (1994), 1760.
- [9] M. Nogami & Y. Moriya, *J. Non-Cryst. Solids* **48** (1982), 359.
- [10] J. Phalippou, M. Prassas & J. Zarzycki, *J. Non-Cryst. Solids* **48** (1982), 17.
- [11] M.A. Villegas & J.M.F. Navarro, *J. Mat. Sci.* **23** (1988), 2464.
- [12] C.C. Harrison & Z. Luo, *J. Sol-Gel Sci. Techn.* **2** (1994), 73.
- [13] M.A. Villegas, J. Sanz & J.M.F. Navarro, *J. Non-Cryst. Solids* **121** (1990), 171.
- [14] N. Tohge & T. Minami, *J. Non-Cryst. Solids* **112** (1989), 432.
- [15] N. Pellegrini, O. De Sanctis & A. Duran, *J. Sol-Gel Sci. Techn.* **2** (1994), 519.
- [16] A.D. Irwin, J.S. Holmgren & J. Jonas, *J. Non-Cryst. Solids* **101** (1988), 249.
- [17] Y. Dimitriev and E. Kashchieva, *J. Mat. Sci.* **10** (1975), 1419.
- [18] L.C. Qin & L.W. Hobbs, *J. Non-Cryst. Solids* **192&193** (1995), 456.
- [19] H. Ohsaki, K. Miura, A. Imai, M. Tada & M. Aegerter, *J. Sol-Gel Sci. Techn.* **2** (1994), 245.
- [20] L.I. Tatarinova, *Electronografia Amorfnykh Veshchestv* (Nauka, Moskva, 1972).
- [21] S. Fujime, *Jap. Journ. Appl. Phys.* **5** (1966), 764.
- [22] P. Moine, A.R. Pelton & R. Sinclair, *J. Non-Cryst. Sol.* **101** (1988), 213.
- [23] B.K. Vainshtein, *Kristallografia* **2** (1957), 29.
- [24] Y. Dimitriev, *Sc.D. Thesis* (VHTI, Sofia, 1991).
- [25] J. Zarzycki, In: *Proc. 10th International Congress on Glass*, Kyoto, 1974, p.12.
- [26] E.A. Porai-Koshits, In: *Survey Papers of the XVth International Congress on Glass*, Leningrad, July 3-7, 1989 (Nauka, Leningrad, 1989), pp. 30-64.

- [27] V.V. Golubkov, *J. Non-Cryst. Solids* **192&193** (1995), 463.
- [28] R.E. Youngman, S.T. Haubrich, J.W. Zwanziger, M.T. Janicke & B.F. Chmelka, *Science* **269** (1995)1416.
- [29] T. Gerber, B. Himmel & P. Weigelt, In: *Proc. 16th Intern. Cong. on Glass*, Madrid, Spain, Oct. 4-9, 1992, Eds. A. Duran and J.M.F. Navarro (S.E. de Ceramica y Vidrio, Madrid, 1992), p. 89.
- [30] A.C. Wright, In: *Experimental Techniques of Glass Science*, Eds. C.J. Simmons and O.H. El Bayoumi (Amer. Ceram. Soc., Westerville, 1993), Chap. 8, p. 70.
- [31] K. Kamiya, M. Wada, J. Matsuoka & N. Nasu, *Bull. Inst. Chem. Res., Kyoto Univ.* **72** (1994), 105.

## SURFACE STUDIES OF BORATE GLASSES

Carlo G. PANTANO, Douglas M. BEALL  
& William CERMIGNANI

*Department of Materials Science and Engineering,  
Pennsylvania State University, University Park, PA, 16802, USA*

X-ray photoelectron spectroscopy and low-energy ion scattering spectroscopy have been used to characterize the surfaces of boron oxide, sodium borate and barium aluminoborate glasses. It is shown that the Bls binding energy cannot distinguish between 3-fold and 4-fold coordinated boron. The ISS analyses show a depletion of modifier-ions in the surface monolayer of the glasses. In the case of melt surfaces, this modification of the surface can be attributed to evaporation and diffusion. In the case of fracture surfaces, it is necessary to consider the effects of ionic fractoemission and surface reconstruction.

### 1. INTRODUCTION

The surface tension of  $B_2O_3$  is one of the lowest for any inorganic oxide glass melt ( $\sim 80$  dyn/cm at  $1000^\circ\text{C}$ ). Qualitatively, at least, this can be attributed to its molecular structure. The planar boron oxide groups can orient themselves in the surface of the melt to minimize their distortion by the asymmetric environment, as well as to minimize the number of dangling bonds [1,2]. These ideas are consistent with the fact that  $B_2O_3$  exhibits a positive temperature coefficient for surface tension. Accordingly, the increasing temperature disorients the low-energy surface structure, and thereby, raises the surface tension. (This is anomalous behavior in the sense that most liquids show a decrease in surface tension as the temperature is increased towards the boiling point.) Kingery, however, suggested that surface orientation is only a minor factor in the observed positive temperature coefficient for surface tension [3]. He attributed it to changes in the liquid structure with increasing temperature; that is, to a decrease in the effective ion size at elevated temperature.

The measurements of surface tension for a series of binary alkali borates by Shartsis & Capps show the classical boron oxide anomaly [4] (although there are numerous statements in the literature that surface tension does not exhibit the anomaly). The fact that the surface tension goes through a maximum is consistent with a higher partial molar surface energy for tetrahedral versus trigonal boron oxide molecular groups. Perhaps of greater significance, though, was their observation that the (positive) temperature coefficient of surface tension was constant up to about 20 mol% alkali oxide. They interpreted this to mean that the surface of these melts was largely  $B_2O_3$ . They attributed the

effect to a surface-localized tendency toward immiscibility.

Altogether, these observations about surface tension suggest that a driving-force exists to segregate and to orient planar boron oxide groups in the surface of glass:

- (1) in the case of pure  $B_2O_3$ , concentration and orientation of the largest groups - presumably boroxyl rings - can be expected;
- (2) in the case of binary alkali borates, segregation and orientation of planar boron oxide groups to the surface, and displacement of tetrahedral groups away from the surface, would occur;
- (3) in the case of more complex borate glasses, such as alkali or alkaline earth aluminoborates, the displacement of high-energy aluminate groups by planar boron oxide seems most likely;
- (4) and in the case of borosilicate glasses, the segregation of boron-oxide to the surface also seems likely.

Some additional consequences of these events would be:

- (5) the absence or depletion of alkali and alkaline earth species in multicomponent borate surfaces since they are most commonly associated with the higher energy tetrahedral boron oxide groups, and
- (6) the preferential spreading of borate-rich phases at the surface of immiscible compositions.

Of course, the extent to which any of these events might occur depends upon the activity and mobility of planar boron oxide species in the bulk of the glass. Moreover, the viscosity/temperature of the glass, as well as the external pressure and atmosphere, can further modify the surface composition and structure due to volatilization and surface reaction. Thus, it is necessary to analyze, directly, the surface composition and structure to further develop these models.

It is evident that although there have been numerous studies of silicate, phosphate and fluoride glasses using surface-sensitive techniques, there has been little comparable evaluation of borates. X-ray photoelectron spectroscopy (XPS) and low-energy ion scattering (ISS) have been widely applied to characterize the non-bridging oxygen activity and atomic arrangement at multicomponent silicate glass surfaces [5,6]. Likewise, XPS has been used to examine the distribution of anion sites in phosphate and fluoride glasses [7,8]. The XPS studies of borate glasses already reported [9-11] did not include compositions or standards to test the sensitivity to non-bridging (NBO) oxygen or boron coordination. In this study, XPS and ISS were evaluated for their capability to characterize borate glass surfaces; specifically,

- to distinguish  $[BO_3]$  versus  $[BO_4]$  groups at glass surfaces,
- to detect the presence and concentration of non-bridging oxygens, and
- to measure the enrichment or depletion of alkali at borate glass surfaces.

## 2. EXPERIMENTAL PROCEDURE

The glasses were melted in platinum crucibles using reagent-grade raw materials. The triphenylboron, triphenylboroxine and borophosphate ( $BPO_4$ ) standards were reagent-grade. The crystalline standards (tourmaline and danburite) were obtained courtesy of the Mineral Museum at the Pennsylva-

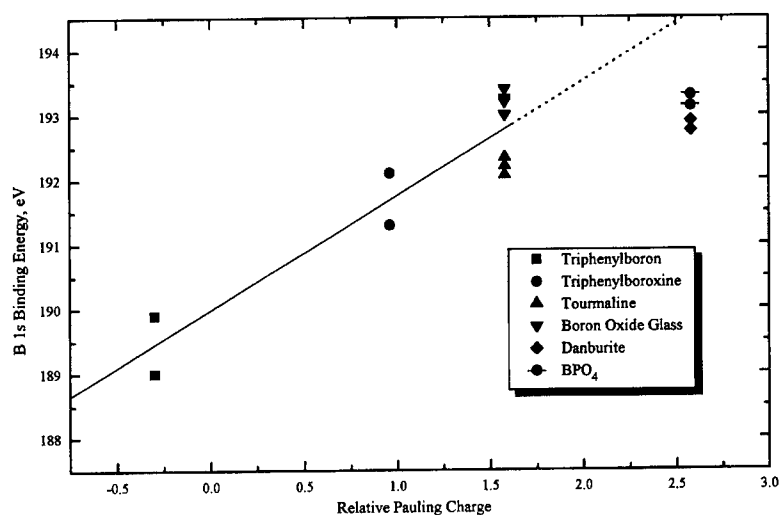


**Figure 1.** Relation between the measured B1s photoelectron binding energy and the charge on boron calculated using equation 1; each measurement was performed 2-3 times on different samples.

nia State University. The surfaces to be analyzed were prepared by fracturing in air and/or in vacuum, or by annealing sessile drops on graphite substrates. The air-sensitive powders were mounted for analysis in a nitrogen-purged glove bag that was interfaced directly to the surface analysis instrument.

The XPS analyses were performed with a Kratos XSAM 800 using Mg Ka radiation (1253.6 eV). In all cases, the XPS data was collected in the high-resolution mode. The binding energy scale was calibrated against Cls at 284.6 eV. The ISS analyses were performed using a Kratos cylindrical mirror analyzer with a  $^3\text{He}^+$  ion beam. The ion beam energy was varied over the range 1000 eV to 3000 eV to vary the scattering depth.

### 3. RESULTS AND DISCUSSION

Figure 1 presents a plot of the B1s photoelectron binding energies measured for a variety of boron-containing molecules, crystals, and glasses. The glasses and crystals were chosen to provide structures wherein the boron coordination is known to be uniquely 3-fold ( $\text{N}_3$ ) or 4-fold ( $\text{N}_4$ ). The molecular standards were chosen to provide lower Pauling charge by substitution of C for O around boron in the planar 3-fold configuration. The glasses and crystals were fractured to provide surfaces whose composition and structure were assumed to be equivalent to the bulk structure. The validity of this assumption is discussed below. The observed binding energies cover the range from ~189 to 194 eV, and verifies the sensitivity of XPS to the short-range order in these materials.

The measured binding energies have been plotted against the Pauling charge. The Pauling charge was calculated on the basis of the known structures of

these materials using:

$$q_i = \sum b_j f_{ij} \quad (1)$$

where,  $q_i$  = Pauling charge on atom  $i$ ,  $b_j$  = number of bonds between atoms  $i$  and  $j$ , and  $f_{ij}$  = fractional ionicity. In these calculations, only the first near-neighbors of the boron ions were considered. If it is assumed that this Pauling charge is sufficient for describing the B1s binding energy dependence upon local structure [12,13], a deviation occurs for structures wherein the boron atoms are uniquely  $N_4$  (Pauling charge = 2.5). This deviation could reflect a reconstruction of these surfaces to yield only  $N_3$  at the surface, but this is considered unlikely because these surfaces were created at room temperature. An alternative interpretation of this deviation concerns the calculated Pauling charge. Since the excess negative charge on  $N_4$  sites must be compensated by second near neighbors (e.g., alkali and alkaline earth ions, or in the case of  $BPO_4$ ,  $P^{+5}$ ), the Pauling charge calculation based solely upon first near-neighbors may be overestimated. In fact, use of the modified Sanderson charge model [14,15], which considers electronegativity equalization between larger groups of atoms and molecules, yields partial charges on the boron which are almost identical for  $B_2O_3$  and  $BPO_4$ . This necessarily implies that the electron density on the boron ion is nearly equivalent in  $N_3$  and  $N_4$  configurations, and consequently, the B1s binding energy, alone, cannot be used to distinguish the coordination number for boron.

Figure 2 summarizes XPS data for a series of Ba-aluminoborate glasses. Over this range of R-values (where  $R = (BaO-Al_2O_3)/B_2O_3$ ), the fraction of boron in tetrahedral coordination ( $N_4$ ) varies from ~0.05 at  $R=0$ , to 0.35 at  $R=0.5$ , and falls to 0.15 at  $R=1.45$ . These characteristics of the bulk structure were independently determined using MAS-NMR. Figure 2(a) shows that the B1s and O1s photoelectron binding energies decrease continuously over this range of compositions. In the range  $R=0$  to 0.5, where the appearance of tetrahedral boron occurs in the bulk, neither the shape nor the width of the B1s spectra suggests any measurable distribution of boron bonding configurations on the surface. A similar trend was observed in the case of Na-borate glasses, although the range of glass compositions that could be examined in this system was limited to R-values up to 0.5. In both cases, though, the modified Sanderson method revealed a linear relationship between the B1s binding energy, and the calculated partial charge on the boron [15]. This indicates that there is an averaging effect of the glass composition upon the electron density at all of the boron sites.

Figure 2(b) shows, however, that the O1s lines for the Ba-aluminoborate glasses with  $R \geq 0.5$  are broadened. This broadening occurs in those compositions where the existing structure models for these aluminoborate glasses would predict the creation of non-bridging oxygens (~5%, 26% and 51% NBO for R-values of 0.5, 0.72 and 1.45, respectively). A deconvolution of the spectra into



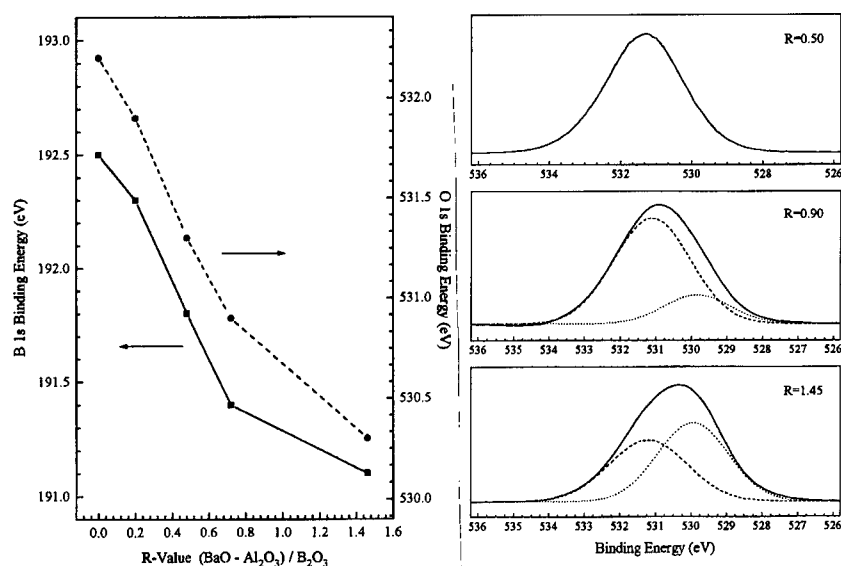


**Figure 2.** XPS data for a series of barium aluminoborate glasses. (a) B1s and O1s binding energy versus composition, and (b) high resolution O1s spectra with deconvolution of bridging and non-bridging oxygen contributions.

two lines - where the lower binding energy component at 529.8 eV corresponds to the NBO - yields ~0, 19% and 54%, respectively, for the percentage NBO in these three compositions. Their agreement with the calculated values suggests that the NBO content of the surface is equivalent to the bulk.

ISS data were collected on two series of borate glasses. One of these is the sodium borate system and the other is the barium aluminoborate system. In low-energy ISS, the incident He ions are almost exclusively scattered in the outermost monolayer of the glass. Thus, this method is exceedingly sensitive to atomic rearrangement or reconstruction of the surface. The most interesting aspect of these measurements concerned the modifier species Na and Ba. The data in Figures 3 and 4 summarize the results. It is clearly evident that the measured ion scattering intensity ratios scale with the bulk concentration ratios. But the plots do not extrapolate through zero. A similar relationship is observed in silicate glasses except that the extrapolation suggests an enrichment of alkali in the surface monolayer. In the case of silicate glasses, this has been attributed to a rearrangement whereby the alkali shields dangling oxygen bonds on the silica tetrahedra, and thereby, is enriched in the surface monolayer.

In the case of these borate glasses, the extrapolation suggests depletion of Na in the case of sodium borate, and depletion of Ba in the case of barium aluminoborate, at the surface. Since the majority of the Na and Ba modifier species are expected to be associated with tetrahedral borate groups, this observation also suggests a depletion of N<sub>4</sub> groups (and/or enrichment in N<sub>3</sub> groups) at the surface, or the presence of electronic defects. The fact that the

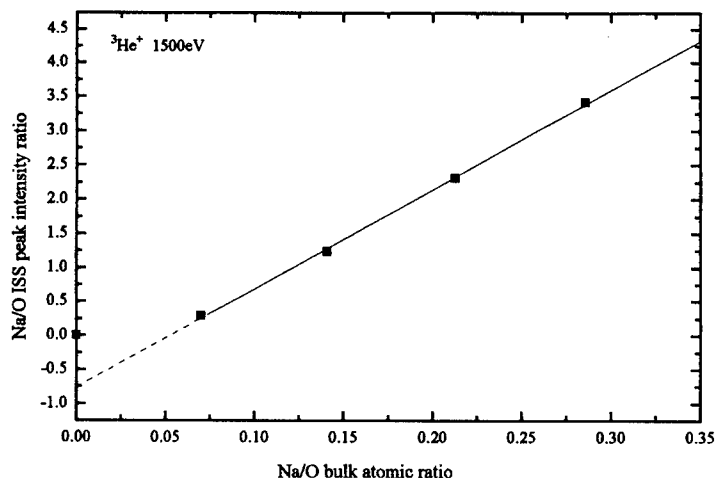


**Figure 3.** ISS data showing the dependence of relative scattering intensity in the surface monolayer of clean fracture surfaces upon the bulk Na/O atomic ratio in  $\text{Na}_2\text{O}-\text{B}_2\text{O}_3$  glasses.

Ba depletion is enhanced in melt surfaces, versus the fracture surfaces, is not surprising. In the case of the melt surfaces, it is likely that evaporation and diffusion could facilitate this surface modification. The fracture surfaces, on the other hand, were created at room temperature. It is possible that a reconstruction of the surface borate groups from  $\text{N}_4$  to  $\text{N}_3$  (due to the higher partial molar surface energy of the  $\text{N}_4$  groups) could create a driving force for the modifier-ion to hop into the sub-surface. The localized heating created during the fracture could enhance this. It is more likely, though, that the fracture event itself participates in the reconstruction. The fracture process is highly ener-

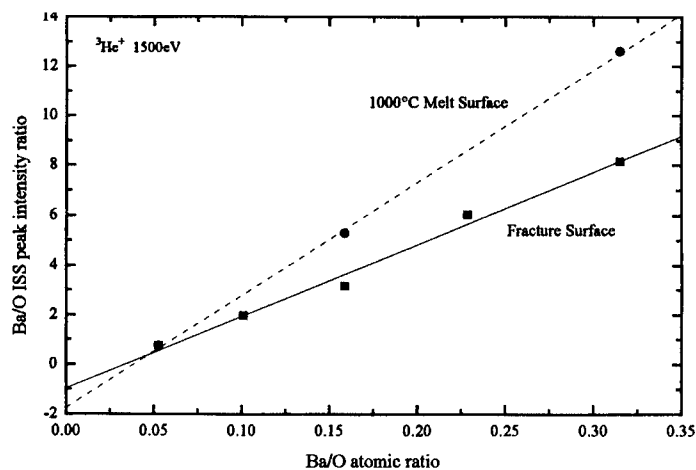


**Figure 4.** ISS data for clean fracture surfaces and melt surfaces of barium aluminoborate glasses.

getic, and in many solids, the emission of electrons, photons and ions accompany the fracture event (so called *fractoemissions*) [16]. The fractoemissions observed during crack-propagation in glasses has been found to include modifier ions [17]. Here, the ionic fractoemission of Ba and O, and the reconstruction of  $N_4$  to  $N_3$ , could facilitate the creation of lower energy surfaces. Although speculative at this time, this model could explain the data reported here and elsewhere, for borate glasses.

#### 4. SUMMARY

The Pauling charge model predicts that the BIs binding energy associated with the  $BO_4$  groups should be measurably greater than that of  $BO_3$  groups. But the analysis of a variety of reference standards and aluminoborate glasses do not show this distinction. The modified Sanderson method for calculating the charge on boron based upon electronegativity equalization over a larger number of atoms shows an excellent correlation with the XPS data (due to space limitations, it could not be included here - see 15). This is consistent with the network model for these glasses, as opposed to models with discrete molecular configurations. The ISS studies showed that the modifier concentrations in the surface monolayer are not equal to their bulk concentrations.

#### ACKNOWLEDGEMENTS

The authors gratefully acknowledge the Office of Naval Research (N00014-93-1-0319) and the Air Force Office of Scientific Research (F49620-93-1-0311) for their financial support.

#### REFERENCES

- [1] A. Dietzel, *Kolloid Z.* **100** (1942), 368.
- [2] W. A. Weyl, in *The Constitution of Glasses* (John Wiley, New York, 1964), pp. 635-645.
- [3] W. D. Kingery, *J. Am. Ceram. Soc.* **42** (1959), 6.
- [4] L. Shartsis & W. Capps, *J. Am. Ceram. Soc.* **35** (1952), 169.
- [5] C. G. Pantano, in *Experimental Techniques of Glass Science*, Eds C. J. Simmons and O. El-Bayoumi, Editors (Am. Ceram. Soc, Ohio, 1993) pp. 129-160.
- [6] J. Kelso, S. Garofalini & C. G. Pantano, *Surf. Sci.* **134** (1984) L543.
- [7] R. K. Brow, R. J. Kirkpatrick & G. L. Turner, *J. Am. Ceram. Soc.* **73** (1990), 2293.
- [8] R. M. Almeida, J. Lau, & J. D. Mackenzie, *Mater. Sci. Forum* **6** (1985), 465.
- [9] B. M. J. Smets & T. P. A. Lommen, *Phys. Chem. Glasses*, **2216** (1981), 158.
- [10] Y. Kaneko & Y. Sugimohara, *Yogyo-Kyokai-Shi* **90**, (1982), 58.
- [11] D. A. Hensley & S. H. Garofalini, *Appl. Surf. Sci.* **81** (1994), 331.
- [12] U. Gelius, *Phys. Scr.* **9** (1974), 133.
- [13] R. K. Brow & C. G. Pantano, *J. Am. Ceram. Soc.* **69** (1986), 314.
- [14] R. T. Sanderson, *Chemical Bonds and Bond Energy* (Academic Press, New York, 1976).
- [15] D. M. Beall, *Surface, Structure and Chemistry in Borate and Boroaluminate Glasses*, PhD Dissertation, The Pennsylvania State University, 1997.
- [16] J. T. Dickinson, et al, *J. Mater. Res.* **6** (1991), 112.
- [17] S. C. Langford, et al, *J. Mater. Res.* **6** (1991), 1358.

## PHYSICAL PROPERTIES OF ALKALI BOROSILICATE GLASSES

Steven A. FELLER, Jason KOTTKE, Joshua WELTER,  
Sumit NIJHAWAN, Rachel BOEKENHAUER,  
Hong ZHANG, David FEIL, Chitra PARAMESWAR,  
Karim BUDHWANI, Mario AFFATIGATO,  
Ajay BHATNAGAR, Gaurav BHASIN,  
Siddhartha BHOWMIK, Joshua MACKENZIE<sup>1</sup>,  
Michael ROYLE, Shyam KAMBEYANDA,  
Ponnappa PANDIKUTHIRA & Monica SHARMA  
*Physics Department, Coe College, Cedar Rapids, IA 52402 USA.*

There is a close correspondence between short range structure, determined spectroscopically, and physical properties in alkali borosilicate glasses. The density and glass transition temperature were measured in all alkali borosilicate glass systems for a very wide range of alkali concentrations, in families of glasses with constant silica to boron oxide ratios. The density data are compared with quantitative structural models as determined by the <sup>11</sup>B NMR work of Bray and coworkers.

### 1. INTRODUCTION

The <sup>11</sup>B NMR work of Phil Bray and coworkers on borosilicate glasses and the consequent development of quantitative structural models [1-4] has led to a much better understanding of the short range order. This laboratory has attempted to elucidate quantitative relationships between these models with measurements of various physical properties over the widest compositional ranges reported to date [5-8]. This paper presents thorough property results from these glass systems and it compares these data with structural information.

### 2. EXPERIMENTAL PROCEDURES

Glass batches were prepared from reagent grade or better silica, boron oxide, boric acid, and either alkali carbonates *or* alkali oxides. These two sets of starting materials were used to broaden glass formation in regions where one set of starting materials was not effective in producing glass [7]. The glasses were made either in platinum or vitreous carbon crucibles. The glasses displayed increasing hygroscopic tendencies with increasing alkali content and such glasses were melted and handled in glove boxes under a dry nitrogen atmosphere.

---

<sup>1</sup> Present Address: Motorola Corporation, Northbrook, IL USA

The well-mixed batches were fused at 1000-1400°C for periods of about twenty minutes. The samples were weighed five minutes before the end of fusion to verify sample composition as reported previously [9]. The samples were reheated and either roller-quenched, plate-quenched, or cast depending on the ease of glass formation.

Density was measured either by a modified sink-float method employing acetone and diiodomethane [6] or through the use of a micropycnometer which used helium gas. The experimental uncertainty is estimated to be  $\pm 0.02$  g/cc. The glass transition temperature was measured on either a Perkin-Elmer DSC-2 or DTA with each operated at a scan rate of 40 K/min. Runs were repeated and the estimated batch-to-batch experimental uncertainty in the onset-defined  $T_g$  is  $\pm 7$  K.

### 3. EXPERIMENTAL RESULTS

#### 3.1 Density

Table 1 lists the densities of these glasses as a function of R with fixed K, where R and K are the molar ratios of alkali oxide and silica to boron oxide, respectively.

**Table 1**

Densities of Alkali Borosilicate Glasses Measured in This Laboratory (in g/cc with an uncertainty of  $\pm 0.02$  g/cc, values in italics are from glasses prepared from alkali oxides)

Lithium					Potassium				
R	K=0	K=0.5	K=1.0	K=3.0	R	K=0	K=1.0	K=2.0	K=4.0
0.00	1.81	1.92,1.91	1.97,1.98		0.00	1.81	1.97,1.98		
0.05	1.88				0.05	1.97			
0.10	1.96	2.03			0.07	2.02			
0.15	2.00				0.10	2.07			
0.20	2.11	2.12	2.12		0.15	2.10			
0.25	2.10				0.20	2.13			
0.30	2.18				0.25	2.16			
0.40	2.22	2.26	2.28		0.30	2.19,2.20	2.27		
0.50	2.27				0.40	2.30,2.27			
0.60	2.28	2.33	2.34		0.50	2.32	2.34	2.40	2.34,2.35
0.70	2.28				0.60	2.30,2.31			
0.80	2.28	2.35	2.37		0.60	2.33			
0.90	2.24				0.70	2.30	2.42,2.42		
1.00	2.23	2.34	2.38	2.32	0.80	2.31,2.31			
1.10	2.24				1.00		2.42	2.46	2.46
1.20	2.19	2.32			1.00		2.40,2.43	2.47,2.48	
1.30	2.18		2.36		1.20			2.45	
1.40	2.18				1.50		2.38	2.46	2.47,2.48
1.50	2.16	2.27		2.39	1.60	2.28			
1.60	2.14		2.33		1.90	2.29			
1.70	2.15				2.00		2.37	2.41,2.41	
1.80	2.11				2.00				2.48,2.48
1.90	2.09				2.10	2.32			
2.00	2.12	2.22	2.30	2.38	2.30	2.32			
2.10	2.09				2.50	2.32	2.39		2.49
2.20	2.09				2.70	2.32			
2.30	2.08				2.90	2.32			

2.40	2.08				3.00		2.37,2.40	2.38,2.39	2.46
2.50	2.07				4.00			2.38,2.39	2.43
2.60	2.10				4.00			2.39	
2.70	2.10				5.00			2.33	2.43
2.75	2.10				6.00				2.44,2.45
3.00		2.14	2.22	2.35	7.00				2.42
4.00		2.13	2.18	2.33					
5.00		2.11	2.16						
6.00			2.14	2.27					
7.00		2.09	2.13						
8.00			2.11						
10.00			2.10						

#### Sodium

R	K=0	K=0.5	K=1.0	K=1.5	K=2.0	K=3.0	K=4.0	K=6.0
0.00	1.81	1.91, 1.92	1.97, 1.98					
0.05	1.92							
0.07	2.00, 2.03							
0.10	2.04							
0.15	2.11, 2.13		2.11					
0.20	2.14	2.16	2.17					
0.25	2.19							
0.30	2.25		2.27					
0.40	2.32	2.35	2.37	2.33				
0.50	2.37	2.41	2.41	2.40	2.43	2.45	2.37	
0.60	2.37	2.45						
0.70	2.37, 2.38		2.47	2.47	2.49			
0.80	2.39							
0.85	2.37							
1.00			2.48,2.50	2.50	2.51, 2.52	2.51	2.50	2.43
1.20		2.43						
1.30	2.36							
1.50		2.47	2.50	2.50, 2.51	2.51	2.52		
1.70	2.39							
1.90		2.43						
2.00	2.39		2.45	2.49			2.52	
2.20	2.39							
2.25								2.51
2.50	2.38	2.42	2.46	2.48		2.51		
2.70	2.39							
3.00	2.39		2.47	2.50		2.51		
3.20	2.39							
3.50	2.34	2.46	2.48	2.49				2.52
4.00				2.51		2.52		
4.80						2.53		
7.00								2.52

#### Rubidium

R	K=0	K=1	K=2	K=4	R	K=0	K=1	K=2	K=4
0.00	1.81	1.97,1.98		0.00	1.81	1.97,1.98			
0.10	2.17,2.18				0.05	2.10			
0.20	2.38,2.41				0.10	2.39			
0.29	2.61				0.15	2.51			
0.30	2.58,2.61				0.20	2.71			
0.40	2.79,2.80				0.25	2.78			
0.50	2.92	2.76,2.81	2.67	2.56	0.30	2.96			
0.52	2.95				0.31	2.97			
0.60	2.99				0.35	3.08			
0.70	3.04				0.40	3.20			
0.80	3.06				0.50		3.12	2.94	2.74

1.00		3.10	2.99	2.85,2.82	0.79	3.57				
1.50		3.16	3.13	2.99,2.99	1.00	3.60	3.16			
1.88	3.38				1.08	3.77				
2.00		3.23	3.20	3.09	1.40	3.89				
2.17	3.40				1.44	3.89				
2.22	3.45				1.50		3.74	3.62	3.37	
2.50	3.47	3.34	3.24	3.16	1.89	3.98				
2.54	3.48				2.00	3.99	3.92	3.78	3.53	
2.69	3.49				2.50			3.93	3.65	
3.00		3.32	3.33	3.24	2.58	4.15				
3.50			3.34	3.29	2.70	4.07,4.08				
4.00			3.35	3.32,3.33	3.00			3.98	3.81	
4.50			3.38	3.36	3.50			4.01	3.88	
5.00				3.38	4.00			4.04	3.96	
5.89				3.39	4.50				4.04	
6.00				3.38	5.00				4.00,4.01	
					6.35				3.98	

### 3.2 Glass Transition Temperature

Table 2 displays the  $T_g$  data obtained from the alkali borate and borosilicate series as a function of R for fixed K families.

**Table 2**

$T_g$  Data for Alkali Borosilicate Glasses Measured in This Laboratory (in K with an uncertainty of  $\pm 7$  K. Values in italics are from glasses prepared from alkali oxides)

Lithium						Potassium					
R	K=0	K=0.5	K=1.0	K=2.0	K=3.0	K=4.0	R	K=0	K=1.0	K=2.0	K=4.0
0.00	533	574	582				0.00	533	582		
0.05	570						0.10	618			
0.10	616	652					0.10	615			
0.15	668	703	733				0.20	675			
0.20	708	734	753				0.30	705	745		
0.20	706						0.40	719			
0.30	757		770				0.50	705	786	843	
0.30	762						0.50			844,846	
0.40	769	770	776				0.60	678			
0.50	773			788	770		0.70	643			903
0.60	756	779	787				1.00		714,713	819,834	
0.70	741						1.50		662		847,855
0.80	730	758	783				2.00		623	682	765
0.90	714						2.50		590		
1.00	694	739	766	791	779		3.00		562	634,630	703,694
1.00		743					3.50		602		
1.20	651	718			782		4.00		574	593	672
1.20	652	720					4.00			601,601	665
1.30			742				5.00			560	647,643
1.50	602	680		768	787		6.00			579	613
1.50	604						7.00				599
1.60			714				7.50				590
1.90	566						8.00				634
2.00	554	624	680	740	771	777					
2.00		624									
2.20	547										
2.40	542										

Lithium						Sodium						
R	K=0	K=0.5	K=1.0	K=2.0	K=3.0	K=4.0	R	K=0	K=0.5	K=1.0	K=2.0	K=4.0
2.50				712			0.00	533	574	582		
2.60	543						0.20	702				
2.70	544						0.30	748		764		
2.75	548						0.40			784		
2.75	544						0.50	752		800	829	848
2.80	546						0.70	715		794	851	
3.00		570	607	677	724		0.80		749			
3.00		571		682	722		1.00		713	752	814	865
3.00	568						1.50		648	692	743	842
3.30						734	1.60	556				
4.00		583	584	605	682	713	2.00	530	589	646	699	799
4.00		582		630			2.50	516	551	602	669	743
4.50		567					3.00	505	536	572		705
4.50		562					3.50		525	557	621	
5.00		548	605	607	638	704	4.00		517			680
5.00				608		680	4.50		508	536	581	
5.00						679	5.00			522		651
5.00						684	5.50				559	
6.00		525	569	619	621	650	6.00					621
6.00						652	7.00				539	601
7.00		510	544	635	623	635	8.00					589
7.50				613			9.00					565
8.00			526	590	629		11.0					554
8.50					636		12.0					548
9.00					627							
9.00			515		611							
9.50					614							
10.00			510		606							
11.00					589							
Rubidium						Cesium						
R	K=0	K=1	K=2	K=4		R	K=0	K=1	K=2	K=4		
0.00	533	574	582			0.00	533	574	582			
0.15	641					0.18	635					
0.18	644,650					0.20	648					
0.30	694					0.36	704,700					
0.36	698					0.40	703,703					
0.40	723					0.50		807				
0.50	700					0.55	688					
0.53	700					0.73	643					
0.58	696					0.89	605					
0.72	651					1.00				895		
0.90	630					1.35	557					
1.00		703		912		1.38	573					
1.50		648		832		1.50		614	689	822		
1.62	550					1.62	539					
1.80	552					1.85	513					
2.00		615	672	766		2.00		583	639	752		
2.25	516					2.18	534					
2.50		587	649	710		2.24	506					
3.00		570	625	702		2.34	460,467					
3.11		567				2.50			593	695		
3.15	495					2.77	507					
3.50			604	679		2.79	501					
4.00			589	633		2.80	503					
4.27			594			2.85	501					
4.50			593	654		3.00			589	653		



5.00	633	3.21	492		
5.89	612	3.28	480		
6.00	610	3.50		574	648
6.89	610	3.62	483		
7.74	605	4.00		543	639
		4.50		548	634
		5.00			612

#### 4. STRUCTURE-PROPERTY RELATIONSHIPS: DENSITY

Generally, the  $^{11}\text{B}$  NMR work of Phil Bray and others [3,4] indicates that the structure of alkali borosilicates can be thought of as consisting of separate borate and silicate networks. The NMR results indicate that initial alkali added to these systems goes preferentially to the borate network until some value for  $R$ , denoted here as  $R_0$ . Above  $R_0$  alkali is shared between the two networks. In the sodium borosilicate system the model proposed by Dell & Bray has some additional features [4].

The structure of the borate aspect in the ternary glass is similar to that of the binary alkali borates. As  $R$  is increased from zero alkali oxide is shared between the borate and silicate parts of the glass. In the borate subsystem with increasing  $R$  trigonal borons convert to the tetrahedral form. With further alkali oxide addition trigonal borons with NBOs appear. The structural models which follow allow fractional quantities of all basic borate groupings to be determined [8].

Recent  $^{29}\text{Si}$  MAS NMR on lithium, sodium, and potassium borosilicates indicates that silicate tetrahedra with varying numbers of NBOs are present in these glasses [10-12]. Sharing of the alkali oxide also is indicated by the chemical shifts observed in the  $^{29}\text{Si}$  MAS NMR data.

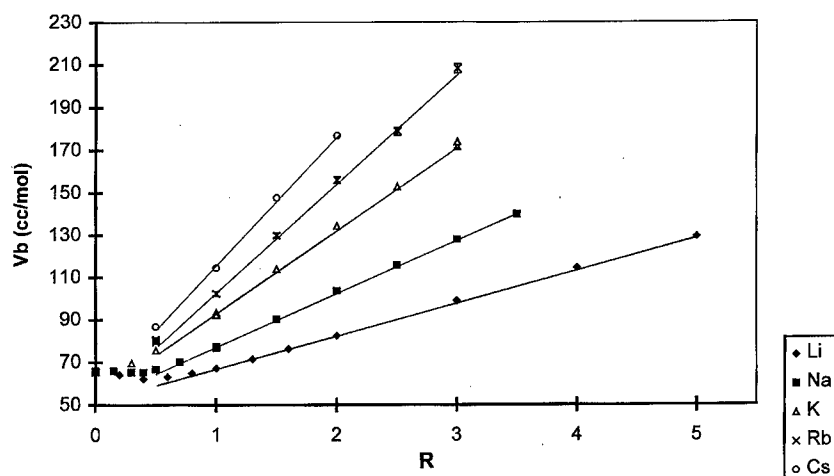


Fig. 1. Volume per mole boron oxide,  $V_b$ , as a function of  $R$  in  $K=1$  alkali borosilicate glasses. The straight lines are meant to serve as guides to the eye.

**Table 3**  
Slopes and Intercepts from  $V_b$  Plots of Alkali Borosilicate Glasses with  $R \geq 0.5$ .

Alkali	K	$V_0$	$\Delta V_0/K$	slope	F	$r^2$
	[SiO <sub>2</sub> ]/[B <sub>2</sub> O <sub>3</sub> ]	(cc/mol)	(cc/mol per unit K)	(cc/mol per unit R)		
Li	0	28.65	—	16.27	0.41	0.998
Li	1	52.60	23.95	15.22	0.44	1.000
Na	0	29.21	—	26.13	0.50	1.000
Na	1	53.01	23.79	24.90	0.52	0.999
Na	2	78.08	24.44	22.93	0.57	0.992
Na	4	125.36	24.04	23.48	0.55	0.999
K	0	30.41	—	40.61	0.66	1.000
K	1	53.96	23.56	39.64	0.68	0.999
K	2	74.54	22.07	41.08	0.66	0.999
K	4	127.05	24.16	38.59	0.70	0.999
Rb	0	31.26	—	49.45	0.65	1.000
Rb	1	53.57	22.31	50.92	0.63	0.999
Rb	2	76.35	22.54	50.50	0.64	0.999
Rb	4	125.73	23.62	48.69	0.66	0.999
Cs	0	30.09	—	63.95	0.65	0.999
Cs	1	55.44	25.35	60.77	0.69	0.999
Cs	2	79.36	24.63	60.83	0.68	0.999
Cs	4	125.36	23.82	60.94	0.68	0.997

A useful way to view the density is to plot the volume per mole boron oxide,  $V_b$ , as a function of  $R$  for fixed  $K$  values. A representative plot is shown in Fig. 1 for the  $K=1$  alkali borosilicates. A close examination of the low alkali regime in the Li and Na glasses shows there is an actual decline in this volume as compression occurs due to the coordination change of the borons. As  $R$  increases beyond 0.5 there is a linear increase in this volume for all of the alkali systems. This is thought to occur because non-bridging oxygens are formed on the silica tetrahedra along with boron tetrahedra being converted back to trigonal borons with various numbers of NBO's. The slopes of the linear regime are alkali dependent and nearly independent of  $K$  while the Y-intercept, defined as  $V_0$ , is very nearly independent of alkali and is a strong function of  $K$  (see Table 3). In Table 3 the quantity  $\Delta V_0/K$  was determined from

$$\Delta V_0/K = (V_0(K) - V_0(K=0))/K \quad (1)$$

and is a measure of the change in the volume of the silica tetrahedra as silica content is varied in the glass. The silica network contracts in each alkali system since the corresponding value for  $V_0$  in silica glass is 27.25 cm<sup>3</sup>/mol. The slopes and values for ionic radii [13-15] allow for a calculation of the differential filled space ratio,  $F$ , (which represents the filling of space as  $R$  changes by unity in a particular  $K$  family), see Table 3. The quantity  $r^2$ , given in Table 3, is the square of the correlation coefficient from the least squares analyses of the data. As the alkali become larger than oxygen (K, Rb, Cs) the value for  $F$  is nearly constant and is approximately that of the random packing of hard spheres (0.64).

## 5. CONCLUSIONS

Extensive physical property data from the alkali borosilicate glass systems are presented. These data have been related to structural models from NMR [1-8, 10-12].

## Acknowledgements

The authors wish to acknowledge the support by the US National Science Foundation under grants DMR 93-01247 and 96-23681. A. C. Wright is acknowledged for his kind hospitality and useful discussions during S. Feller's sabbatical stay at Reading University (UK) during 1996. The UK/US Fulbright Commission is thanked for supporting S. Feller in England. P. Venhuizen helped with the preparation of the manuscript.

## REFERENCES

- [1] P.J. Bray & J.G. O'Keefe, *Phys. Chem. Glasses* **4** (1963), 37.
- [2] P.J. Bray, S.A. Feller, G.E. Jellison, Jr. & Y.H. Yun, *J. Non-Cryst. Solids* **38/39** (1980), 93.
- [3] J. Zhong, X.Wu, M.L. Liu & P.J. Bray, *J. Non-Cryst. Solids* **107** (1988), 81.
- [4] W.J. Dell & P.J. Bray, *J. Non-Cryst. Solids* **58** (1983), 1.
- [5] M. Shibata, C. Sanchez, H. Patel, S. Feller, J. Stark, G. Sumcad & J. Kasper, *J. Non-Cryst. Solids* **85** (1986), 29.
- [6] B.C.L. Chong, S.H. Choo, S. Feller, B. Teoh, O. Mathews, E. J. Khaw, D. Feil, K. Chong, M. Affatigato, D. Bain, K. Hazen & K. Farooqui, *J. Non-Cryst. Solids* **109** (1989), 105.
- [7] M. Royle, M. Sharma, S. Feller, J. MacKenzie & S. Nijhawan, *Phys. Chem. Glasses* **34** (1993), 149.
- [8] D. Feil & S. Feller, *J. Non-Cryst. Solids* **119** (1990), 103.
- [9] H. Zhang, S. Koritala, K. Farooqui, R. Boeckenhauer, D. Bain, S. Kambeyanda & S. Feller, *Phys. Chem. Glasses* **32** (1991), 185.
- [10] S.W. Martin, S. Feller, D. Bain & K. Budhwani, *J. Am. Ceram. Soc.* **75** (1992), 1117.
- [11] S.W. Martin, A. Bhatnagar, C. Parameswar, S. Feller & J. MacKenzie, *J. Am. Ceram. Soc.* **78** (1995), 952.
- [12] S.W. Martin, J.W. MacKenzie, A. Bhatnagar, S. Bhowmik, S.A. Feller & M.L. Royle, *Phys. Chem. Glasses* **36** (1995), 82.
- [13] R.D. Shannon, *Acta Crystallogr. A* **32** (1976), 751.
- [14] R.L. Warren & B.E. Warren, *J. Appl. Crystallog.* **3** (1970), 251.
- [15] W.H. Zachariasen, *Acta Crystallogr.* **17** (1963), 749.

## CRYSTALLIZATION KINETICS IN Ca, Sr AND Ba BOROPHOSPHATE SYSTEMS

Galina A. SYCHEVA

Structure-Physical Laboratory, Institute of Silicate Chemistry,  
Odoevskogo 24 - 2, St.Petersburg, 199155, Russia

and

Vladimir N. SIGAEV

*Mendeleev University of Chemical Engineering,  
Miusskaya pl. 9, Moscow, 125190, Russia*

Optical microscopy, x-ray powder diffractometry, and differential thermal analysis techniques have been utilised to determine differences in the nucleation rates,  $I$ , between wet and dry Ca, Sr and Ba borophosphate glasses. It is apparent that small amounts of water affect the nucleation rates, which will control the final microstructure. The effect of water vapor soaking has been tested to find the best way to promote the crystallisation.

### 1. INTRODUCTION

Glass-forming in alkali and alkali-free borophosphate systems and in the  $\text{MeO-B}_2\text{O}_3\text{-P}_2\text{O}_5$  system has been described in several papers [1-4]. As regards structural glass formation and the physical as well as the chemical properties of glasses, the systems  $\text{R}_2\text{O-B}_2\text{O}_3\text{-P}_2\text{O}_5$  ( $\text{R}=\text{Li, Na, K, Ag}$ ) have been subject to the most systematic study [5-11]. Previous work [12-14] has been concerned with the study of borophosphate glass-forming systems containing RO oxides ( $\text{R}=\text{Mg, Ca, Sr, Ba}$ ), with respect to the glass structure and its physical and chemical nature. In Ref. [14] the results are reported from an investigation of glasses in the system  $\text{SrO-B}_2\text{O}_3\text{-P}_2\text{O}_5$ , including the crystallisation ability, softening-point temperature, chemical stability and electrical resistivity of the glasses. Work [15] has been reported regarding the formation of structural groups during synthesis, as well as those existing in the glass-forming system  $\text{BaO-B}_2\text{O}_3\text{-P}_2\text{O}_5$ , and is concerned with the chemical reactions that occur during the thermal processing of  $\text{BaO-B}_2\text{O}_3\text{-xP}_2\text{O}_5$  ( $x=0\text{-}60\text{ mol\%}$ ) mixtures and the structure of the glasses that evolve with the gradual addition of  $\text{P}_2\text{O}_5$ . The assumption that chemical compound formation among the constituents determines the structure and properties of the glass prior to melting is the major premise of this work. Glass formation regions, following quenching from

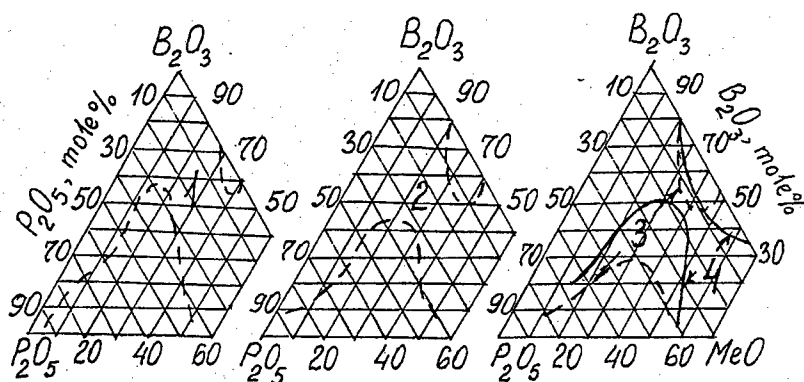


Fig. 1. The glass formation regions in the systems  $\text{MeO-B}_2\text{O}_3\text{-P}_2\text{O}_5$ , 1,  $\text{Me}=\text{Ca}$ ; 2,  $\text{Sr}$ ; 3 and 4,  $\text{Ba}$  (4 from Ref. [1]).

1200°C, were also studied in Ref. [15]. Reference [13] is devoted to a study of the glass-formation and some of the physicochemical properties of glasses in the  $\text{MeO-B}_2\text{O}_3\text{-P}_2\text{O}_5$  system, where  $\text{Me}=\text{Mg}$ ,  $\text{Ca}$ ,  $\text{Sr}$ ,  $\text{Ba}$ ,  $\text{Zn}$  and  $\text{Cd}$ .

No previous work has been reported regarding the crystallisation kinetics of  $\text{Ca}$ ,  $\text{Sr}$  and  $\text{Ba}$  borophosphate glasses and so, in this work, the crystallisation kinetics of  $\text{MeO-B}_2\text{O}_3\text{-P}_2\text{O}_5$  glasses are investigated. The choice of this system was dictated by several interrelated factors. First,  $\text{MeO}$  borophosphate glasses are of practical importance, as the basis of the production of stillwellite glass-ceramics. Second, for these glasses, not only the surface crystallisation, but also volume nucleation is observed.

The glass formation regions in these systems are shown in Fig.1. A feature of all the systems is the presence of two glass-forming regions, which do not overlap: the first "high-phosphate" is contiguous with the  $\text{MeO-P}_2\text{O}_5$  line, and second "borate" is close to the  $\text{MeO-B}_2\text{O}_3$  line.

## 2. EXPERIMENTAL

### 2.1. Glass Synthesis

The batch to be conventionally melted was prepared from reagents of analytical purity: phosphoric acid, boric acid and  $\text{Ca}$ ,  $\text{Sr}$  and  $\text{Ba}$  carbonates. The glasses were melted at 1300°C for 2 h, except for the  $\text{Ca}$ -containing glasses, which were melted at 1400°C for 2 h. The samples were produced by a single pouring onto a steel plate to yield thicknesses of 5-7 mm, 3-4 mm and  $\ll 0.5$  mm, respectively, for the  $\text{Ba}$ -,  $\text{Sr}$ - and  $\text{Ca}$ -containing glasses. A dry atmosphere was obtained by flowing an inert gas ( $\text{Ar}$ ) through the glass melt, while water was introduced by passing water vapour through the primary melt on several occasions. As was shown in Ref. [16], the water content of the glasses depends on the melting temperature, the melting time and on the flow rate of the water vapor through the melt. It has been established [17] that the water content of initial samples of silicate glasses was no more than 0.05 mol% and was equal

**Table 1**  
Glass composition (mol%) and preparation of glass samples.

No.	CaO	SrO	BaO	P <sub>2</sub> O <sub>5</sub>	B <sub>2</sub> O <sub>3</sub>	Preparation	T <sub>g</sub> (°C)	n (T <sub>m</sub> ) (mm <sup>-3</sup> ) t=50 h T=565°C
1	40	-	-	30	30	Conventionally melted	-	-
2	50	-	-	25	25	Conventionally melted	605	-
3	-	40	-	30	30	Conventionally melted	-	-
4	-	50	-	25	25	Conventionally melted	600	-
5	-	-	40	30	30	Conventionally melted	-	-
6	-	-	50	25	25	Ar drying, 20'	585	500
7	-	-	50	25	25	Ar drying, 10'	-	1060
8	-	-	50	25	25	Conventionally melted	580	2484
9	-	-	50	25	25	Water, 250 ml/h for 2h	560	16000
10	-	-	50	25	25	Water, 250 ml/h for 3h	558	20000
11	-	-	50	25	25	Water, 250 ml/h for 4h	558	21000

0.12 and 0.2 mol% after passing water vapor through the primary melt for 1 and 2 h, respectively. In phosphate glasses, the water content was found to range from about 0.06 to 0.63 mol% [16].

In this work, the effect of varying the water content of Ba borophosphate glasses on the number of crystals nucleated at the temperature T<sub>m</sub>, where the stationary nucleation rate has a maximum, has been studied and the relationship between the number of crystals and the preparation procedure can be seen from Table 1.

## 2.2. Differential Thermal Analysis

Differential thermal analysis (DTA) was performed, using a derivatograph (MOM, Hungary) under precisely fixed conditions (a corundum crucible, 0.6 g sample, and a constant heating rate of 10 K/min), and used to determine the glass transition temperatures, the crystallisation tendency and the melting temperatures of the glasses mentioned above. The glass transition temperature, T<sub>g</sub>, was determined from the DTA curve by the tangent-line method, in the endothermic region due to the glass transition. Typical DTA curves for the glasses are presented in the Fig. 2. This technique was used also to estimate the temperature range for crystal nucleation as the region of the endothermic effect in the DTA curve. The optimum development temperature corresponded to the exothermic peak observed in the DTA curve.

## 2.3. X-ray powder diffractometry.

X-ray diffraction analysis was performed using standard procedures (Rigaku diffractometer, Cu K<sub>α</sub> radiation, and a Ni filter). It was employed for the identification of crystalline phases and showed the absence of any crystalline phases in the initial glasses. The crystalline phase were identified by comparing the powder patterns obtained from the devitrified glasses with ASTM data for

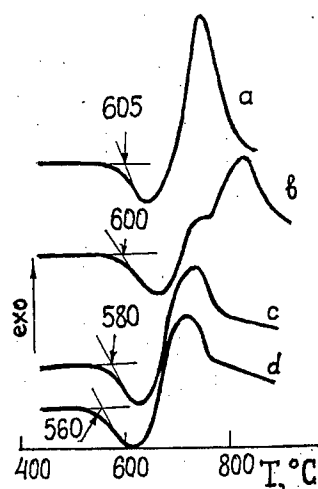


**Fig. 2.** DTA curves for the following glasses: (a)  $2\text{CaO} \cdot \text{B}_2\text{O}_3 \cdot \text{P}_2\text{O}_5$ ; (b)  $2\text{SrO} \cdot \text{B}_2\text{O}_3 \cdot \text{P}_2\text{O}_5$ ; (c)  $2\text{BaO} \cdot \text{B}_2\text{O}_3 \cdot \text{P}_2\text{O}_5$  (all without water additions and Ar drying) and (d)  $2\text{BaO} \cdot \text{B}_2\text{O}_3 \cdot \text{P}_2\text{O}_5$  (water addition, 250 ml/h for 2 h).

known compounds likely to occur in the present systems. Some unidentified lines were observed but the predominant phases found were  $\text{MePO}_4$ ,  $\text{Me}_2\text{P}_2\text{O}_7$  and Me Borate Phosphate.

## 2.4. Procedure for Investigating the Kinetics of Crystallisation

**2.4.1. Optical microscopy technique** - The stationary rate of crystal nucleation,  $I_{st}$ , and the time of nonstationary nucleation,  $\tau$ , are the basic parameters that describe the kinetics of crystal nucleation in glasses. The parameter  $I_{st}$  is directly determined experimentally and the time of nonstationary nucleation,  $\tau$ , is estimated using the induction period,  $t_{ind}$ . As was shown in Ref. [18],  $\sqrt{t_{ind}} = \pi^2/6\tau$ .

The optical microscopy technique was used to determine the above parameters. In this technique, nuclei are formed at a low temperature and subsequently grown at a higher (development) temperature, where little or no further nucleation occurs. A planar cross-section of the sample is made and the number of nuclei per unit volume,  $n$ , is determined using standard stereological techniques [19].

In glasses 6-11, crystals of complex composition - barium borate phosphate (predominantly) plus  $\text{Ba}_2\text{P}_2\text{O}_7$  (traces) - nucleated and grew. These have the form of spherulites, ellipsoids with semi-axes  $R_1$  and  $R_2$  and  $R_1/R_2 = 1/2.25$  to  $1/3.08$ . The glasses were held at low temperatures,  $T$ , in the range 540 to 620°C for a different times,  $t$ . The development temperature  $T_d$  was 680°C and the development time 10 min. Figure 3 (a) shows typical curves for  $n(T, t)$ . These curves can be used to determine the rate of stationary nucleation,  $I_{st} = dn/dt$  at  $t > t_{ind}$ , where  $t_{ind}$  is determined from the point of intersection of the straight-line part of  $n(T, t)$  with  $t$  axis. At  $t > t_{ind}$ , the nucleation rate is constant:  $I(T, t) = I_{st}(T)$ .

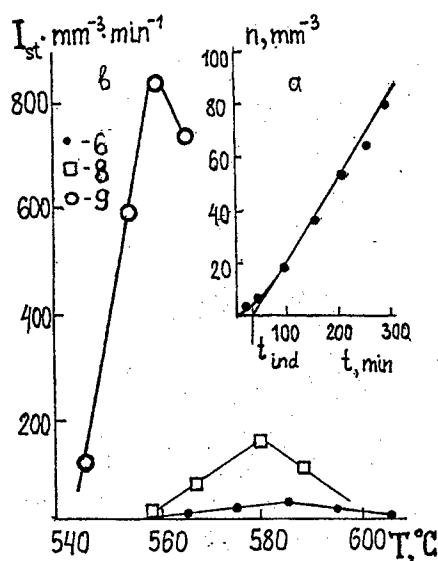


**Fig.3.** (a) The number,  $n$ , of crystals, plotted against the time of low-temperature heat treatment at  $565^{\circ}\text{C}$ , for glass 8. (b) Nucleation rate from optical microscopy measurements for glasses 6, 8 and 9 (development temperature  $680^{\circ}\text{C}$ , development time 10 min).

The stationary nucleation rate,  $I_{st}(T)$ , was calculated as the slope of the linear portion of the  $n(t)$  curve. Fig. 3 (b) shows plots of  $I_{st}$  vs temperature for glasses 6-9, under the conditions indicated in the figure caption. With increasing water content, the temperature of the nucleation rate maximum,  $T_m$ , shifts to the lower temperature. The longer the Ar drying, the higher value of  $T_m$ , while the value of  $I_{st}(T_m)$  increases with the increasing of water content.

**2.4.2. X-ray quantitative analysis** - Since the glasses in the Ca and Sr borophosphate systems were produced in thin layers, it was impossible to study their crystallisation kinetics by the development technique. For the reason, the process of crystallisation was investigated by X-ray analysis using the Rigaku diffractometer and  $\text{CuK}_{\alpha}$  radiation. The estimation of the amount of crystalline phase formed was conducted using a reference sample and data for both the integrated intensity of a selected diffraction peak and the height of the peak. For barium borate phosphate this peak is located at a scattering angle,  $2\theta$ , of  $25^{\circ}$ , while for strontium-borate-phosphate and calcium borate phosphate the corresponding peak occurs at  $30.12^{\circ}$  and  $30.94^{\circ}$ , respectively.

For characterising the degree of crystallinity, the ratio  $\alpha = V(T, t)/V_{\max}$  was used,  $V(T, t)$  being the volume of the crystalline phase formed at a temperature  $T$  and up to the time  $t$  and  $V_{\max}$  being the volume of this phase corresponding to the full duration of the experiment. To eliminate the effect of texturing, the scattered intensity was recorded for several runs and the average magnitude used. The number of runs was five for the reference sample and three for the



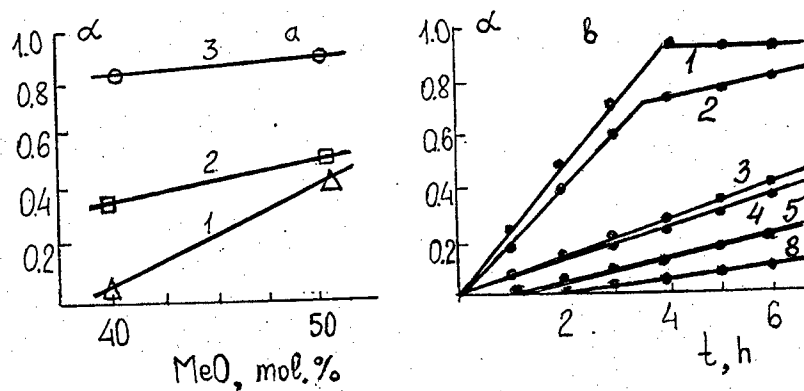


Fig.4 (a) Dependence of degree of crystallinity,  $\alpha$ , on the amount of MeO: 1, BaO; 2, SrO and 3, CaO. (Heat treatment conditions: 565°C for 240 min; development temperature 680°C; development time, 10 min). (b) Dependence of degree of crystallinity,  $\alpha$ , on the time of heat treatment (temperature 565°C). Numbers near the curves correspond to the glass number in Table 1.

sample under investigation. The error in determining the amount of the crystalline phase is less than 12%.

Figure 4 (a) demonstrates the dependence of the degree of crystallinity,  $\alpha$ , on the amount of Ba, Sr or Ca oxide. As may be seen,  $\alpha$  increases with increasing oxide content. Figure 4 (b) shows the dependence of  $\alpha$  on the time of heat treatment at 600°C and indicates that  $\alpha$  generally increases with time. Similar dependencies were obtained for temperatures of 550, 580 and 620°C. As is seen from Fig. 4, the crystallisation ability for Ba containing glasses is lower than that for Sr and Ca containing borophosphate glasses.

### 3. DISCUSSION

The graphs of the number,  $n$ , of crystals plotted against the time of low-temperature heat treatment and the temperature dependence of the nucleation rate for the wet and dry glasses, as determined by development method, are shown in Fig. 3. The wet glass exhibits a maximum in nucleation rate at a lower temperature than the dry glass, with a higher rate of nucleation at the maximum. This increase in nucleation rate with increasing water content corresponds closely to the results obtained in other systems [16,17,20]. In Ref. [20], crystallisation was promoted only when an adequate amount of water was present in the glass. It is well known that the presence of water can decrease the viscosity of a glass. The glass transition temperature,  $T_g$ , is the temperature corresponding to a viscosity of about  $10^{13}$  poises, irrespective of the kind and chemical composition of the substance. This is regarded as the temperature where the atoms or atomic groups composing the network cease translational motion on the cooling of a supercooled liquid. Accordingly, the lowering of  $T_g$  with increasing water content is equivalent to a lowering of the

viscosity.  $T_g$  decreases with increasing water content in all glasses.

Homogeneous nucleation theory leads to theoretical formulae for  $I_{st}$ ,  $t_{ind}$  and  $\tau$  [17]. The nucleation rate is mainly determined by three parameters: (1) the difference,  $\Delta\phi = \phi_g - \phi_c$ , in the free energies of the glass,  $\phi_g$ , and crystal,  $\phi_c$ , per unit volume of the nucleus; (2) the surface free energy,  $\sigma$ , and (3) the activation free energy,  $\Phi_i$ . The nucleation rate can be increased both by decreasing the glass viscosity, as a result of introducing water into the glass, and by decreasing the surface energy at the nucleus/glass interface, owing to the water concentrating at this interface.

Consider the data on the influence of the water content on the nucleation of barium borate phosphate "spherulites" in glasses 6-11. The number of development crystals increases from 500 to 21 000. This increase is due to the rapidly growing influence of the water content on the heterogeneous nucleation of barium borate phosphate. If the concentration of OH groups is exhausted, the number of crystals,  $n(T_m)$ , stops increasing (transition from glass 10 to glass 11).

It is known [16] that the water content of phosphate glasses greatly depends on the ratio  $M/P$ ,  $M$  being the concentration of alkali metal ion and  $P$  the concentration of phosphorus. The water content in phosphate glasses is described by an exponential-like dependence, which rapidly decreases with decreasing  $P_2O_5$  content. When the  $P_2O_5$  content is lower than 45 mol%, the water content becomes negligible.

In the case of the  $BaO-B_2O_3-P_2O_5$  system, the water content similarly depends on the ratio  $M/(P+B)$ ,  $P+B$  being the sum of the concentrations of phosphorus and boron oxides. As for the phosphate glasses investigated in Ref. [16], the water content of  $BaO-B_2O_3-P_2O_5$  glasses depends on the melting temperature, the melting time and on the rate of flow of water vapor through the melt.

## CONCLUSIONS

A study of the crystallization kinetics in borophosphate systems has been made. The degree of crystallinity has been determined in the glasses as a function of temperature and RO content in the interval 40-50 mol%. The observed phenomena have been explained in terms of the crystal nucleation theory for complex glasses.

## REFERENCES

- [1] A.G. Pincus, *J. Soc. Glass Technol.* **34** (1950), 140.
- [2] Z.M. Syritskaya, in: *The Vitreous State* [in Russian], vol.3, no 4, Minsk (1964), p.8.
- [3] D.G. Grossman and C.I. Philips, *J. Am. Ceram. Soc.* **47** (1964), 471.
- [4] G.P. Sedmale, Dissertation Abstract, Riga Polytechnic Institute, Riga (1971).
- [5] K. Takahashi, *Advanced Glass Technology*. Proc. 6th Int. Congr. on Glass, vol.1 (Plenum, New York, 1962) p. 366.
- [6] H. Bauer, Habilitationsschrift, Karlsruhe, 1963.
- [7] P. Beckenkamp, *Philips Res. Rep. Suppl.* (1966), 89.

- [8] I.N. Yun & P.J. Bray, *J. Non-Cryst. Solids* **30** (1978), 45.
- [9] T. Tsuchia & T. Moriya, *J. Non-Cryst. Solids* **38-39** (1980), 323.
- [10] J. Lesko, M. Doruskova & J. Trzil, *Coll. Czech. Chem. Commun.* **49** (1984), 2355.
- [11] M. Seaglotti, M. Villa & G. Chiodelli, *J. Non-Cryst. Solids* **93** (1987), 350.
- [12] P. Ramamorthy & T.J. Rockett, *J. Am. Ceram. Soc.* **57** (1974), 501.
- [13] D.F. Ushakov & N.F. Baskova, *Sov. J. Glass Phys. Chem.* **2** (1976), 38.
- [14] A.P. Molotshko, Z.N. Shalimo & I.L. Rakov, *Isv. Akad. Nauk Belorusskoi SSR* (1980), 115 (in Russian).
- [15] G. Sedmale, J. Vaivads, V. Sedmalis, V.O. Kabanov & O.V. Yanush, *J. Non-Cryst. Solids* **129** (1991), 284.
- [16] G.A. Sycheva, T.G. Kostyreva & I.G. Poljakova, Collected papers XVII Int. Congr. on Glass, Beijing, P.R.China, 1995, vol.2, pp 426-432.
- [17] A.M. Kalinina, V.M. Fokin, G.A. Sycheva & V.N. Filipovich. Collected papers, XIV Int. Congr. on Glass (Indian Ceram. Soc., Calcutta, 1986), vol.1, pp 366-373.
- [18] J.H. Hollomon & D. Turnbull *Nucleation*, in: Progress in Metal Physics, vol. IV ed. B. Chalmers. (Interscience N.J., 1953) p. 403.
- [19] R.T. Dehoff & F.N. Rhines. *Trans AIME*, **221**, (1961), 975. ???????????
- [20] R. Ota, H. Kuribayashi, J. Fukunaga & T. Taguchi, *J. Non-Cryst Solids* **144** (1992), 81.

## STRUCTURE AND PROPERTIES OF ALKALI THIOBORATE GLASSES: UNIQUE CHEMISTRIES AND UNUSUAL PROPERTIES

Steve W. MARTIN

*Department of Materials Science & Engineering,  
Iowa State University of Science & Technology, Ames,  
IA 50011, USA*

Sulphide analogs of alkali borate glasses were first prepared more than 10 years ago as possible solid electrolyte materials in solid state lithium batteries. Although they were found to exhibit exceptional ionic conductivities, as high as  $10^{-3} \text{ (Wcm)}^{-1}$  at room temperature, they were not fully explored as a new glass forming family with possibly interesting correlations to their well characterised alkali borate neighbours. In this paper, the glass forming ranges, structure-property relationships between the alkali thioborate and alkali borate physical properties will be extensively reviewed. In general it is found that quite large glass forming ranges exist for these glasses out to exceeding 80 mol% alkali sulphide. The density of these glasses increases quite dramatically with increasing alkali content in a manner similar to that observed with the alkali borate glasses and is associated with the increasing fraction of small volume but heavy mass tetrahedral boron group. Contrasting this behaviour is the  $T_g$  which shows a dramatic anti-correlation with alkali content and decreases some  $150^\circ\text{C}$  as the alkali fraction increase out to  $\sim 30$  mol%. This is to be compared to the  $T_g$  behaviour in the alkali borate glasses where  $T_g$  increases more than  $200^\circ\text{C}$  for the same alkali content. To probe these differences, a detailed structural study of these glasses has been undertaken. Infrared, Raman, NMR, and MAS NMR studies of these glasses have been made. We will review these studies paying particular attention to understand the dramatic differences in the structure-property relationships between the alkali thioborate and alkali borate glasses.

# ANALYTICAL AND MOLECULAR ORBITAL MODELLING APPROACH TO THE CHEMICAL BONDING STATES OF F<sup>-</sup> IONS IN OXYFLUOROBORATE GLASSES

Satoshi HAYAKAWA & Akiyoshi OSAKA  
*Biomaterials Laboratory, Faculty of Engineering, Okayama  
University, Tsushima, Okayama-shi, 700, Japan*

The structure of NaF-B<sub>2</sub>O<sub>3</sub> glasses was investigated by means of <sup>11</sup>B and <sup>23</sup>Na MAS NMR and X-ray photoelectron spectroscopies. The chemical bonding states of F<sup>-</sup> ions in the glasses were estimated from the F1s XPS analysis. The BO<sub>(4-y)</sub>F<sub>y</sub><sup>-</sup>/(BO<sub>3</sub>+BO<sub>(4-y)</sub>F<sub>y</sub><sup>-</sup>) fraction (N<sub>4</sub>%) was determined from <sup>11</sup>B MAS NMR spectra. It was deduced that the addition of NaF caused the formation of tetrahedral four-coordinated boron atoms, BO<sub>3</sub>F<sup>-</sup>. The conversion of BO<sub>3</sub> units into BO<sub>3</sub>F<sup>-</sup> units depended on the melting temperature. The proposed structural models were confirmed by a molecular orbital calculation. The F-B and F-Na bonds present in the glasses were found to be relatively covalent, whereas ionic F<sup>δ-</sup>(-Na<sup>δ+</sup>)<sub>n</sub> bonds as found in crystalline NaF were not present in the glasses.

## 1. INTRODUCTION

Boron trioxide, B<sub>2</sub>O<sub>3</sub> is one of the glass-forming oxides [1] and many multi-component glasses containing B<sub>2</sub>O<sub>3</sub> have been reported [2-6]. It is accepted that the network structure of binary alkali borate glasses contains trigonal three-coordinated planar boron atoms, BO<sub>3</sub>, and tetrahedral four-coordinated boron atoms, BO<sub>4</sub><sup>-</sup> [3]. It is known that the variation of several properties in borate glasses, such as the glass transition temperature (T<sub>g</sub>), the thermal expansion coefficient, and the ionic conductivity closely follows the variation of the BO<sub>4</sub><sup>-</sup>/(BO<sub>3</sub>+BO<sub>4</sub><sup>-</sup>) ratio (N<sub>4</sub>) which is a strong function of the alkali metal oxide content [2-4]. The coordination state of boron varies when an alkali metal fluoride, MF is added in place of an alkali metal oxide [4-6]. It has been reported that the local environments around a boron atom in sodium oxyfluoroborate glasses are BO<sub>3</sub>F<sup>-</sup> [6], BO<sub>3</sub>F<sup>-</sup> and BO<sub>2</sub>F<sub>2</sub><sup>-</sup> [3,4], or BO<sub>3</sub>F<sup>-</sup>, BO<sub>2</sub>F<sub>2</sub><sup>-</sup> and BOF<sub>3</sub><sup>-</sup> units [5]. These structural models vary with the researchers [4-6]. Therefore, the coordination state of boron in these glasses and its compositional dependence has not yet been fully understood. It is noted that the melting temperature varies with the researchers and ranges from 850 to 1000°C. It is possible that the conversion of BO<sub>3</sub> units into BO<sub>(4-y)</sub>F<sub>y</sub><sup>-</sup> units on the addition of MF addition does not always proceed to completion. In the present

experiment, NaF-B<sub>2</sub>O<sub>3</sub> glasses were prepared by the conventional quenching method with different melting temperatures and the structure of these glasses was investigated by <sup>11</sup>B and <sup>23</sup>Na MAS NMR and X-ray photoelectron spectroscopies in order to discuss the effect of melting temperature on the chemical states of boron and fluorine. To check the structural model obtained, we performed semiempirical molecular orbital calculations for several molecular clusters.

## 2. EXPERIMENTAL

Glasses of the composition xNa<sub>2</sub>F<sub>2</sub>(100-x)B<sub>2</sub>O<sub>3</sub> (x=10, 20 and 30) were prepared. The starting materials were reagent grade NaF and B<sub>2</sub>O<sub>3</sub> (Nacalai Tesque, Inc). The appropriate amounts of starting materials were mixed and melted in a Pt crucible using an electric furnace at 900 and 1100°C for 15 min. The melts were poured onto a steel plate and immediately pressed by another steel plate. X-ray photoelectron spectra (XPS) measurements were made with an S-Probe ESCA SSX100S (Fisons Instruments) using a monochromatic Al K $\alpha$  radiation (h $\nu$ =1486.6 eV). The glass samples were analyzed using the fresh surfaces just after being fractured in ultra high vacuum ( $\sim 7 \times 10^{-8}$  Pa). Neutralization of the surface charge of the sample was performed by setting a Ni mesh screen 1 mm above the sample surface and flooding with low energy (5-7 eV) electrons. Corrections of the binding energy were made by referring the measured binding energy to the C1s peak at 284.6 eV. Magic-Angle-Spinning (MAS) NMR spectra of powdered samples were recorded at 9.4 T on a JEOL JNM-GX400 FT-NMR spectrometer, equipped with TU-GSX400MAS probe. The sample spinning speed at the magic angle to external field was 5-6 kHz. <sup>11</sup>B MAS NMR spectra were measured at 128 MHz with 1.5  $\mu$ s pulses and 2.5 s recycle delays. About 16 pulses were accumulated. BPO<sub>4</sub> { $\delta = -3.6$  ppm against (C<sub>2</sub>H<sub>5</sub>)<sub>2</sub>O.BF<sub>3</sub>,  $\delta = 0$  ppm} was used as the secondary external reference substance to determine the <sup>11</sup>B chemical shifts. We estimated the BO<sub>(4-y)</sub>F<sub>y</sub><sup>-</sup>/(BO<sub>3</sub>+BO<sub>(4-y)</sub>F<sub>y</sub><sup>-</sup>) ratio (N<sub>4</sub>%) from the ratio of the intensity of the resonance peak for BO<sub>3</sub> to that for BO<sub>(4-y)</sub>F<sub>y</sub><sup>-</sup>. <sup>23</sup>Na MAS NMR spectra were measured at 105 MHz with 1.5  $\mu$ s pulses and 2.5 s recycle delays. About 40 pulses were accumulated. NaCl crystal ( $\delta = 0$  ppm) was used as the external reference substance to determine the <sup>23</sup>Na chemical shifts.

## 3. THEORETICAL

Semiempirical molecular orbital calculations were performed to obtain the heat of formation,  $\Delta H_{298}^\circ$ , and the entropy term,  $T\Delta S_{298}^\circ$ , for proposed borate polymers in various fluorinated environments. The calculations were performed by using the AM1 routine in the MOPAC Ver. 6.02 computer program package [7]. The convergence of the self-consistent field calculation was ensured by using the keyword PRECISE and thermodynamic quantities were obtained by using the keywords FORCE and THERMO. The calculation technique used here has already been discussed elsewhere [8]. Here, we estimate the Gibbs free energy change,  $\Delta G_{298}^\circ$ , from  $\Delta H_{298}^\circ$  and  $T\Delta S_{298}^\circ$ . This quantifies the reliability of the chemical states of the F<sup>-</sup> ions in the structural models.

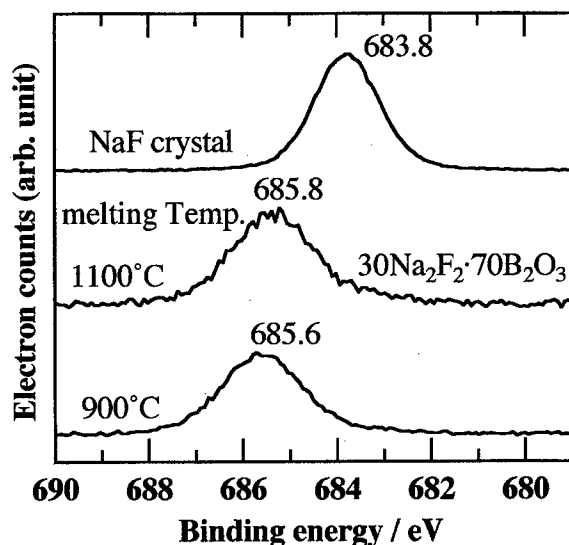


Fig. 1. F 1s XPS spectra of NaF and  $30\text{Na}_2\text{F}_2 \cdot 70\text{B}_2\text{O}_3$  glasses.

## 4. RESULTS

### 4.1. X-ray Photoelectron Spectra

The differences in atomic % between the fresh fracture surface composition, which was determined from wide scan XPS spectra for the  $30\text{Na}_2\text{F}_2 \cdot 70\text{B}_2\text{O}_3$  glasses quenched from 900 and 1100°C, are less than 2%. This indicates that the effect of the melting temperature on the vaporization of components from the melt was negligible.

Figure 1 shows the F 1s XPS spectra of NaF and  $30\text{Na}_2\text{F}_2 \cdot 70\text{B}_2\text{O}_3$  glasses quenched from 900 and 1100°C. The F 1s XPS spectrum of NaF shows one sharp symmetrical peak at about 683.8 eV. The F 1s XPS spectra of the glasses with melting temperatures of 1100°C and 900°C show one broad symmetrical peak at about 685.8 eV.

### 4.2. $^{11}\text{B}$ MAS NMR Spectra

Figure 2(a) and 2(b) show the  $^{11}\text{B}$  MAS NMR spectra of  $x\text{Na}_2\text{F} \cdot (100-x)\text{B}_2\text{O}_3$  glasses ( $x=10, 20$  and  $30$ ) quenched from 900 and 1100°C, respectively. The resonance peak due to tetrahedrally coordinated boron denoted by  $\text{BO}_{(4-y)}\text{F}_y^-$  is superimposed on the weak quadrupolar splitting resonance peaks of three-coordinated planar boron in  $\text{BO}_3$ . The  $\text{BO}_{(4-y)}\text{F}_y^-$  resonance peak can be obtained by subtracting the resonance peak for the quadrupolar splitting of  $\text{BO}_3$  in crystalline  $\text{B}_2\text{O}_3$  from the composite spectrum and can be simulated by a Gaussian function on the basis of the least-square fit shown in Fig. 2(a).  $N_4$  is plotted as a function of  $\text{Na}_2\text{F}_2$  content in Fig. (3). For comparison, the solid curve is the correlation found by Kline & Bray  $\{N_4=x/(100-x)\}$  when  $\text{BO}_3\text{F}^-$  units were formed [3]. This correlation would indicate an apparent stoichiom-

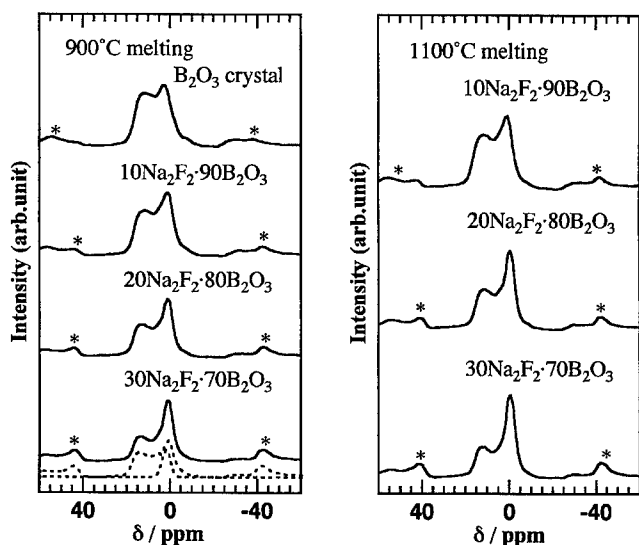
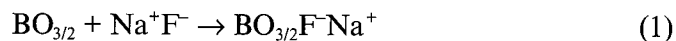


Fig. 2.  $^{11}\text{B}$  MAS NMR spectra of  $x\text{Na}_2\text{F}_2 \cdot (100-x)\text{B}_2\text{O}_3$  glasses ( $x=10, 20, 30$ ). Asterisks denote spinning side bands.

etry defined as follows:



Note that  $N_4$  for the glasses made from the melt at  $900^\circ\text{C}$  do not correspond to the values predicted by the theoretical  $x/(100-x)$  curve and lie below these values, while for  $N_4$  of the glasses made from the melt at  $1100^\circ\text{C}$  almost correspond to the theoretical values. Provided that the reaction between  $\text{B}_2\text{O}_3$  and  $\text{NaF}$  follows reaction (1), the percentages of the conversion of  $\text{BO}_3$  into  $\text{BO}_3\text{F}^-$ ,  $R$ , are defined

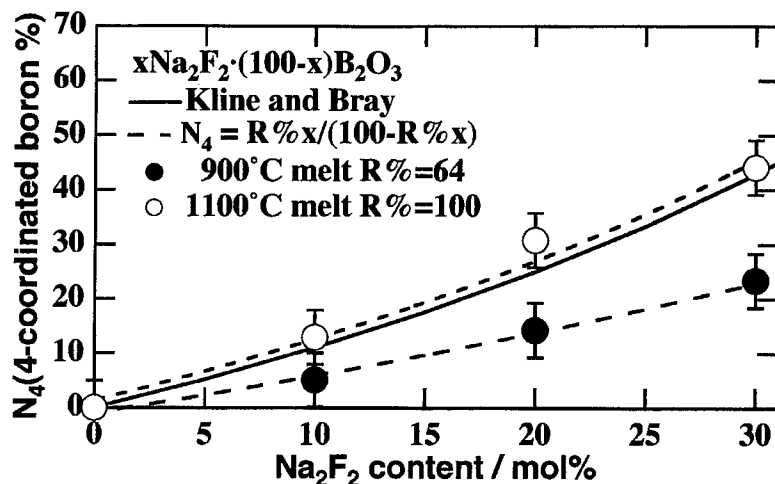


Fig. 3.  $N_4$  (%) versus  $\text{Na}_2\text{F}_2$  content.



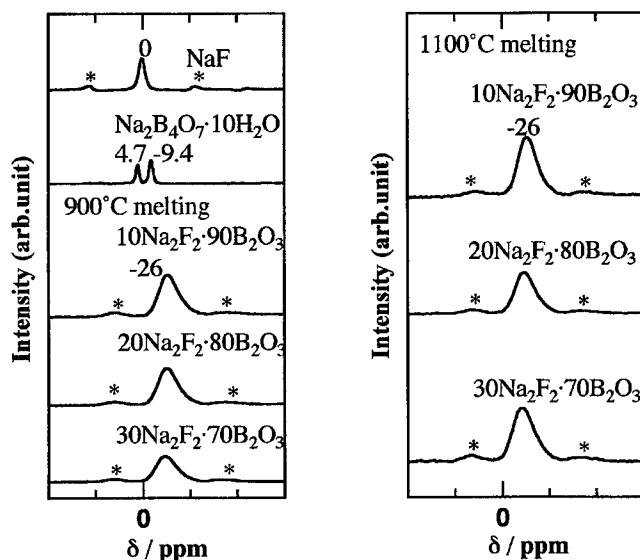


Fig. 4.  $^{23}\text{Na}$  MAS NMR spectra of  $x\text{Na}_2\text{F}_2 \cdot (100-x)\text{B}_2\text{O}_3$  glasses ( $x=10, 20, 30$ ). Asterisks denote spinning side bands.

as shown in Fig. (3).

#### 4.3. $^{23}\text{Na}$ MAS NMR Spectra

Figure 4(a) and 4(b) show the  $^{23}\text{Na}$  MAS NMR spectra of  $x\text{Na}_2\text{F}_2 \cdot (100-x)\text{B}_2\text{O}_3$  glasses ( $x=10, 20, 30$ ) quenched from 900 and 1100°C, respectively. For comparison,  $^{23}\text{Na}$  MAS NMR spectra for crystalline NaF and  $\text{Na}_2\text{B}_4\text{O}_7 \cdot 10\text{H}_2\text{O}$  are also shown. The line profile for crystalline NaF is symmetric and very sharp. On the other hand, the line profiles of all for the glasses are asymmetric and broad. The  $^{23}\text{Na}$  MAS NMR peak positions of the glasses range from -22 to -26 ppm. The line profiles and peak positions for the glasses do not depend on the melting temperature.

#### 4.4. Calculated Thermodynamic Properties for Molecular Clusters

The MO calculations were performed on the basis of two isolated molecular clusters,  $\text{H}_4\text{B}_2\text{O}_5$  and NaF. In view of the experimental results, we can expect that the conversion of  $\text{BO}_3$  units into  $\text{BO}_3\text{F}^-$  units or  $\text{BO}_2\text{F}_2^-$  units occurs. Maya has already reported a model comprising local structures [6]. We used several isolated molecular clusters based on Maya's local structure model, in order to investigate the chemical reaction between  $\text{B}_2\text{O}_3$  and NaF in the melt. The calculated properties of the molecular clusters are listed in Table 1 and the optimized geometries for the molecular clusters, unmodified and modified by NaF molecules, are shown in Fig. 5.

#### 4.5. Gibbs Free Energy Change in the Reaction between Molecular Clusters

**Table 1**  
Heat of Formation,  $\Delta H_{298}^\circ$  at the Optimized Geometries for Several Molecular Clusters

Molecular Clusters	$\Delta H_{298}^\circ/\text{kcal}$	Molecular Clusters	$\Delta H_{298}^\circ/\text{kcal}$
(a) $\text{H}_4\text{B}_2\text{O}_5$	-419.844	(b) $\text{H}_4\text{B}_2\text{O}_5\text{FNa}$	-619.864
(c) $\text{H}_4\text{B}_2\text{O}_5\text{F}_2\text{Na}_2$	-793.849	(d) $\text{H}_2\text{BO}_3\text{Na}$	-323.778
(e) $\text{H}_2\text{BO}_2\text{F}$	-254.304	(f) $\text{H}_2\text{BO}_2\text{F}_2\text{Na}$	-439.073
(g) $\text{H}_2\text{BO}_3\text{FNa}_2$	-478.158	(h) $\text{NaF}$	-83.543

The important chemical reactions are F-coordination and F-substitution. The calculated thermodynamic properties for these reactions are listed in Table 2 together with the reaction formula. The F-coordination reaction for reactions (2) and (3) is equivalent to reaction (1). We find that the Gibbs free energy change for the first reaction (2) is  $\Delta G_{298}^\circ = -106.3$  kcal and for the second reaction (3)  $\Delta G_{298}^\circ = -77.7$  kcal, which were calculated from the data in Table 2. In these reactions, we can expect that the  $\text{BO}_3$  unit is progressively converted into the  $\text{BO}_3\text{F}^-$  unit. The F-substitution reaction gives a  $\text{BO}_2\text{F}$  unit and a non-bridging oxygen  $\text{O}(-\text{Na})$  at the expense of the bridging  $\text{B}-\text{O}-\text{B}$  bond (Fig. 5(a)) in reaction (4). We estimate  $\Delta G_{298}^\circ = -77.3$  kcal. Next, the F-substitution reaction of interest gives  $\text{BO}_2\text{F}$  or  $\text{BO}_2\text{F}_2^-$  units at the expense of the bridg-

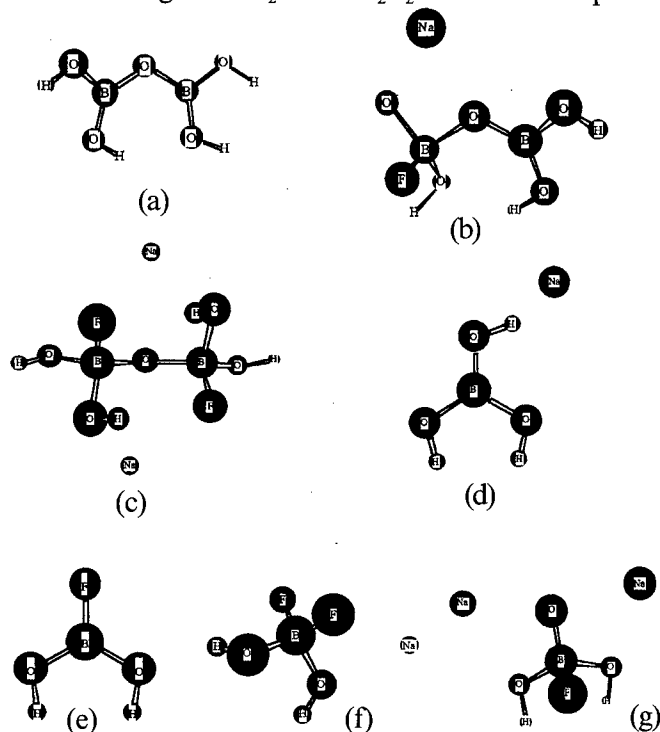


**Fig. 5.** Optimized Geometries for Proposed Borate Clusters.

**Table 2**  
Standard Enthalpy Change,  $\Delta H_{298}^\circ$  and Standard Entropy Change,  $\Delta S_{298}^\circ$

Reaction	$\Delta H_{298}^\circ$ (kcal/mol)	$T\Delta S_{298}^\circ$
(2) $H_4B_2O_5 + NaF \rightarrow H_4B_2O_5FNa$	-116.5	-10.2
(3) $H_4B_2O_5FNa + NaF \rightarrow H_4B_2O_5F_2Na_2$	-90.4	-12.7
(4) $H_4B_2O_5 + NaF \rightarrow H_2BO_3Na + H_2BO_2F$	-74.7	2.6
(5) $H_4B_2O_5FNa + NaF \rightarrow H_2BO_3Na + H_2BO_2F_2Na$	-59.4	3.5
(6) $H_4B_2O_5FNa + NaF \rightarrow H_2BO_2F + H_2BO_3FNa_2$	-29.1	4.0
(7) $H_4B_2O_5F_2Na_2 + NaF \rightarrow H_2BO_3FNa_2 + H_2BO_2F_2Na$	-39.8	4.4

ing B–O–B bond in reactions (5), (6) and (7). We find that the Gibbs free energy change for Eq. (5) is  $\Delta G_{298}^\circ = -62.9$  kcal, that for Eq. (6) is  $\Delta G_{298}^\circ = -33.1$  kcal and that for Eq. (7) is  $\Delta G_{298}^\circ = -44.2$  kcal. The the Gibbs free energy change for Eqs. (2) and (3) are significantly lower than those for Eqs. (5), (6) and (7). This indicates that the conversion of  $BO_3$  into  $BO_3F^-$  is most favorable in the reaction between  $H_4B_2O_5$  molecule and NaF molecule.

## 5. DISCUSSION

Since  $N_4$  for the glasses quenched from the melt at 1100°C almost correspond to the theoretical values, we can deduce that the local structure of these glasses consists mainly of  $BO_3$  and  $BO_3F^-$  units. Assuming that the conversion of  $BO_3$  units into  $BO_{(4-x)}F_x^-$  units by the addition of NaF does not progress sufficiently in the glass quenched from the melt at 900°C, the existence of NaF cluster is postulated. However, as is evident from Fig. 1, we could not deconvolute the F 1s XPS spectra of the glasses into two kinds of peaks assigned to covalent F–B bonds and ionic  $F^{\delta-}(-Na^{\delta+})_n$  bonds. The symmetrical F 1s XPS peak at 685.8 eV indicates that both the F–B and F–Na bonds present in the glasses are relatively covalent and that ionic  $F^{\delta-}(-Na^{\delta+})_6$  bonds as found in crystalline NaF are not present in the glasses. Therefore, the NaF cluster in the glasses may consist of covalent F–Na bonds. Since the quadrupolar  $^{23}Na$  nucleus is subjected not only to magnetic field but also to electric field gradients, the  $^{23}Na$  MAS NMR line profiles should be related to the magnitude of the electric field gradient around the  $^{23}Na$  nucleus which depends on the fluorine and oxygen coordination states around the Na atoms. It is likely that, the  $Na(-O)_n$  or  $Na(-F)_n$  bonds in the glasses may be anisotropic, in contrast to the isotropic  $Na^{\delta+}(-F^{\delta-})_6$  bonds in crystalline NaF. Furthermore, from the results of for the calculated Gibbs free energy change,  $\Delta G_{298}^\circ$ , it appears that the tendency for the formation of  $BO_3F^-$  units is greater than those for  $BO_2F_2^-$  and  $BO_2F$  units. Although the formation of  $BO_2F_2^-$  and  $BO_2F$  units should accompany the formation of non-bridging oxygen,  $O(-Na)_n$  at the expense of the bridging B–O–B bond, we could not detect the presence of the non-bridging oxygen atom from the O 1s XPS spectra of the glasses, which are not shown here. These results emphasize that the conversion of  $BO_3$  units into  $BO_3F^-$

units (F-coordination) may be the dominant change, rather than the formation of  $\text{BO}_2\text{F}_2^-$  and  $\text{BO}_2\text{F}$  units.

## 6. CONCLUSIONS

The structure of  $x\text{Na}_2\text{F}_2 \cdot (100-x)\text{B}_2\text{O}_3$  glasses was investigated by means of  $^{11}\text{B}$  and  $^{23}\text{Na}$  MAS NMR and X-ray photoelectron spectroscopies. The addition of the NaF caused the formation of tetrahedral four-coordinated boron atoms,  $\text{BO}_3\text{F}^-$ . The conversion of  $\text{BO}_3$  units into  $\text{BO}_3\text{F}^-$  units depended on the melting temperature. F-B and F-Na bonds present in the glasses were found to be relatively covalent, whereas ionic  $\text{F}^\delta-(-\text{Na}^\delta+)_n$  bonds as found in crystalline NaF were not present in the glasses. The calculated Gibbs free energy change supported the suggestion that the local structure of these glasses consisted mainly of  $\text{BO}_3$  and  $\text{BO}_3\text{F}^-$  units.

## 7. Acknowledgements

The authors thank Prof. Y. Miura of Okayama University in Japan for his assistance in the XPS measurements. The authors thank Prof. T. Yoko of Kyoto University in Japan for his assistance in the NMR measurements.

## REFERENCES

- [1] W.H. Zachariasen, *J. Am. Chem. Soc.*, **54** (1932), 3841.
- [2] C.C. Hunter & M.D. Ingram, *Solid State Ionics*, **14** (1984), 31.
- [3] D. Kline & P.J. Bray, *Phys. Chem. Glasses*, **7** (1966), 41-51.
- [4] J.E. Shelby and L. K. Downie, *Phys. Chem. Glasses*, **30**[4](1989) 151.
- [5] W. Poch, *Glastech. Ber.*, **40** (1967), 261.
- [6] L. Maya, *J. Am. Ceram. Soc.*, **60** (1977) 323.
- [7] MOPAC Ver. 6.00(QCPE No. 445), J.J.P. Stewart, *QCPE Bull.* **10** (1990), 86; T. Hirano, *JCPE Newsletter*, **2** (1991), 39; Revised as Ver. 6.02 by J. Toyoda.
- [8] M.J.S. Dewar, E.G. Zoebisch, E.F. Healy & J.J.P. Stewart, *J. Am. Chem. Soc.*, **107** (1985), 3902.

## PREPARATION OF LITHIUM CHLOROBORACITE BY THE SOL-GEL METHOD

Toshimi NAGASE, Kohji SAKANE & Hideo WADA  
*Shikoku National Industrial Research Institute,  
2217-14 Hayashi, Takamatsu 761-03, Japan*

Lithium chloroboracite ( $\text{Li}_4\text{B}_7\text{O}_{12}\text{Cl}$ ) powder and film were prepared by the sol-gel method from inorganic lithium and boron compounds with hydrochloric acid or/and ammonium chloride. Single-phase  $\text{Li}_4\text{B}_7\text{O}_{12}\text{Cl}$  powder was prepared under conditions similar to those used in its preparation from methoxides. In the preparation of films, however, maintaining the stoichiometric amount of chlorine necessitated a chlorine-rich heating environment. The chlorine composition in the sol solution also produced a difference in the chlorine content of films, and in the crystallization of  $\text{Li}_4\text{B}_7\text{O}_{12}\text{Cl}$  and a by-product, lithium tetraborate.

### 1. INTRODUCTION

Lithium boracites ( $\text{Li}_4\text{B}_7\text{O}_{12}\text{X}$ , X=halogen) are known as lithium-ion conductors. The representative compound,  $\text{Li}_4\text{B}_7\text{O}_{12}\text{Cl}_{0.68}\text{Br}_{0.32}$ , shows a high conductivity of  $2 \times 10^{-6} \Omega^{-1}\text{cm}^{-1}$  at 298 K and  $0.9 \times 10^{-2} \Omega^{-1}\text{cm}^{-1}$  at 520 K [1]. Lithium boracites are stable in air and insoluble in water. Although  $\text{B}_2\text{O}_3-x\text{Li}_2\text{O}-y\text{LiX}$  (X=halogen) glasses also possess high ionic conductivities [2], they are chemically and physically less stable. Lithium boracites have a potential application as a solid electrolyte in thin film batteries. Such an application, however, requires lithium boracite films. To date, only powders have been prepared by a flux or hydrothermal method [1]. The decomposition of lithium boracites at high temperature makes it difficult to sinter the powder or to grow a crystal from the melt.

Among the various methods for preparing functional films, the sol-gel method has the advantages of precise composition control [3] and no need for a vacuum. From this point of view, we have applied the sol-gel method to the preparation of lithium boracite films. Lithium chloroboracite ( $\text{Li}_4\text{B}_7\text{O}_{12}\text{Cl}$ ) was selected here as a model compound to examine the preparation conditions and the reaction process. We have already reported the preparation of  $\text{Li}_4\text{B}_7\text{O}_{12}\text{Cl}$  powder from lithium methoxide, boron methoxide, and hydrochloric acid or ammonium chloride [4].

In this study we attempted to prepare both  $\text{Li}_4\text{B}_7\text{O}_{12}\text{Cl}$  powder and film from inorganic lithium and boron compounds. This selection of lithium and boron sources has advantages in ease of handling as well as low cost. The preparation conditions for  $\text{Li}_4\text{B}_7\text{O}_{12}\text{Cl}$  powder and the reaction process during heating were

investigated and compared with the previous results on the preparation of  $\text{Li}_4\text{B}_7\text{O}_{12}\text{Cl}$  powder from methoxides. The conditions for preparing  $\text{Li}_4\text{B}_7\text{O}_{12}\text{Cl}$  film were also investigated with a view to suppressing chlorine evaporation.

## 2. EXPERIMENTAL

### 2.1. Preparation of Powder

Lithium hydroxide monohydrate ( $\text{LiOH}\cdot\text{H}_2\text{O}$ ) was dissolved into methanol, and boric acid ( $\text{H}_3\text{BO}_3$ ) was added to the methanol solution in the molar ratio of B/Li of 7/4. The resulting methanol solution was diluted with methanol to a concentration of 0.8 M for lithium and 1.4 M for boron, and stirred for 1 day at 318 K. All the above operations were performed in an argon atmosphere. To the diluted solution, water and various amounts of hydrochloric acid (HCl) were added. The molar ratio of  $[\text{total water}^*]/([\text{lithium}] + 3 \times [\text{boron}])$  was fixed at 5, while the molar ratio of HCl/Li was varied from 0.25 to 0.9. The latter molar ratio is hereafter designated as  $R_H$ . Stirring the solutions further for 1 day at room temperature gave clear sol solutions. The solvents of the solutions were then gradually evaporated by heating at 323 K for 2 days and the residues were dried further at 373 K for 1 day. Finally the dried residues were heated at 973 K for 1 h in air. Hereafter, the dried and heated residues are designated as Dried Powders and Heated Powders, respectively.

### 2.2. Preparation of Film

Coating solutions were prepared in a way similar to that for the powder preparation.  $\text{LiOH}\cdot\text{H}_2\text{O}$  and  $\text{H}_3\text{BO}_3$  were dissolved in methanol and the solution was diluted with methanol to a concentration of 0.6 M for lithium and 1.05 M for boron. The mixed solution was stirred at 318 K until it became transparent. Water and chlorine sources were then added. The molar ratio of  $[\text{total water}^*]/([\text{lithium}] + 3 \times [\text{boron}])$  was fixed at 2.5. Hydrochloric acid and ammonium chloride ( $\text{NH}_4\text{Cl}$ ) were used as chlorine sources. The molar ratio of  $\text{NH}_4\text{Cl}/\text{Li}$  is designated as  $R_N$ . Three types of solutions were prepared: 1)  $R_N=0.675$  and  $R_H=0$ , 2)  $R_N=1.35$  and  $R_H=0$ , 3)  $R_N=0.675$  and  $R_H=0.675$ . Stirring the solutions further for 1 day at room temperature gave clear coating solutions.

Silicon (111) wafers coated with platinum by sputtering were used as substrates. Films were formed by depositing one of the three coating solutions with a spin-coating machine rotating at speed of 3000 rpm. The resulting gel films were dried at 473 K for 10 min on a hot plate in air. Repeating the above depositing and drying procedures twelve times gave a film thickness of about 2  $\mu\text{m}$ . The dried films were then heated at 873 K for 1 h in a nitrogen atmosphere as follows: (A) Two films of the same composition were stacked on each other face to face to make a pair; (B) Additionally, each pair of films was double wrapped in nickel foil; (C) Furthermore, Dried Powder with  $R_H$  of 0.9 was

\*Total water content includes the amounts of water in  $\text{LiOH}\cdot\text{H}_2\text{O}$  ( $(1/2)\text{Li}_2\text{O}\cdot(3/2)\text{H}_2\text{O}$ ) and  $\text{H}_3\text{BO}_3$  ( $(1/2)\text{B}_2\text{O}_3\cdot(3/2)\text{H}_2\text{O}$ ). In the preparation of powder, the total amount of water amount was the same as in the preparation from methoxides [4].

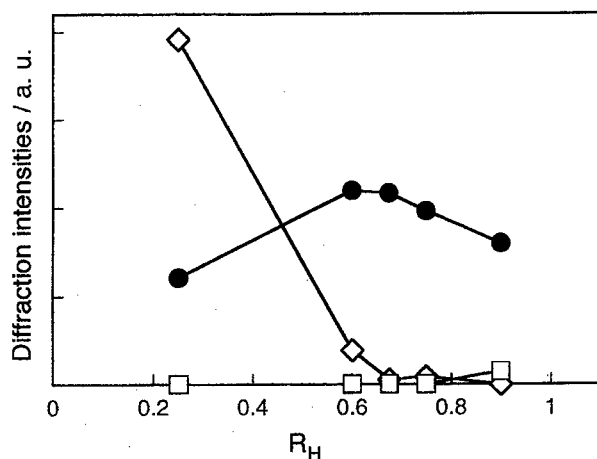


Fig. 1. Change in diffraction intensities of phases in Heated Powders with amounts of hydrochloric acid.

●, ◇, and □ denote the intensities of  $\text{Li}_4\text{B}_7\text{O}_{12}\text{Cl}$ ,  $\text{Li}_2\text{B}_4\text{O}_7$  and  $\text{Li}_2\text{B}_2\text{O}_4$ , respectively.

inserted into the nickel foil around each pair of films. These three kinds of environments are hereafter designated as Environment A, B, and C, respectively. The dried and heated films are referred to as Dried Films and Heated Films, respectively.

### 2.3. Analysis

Heated Powders and Heated Films were identified on an X-ray diffractometer (RINT-1200, Rigaku) with powder and thin-film attachments, respectively. Dried Powder was also analyzed with a differential thermal analysis - thermogravimetric analyzer (System 001, TG-DTA 2000, MAC Science) at a heating rate of 10 K/min. Dried Powder prepared from methoxides [4] was also analyzed in the same manner for comparison. The chlorine content of the powders and films was determined with an X-ray fluorescence spectrometer (RIX-3000, Rigaku). From the intensities of a fluorescent  $\text{Cl-K}\alpha$  line, the concentrations were calculated by a fundamental parameter procedure. In the analysis of films, the intensities of a fluorescent  $\text{Si-K}\alpha$  line from the silicon substrates were also measured and then the total amounts of deposited films were estimated from the decay of the  $\text{Si-K}\alpha$  intensities. Heated Film was examined on a scanning electron microscope (S-2460N, Hitachi) with an energy dispersive X-ray spectrometer (DX-4, EDAX International).

## 3. RESULTS AND DISCUSSION

### 3.1. Preparation of Powder

**3.1.1. Preparation condition of powder** - X-ray diffraction analysis of Heated Powders showed that  $\text{Li}_4\text{B}_7\text{O}_{12}\text{Cl}$  formed either with or without by-products: lithium tetraborate ( $\text{Li}_2\text{B}_4\text{O}_7$ ), lithium metaborate ( $\text{Li}_2\text{B}_2\text{O}_4$ ) and a trace of

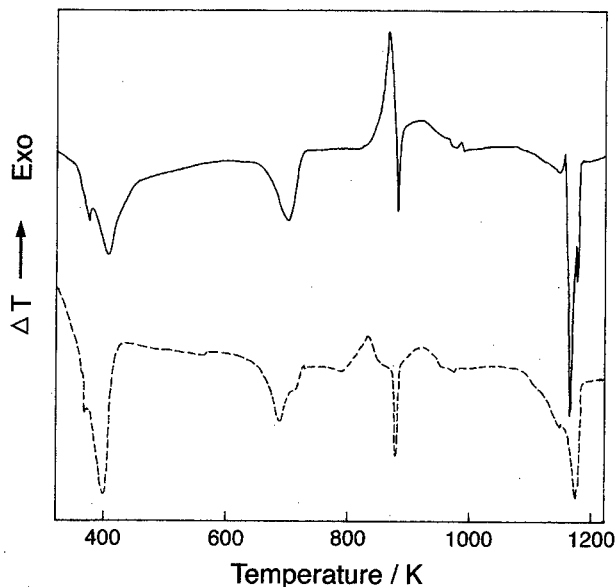


Fig. 2. DTA curves of Dried Powders with  $R_H$  of 0.675. Solid and broken lines denote Dried Powders prepared from inorganic compounds or methoxides, respectively.

unknown compounds. The formation of these by-products depended on the amounts of hydrochloric acid, i.e.  $R_H$ . In Fig. 1 the diffraction intensities of the unique peaks of  $\text{Li}_4\text{B}_7\text{O}_{12}\text{Cl}$ ,  $\text{Li}_2\text{B}_4\text{O}_7$ , and  $\text{Li}_2\text{B}_2\text{O}_4$  ( $32.84^\circ$ ,  $21.78^\circ$  and  $30.56^\circ$  in  $2\theta(\text{Cu K}\alpha)$ , respectively) are plotted versus  $R_H$ . At  $R_H=0.25$  a large amount of  $\text{Li}_2\text{B}_4\text{O}_7$  was formed. With increasing  $R_H$  the formation of  $\text{Li}_2\text{B}_4\text{O}_7$  was suppressed and subsequently at  $R_H=0.675$  or above was totally suppressed. In contrast,  $\text{Li}_2\text{B}_2\text{O}_4$  formed only at  $R_H=0.9$ . When  $R_H$  was from 0.675 to 0.75,  $\text{Li}_4\text{B}_7\text{O}_{12}\text{Cl}$  formed as a single-phase. These  $R_H$  values agreed well with the figure of 0.675 when preparing  $\text{Li}_4\text{B}_7\text{O}_{12}\text{Cl}$  powder from methoxides under the same heating condition. The by-product formation of  $\text{Li}_2\text{B}_4\text{O}_7$  and  $\text{Li}_2\text{B}_2\text{O}_4$  also depended on  $R_H$  in a similar manner.

**3.1.2. Reaction process during heating** - DTA-TG analysis was performed on Dried Powders prepared from the inorganic compounds or methoxides with  $R_H$  of 0.675, when a single-phase of  $\text{Li}_4\text{B}_7\text{O}_{12}\text{Cl}$  formed. The two TG curves of these powders showed similar decreases. Figure 2 shows the DTA curves of these powders. Both curves exhibit similar endothermic and exothermic reactions. Referring to our results in preparation from methoxides and the literature, the observed peaks were assigned as follows: about 350 to 450 K (endo), evaporation of methanol and adsorbed water; 630 to 730 K (endo), decomposition of  $\text{Li}_2\text{B}_{10}\text{O}_{16}\cdot\text{H}_2\text{O}$  with dissipation of water of crystallization; 810 to 878 K (exo), crystallization of an intermediate of  $\text{Li}_2\text{B}_4\text{O}_7$ ; 883 K (endo), melting of  $\text{LiCl}$



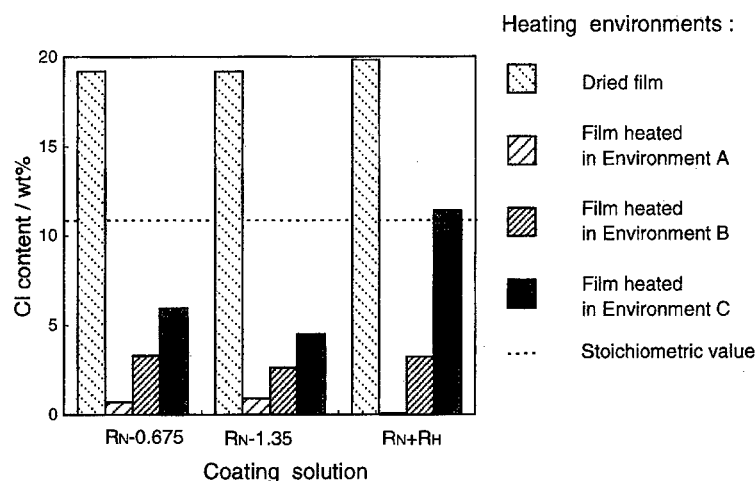


Fig. 3. Chlorine content of films prepared from various coating solutions and heated in various environments.

$R_N=0.675$ ,  $R_N=1.35$  and  $R_N+R_H$  denote the chlorine composition in the coating solutions:  $R_N=0.675$ ,  $R_H=0$ ;  $R_N=1.35$ ,  $R_H=0$ ;  $R_N=0.675$ ,  $R_H=0.675$ , respectively.

(lit., 887 K); 893 to 960 K (exo), crystallization of  $\text{Li}_4\text{B}_7\text{O}_{12}\text{Cl}$ ; a broad peak from 1080 to 1155 K (endo), decomposition of  $\text{Li}_4\text{B}_7\text{O}_{12}\text{Cl}$  (lit.[5], beginning from 1137 K in Ar); sharp peak from 1155 to 1190 K (endo), melting of a material decomposed of  $\text{Li}_2\text{B}_4\text{O}_7$  (lit.[6], 1190 K), where the terms endo and exo in parentheses refer to endothermic and exothermic reactions, respectively.

The temperature ranges for crystallization of  $\text{Li}_2\text{B}_4\text{O}_7$  and  $\text{Li}_4\text{B}_7\text{O}_{12}\text{Cl}$  in DTA analysis, however, did not coincide closely with those in high-temperature XRD [4], probably due to the difference in heating rates. The similarity of the two DTA curves shows that the kind of lithium and boron sources had little effect on the reaction process in the preparation of  $\text{Li}_4\text{B}_7\text{O}_{12}\text{Cl}$  powder. Therefore, the inorganic compounds were used as the lithium and boron sources for the preparation of  $\text{Li}_4\text{B}_7\text{O}_{12}\text{Cl}$  film.

### 3.2. Preparation of Film

**3.2.1. Problem of lack of chlorine** - Film prepared with hydrochloric acid added at  $R_H=0.675$  was too thin ( $<0.3 \mu\text{m}$ ) for characterization. Therefore, ammonium chloride, which was found to produce single-phase  $\text{Li}_4\text{B}_7\text{O}_{12}\text{Cl}$  powder in a way similar to hydrochloric acid, was tried as a chlorine source. When prepared with ammonium chloride added at  $R_N=0.675$  and heated at 873 K for 1 h in a nitrogen atmosphere,  $\text{Li}_2\text{B}_4\text{O}_7$  formed, but not  $\text{Li}_4\text{B}_7\text{O}_{12}\text{Cl}$ . In order to clarify the difference between the preparation of powder and film, the chlorine content of the above Dried and Heated Films was analyzed and compared with that of single-phase  $\text{Li}_4\text{B}_7\text{O}_{12}\text{Cl}$  powder, which was prepared with  $R_H$  of 0.675 and heated at 973 K for 1 h. The powder contained 10.6 wt% of chlorine, which agrees well with the stoichiometric value for  $\text{Li}_4\text{B}_7\text{O}_{12}\text{Cl}$  (10.7 wt%). However,

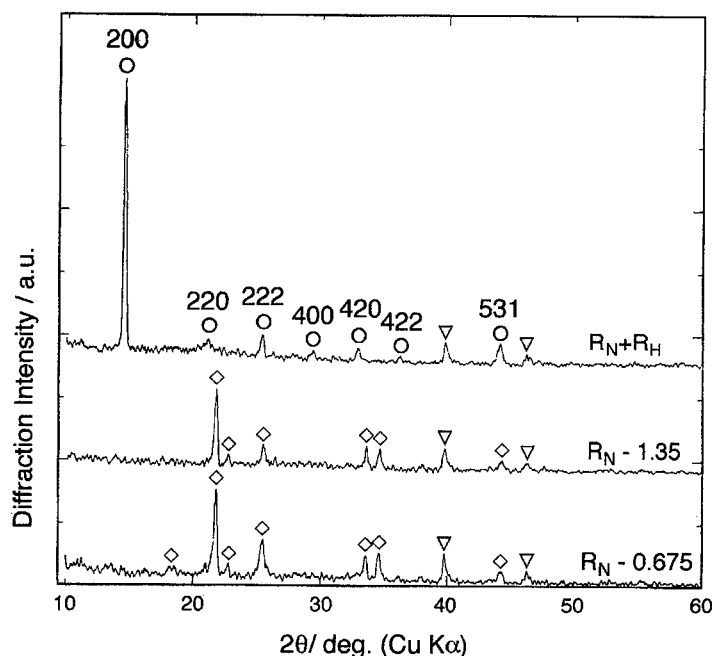


Fig. 4. X-ray diffraction patterns of the films prepared from various coating solutions and heated in Environment C.

o, ◇, and ▽ denote the peaks due to  $\text{Li}_4\text{B}_7\text{O}_{12}\text{Cl}$ ,  $\text{Li}_2\text{B}_4\text{O}_7$  and Pt, respectively.

$R_N=0.675$ ,  $R_N=1.35$  and  $R_N+R_H$  denote the chlorine composition in the coating solutions:

$R_N=0.675$ ,  $R_H=0$ ;  $R_N=1.35$ ,  $R_H=0$ ;  $R_N=0.675$ ,  $R_H=0.675$ , respectively.

in the films, the chlorine content declined from 19.2 wt% to only 0.6 wt% as a result of heating. These results show that chlorine evaporated more easily from films than from powders. Therefore, a different approach was required to suppress the evaporation of chlorine.

**3.2.2. Suppression of chlorine evaporation** - We attempted to suppress chlorine evaporation by modifying both the chlorine composition in the coating solutions and the environment for heating Dried Films. Figure 3 shows the chlorine content of films prepared from different coating solutions and then heated in different environments. Among the films prepared from the same coating solution, the chlorine exists in the following order: (Dried Film) > film heated in Environment C > that in Environment B > that in Environment A. This order coincides with the decreasing order of chlorine content in the heating environments. This shows that higher chlorine content in the surrounding environment suppresses chlorine evaporation from the film.

Increasing the amount of ammonium chloride from 0.675 to 1.35 in  $R_N$  did not suppress chlorine evaporation at all, even in Environment C, because both films lacked chlorine. Only when film was prepared from the coating solution

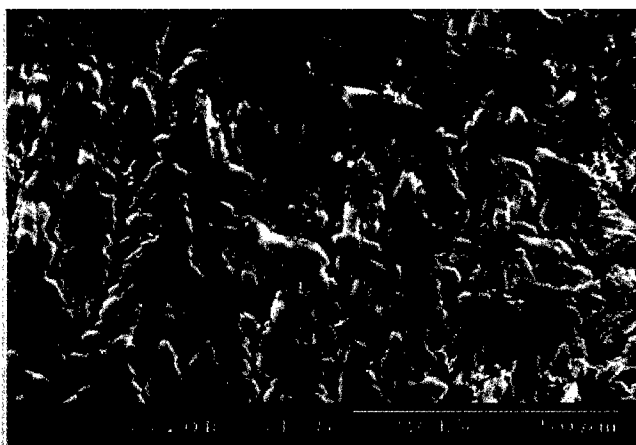


Fig. 5. SEM image of  $\text{Li}_4\text{B}_7\text{O}_{12}\text{Cl}$  film prepared from the solution with  $R_N=0.675$  and  $R_H=0.675$  and heated in Environment C.

with  $R_N=0.675$  and  $R_H=0.675$ , and heated in Environment C was the chlorine content preserved at the stoichiometric value.

**3.2.3. Characterization of film** - The phases in the films heated in Environment C were identified by XRD. Figure 4 shows the X-ray diffraction patterns. The chlorine composition in the solutions also affected the crystallization of  $\text{Li}_4\text{B}_7\text{O}_{12}\text{Cl}$  and  $\text{Li}_2\text{B}_4\text{O}_7$ . In the films prepared with only ammonium chloride,  $\text{Li}_2\text{B}_4\text{O}_7$  alone formed and crystallization of  $\text{Li}_4\text{B}_7\text{O}_{12}\text{Cl}$  was not observed at all, even though there is about half the stoichiometric amount of chlorine. On the other hand, in the film prepared from the coating solution with  $R_N=0.675$  and  $R_H=0.675$ , when the chlorine content coincided with the stoichiometric value,  $\text{Li}_4\text{B}_7\text{O}_{12}\text{Cl}$  formed as a single-phase.

Furthermore, in the prepared  $\text{Li}_4\text{B}_7\text{O}_{12}\text{Cl}$  film the relative intensity of the (200) peak was quite strong in comparison with that in the JCPDS data files [7] or in the Heated Powder patterns. This indicates that the  $\text{Li}_4\text{B}_7\text{O}_{12}\text{Cl}$  film is highly oriented along the (100) plane. The direction of the orientation is expected to enhance the ionic conductivity of the film, because the direction fits that of lithium-ion channels in lithium boracite crystal.

Figure 5 shows the SEM image of the  $\text{Li}_4\text{B}_7\text{O}_{12}\text{Cl}$  film. The surface was not smooth but had a structure like leaves, although the surface of the Dried Film was smooth. EDX analysis of the  $\text{Li}_4\text{B}_7\text{O}_{12}\text{Cl}$  film showed that the Cl/O intensity ratio was approximately the same everywhere on the leaf-shaped deposits, but outside the deposits chlorine was scarcely detected and instead the Si intensity increased. These SEM and EDX results showed that the deposits were  $\text{Li}_4\text{B}_7\text{O}_{12}\text{Cl}$ , with the substrate exposed partly between the deposits. In order to prepare smoother  $\text{Li}_4\text{B}_7\text{O}_{12}\text{Cl}$  film, which is required to examine its conductivity, further study of the heating procedure is necessary.

#### 4. CONCLUSIONS

$\text{Li}_4\text{B}_7\text{O}_{12}\text{Cl}$  powder and film were prepared by the sol-gel method from inorganic lithium and boron compounds with hydrochloric acid or/and ammonium chloride. Single-phase  $\text{Li}_4\text{B}_7\text{O}_{12}\text{Cl}$  powder was obtained from a sol solution with the  $\text{HCl/Li}$  molar ( $R_H$ ) ratio of 0.675 to 0.75, in a manner similar to that in its preparation from lithium and boron methoxides. The kind of lithium and boron sources had little effect also on the reaction process during heating.  $\text{Li}_4\text{B}_7\text{O}_{12}\text{Cl}$  film was much more difficult to synthesize, because chlorine evaporated easily from the films during heating. Single-phase  $\text{Li}_4\text{B}_7\text{O}_{12}\text{Cl}$  film was prepared only from the sol solution with  $R_H$  of 0.675 and  $\text{NH}_4\text{Cl/Li}$  molar ratio ( $R_N$ ) of 0.675 and under a chlorine-rich heating environment. The prepared  $\text{Li}_4\text{B}_7\text{O}_{12}\text{Cl}$  film was highly oriented along the (100) plane.

#### REFERENCES

- [1] W. Jeitschko, T.A. Bither & P.E. Bierstedt, *Acta Cryst.* **B33** (1977), 2767.
- [2] A. Levasseur, J.C. Brethous, J.M. Reau, P. Hagenmuller & M. Couzi, *Solid State Ionics* **1** (1980), 177.
- [3] S. Sakka, In: *Sol-Gel Fibers and Coating Films*, Eds. M.A. Aegerter, M. Jafeliecci, Jr., D.F. Souza and E.D. Zanotti (World Scientific, Singapore, 1989), pp 346-374.
- [4] T. Nagase, H. Wada, K. Sakane & T. Kitamura, In: *Proc. Int. Conf. on Sol-Gel-Production*, Oct. 10-13, 1993, Saarbrücken, Germany, (to be published).
- [5] P. Tissot, J. Painot, J.P. Rivera & H. Schmid, *Thermochimica Acta*, **56** (1982), 359.
- [6] B.S.R. Sastry & F.A. Hummel, *J. Am. Ceram. Soc.* **42** (1959), 216.
- [7] JCPDS data file numbers 24-0602 and 34-0742.

## DENSITIES OF THE ALKALI THIOBORATE GLASSES AS A FUNCTION OF SHORT RANGE ORDER

Michael ROYLE, Jaephil CHO & Steve W. MARTIN  
*Department of Materials Science and Engineering,  
Iowa State University of Science and Technology,  
Ames, IA 50011, USA*

Densities of the alkali thioborate glasses,  $xM_2S \cdot (1-x)B_2S_3$  ( $M=Na, K, Rb, Cs$ ), have been measured over a wide range of compositions. The density trend of each alkali family shows a strong dependence on the fraction of tetrahedral boron sites ( $M^+BS_2^-$ ),  $N_4$ , in the glass.  $^{11}B$  NMR studies have shown that the conversion rate,  $\alpha$ , of trigonal boron sites ( $BS_{3/2}$ ) to tetrahedral sites varies from alkali to alkali; the conversion rate varies from  $\alpha=2$  for cesium to  $\alpha=7.2$  for sodium. In the low alkali region, the densities all show a monotonic increase due to the growth of  $N_4$  in the glass. However, at high alkali content, the heavier alkali glasses show a different behavior than the lighter alkali. The densities of the heavier alkali continue to increase throughout the glass forming region, whereas the lighter alkali reach a maximum and decrease as the  $N_4$  diminishes. This may be due to the larger alkali ions dominating the packing, giving a more densely packed system; whereas, the smaller alkali ions are dominated the trigonal planar units causing a less densely packed system.

### 1. INTRODUCTION

With the increased interest in  $B_2S_3$ -based glasses as solid state electrolytes [1-8], research on the correlation between the short range order (SRO) and the physical properties of these glasses has become more important. Infrared (IR) [9-12] and NMR [13-16] spectroscopic studies have been used extensively to characterize the SRO in these systems. The IR and NMR data show that the SRO structural groups of the alkali thioborate glasses are similar to the alkali borate glasses [17-23]. In the low alkali region, the trigonal planar groups,  $B3(0)$  (where the 3 represents the coordination number of the boron and the number in parentheses represents the number of non-bridging sulfurs (NBS)), are replaced by the tetrahedral groups,  $B4$ . In the high alkali region, the  $B4$  groups are replaced by the trigonal planar groups with one NBS,  $B3(1)$ , and trigonal planar groups with three NBS,  $B3(3)$ . This same behavior is seen the borate glasses, with the addition of a trigonal group with two non-bridging oxygen (NBO), the analogous group with two NBS are not found in the thioborate glasses.

One enigmatic result of the NMR data is the variation of the conversion rate,  $\alpha$ , of  $B3(0)$  groups to  $B4$  groups in thioborate glasses. NMR data show

that  $\alpha=7.2$  for the sodium thioborate glasses, which is exceptionally large when compared to  $\alpha=2$  for the sodium borate glasses. As the size of the alkali ion is increased, the conversion rate decreases to  $\alpha=2$  for the cesium thioborate glasses, which is comparable to the cesium borate glasses. These data are important when analyzing the density data of these glasses.

Using the four coordinated boron group fraction,  $N_4$ , data of the alkali thioborate glasses, the density can readily be modeled. The density can be defined as [24]:

$$\rho = \frac{\sum_{i=1}^5 f_i m_i}{\sum_{i=1}^5 f_i V_i} \quad (1)$$

where  $f_i$ ,  $m_i$ , and  $V_i$  are the fraction, molar mass, and molar volume of the  $i^{\text{th}}$  unit, respectively. If the volumes, masses, and fractions of the SRO groups are known, this makes modeling the density a straight forward task. However, not all of the volumes and fractions are known; for example, the only volumes which cannot be directly calculated from the density are the volumes of the B4 and B3(1) groups. Also, the only fraction which cannot be calculated from the  $N_4$  data is the post maximum region of the B3(1) group. These unknowns were consequently fit to the density data in order to obtain the best values. An iterative Newtonian search algorithm was employed to perform this operation. This paper will present the data and the structural model developed from the data.

## 2. EXPERIMENTAL DATA

Figures 1(a)-(d) show  $N_4$  as a function of composition for the various alkali thioborate glasses. Superimposed on the experimental data are plots of  $x/(1-x)$ ,  $2x/(1-x)$ ,  $3x/(1-x)$ , and  $4x/(1-x)$ . The sodium  $N_4$  data fall between  $3x/(1-x)$  and  $4x/(1-x)$ , indicating a conversion rate between 6 and 8 B4 groups for every B3(0) group. The potassium and rubidium  $N_4$  data gives a conversion rate between 2 and 4, with the conversion rate in the potassium system being larger than that of the rubidium system. Lastly, the cesium  $N_4$  data fall on the  $x/(1-x)$  curve indicating a conversion rate of 2. The precise conversion rate is calculated by fitting Eq. (2) to the  $N_4$  data. The fitting was performed using the built in Microsoft Excel solver routine. The calculated rates for the alkali thioborate glasses are given in Table 1. Figure 2 shows all of the alkali  $N_4$  data as a function of composition. The sodium system with the larger conversion rate increases

**Table 1.**  
Conversion rates of the various alkali thioborate glasses.

	Na	K	Rb	Cs
Conversion Rate	7.2	3.1	2.3	2

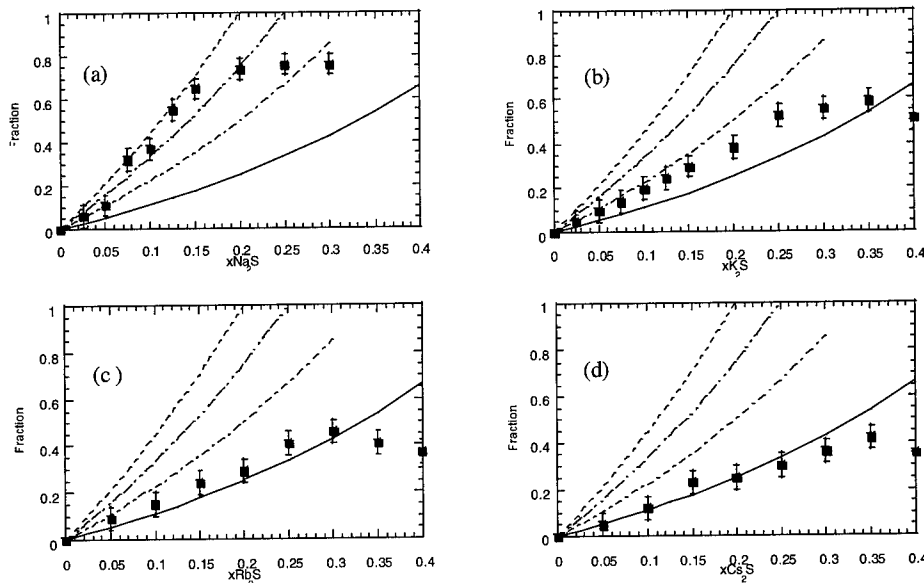


Fig. 1 (a)-(d). The  $N_4$  data plotted against  $x/(1-x)$  [—],  $2x/(1-x)$  [— · —],  $3x/(1-x)$  [- - -],  $4x/(1-x)$  [- · - ·].

sharply and reaches its maximum at a lower composition than the other alkali

$$f_2 \equiv N_4 = \frac{\alpha x}{2(1-x)} \quad (2)$$

families. As the size of the alkali ion is increased, the slope of the conversion rate decreases, the maximum is lowered, and the position of the maximum is shifted to higher alkali content glasses.

The density data is similar throughout the alkali families. In the low alkali region, every family shows a monotonic increase which can be attributed to increasing  $N_4$  in this region. The density data can be seen in Fig. 3. As  $N_4$  maximizes, the density also maximizes for the smaller alkali families; however, the density of the larger alkali families continues to increase throughout the glass-forming region. Qualitatively, these density trends in the high alkali region can be explained by examining the size of the alkali ion in relation to the structural groups. Sodium and potassium ions are similar or smaller in size to the structural groups which causes the network to limit the packing ability of the glass. In the high alkali region, the less dense trigonal planar groups dominate, giving a lower density than in the low alkali region where the glass is comprised of more dense tetrahedral groups. On the other hand, the rubidium and cesium ions are much larger than the structural groups, thereby allowing the alkali ions to determine how efficiently the glass is packed, with the network groups acting as space fillers. This same behavior is found in the alkali

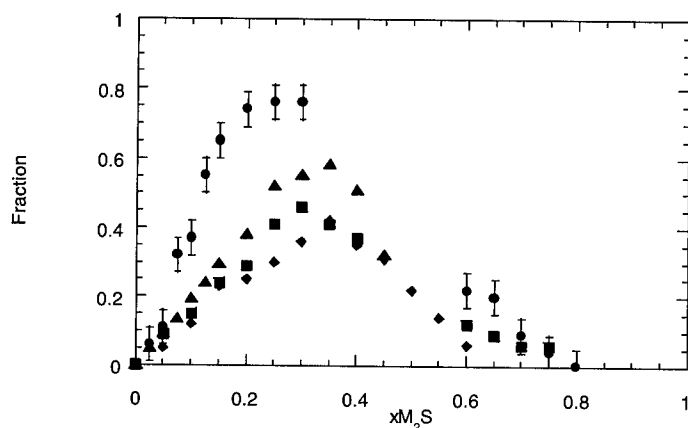


Fig. 2. A compilation of alkali thioborate  $N_4$  data, Na ( $\circ$ ), K ( $\Delta$ ), Rb ( $\blacksquare$ ), Cs ( $\diamond$ ), with a representative error bar inserted into the graph.

borate glasses [25]. One interesting fact to note is that the  $0.5\text{Na}_2\text{S}+0.5\text{B}_2\text{S}_3$  glass (which is not possible in the sodium borate system) can be made through the use of roller quenching. This may be attributed to the lower melting point of the sulfide system as well as the larger size of the sulfur atom which increases the viscosity and allows it to vitrify more readily.

### 3. MODEL

A more quantitative model can be developed using Eq. (1). In order to build a model, the fractions of the various SRO groups must be found. As stated above, the  $N_4$  data was modeled by fitting Eq. (2) or straight lines to the data.

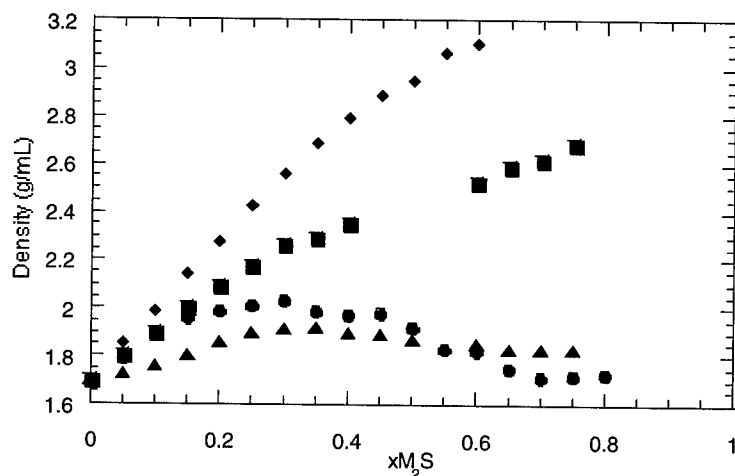


Fig. 3. A compilation of alkali thioborate  $N_4$  data, Na ( $\circ$ ), K ( $\Delta$ ), Rb ( $\blacksquare$ ), Cs ( $\diamond$ ), the experimental error is within the data points.



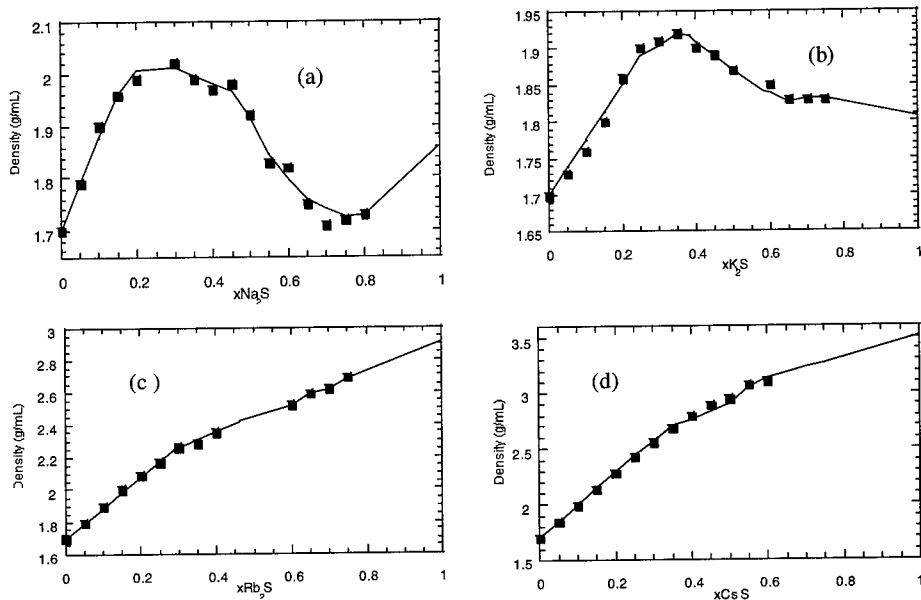


Fig. 4 (a)-(d). Densities of the alkali thioborate glasses (■) with the model (—), the experimental error is within the data points.

From these data and the fact that the sum of the fractions at all compositions must equal unity, most of the other fraction information can be elucidated. For instance, in the low alkali region, only the B3(0) and B4 groups exist. Therefore, the fraction of the B3(0) group is equal to one minus  $N_4$ . Upon the formation of the B3(1) group, it is assumed that the fraction B3(0) group falls to zero at the same rate as for lower  $x$  and hence the fraction of the B3(1) group can be found. When the fraction of the B3(1) group reaches its maximum, the B3(3) group is formed. Without knowing the B3(1) and B3(3) fractions, the model cannot be completed since two unknowns exist in this region. The two unknowns can be simplified by assuming the B3(3) fraction is equal to one minus the other fractions. This leaves the decreasing portion of the B3(1) fraction as an unknown.

In addition to the unknown fractions, some of the molar volumes are unknown. The volumes of the B3(0) and molecular  $M_2S$  can be found using the density of  $v\text{-B}_2\text{S}_3$  and  $c\text{-M}_2\text{S}$ . The density of crystalline  $M_2S$  is used because it has been shown [26] that past the orthothioborate composition,  $M_2S$  remains in the glass. The use of the crystalline volume of the alkali sulfide creates some error in the model; however, the effect of this error is only seen past  $x=0.75$  and therefore is minimal. Reference 26 also shows that the molar volumes of the B3(0), B3(1), and B3(3) groups have a linear relationship. This relationship is employed in the calculations to insure accuracy of the model, as well as to reduce the number of unknowns. The only exception to these formulations is

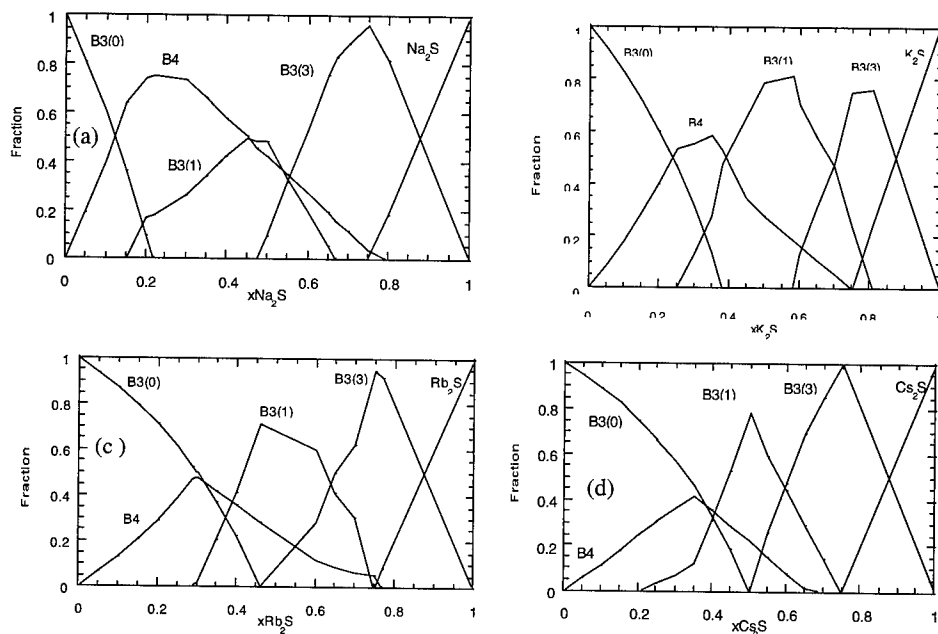


Fig. 5 (a)-(d). Modeled fractions of the SRO groups of the alkali thioborate glasses.

the sodium system. IR data of the sodium thioborate glasses show that at  $x \approx 0.75$  the fraction of the B3(3) group approaches unity. Therefore, the  $0.75\text{Na}_2\text{S} + 0.25\text{B}_2\text{S}_3$  glass can be used to find the volume of the B3(3) group. In either case, there exists two unknowns associated with the volumes of the SRO groups: the volume of the B4 group and either the volume of the B3(1) group or the slope of the equation relating the volumes of the trigonal boron groups.

The two unascertained volume terms and the unknown fractions can be found by employing an iterative Newtonian search algorithm. This method for modeling the density is based on the iterative use of the built-in solver function of Microsoft Excel. This solver function uses a Newtonian search algorithm to vary user defined variables to minimize a target cell, in this case the sum of the square of the differences between the model and experimental data. This function was used

Table 2.  
Molar Volumes (mL/mol) of the SRO Groups of the alkali thioborate glasses.

	Na	K	Rb	Cs
B3(0)	34.7	34.7	34.7	34.7
B4	47.4	57.3	62.0	63.6
B3(1)	52.3	61.9	68.2	74.2
B3(3)	102.3	122.6	135.2	154.7
M <sub>2</sub> S	42.1	52.18	64.19	80.29

iteratively by varying the volume terms, and then the fraction terms until the sum was unchanging to  $10^{-5}$ . Figures 4 (a)-(d) show the alkali thioborate density data with the models superimposed upon them. These figures show the accuracy of the computer calculations. These calculations give important information, such as the volumes and fractions of the SRO groups. Table 2 gives the volumes of the SRO groups, both calculated directly from the density data and calculated with an iterative Newtonian search. As well as obtaining the previously unknown molar volumes, the fractions of the various SRO groups were also found. These fractions are graphically represented in Fig. 5 (a)-(d). However, the calculated fractions do not accurately represent what is seen in the IR data. The B3(3) fractions of the cesium thioborate glasses do not reach unity as shown by this data. This could be an artifact of assuming that the cesium sulfide begins to remain in the glass at  $x=0.75$ .

#### 4. CONCLUSIONS

This model cannot be used as a predictive model since experimental data were used in calculations. However, it does give some insight into the structure of the glass. One of the most important results from this model is the calculated B3(1) fractions. Without conclusive NMR data in this composition region, relating physical properties to structures is very difficult. This model gives experimentally determined fractions which can be the basis of other models. This work will help researchers to obtain a better understanding of the nature of the alkali thioborate glasses, which may, in turn, help in the development of technologically useful products.

#### REFERENCES

- [1] A. Levasseur, R. Olazcuaga, M. Kbala, M. Zahir & P. Hagenmuller, *C.R. Acad. Sci.* **293** (1981), 563.
- [2] M. Makytá, A. Levasseur & P. Hagenmuller, *Mater. Res. Bull.* **19** (1984), 1361.
- [3] M. Menetrier, A. Hojjaji, C. Estournes & A. Levasseur, *Solid State Ionic.* **48** (1991), 325.
- [4] S. W. Martin, *J. Amer. Ceram. Soc.* **74** (1991), 1767.
- [5] A. Pradel & M. Ribes, *J. Solid State Chem.* **96** (1992), 247.
- [6] H. Patel, *Ph.D. Thesis* (Iowa State University, 1993).
- [7] J. Kincs, *M.S. Thesis* (Iowa State University, 1994).
- [8] J. H. Kennedy, *Materials Chem. and Phys.* **23** (1990), 29.
- [9] J. Cho, *M.S. Thesis* (Iowa State University, 1992).
- [10] D.R. Bloyer, *M.S. Thesis* (Iowa State University, 1989).
- [11] J. Cho & S. W. Martin, *J. Non-Cryst. Solids* **170** (1994), 182.
- [12] J. Cho, *Ph.D. Thesis* (Iowa State University, 1995).
- [13] J. Sills, *Ph.D. Thesis* (Iowa State University, 1993).
- [14] J. Sills, S. W. Martin & D. R. Torgeson, *J. Non-Cryst. Solids* **168** (1994), 286.
- [15] J. Sills, S. W. Martin & D. R. Torgeson, *J. Non-Cryst. Solids* **175** (1994), 270.
- [16] J. Cho, S. W. Martin, K. Kim & D. R. Torgeson, *J. Non-Cryst Solids* In Press.
- [17] P. J. Bray & J. G. O'Keefe, *Phys. Chem. Glasses* **4** (1963), 37.
- [18] E. I. Kamitsos, A. P. Patsis, G. D. Chryssikos & M. A. Karakassides, *Mat. Sci. Eng.* **B7** (1990), 1.
- [19] E. I. Kamitsos, M. A. Karakassides & G. D. Chryssikos, *Phys Chem. Glasses* **30** (1989), 229.

- 
- [20] J. Krogh-Moe, *Phys. Chem. Glasses* **6** (1965), 45.  
[21] E. I. Kamitsos, M. A. Karakassides & G. D. Chryssikos, *J. Non-Cryst. Solids* **116** (1990), 115.  
[22] J. Krogh-Moe, *Phys. Chem. Glasses* **1** (1960), 26.  
[23] G. E. Jellison, Jr. & P. J. Bray, *J. Non-Cryst. Solids* **29** (1978), 187.  
[24] A. Karki, S. Feller, H. P. Lim, J. Stark, C. Sanchez & M. Shibata, *J. Non-Cryst. Solids* **92** (1987), 11.  
[25] M. Royle, M. Sharma, S. Feller, J. MacKenzie & S. Nijhawan, *Phys. Chem. Glasses* **34** (1993), 149.  
[26] J. Cho & S. W. Martin, *J. Non-Cryst. Solids* In Press.

## AN XPS STUDY OF THE CHEMICAL STRUCTURE OF AgI–Ag<sub>2</sub>O–B<sub>2</sub>O<sub>3</sub> GLASSES

H. JAIN

*Materials Science and Engineering Dept., Lehigh University,  
Bethlehem, PA 18015, USA*

A. C. MILLER

*Zettlemoyer Center for Surface Studies, Lehigh University,  
Bethlehem, PA 18015, USA*

E. I. KAMITSOS & J.A. KAPOUTSIS

*National Hellenic Research Foundation, Athens 11635, Greece*

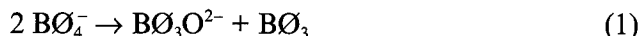
The chemical structure of six glasses within the  $x\text{AgI}:(1-x)[\text{Ag}_2\text{O}:n\text{B}_2\text{O}_3]$  system, and polycrystalline AgI has been determined using high resolution x-ray photoelectron spectroscopy. The O 1s spectra reveal a new kind of oxygen atom with charge density lower than that on bridging oxygens. These low charge density oxygens (LCDO) are believed to result from a predominantly covalent bonding with Ag. The concentration of LCDO increases with the initial addition of Ag<sub>2</sub>O to B<sub>2</sub>O<sub>3</sub>, or AgI to Ag<sub>2</sub>O:B<sub>2</sub>O<sub>3</sub> glasses. For  $n=1$ , with increasing  $x$ , Ag and I approach the chemical state of crystalline AgI. There is no obvious indication of distinct AgI microdomain formation at low AgI content.

### 1. INTRODUCTION

Among the various halogenated borate glasses, the structure of silver iodoborates has been investigated most because of their potential application as a solid electrolyte [e.g. 1-11]. In these studies much attention has been given to the structural significance of AgI, since it is the high conductivity component in the AgI–Ag<sub>2</sub>O–B<sub>2</sub>O<sub>3</sub> system. In this regard two conflicting views are prevalent in the literature: (A) AgI maintains its identity within the glass structure forming microdomains or clusters such that fast conduction of Ag<sup>+</sup> ions occurs along these regions [8,12-16]. Then silver ions must have at least two different environments, although a greater variety of silver coordinations is possible. For example, Minami *et al.* [9] have proposed three environments of silver ions corresponding to (i) bonding with a non-bridging oxygen (NBO) in BO<sub>3</sub> groups, (ii) bonding only to I and (iii) bonding to BO<sub>4</sub> groups. Further, a fourth kind of

environment is proposed corresponding to two intermediate size structural units, and different ion conduction rates are assumed for the silver atoms in the various environments [3]. The recent far infrared results show two energetically different Ag sites in a silver borate glass and a third kind of site is introduced with the addition of AgI [6]. (B) AgI is uniformly dispersed in the glass network so that all silver ions perceive an average uniform environment. Then the conductivity is enhanced because the average environment in AgI containing glass provides a lower energy barrier for ion migration.

The structural interpretation of fast ion conduction in the system  $x\text{AgI}:(1-x)[\text{Ag}_2\text{O}:n\text{B}_2\text{O}_3]$  becomes considerably more complex when one considers also the glass network. One set of spectroscopic data including NMR [2], Raman [7,8] and neutron scattering [14] indicate that the borate network is not affected by the introduction of AgI. The latter simply occupies and expands the interstitial space without significantly affecting the network. On the contrary, infrared investigations show significant changes in the borate network [6,9,10], which should indirectly influence the silver ion migration. In particular, for  $n=1$  AgI promotes the following structural transformation



where  $\emptyset$  represents a bridging oxygen (BO). Thus, there are several diverse and, in some ways, contradictory views of the glass structure which should be important for Ag conduction in the glasses of interest. However, so far no attempt has been made to characterize the chemical structure of silver borate glasses by x-ray photoelectron spectroscopy (XPS). In this paper we present a preliminary analysis of our high resolution XPS results on  $x\text{AgI}:(1-x)[\text{Ag}_2\text{O}:\text{B}_2\text{O}_3]$  glasses. Considering that the chemical structure strongly influences both the transport and dielectric properties of a glass [18,19], such information should be useful for establishing a structural basis of conductivity in silver based fast ion conducting glasses.

## 2. EXPERIMENTAL

The glasses were prepared by mixing and then melting in a platinum crucible appropriate amounts of  $\text{Ag}_2\text{O}$ ,  $\text{B}_2\text{O}_3$  and AgI powders at 700-1000°C depending on the composition. The homogenized clear melt was then splat quenched between two polished copper blocks, which resulted in glass specimens with a good surface. The specimens were stored in the dark to prevent any light induced changes. The XPS spectra were obtained using a Scienta spectrometer (ESCA-300) with monochromatic Al  $K\alpha$  X-rays (1486.6 eV). To avoid surface contamination, the sample was fractured in situ in a vacuum better than  $4.0 \times 10^{-9}$  Torr. The surface was flooded with  $\approx 2$  eV electrons to minimize the surface charging of our electrically insulating samples. Data analysis was conducted with the ESCA-300 software package using a Voigt function and Shirley background subtraction [20]. The B 1s and O 1s peaks for  $\text{B}_2\text{O}_3$  glass inherently show a small asymmetry [25]. Therefore, these spectra for all the present glasses were analyzed with the same asymmetry parameter (0.11 and 0.12, respectively).

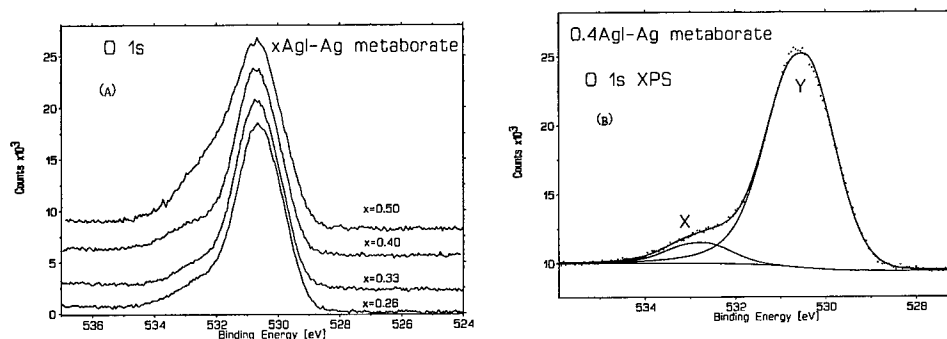


Fig. 1. O 1s x-ray photoelectron spectra for  $x\text{AgI}:(1-x)[\text{Ag}_2\text{O}:\text{B}_2\text{O}_3]$  glasses. (a) Comparison of the spectra for  $x=0.26$ - $0.50$ . (b) Decomposition of the spectrum for  $x=0.40$  into two components.

### 3. RESULTS

To obtain a complete picture of the changes in bonding of the various elements, the x-ray photoelectron spectra have been obtained for the Ag 3d, B 1s, O 1s and I 3d electrons in four  $x\text{AgI}:(1-x)[\text{Ag}_2\text{O}:\text{nB}_2\text{O}_3]$  glasses with  $n=1$ . For comparison, spectra for the binary  $\text{Ag}_2\text{O}:\text{2B}_2\text{O}_3$  ( $x=0$ ,  $n=2$ ) and  $\text{Ag}_2\text{O}:\text{9B}_2\text{O}_3$  ( $x=0$ ,  $n=9$ ) glasses were also obtained. The silver diborate glass is the one which could be prepared with the highest  $\text{Ag}_2\text{O}$  content without adding AgI. Compared to binary silver borate glasses, the AgI containing glass surfaces showed relatively little charging. Nevertheless, we could not be completely sure that a sample remained at the ground potential. Therefore, all the binding energies (b.e.) reported here are referenced (somewhat arbitrarily) to B 1s as being at 191.0 eV. We have chosen B 1s as an internal reference because generally cation energy levels do not shift much with composition. Furthermore, at least for the metaborate series the B/O ratio remains fixed and no variation is observed in the full width at half maximum (FWHM, D) of the B 1s peak.

The O 1s spectrum shows the strongest variation with the addition of AgI, as shown in Fig. 1. At least two peaks are required to describe it, indicating two distinguishable chemical environments of the oxygen atoms. Therefore, each O 1s spectrum is fitted with two components: a peak 'X' at high b.e. and a peak 'Y' at low b.e. as shown, for example, in Fig. 1(b) for the  $0.4\text{AgI}:\text{0.6}[\text{Ag}_2\text{O}:\text{B}_2\text{O}_3]$  glass. The dots are actual data points and the upper solid curve is the best fit to data. The following procedure was adopted for curve fitting: since the spectrum shows strong asymmetry on the high binding energy side, the dominant peak is selected to parallel the height and slope of the spectrum on the low binding energy side. Then a second peak is added with its maximum corresponding to that of the shoulder on the high binding energy side. With these two peaks as initial input, the ESCA-300 computer program obtained the two component peaks with the best least-square fit to the experimental data. The fitting procedure is initially constrained to assign the same value of D for both the components. Subsequently D for the two components was made independent. For the case of  $x=0.4$  and  $0.5$ , the high b.e. shoulder is sufficiently strong for unambiguously determining its approximate position and

height. For the case of  $x=0.26$  and  $0.33$ , the shoulder location is not obvious. Then the peak position of the shoulder for the  $x=0.4$  glass was used as the initial peak position input. The results of the deconvolution of the O 1s spectra are listed in Table 1, which includes the binding energy, FWHM and % area (%A) of the two component peaks. The error in b.e. from the curve fitting procedure is estimated to be  $\pm 0.1$  eV. Then the b.e. of the X and Y peaks remains nearly independent of composition. By comparison the %A of the X component increases with increasing  $x$  or decreasing  $n$ .

In contrast to the O 1s spectrum, the Ag 3d and I 3d spectra are nearly symmetric and can be described reasonably well by single peaks as characterized by the parameters given in Table 1 (Ag 3d spectrum for  $n=9$ , as an exception, consists of two peaks). At the same time  $D$  for these two peaks is significantly larger for the present glasses than for crystalline AgI, particularly for the Ag 3d peak. Further,  $D$  for both the peaks decreases appreciably with increasing  $x$  (Table 1). In general, given the relatively large scatter in data, the B 1s spectra can be described approximately by a single peak with the small asymmetry found for  $B_2O_3$  glass [25], but with a  $D$  much larger than for the Ag and I peaks.

#### 4. DISCUSSION

Typical O 1s spectra for alkali silicate glasses consist of a large peak at high b.e. and a small peak at low b.e. corresponding to BOs and NBOs respectively (e.g [21,22] and references therein). The fractional area of the low b.e. peak remains directly proportional to the alkali content. The O 1s spectra of alkali germanate glasses can also be fitted with a large and a small component at high and low b.e. respectively, but in this case the area ratio does not have a

**Table 1.**

Binding Energy (b.e.), Full Width at Half Maximum ( $\Delta$ ) and Percent Area (%A) of the Various XPS Peaks for the  $xAgI:(1-x)[Ag_2O:nB_2O_3]$  Glass System.

Material	O 1s b.e.	$\Delta$	%A	I 3d <sub>5/2</sub> b.e.	$\Delta$	Ag 3d <sub>5/2</sub> b.e.	$\Delta$	B 1s b.e.	$\Delta$
$x=0.26, n=2$	530.4	1.82	94	619.7	1.13	368.0	1.08	191.0	1.24
	532.6	1.48	6						
$x=0.33, n=2$	530.5	1.79	96	619.7	1.10	368.1	1.04	191.0	1.21
	532.6	1.16	4						
$x=0.40, n=2$	530.4	1.76	92	619.6	1.07	368.1	1.00	191.0	1.17
	532.7	1.67	8						
$x=0.50, n=2$	530.5	1.97	83	619.4	1.06	368.0	0.95	191.0	1.44
	532.4	1.72	17						
$x=0, n=9$	530.6	2.19	96			366.8	1.60*	191.0	2.02
	532.3	1.97	4			368.5	1.56*		
$x=0, n=2$	530.6	1.76	89			367.3	1.17	191.0	1.38
	532.2	1.61	11						
AgI				620.0	0.93	368.8	0.66		
B <sub>2</sub> O <sub>3</sub> [25]	530.6	1.77						191.0	1.68

\*Consists of two components with areas 89% and 11%, indicating possible phase separation.



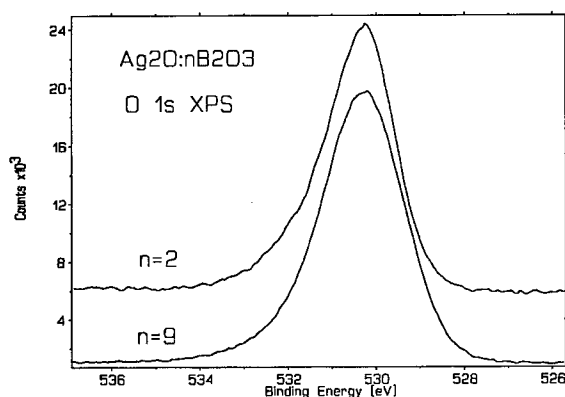


Fig. 2. O 1s x-ray photoelectron spectra for  $\text{Ag}_2\text{O}:9\text{B}_2\text{O}_3$  and  $\text{Ag}_2\text{O}:2\text{B}_2\text{O}_3$  glasses.

simple relationship with the alkali content because the latter induces  $\text{GeO}_4 \rightarrow \text{GeO}_6$  conversion in addition to the formation of NBOs [23,24]. Nonetheless, for both alkali silicate and alkali germanate glasses the dominant BO peak is on the higher b.e. side. By contrast, the dominant O 1s component (Y) for the present silver iodoborate and binary silver borate glasses is at lower b.e. (see Figs 1 and 2; Table 1). Clearly, the structure around O in the present silver borate glasses is significantly different from that in alkali germanate and silicate glasses. The following points may be noted for determining the origin of the two (or possibly more) components of the O 1s spectra in Fig. 1:

(a) The b.e. difference between the peaks X and Y,  $\delta_{XY}=1.6-2.3$  eV, is typical of the values reported for the BO and NBO in silicate and germanate glasses [21-24]. Thus it is tempting to assign X to BOs and Y to NBOs, but for the following reasons that will be inappropriate.

(b). It is reasonable to assume that in  $\text{B}_2\text{O}_3$  all O atoms form bridges between two B atoms. For this glass, the difference between the B 1s and O 1s peaks,  $\delta_{BO}=339.6$  eV [25]. When silver is added to  $\text{B}_2\text{O}_3$ , a component grows on the high b.e. side (see Fig. 2), similar to the X peak in Fig. 1. Table 1 indicates that  $\delta_{BO(X)}=341.3$  and  $341.2$  eV for this component for the binary glasses with  $n=9$  and  $2$ , respectively. On the other hand, for the dominant component  $\delta_{BO(Y)}=339.6$ , which is identical to the value for  $\text{B}_2\text{O}_3$ . Therefore, we should assign the Y peak to BOs similar to those in  $\text{B}_2\text{O}_3$ .

(c) Since the b.e. of the 'X' peak is larger than that of the 'Y' peak, the former represents O atoms with a smaller electron density. So if the dominant peak 'Y' represents BO, X should represent an O atom with even smaller electron density. To the best of our knowledge the new low charge density oxygen (LCDO) atoms have not been previously observed in the XPS of any alkali containing oxide glass.

Generally, Ag is considered iso-structural to alkali atoms in oxide glasses [26]. That is, silver should be donating its electron to an oxygen atom or polyhedron forming an NBO or inducing a network conversion of the type  $\text{GeO}_4 \rightarrow \text{GeO}_6$  or  $\text{BO}_3 \rightarrow \text{BO}_4$ . In this picture, the addition of a silver atom can only increase

the electron density more or less on a BO. However, the present results show that the addition of silver decreases electron density away from at least an appreciable fraction of the network oxygen atoms. Now if we consider the electronegativity values of O (3.44), B (2.04), Ag (1.93) and the alkali atoms (0.79-0.98) [27], we find that Ag is much more like B than an alkali atom. That is, Ag should be forming a relatively covalent bond just like B. Obviously, this inference must be appropriately modified to reflect the differences in sizes and coordinations of the two atoms. In any case, from electronegativity arguments we may anticipate that at least a fraction of Ag atoms is bonded to O much like B. With the  $\text{Ag}_2\text{O}$  addition the formation of predominantly covalent Ag-O-B linkages appears feasible with lower electron density on O atoms than those in B-O-B linkages. This proposal of a relatively covalent Ag-O bond is consistent with the suggestion of Tarashima *et al.* [28] and the most recent far IR results of Kapoutsis *et al.* [29]. In this connection note that XPS, unlike infrared (IR) spectroscopy, does not directly detect the bond linkages but only the changes in a particular energy level by the changes in chemical environment. The relative fraction of X oxygen atoms,  $f_x$ , increases from about 4% to 11% when  $n$  decreases from 9 to 2, indicating that indeed the X peak is associated with Ag atoms. Note that for the  $n=9$  and  $n=2$  silver borate glasses Ag/O ratio is 0.0714 and 0.286, respectively. Apparently, more than one Ag atom is needed to produce an LCDO. A simple evaluation of the composition dependence of the X peak, the density of states near the Fermi level and visual observations do not indicate that the LCDO could be a color center produced by x-irradiation. Nonetheless, we are pursuing a systematic investigation to experimentally rule out this possibility or an impurity origin of this peak.

Both the NMR [26] and IR [29] studies show that the addition of up to 25-30 mol%  $\text{Ag}_2\text{O}$  to  $\text{B}_2\text{O}_3$  is accompanied by  $\text{BO}_3 \rightarrow \text{BO}_4$  conversion. For higher mol%  $\text{Ag}_2\text{O}$ , NBOs are presumed to be produced at the expense of  $\text{BO}_4$  tetrahedra. However, the XPS spectra do not show a clear evidence of NBOs in any of the present glasses, thus suggesting that either the concentration of NBOs is too small or that their electron density is not sufficiently different from that of BOs. In principle, the Y component can be deconvoluted into a BO and an NBO component, but we have refrained from any deconvolution which is not sufficiently unique and necessary.

Unfortunately, an  $\text{Ag}_2\text{O}:\text{B}_2\text{O}_3$  reference glass could not be prepared without crystallizing the melt. So, if we extrapolate the observed increasing trend of  $f_x$  with increasing  $\text{Ag}_2\text{O}$  mol%, we expect the X component to be about 20% of the total O in silver metaborate glass. None of the AgI containing silver metaborate compositions have this high value of  $f_x$ . In fact,  $f_x$  decreases with decreasing AgI content (the curve fitting error in %A is  $\pm 2\%$ ). That is, the silver metaborate glass appears to have significantly fewer LCDOs than predicted by the two lower  $\text{Ag}_2\text{O}$  content binary glasses, perhaps because they are being replaced by some other type of BOs in a complex structural unit or NBOs [29].

An important message from the present data is that in contradiction to the assumption that AgI has no influence on the network structure [2,7,8,14], the

O 1s spectrum is significantly influenced by the addition of AgI. The changes from AgI addition in the electron distribution within the network parallel those from the addition of  $\text{Ag}_2\text{O}$  to  $\text{B}_2\text{O}_3$ . In both cases the migration of silver is facilitated by the changes in the network. The previous IR work on the same glasses led to eq. (1) above [29], with the conclusion that AgI destroys  $\text{BO}_4^-$  units. The present results cannot be expressed in the classical simplified picture made of well defined ionic species. Further analysis and modeling of the O 1s spectra are needed to verify the predictions of eq. (1).

As mentioned before, the Ag 3d spectra can be reasonably well described by a single peak. However, the FWHM of the peak is significantly larger than that of Ag in AgI (for which  $\Delta=0.66$  eV) but comparable to that for silver diborate (1.17 eV), thus indicating that there is a range of chemical environments of silver. Unfortunately, the Ag 3d XPS line is relatively insensitive to the chemical environment and therefore we are investigating the change in the Ag Auger parameter which is a better indicator of the Ag environment. A close examination of the Ag  $3d_{5/2}$  XPS peak shows a small but significant change with the addition of AgI: the FWHM of this peak decreases slightly. This is an indication of increased homogenization of the average charge distribution around Ag with increasing AgI.

The I  $3d_{5/2}$  spectra show a variation which complements that of Ag  $3d_{5/2}$ . With respect to B 1s there is no change in the b.e. of I  $3d_{5/2}$ , indicating that the I atoms remain unaffected by the rest of the glass structure. Furthermore, the b.e. difference between the Ag and I XPS peaks,  $d_{\text{Ag-I}}$ , decreases from 251.7 to 251.4 eV as  $x$  increases from 0.26 to 0.5, approaching 251.2 observed for the AgI powder. Thus, the charge density difference within the Ag-I bond decreases and it becomes a more covalent bond with the addition of AgI. The same conclusion is found from the increase of the far IR absorption frequencies representing the rattling of Ag atoms in a mostly covalent environment [6,29]. Finally, the I  $3d_{5/2}$  peak also becomes narrower with increasing  $x$ , much like the Ag  $3d_{5/2}$  peak, becoming more like the same peak for AgI ( $\Delta=0.93$  eV). These observations support the IR observations [10] and suggest the following model: The addition of AgI distinctly modifies the borate network. In particular, the charge distribution in the glass changes much like that which occurs with the initial addition of  $\text{Ag}_2\text{O}$  to  $\text{B}_2\text{O}_3$ . An I atom simply enters as an interstitial without actively affecting the network. Only at high AgI concentration, do the Ag and I atoms become like those in AgI crystal. Therefore, for the same reason, at small  $x$  there should not be any microdomains reminiscent of crystalline AgI. There appears to be a gradual conversion of Ag atoms surrounded predominantly by O atoms to those predominantly coordinated by I atoms, ultimately approaching the AgI structure.

## 5. CONCLUSIONS

The x-ray photoelectron spectroscopy of four silver iodoborate and two silver borate glasses reveals that silver affects the bonding within the glass network differently than do any alkali atoms in silicates, borates or germanates. Most notably, the charge density on a fraction of O atoms decreases with the addition

of Ag<sub>2</sub>O or AgI. The observation of these low charge density oxygen (LCDO) appears to be the first one for any oxide glass containing monovalent cations. The observation is opposite to that expected from the formation of NBOs or the usual negatively charged BO<sub>4</sub> tetrahedra. The unusual kind of O bonding in the present glasses is explained in terms of a predominantly covalent bonding of Ag resulting from its high electronegativity, comparable to that of B.

The addition of AgI to silver metaborate glass induces the formation of low electron density O in the structure. With increasing AgI content in the glass, both Ag and I atoms gradually approach the chemical state of crystalline AgI, but there is little support for the existence of AgI microdomains at low AgI content.

#### Acknowledgment

This work is supported by grants from NATO (CRG. 931213), National Science Foundation (DMR-9225072) and National Hellenic Research Foundation.

#### REFERENCES

- [1] L. Cervinka & F. Rocca, *J. Non-Cryst. Solids* **192 & 193** (1995), 125.
- [2] G. Chiodelli, A. Magistris, M. Villa & J.L. Bjorkstrom, *J. Non-Cryst. Solids* **51** (1982), 143.
- [3] S. Hayashi & K. Hayamizu, *J. Non-Cryst. Solids* **111** (1989), 214.
- [4] J. Swenson, L. Borjesson & W.S. Howells, *Phys. Rev. B* **52** (1995), 9310.
- [5] S.H. Chung, K.R. Jeffrey & J.R. Stevens and L. Borjesson, *Phys. Rev. B* **41** (1990), 6154.
- [6] E.I. Kamitsos, J. A. Kapoutsis, G. D. Chryssikos, J. M. Hutchinson, A. J. Pappin, M. D. Ingram & J. A. Duffy, *Phys. Chem. Glasses*, **36** (1995), 141.
- [7] J.P. Malugani & R. Mercier, *Solid St. Ionics* **13** (1984), 293.
- [8] G. Carini, M. Cutroni, A. Fontana, G. Mariotto & F. Rocca, *Phys. Rev. B* **29** (1984), 3567.
- [9] T. Minami, T. Shimuzu & M. Tanaka, *Solid St. Ionics* **9-10** (1983), 577.
- [10] E. I. Kamitsos, J. A. Kapoutsis, G.D. Chryssikos & G.D. Patsis, *Proc. XVI Int. Congr. Glass*, Madrid, 1992, vol. 4, p. 403.
- [11] S.W. Martin, H.J. Bishoff, M. Mali & D. Brinkmann, *Solid. State Ionics* **18 & 19** (1986), 421.
- [12] T. Minami, *J. Non-Cryst. Solids* **73** (1985), 273.
- [13] A. Schiraldi, E. Pezzati & P. Baldini, *J. Phys. Chem.* **89** (1985), 1528.
- [14] M. Tachez, R. Mercier, J.P. Malugani & P. Chieux, *Solid State Ionics* **44** (1991), 151.
- [15] M. Mangion & G.P. Johari, *Phys. Rev. B* **36** (1987), 8845.
- [16] M.D. Ingram, J.M. Hutchinson & A.P. Pappin, *Phys. Chem. Glasses* **32** (1991), 121.
- [17] L. Borjesson, R.L. McGreavy & W.S. Howells, *Phil. Mag. B* **65** (1992), 261.
- [18] C.H. Hsieh & H. Jain, *J. Non-Cryst. Solids* **183** (1995), 1.
- [19] C.H. Hsieh, H. Jain & E.I. Kamitsos, *J. Appl. Phys.* **80** (1996), 1704.
- [20] D.A. Shirley, *Phys. Rev. B* **5** (1972), 4709.
- [21] R. Bruckner, H. Chun & H. Goretzki, *Glastech. Ber.* **51** (1978), 1.
- [22] C.H. Hsieh, H. Jain, A.C. Miller & E. I. Kamitsos, *J. Non-Cryst. Solids* **168** (1994) 247.
- [23] W.C. Huang, H. Jain & M.A. Marcus, *J. Non-Cryst Solids* **180** (1994), 40.
- [24] X. Lu, H. Jain & W.C. Huang, *Phys. Chem. Glasses* **37** (1996), 201.
- [25] S. K. Saha, Ph.D. Thesis, Lehigh University, Bethlehem, PA, 1996.
- [26] K.S. Kim & P.J. Bray, *J. Nonmetals* **2** (1974), 95.
- [27] A.L. Allred, *J. Inorg. Nucl. Chem.* **17** (1961), 215.
- [28] K. Tarashima, S.H. Kim & T. Yoko, *J. Am. Ceram. Soc.* **78** (1995), 1601.
- [29] J.A. Kapoutsis, E.I. Kamitsos & G.D. Chryssikos, *Proc. Second Int. Conf. on Borates Glasses, Crystals and Melts*, 303.

# THE ROLE OF SILVER IN THE STRUCTURE OF (AgI)<sub>x</sub>(Ag<sub>2</sub>O.*n*B<sub>2</sub>O<sub>3</sub>)<sub>1-x</sub> BORATE GLASSES AND THEIR FAST ION CONDUCTING PROPERTIES

Francesco ROCCA

*CeFSA-Centro CNR-ITC di Fisica degli Stati Aggregati,  
38050 Povo (Trento), Italy.*

Giuseppe DALBA, Paolo FORNASINI

*Istituto Nazionale di Fisica della Materia-Dipartimento di Fisica,  
Università di Trento, 38050 Povo (Trento), Italy.*

and

Francesca MONTI

*Facoltà di Scienze, Università di Verona, Strada le Grazie,  
37134 Verona, Italy.*

The paper presents a summary of research performed during recent years on (AgI)<sub>x</sub>(Ag<sub>2</sub>O.*n*B<sub>2</sub>O<sub>3</sub>)<sub>1-x</sub> glasses using X-ray Absorption Spectroscopy (EXAFS and XANES) and diffraction techniques. Short and intermediate range ordered structures typical of these systems are presented and discussed. The unusual very low coordination number of silver with oxygen (N=2) shown by EXAFS analysis is confirmed by a comparison with the local coordination of silver in borate crystals. Silver borate glasses can accommodate high concentrations of AgI and show fast ion conducting properties. Even the best superionic glasses prepared by conventional melt quenching do not show evidence for crystallinity of AgI; on the contrary, by fast roller quenching techniques it is possible to stabilise the crystalline superionic  $\alpha$ -phase of AgI even at room temperature. The peculiar role of the covalent Ag-O bond in the borate network can explain these experiments.

## 1. INTRODUCTION

The B<sub>2</sub>O<sub>3</sub> glass network can be easily changed by insertion of a modifier alkali metal oxide (M<sub>2</sub>O). This is mainly due to the possibility of gradually changing the local configuration of some boron atoms from neutral planar BO<sub>3</sub> triangles to negatively charged BO<sub>4</sub> tetrahedra. Glassy systems of general formula M<sub>2</sub>O.*n*B<sub>2</sub>O<sub>3</sub>, (where *n* is the molar ratio [B<sub>2</sub>O<sub>3</sub>]/[M<sub>2</sub>O]) can be easily obtained by melt quenching over a wide range of composition.

It is generally believed that a direct and universal relationship exists between the fraction of three- and four-coordinated boron atoms and the concentration of M<sub>2</sub>O [1]: starting from the pure B<sub>2</sub>O<sub>3</sub> structure (formed only from triangular units, partly organised to form three-membered boroxol rings), there is a continuously increasing number of BO<sub>4</sub> units with increasing M<sub>2</sub>O concentration, within a glass network where each oxygen is bridging between two boron atoms, the maximum fraction of tetrahe-

dra being reached for  $n \approx 2$ . On further increasing the  $M_2O$  content, nonbridging oxygen (NBO) atoms appear, yielding  $BO_3^-$  units, and the relative number of  $BO_4$  tetrahedra is reduced. The  $BO_3$  and  $BO_4$  basic units can link to form different, larger superstructural groups, originally recognised and classified by Krogh-Moe on the basis of X-ray structural investigations of crystalline compounds having a similar composition [2]. All of these intermediate range (IRO) units contain modifications of the original  $B_3O_6$  three-membered, planar boroxol ring: of course, the presence of  $BO_4$  tetrahedra forces a three-dimensional arrangement of the B–O bonds and in some cases results in a stronger rigidity of the unit as, for example, in the case of the diborate group.

The kind, fractional content and interconnection of these IRO units varies as a function of the alkali metal oxide content, both in crystals and in glasses. It should be noted here that, contrary to the universal trend shown by the relative number of  $BO_3$  and  $BO_4$  units as a function of  $n$ , the modifier oxide plays an important role in determining the structure of alkali borate compounds: it is evident from a comparison of the works of Krogh-Moe that the IRO and the medium range order (MRO) structures are different for crystalline systems of the same chemical composition but with different cations.

The fundamental role of each network modifying cation is probably increased in glasses, because the long range order of the crystal is lost and there are extra degrees of freedom for the IRO and MRO structures: from this point of view it is important to study more deeply the local coordination of the cations, going beyond the concept of a *mean* coordination number and distance, by trying to understand what function a cation is playing in each identified or proposed local site: for example, the cation can directly participate in the network, bridging between different oxygens, or it can simply compensate the negatively charged sites, being free to jump between adjacent similar sites. This kind of study will greatly enhance the understanding of the ion conducting properties shown by borate glasses: indeed, a microscopic theory soundly based on direct structural information is still lacking.

Borate glasses are even more appealing for technological application when a metal halide salt (e.g. LiI, LiCl, AgI, AgBr, etc.) is added to form a pseudo-binary glass of general formula  $(MX)_x(M_2O.nB_2O_3)_{1-x}$  ( $M=Li$  or  $Ag$ ;  $X=Cl, Br$  or  $I$ ) since these systems show a very high room temperature ionic conductivity, typically  $1\sim5$  (ohm cm) $^{-1}$ . The highest values of ionic conductivity are obtained for silver borate glasses doped with AgI.

A research project on  $(AgI)_x(Ag_2O.nB_2O_3)_{1-x}$  glasses has been under way in the authors' Institutes for many years [3], aiming at a deeper knowledge of the local structure around the silver and iodine atoms and, more generally, of the IRO and MRO characteristics of silver borate glasses [4]. This paper presents a summary of these studies, using x-ray absorption spectroscopy (XANES and EXAFS) and diffraction techniques. Details of the experiments can be found in the original papers [4-5].

## 2. SHORT RANGE ORDER

X-ray Absorption Spectroscopy (XAS) can provide local structural information about the environment of the absorbing atom. In particular, EXAFS studies allow the determination of the radial distribution function around the absorbing atoms in terms of coordination number, interatomic distance and degree of distortion from a symmetric coordination. A careful analysis of the EXAFS Debye–Waller factor as a function of

temperature can also provide information about the local vibrational dynamics, since it is related to the Mean Square Relative Displacement (MSRD) of atoms. On the other hand, the analysis of XANES (X-ray Absorption Near Edge Structures) is useful for studying the electronic structure and the chemical bonding of the absorbing atom.

## 2.1. X-ray Absorption Results

**2.1.1. EXAFS analysis of  $(\text{Ag}_2\text{O} \cdot n\text{B}_2\text{O}_3)$**  - The EXAFS was measured at room temperature at the K and L edges of Ag. The quantitative analysis of the first coordination shell for glasses with  $n=2,3,4$  and 6 was made using crystalline  $\text{Ag}_2\text{O}$  as a reference. This compound has a highly symmetric structure: silver atoms are linearly coordinated by oxygen and oxygen atoms are tetrahedrally coordinated by silver. The first Ag–O distance in the crystal is 2.044 Å [6]. The EXAFS for glasses with  $n>2$  is very similar: the average Ag–O distance is found to be  $2.27 \pm 0.05$  Å, about 0.3 Å larger than in c- $\text{Ag}_2\text{O}$ . For the glass with  $n=2$ , the best fit to the experimental data is obtained by considering two different Ag–O distances,  $2.02 \pm 0.05$  Å and  $2.27 \pm 0.05$  Å: this new shorter distance has been attributed to silver coordinated by non-bridging oxygens, which are expected at this high Ag content on the basis of NMR results [7]. The average coordination number obtained for the oxygens in the first shell is  $N=2$ , the same as for  $\text{Ag}_2\text{O}$ . The shortest distance coincides with the Ag–O bond length in c- $\text{Ag}_2\text{O}$ , suggesting the presence of a very similar local structure in the glass with  $n=2$ . The Debye–Waller (DW) factor at room temperature is found to be very similar for the glasses and the reference crystal. On the contrary, more recent measurements at low temperature, using the wider energy range available at the k edge, showed that the MSRD for the O–Ag–O distances behaves differently in  $\text{Ag}_2\text{O}$  and the glasses: this is mainly due to the static disorder contribution in the glasses, which is constant with temperature. New EXAFS measurements are planned to better study this fact.

The similarity between the DW factors indicates that the first coordination shell of silver in the glasses is characterised by a high degree of order. This means that silver is not randomly dispersed within the glass network: if so, the DW factor would be much higher than that measured. This important point, together with the low value of the coordination number, will be discussed in greater detail below.

**2.1.2. Near edge analysis of  $(\text{Ag}_2\text{O} \cdot n\text{B}_2\text{O}_3)$**  - The absorption measurements at the  $L_3$ ,  $L_2$  and  $L_1$  edges of silver are very interesting, because the high experimental energy resolution allows the electronic structure, characteristic of the Ag–O bonds in the glasses, to be studied more deeply.

The XANES region at the  $L_3$  edge of  $\text{Ag}_2\text{O}$  is very highly structured and shows a characteristic white line peak. This feature has been attributed to a direct transition of the photoelectron from the  $2p$  core level to the Ag- $4d$  partial density of electronic states [8]. Alternatively, the white line peak may be regarded as a fingerprint of the incorporation of Ag- $4d$  states (from a nominally closed  $d^{10}$  subshell) in the chemical bonding. If this  $d$  band is totally filled, as can be expected for metallic silver or for an  $\text{Ag}^+$  free ion, the white line is absent. In c- $\text{Ag}_2\text{O}$ , this band is only about 90% filled: the unoccupied states are present at the bottom of the conduction band, thus contributing to the first peak of the spectrum. The presence of a very similar peak in the XANES spectra for  $(\text{Ag}_2\text{O} \cdot n\text{B}_2\text{O}_3)$  glasses was interpreted as an indication

that the same kind of bond is still present in the glasses: the present authors have suggested a strongly localised bond, and a quasi-linear O–Ag–O coordination [5b].

This has been partially confirmed by Behrens [9], who made a careful analysis of the  $L_3$  edge for different oxidic  $Ag^+$  compounds (crystals and glasses): he confirmed that the white line peak is proportional to the covalent part of the Ag–O bond and showed that this is a common feature of these compounds. On the contrary, the proposed linear coordination is not supported (but not excluded) by the mere presence of the white line, because this peak is present in compounds having three- or four-fold coordination.

**2.1.3. Analysis of  $(AgI)_x(Ag_2O \cdot nB_2O_3)_{1-x}$**  - The EXAFS was measured at room temperature, at the K and L edges of silver and at the L edges of iodine, only for glasses with  $n=4$ .

The EXAFS data show that the well defined Ag–O bond previously identified remains unchanged when the AgI content increases up to  $x=0.55$  (the maximum concentration possible for this glass): a quantitative analysis of the edge structures shows that the fraction of Ag cations bonded to oxygen is that expected from the stoichiometry. This is a further confirmation that the main features of the borate network are not appreciably affected by the progressive introduction of AgI.

From the Ag–K EXAFS, a second feature, related to the Ag–I coordination, is clearly resolved: the mean Ag–I distance is 2.75 Å, slightly lower than in crystalline  $\beta$ -AgI. This is confirmed by temperature dependent measurements performed at the  $L_3$ -edge of iodine. The coordination number of silver ions around the absorbing iodine, estimated for different samples and temperatures, is  $N=4$ . This value is constant and is the same for  $\beta$ -AgI and the glasses. A careful analysis, however, shows a significative difference in the radial distribution function for  $\beta$ -AgI crystal and the glasses: the asymmetry of the I–Ag shell in the glasses is higher, because the static disorder is strongly enhanced (much more than for the Ag–O coordination). Even at the highest AgI content, the EXAFS data do not show evidence of the iodine–iodine coordination expected for the tetrahedral coordination of  $\beta$ -AgI. On the contrary, only at low AgI content evidence for an I–Ag–O coordination can be found.

This means that, at low AgI content, very small (AgI) units are dispersed in the empty space of the glass matrix, directly bonded to the nearest available O–Ag dangling bonds. The high static disorder already present in the first coordination shell excludes any ordering of the AgI in terms of a crystalline phase. The difference in the long range order between  $\beta$ -AgI and the glasses is confirmed by the analysis of the XANES region at the  $L_3$  and  $L_1$  edges of iodine. An attempt is made to discuss the origin of this fact in Section 4.

### 3. MEDIUM RANGE ORDER

Before presenting and discussing neutron and X-ray diffraction measurements on glasses, it is useful to remember the fundamental studies of Krogh-Moe, who succeeded in crystallising many different alkali borate compounds over a wide range of composition. His attention was mainly focused on the determination and discussion of the ordering of the superstructural units, but it will be seen that important information about the different cation effects can also be identified.

Following the suggestions of Krogh-Moe, the glass random network should be modelled



by connecting (or disconnecting) the same superstructural units found in the crystals. The most simple way is to arrange exactly the same superstructural units as determined by X-ray diffraction for a crystal having the right composition. However, this procedure is complicated for three reasons: (1) there are several ways in which the borate anion groups may polymerise for a given chemical composition (e.g.  $\text{Na}_2\text{O} \cdot 3\text{B}_2\text{O}_3$  has three different crystalline triborate phases); (2) for a given stoichiometry, the structure of crystals may be strongly different when the cation is changed (e.g.  $\text{Na}_2\text{O} \cdot 2\text{B}_2\text{O}_3$  is very different from  $\text{Li}_2\text{O} \cdot 2\text{B}_2\text{O}_3$  such that the diborate group is not even present) and (3) the same long but quite flexible chain of superstructural units may be present in crystals with very different composition (for example the triborate-pentaborate sequence can be found in both sodium diborate and silver tetraborate). Another important consideration can help us in modelling the glass (or, perhaps, a part of it): the alkali borate crystals usually contain two identical interpenetrating boron-oxygen networks. The whole crystalline structure is stabilised by the presence of cations, which can have a different position and role, depending on their covalency.

### 3.1. Analysis of Neutron and X-ray Diffraction Measurements

The experimental studies of the medium range order in alkali borate glasses are quite recent, compared to the hundreds of papers published in this field during at least thirty years: at most, authors were interested in debating whether rings are present or not. The first experimental evidence for intermediate-range ordering in superionic borate glasses was found in 1989 by Börjesson *et al.* [10] from neutron diffraction measurements on  $(\text{AgI})_x(\text{Ag}_2\text{O} \cdot 2\text{B}_2\text{O}_3)_{1-x}$ : the main result was the presence of a strong diffraction peak at an anomalously-low-value of the scattering vector,  $Q$ , of  $0.8 \text{ \AA}^{-1}$ , which is shown only in the AgI-rich glasses and indicates a structural correlation length of about  $8 \text{ \AA}$ . The presence of this first sharp diffraction peak (FSDP) was attributed either to the formation of AgI clusters or to voids within the boron-oxygen network. Subsequently, other neutron experiments have been performed on borate glasses containing Li, Na and Ag [11], and the present authors have performed X-ray diffraction measurements on silver borate glasses [12]. This set of complementary data allows some models to be proposed for the MRO in borate glasses [4,12].

The work is being performed in collaboration with L. Cervinka (Academy of Sciences, Prague). Starting from simple structural models for the glass network, scattering curves can be directly calculated (for comparison with the X-ray or neutron experiments) by using the classical Debye formula [13]. This equation gives the average scattered intensity for an array of atoms or identical objects (i.e. superstructural units) with a completely random orientation in space. Of course, the modelling must use a small number of atoms and does not allow the averaging of slightly distorted objects, but it is very powerful in understanding the main features of diffraction experiments on amorphous materials.

The starting models for our calculations were the IRO units identified in the Li diborate [14] and Ag tetraborate crystals [15] (unfortunately the crystalline structure of Ag-diborate is not known). Comparing the diffraction experiments on Li- and Ag-diborate glasses it is evident that these isostructural compounds have a completely different ordering of the  $\text{BO}_3$  and  $\text{BO}_4$  basic units: the MRO structure of Li diborate glass does not involve large units such as diborate, triborate and pentaborate, while the Ag diborate glass can be modelled on the basis of chains of superstructural units, ordered at a well-identified mutual separation.

The Li glass can be modelled by a simple random network composed of small  $\text{BO}_3$  and  $\text{BO}_4$  basic units. However, the trigonal and tetrahedral units preserve MRO at two characteristic periodicities, 4.5 Å and 4 Å respectively, as shown by the relatively large neutron scattering peak at  $1.5 \text{ Å}^{-1}$ . This conclusion does not imply that bigger units are absent in the Li diborate glass but simply that, if present, they are randomly dispersed and do not contribute to the MRO.

The analysis of the data for the  $(\text{Ag}_2\text{O}.n\text{B}_2\text{O}_3)$  glasses ( $n=2,4,8$ ) has been improved by complementary X-ray studies because of the higher sensitivity to silver electron density. The glasses with  $n=2$  show the presence of a periodicity of about 6 Å, which is responsible for the first main peak in neutron scattering data. This feature can be modelled quite well by an ordering at a distance of 6 Å, arising from long chains composed of two or three diborate units and/or of a succession of triborate and pentaborate-like units [11-12]. The silver atoms are attached to these chains by short bonds (1.8-2.1 Å), but they are also mutually correlated at a characteristic distance 3.30 Å. At lower silver content, the characteristic Ag-Ag distance increases to 3.75 Å for the octaborate, accompanied by a decreasing importance of the diffraction peak corresponding to the periodicity of 6 Å. In fact, the MRO for the silver octaborate glass is very similar to that for the Li diborate glass. It may thus be concluded that silver is playing an important role in the stabilisation of long chains of superstructural units in the glasses, and in their relative ordering at medium range distances.

The incorporation of AgI into the diborate glasses results in an expansion of the characteristic glass network distance, in order to accommodate a high quantity of the doping salt: as clearly indicated by the presence of the FSDP at  $0.8 \text{ Å}^{-1}$ , which is enhanced (but does not move significantly) with increasing AgI content. The presence of a different sharp peak from that found for the  $(\text{Ag}_2\text{O}.2\text{B}_2\text{O}_3)$  glass indicates that the MRO in the borate network is modified by the presence of AgI, which does not influence the short range units but does influence the ordering of the IRO chains, as characterised by a periodicity of about 8 Å.

The ordering which is characteristic of the Ag-Ag distance in the diborate glass, is not so well defined when AgI is added. The presence of AgI in the "empty" part of the borate network (with defined inter chain distance) forces a rearrangement of the Ag-Ag mutual ordering, while the characteristic 8 Å distance between borate cages determines the upper limit for the dimension of a hypothetical cluster of AgI. This is a very small dimension: the space is restricted and the rigidity of the chain is so great that AgI cannot grow as it does in the crystal but, during the cooling process from the melt, is only able to maintain the short range order.

#### 4. THE LOCAL ORDER AROUND SILVER

The modelling of the IRO and MRO structure presented previously was achieved by using information from crystalline Ag-tetraborate, Li-diborate and, more recently, from Ag-metaborate [16] and Ag-orthoborate [17]. Hence it is now useful to discuss the local coordination of silver in crystalline materials.

Silver tetraborate [15] is composed of two separate, identical, three-dimensional, interlocking networks each one comprising triborate and pentaborate groups. There are two different sites for silver, Ag(1) and Ag(2), characterised by a wide spread of distances. However, it is possible to identify the nearest Ag-O bonds. Ag(1) is coordinated

by three oxygen atoms in the same plane, perpendicular to the  $a$  axis. The shortest bonds (2.25 Å and 2.37 Å) are quasi-linearly bridging to the oxygen atom connecting different pentaborate units and to an oxygen belonging to a different IRO unit. Ag(1) is thus contributing to the mutual alignment of the IRO units of the chain, but only in the  $cb$  plane. The shortest Ag(2) bonds (2.39 Å, 2.43 Å and 2.46 Å) are more randomly distributed. The crystal contains big holes, with all the silver atoms on their surface.

Silver metaborate [16] contains infinite parallel chains of corner sharing tetrahedra, with the other corner-oxygens linked by a triangular unit to a similar oxygen of the nearest tetrahedron. The chains are aligned along the  $b$  axis, in thin layers (perpendicular to the  $c$  direction) composed of very close independent chains. One half of the NBO vertices of the triangular units of the closest chains are pointing along the  $c$  direction, towards the interior of the layer; the others are quasi parallel to the  $ac$  plane aligned at the external sides of the layer. Five different sites have been characterised for silver in this very ordered structure: the shortest Ag–O bond (2.15 Å) corresponds to a silver atom situated between the closest chains, coordinated by the nonbridging oxygen of a triangular unit and very near to an opposite tetrahedron face. In the same internal region of the layer there is a silver atom which is linearly coordinated by two oxygens at a distance of 2.16 Å: these oxygens are at the corners of tetrahedra linked by triangular units. The third short Ag–O distance (2.18 Å) is related to a silver atom which is in the larger region outside the layers: it is trigonally coordinated (the other Ag–O distances are longer than 2.7 Å) and seems to be responsible for determining the intra-layer distance.

Crystalline silver orthoborate is very different in that it contains only isolated trigonal  $\text{BO}_3$  units lying parallel to the  $ab$  plane, and Ag/O chains as structure-building elements. The two shortest Ag–O bonds are non-linear, but still quite short (2.12 Å).

These crystals are very interesting because they contain silver atoms with short interatomic distances, characterised by low coordination numbers and in some cases by linear bonding. The covalent character of the Ag–O bond shown by our XAS studies is confirmed by the ability of Ag to stabilise the structure and the relative ordering of the IRO borate chains. The rigidity of the glass network is probably due to the ability of silver to form short linear bonds, which also explains the low DW factor for the Ag–O interaction, as measured by EXAFS experiments.

It has already been pointed out that the rigidity of the borate chains and their arrangement with a well-defined characteristic distance prevents an ordering of the AgI as in  $c\text{-AgI}$ . When the AgI content is increased too much, the melt quenched glass contains large particles of  $\beta\text{-AgI}$ , but the ionic conductivity greatly decreases. Conversely, it has recently been shown that, by the fast roller quenching technique and in a quite narrow composition range, it is possible to stabilise the superionic conducting  $\alpha$ -phase of AgI in silver borate glasses at room temperature [18–19], thus obtaining an enhancement of the ionic conductivity. The microstructure of the  $\alpha\text{-AgI}$  frozen composite is characterised by discrete small particles of AgI, homogeneously dispersed in the glass matrix, having a typical size in the range 20–40 nm. It is very interesting to note that when  $\beta\text{-AgI}$  is obtained instead of  $\alpha\text{-AgI}$ , the crystalline phase grows to a much larger dimension [20]. The authors consider this to be a further evidence of the strong interaction between the silver borate network and the AgI arrangement: in the fast ion conducting compounds (either glassy or containing  $\alpha\text{-AgI}$ ), the viscosity of the melt and

the rigidity of the IRO arrangement can prevent the normal ordering of AgI. For glasses, the quench rate is not so fast and a disordered AgI configuration is obtained on a very small scale for AgI while, for more rapidly quenched materials, both during the fast cooling process and in the resulting composite, the superionic phase of AgI is stabilised on a relatively larger scale because the transformation to the normal  $\beta$ -phase is stopped by the stress imposed by the rigidity of the silver borate network.

## 5. CONCLUSIONS

The short range structure around modifier alkali ions in borate glasses has been generally understood in terms of a random insertion of the alkali ions in the free space of the glass network. This should result in a first coordination shell having a high mean coordination number and a broad distribution of distances.

This paper shows that the local structure of silver ions can be better described taking into account the shortest Ag–O bonds, characterised by a low coordination number and in many cases by a quasi-linear two-fold coordination, similar to c-Ag<sub>2</sub>O.

The covalent character of the Ag–O bond strongly influences the resulting properties of the glass, increases the rigidity of the network and can explain the ability of silver borate glasses to accommodate a high quantity of AgI thus increasing a lot the ion conductivity.

## REFERENCES

- [1] S.A. Feller, W. J. Dell & P. J. Bray, *J. Non-Cryst. Solids* **15** (1982), 21.
- [2] J. Krogh-Moe, *J. Non-Cryst. Solids* **1** (1969), 269.
- [3] F. Rocca, G. Dalba & P. Fornasini, *Mater. Chem. Phys.* **23** (1989), 85.  
F. Rocca, *J. de Physique* **IV C2** (1992), 97.
- [4] L. Cervinka, F. Rocca, P. Fornasini & G. Dalba, *J. Non-Cryst. Solids* **150** (1992), 140.  
L. Cervinka & F. Rocca, *J. Non-Cryst. Solids* **192&193** (1995), 125.
- [5] G. Dalba, P. Fornasini, F. Rocca, E. Bernieri, E. Burattini & S. Mobilio, *J. Non-Cryst. Solids* **91** (1987), 153; G. Dalba, P. Fornasini, F. Rocca & E. Burattini, *J. de Physique* **C8-47** (1986), 749; G. Dalba, P. Fornasini, A. Fontana, F. Rocca & E. Burattini, *Solid State Ionics* **28-30**, (1988) 713; F. Rocca, G. Dalba & P. Fornasini, *Solid State Ionics* **53-56** (1992), 1253.
- [6] W. G. Wyckoff, *Crystal Structures* (Wiley, New York, 1963)
- [7] G. Chiodelli, A. Magistris, M. Villa & J. L. Bjorkstam, *J. Non-Cryst. Solids* **51** (1983), 143; S.A. Feller, W. J. Dell & P. J. Bray, *J. Non-Cryst. Solids* **51** (1982), 21.
- [8] M. T. Czyzyk, R. A. de Groot, G. Dalba, P. Fornasini, A. Kiesel, F. Rocca & E. Burattini, *Phys. Rev. B* **39** (1989), 9831.
- [9] P. Behrens, *Solid State Commun.* **81** (1989), 235.
- [10] L. Börjesson, L. M. Torell, U. Dahlborg & W. S. Howells, *Phys. Rev. B* **39** (1989), 3404; L. Börjesson, L. M. Torell & W. S. Howells, *Phil. Mag* **B59** (1989), 105.
- [11] J. Swenson, L. Börjesson & W. S. Howells, *Phys. Rev. B* **52** (1995), 9310.
- [12] L. Cervinka, F. Rocca, L. Börjesson & J. Swenson, *Phys. Rev. B*, to be published
- [13] L. Cervinka, *J. Non-Cryst. Solids* **106** (1988), 291.
- [14] J. Krogh-Moe, *Acta Crystallogr.* **15** (1962), 190; J. Krogh-Moe, *Acta Crystallogr.* **B24** (1968), 179.
- [15] J. Krogh-Moe, *Acta Crystallogr.* **18** (1965), 77.
- [16] G. Brachtel & M. Jansen, *Z. anorg. allg. Chem.* **478** (1981), 13.
- [17] M. Jansen & W. Scheld, *Z. anorg. allg. Chem.* **477** (1981), 85.
- [18] M. Tatsumisago, Y. Shinkuma & T. Minami, *Nature* **354** (1991), 217.
- [19] G. Dalba, P. Fornasini, F. Monti, F. Rocca, T. Minami, M. Tatsumisago, N. Torata, M. Adachi & S. Kishimoto, *J. Non-Cryst. Solids* **192&193** (1995), 347
- [20] T. Saito, M. Tatsumisago, N. Torata & T. Minami, *Solid State Ionics* **79** (1995), 279.

## A STRUCTURAL STUDY OF SILVER BORATE GLASSES BY INFRARED REFLECTANCE AND RAMAN SPECTROSCOPIES

John A. KAPOUTSIS, Efstratios I. KAMITSOS  
& Georgios D. CHRYSSIKOS  
*Theoretical and Physical Chemistry Institute, NHRF,  
48, Vass. Constantinou Ave., 116 35 Athens, GREECE*

A vibrational spectroscopic study of  $x\text{Ag}_2\text{O} \cdot (1-x)\text{B}_2\text{O}_3$  glasses has been performed to investigate the short- and medium-range structure and the nature of Ag-O bonding as a function of  $\text{Ag}_2\text{O}$  content. The results indicate that the effect of silver oxide on the short-range structure is similar to that of alkali metal oxides, and in particular  $\text{Li}_2\text{O}$ . The rate of conversion of  $\text{B}\text{O}_3$  triangles into  $\text{B}\text{O}_4$  tetrahedra ( $\text{O}$ =bridging oxygen atom) follows the  $x/(1-x)$  law up to  $ca\ x=0.25$ , and then it deviates at higher values of  $x$  because of the formation of non-bridging oxygen-containing  $\text{B}\text{O}_2\text{O}^-$  triangles. Boroxol rings and other borate arrangements such as, penta-, tri- and di-borate groups, were also identified in Ag-borate glasses with increasing  $\text{Ag}_2\text{O}$  content. The analysis of the far infrared spectra suggests an inhomogeneous distribution of  $\text{Ag}^+$  ions in the glass matrix. Silver ions in Ag-poor regions behave as pseudo-alkalis and their interactions with the network sites are predominantly ionic, while ions occupying sites in the Ag-rich regions are characterised by a considerable degree of covalency in the Ag-O bonding.

### 1. INTRODUCTION

Borate glasses have attracted the interest of numerous investigators during the last thirty years. Considerable effort has been directed towards the elucidation of glass structure and its dependence on the content and type of alkali metal oxide,  $\text{M}_2\text{O}$ . It is well demonstrated that addition of  $\text{M}_2\text{O}$  to  $\text{B}_2\text{O}_3$  causes the gradual change of boron coordination number from three to four, and the formation of non-bridging oxygen atoms at higher modification levels [1-3]. The nature and relative abundance of the various borate arrangements depend strongly on the type of alkali cation [4-6]. It is believed that Ag ions in borate glasses play a role similar to that of the alkalis. Indeed, the results of previous studies have shown that the short-range order of Ag-borate glasses resembles that of alkali borates of the same metal oxide content [7-13].

Interest in silver-borate glasses,  $x\text{Ag}_2\text{O} \cdot (1-x)\text{B}_2\text{O}_3$ , has been renewed lately because such compositions can yield superionic glassy conductors after doping with silver halide salts [14]. Kamiya et al [15] proposed on the basis of

their X-ray diffraction study that the enhanced ionic conductivity of Ag-borate glasses originates from a clustering of  $\text{Ag}^+$  ions, which results in shortening of the jump distance required for the migration of  $\text{Ag}^+$  charge carriers. Recent molecular dynamics (MD) simulations of the structure of Ag-borates by Abramo et al [16,17] showed that the distribution pattern of silver ions is very sensitive to the choice of silver radius; a small radius (0.63 Å) leads to clustering of  $\text{Ag}^+$  ions, while the use of a larger radius (1.1 Å) in the simulation process favours their homogeneous distribution.

Besides their high ionic conductivity, silver borate glasses exhibit interesting nonlinear optical properties. It was found recently that the third-order susceptibility,  $\chi^{(3)}$ , of Ag-borates is much higher than that of Cs-borates, even though  $\text{Cs}^+$  ions have a larger polarizability than  $\text{Ag}^+$  ions [18]. To explain such differences it was proposed that the Ag–O bond has considerable covalency as compared to the Cs–O bond which is ionic [18].

In view of this current interest in silver borate glasses, we present in this paper a systematic study of the  $x\text{Ag}_2\text{O} \cdot (1-x)\text{B}_2\text{O}_3$  ( $0 \leq x \leq 0.33$ ) system by infrared reflectance and Raman spectroscopic techniques. The purpose of the work is to investigate the effect of  $\text{Ag}_2\text{O}$  on the glass structure and the distribution of  $\text{Ag}^+$  ions, as well as on the nature of the Ag–O bonding.

## 2. EXPERIMENTAL

Stoichiometric amounts of reagent grade  $\text{Ag}_2\text{O}$  and  $\text{B}_2\text{O}_3$  were mixed and melted in Pt crucibles at  $1000^\circ\text{C}$  for about 30 min. Splat quenching the melts between two polished copper blocks yielded flat samples with surfaces of good quality, which were used for spectroscopic measurements without any further treatment. Clear glasses were prepared in the composition range  $0 \leq x \leq 0.33$ .

Raman spectra were measured on a Ramanor HG 2S Jobin-Yvon spectrometer at  $90^\circ$  scattering geometry, employing the 514.5 nm line of a Spectra Physics 165 argon laser for excitation. Strong fluorescence prevented the measurement of the Raman spectra of the glasses with  $x > 0.20$ . Infrared reflectance spectra were recorded on a Fourier-transform Bruker IFS 113v spectrometer in the region  $30\text{--}4000\text{ cm}^{-1}$ . The absorption coefficient spectra reported in this work were calculated from the reflectivity spectra through the Kramers-Kronig inversion technique [19].

## 3. RESULTS AND DISCUSSION

### 3.1. The Structure of the Borate Network

**3.1.1. Mid-infrared spectra** - Infrared absorption spectra of silver borate glasses are presented in Fig. 1. Three spectral regions, characteristic of vibrational modes of the borate network, can be distinguished in the mid infrared part of the spectra:  $1200\text{--}1550\text{ cm}^{-1}$  (B–O stretching vibrations of trigonal  $\text{BO}_3$  units),  $850\text{--}1200\text{ cm}^{-1}$  (B–O stretching vibrations of tetrahedral  $\text{BO}_4$  units), and  $600\text{--}800\text{ cm}^{-1}$  (bending vibrations of various borate segments) [1,19]. The most obvious effect of the addition of  $\text{Ag}_2\text{O}$  to  $\text{B}_2\text{O}_3$  is the progressive development

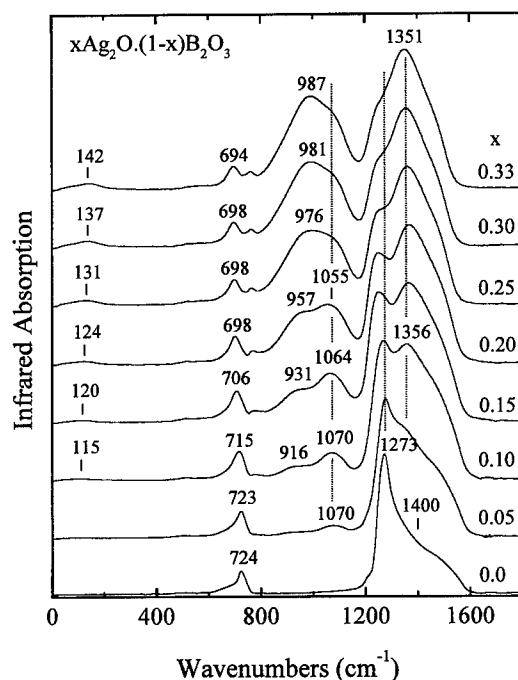
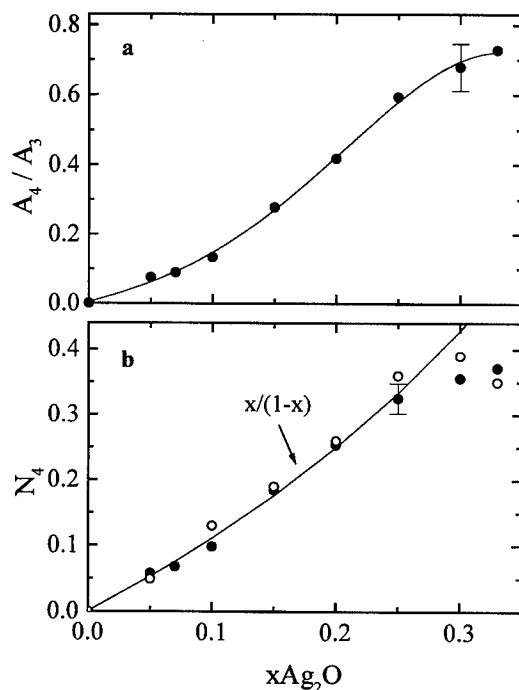


Fig. 1. Infrared absorption spectra of  $x\text{Ag}_2\text{O} \cdot (1-x)\text{B}_2\text{O}_3$  glasses.

of a complex absorption envelope in the region  $850\text{--}1200\text{ cm}^{-1}$ . Glassy  $\text{B}_2\text{O}_3$  ( $x=0$ ) which is known to consist of boroxol rings and independent  $\text{BO}_3$  trigonal units [20] shows no infrared activity in this region. Thus, the increase of the relative intensity of the  $850\text{--}1200\text{ cm}^{-1}$  envelope with  $x$  is indicative of the progressive transformation of  $\text{BO}_3$  triangles into  $\text{BO}_4$  tetrahedral units. This observation suggests that  $\text{Ag}_2\text{O}$  plays a role similar to that of alkali oxides, therefore confirming the network modifying nature of  $\text{Ag}_2\text{O}$  suggested in previous studies [7-13].

Increasing the  $\text{Ag}_2\text{O}$  content in the range  $0 < x \leq 0.15$  results in the appearance of two bands at *ca*  $930$  and  $1065\text{ cm}^{-1}$ , while for higher  $x$  values a third band develops at *ca*  $980\text{ cm}^{-1}$ . Comparison with the infrared spectra of alkali borate glasses and crystals suggests that the first two bands can be attributed to B-O stretching vibrations of  $\text{BO}_4$  tetrahedra in pentaborate units, while the corresponding vibrations of triborate and diborate groups should be responsible for the latter feature [19]. Hence, the compositional dependence of the spectra denotes that the initially formed pentaborate units ( $x \leq 0.15$ ) are gradually replaced by triborate and diborate groups. The presence of such borate groups, with well defined medium-range order, is in agreement with the propositions of Krogh-Moe [1] and Boulou & Kreidl [8].

The emerging structural picture is supported also by the composition dependence of the  $1273\text{ cm}^{-1}$  band, which has been attributed to the stretching



**Fig. 2.** (a) Effect of  $\text{Ag}_2\text{O}$  on the relative integrated intensity  $A_4/A_3$ . The line is drawn to guide the eye. (b) The fraction  $N_4$  calculated through Eq. (1) is depicted by closed symbols. The continuous line represents the theoretical  $N_4 = x/(1-x)$  behaviour. Open circles represent NMR data of Kim & Bray [7].

vibration of B–O–B linkages characteristic of boroxol rings, pentaborate and triborate groups [1]. The destruction of pentaborate groups in favour of diborates with increasing  $x$  is consistent also with the development of the  $1351\text{ cm}^{-1}$  feature which is characteristic of the latter arrangements [19] ( $x=0.33$ ). Along the same lines is the activity exhibited by the bending vibrations: pentaborate units are active at  $\sim 710\text{ cm}^{-1}$  and diborate ones at  $\sim 695\text{ cm}^{-1}$  [19].

The effect of  $\text{Ag}_2\text{O}$  on the short-range structure can be quantified by obtaining the integrated intensity of the absorption profiles:  $800\text{--}1200\text{ cm}^{-1}$  (denoted by  $A_4$ ) and  $1200\text{--}1550\text{ cm}^{-1}$  (denoted by  $A_3$ ), which are characteristic of  $\text{BO}_4$  tetrahedra and  $\text{BO}_3$  triangular units, respectively. The relative integrated intensity,  $A_r = A_4/A_3$ , was calculated and is shown in Fig. 2(a) versus  $\text{Ag}_2\text{O}$  content. The change of boron coordination from three to four with increasing  $x$  is well demonstrated. As shown previously [21] the relative integrated intensity  $A_r$  can be employed to calculate the fraction of four-coordinated boron atoms,  $N_4$ , through the expression,

$$N_4 = A_r / (\alpha + A_r) \quad (1)$$

where  $\alpha$  is the relative absorption coefficient of boron tetrahedra versus boron



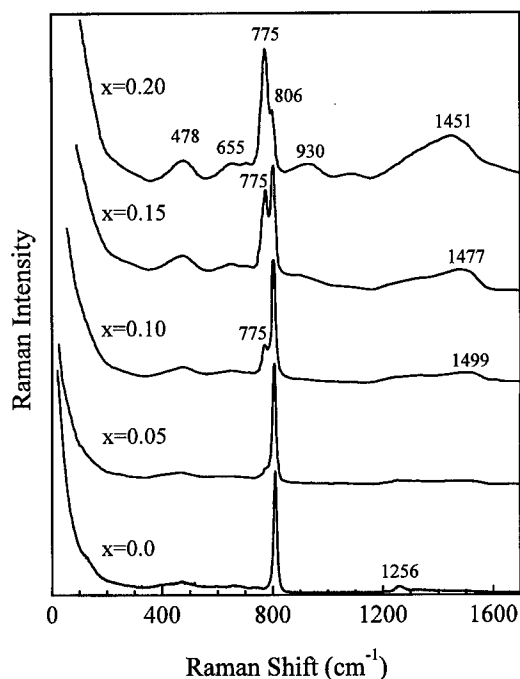


Fig. 3. Raman spectra of  $x\text{Ag}_2\text{O} \cdot (1-x)\text{B}_2\text{O}_3$  glasses.

triangles. At very low  $\text{Ag}_2\text{O}$  contents the structural modification mechanism involves mainly the transformation of boron-oxygen triangles into borate tetrahedra, and thus the law  $N_4 = x/(1-x)$  is obeyed. On these grounds, the experimental  $A_r$  values of the  $x=0.05$  and  $x=0.07$  glasses and Eq.(1) give the average value  $\alpha=1.25$ . With the assumption that this value of  $\alpha$  is independent of  $x$ , Eq. (1) is employed to calculate  $N_4$  using the infrared data ( $A_r$ ). The results are shown in Fig. 2(b) where a comparison with the theoretical values ( $x/(1-x)$ ) and the NMR results of Kim & Bray [7] is also made. It can be seen that the agreement between infrared and NMR results is good, both showing that the fraction of four-coordinated boron atoms follows the theoretical curve very closely up to  $x \approx 0.25$ . The deviations observed for  $x \geq 0.25$  are attributed to formation of non-bridging oxygen containing metaborate triangles,  $\text{B}\text{O}_2\text{O}^-$ , in general agreement with the results of previous investigations [7-13].

The isomerization process  $\text{B}\text{O}_4^- \leftrightarrow \text{B}\text{O}_2\text{O}^-$  is of special importance for understanding the factors affecting the structure of alkali borate glasses below the metaborate composition,  $x \leq 0.50$  [22]. High field strength cations (e.g.  $\text{Li}^+$ ) favour the formation of  $\text{B}\text{O}_4^-$ , but low field strength cations (e.g.  $\text{Cs}^+$ ) induce a higher rate of  $\text{B}\text{O}_2\text{O}^-$  creation. Indeed, the  $N_4$  values of Li-borate glasses follow the theoretical curve up to  $ca\ x=0.25$ , but increasing deviations were observed in the series  $\text{Li} < \text{Na} < \text{K} < \text{Rb} < \text{Cs}$  [4]. Therefore, the results depicted in Fig. 2(b) suggest that the effect of silver ions on the short-range order of bo-

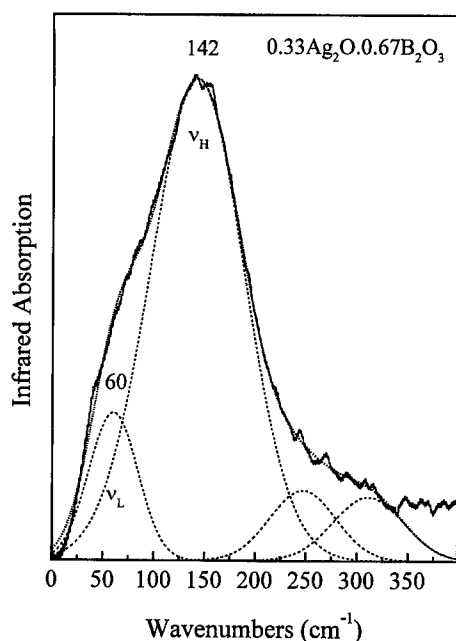


Fig. 4. Deconvoluted far infrared spectrum of the  $0.33\text{Ag}_2\text{O} \cdot (1-x)\text{B}_2\text{O}_3$  glass.

rate glasses is very similar to that of lithium ions.

The change of boron coordination number from 3 to 4 enhances the coherence of the borate network because of the additional B–O–B crosslinks developed, while the formation of non-bridging oxygens results in network depolymerisation. These drastic changes of the short-range structure are manifested in the composition dependence of macroscopic glass properties, such as the glass transition temperature,  $T_g$ , and the thermal expansion coefficient,  $\alpha$ . For silver borate glasses  $T_g$  shows a maximum at  $x=0.25$ , and  $\alpha$  passes through a well defined minimum at  $x=0.20$  [8,11].

**3.1.2. Raman spectra** - Figure 3 shows the Raman spectra of silver borate glasses. The spectrum of glassy  $\text{B}_2\text{O}_3$  ( $x=0$ ) is dominated by the sharp band at  $806\text{ cm}^{-1}$ , assigned to the ring-breathing vibration of boroxol rings [23]. Addition of  $\text{Ag}_2\text{O}$  causes the progressive decrease of the intensity of the boroxol band and the development of a new band at  $775\text{ cm}^{-1}$ , which dominates eventually the spectrum of the  $x=0.20$  glass. A similar band in the spectra of alkali borate glasses has been attributed to the symmetric ring-breathing vibration of six-membered rings bearing one or two  $\text{BO}_4^-$  tetrahedra [22,24].

Increasing  $x$  induces changes in other regions of the Raman spectra as well. In particular, broad and asymmetric bands appear at  $350\text{--}550\text{ cm}^{-1}$ ,  $600\text{--}700\text{ cm}^{-1}$ ,  $850\text{--}1000\text{ cm}^{-1}$  and  $1300\text{--}1550\text{ cm}^{-1}$ . In analogy with alkali borates, the bands at  $350\text{--}550\text{ cm}^{-1}$ , *ca*  $650\text{ cm}^{-1}$  and  $850\text{--}1000\text{ cm}^{-1}$  can be attributed to the

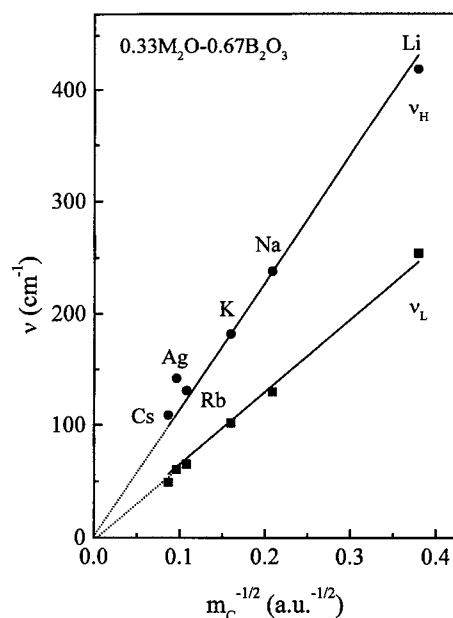


**Fig. 5.** Cation motion frequencies ( $\nu_H$ ,  $\nu_L$ ) versus  $m_C^{-1/2}$ , where  $m_C$  is the metal ion mass, for silver- and alkali-diborate glasses ( $x=0.33$ ). Lines are least square fittings to the alkali vibration frequencies. Error bars are of the size of symbols.

vibrations of borate tetrahedra containing borate groups, i.e. pentaborate, and triborate groups. The 1300-1550  $\text{cm}^{-1}$  band envelope changes in shape and increases in relative intensity with  $x$ . Bands in this high-frequency region have been assigned to the localised stretching vibrations of terminal B–O<sup>-</sup> bonds of metaborate triangles,  $\text{B}\text{O}_2\text{O}^-$  [22]. As shown in Fig. 3, the 1300-1550  $\text{cm}^{-1}$  envelope can be observed already at  $x=0.10$  but attains considerable relative intensity for  $x \leq 0.15$ , indicating an increasing rate of formation of non-bridging oxygens. At the moment, it is difficult to quantify this effect because the corresponding Raman cross section is not known. The Raman results presented in this section are in reasonable agreement with the trends observed in the corresponding infrared spectra.

### 3.2. Far Infrared Spectra and the Nature of the Ag–O Bond

The nature and distribution of anionic sites hosting  $\text{Ag}^+$  ions can be revealed from the study of the far infrared spectra. It is seen in Fig. 1 that the far infrared region is characterised by the presence of a weak feature, whose intensity and frequency are increasing with  $\text{Ag}_2\text{O}$  content. This band is attributed to the rattling motion of  $\text{Ag}^+$  ions against their network sites [25].

A typical far infrared spectrum is shown in Fig. 4 in an expanded frequency and intensity scale. The pronounced low frequency asymmetry of the  $\text{Ag}^+$  motion band can be described well by two Gaussian components, using the

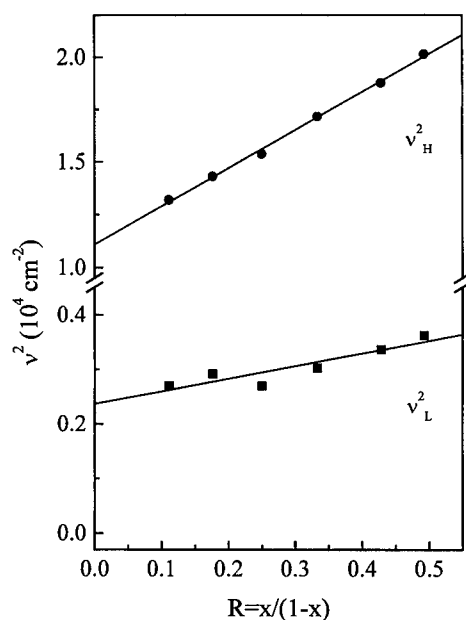


Fig. 6. Dependence of  $v_H^2$  and  $v_L^2$  on  $R=x/(1-x)$  in  $x\text{Ag}_2\text{O} \cdot (1-x)\text{B}_2\text{O}_3$  glasses. The lines are least squares fittings. Error bars are of the size of symbols.

deconvolution procedure applied previously to binary and ternary glasses [19,25-27]. The two weaker components which describe absorption between 200-350  $\text{cm}^{-1}$  can be assigned to borate network modes [27]. The two far infrared components, with frequencies designated by  $v_H$  and  $v_L$ , are attributed to vibrations of  $\text{Ag}^+$  ions in two distributions of anionic site environments. It is of interest to note that the far-infrared spectra of silver borates could be described always by two  $\text{Ag}^+$  ion motion components, despite the continuous variation of the short- and medium-range structure induced by  $\text{Ag}_2\text{O}$  addition. The existence of two different distributions of  $\text{Ag}^+$  sites can originate from the inhomogeneous dispersion of  $\text{Ag}^+$  ions in the glass matrix, that may result in Ag-rich and Ag-poor regions, as suggested by Kamiya et al [15].

The  $\text{Ag}^+$  motion frequencies ( $v_H, v_L$ ) for the  $x=0.33$  glass (diborate composition), and the corresponding frequencies of alkali ions in diborate glasses [27] are plotted in Fig. 5 versus  $m_c^{-1/2}$ , where  $m_c$  is the metal ion mass. The silver motion frequencies are excluded from the linear least square fits shown in this figure. It can be seen that the  $\text{Ag}^+$  ions giving rise to frequency  $v_L$  behave as pseudo-alkalis, in contrast to those vibrating at frequency  $v_H$ . Clearly  $v_H(\text{Ag}^+)$  is ca 30% higher than the  $v_H$  frequency of an alkali-like ion with the mass of silver. The Ag- and alkali-motion frequencies in borate sites were compared for various other metal oxide contents ( $x$ ) and found to exhibit trends very similar to those in Fig. 5. We interpret these results as suggesting that Ag ions vibrating with frequencies  $v_L$  interact with their sites ionically, while those giv-

ing rise to  $\nu_H$  are characterised by Ag–O bonding with considerable covalency. These findings lend support to the proposition of Tarashima and co-workers discussed in the introduction [18].

Figure 6 displays the silver ion frequencies squared ( $\nu_H^2$ ,  $\nu_L^2$ ) as a function of the structural parameter  $R = x/(1-x)$ , which represents the average formal negative charge per boron–oxygen polyhedron. The observed linear increase of  $\nu_H^2$  and  $\nu_L^2$  with  $R$  can result from the creation of network sites with increasing anionic charge density, and/or from the progressive decrease of the Ag–O bond distance [28]. Both effects point to the increasing covalency in the Ag–O interactions as the content of glass in silver oxide increases.

#### 4. CONCLUSIONS

The analysis of the mid-infrared and Raman spectra of silver borate glasses has demonstrated the modifying role of  $\text{Ag}_2\text{O}$  on the glass structure. Thus, boroxol rings are progressively destroyed in favour of  $\text{BO}_4$ -containing six-membered rings, resulting in the change of boron coordination number from 3 to 4. The fraction of four-coordinated boron atoms,  $N_4$ , was found to follow the theoretical values,  $x/(1-x)$ , for compositions in the range  $0 < x \leq 0.25$ . For glasses with higher silver oxide contents, both infrared and Raman spectra showed the creation of borate groups containing non-bridging oxygens.

The broad and asymmetric far infrared profiles in the range of  $\text{Ag}^+$  ion motion were deconvoluted by two Gaussian bands having frequencies ( $\nu_H$ ,  $\nu_L$ ) and intensities which increase with  $x$ . These bands were assigned to vibrations of  $\text{Ag}^+$  cations in two different distributions of network sites, suggesting the inhomogeneous dispersion of silver ions in the glass matrix.  $\text{Ag}^+$  cations vibrating in their sites with frequency  $\nu_H$  exhibit covalent character in their Ag–O interactions.

#### REFERENCES

- [1] J. Krogh-Moe, *Phys. Chem. Glasses* **6** (1965), 46.
- [2] G. E. Jellison & P.J. Bray, *J. Non-Cryst. Solids* **29** (1978), 187.
- [3] S. A. Feller, W. J. Dell & P.J. Bray, *J. Non-Cryst. Solids* **51** (1982), 21.
- [4] J. Zhong & P.J. Bray, *J. Non-Cryst. Solids* **111** (1989), 67.
- [5] E.I. Kamitsos, G.D. Chryssikos & M.A. Karakassides, *Phys. Chem. Glasses* **29** (1988), 121.
- [6] G.D. Chryssikos, E.I. Kamitsos & M.A. Karakassides, *Phys. Chem. Glasses* **31** (1990), 109.
- [7] K.S. Kim & P.J. Bray, *J. Non-cryst. Solids* **2** (1974), 95.
- [8] E.N. Boulou & N.J. Kreidl, *J. Am. Ceram. Soc.* **54** (1971), 368.
- [9] G. Carini, M. Cutroni, A. Fontana, G. Mariotto & F. Rocca, *Phys. Rev. B* **29** (1984), 3567.
- [10] G. Carini, M. Cutroni, M. Federico, G. Galli & G. Tripodo, *Phys. Rev. B* **30** (1984), 7219.
- [11] J.L. Piguet & J.E. Shelby, *J. Am. Ceram. Soc.* **68** (1985), 450.
- [12] G. Dalba, P. Fornasini, F. Rocca, E. Bernieri, E. Burattini & S. Mobilio, *J. Non-Cryst. Solids* **91** (1987), 153.
- [13] J. Swenson, L. Börjesson & W.S. Howells, *Phys. Rev. B* **52** (1995), 9310.
- [14] G. Chiodelli, G. Campari Vigano, G. Flor, A. Magistris & M. Villa, *Solid State Ionics* **8** (1983), 311.
- [15] K. Kamiya, S. Sakka, K. Matusita & Y. Yoshinaga, *J. Non-Cryst. Solids* **38&39** (1980), 147.
- [16] M.C. Abramo, G. Carini & G. Pizzimenti, *J. Phys. C: Solid State Phys.* **21** (1988), 527.
- [17] M.C. Abramo, G. Pizzimenti & G. Carini, *Solid State Ionics* **28-30** (1988), 148.

- [18] K. Tarashima, S.H. Kim & T. Yoko, *J. Am. Ceram. Soc.* **78** (1995), 1601.
- [19] E.I. Kamitsos, A.P. Patsis & G.D. Chryssikos, *J. Non-Cryst. Solids* **126** (1990), 52.
- [20] A.C. Hannon, R.N. Sinclair, J.A. Blackman, A.C. Wright & F.L. Galeener, *J. Non-Cryst. Solids* **106** (1988), 116.
- [21] G.D. Chryssikos, J.A. Kapoutsis, E.I. Kamitsos, A.P. Patsis & A.J. Pappin, *J. Non-Cryst. Solids* **167** (1994), 92.
- [22] E.I. Kamitsos & G.D. Chryssikos, *J. Mol. Struct.* **247** (1991), 1.
- [23] C.F. Windisch & W.M. Risen Jr., *J. Non-Cryst. Solids* **48** (1982), 281.
- [24] T.W. Brill, *Phillips Res. Rep., Suppl. No. 1* (1975), 1.
- [25] E.I. Kamitsos, J.A. Kapoutsis, G.D. Chryssikos, J.M. Hutchinson, A.J. Pappin, M.D. Ingram & J.A. Duffy, *Phys. Chem. Glasses* **36** (1995), 141.
- [26] J.A. Kapoutsis, E.I. Kamitsos, G.D. Chryssikos, Y.D. Yiannopoulos, A.P. Patsis & M. Prassas, *Chim. Chron. New Series* **23** (1994), 271.
- [27] E.I. Kamitsos, A.P. Patsis & G.D. Chryssikos, *J. Non-Cryst. Solids* **152** (1993), 246.
- [28] E.I. Kamitsos, G.D. Chryssikos, A.P. Patsis & J. A. Duffy, *J. Non-Cryst. Solids* **196** (1996), 249.

## HISTORY OF THE USE OF $B_2O_3$ IN COMMERCIAL GLASS

Robert A. SMITH

U. S. Borax Inc., 26877 Tourney Road, Valencia, CA, 91355, USA

The early history of boron and its first use in glass including optical, Pyrex low expansion, fiberglass, and enamel and ceramic glaze are reviewed. Glass as a science began in the 19<sup>th</sup> century, starting with Faraday and followed by the classic work of Schott and Abbé in optical glass. These studies led to the first practical, durable, and at the same time low expansion borosilicate type glasses. Borate was instrumental in the commercialization of both insulation and textile fibers, leading to the largest single commercial use of  $B_2O_3$  today. The most important properties that  $B_2O_3$  brings to glass making and finished glass products are considered.

### 1. EARLY HISTORY OF $B_2O_3$

It is often assumed that the well-known use today of  $B_2O_3$  in glass, enamels, and ceramic glazes was also known to the older civilizations which developed these arts. Just how long borax has been used by man is a question unlikely to be resolved. According to legend, the Babylonians brought borax from the Far East more than four thousand years ago to be used by the goldsmiths, and writings have frequently cited the ancient Egyptians as users of borax in metallurgy, medicine and mummification, but none of this has been substantiated. The *nitron Baurak* of the Greeks, the *borith* of the Hebrews, the *baurack* of the Arabians, the *boreck* of the Persians, the *burack* of the Turks, the *borax* of the Romans, all might appear to express one and the same substance, the borate of soda. However, there is little evidence to support when or whether these names described the substance we know as borax today. These words from which the name borax is derived are varying transliterations of the Arabic word meaning to glitter or shine [1].

In The Tincal Trail [1], Norman Travis and John Cocks consider writings in ancient texts of minerals that appear to be associated with borax, but conclude that the writers were really referring to ores other than borates, most commonly to soda ash or trona. Nevertheless, it has been speculated that authentic borax was known to and used by craftsmen, scholars, and alchemists of the great Islamic civilization sometime before 800 AD, though its source is uncertain. Also it is possible that Harun-al-Rashid's traders took borate to China during the latter part of the T'ang dynasty (618-907 AD). However, it wasn't until sometime in the Middle Ages that borax from the remote regions of Ti-

bet was regularly imported into Europe. It was costly, and this limited it principally to the precious-metal trade. Gold- and silversmiths and jewelers used it as a soldering agent and in the refining of metals and assaying of ores. In these times, the quantities used were small, being traded as an exotic commodity in the same category as spices. Its method of production was guarded as a secret, and its source remained a mystery until well into the second half of the eighteenth century.

## 2. EARLY HISTORY OF $B_2O_3$ IN GLASS

By the 1500's glass making was widely practiced in Northern Europe, however there are no references to the use of borax. In trying to fix the first use of borax as well as its first use in glass, it needs to be remembered that, prior to the nineteenth century, many of the accounts of glass and allied technology were written by scholars and observers who were not themselves involved in the art. The secrets were passed on by word of mouth and practical instruction, and those who knew most were not given to writing for the benefit of others [1].

To date there is no analytical evidence to support early use of borate in glass. The earliest reference to borosilicate glass was in China, 1225, in which Zhao Ru-kuo described the maritime trade of his homeland in the time of the Sung dynasty (960 to 1279 AD) reporting about the glass making of the Arabs and others [2]: "borax is added so that the glass endures the most severe thermal extremes and will not crack." The earliest European mention of borax in glass occurs in a German work by Johann Kunckel in 1679, which includes borax in the description of several glass compositions used for making artificial precious stones [3].

It seems unlikely that borax was in use in the glass industry in Europe until well into the eighteenth century and then in a very limited way. Johann Cramer in 1739 in Germany recommended for crystal glass 3 parts of prepared flints (silica), 1 part of the purest alkaline salt (potash), and 1 part burnt borace (borax) [4]. In 1758 Robert Dossie reported that the best looking-glass plates were ones containing 56% white sand, 23.5% pearl ashes (potash), 14% saltpeter, and 6.5% borax—he also notes that borax helps glass to receive certain colors [5].

## 3. EARLY USE OF $B_2O_3$ IN ENAMEL AND CERAMIC GLAZE

The art of enameling began to take definite form in the early Byzantine era, but in spite of the important role which borax played later it seems it was not used in enamel frits applied to metals until the middle of the eighteenth century. The early borate-containing frits were colored ground glass used almost entirely for decorative purposes, and then in small quantities. But the main increase in the use of borax in enamel-work did not come about until the enameling of iron created a new industry in the nineteenth century [1].

Enamel was first applied to sheet iron and steel in Austria and Germany about 1850. Cast-iron shapes such as cooking pots were heated in furnaces,



and enamel frit was dusted onto the metal as a dry powder which melted and stuck to the iron. The article was then returned to the furnace and the enamel melted to a smooth glaze, other coats of enamel being added later. The enamel had to be easily fusible, and borax became an important ingredient. By the end of the century, a worldwide trade had developed in all kinds of household goods such as dishes, bowls, buckets, bathtubs, as well as durable advertisement displays, street names and signs of all kinds. A highly technical frit industry, working closely with iron and steel fabricators, evolved and the improved quality of borax, soda ash, and other raw materials enabled rapid progress to be made. By the start of the twentieth century, enamel frit was the largest single use of borax [1].

Allied to enameling is the glazing and decoration of porcelain, pottery and ceramics. The history of glazes, starting with the ancient Egyptian, Chinese, Babylonian and Greek civilizations, is lengthy and complex. The earliest evidence of  $B_2O_3$  use was in China during the Liao dynasty (916 to 1125 AD) in recently discovered green glazed shards: 55%  $SiO_2$ , 6%  $Al_2O_3$ , 13%  $B_2O_3$ , 10%  $Na_2O$ , 1%  $K_2O$ , 6%  $CaO$ , 2%  $MgO$ , 6%  $CuO$ , 0.5%  $PbO$  [6]. The next earliest reference skips ahead to the reign of Kangxi (1662 to 1722) in China, where  $B_2O_3$  was discovered in opaque porcelain enamel glaze, and to Japan in the year 1699 [7]. Earlier, the Chinese had relied on lime and potash for good-quality glazes. From the middle of the nineteenth century, developments in enamelware, pottery, and china saw a rapid increase in demand for borate. This coincided with the increasing availability of boric acid from Italy and a substantial reduction in price, which enabled it to be used in entirely new applications. A typical glaze on Staffordshire earthenware or soft porcelain often contained between 12 and 25% of borax [1].

As for ceramic glazes,  $B_2O_3$  is unique in that it acts simultaneously as a glass former, as a flux, and as a viscosity stabilizer by preventing the glaze from running too much as it is fired. Perhaps most important of all,  $B_2O_3$  reduces the thermal expansion of the glaze so it can be properly matched to the ceramic body and thus prevent crazing. At the same time, it improves aqueous and chemical durability while adding to the brilliance of the glaze.

#### 4. BEGINNING OF GLASS AS A SCIENCE

In the 19<sup>th</sup> century, optical glass played an important role in the development of all types of glasses. The needs of optical glass to be sufficiently perfect to meet the exacting requirements of optical instruments contributed enormously to advances in the knowledge of glass technology. In 1824, Michael Faraday was commissioned by the Royal Society to carry out an experimental program to improve optical glasses [8]. Little of significance resulted from several years' work, but he did develop a lead borate glass of remarkably high refractive index containing 20% boric oxide, 70% lead oxide, and 10% silica, known as Faraday's heavy glass, but it was not durable enough to have any practical use in optical work. However, many years later in 1845 its presence in

Faraday's laboratory was a direct factor in his well-known discovery that a magnetic field could cause plane polarized light to rotate, known today as the magneto-optical effect or "Faraday effect". Work in England by William Vernon Harcourt, starting in 1834 and later with Sir George Stokes, was carried out to correlate glass physical properties by varying the glass composition, but without any commercial success. Maes in France in the year 1851 reported the first attempts at industrial scale production of a borosilicate glass, however melting control and equipment were inadequate. His glass comprised 56% SiO<sub>2</sub>, 7% B<sub>2</sub>O<sub>3</sub>, 17% K<sub>2</sub>O, 2% CaO, 14% ZnO, and 4% PbO [9].

An understanding of the way in which B<sub>2</sub>O<sub>3</sub> could enhance the quality and performance of glass first began when Otto Schott persuaded Ernst Abbé from the University of Jena to join him and Carl Zeiss in forming the Jena Glassworks of Schott and Sons in Germany in 1884 [2]. Up to this time, there were only six elements commonly used in glass, Si, O, Na, K, Ca, and Pb—all others were normally only present in minor amounts and usually only as impurities. Schott and Abbé systematically investigated the introduction of a wide range of chemical elements into glass compositions. From this work they found that, in the visible spectrum, glass containing B<sub>2</sub>O<sub>3</sub> affected short wavelength dispersion so that it became a valuable constituent of optical glasses.

Schott and Abbé succeeded where others had failed in improving the optical properties of glass, and at the same time increasing its resistance to water and chemical attack. They also discovered that glasses containing B<sub>2</sub>O<sub>3</sub> could be formulated which would withstand sudden changes in temperature, and from 1892 onward they manufactured many products based on borosilicate glasses [1]. They invented a group of borosilicate glasses that was commercialized in 1917 under the name of "Jena Apparatus Glass". This glass was resistant to thermal shock, but still the glassware had to be made fairly thin-walled in order to be suitable for the chemical laboratory. By lowering the alkali content

**Table 1**  
Early Low Expansion Glass [10]

	Jena Apparatus Glass 1917	Jena Supremax	Pyrex 1915
SiO <sub>2</sub>	64.3	56.0–54.3	81.0
Al <sub>2</sub> O <sub>3</sub>	6.3	20.0–21.0	3.0
B <sub>2</sub> O <sub>3</sub>	10.3	9.0–7.5	11.5
Na <sub>2</sub> O	7.4	1.0–1.3	4.5
K <sub>2</sub> O		1.0	
CaO		5.0–15.1	
MgO		8.0	
ZnO	11.7		
BaO		0.8	

and increasing alumina, another group of glasses was developed which became known under the name "Supremax" glass of Schott and Genossen. These early Jena glasses are shown in Table 1. In some cases  $B_2O_3$  was partly replaced by  $P_2O_5$ . "Duran", developed sometime during World War II and introduced in 1950 by Schott, was derived from these early borosilicate glasses.

The first low expansion borosilicate glass was produced in the United States in 1912 for use by the railroad in signal lantern glass. With the outbreak of war in 1914, supplies of laboratory glassware from Germany were no longer available, and Corning Glass Works, operating in the United States since 1868, became a new center for the production of borosilicate glasses. In 1908, they established one of the first US industrial research centers, and in 1915 Sullivan and Taylor patented a low expansion borosilicate glass, that was to become known as "Pyrex" that revolutionized laboratory glassware and brought glass into the kitchen as cooking-ware [11-12], Table 1.

Compared to the Jena glass, it did not contain alkaline earth oxides and its alumina and alkali content were low. This high silica glass was a challenge to melt due to its high viscosity, and initially large amounts of arsenic and antimony oxide were used to ensure proper melting and fining. Later, Hood (1936) [13] found these oxides could be replaced by sodium chloride. Laboratory ware was followed by battery jars and the now familiar heat-resistant oven-ware for domestic use. In these low expansion Jena and Pyrex type glasses, the fluxing action of boric acid allows these low alkali glasses to be melted and fined at commercially feasible temperatures without sacrificing chemical durability.

Phase separated borosilicate glasses were first discovered by Hood and Norbert in 1934. This led to the invention of a process for producing high silica laboratory ware by treating a phase separated  $B_2O_3$ - $SiO_2$  glass with acid [14]. The borate rich phase was leached away leaving a silica rich, 96-98%  $SiO_2$ , glass phase that was sold under the name of "Vycor".

The price at which borax and boric acid was now available enabled wider use in glass to take place. By the end of the nineteenth century, world production of borates was shared between the United States, Chile, Peru, and Turkey as calcium borates, and Italy as crude boric acid. After Tibet, boric acid became available from Italy beginning in 1820. The extensive sodium and calcium borate deposits in Turkey were first mined in 1865 [15], and borate was first discovered in the United States in California (1856), within mineral springs, and later in Death Valley and Searles Lake by the 1870's. By 1900, the borax trade from Tibet was reduced to a few hundred tons a year, and this seems to have ceased altogether in the early years of the twentieth century. By 1910, the United States and Chile were the main producers providing 85 percent of world production [16]. After the discovery of a massive deposit of sodium borate in the Mojave Desert in California, first mined in 1926, the United States dominated the world borate market until the resources in Turkey have more recently been developed. Today, Turkey and the United States are the major world suppliers.

## 5. TEXTILE OR CONTINUOUS FILAMENT FIBERGLASS

The largest use of borates in the world today is in insulation and textile fiberglass [17]. The French physicist René Antoine Ferchault de Réaumur (1683-1757) foresaw that, "if they succeed in making glass threads as fine as those of spiders webs, they will have glass threads of which woven stuffs may be made" [18]. He also appears to have drawn fibers himself, not from a glass rod, but from a pool of molten glass straight onto a rotating wheel. However, this glass was no more than a novelty.

In 1893, Edward Drummond Libbey exhibited a dress made of glass fiber and silk at the Columbian Exhibition in Chicago. At about the same time, a small workshop in Paris was making textiles combining silk or cotton with glass fibers and selling them for 100 francs per meter. While these were luxury curiosities not likely to develop into a big market, it nevertheless demonstrated that glass fibers could be manufactured and, perhaps, used. Then during the First World War the Germans developed a method of producing glass fibers based on single strands drawn through an orifice. Later, in the 1930's, a process was developed in the United States whereby a continuous filament was formed by multiple strands of glass extruded from a heated platinum box or bushing with many tiny holes. These early fibers were generally made from soda-lime-silica glass, known as Type A glass, having poor durability (see Table 3).

Phase equilibrium relationships in glass forming systems were developed in the 1930's that led to compositions suitable for high temperature electrical insulation applications where the glass must have both high electrical resistivity and low surface conductivity. This required a glass low in alkali, less than 1.0 wt%. Study of glasses in the systems  $\text{CaO-Al}_2\text{O}_3\text{-SiO}_2$  and  $\text{CaO-MgO-Al}_2\text{O}_3\text{-SiO}_2$  led to development of the first electrical glass patented as alkali- and  $\text{B}_2\text{O}_3$ -free in 1937 (first column in Table 2) then by addition of  $\text{B}_2\text{O}_3$  and fluorine to a near eutectic composition in the  $\text{CaO-MgO-Al}_2\text{O}_3\text{-SiO}_2$  system. This was soon replaced by a 1943 patented composition issued to Owens-Corning, and this well chosen composition became the highly successful 'original E-Glass' (second column in Table 2). This low alkali formulation was more easily processed, and still solved the durability problems lacking in the earlier Type A textile glass. Fluxing in this high temperature glass depended on  $\text{B}_2\text{O}_3$  and  $\text{F}_2$  in the absence of alkali.

The E-Glass fiber was quickly adopted into many other non-electrical reinforcement applications. In 1935, the first patents appeared covering thermosetting resins which cured at room temperature, e.g. polyesters. These, when reinforced with E-Glass fibers, could be used for structural shapes and gave rise to the reinforced plastics industry in the early 1940's. In the ensuing years, a number of modifications were made. E-Glass "621" was formulated when it was found that dissolution of zirconium oxide from the refractories used at that time had a negative effect on the liquidus temperature [23]. To circumvent this problem, all the  $\text{MgO}$  was replaced by  $\text{CaO}$ , giving a sufficiently low liquidus temperature to accommodate the refractory derived zirconium oxide [24]. In more recent years it has become possible to operate at higher furnace tempera-

**Table 2**  
E-Glass - Continuous Filament Fiberglass

		"Original"		B&F-Free		
	Early E-Glass 1940[19]	E-Glass Schoenlaub 1943[20]	"816" Haggerty 1979[21]	McWilliams Watson 1988[22]	E-Glass Typical 1990s	C-Glass Bowes 1943[27]
SiO <sub>2</sub>	60	54.0	58.0	59.0	54.0	65.0
Al <sub>2</sub> O <sub>3</sub>	9	14.0	11.0	12.1	14.0	4.0
B <sub>2</sub> O <sub>3</sub>		10.0			6.1	5.5
R <sub>2</sub> O		1.0	1.0	0.9	1.0	8.5
CaO	27	17.5	22.5	22.6	23.3	14.0
MgO	4	4.5	2.6	3.4	0.4	3.0
ZnO			2.6			
TiO <sub>2</sub>			2.4	1.5	0.5	
Fe <sub>2</sub> O <sub>3</sub>			0.1	0.2		
F <sub>2</sub>		0.5	0.01		0.6	

tures as refractories and fiber-forming bushings have improved allowing use of somewhat lower levels of B<sub>2</sub>O<sub>3</sub>, typically 6 to 8%. Composition "816" (known as 8525 glass in Canada) is an example of a B<sub>2</sub>O<sub>3</sub>-free glass intended as an E-Glass replacement, but this glass has a high liquidus temperature and there appears to be little economic advantage compared to today's conventional E-Glass. Another example of an E-Glass replacement free of both B<sub>2</sub>O<sub>3</sub> and fluorine is shown in Table 2. Production of these B<sub>2</sub>O<sub>3</sub>-free glasses is small and they are not a true 'E-Glass' but can be suitable for some reinforcement applications, notably in concrete. Trends have been toward lower B<sub>2</sub>O<sub>3</sub> compositions because of raw material cost and volatility from the furnace.

Another type of textile fiberglass known as C-Glass (Chemical) was developed for its greater chemical resistance, particularly to acids [27]. Compared with E-Glass, it has higher silica and soda, lower alumina, and about 5 to 6% B<sub>2</sub>O<sub>3</sub> (Table 2).

## 6. INSULATION OR WOOL FIBERGLASS

Insulation fiberglass, also known as glass wool, is the other major category of commercial fiberglass. Its development followed on to technology from the 1800's invented for manufacture of mineral wool insulation from molten slag. From about the turn of the century, the first glass considered for glass wool, as opposed to mineral wool, was a common early soda-lime-silicate container glass composition designated Type A in Table 3. However, this glass had a high fiberizing temperature and produced fibers of low durability.

Up to this point, insulation fiberglass was of little commercial importance.

**Table 3**  
Insulation Fiberglass

	Type A	Type T <sub>1</sub> Bowes 1943 [27]	Type T <sub>2</sub> Welsch 1959[28]
SiO <sub>2</sub>	72.0-72.5	63	58.6
Al <sub>2</sub> O <sub>3</sub>	0.2-0	5	3.2
B <sub>2</sub> O <sub>3</sub>		5	10.1
Na <sub>2</sub> O+K <sub>2</sub> O	10.0-16.0	10	15.1
CaO	5.5-10.0	14	8.0
MgO	2.5-4.0	3	4.2

The fiberglass revolution began in the 1930's with the development of a new process for producing glass fibers on an industrial scale. The Owens-Illinois Glass Company of Newark, OH (Owens-Corning today) made significant improvements to the process of glass fiber manufacture which made it economically viable [25]. In about 1940, the earlier Type A glass was replaced by Type T<sub>1</sub>, or Thermal glass, containing about 5% B<sub>2</sub>O<sub>3</sub> (Table 3), suitable for the steam blown fiberization process invented in 1932 and later for the air attenuated and flame attenuated fiberization processes [26]. Compared to Type A glass, the melt viscosity was reduced by the presence of B<sub>2</sub>O<sub>3</sub> in combination with higher CaO and lower SiO<sub>2</sub>, while the durability was dramatically improved with B<sub>2</sub>O<sub>3</sub> along with increased Al<sub>2</sub>O<sub>3</sub>. In addition, B<sub>2</sub>O<sub>3</sub> had a favorable effect on the liquidus temperature as well as the rate of devitrification. This became the first commercially successful insulation fiberglass having both high durability and improved fiber-forming characteristics.

A major change in glass formulation was again made necessary with the introduction of the rotary fiberization process in about 1955 that today is the preferred process for making commodity insulation fiberglass. The advantage of this process is significantly higher rates of production, but demands on the glass are greater. Glass having a low enough working temperature and liquidus temperature was required for contact with high temperature metal alloys used in fiberizing spinners while still maintaining good finished fiber durability. This was accomplished by increasing both B<sub>2</sub>O<sub>3</sub> and Na<sub>2</sub>O at the expense of SiO<sub>2</sub> in Type T<sub>2</sub> glass (Table 3). This glass composition has been modified over the years as high temperature spinner alloys and design have improved. The drive to reduce cost results in a range of glass compositions produced today typically containing about 4 to 6% B<sub>2</sub>O<sub>3</sub>.

## 7. SUMMARY

It is unlikely that borax was known in ancient times, but may have been first discovered during the great Islamic civilization sometime before 800 AD. By the Middle Ages, it is known that small amounts of borax from remote regions

of Tibet were imported into Europe, for use principally by the precious-metal trade, however, its source was unknown until the middle of the eighteenth century. The earliest analytical evidence of borax in glass comes from China, sometime during the Liao dynasty (916 to 1125), in recently discovered pottery shards with a green glaze that contains 13 wt%  $B_2O_3$ . Early in the nineteenth century new sources of borax were discovered first in Italy, followed by Turkey, the United States and South America. This increase in availability led to wider use first in enamel glaze, then ceramic glaze and glass. By the end of the nineteenth century the practical needs for high quality optical glass led to the discovery of low expansion borosilicate glass that was soon used in laboratory ware and domestic heat resistant oven-ware. The technology for the commercial manufacture of fiberglass was developed in the 1930's and 1940's and is today the largest single commercial use for borates.

Today's use of  $B_2O_3$  in commercial glass is driven both by finished glass properties as well as requirements in the glass making process. Finished glass properties include durability—the resistance to attack by moisture; a low coefficient of expansion—the resistance to thermal shock; a high electrical resistance in low alkali glass; and optical dispersive properties—the variation in index of refraction with wavelength. In the glass making process,  $B_2O_3$  acts as a flux (assisting the fusion of batch raw materials into a vitreous state), contributes to working or forming properties by lowering the forming temperature and liquidus temperature, and reduces the rate of devitrification. At least one and usually a combination of these properties are important in the manufacture and end application of commercial borosilicate glass. In the category of lighting glass, for example, a low thermal expansion is important to match and seal refractory electrical leads, W and Mo, as well as for thermal shock resistance.

Today, insulation (glass wool) and textile (continuous filament) fiberglass represent the largest commercial category for  $B_2O_3$ . The above attributes of  $B_2O_3$  are particularly important in the production of fiberglass. Durability is a most important property for the high surface area associated with very fine or small diameter fibers. An important characteristic of  $B_2O_3$  in fiberglass is that it provides high durability in the finished glass products and at the same time provides required low temperature forming properties dictated by the temperature constraints of metal alloys used in fiberizing equipment. No other commercially available oxide can provide all these features economically in a single batch raw material.

## REFERENCES

- [1] N. J. Travis & E. J. Cocks, *The Tincal Trail*, (Harrap Limited, London, 1984).
- [2] J. Steiner, *Glastech. Ber.* **66** (6/7) (1993), 165.
- [3] J. Kunckel, *Ars Vitraria Experimentalis* (Frankfurt and Leipzig, 1679), Part I, p. 206; Part II pp. 57-9.
- [4] J. Cramer, *Elementa Artis Documasticae* (Leyden, 1739). English translation *Elements of the Art of assaying metals* (London, 1741), p 440, n. 33.
- [5] R. Dossie, *Handmaid of the Arts* (London, 1796), New Edition, Vol II, pp 171, 188-9 *op. cit.*

- [6] N. Wood, *Borax Review* **8** (1990), 3.
- [7] Bernard Leach, *Kenzan & His Tradition* (London, 1966).
- [8] M. Faraday, *Experimental Researches in Chemistry & Physics*, (London, 1859), p 231, 256.
- [9] E. Zchimmer: *Die Glasindustrie in Jena*, Eugen Diederichs Verl., Jena, 1912.
- [10] W. A. Weyl, *The Glass Industry* **2** (1948), Parts I-IX, pp. 131, 200, 264, 328, 388, 444, 500, 559, 632.
- [11] E. C. Sullivan & W. C. Taylor, *J. Soc. Eng. Chem.* **7** (1915), 1064.
- [12] E. C. Sullivan & W. C. Taylor, U. S. Patent 1,304,623 (1919), Corning Glass.
- [13] H. P. Hood, U. S. Patent 2,035,318 (1936), Corning Glass.
- [14] H. P. Hood & M. E. Norberg, U. S. Patent 2,106,744 (1938) & 2,221,709 (1940), Owens-Corning.
- [15] W. Bühler, *Borazit, The Story of the Turkish Boron Mines & their Impact on the Boron Industry*, (Imprimerie Chabloz SA, Switzerland, 1996).
- [16] C. G. Vale & H. S. Gale, *The Production of Borax in 1911 US Geological Survey* (Washington, 1912), p. 6. Production Statistics.
- [17] K. L. Loewenstein, *The Manufacturing Technology of Continuous Glass Fibres*, Glass Science and Technology **6**, 3<sup>rd</sup> Edition, (Elsevier 1993).
- [18] A. De Dani, *Monthly Bulletin for the Glass Industry*, C. E. Ramsden & Co. Ltd., May **370** (1965).
- [19] Naamlooze Vennootschap Maatschappij tot Beheer en Exploitatie van Octrooien, GB Patent 520 247 (1940).
- [20] R. A. Schoenlaub, U. S. Patent 2,334,961 (1943), Owens-Corning.
- [21] W. N. Haggerty, CA Patent 1,067,230 (1979), Owens-Corning.
- [22] D. E. McWilliams & J. C. Watson EP Patent 275,541 (1988), PPG.
- [23] P. F. Aubourg & W. W. Wolf, In: *Commercial Glasses, Advances in Ceramics Vol 18*, Eds D. C. Boyd & J. F. MacDowell (Amer. Ceram. Soc., Ohio, 1986), 51.
- [24] R. L. Tiede & F. V. Tooley, U. S. Patent 2,571,074 (1951), Owens-Corning.
- [25] W. W. Boeschstein, *Glass Industry*, July (1995), 26.
- [26] L. V. Gagin, *Canadian Clay & Ceramics*, July/August (1980), 10.
- [27] U. E. Bowes, U. S. Patent 2,308,857 (1943), Owens-Corning.
- [28] W. W. Welsch, U. S. Patent 2,877,124 (1959), Owens-Corning.



## **MICROFLOAT TECHNOLOGY—A NEW CHALLENGE TO THE PRODUCTION OF HIGHTECH BOROSILICATE FLAT GLASSES**

Thomas KLOSS, K. SCHNEIDER, G. LAUTENSCHLÄGER  
*JENA<sup>er</sup> Glaswerk GmbH, 07745 Jena, Germany*

P. KELLER, W. LINZ  
*Schott Glaswerke Mainz, Germany*

T. KIMURA & Y. TAKAHASHI  
*Asahi Glass Corp., Tokyo, Japan*

There is no doubt that the borosilicate glass family is outstanding among all others for its countless variety of technical glass applications. Due to the inexhaustible possibilities for compositional variations, special borosilicate glasses can meet extraordinary properties. In particular, their high chemical resistance, high resistance to temperature changes combined with low thermal expansion, and now their unique ability to be prepared as a toughened safety glass have led experts to think further about the potentials for new high tech applications. These are discussed in the present paper, which describes the role of borosilicate glasses in advanced flat glass technology.

The Schott glasses of the DURAN<sup>®</sup> and SUPRA<sup>®</sup> type were the first borosilicates in the world to be prepared using the Microfloat process and are named BOROFLOAT<sup>®</sup> 33 and BOROFLOAT<sup>®</sup> 40 glass, respectively (trademark of Jena<sup>er</sup> Glaswerk GmbH). The successful floating of these different borosilicate glass compositions impressively demonstrates the flexibility and performance of the new Microfloat equipment in Jena. Some of the very special requirements for floating high quality, low expansion borosilicate glasses are discussed, especially the temperature dependence of the evaporation of alkaline borates and the effect this has on quality.

A few of the most important physical and chemical characteristics of the BOROFLOAT<sup>®</sup> glasses are summarised and some structural data are given, based on Raman spectroscopy. Potential new future applications are also discussed.

## THE USE OF BORON OXIDE IN GLASS FIBER FORMULATIONS

Foster L. HARDING, Jon F. BAUER, Harry H. RUSSELL III  
& Xiaojie XU

*Schuller International, Mountain Technical Center,  
P. O. Box 625005, Littleton, CO 80162-5005, USA*

Because of its unique contribution to glass properties, boron oxide is a constituent in almost all commercial fiber glass formulations. Specifically, (1)  $B_2O_3$  moves fiber glass formulations toward lower viscosity while decreasing liquidus temperature and improving moisture resistance. (2)  $B_2O_3$  enables creation of glass formulations whose fibers are reasonably soluble in relevant biological fluids, while at the same time preserving resistance to moisture. (3)  $B_2O_3$  lowers glass surface tension, which is thought to result in easier fiber formation. (4)  $B_2O_3$  lowers glass coefficient of thermal expansion (CTE), which is important for some emerging applications.

### 1. INTRODUCTION

Despite its relatively high cost, the use of  $B_2O_3$  is pervasive in fiber glass formulations because of its unique influence on properties that are critical to product manufacturing and performance. Because E-glass is restricted to very low alkali levels [1], the fluxing action and lower viscosity from  $B_2O_3$  has been necessary in textile fibers from the beginning. Since the function of boron in E-glass seems obvious, this paper will focus on the use of  $B_2O_3$  in fiber glass insulation.

### 2. PROPERTIES IMPORTANT TO THE HISTORICAL USE OF BORON

While many glass properties are important in manufacturing and marketing fiber glass products, viscosity, liquidus temperature, durability, and surface tension have had particular importance in establishing the common use of  $B_2O_3$  in glass formulations.

Insulation glass fibers are formed using expensive and highly specialized alloy components, which must resist both high temperature creep and molten glass corrosion. The strong temperature dependence of these key alloy properties has provided a driving force toward lower operating temperatures via use of lower viscosity glass formulations.

High Temperature Viscosity (HTV),  $\log(\text{viscosity})=3$ , is often chosen to represent the viscosity/temperature point at which commercial fiberization takes place. If the difference between the HTV and liquidus temperature is too small, crystal formation can occur in cooler regions of the molten glass and severely

**Table 1**  
Schuller 901F Insulation Fiber Glass Formula

Oxide	Weight Percent
SiO <sub>2</sub>	56.20
Al <sub>2</sub> O <sub>3</sub>	4.90
B <sub>2</sub> O <sub>3</sub>	8.60
Na <sub>2</sub> O	16.74
K <sub>2</sub> O	1.06
CaO	7.00
MgO	4.90
Property	Value
HTV	1001°C
Liquidus T.	919°C
FRP	18.75

disrupt fiber production. Depending on the fiberization process, liquidus temperature must be at least 40 to 120°C below the HTV.

Glass durability is also important because fibers are required to resist loss of strength under end-use conditions or when stored under compression in humid climates.

In most commercial silicate glasses, RO (CaO and MgO) and R<sub>2</sub>O (Na<sub>2</sub>O and K<sub>2</sub>O) are important ingredients for adjusting glass viscosity, while Al<sub>2</sub>O<sub>3</sub> is commonly used to enhance glass durability. The following discussion explains why it is quite difficult to simultaneously optimize viscosity, liquidus, and du-

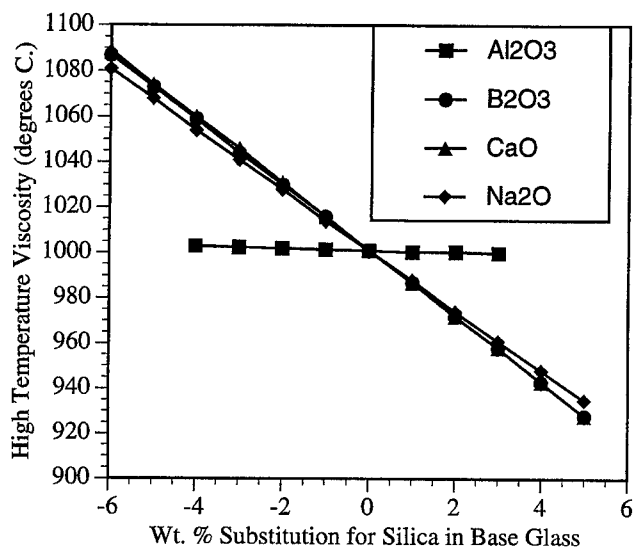


**Fig. 1.** Influence of Al<sub>2</sub>O<sub>3</sub>, B<sub>2</sub>O<sub>3</sub>, CaO, and Na<sub>2</sub>O substitutions for SiO<sub>2</sub> on high temperature viscosity (HTV) of Schuller 901F glass.

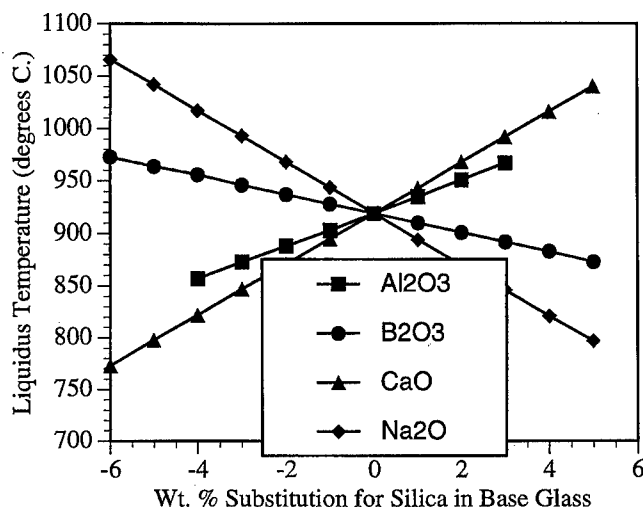


Fig. 2. Influence of  $\text{Al}_2\text{O}_3$ ,  $\text{B}_2\text{O}_3$ ,  $\text{CaO}$ , and  $\text{Na}_2\text{O}$  substitutions for  $\text{SiO}_2$  on the liquidus temperature of Schuller 901F glass.

rability in fiber glasses without also using  $\text{B}_2\text{O}_3$ .

Table 1 shows a commercial fiber glass building insulation formula (Schuller 901F) which exhibits a typical balance amongst HTV, liquidus temperature, and durability. Fatigue Resistance Parameter (FRP) is an exponent in the static fatigue equation given by Charles [2]. It was calculated using a model developed at Schuller from fiber tensile strength data collected under various temperature and humidity conditions [3]. The higher the FRP, the more resistant a glass is to moisture attack. Depending on end-use application, an FRP value of 16 or higher is typically required for commercial fiber glass products. 901F glass was used as the base for calculating relationships between glass composition and properties as reported throughout this paper.

Figure 1 shows that  $\text{Na}_2\text{O}$ ,  $\text{CaO}$ , and  $\text{B}_2\text{O}_3$  are about equally effective at lowering HTV when substituted for  $\text{SiO}_2$ , while  $\text{Al}_2\text{O}_3$  for  $\text{SiO}_2$  substitutions have very little effect on HTV. The HTV values were calculated using an internal Schuller model [4] which is based upon experimental values measured using concepts similar to those described by Tiede [5]. A rotary viscosimeter was modified with a furnace and platinum parts to permit high temperature glass viscosity measurements.

Figure 2 shows that  $\text{CaO}$  for  $\text{SiO}_2$  substitutions have a strong tendency to raise liquidus temperature as the HTV decreases, so  $\text{CaO}$  has limited value as a means of decreasing viscosity. The liquidus temperatures were calculated using an internal Schuller model based upon original gradient furnace liquidus determinations [4].

Figure 3 shows that  $\text{CaO}$ , and particularly  $\text{Na}_2\text{O}$ , substitutions for  $\text{SiO}_2$ , cause a decrease in the resistance of the glass to moisture attack. The FRP values were calculated using Schuller's internal model as noted above [3]. Figures 1-3 show that only  $\text{B}_2\text{O}_3$  substitutions for  $\text{SiO}_2$  possess the combination of property trends which decrease HTV, lower liquidus temperature, and increase

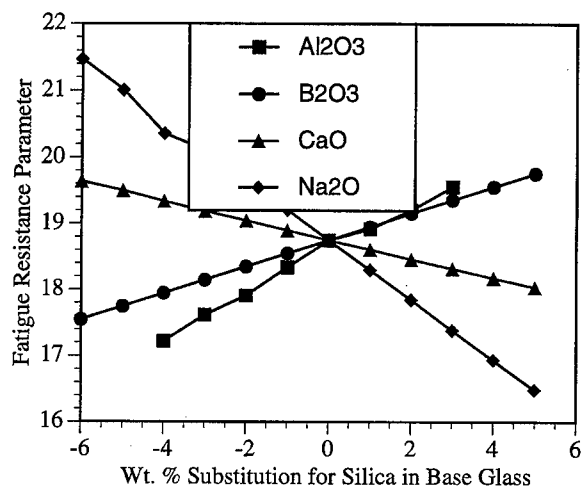


Fig. 3. Influence of  $\text{Al}_2\text{O}_3$ ,  $\text{B}_2\text{O}_3$ ,  $\text{CaO}$ , and  $\text{Na}_2\text{O}$  substitutions for  $\text{SiO}_2$  on the fatigue resistance parameter (FRP) of Schuller 901F glass.

moisture resistance. This combination of properties has been the driving force behind the historical development of fiber glass formulations containing  $\text{B}_2\text{O}_3$ .

Over the years, better fiberization efficiency and "easier" production operations have often been associated with glass formulas which contain higher levels of  $\text{B}_2\text{O}_3$ . Figure 4 shows the influence of  $\text{Al}_2\text{O}_3$ ,  $\text{CaO}$ ,  $\text{Na}_2\text{O}$ , and  $\text{B}_2\text{O}_3$  substitutions for  $\text{SiO}_2$  on glass surface tension, based upon calculations using Deitzel's composition vs. surface tension model [6]. Substitutions of both  $\text{Al}_2\text{O}_3$  and  $\text{CaO}$  for  $\text{SiO}_2$  increase surface tension, while substitutions of both  $\text{Na}_2\text{O}$  and  $\text{B}_2\text{O}_3$  decrease surface tension. Combining this information with the data plotted in Figure 3 demonstrates that  $\text{B}_2\text{O}_3$  is unique in lowering surface tension while simultaneously improving product resistance to atmospheric moisture. While we are not aware of studies which firmly establish the correlation, we believe this lowering of surface tension is at least part of the reason for the empirical performance observations that have supported the use of  $\text{B}_2\text{O}_3$  in fiber glass formulations.

### 3. TWO PROPERTIES WHICH HAVE RECENTLY ADDED TO THE REASONS FOR USE OF BORON IN FIBER GLASS

Over the past decade, events have provided two other driving forces which further strengthen fiber glass industry reliance upon  $\text{B}_2\text{O}_3$  as a key glass formulation component.

#### 3.1 Biosolubility

The tragedy of lung disease caused by inhalation of respirable asbestos fibers has caused society to question whether all respirable fibers might be harmful to human health. However, the weight of evidence from extensive epidemio-

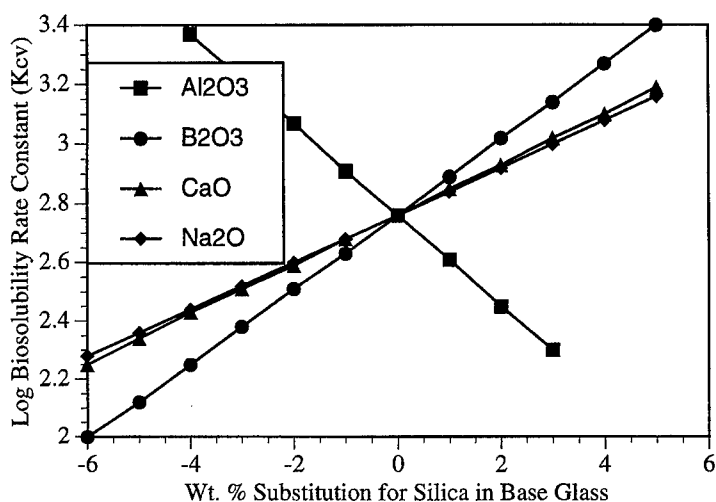


Fig. 4. Influence of  $\text{Al}_2\text{O}_3$ ,  $\text{B}_2\text{O}_3$ ,  $\text{CaO}$ , and  $\text{Na}_2\text{O}$  substitutions for  $\text{SiO}_2$  on the surface tension of Schuller 901F glass.

logical and laboratory research strongly supports the conclusion that occupational exposure to glass fibers does not increase the risk to humans of respiratory system cancer (for example, see Lee et al. [7]). Logic does suggest that fibers which can be readily dissolved by the fluids naturally found in the lung will provide an extra margin of safety against incidence of lung disease. This is also supported by research results [8, 9]. It may therefore prove highly desirable to develop glass fiber formulations which are quite soluble in lung fluid, while at the same time being resistant to attack by atmospheric moisture.

Figure 5 indicates the influence of several glass making oxides on the

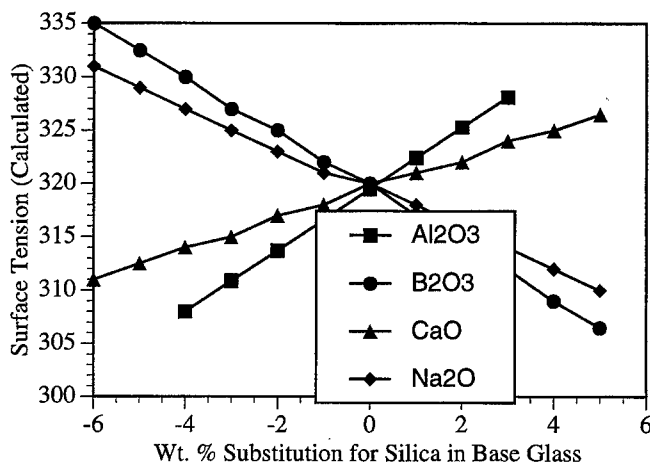


Fig. 5. Influence of  $\text{Al}_2\text{O}_3$ ,  $\text{B}_2\text{O}_3$ ,  $\text{CaO}$ , and  $\text{Na}_2\text{O}$  substitutions for  $\text{SiO}_2$  on biosolubility of Schuller 901F glass fibers.

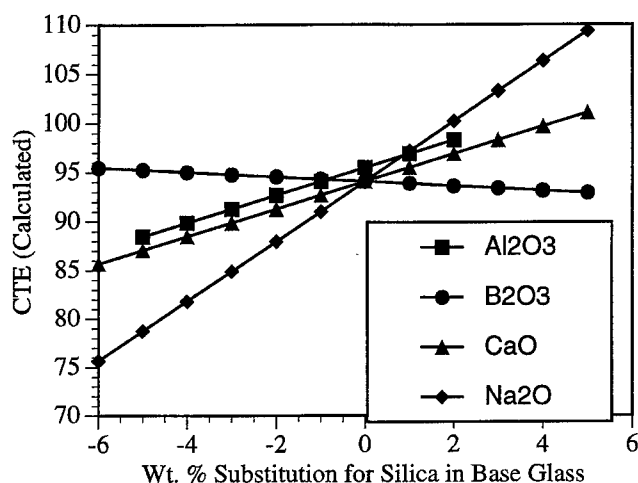


Fig. 6. Influence of  $\text{Al}_2\text{O}_3$ ,  $\text{B}_2\text{O}_3$ ,  $\text{CaO}$ , and  $\text{Na}_2\text{O}$  substitutions for  $\text{SiO}_2$  on Schuller 901F glass coefficient of thermal expansion (CTE).

“biosolubility” constant  $K_{CV}$ ; that is, the solubility constant of glass fibers exposed to an artificially prepared lung fluid. The curves were calculated using a model developed at Schuller based upon *in vitro* experiments by Bauer et al. [10, 11]. It is clear that one useful strategy for enhancing biosolubility is to lower the  $\text{Al}_2\text{O}_3$  level in the glass. However, this action will also make the glass more vulnerable to moisture attack.

Comparing Figures 3 and 5, it is clear that  $\text{B}_2\text{O}_3$  has a unique ability to enhance biosolubility while simultaneously increasing atmospheric moisture resistance. This could become another very important reason for use of  $\text{B}_2\text{O}_3$  in fiber glass formulations, and may actually result in higher  $\text{B}_2\text{O}_3$  levels than have been historically typical.

### 3.2 Thermal Expansion

Figure 6 reflects glass coefficient of thermal expansion (CTE) calculations using the methods of Winkelmann & Schott [12]. It demonstrates that  $\text{B}_2\text{O}_3$  is a key ingredient in formulating glasses with low CTE. If it is desired to significantly lower the thermal expansion of glass while retaining a similar viscosity, Figures 1 and 6 suggests that  $\text{B}_2\text{O}_3$  substitutions for alkali and/or alkaline earth oxides offer a logical approach. This area has generated new interest since the recent introduction of bicomponent glass fibers where the difference in CTE of the two glasses creates a natural curl and twist similar to that seen in wool and in some synthetic (polymer) fibers.

## 4. DISCUSSION

The fluxing attributes of  $\text{B}_2\text{O}_3$  and its improvement of glass moisture resistance in comparison to other additives is reflected in its thermodynamic properties. For

example, calculated free energies of hydration ( $\Delta G_{\text{HYD}}$ ) for  $\text{B}_2\text{O}_3$  in glasses clearly show an advantage over alkali or alkaline earth oxides with regard to chemical durability in aqueous systems. Hydration of  $\text{B}_2\text{O}_3$  results in a  $\Delta G_{\text{HYD}}$  of only  $-9.9$  kcal/mol as compared with  $-28.8$  kcal/mol for  $\text{Na}_2\text{O}$ ,  $-41.7$  kcal/mol for  $\text{K}_2\text{O}$ , and  $-16.1$  kcal/mol for  $\text{CaO}$  [13]. This means that the substitution of  $\text{B}_2\text{O}_3$  into glass for  $\text{SiO}_2$  results in far less moisture resistance "penalty" than  $\text{R}_2\text{O}$  or  $\text{RO}$  substitutions.

However, this is not reflected in the dissolution rates of  $\text{B}_2\text{O}_3$  in glasses exposed to simulated lung fluids, where boron behaves similarly to calcium and sodium in being readily leached from the glass structure [11]. The reason for this behavior is not known, but it may be related to the specific structural environment of the boron atoms. Little detailed structural data are available for borosilicate formulations as complex as commercial fiber glass. Typical formulas contain alkali in molar percentages greater than  $\text{B}_2\text{O}_3$ . As alkali concentration is increased in boron-containing glasses, several structural changes are believed to occur, eventually resulting in trigonal  $\text{BO}_3^{n-}$  containing from one to three non-bridging oxygen ions [14]. Alkali ions may be affiliated with the trigonal  $\text{BO}_3^{n-}$  ions strongly enough to allow ion exchange reactions to proceed with coupled release of alkali and boron. It is very likely that formation of boron oxyanions in the glass structure is important in decreasing melt viscosity and also in determining other liquid state properties. Much remains to be learned about the complex chemistry of boron in silicate glasses and its influence on glass properties which are important to the manufacture and durability of glass fibers.

Despite the above-documented advantages of  $\text{B}_2\text{O}_3$  in glass fiber formulations, its use is accompanied by practical problems. Boron minerals are expensive with glass makers often spending as much for boron raw materials as for all other raw materials combined. Boron volatilization, especially combined with alkali volatilization, causes particularly aggressive attack on glass furnace superstructure refractories. Condensation of the same volatile components in furnace exhaust systems also contributes to particulate air emissions. Hydrated boron minerals often contribute to batch dust carryover from glass furnaces when their water of hydration is released with explosive force.

## 5. CONCLUSION

On balance, the unique contribution of  $\text{B}_2\text{O}_3$  to the combination of glass properties required for fiber glass manufacturing and product service conditions far outweighs the problems and assures its continued importance for many years to come.

## REFERENCES

- [1] W. Eastes, ed., *Man-made Vitreous Fibers: Nomenclature, Chemical and Physical Properties*. (North American Insulation Manufacturers Assoc., Alexandria, VA, 1993), p. 43.
- [2] R.J. Charles, *J. Appl. Phys.* **29** (1958), 1657.
- [3] R.K. Ware, Schuller Internal Research Report 436-651 (1981).



- [4] R.K. Ware, Schuller Internal Research Report 436-710 (1981).
- [5] R.L. Tiede, *J. Am. Ceram. Soc.* **42** (1959), 537
- [6] A. Dietzel, *Sprechsaal*, **75** (1942), 82.
- [7] I. Lee, C.H. Hennekens, D. Trichopoulos & J. E. Buring, *J. Occup. Env. Med.* **37** (1995), 725.
- [8] J.F. Bauer, B.D. Law & K.A. Roberts, (presentation at) *TAPPI Non-Wovens Conf.* (1988), available from author.
- [9] R.M. Potter & S.M. Mattson, *Glastech. Ber.* **64** (1991), 16.
- [10] J.F. Bauer, B.D. Law & T.W. Hesterberg, *Env. Health Perspectives*, **102** (1994), 61.
- [11] J.F. Bauer & B.D. Law, Schuller Internal Research Report 436-3167 (1995).
- [12] A. Winkelmann, O. Schott, *Ann. Phys. (Leipzig)* **51** (1894), 735.
- [13] C.M. Jantzen, *J. Am. Ceram. Soc.* **75** (1992), 2433.
- [14] R.A. Smith, *J. Non-Cryst. Solids* **84** (1986), 421.

## INFLUENCE OF SMALL QUANTITIES OF BORON OXIDE ADDITIVES ON THE MICROSTRUCTURE AND OPTICAL PROPERTIES OF DENTAL GLASS-CERAMICS

Wolfram HÖLAND, Martin FRANK  
& Volker RHEINBERGER

*IVOCLAR Ltd., FL - 9494 Schaan, Principality of Liechtenstein*

Although opal glasses for technical uses have been available for some time, entirely new requirements must be fulfilled in the development of opal products for dental applications. A thermal expansion of  $90\text{--}160 \times 10^{-7} \text{ K}^{-1} \text{ m/m}$  is required. Furthermore, the opalescence of the material must be similar to that of natural teeth. This paper will show that special products can be developed to meet these requirements. Hence, glass-ceramics derived from the  $\text{SiO}_2\text{--Al}_2\text{O}_3\text{--K}_2\text{O}$  system were produced by adding  $\text{P}_2\text{O}_5$ ,  $\text{Na}_2\text{O}$ ,  $\text{ZrO}_2$ ,  $\text{TiO}_2$  and small amounts of  $\text{B}_2\text{O}_3$ . The development of opalescent dental products was carried out by controlling two mechanisms in the glass: microstructure development, and nucleation and crystallization. The microstructure of the glass matrix was formed as a special microheterogenic liquid-liquid phase separation. The diameter of the droplet phase measured approx. 40-500 nm. It was even possible to control this reaction with phosphate additives and small quantities of  $\text{B}_2\text{O}_3$ . The surface nucleation of the glass granules lead to the crystallization of leucite-type crystals, which produced a high thermal expansion coefficient. The new products were highly translucent and the opalescence was comparable to that of natural teeth.

### 1. INTRODUCTION

Glasses with opalescent properties are well known in both the fields of technical and optical glasses. Often this opalescence is used for decorative purposes (e.g. tableware) or for producing optical effects in technical building components (e.g. in the electrotechnical industry).

In the development of an opal effect in technical glasses, different solutions were achieved. The opal effect was found by precipitating microcrystals as well as by specifically developing a special microstructure by influencing phase separation. Therefore, fundamental research was also concentrated on the glass microstructure processes. Significant fundamental research of phase separation in glasses is documented in [1-3].

The following glass systems were particularly important with regard to the glass formation systems that were used in the development of opal glasses:

- silicate glasses with fluoride additives [4,5]
- borosilicate glasses [6]

- phosphosilicate glasses with different additives [7,8].

In these glasses, the opalescence was produced with special phase separation processes or with the precipitation of microcrystals [9].

In his study on the structure of borate glasses, Bray [10,11] achieved revolutionary results with regard to fundamental research and materials development. Thus Bray's [9,10] findings also served as a guideline for the developments described in this paper. Furthermore, we are grateful for having been able to draw on numerous technical discussions with Professor Bray, a colleague of many years.

Since the opal effect of technical products differs from that of natural teeth, new objectives had to be set in the development of biomaterials for dental restorations. In addition, these biomaterials must demonstrate a high expansion capability, so that they can adapt to the natural tooth as well as to other biomaterials, which are processed together with the opal biomaterial. Therefore, linear coefficients of thermal expansion of approx.  $9.0\text{--}16.0 \times 10^{-6} \text{ K}^{-1} \text{ m/m}$  are required. Furthermore, the opalescence of these glasses must be similar to that of natural teeth. To ensure the optical qualities, the opal effect should remain virtually unchanged, even after repeated heat treatment of the final product.

## 2. EXPERIMENTAL

The experimental work was focused on producing a glass system that would permit the development of an opal glass for restorative dental applications on the basis of specifically controlled structural processes of the glass. In addition to the special opal effect, a high coefficient of thermal expansion and high temperature stability of all the properties (the opal effect and the coefficient of thermal expansion in particular) after various heat treatments up to approximately  $920^\circ\text{C}$  had to be achieved. To achieve crystal phases with high linear coefficients of thermal expansion, a glass formation system was selected, which would allow controlled phase separation and serve as a base glass for a glass-ceramic. Therefore, a base glass from the  $\text{SiO}_2\text{--Al}_2\text{O}_3\text{--K}_2\text{O--CaO--P}_2\text{O}_5$  system was selected. The main results of this study were the optimized chemical composition range of the glass-ceramic, the process of controlling the microstructure of the glassy matrix, and the mechanism of controlled crystallization.

In the experimental part, the glasses were melted between  $1500$  and  $1600^\circ\text{C}$ . Following appropriate homogenization and cooling, a glass frit was produced. The phase development and the microstructure of the glass were examined. The glass examined with regard to its phase development and microstructure had a grain size of less than  $90 \mu\text{m}$ . Opal glass-ceramic in monolithic form was produced from these glass grains with subsequent heat treatment of  $900\text{--}920^\circ\text{C}$  for  $1\text{--}1\frac{1}{2}$  hours, followed by graining and additional sintering at  $920^\circ\text{C}$  for 1 min.

Microstructure development was examined using scanning electron microscopy (Carl Zeiss, DSM 962) and possible crystal phase development using X-ray diffraction (Siemens D500, diffractometer using  $\text{Cu-K}_{\alpha}$ -radiation).

Thermal properties were determined with a dilatometer (Netsch, 402 TMA).

For the dilatometric measurements, samples measuring  $26 \times 6.5 \times 5$  mm were produced. Subsequently, plane-parallelism of the reference surfaces for the measurement of length were achieved by grinding and polishing. The test parameters for the dilatometric measurements were: heating rate of 5 K/min and an atmosphere of still air.

### 3. RESULTS

By systematically varying the experimental conditions, the chemical composition, the grain size of the base glass, and the thermal treatment of the base glass for controlled crystallization in particular, various opal glass-ceramics, have been developed for use in restorative dentistry. The initial results of these developments are particularly interesting with regard to the high coefficient of thermal expansion [12,13].

This paper focuses on the processes involved in the development of glass microstructures and the controlling of crystallization, paying particular attention to the effects of small quantities of additives and of  $B_2O_3$  in particular.

The opalescent biomaterial was achieved in the following composition range (in wt%) 53-59 $SiO_2$ , 13-17 $Al_2O_3$ , 9.5-12.5 $K_2O$ , 8-11 $Na_2O$ , 1.5-3.5 $CaO$ , 1.5-3.5 $P_2O_5$  with approx. 1-5% additives. Within this range of 1 to 5% additives, approx. 1 wt%  $B_2O_3$  demonstrated a favourable influence on the formation of the glass microstructure. The results are clearly visible in scanning electron micrographs.

The other additives used were 0.5%  $CeO_2$  and 1.0-3.0%  $ZrO_2$ .

#### 3.1. Surface crystallization

Figure 1 shows the microstructure of a glass-ceramic that was produced by heat treating a powder at 920°C. The process for manufacturing a powder that

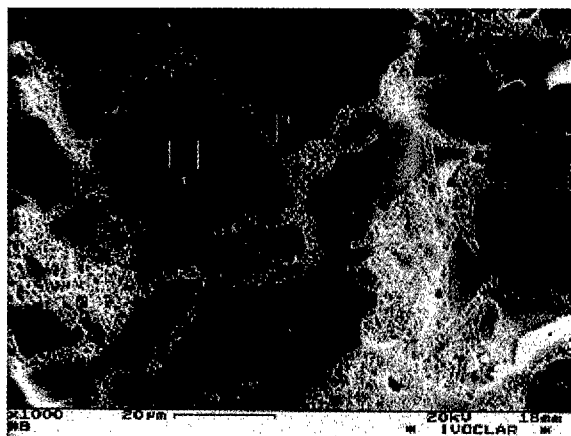


Fig. 1. Opal glass-ceramic after sintering at 920°C. Scanning electron micrograph, after HF etching (2.5% HF for 10 s) [12].

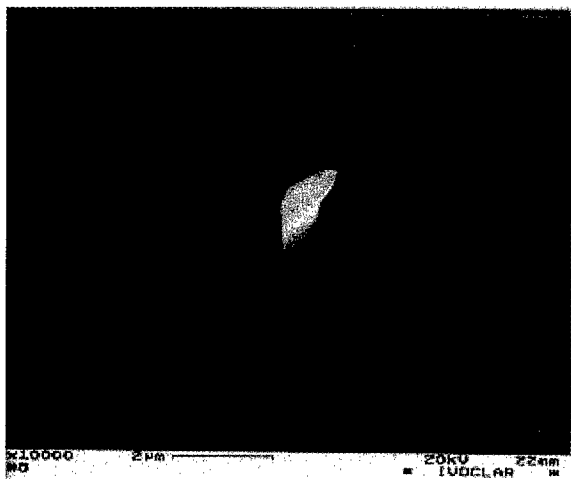


Fig. 2. Leucite nucleating two-dimensionally. Scanning electron micrograph.

can be sintered to form a dense glass-ceramic at approx. 920°C is characterized by the fact that the base glass powder with an average content of approx. 2.5 wt%  $P_2O_5$  and approx 0.9 %  $B_2O_3$  is initially heat treated. During the heat treatment of the base glass powder at 920°C, glass microstructure formation, sintering of the powder, and primary processes of nucleation and crystallization occur almost simultaneously. After the heat treatment, this glass-ceramic product is converted into a glass-ceramic powder and was additional heat treatment at 920°C, given the type of microstructure shown in Fig. 1.

Furthermore, Fig. 1 shows that sintering produces a dense product and reduces porosity. Figure 1 also reveals that crystallization has taken place at the



Fig. 3. Crystallization of leucite, originating from a nucleating centre. Petal-shaped growth pattern: SEM.

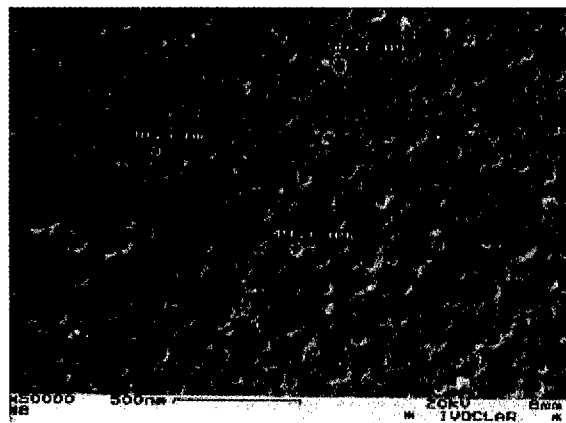


Fig. 4. Phase separation of the glass matrix according to excerpt 1 in Figure 1. The glassy droplet phase measures approx. 40-60 nm. SEM [12].

inner grain boundary. These inner grain boundaries are also called “ghost surfaces”, since the process of controlled surface nucleation and crystallization progress along them.

X-ray diffraction analysis has revealed that leucite,  $\text{KAlSi}_2\text{O}_6$ , develops during surface crystallization. The mechanism of the surface crystallization of leucite is comparable to that of cordierite,  $\text{Mg}_2\text{Al}_4\text{Si}_5\text{O}_{18}$ , which develops in an entirely different material system. The leucite nuclei are almost flat two-dimensional particles. These nuclei are clearly visible in a  $\text{P}_2\text{O}_5$  - and  $\text{CaO}$ -free base glass (Fig. 2) [14].

The crystalline leucite continues to develop from the nucleating centre. The small crystals grow around the nucleating centre like the petals of a flower (Fig. 3).

Glass-ceramics with different coefficients of thermal expansion were produced with leucite crystals of different sizes and densities. The tetragonal modification of leucite is known to have a very high coefficient of thermal expansion. Therefore, glass-ceramics with a coefficient of thermal expansion between  $12.0 \times 10^{-6} \text{ K}^{-1} \text{ m/m}$  and  $15.5 \times 10^{-6} \text{ K}^{-1} \text{ m/m}$  were developed. These materials were then used to develop glass-ceramics for dental applications.

### 3.2. Glass microstructure formation

The development of a reproducible and adjustable microstructure for the residual glass matrix presented an equally complex solid state reaction parallel to the surface crystallization of leucite.

Figures 4 and 5 show two excerpts (numbered 1 and 3) from Fig. 1, magnified by a factor of 50 000.

Figure 4 demonstrates that it was possible to produce a special type of phase separation of the residual glass matrix using the combined effects of  $\text{CaO}$ ,  $\text{P}_2\text{O}_5$ , and  $\text{B}_2\text{O}_3$ . This phase separation demonstrated an adequately high thermal stability to maintain the size of the droplet glass phase, even after a number

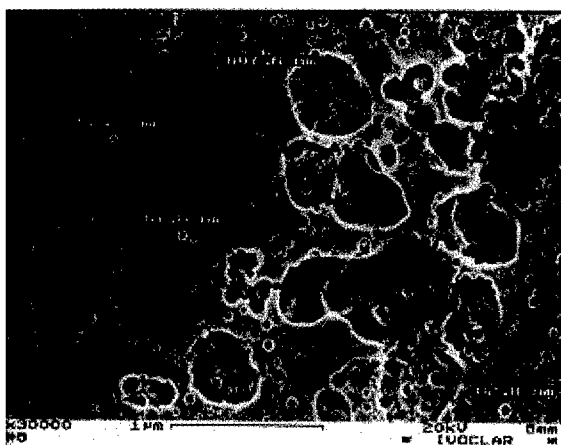


**Fig. 5.** Interface between two crystallized glass grains, showing etched leucite crystals and a phase separated glass microstructure (excerpt 3 in Figure 1) SEM [12].

of heat treatments at approx. 920°C. The glass phase neither dissolved in the glass matrix nor recrystallized. As a result, the opal effect was maintained.

Figure 5 shows the interface between two grains of crystallized glass powder. Clearly controlled surface crystallization has occurred. After nucleation was initiated, however, crystallization proceeded only partially and the growth of the leucite crystals was halted. As a result, growth towards the grain center also stopped.

#### 4. DISCUSSION

The results show that it is possible to produce glass-ceramics and at the same time control entirely different properties in a relatively complex system featuring multiple components. The properties involved were opalescence, a high coefficient of thermal expansion, and thermal stability of the glass-ceramic. These characteristics in addition to the required biocompatibility make the glass-ceramic suitable for use as a biomaterial.

In the development of this glass-ceramic two main mechanisms were controlled which would, from the point of view of materials science, usually influence each other directly. Under the experimental conditions selected, however, the processes were controlled almost separately by halting the surface crystallization of leucite in the kinetic growth process. Normally, an excessively high crystal content would negatively influence the transmission of light through the glass-ceramic and the desired opal effect would not have been visible. In this case, however, an adequate amount of crystals were formed to achieve a high coefficient of thermal expansion as well as a high degree of translucency. Therefore, the opal effect of the glass matrix was visible.

The liquid-liquid phase separation of the glass matrix phase is predominantly caused by the formation of a Ca(II)- and P<sub>2</sub>O<sub>5</sub>-rich droplet glass phase.

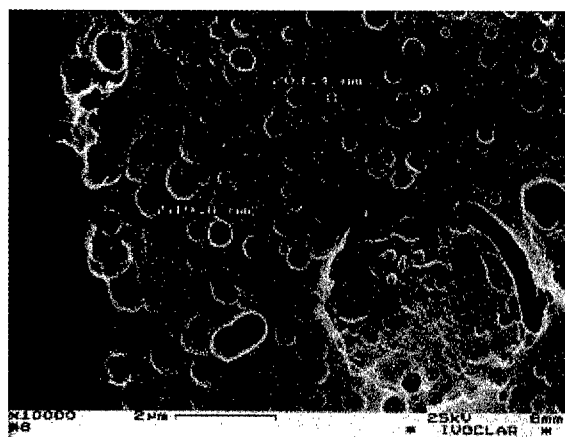


Fig. 6. Scanning electron micrograph of an opal glass-ceramic with leucite crystals and a high content of a glassy droplet phase.

This effect is in line with the fundamental research conducted on the phase separation for these glass systems. However, it has been observed that very small amounts of  $B_2O_3$  positively influence the process of phase separation, without initiating nucleation and crystallization in this glass phase.

Figure 6 shows the microstructure of a glass-ceramic demonstrating a droplet glass phase of up to 500 nm. This size is clearly the upper limit at which

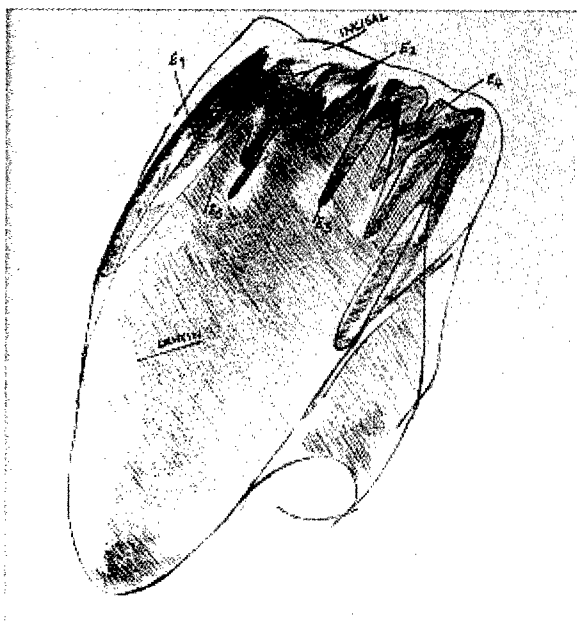


Fig. 7. Diagram of the application of five types of opal materials (E1-E5).



transmission is not significantly impaired.

At the same time, however, an adequate amount of droplet phases between 100 and 200 nm are present. These phases are responsible for the development of the opal effect.

## 5. CONCLUSION

The biomaterial which was developed is suitable for dental applications because of its favourable properties. Figure 7 shows five products (labeled E1 to E5) with chemical compositions in the range discussed. They have a different degree of opalescence and transmission [15]. Each of these glass-ceramics is applied to a different part of the incisal of dental crowns in a sintering procedure. In this way, artificial crowns, even those with metal superstructures as shown in Fig. 7, can be reconstructed according to their natural counterpart. The result is a restoration that is virtually indistinguishable from the natural tooth from an optical, functional, and biochemical perspective.

## 6. REFERENCES

- [1] W.D. Kingery, H.K. Bowen & D.R. Uhlmann, *Introduction to Ceramics*. John Wiley & Sons, New York (1975).
- [2] W. Vogel, *Glaschemie*, Deutscher Verlag für Grundstoffindustrie, Leipzig (1979).
- [3] D.R. Uhlmann & N.J. Kreidl, *Glass, science and technology*, Vol. 1 Glass-forming systems. Academic Press, Orlando (1983).
- [4] J.M. Parker, J.A.M. Al-Dulaimy & Q.A. Juma, *Glass Technol.* **25** (1984) 180.
- [5] P.P. Pirooz, US Patent 3 647 490 (1972).
- [6] W. Haller, D.H. Blackburn, F.E. Wagstaff & R.J. Charles, *J. Am. Ceram. Soc.* **53** (1970) 34.
- [7] W. Sack, German patent DE 2313074 (1973).
- [8] N.T. E.A. Baak & C.F. Rapp, US Patent 3 506 464 (1970).
- [9] T.F. Bates & M.V. Black, *Glass Ind.* **29** (1948) 487.
- [10] P.J. Bray, *J. Non-Cryst. Solids* **75** (1985) 29.
- [11] P.J. Bray, In: W. Vogel, *Glaschemie*, (Dt. Verlag für Grundstoffindustrie, Leipzig 1979), pp. 81-91.
- [12] W. Höland, M. Frank & V. Rheinberger, *Thermochim. Acta* **280-1** (1996), 491.
- [13] W. Höland, M. Frank, M. Schweiger & V. Rheinberger, *Glastech. Ber. Glass Sci. Technol.* **67 C** (1994) 117.
- [14] W. Höland, M. Frank & V. Rheinberger, *J. Non-Cryst. Sol.* **180** (1994) 292-307.
- [15] W. Höland, V. Rheinberger, M. Frank & S. Wegner, *Bioceramics* **9** (1996), 445.

## HALOBORATE GLASS-CERAMICS AS X-RAY STORAGE PHOSPHORS

K. PAPADOPOULOS

*Materials Science & Engineering Division,  
Eastman Kodak Company, Rochester, NY 14650-2022, USA*

and

K. SIEBER

*Coating Technologies Division, Eastman Kodak Company,  
Rochester, NY 14650-2033, USA*

Extensive glass formation has been shown in barium haloborate systems. Thermal treatment of selected glasses has precipitated crystalline phases which, in the presence of an activating dopant, act as x-ray storage phosphors. Glass-ceramics have been demonstrated which have a potential use as x-ray storage materials.

### 1. INTRODUCTION

Certain crystals, when doped with a suitable activator such as  $\text{Eu}^{2+}$ , act as x-ray storage phosphors. X-rays produce metastable defects called F-centres, whose stored energy is released on exposure to light as photostimulated luminescence (PSL), or to heat as thermally stimulated luminescence. PSL is used in storage screens; the x-rays form a latent image, which can be "read" by laser scanning and stored digitally in a computer file for later retrieval. The latent image can be erased and the screen reused. This technology is known as computed radiography [1]. Currently, x-ray storage screens are made by coating dispersions of phosphor particles onto flexible supports, by techniques common in the photographic industry.

This work was prompted by the idea that the technology of glass-ceramics might be useful in making x-ray storage screens, if a storage phosphor could be precipitated. The resolution of a radiographic imaging screen depends largely on the phosphor particle size and its distribution. Glass-ceramics offer the possibility of controlling both of these variables to prepare improved imaging plates, and one can envisage storage screens which would be mechanically tough and chemically resistant to repeated cleaning. Several barium-containing halides exhibit PSL when host to suitable activators. Examples are  $\text{BaFBr}$  [2],  $\text{BaFBr}_x\text{I}_{(1-x)}$  [3], both now used in storage screens, and  $\text{Ba}_2\text{B}_5\text{O}_9\text{Br}$  [4]. (In the remaining text, any reference to a storage phosphor implies the presence of an activating species).

Oxide and halide glass systems are familiar in technology and industry. However, except for fluoride-containing systems, overlap between them is relatively uncommon. Container- and flat-glasses have no significant halide, while the fibre optic community requires halide glasses to be as oxide-free as possible, to minimize infrared absorption. Known oxyhalide glass systems with halides other than fluoride include  $B_2O_3$ - $Na_2O$ - $NaCl$  [5],  $B_2O_3$ - $Li_2O$ - $LiCl$  [6,7],  $B_2O_3$ - $SiO_2$ - $Li_2O$ - $LiCl$  [7], and  $B_2O_3$ - $AgX$ - $Ag_2O$  ( $X=Cl, Br, I$ ) [8], which are of interest as fast-ion conductors. Luminescent glasses are reported in the  $B_2O_3$ - $BaF_2$ - $BaBr_2$  system [9], and optical glasses involving  $TeO_2$  [10] and  $Sb_2O_3$  [11,12] with various metal halides have been prepared. In this work, extensive glass formation was shown in the systems  $B_2O_3$ - $BaO$ - $BaBr_2$  and  $B_2O_3$ - $BaO$ - $BaFBr$ , which provided precursor compositions for glass-ceramics, and  $B_2O_3$ - $BaO$ - $BaCl_2$ , whose devitrification behaviour was not investigated.

## 2. EXPERIMENTAL

Compositions intended only to show glass formation were melted in a box furnace in air, in 5-10 g quantities. To evaluate PSL behaviour, Eu was introduced as an activator; glasses were melted in a horizontal fused silica tube furnace under a reducing atmosphere (4%  $H_2$  in Ar), to convert  $Eu^{3+}$  to  $Eu^{2+}$ . Porcelain or alumina crucibles were used. By the examination of corrosion profiles under a microscope, it was estimated that dissolved crucible material did not exceed ~0.5 wt% of the glass.

### 2.1. Undoped Glasses

Mixtures of  $B_2O_3$ ,  $BaCO_3$  and the appropriate barium halide(s) were prereacted at 700°C, then melted at 950-1100°C, depending on composition. Prereaction avoided too rapid an evolution of  $CO_2$  from the  $BaCO_3$ , which would cause the melt to "boil over". After 30 min. at the final temperature, melts were poured into a graphite mould and put into an annealing furnace at ~450°C, which was allowed to cool to room temperature at its natural rate. Some melts outside the glass-forming region crystallized uncontrollably on cooling. In others, two immiscible liquids were visible as distinct layers when poured. Still others did not completely melt up to 1100°C, the upper limit of the furnace.

### 2.2. Europium-doped Glasses

Europium was introduced into the major ingredients as  $Eu_2O_3$ . Batches were prereacted overnight at 650-700°C to ensure complete reduction of  $Eu^{3+}$  to  $Eu^{2+}$ . The furnace was programmed to heat up over 1.5 h to the melting temperature, which was maintained for 0.5 h. The glass was quickly poured into carbon moulds and cooled gradually to room temperature from 450°C. Europium content was normally calculated as an equimolar substitution of  $EuO$  for  $BaO$ .

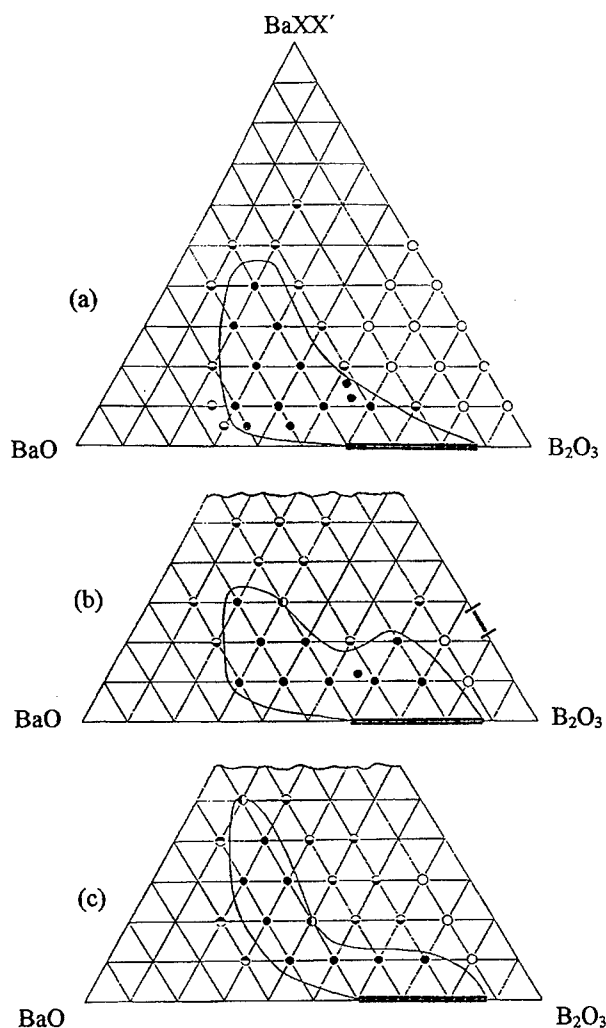


**Fig. 1.** Glass-forming regions in the systems  $B_2O_3$ -BaO-BaXX': (a)  $X=X'=\text{Br}$ ; (b)  $X=\text{F}$ ,  $X'=\text{Br}$ ; (c)  $X=X'=\text{Cl}$ . ● glass former; ◐ borderline glass-former; ◑ crystallization; ○ two liquids; ⊖ did not melt  $<1100^\circ\text{C}$ ; — approximate range of Ref. [9] glasses; -----  $B_2O_3$ -BaO glass-forming region [13].

### 3. GLASS FORMATION AND DEVTRIFICATION

#### 3.1. Glass-forming Compositions

Glass-forming regions in the  $B_2O_3$ -BaO-BaBr<sub>2</sub>,  $B_2O_3$ -BaO-BaFBr and  $B_2O_3$ -BaO-BaCl<sub>2</sub> systems, determined from this work, are shown in Fig. 1; they are remarkably extensive, occupying 20-25% of the available composition space. Glass formation is reported along the  $B_2O_3$ -BaFBr binary [9], but was not found in  $B_2O_3$ -BaBr<sub>2</sub> and was not investigated in  $B_2O_3$ -BaCl<sub>2</sub>.

One glass-forming composition in the  $B_2O_3$ -BaO-BaBr<sub>2</sub> system is  $5B_2O_3 \cdot 3BaO \cdot BaBr_2$ . It has the same stoichiometry as the known crystal  $Ba_2B_5O_9Br$ , which behaves as a storage phosphor. This is the first known example of a storage phosphor also forming a glass.

In the system  $B_2O_3$ -BaO-BaFBr, the composition  $2B_2O_3 \cdot 5BaO \cdot 3BaFBr$  ("2:5:3"), as a glass-former nearest to the BaFBr apex, was chosen for devitrification studies. However, quantities larger than ~5 g crystallized on cooling. To try to stabilize the glass, some of the  $B_2O_3$  was substituted by  $SiO_2$ , with only slight improvement. Further into the vitreous region,  $SiO_2$  substitution was more effective; in some cases up to a third of the  $B_2O_3$  could be replaced to give stable glasses which melted at temperatures up to 1100°C.

### 3.2. Devitrification Behaviour

**3.2.1.  $B_2O_3$ -BaO-BaBr<sub>2</sub>** - When  $Ba_2B_5O_9Br$  with EuO at a mole fraction of 0.01 was melted, it formed a yellow glass. After a heat-treatment of 2 h in air at 700°C, the glass became opaque and pale yellow. The devitrified product retained its integrity and strength when quenched directly into water. Three forms of  $Ba_2B_5O_9Br$  were examined by x-ray powder diffraction. As expected, the glass showed no Bragg peaks. The crystalline compound (made by reacting the raw materials in the solid state at 800°C) and the devitrification product showed identical peaks, but  $BaB_2O_4$  and another unidentified phase were also indicated in the latter.

A series of melts was made, in which EuO from 0.0001 to 0.1 was substituted for the equivalent mole fraction of BaO. Glass colour ranged from pale yellow to amber as the Eu content increased. Each glass was devitrified and the PSL of the resulting glass-ceramic measured.

**3.2.2.  $B_2O_3$ -BaO-BaFBr** - In contrast to  $Ba_2B_5O_9Br$ , BaFBr is an established commercial storage phosphor, and glasses in which it is a major component are therefore of interest. In the system  $B_2O_3$ -BaO-BaFBr, it should crystallize from glasses nearest to the BaFBr apex. X-ray powder diffraction confirmed its presence in the devitrified 2:5:3 composition.

## 4. PHOTOSTIMULATED LUMINESCENCE OF DEVITRIFIED GLASSES

### 4.1. $B_2O_3$ -BaO-BaBr<sub>2</sub>

Table 1 shows PSL data for the three forms of  $Ba_2B_5O_9Br$  with EuO = 0.01, and a BaFBr:Eu reference phosphor. The response is the peak voltage generated by a photomultiplier from samples irradiated with a He-Ne laser. Vitre-

Table 1

PSL (Volts) for Different Forms of  $Ba_2B_5O_9Br$ :Eu and a BaFBr:Eu Reference Phosphor

X-ray dose (Rem)	Crystalline	Glass	Glass-ceramic	Reference
0.0015	0	0	0	3.8
17.7	5.6	0	0.6	Not measured

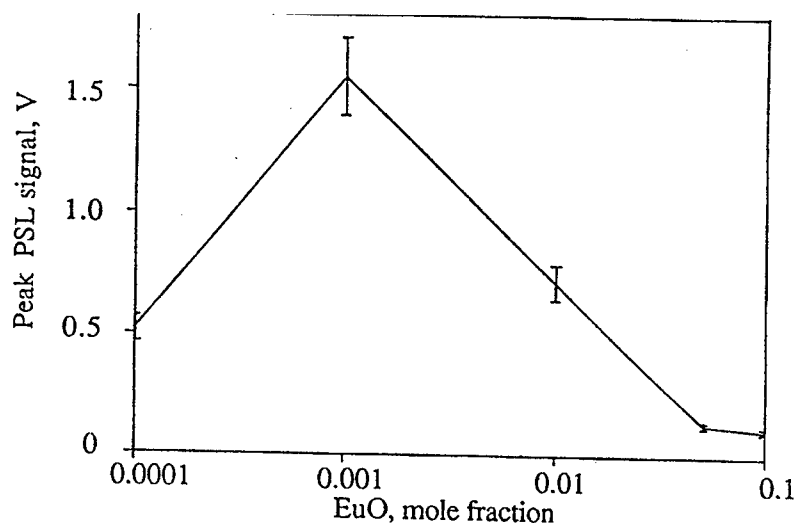


Fig. 2. Effect on PSL of EuO substitution for BaO in  $\text{Ba}_2\text{B}_5\text{O}_9\text{Br}$ . EuO concentration is relative to 1 mole of the equivalent  $0.56\text{B}_2\text{O}_3 \cdot 0.33\text{BaO} \cdot 0.11\text{BaBr}_2$ . The glasses were devitrified at  $675^\circ\text{C}$  for 16 h and exposed to an x-ray dose of 17.7 Rem.

ous  $\text{Ba}_2\text{B}_5\text{O}_9\text{Br}$  gave no response. More surprisingly, the crystals and glass-ceramic responded only to a high x-ray dose. Fig. 2 shows the PSL of the glass-ceramic EuO series referred to earlier. Even the peak response, at  $\text{EuO} = 0.001$ , was still very weak.

#### 4.2. $\text{B}_2\text{O}_3$ -BaO-BaFBr

Melts of 2:5:3 with 0.1 mol% EuO were made in a 25 mm diameter carbon mould at  $975^\circ\text{C}$  in a reducing atmosphere, then cooled to  $800^\circ\text{C}$  over 3 h. The resulting buttons emerged opaque and yellow, with a coarse crystalline appearance, and pits in the surface where bubbles had formed. However, in contrast to any previous sample, the material showed PSL after exposure to 1.5 mRem, a low x-ray dose similar to those used in medical radiography.

### 5. COMPOSITION FOR X-RAY IMAGING TESTS

The silica-stabilized composition  $22\text{B}_2\text{O}_3 \cdot 5\text{SiO}_2 \cdot 49.9\text{BaO} \cdot 0.1\text{EuO} \cdot 0.23\text{BaFBr}$  was chosen for imaging tests. Gold was introduced to promote uniform nucleation. The gold source was an atomic absorption standard gold solution (1 mg Au per ml in 5% HCl), diluted so that the required amount of Au was added via 1 ml of solution per 10 g of prereacted batch. This wet the batch uniformly without flooding. After drying, the batch was ground in a mortar and mixed well before melting.

Samples with increasing Au levels were heat-treated at  $775^\circ\text{C}$  (previously determined from screening experiments as a suitable temperature) for 4 and 16 h. Their PSL responses, plotted against Au content in Fig. 3, are higher for the

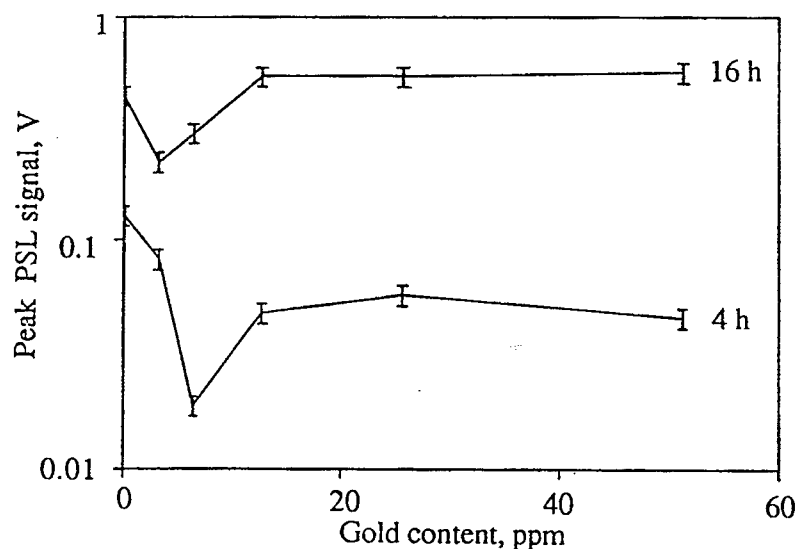


Fig. 3. Effect of the concentration of Au nucleating agent on peak PSL. Glasses of the composition  $22\text{B}_2\text{O}_3 \cdot 55\text{SiO}_2 \cdot 49 \cdot 9\text{BaO} \cdot 0 \cdot 1\text{EuO} \cdot 23\text{BaFBr}$  were heated to  $775^\circ\text{C}$  for 4 or 16 h, then exposed to an x-ray dose of 1.5 mRem.

16 h samples; the PSL falls at first, then recovers to a plateau at ~13 ppm Au. Except for initial additions, then, gold does not degrade the PSL response. Although higher Au levels might promote more uniform crystallization, it was decided to scale up to 75 g melts with 13 ppm of gold.

Batches were prereacted at  $675^\circ\text{C}$  for 16 h in a reducing atmosphere, heated slowly to  $1000^\circ\text{C}$ , held for 20 min, and poured into 70 mm diameter graphite moulds in which the resulting glass was cooled in an annealing furnace from  $450^\circ\text{C}$  to room temperature. The clear greenish discs were then heat-treated at  $775^\circ\text{C}$  for 16 h, under the reducing atmosphere, and cooled slowly to room temperature. The products showed considerable shrinkage. They were opaque and light green, but with some patches of white speckles. For the imaging tests, each disc was ground flat on both faces to a thickness of ~4 mm.

## 6. IMAGING TESTS

The glass-ceramic plates were used as sensors in the imaging tests. Images were acquired by a computed radiography scanning system which was constructed at the Kodak Research Laboratories. Scans were taken using a 30 mW laser at 633 nm with a  $100\text{ }\mu\text{m}$  pixel size. The scan rate was  $17 \cdot 5\text{ }\mu\text{s}$  per pixel. Initial examinations of noise were done using a Faxitron x-ray generator, with a tungsten source operating at 80 kV with 0.5 mm Cu and 1.5 mm Al filtration. The actual dose under these conditions was about 80 mRem.

The flat-field exposure showed considerable noise which was largely correlated with the patchy areas visible to the naked eye. Images of a lead bar taken

at 50 kV using a 30 s exposure with 1.5 mm Al beam filtration showed visual resolution out to 3 cycles/mm. This result is surprisingly good, given the flat field noise and large sample thickness, and suggests that a small crystallite size is present in the glass-ceramic. However, the flat-field noise made it difficult to see any detail in images of bone fragments.

## 7. DISCUSSION

Unexpectedly extensive glass formation in the barium haloborate systems has allowed the precipitation of known storage phosphors by the glass-ceramic process, and the fabrication of photostimulable x-ray imaging plates. This suggests that other haloborate systems, and perhaps other mixed halide-oxide systems, may be ripe for investigation. For example, one may envisage glasses in the  $\text{SiO}_2\text{--BaO--BaBr}_2$  and  $\text{GeO}_2\text{--BaO--BaBr}_2$  systems, from which the storage phosphors  $\text{Ba}_5\text{SiO}_4\text{Br}_6$  [14] and  $\text{Ba}_5\text{GeO}_4\text{Br}_6$  [15] might be precipitated. Also, one might be able to produce and identify hitherto unknown phases which would otherwise come to light only after extensive and laborious solid-state syntheses.

The imaging plates which were demonstrated are far from uniform. However, bearing in mind that this was only a preliminary study to demonstrate feasibility, it is very likely that, by modifying melt compositions and properties, and by better control of the melting and devitrification processes, one could fabricate much improved materials.

## 8. CONCLUSION

Extensive glass formation has been shown in barium haloborate systems (sometimes with added silica) and may be expected in other oxyhalide systems. It is possible by thermal treatment to form glass-ceramics in which a storage phosphor is present as the crystalline phase. Radiographic imaging experiments with glass-ceramic plates as x-ray sensors indicate that they do indeed function as photostimulable x-ray imaging plates.

## Acknowledgments

The authors gratefully acknowledge the following members of the Health Imaging Research Laboratory, Eastman Kodak Company: D. Trauernicht for performing the x-ray imaging evaluations, and P. Bryan for his support of this work.

## REFERENCES

- [1] G. Luckey, U.S. Pat. no. 3 859 527 (January 7, 1975).
- [2] K. Takahashi, J. Miyihara & Y. Shibahara, *J. Electrochem. Soc.* **132** (1985), 1492.
- [3] K. Takahashi, Y. Hosoi & Y. Kojima, Eur. Pat. no. 0 142 734 (May 29, 1985).
- [4] A. Meijerink & G. Blasse, *J. Lumin.* **43** (1989), 283.
- [5] F.Y. Tsang, U.S. Pat. no. 3 829 331 (August 13, 1974).
- [6] D.P. Button, R.P. Tandon, H.L. Tuller & D.R. Uhlmann, *J. Non-Cryst. Solids* **42** (1980), 297.
- [7] K. Otto, *Phys. Chem. Glasses* **7** (1966), 29.



- [8] T. Minami, T. Shimizu & M. Tanaka, *Solid State Ionics*, **9-10** (1983), 577.
- [9] C. Bueno, R. A. Buchanan & H. Berger, *Proc. SPIE* **1327** (1990), 79.
- [10] V. Kozhukharov, M. Marinov, I. Gugov, H. Bürger & W. Vogel, *J. Mater. Sci.* **18** (1983), 1557.
- [11] B. Dubois, H. Aomi, J. Portier & P. Hagenmuller, *Mater. Res. Bull.* **19** (1984), 1317.
- [12] J. Portier, J.J. Videau, B. Dubois & J. Cottrant, *Mater. Sci. Forum* **5** (1985), 155.
- [13] H. Rawson, *Inorganic Glass-Forming Systems* (Academic Press, London, 1967), p 98.
- [14] A. Meijerink & G. Blasse, *Mater. Chem. Phys.* **21** (1989), 261.
- [15] A. Meijerink & G. Blasse, *J. Phys. D: Appl. Phys.* **24** (1991), 628.

## LIQUID-GLASS TRANSITION IN $B_2O_3$

Lars BÖRJESSON

*Department of Applied Physics,  
Chalmers University of Technology,  
S- 412 96 Goteborg, Sweden*

The dynamics of the liquid-glass transition, as well as the dynamics of glasses in general, are much debated current issues in condensed matter physics. It is well known that various inorganic, polymeric and organic liquids can easily be supercooled down to the solid glassy state, but it is an open question whether the dynamics in the transition region of systems with such different microscopic interactions follow some general scenario. An enormous experimental interest in the phenomena has been triggered by the recent theoretical progress of the mode-coupling theory for the understanding of the transition. Inspired by the predictions of the mode-coupling theory most recent experimental studies of the transition scenario have concentrated on the so called fragile glassformers, i.e. those with weak interparticle forces such as molecular and ionic glassformer, and found at least qualitative agreement with the theory. In order to extend the experimental tests also to stronger network glass we have investigated the dynamics in the glass transition region as well as in the glassy state of the relatively strong glassformer  $B_2O_3$  with light and neutron scattering techniques. A review of the results will be given and they will be discussed in relation to current theories for the liquid-glass transition.

## RELAXATION PROCESSES IN BORATE MELTS

Brian J. REARDON, John KIEFFER, John E. MASNIK  
*Department of Materials Science and Engineering*

and

Jay D. BASS  
*Department of Geology, University of Illinois,  
Urbana, IL 61801, USA*

Using Brillouin light scattering we have measured the complex mechanical modulus, describing the dynamic behavior of molecular structures in liquid borates, as a function of temperature and composition. The determination of shear and bulk viscosities, as well as the complex Poisson ratio at GHz frequencies, provides detailed insight into the structural evolution during glass formation. Accordingly, the boron-oxygen network undergoes two distinct structural reorganizations when cooled from its most fluid state to a rigid glass. One reorganization is between the completely dissociated structure and a three-dimensional random network. This process is activated above 1300°C. A second reorganization, between 1300°C and  $T_g$ , yields percolating domains of a more ordered and rigid structure, possibly containing layers with a large concentration of boroxol rings.

### 1. INTRODUCTION

Due to their low melting temperatures, borate glasses are attractive for applications, ranging from solid electrolytes in batteries and sensors [1,2], to in-line optical amplifiers [3,4]. The rather poor chemical durability of borates, in particular in the presence of water, has prompted a continuing quest for improvements in these properties through alloying with stabilizing compounds. At the same time, the glass forming ability of the substance cannot be compromised. Our research focuses on the fundamental aspects of glass formation, i.e. on the structural dynamics of a glass forming melt upon cooling.

Using Brillouin light scattering, we determine the complex mechanical modulus of molecular scale structures. These structures are probed in the GHz frequency regime, making this technique sensitive to features with correlation lengths of about 100 nm (i.e. the wavelength of thermal phonons at that frequency). Furthermore, energy dissipating processes revealed in this experiment have a lifetime of the order of nanoseconds, and include elementary transport phenomena and reorientation of small structural entities. These time- and length domains

are most relevant for processes that become thermally activated in the vicinity of the glass transition. In this paper we summarize the results for boron oxide and binary alkali borates, and show how the mechanical impedance, measured on this scale, can elucidate the structural dynamics of supercooled liquids.

## 2. EXPERIMENTAL

Details concerning the experimental setup and the measurement procedure have been given elsewhere [5,6]. In short, glasses were prepared from powders of boric acid and alkali carbonates, with a total impurity content of less than 0.2% by weight. Specimens were suspended in a platinum wire loop and mounted in a gas-tight furnace. In order to reduce their water contamination, samples were first heated to the highest temperature and held for about 12 to 16 h. During this time, and throughout the measurements, the furnace chamber was purged with dried air, containing less than 3 ppm of water.

Incident light was provided by a Ar laser at a wavelength of 514.5 nm. The scattered light was collected at 90° with respect to the incident direction, and was analyzed using a six-pass tandem Fabry-Perot interferometer. The frequency spectrum of the scattered light was deconvoluted, to free it from instrumental broadening, and was then fitted with the expression for the dynamic structure factor,  $S(\mathbf{q}, \omega)$ , derived in the framework of the generalized hydrodynamic theory [7]. Accordingly, the frequency of the inelastically scattered light is shifted from that of the incident light by the amount  $c_0 q$ , where  $c_0$  is the velocity of sound and  $\mathbf{q}$  the scattering wavevector, which is defined by the scattering geometry. From the sound velocities one can evaluate the elastic constants, which in the case of longitudinal sound waves corresponds to the longitudinal storage modulus,  $M'$ , and for transverse waves to the shear modulus,  $G'$ . In an isotropic medium, these two measures are sufficient for the determination of all elastic constants.

The linewidth  $\Gamma$  of the Brillouin peak is controlled by the combined effects of viscosity and thermal diffusivity. The latter quantity can be eliminated with the help of the Rayleigh peak width, to yield the viscosity,  $\eta'(\omega)$ . Finally, assuming linear viscoelasticity, one can relate the viscosity to the loss modulus,  $M''$ , by means of the simple relationship,  $M'' = (c_0 q) \eta'$ . Hence, as long as we can discern the spectral features corresponding to both the longitudinal and the transverse sound waves, we are in a position to not only obtain all elastic constants for the melts, but we can get the complex values of these moduli. In particular, based on the relationship between longitudinal and shear moduli,  $M^* = K^* + 4/3 G^*$ , we can extract the complex bulk modulus, of which the real component corresponds to the reciprocal of the compressibility of the liquid, and the imaginary component to the bulk viscosity multiplied by the probing frequency.

## 3. RESULTS

In Fig. 1, we show the longitudinal storage and loss moduli of selected sodium borate systems, as a function of temperature. The storage modulus of the glasses has a weak temperature dependence. The glass transition is marked by a change of

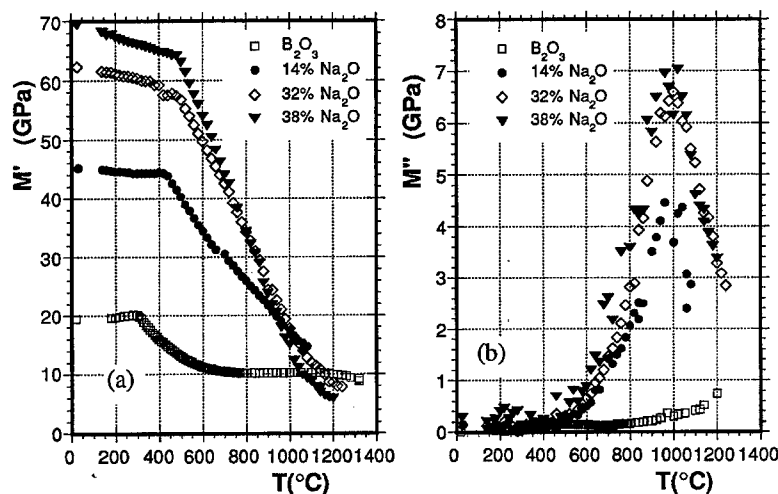


Fig. 1. Storage (a) and loss (b) modulus of sodium borates as a function of the temperature, and for various compositions.

slope in the data, and above  $T_g$ , the rate of structural degradation increases with increasing fragility of the liquid. At the highest temperatures of these measurements, the values of the storage moduli for different systems are rather close. At these temperatures, any resistance to shear deformation in the liquids is likely to be lost, and the value of the longitudinal modulus amounts to that of the bulk modulus. The loss modulus exhibits a maximum on the temperature scale, and the peak intensity is larger the higher the alkali concentration.

At first sight, the combination of storage and loss moduli appear to follow closely the behavior expected of those of linear-viscoelastic media, i.e., the loss modulus peaking at conditions where the substance transforms from a rigid to a fluid structure. However, thermo-rheological simplicity requires that the maximum loss modulus amounts to half of the difference between the storage moduli of the rigid and fluid state of the substance [8]. Comparing scales in Figs 1a and 1b, this is obviously not the case, especially in systems with low alkali concentrations.

In Fig. 2, the loss modulus of pure  $B_2O_3$  is shown as a function of temperature. The appearance of a small hump at low temperatures suggests that several distinct mechanisms are invoked upon changing the structure of boron oxide from the glass to the high-temperature melt. The data has therefore been fitted with a linear combination of Debye terms,

$$M'' = \sum_j \left( M_{2,j} \frac{\omega \tau_{0,j} e^{E_{A,j}/k_B T}}{1 + \omega^2 \tau_{0,j}^2 e^{2E_{A,j}/k_B T}} \right) \quad (1)$$

where  $M_{2,j}$  is the relaxational modulus,  $\tau_0$  is the relaxation time constant, and

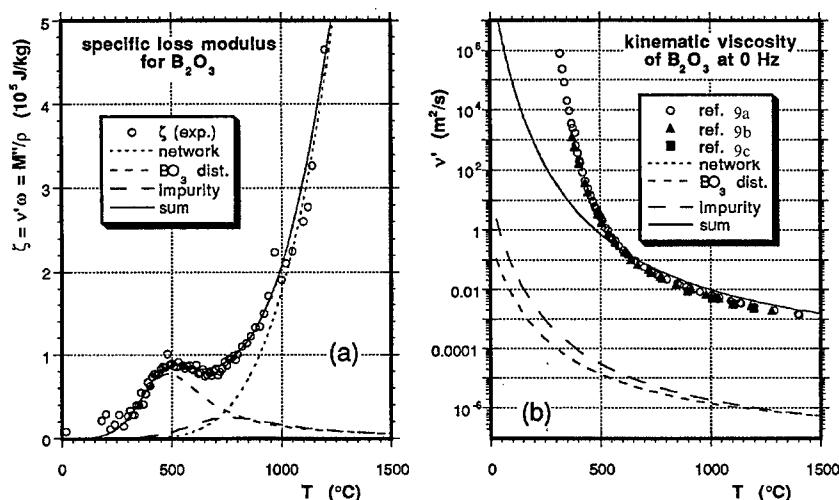


Fig. 2. (a) High-frequency viscosity of boron oxide, as extracted from Brillouin spectra, and (b) comparison with rotational viscometry data [9], after conversion to zero frequency.

$E_A$  the activation energy of the relaxation process. The index  $j$  refers to a particular mechanism. A total of three terms, representative of three different mechanisms, provides a reasonably good agreement. When dividing the loss modulus by the probing frequency, and when setting the remaining  $\omega$  in the denominator of Eq. (1) to zero, one obtains the zero-frequency viscosity. This has been done for each term in the linear combination describing the Brillouin data, and is shown in Fig. 2b. The dashed patterns for the lines representing individual mechanisms has been preserved between the two graphs. However, the curve corresponding to high-temperature mechanism cannot be resolved from that of the sum of all contributions, in Fig. 2b. Also shown in this figure are viscosity data obtained by rotating cylinder viscometry, from three different sources. The agreement between the rotational viscometry data and that extrapolated from the Brillouin results is rather good, but only above 500°C. On the other hand, the viscous dissipation during fluid flow appears to be dominated by the high-temperature mechanism, and as can be seen in Fig. 2a, is registered by the Brillouin technique only above 500°C. Hence, the disagreement below that temperature is not between measured quantities, but because of a change in the dominant relaxation mechanism. On the other hand, the comparison made in Fig. 2b shows that the magnitude of the loss modulus is not flawed due to the neglect of any procedural peculiarities.

#### 4. DISCUSSION

While the Brillouin probe is no longer sensitive to the slow processes which dissipate energy in macroscopic flow, it still is capable of detecting some low-energy mechanisms of structural rearrangement, which become activated immediately above  $T_g$ . The hump in the loss modulus (or viscosity) data, observed

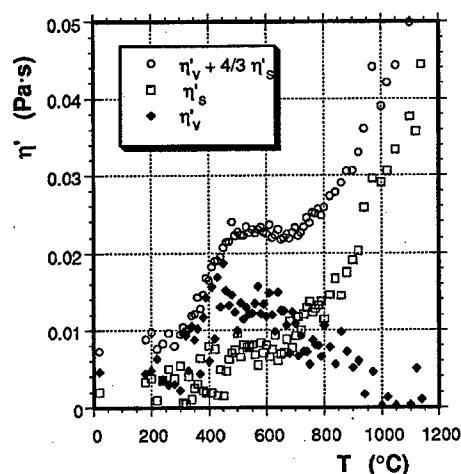


Fig. 3. Longitudinal, shear, and bulk viscosities of boron oxide as a function of temperature.

between 300°C and 800°C, is very reproducible. Due to a series of experiments described earlier [10], we can rule out impurities as the cause for this hump. However, an interesting observation can be made when extracting bulk and shear viscosities separately from the Brillouin data. The results are shown in Fig. 3. It turns out that the hump at low temperatures can be almost entirely attributed to energy losses during isotropic compressional deformations, while at higher temperatures most losses occur upon shear deformations.

As mentioned earlier, the measurement at high frequencies allows one to determine both complex conjugate components of mechanical moduli. The same holds true for the Poisson ratio, since it can be expressed as a function of the longitudinal and shear moduli, according to

$$\nu = \frac{M^* - 2G^*}{2(M^* - G^*)} = \nu' + i\nu'' \quad (2)$$

The real and imaginary component of the Poisson ratio for  $B_2O_3$  are shown in Fig. 4, as a function of temperature. The glass transition and structural degradation towards higher temperatures is quite obvious from the real part of  $\nu$ . Interestingly, though,  $\nu$  plateaus before reaching the value of 0.5, which would be characteristic of an incompressible liquid. Moreover, the imaginary component of  $\nu$  is non-zero. This means that in an oscillatory deformation there is a phase shift between elongation in direction of the applied stress and contraction perpendicular to that direction. One can show that negative values for  $\nu''$  mean that the perpendicular contraction lags behind the elongation in the direction of the applied stress. If  $\nu''$  is positive, on the other hand, the opposite is true [11].

This latter scenario is perhaps less intuitive, and we suggest the following

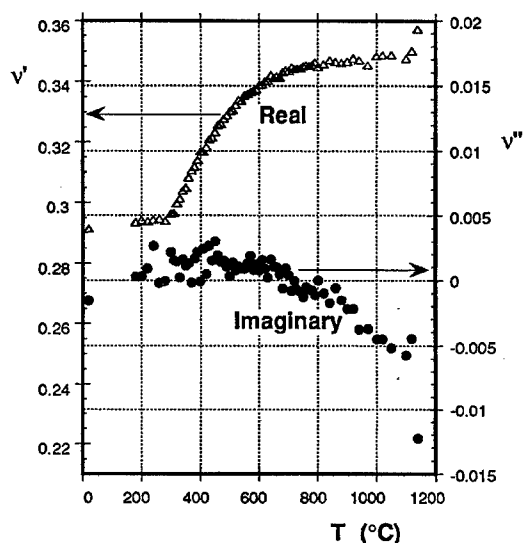


Fig. 4. Complex Poisson ratio for boron oxide as a function of temperature.

interpretation: The structure of  $B_2O_3$ , just above  $T_g$ , must be such that compression is required to facilitate some kind of disengagement mechanism, and render the structure more compliant. One possible scenario amenable to this picture would be the breakdown of boroxol rings. Suppose that in a configuration with large concentration of boroxol rings [12], these rings would arrange in an energetically stable manner, i.e. by seeking to pair the borons of one ring with the oxygens of a neighboring ring, and vice versa. When rings approach closely, say as a result of thermal motion, and the boron moves out from its  $BO_3$  plane, it can become temporarily coordinated with four oxygens, and can then be pulled into a new triangle containing one oxygen which is different. Such a mechanism has been observed in molecular dynamic computer simulations of  $B_2O_3$  [13]. The boron and oxygen which each have lost a bonding partner in this process are next to bond. Hence, all coordination requirements remain preserved, but the topology within the structure has changed. In effect, the average ring size increases, creating a more flexible structure.

While this proposed mechanism can account for the positive values of the imaginary part of the Poisson ratio between  $T_g$  and  $800^\circ C$ , and for the fact that within the same temperature range, viscous dissipation mostly results from collisions during dilatational deformations, the mechanism also implies the existence of topologically and energetically distinct structural states, and the transformation between them as a result of temperature changes. The assumption of such distinct structural states was underlying to the development of a modified viscoelastic model, which can explain the discrepancy between the magnitudes of the maximum loss modulus and of the decrease in storage modulus. This model can easily be generalized to encompass a distribution of



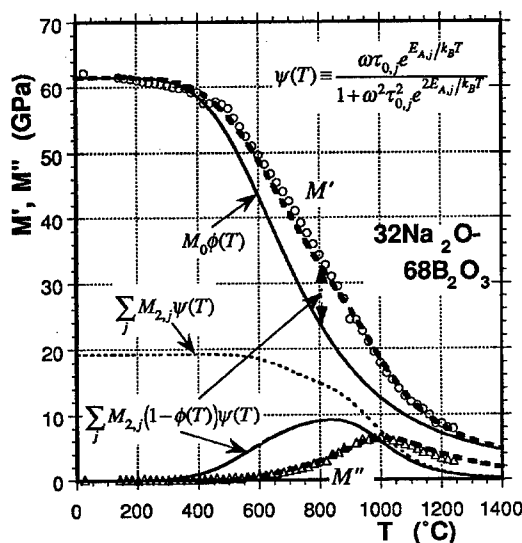


Fig. 5. Storage and loss modulus of a sodium borate system as a function of temperature, and best fit curves using the modified Maxwell model.

structural states, as long as the extremes in mechanical behavior are properly accounted for. For our model we considered one state to be ideally elastic and representative of a room-temperature glass, and the other one to be viscoelastic, like a glass melt. The volume fraction of structure found in the rigid state,  $\phi(T)$ , can be estimated using Boltzman statistics, with knowledge of the free energy difference between the structural states,

$$\phi(T) = \left[ 1 + e^{-Q(1-T/T_c)/k_B T} \right]^{-1} \quad (3)$$

where  $Q$  is an energy comparable to the enthalpy of fusion, and  $T_c$  a critical temperature between the glass transition and equilibrium melting temperatures of the substance. Multiplying  $\phi(T)$  with a constant  $M_0$ , the static modulus at 0 K, yields the temperature dependent static modulus, and the expression for the modified Maxwell model is [11]

$$M^*(\omega, T) = M_0 \phi(T) + \sum_j \left( M_{2,j} (1 - \phi(T)) \frac{\omega^2 \tau_{0,j}^2 e^{2E_{A,j}/k_B T} + i \omega \tau_{0,j} e^{E_{A,j}/k_B T}}{1 + \omega^2 \tau_{0,j}^2 e^{2E_{A,j}/k_B T}} \right) \quad (4)$$

Note that the relaxational modulus now depends on the temperature also via the term  $(1 - \phi(T))$ . It reflects changes in thermodynamic conditions, which bring about a gradual release of rigid structure, and result in an increase of the relaxational modulus with temperature. As formulated, the model makes no assumptions about the spatial arrangement of regions corresponding to either structural state. However, it is reasonable to presume that the rigid state would

be found in three-dimensional percolating domains, even at modest concentrations, and that the transformation between structural states occurs at the domain boundaries, just like a growth process.

The capability of this model is demonstrated in Fig. 5, where the best fits of Eq. (4) to the data for a sodium borate system is shown. This example is typical, and for a more complete analysis consider Ref. [11]. Accordingly, a large fraction of the decrease in storage capacity is due to irreversible structural changes. The energy dissipated in the molecular motion which leads from one structural state to the other, does not amount to the lost storage capacity. This is because the states corresponding to the beginning and the end of the deformation are structurally different. In other words, the mechanisms of structural rearrangement in a supercooled liquid require less energy than it takes to inelastically deform a stable structure.

## 5. CONCLUSIONS

Brillouin light scattering allows one to determine the complex mechanical modulus of molecular structures. This measure can provide important insights with regard to the intermediate and extended range order. In the case of boron oxide we found that viscous dissipation immediately above  $T_g$  involves predominantly dilatational deformations. Furthermore, these deformations are underlying to irreversible structural modifications. While the glass structure draws its rigidity from a relatively ordered arrangement of small rings, the supercooled liquid is characterized by larger rings that make up a continuous random network. The mechanism of transition between structural states requires little energy, and involves a transient configuration with four-coordinated borons.

## REFERENCES

- [1] L. Börjesson, L.M. Torell, U. Dahlborg & W.S. Howells, *Phys. Rev. B* **39** (1989), 3404.
- [2] L. Cervinka & F. Rocca, *J. Non-Cryst. Solids* **192-193** (1995), 125.
- [3] D.H. Cho, K. Hirao & N. Soga, *J. Non-Cryst. Solids* **189** (1995), 181.
- [4] K. Gatterer, G. Pucker, H.P. Fritzner & S. Arafa, *J. Non-Cryst. Solids* **176** (1994), 237.
- [5] J.E. Masnik, J. Kieffer & J.D. Bass, *J. Am. Ceram. Soc.* **76** (1993), 3073.
- [6] J. Kieffer, J.E. Masnik, B.J. Reardon & J.D. Bass, *J. Non-Cryst. Solids* **183** (1995), 51.
- [7] J.P. Boon and S. Yip, *Molecular Hydrodynamics* (Dover, New York, 1991).
- [8] T.A. Litovitz, T. Lyon & L. Peselnick, *J. Acoust. Soc. Am.* **26** (1954), 566.
- [9] A. Napolitano, P.B. Macedo, E.G. Hawkins, *J. Am. Ceram. Soc.* **48** (1965), 613; R.E. Eppler, *J. Am. Ceram. Soc.* **49** (1966), 679; G.H. Kaiura & J.M. Toguri, *Phys. Chem. Glasses* **17** (1976), 62.
- [10] J. Kieffer, *Phys. Rev.* **B50** (1994), 17.
- [11] J.E. Masnik, J. Kieffer & J.D. Bass, *J. Chem. Phys.* **103** (1995), 9907.
- [12] G.E. Jellison, L.W. Panek, P.J. Bray & G.B. Rouse, *J. Chem. Phys.* **66** (1977), 802; A.C. Hannon, D.I. Grimley, R.A. Hulme, A.C. Wright & R.N. Sinclair, *J. Non-Cryst. Solids* **177** (1994) 299.
- [13] J. Kieffer, unpublished results.

## HIGH-PRESSURE INDUCED PHENOMENA IN GLASSES

Michael I. KLINGER

*Department of Physics, Bar Ilan University,  
Ramat Gan (Tel Aviv), 52900, Israel*

and

Sergei N. TARASKIN

*Moscow Engineering-Physics Institute,  
Moscow, 115400, Russia*

Pronounced pressure-induced phenomena in dynamical and electronic properties of glasses have been theoretically predicted at accessible high pressures,  $p \approx 10^4$ – $10^5$  bar, for temperatures far below the glass-transition temperature. Their origin is eventually related to atomic "soft configurations" on the nanometer scale, characteristic of glassy materials and anomalously sensitive to pressure.

### 1. INTRODUCTION

The influence of hydrostatic pressure ( $p$ ) on dynamical (and electronic) properties is different for glasses, including borate glasses, and the respective crystalline materials. For the latter, generally speaking, macroscopic changes in properties may be expected to occur at  $p \geq p^0 = E_b/z_0(5a)^3$ , so that  $p^0$  is very high,  $p^0 \geq 10^7$  bar, for "rigid" materials in which covalent (ionic) or metallic bonding predominates with the typical energy  $E_b \geq 1$  eV, mean coordination number  $z_0$ ,  $2 \leq z_0 \leq 10$ , and atomic spacing  $a \approx 2$ – $3$  Å. Phase transitions at lower pressure,  $p < 10^6$  bar are observed only in single-crystals in which appropriate soft-phonon modes are available. One may conclude that some softness is needed for realizing macroscopic changes in properties of solids at  $p \ll p^0$ . Hence, the difference between crystals and glasses may be related to the different kinds of softness in the two classes of solids. Actually, glasses at ambient pressure ( $p \equiv 0$ ) are characterized by localized softness randomly distributed in "soft configurations" of typical atomic relative concentration  $c_a^0 \equiv N_a^0/N_0 = c_a(p=0, T=0) \approx 10^{-2}$  at  $T \ll T_g$  ( $N_0 = a^{-3}$ ) [1]. The universal low-energy dynamics and low-temperature properties of glasses [2] are related to the soft configurations, each containing a group of  $n_{sm}$  atoms moving in the associated localized soft mode, with  $10 \leq n_{sm} \leq 10^2$ , e.g.  $n_{sm} \approx 30$  [1,3]. The harmonic-force constant  $k$  in the soft mode is anomalously small,  $k \ll k_0 \approx M_{sm} \omega_0^2 \approx 10^2$  eV/Å<sup>2</sup>, and the generalized susceptibility to distortions is high,  $\chi = k^{-1} \gg \chi_0 = k_0^{-1}$  ( $\omega_0 \approx 10^{13}$ /s,  $M_{sm} = n_{sm}M$  and  $M$  is the average atomic mass). In this connection the ensemble of the soft configurations is anomalously sensitive to pressure, so that even accessible, not

very high pressure  $p \leq 10^5 \text{ bar} \ll p^0$  can give rise to macroscopic changes in the properties of glasses.

On the other hand, the essential electron properties of semiconducting glasses (SGs) at ambient pressure are related to the basic charge carriers in the mobility gap, of typical relative concentration  $c_2^0 = c_2(p=0, T=0) \approx 10^{-3} - 10^{-4}$  for  $T \ll T_g$  (see, e.g. Refs [1,4]). The charge carrier is identified with a singlet electron (hole) pair self-trapped in a typical soft configuration, or a negative-U centre: its pair-correlation energy  $U$  is negative, at inter-electron attraction, and anomalously large in magnitude being comparable to the mobility-gap width  $E_g^0 = E_g(p=0)$  [1]. In this connection, the hybridization of the electron conduction-band state under self-trapping with the valence-band states in the gap is decisive in this type of self-trapping, unlike the situation in the common polaronic self-trapping [1,5]. The essential gap states eventually are the self-trapped negative-U states fully occupied by the singlet pairs, forming the negative-U centres in the mobility gap. Thus, the negative-U centres also exhibit anomalously high sensitivity to pressure, so that the high pressures ( $p \approx 10^4 - 10^5$ ) bar can also give rise to fundamental transformations in the electron structure and properties of the SGs.

## 2. TRANSFORMATIONS IN GLASSY LOW-ENERGY ATOMIC DYNAMICS AND ELASTIC PROPERTIES

The glassy features implied in what follows are associated with the soft configurations basically characterized by their random softness parameter which is small in magnitude,  $|\eta| \leq \eta^* = \text{const} \approx 0.1$ , and by its distribution density  $H(\eta)$  [1]. The main question is how pressure affects the distribution density and the related total atomic concentration,  $c_a$  of the soft configurations.

A plausible model of  $H(\eta)$  is a Gaussian-like function (see, e.g. Refs [1,4]):

$$H(\eta) = H_0(\eta) \exp[-\eta_c^{-1}(1 - \eta/\eta_0)^2] \quad (1)$$

where  $H_0(\eta) \equiv H_0 = \text{constant}$  at least for pronounced single-well and double-well potentials at  $|\eta| > 0.1$ . Here  $\eta_0 \approx 1$  corresponds to the typical, "rigid", atomic configurations at  $k \approx k_0$  for the vast majority ( $\approx 99\%$ ) of atoms in the glass. The approximation (1) enables us to estimate the atomic concentration  $c_a$  of the soft configurations applying the formula

$$c_a = \int_{-\infty}^{\eta^*} d\eta H(\eta) \quad (2)$$

so that in fact (see Section 1)  $c_a^0 \approx 10^{-2}$  at ambient (and low) pressure.

The basic parameter in Eqs. (1) and (2), which may noticeably depend on pressure, is  $\eta_c = \eta_c(p)$ , characterizing the variation scale for  $H(\eta)$ , whereas both  $\eta^*$  and  $\eta_0$  by their definition are universal constants. Two arguments are helpful for finding  $\eta_c(p)$ , for some series of non-metallic amorphous materials at least (cf. Ref. [6]). One is that the glassy low-temperature properties at ambient pressure are observed to be suppressed with growing effective (average) coordination number  $z$ . That is certainly the case for amorphous semiconductors which are covalent glasses at  $z < z_c$ , the "critical" value of  $z$  (e.g.  $z(\text{g-Se}) = 2$  or

$z(\text{g-GeSe}_2)=2.67 < z_c$ ), whereas non-glassy covalent materials (with no pronounced glassy low-temperature properties) correspond to  $z_c < z < z_{\max}=4$ , e.g. a-Si ( $z=4$ ) and probably a-As ( $z=3 > z_c$ ) [1,7]. Furthermore, a global elastic transition (not necessary a phase transition) is observed in the materials in the sense that the elastic modulus  $B(z)$  rather sharply increases at  $z > z_c$ , from  $B(z < z_c) \approx 10^5$  bar for SGs to  $B(z=4) \approx 10^6$  bar for a-Si; see, e.g. Ref. [7]. As noted in the latter, these features appear to reflect the remarkable dichotomy of cohesion forces, "strong" (e.g. covalent) and "weak" (e.g. of van der Waals origin) in the relatively soft glasses at  $z < z_c$ , as opposed to the negligible role of the "weak" forces in the more rigid non-glassy materials at  $z > z_c$ . The "weak" forces characterize the interactions between appropriate random quasimolecular units related to the medium-range-order (MRO) composing the glass, the atoms of each unit being bound to each other by the "strong" forces. It may be assumed in this connection that  $z = z_0 + \Delta z$ , with  $z_0$  and  $\Delta z$  the contributions of the "strong" and "weak" forces, at  $0 < \Delta z \ll z_0$  for ambient pressure (see, e.g. Refs [7,8]). Actually  $z_0$  is characteristic of the ensemble of decoupled quasimolecular units of which the effective dimensionality is  $d_{\text{eff}}^0 = 0$ . On the other hand,  $\Delta z$  is the measure of the contribution of more extended random structures of the "weakly" bound quasimolecular units (as if those are cross-linked), of higher effective dimensionality  $d_{\text{eff}} \leq 3$ .

Within the framework of the previously mentioned theoretical soft-configuration model of glasses [1], the suppression of the glassy low-temperature properties with increasing  $z^3 z_c$  at ambient pressure means that in the SGs

$$0 \gtrsim d\eta_c^0/dz \text{ and } 0 \gtrsim dc_a^0/dz \text{ at } \eta_c^0 \equiv \eta_{c,\max} \equiv 0.1 \text{ and } c_a^0 \equiv c_{a,\max} \approx 10^{-2} \quad (3)$$

for  $z < z_c$ , whereas both  $\eta_c^0$  and  $c_a^0$  more strongly decrease,

$$d\eta_c^0/dz < 0 \text{ and } dc_a^0/dz < 0 \quad (4)$$

for  $z_c \leq z \leq z_{\max}$ . Moreover,

$$\eta_c^0(z = z_{\max}) < \eta_c^0(z_c) < \eta_c^0(z < z_c) \text{ at } \eta_c^0(z = z_{\max}) \ll \eta_c^0(z < z_c) \equiv 0.1 \text{ and } c_a^0(z = z_{\max}) \ll c_a^0(z_c) \ll c_a^0(z < z_c) \approx 10^{-2} \quad (5)$$

Another argument for estimating  $\eta_c(p)$  is that some empirical data, concerning pressure effects for the optical-absorption edge, the bulk modulus and the glass-transition temperature may give rise to the following estimation [7,8]:

$$0 < dz/dp \leq 10^{-5}/\text{bar} \quad (6)$$

so that  $(0 <) dz(p) \equiv z(p) - z(0) \leq 1$  at the applied pressure,  $10^5 \leq p < 10^6$  bar. This may be interpreted within the framework of the model as follows: actually the "strong" (e.g., covalent) bonds remain intact while the "weak" forces may enhance, continuously transforming to a kind of "strong" interaction, with increasing pressure up to the range  $10^5 \leq p < 10^6$  bar  $\ll p^0$ . This transformation, as well as the related transformation of the glass to a non-glassy material at

$z=z(p)>z_c=z(p_c)$ , is due to the decrease of the average distance between the quasimolecular units (densification) until the dichotomy of forces disappears at a characteristic pressure  $p_c$  and only "strong" forces exist in the resulting "continuous random network" structure of higher effective dimensionality  $d_{\text{eff}}$  (e.g.  $2 \leq d_{\text{eff}} < 3$ ), at  $p \geq p_c$  and  $dz \approx 1$ . In other words, one may assume that

$$dz/dp \equiv d\Delta z/dp \gg |dz_0/dp| \text{ and } 10^5 \text{ bar} \leq p_c \ll p^0 \quad (7)$$

and, from continuity considerations and the formulae (3)-(6), that  $z = z(p)$  is a simple function. Then, the following properties appear to be characteristic of  $\eta_c = \eta_c(p) \equiv \eta_c[z(p)]$  and  $c_a = c_a(p) \equiv c_a[z(p)]$ :

$$d\eta_c/dp \equiv 0 \equiv dc_a/dp \text{ at } \eta_c \equiv \eta_c^0 \approx 0.1 \text{ and } c_a \equiv c_a^0 \approx 10^{-2} \quad (8)$$

for  $p \ll p_c$ , i.e.  $z(p) < z_c$ , whereas  $\eta_c$  and  $c_a$  monotonically decrease with increasing  $p$  for  $p_c \leq p \leq p_{\text{max}}$  at  $z_{\text{max}} = z(p_{\text{max}})$ ,

$$\eta_c(p_{\text{max}}) < \eta_c(p_c) < \eta_c^0, \text{ or } \eta_c(p_{\text{max}}) \equiv \eta_c^* \ll \eta_c^0, \text{ e.g. } \eta_c^* \approx 0.1 \eta_c^0 \quad (9)$$

$$c_a(p_{\text{max}}) \ll c_a(p_c) \ll c_a^0$$

It follows from Eqs. (3)-(9) that the approximation

$$\eta_c(p) \equiv \eta_c^* + \eta_c^0(1-p/p_\eta)\theta(p_\eta-p) \quad (10)$$

may be applied for estimating  $\eta_c(p)$ , with the characteristic pressure  $p_\eta$  close to  $p_{\text{max}}$ ,  $p_{\text{max}} \geq p_\eta \geq p_c$ . In Eq. (10):  $\theta(x) \equiv \{1 \text{ at } x > 0; 0 \text{ at } x < 0\}$ . The approximation (10) may be interpreted as follows: the distribution density  $H(\eta)$  is strongly narrowed at  $\eta_c$  decreasing from  $\eta_c^0$  to  $\eta_c^* \ll \eta_c^0$ , so the soft configurations are strongly suppressed and the related glassy features are lost, as the atomic concentration  $c_a(p)$  is diminished by orders of magnitude at the high  $p \geq p_c$ ,  $c_a(p) \ll 0.1 c_a^0 \approx 10^{-3}$ . In this connection,  $p_\eta$  may be estimated from the formulae (6)-(10) as follows:

$$10^5 \text{ bar} \leq (dz/dp)^{-1} \leq p_\eta < 10^6 \text{ bar} \quad (11)$$

(see also Eqn. (15) in Section 3). As may be concluded, the general suppression of the soft configurations with growing pressure appears to be characteristic at least of the glasses exhibiting the dichotomy of forces.

On the other hand, the prediction follows from above that the global elastic transformation is expected also to occur in the given glass ( $z(p=0) < z_c$ ) at high  $p \approx p_c$  at which  $z(p) \approx z(p_c) = z_c$ . Since  $z_c - z(p=0) \leq 1$  at least for the SGs, one may conclude also that the "critical" pressure  $p_c$  is of the same scale as (though probably lower than)  $p_\eta$ , so that

$$10^5 \text{ bar} \leq p_c \leq p_\eta < 10^6 \text{ bar} \quad (12)$$

It is worthy of note that for a molecular crystal, for which van der Waals bonding is determinative with the typical energy  $E_b^* \approx 0.05-0.10$  eV, the characteristic pressure  $p^* = E_b^*/z_0 a^3 \approx 10^5-10^6$  bar  $\ll p^0 \approx 10^7-10^8$  bar (see Section 1), i.e.  $p^*$  is of the same scale as  $p_c$  in the covalent (or other similar) glasses under discussion.

The estimations (11) and (12) appear to be evidence for a correlation between the predicted strong suppression of the soft configurations and a global elastic transformation at the accessible high  $p \geq p_c$ , at which the glass under consideration is transformed to the respective non-glassy material. Some correlation also may exist between the general suppression phenomenon under discussion and the "rigidity-percolation" phase transition introduced earlier (see, e.g. Ref. [9]) as a model for the global elastic transformation at a "critical" value  $z_c$  of  $z$  in amorphous materials at ambient pressure. These and other correlations and the related quantitative theory of the revealed basic transformations in elastic and dynamical properties of the glasses at high pressures will be discussed in detail elsewhere.

It is worth adding that the general suppression phenomenon ( $c_a(p) \ll c_a^b \equiv c_a(0) \approx 10^{-2}$ ), at high pressures in the range  $p_{\eta} \geq p > p^* \approx p_{\eta} \eta_c^0 \approx 0.1 p_{\eta} \geq 10^4$  bar, is predicted for the glasses for which relationships (3)-(6) hold. If, however, for other glasses one of the relationships (4)-(6) does not hold, e.g.  $dz/dp \leq 0$ , the situation may differ, so that Eqs.(7)-(10) are violated, e.g.  $dc_a/dp \geq 0$  and  $c_a(p)$  increases or weakly changes with growing  $p$  in the appropriate pressure range. Such a behaviour may be compatible with the recently observed pressure-induced growth of the atomic concentration of the anharmonic (double-well) soft-mode potentials with increasing  $p \leq 10^4$  bar ( $\ll p_c$ ) [10] in vitreous silica. In the latter, as well as probably in general in the "strong" glasses, the dichotomy of forces may be less essential and therefore the pressure-induced phenomena may differ from those in the fragile (covalent) glasses considered above.

### 3. PRESSURE-INDUCED PHENOMENA IN ELECTRONIC PROPERTIES

The basic question is how pressure mainly affects the electron properties of the SGs, which are related to the negative-U centres (see Section 1). The recently developed theory [5] characterizes the situation in detail. Let us focus here on the qualitative aspects of the most pronounced predicted phenomenon - the non-monotonic variation of the thermal-equilibrium concentration  $c_2(p)$  of the negative-U centres with growing pressure at  $T \ll T_g$ . The phenomenon may be derived from the basic distribution density  $H(\eta)$  for the random softness parameter at its effective value  $\eta = \eta_{\text{eff}}$  for the vast majority of the negative-U centres. The parameter is linked to both the mobility gap-width  $E_g$  and to the material constants  $\gamma^*$  and  $U_d$  [5],

$$\eta_{\text{eff}}(p) = \gamma^*/(E_g(p) + U_d) \quad (13)$$

Here  $\gamma^*$  is the effective electron-soft-mode coupling energy and  $U_d$  is the effective electron-electron repulsion (Hubbard) energy, of typical values  $\gamma^* \approx (0.1-0.2)E_g^0 \geq U_d = 0.1E_g^0$ . The gap width  $E_g$  for the SGs exhibits an approximately linear decrease with growing pressure,

$$E_g = E_g(p) \equiv E_g^0(1 - p/p_g) \quad (14)$$

in the pressure range under consideration, at  $0 \leq p < p_g = q \times 10^5$  bar and  $1 \leq q < 10$ ,

at which the global semiconductor-metal transition occurs [8,11,12]. Since no global elastic transformation is observed in the SGs at  $p < p_g$ , one may conclude that

$$p_g \leq p_c \leq p \quad (15)$$

It is derived in the theory, in accordance with the above considerations, that the basic feature of the pressure dependence of  $c_2(p)$  may be characterized by the following expression:

$$c_2(p) \sim \eta_{\text{eff}}(p) \exp[-\eta_c^{-1}(p)(1-\gamma\eta_{\text{eff}}(p))^2] \quad (16)$$

at  $g \approx 1$ , which in particular gives rise to the estimation  $c_2^0 \equiv c_2(p=0) \approx 10^{-3}-10^{-4}$  at typical values of the parameters involved ( $\eta_{\text{eff}}^0 \equiv \eta_{\text{eff}}(0) \approx 0.1-0.2$ ,  $\eta_c^0 \approx 0.1$  and  $p_g/p_\eta \approx 0.5-1.0$ ).

As seen from Eqs. (13), (14) and (16),  $c_2(p)$  varies non-monotonically with increasing pressure. The latter is due to growth in both  $\eta_{\text{eff}}(p)$ , from  $\eta_{\text{eff}}^0 \approx 0.1$  to  $\eta_{\text{eff}}(p_g) \approx 1$ , and  $\eta_c^{-1}(p)$ , from  $(\eta_c^0)^{-1} \approx 10$  to  $(\eta_c^*)^{-1} \gg 10$ . Therefore,  $c_2(p)$  at first decreases, exhibits a minimum at  $p = p_{\text{min}}(U_d/E_g^0, p_g/p_\eta)$  and then increases rapidly up to  $c_2(p_g) \geq 10c_2^0$ . In the approximation (16), the upper limit estimation,  $p_{\text{min}}^0$ , for  $p_{\text{min}}$  can be obtained:

$$p_{\text{min}}/p_g \leq p_{\text{min}}^0/p_g = p_0/p_g - (2\gamma^*p_\eta/E_g^0p_g)^{1/2} \quad (17)$$

where  $\eta_{\text{eff}}(p_0) = \eta_0 \approx 1$  and  $p_0 \leq p_g$  at realistic  $\gamma^* \geq U_d$ , and  $p_0$  is close to  $p_g$ . For actual  $\gamma^*/E_g^0 \approx 0.15$  one finds that  $p_{\text{min}} \leq p_{\text{min}}^0 \approx (0.4-0.5)p_g$  at  $\xi \equiv p_g/p_\eta \leq 1$ , e.g.  $p_{\text{min}} \approx 0.35p_g$  is found from Eq. (17) at a realistic  $U_d/E_g^0 = 0.1$  and a possible  $p_g/p_\eta \approx 1$ . Moreover,  $p_{\text{min}}$  weakly shifts to lower values,  $dp_{\text{min}}/d\xi > 0$ , as  $\xi$  decreases. Note that the value of the parameter  $p_\eta = \xi p_g$ , with the related values of  $U_d/E_g^0$ ,  $\gamma^*/E_g^0$  and experimentally measured  $p_g$ , can be obtained as far as the empirical value of  $p_{\text{min}}$  is found (the same holds true for  $U_d/E_g^0$ , if the values of  $\xi$  and  $\gamma^*/E_g^0$  are known).

Two basic effects and their competition are responsible for the predicted non-monotonic behaviour of  $c_2(p)$ . One is the general pressure-induced suppression of the soft configurations (Section 2) and then of the "strong" negative-U centres of which the negative pair correlation energy  $U_{\text{eff}}(p)$  is large in magnitude:  $E_g^0/4 < |U_{\text{eff}}(p)| \leq E_g^0/2 \approx 1$  eV at rather low  $p < p_{\text{min}} < p_g/2$ . Another effect is that the effective softness  $\eta_{\text{eff}}(p)$  of the local atomic configurations, involved in the formation of the negative-U centers, increases with growing  $p$ . Since the distribution density  $H(\eta)$  increases as  $\eta$  varies from  $\eta=0$  to  $\eta=\eta_0 \approx 1$ ,  $c_2(p)$  increases rapidly with growing  $\eta = \eta_{\text{eff}}(p)$  for the "weak" negative-U centres of which  $U_{\text{eff}}$ , remaining negative due to the hybridization of states (Section 1), becomes small in magnitude,  $|U_{\text{eff}}(p)| \ll E_g^0/2$ . In fact the "weak" negative-U centres can be created even in the typical "rigid" configurations at  $\eta_{\text{eff}}(p) \leq \eta_{\text{eff}}(p_0) = \eta_0 \approx 1$  and  $p_{\text{min}} < p \leq p_0$ , as far as  $E_g(p)$  becomes small enough,  $E_g(p) \ll E_g^0$ , so the hybridization of the conduction-band and valence-band states in the mobility gap is still determinative for the formation of those negative-U centres.



Let us note that the other thermal-equilibrium electron properties of the SGs related to the negative-U centres, such as their contribution to specific heat  $\Delta C_e$  and magnetic susceptibility  $\Delta \kappa_e$ , largely exhibit a similar pressure dependence for high  $p \leq 10^5$  bar, since  $\Delta C_e \propto c_2(p)$  and  $\Delta \kappa_e \propto c_2(p)$ . Furthermore, the intensities of non-equilibrium processes (e.g. d.c. conductivity, luminescence and optical absorption) related to the negative-U centres,  $I(p) \propto c_2(p)W(p)$ , also behave with growing  $p$ , for high  $p \leq 10^5$  bar, similarly to  $c_2(p)$ , as far as the respective transition (excitation) probability  $W(p)$  can be shown to depend more weakly on pressure.

#### 4. CONCLUDING REMARKS

The accessible high pressures  $10^4 \leq p < 10^6$  bar are predicted to give rise to the general suppression of the soft configurations and the related macroscopic changes in the low-energy atomic dynamics and elastic properties of glasses, this being explicitly argued for the glasses with the dichotomy of cohesion forces as the most bright example. These pressures also determine the macroscopic changes in the electron properties of semiconducting glasses.

As the generalized susceptibility of the typical soft configuration with respect to atomic distortions is high (Section 1),  $\chi \approx 30\chi_0$  and so  $c_a^0 \chi \approx 0.3c_{\text{tot}}\chi_0$  (with the total atomic concentration  $c_{\text{tot}}=1$ ), the role of the soft configurations is comparable to that of the vast majority of atoms of the glass at ambient pressure for properties related to the distortions. The problem is what are the properties in question (e.g. is some aspect of the glass transition related to this basic feature of the soft configurations?) and what are the high-pressure induced changes in these properties.

There are also competing pressure effects in the electron properties of the SGs at the highest pressures in question. One is a kind of the Anderson-Mott delocalization of the negative-U centres. The problem is to characterize the contribution of the competing pressure effects to the electron properties mentioned.

#### REFERENCES

- [1] M.I. Klinger, *Phys. Rep.* **165** (1988), 275.
- [2] *Amorphous Solids* Ed. W.A. Phillips, (Springer, Berlin, 1981).
- [3] H.R. Schober & C. Oligschlegel, *Phys. Rev. B* **53** (1996), 11469.
- [4] N.F. Mott & E.A. Davis, *Electron processes in Non-Crystalline Materials* (Clarendon, Oxford, 1979).
- [5] M.I. Klinger & S.N. Taraskin, *Phys. Rev. B* **52** (1995), 2557; *J. Phys.: Condens. Matter*, in press (1997).
- [6] M.I. Klinger, *Solid State Commun.* **70** (1989), 79.
- [7] K. Tanaka, *Solid State Commun.* **60** (1986), 295; **54** (1985), 867.
- [8] K. Tanaka, *Phys. Rev. B* **30** (1984), 4549; K. Tanaka, *J. Non-Cryst. Solids* **90** (1987), 363; K. Tanaka, *J. Non-Cryst. Solids* **97&98** (1987), 391.
- [9] M.F. Thorpe, *J. Non-Cryst. Solids* **76** (1985), 109.
- [10] D. Tielburger, R. Merz, R. Ehrenfels & S. Hunklinger, *Phys. Rev. B* **45** (1992), 2750.
- [11] B. Weinstein, *Phil. Mag. B* **50** (1984), 709.
- [12] I. Berman & N. Brandt, *Sov. Phys. Low Temper.* (in Russian) **16** (1990), 1227.

## THE BRAY AND LANDA-PATASHINSKII MODELS, AND POLYMORPHISM IN BOROSILICATE GLASSES AND MELTS

Leonid M. LANDA & Ksenia A. LANDA  
*LANCER TECH, INC., R.D. 6, Box 514, Greensburg,  
PA 15601, USA*

Latent heats were measured and the temperatures of the glass $\rightleftharpoons$ melt and melt $\rightarrow$ melt transitions were determined for the structures that have been formed under normal and high pressure. Polymorphism in borosilicate glasses and melts is accounted for, on the basis of the Bray model for boric oxide and the Landa-Patashinskii model for silica, and within the framework of the Landau theory of phase transitions.

### 1. INTRODUCTION

The Bray model [1] and the ensuing Landa-Patashinskii model [2] suggest that a relationship exists between the external conditions under which the structure of a glass or a melt has been formed, and the number of elementary boron-oxygen groups (boroxol rings) or silicon-oxygen groups (tetrahedra) in the structural units, the size of which can reach 15-20 Å. A change in the number of groups in the units is possible in both solid glasses and liquid melts, while the presence of latent heat upon this change is indicative of a first-order phase transition [2,3].

Modern theories of glass formation and vitrification [4,5] proceed from the existence of crystalline modifications in a chemical system. A structural unit within 2-3 coordinative spheres, in both the glass and melt, replicates the local order of a crystal (see the definition of a "crystalloid" as a structural unit in Ref. [3]). Vogel [6] notes that a "crystalloid" of Ref. [3] differs from a crystallite by lacking translation symmetry and from a random network by local crystal similarity (by the coordination of a glass-forming element, the number of elementary groups in a ring or the number of rings in a cycle which represents a structural unit).

The Bray and the Landa-Patashinskii models can also account for polymorphism in the case that no crystalline modifications exist in a chemical system: a change in the symmetry of the phases, as well as a change in the number of groups in a ring and the rings in a unit, occur independently of the possibility of forming long-range order out of such rings and units.

## 2. MATERIALS AND INVESTIGATION METHODS

The glass studied in this work was a non-miscible, highly homogeneous borosilicate glass (crown type) which has the composition  $69\text{SiO}_2$ ,  $11\text{B}_2\text{O}_3$ ,  $10.5\text{Na}_2\text{O}$ ,  $6.5\text{K}_2\text{O}$  (in mol%), a glass transition temperature,  $T_g=813\text{ K}$  and a molar weight of  $64\text{ g}$ .

The samples weighing  $0.05\text{ g}$ , of the powdered virgin glass (glass V), with  $0.2\text{ g}$  of benzoylperoxide, were subjected to explosion in a  $340\text{ cc}$  volume, oxygen-filled calorimetric bomb, at an initial pressure of  $3\text{ MPa}$ , with alumina as a standard. Ultrafine powder, obtained as a result of repeated explosions (glass E) and the glass V were tested using differential scanning calorimetry (DSC), in heating and cooling experiments performed at  $0.02\text{ K s}^{-1}$ , and in a solution calorimeter with an  $80\text{ cc}$  solution of composition  $\text{HF}:\text{H}_2\text{SO}_4:\text{H}_2\text{O}=1:1:40$ , at  $298\text{ K}$ . The resulting heating effects were measured with an experimental error of  $3\text{--}5\%$ .

## 3. EXPERIMENTAL RESULTS

The results of the solution calorimetry reveal that the enthalpy of glass V is  $13\text{ kJ/mol}$  higher than that of glass E. Therefore, these glasses represent different phases, which may differ in the number of elementary groups in the structural units.

Figure 1 shows the DSC data for glass V and glass E. As it is evident from Fig. 1, at a certain temperature  $T_{m,E}=860\text{ K}$ , glass E transforms into melt E with absorption of about  $10\text{ kJ/mol}$ ; while at  $1165\text{ K}$  melt E transforms into melt V, releasing  $3.5\text{ kJ/mol}$ . Melt V, obtained from melt E, transforms into glass V on cooling. If the cooling of glass E begins before it has reached  $1165\text{ K}$  on heating, then it returns to the initial state of glass E at a temperature  $T_{c,E}=920\text{ K}$ .

There are three characteristic temperatures for sample V:

- (a) a temperature  $T_{c,V}=778\text{ K}$ , at which a DSC graph,  $\Delta T=f(t)$ , undergoes a change in slope and, in addition,  $0.27\text{ kJ/mol}$  is absorbed on heating;
- (b) a temperature  $T_{a,V}=813\text{ K}$ , at which  $0.025\text{ kJ/mol}$  of heat is released, while  $0.19\text{ kJ/mol}$  is absorbed, and which is identified as  $T_g$ ;
- (c) a temperature  $T_{d,V}=910\text{ K}$ , at which  $0.031\text{ kJ/mol}$  of heat is released and  $0.35\text{ kJ/mol}$  absorbed.

Low latent heat in case of structure V and, mainly, the absence of a hysteresis on its heating and cooling, mean that phase transitions occur in the melt at  $813\text{ K}$  and  $910\text{ K}$ , which are intermediate between first- and second-order phase transitions. It is possible that those are conditioned by the rise of new kinds of oscillatory and rotational movements.

## 4. STRUCTURAL, KINETIC AND THERMODYNAMIC DIFFERENCES BETWEEN THE GLASS AND MELT

The conversion of a melt into a glass is realized by common (for phase transitions) ways of increasing the free energy,  $G$ , of the initial phase: by cooling the melt and/or increasing pressure. However, within the existing literature on non-

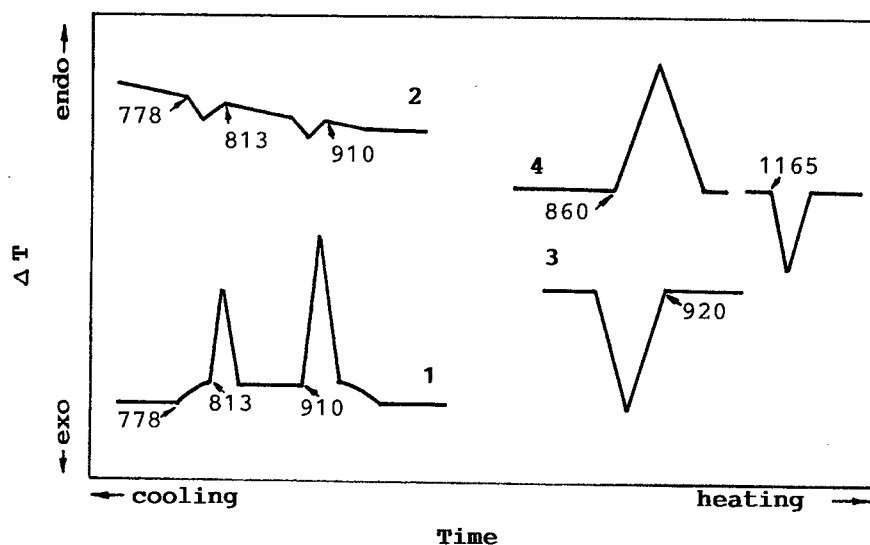


Fig. 1. Differential scanning calorimetry (DSC) for glasses V (1,2) and E (3,4), on heating (1,4) and cooling (2,3).

metallic glasses, it has become accepted, that the idea of a phase transition is only applicable to systems in equilibrium [7], that a phase transition and a relaxation process should necessarily be considered as alternatives [8] and therefore that the transition of a melt into a glass is not a phase transition [7,8].

Modern physics considers phase transitions otherwise [9]: it proceeds from the different symmetry of the phases above and below the transition point,  $T_c$ , rather than from the phase equilibrium (equilibrium is impossible for the second-order phase transitions). The time of relaxation (in the case of non-equilibrium phases) and the symmetry, undergo abrupt changes at the transition point. At the point of a second-order phase transition, the phase that is less symmetric (i.e. more non-symmetric phase) transforms into a more symmetric phase, so that only the latter phase exists in this point.

A change in the phase symmetry is quantitatively described by an order parameter,  $\eta$ , [9], which is equal to zero in the area of existence of a symmetric phase, while for a non-symmetric phase it is given by

$$\eta^2 = \{a(P)/2B(P)\}(T_c - T) \quad (1)$$

while

$$G = G(P, T, \eta) = G(P, T) + a(P)\{T - T_c\}\eta^2 + B(P)\eta^4 \quad (2)$$

In Eqs. (1) and (2),  $P$  is the pressure;  $B(P) > 0$ . As a rule,  $a(P) > 0$ , and a non-symmetric phase is a low-temperature one ( $T < T_c$ ). Exceptions to this rule are possible when  $a(P) < 0$ , and the non-symmetric phase is a high-temperature one ( $T > T_c$ ) [9]. The last case is realized in the "melt-glass" systems.

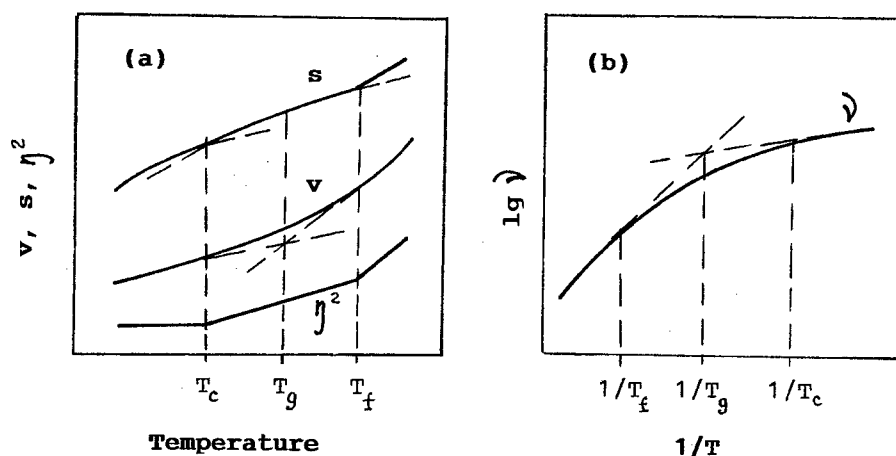


Fig. 2. Characteristics of glass ( $T \leq T_c$ ), a non-equilibrium liquid ( $T_c < T < T_f$ ), equilibrium liquid ( $T \geq T_f$ ): (a) specific volume,  $v$ , specific entropy,  $s$ , order parameter,  $\eta$ ; (b) viscosity,  $v$ .

Irrespective of the location of the phases on the temperature scale both the compressibility and the specific heat increase upon the transition to a non-symmetric phase, while the time of relaxation increases upon the transition to a symmetric phase [9].

The transition melt  $\rightarrow$  glass is a phase transition, because it is possible: (a) to determine the different symmetry of the phases involved in it, (b) to choose an order parameter,  $\eta$  and by doing so, (c) to determine the transition temperature, at which  $\eta$  becomes equal to zero.

For the glass, in contrast to the melt, the ergodic theorem is not observed [10], and the level of the thermal density fluctuations is frozen in [11]. Therefore, we consider glass (see Ref. [12]) to be a symmetric phase with respect to a non-equilibrium melt which is a non-symmetric phase: the properties of a melt are invariant in the spatial coordinates, while those of a glass are invariant in the spatial-temporal coordinates.

The same conclusion follows from Eq. (1). Upon relaxation, in a non-equilibrium glass-forming system, the volume decreases spontaneously, while the entropy of the system increases - otherwise the process would be neither relaxation, nor spontaneous. Hence, it follows that the pressure in the system is negative. This is caused by the stresses that arise in the system on fast cooling. If the pressure is negative, then  $a(P)$  is also negative, and the symmetric phase is a low-temperature one.

The dependence of the glass transition temperature on the rate of cooling a melt, the increase of the specific heat and the compressibility on the transition from glass to melt and the relation  $T_{m,E} < T_{c,E}$  (see Fig. 1) are the consequences of the unusual location of a symmetric phase versus a non-symmetric phase on the temperature scale. All these regularities follow from the theory of phase transitions [9], if vitrification is considered from the point of view of a change

of the symmetry of the phases, rather than a change of the temperature of a system.

The freezing-in of the relaxation process, i.e. the transition from a non-equilibrium melt that exists at  $T > T_c$ , to a glass that exists at  $T < T_c$ , is a phase transition. At  $T_c$ , the time of relaxation undergoes an abrupt change, while the level of the thermal density fluctuations remain dependent on temperature. An order parameter for the system ( $\eta^2$ ) is the difference in the levels of the heat fluctuations of density at  $T$  and  $T_c$  [12,13].

In Refs. [12-14] the temperature of the phase transition from glass to melt,  $T_c$ , is lower than the glass transition temperature,  $T_g$ , if  $T_g$  is being determined by the method of tangents, rather than after Tammann [15]. Tammann introduced the symbol  $T_g$  in order to indicate a certain temperature at which a system acquires brittleness, a property inherent in solids. The temperature of the phase transition,  $T_c$  in Refs. [12-14], as well as the  $T_g$  in Ref. [15], is the solid-liquid boundary (Fig. 2). The method of tangents shifts  $T_g$  to the liquid state range - by 50 K for  $B_2O_3$ , by 30 K for  $GeO_2$ , by 200 K for  $SiO_2$  [12] and by 35 K for glass V studied in this work.

At temperatures  $T_c$  and  $T_f$  (not at  $T_g$ ), the radii of curvature of the temperature dependences of the specific volume,  $v$ , the specific entropy,  $s$ , and the viscosity,  $\nu$ ,  $v(T)$ ,  $s(T)$  and  $\log \nu(1/T)$ , undergo a change. Consequently, the derivatives of these functions,  $(dv/dT)$ ,  $(ds/dT)$  and  $\{(1/\nu)(d\nu/d(1/T))\}$ , undergo an abrupt change (see Fig. 2). The relaxation time also undergoes an abrupt change at these points, which confine the area of existence of a non-equilibrium liquid.

Rapid phenomena are possible, for which an equilibrium and a non-equilibrium liquids are different phases. In this case it is possible to disregard the relaxation processes in a non-equilibrium liquid which would appear to be symmetric versus an equilibrium liquid.

It is worth mentioning that the existence of negative pressure in a system prevents the densification which is necessary for the crystallization of a melt. For  $B_2O_3$ , densification is about 30% upon crystallization, which is why it crystallizes poorly at normal ambient pressure but easily at a pressure of 3.5-4.0 GPa. At such pressure a densification of the  $B_2O_3$  melt by 30% is possible since its compressibility at normal pressure is about  $1.3 \times 10^{-10} \text{ GPa}^{-1}$ .

## ACKNOWLEDGEMENTS

This work was supported by the Ben Franklin Technology Center of Western Pennsylvania, under the Challenge Grant program for Research and Development No. 95W. CM00151R-1.

## REFERENCES

- [1] P.J. Bray, S.A. Feller & Y.H. Yun, *J. Non-Cryst. Solids* **38 & 39** (1980), 93.
- [2] L.M. Landa & A.Z. Patashinskii, In: *Relaxation Mechanisms in Glass Systems*, (Siberian Branch of the Academy of Sciences, Ulan-Ude, 1985. In Russian), pp. 69-72.
- [3] L.M. Landa & K.A. Landa, In: *The Physics of Non-Crystalline Solids*, Eds L.D. Pye,

- W.C. LaCourse and H.J. Stevens (Taylor & Francis, London, 1992), pp. 376-380.
- [4] I. Gutzow, L.D. Pye & A. Dobrev, *J. Non-Cryst. Solids* **180** (1995), 107.
- [5] D.R. Uhlmann, *J. Am. Ceram. Soc.* **66** (1983), 95.
- [6] W. Vogel, *Glass Chemistry* (Springer-Verlag, Berlin Heidelberg New York, 1994), p. 54.
- [7] A. Feltz, *Amorphous and Glassy Inorganic Solids* (Academic-Verlag, Berlin, 1983).
- [8] O.V. Mazurin, *Steklovanie* (Nauka, Leningrad, 1986. In Russian).
- [9] L.D. Landau & E.M. Lifshitz, *Statistical Physics* (Pergamon Press, New York, 1980).
- [10] W. Gotze, *Z. Phys.* **B56** (1984), 139.
- [11] A.M. Levelut & A. Guiner, *Bull. Soc. Fr. Mineral. Crystallogr.* **90** (1967), 445.
- [12] L.M. Landa & K.A. Landa, In: *Proc. XVII Int. Congress on Glass*, Beijing, China, Oct. 9-14, 1995, Ed Gong Fangtian (International Academic Publishers, Beijing, 1995) **7**, pp. 90-94.
- [13] L.M. Landa & K.A. Landa, In: *Proc. XVII Int. Congress on Glass*, Beijing, China, Oct. 9-14, 1995, Ed Gong Fangtian (International Academic Publishers, Beijing, 1995) **2**, pp. 52-57.
- [14] J.H. Gibbs & E.A. DiMarzio, *J. Chem. Phys.* **28** (1958), 373.
- [15] G.A. Tammann, *Glassy State* (Voss, Leipzig, 1933).

## THE STRUCTURE OF DEFECTS INDUCED IN SILICA GLASS BY BORON IMPLANTATION

Ken-ichi KAWAMURA, Hideo HOSONO, Hiroshi KAWAZOE  
*Materials and Structures Laboratory, Tokyo Institute of  
Technology, Nagatsuta, Yokohama 226, Japan*

Masayuki SETO & Satoru FUJITSU  
*Shonan Institute of Technology, Department of Materials  
Science and Ceramic Technology, Tsujido-Nishikaigan,  
Fujisawa, Kanagawa 251, Japan*

Boron implantation in wet synthetic silica glass plates of thickness 1 mm was carried out at room temperature. The acceleration voltage and flux of boron ions were 1.5 MV and  $3 \times 10^{16}/\text{cm}^2$ . Optical absorption bands were induced in the implanted layer at about 5.1, 5.9 and 7.6 eV. Si-Si direct bonding was the major defects formed in the layer. The concentration profile of the Si-Si bonding was found to be the same as that of the implanted boron. The intensities of the defects lines assigned to 3- and 4-membered ring structures for the Raman spectra of silica glasses increased upon implantation. This is an indication of the bond switching involved in the relaxation process during implantation.

### 1. INTRODUCTION

Ion implantation is a unique technique for modification of the surface layer in solids because it enables one to introduce simultaneously foreign chemical species and energy within a restricted space whose thickness is of the order of submicrometer to micrometer. The kinetic energy of the implanted ions is transferred to or consumed by the host lattice through electronic excitations and nuclear collision processes. In other words the implanted region is subjected to a transient high temperature and pressure, while the surrounding structures remain cold. A wide variety of chemical reactions is expected between the implanted species and the host material depending on the types of implanted species and host materials. The above mentioned characteristics and constraints for chemical reactions are said to constitute a new chemical reaction field.

Silica glass has been a useful material in optics and optical communication systems, because of its unique characteristics such as a wide transmission wavelength region, extraordinarily high optical transmission, and high thermal-, mechanical-, chemical- and photochemical-stabilities. The establishment of tech-



nologies for the fabrication of high purity silica glasses played a central role in utilizing some of these characteristics. In addition, silica glass is a good solvent for a wide variety of materials. The discovery of active functions in doped silicas such as second-harmonic generation [1] and grating formation [2] seem to have stimulated studies of the surface modification of silica glasses [3,4].

A knowledge of the physical and chemical reactions during and after ion implantation constitutes the essential basis for designing active waveguides using silica as a substrate. In a series of studies of such chemical reactions we concentrate here on boron implantation into synthetic silica glasses. The formation of oxygen deficient defects is reported, and changes in the network structure during the implantations are discussed.

## 2. EXPERIMENTAL

The substrates used in the present study were type III synthetic silica plates of 1 mm thickness with an OH concentration of  $3 \times 10^{19}/\text{cm}^3$ . Boron implantations were carried out at an acceleration voltage of 1.5 MV. The total surface density of the implanted ions was  $3 \times 10^{16}/\text{cm}^2$ . The temperature of the samples during the implantation was lower than 70°C and no intentional cooling was done. The depth and energy loss profiles were calculated by using the TRIM Code [5].

Implantation induced defects were identified mostly by optical absorption measurements. In order to estimate changes in optical absorptions within an implanted layer, the sample surface was stepwisely etched off, and optical absorption measurements were done repeatedly at each etching step. The etchant was diluted  $\text{H}_2\text{SO}_4$ -HF aqueous solution. During the chemical etching both sides of the silica glass plates, implanted and unimplanted, were dissolved into the acid. The thickness of the etched layer in each step was calculated from the corresponding weight loss. A correction was made to take into account the difference in etching rates of the implanted and unimplanted surface. The experimental uncertainty of the depth removed by etching was  $\sim \pm 10\%$ . As a consequence, the uncertainty of the Si-Si bond concentration was also  $\sim \pm 10\%$ , because the uncertainty of the absorbance of 7.6 eV in VUV spectra was much smaller ( $\sim 1\%$ ) than that of removed thickness.

Optical absorption spectra in the visible-ultraviolet region were measured on a Hitachi U-4000 spectrometer and those in the vacuum ultraviolet range were measured on a JASCO VUV-200 spectrometer. There was a small overlapping window in the wavelengths of the two measurements, and the vuv absorption spectrum was smoothly connected to the uv spectrum. The Raman spectrum from the implanted surface region was measured on a JASCO NR-1100 spectrometer with an optical microscope. The emission from an Ar ion laser (488 nm) was used as an excitation. All optical measurements were done at room temperature.

## 3. RESULTS

### 3.1. Energy Dissipation Process

It is well known that the kinetic energy of implanted ions is transferred to the lattice of host substrates by two processes, electronic excitations and nuclear colli-

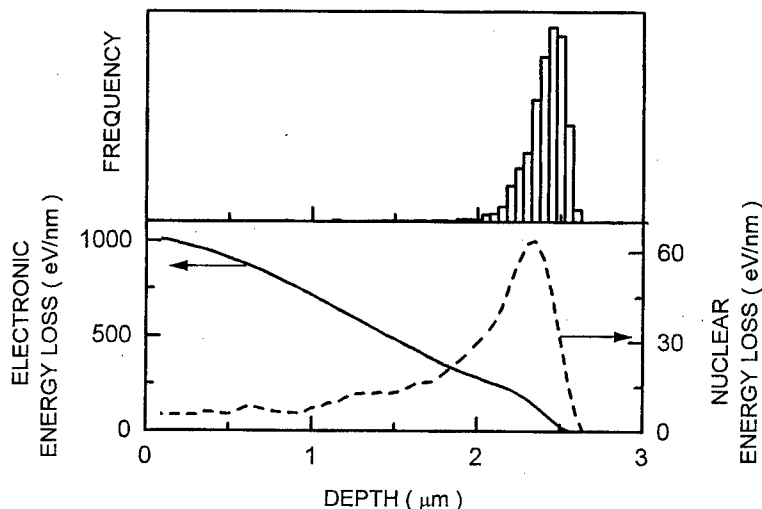


Fig. 1. Concentration profile of the implanted borons (upper) and dissipated energies through electronic excitations and nuclear collisions as a function of depth bottom.

sions. Figure 1 shows the simulated energy losses through electronic excitations and nuclear collisions upon the implantation of boron in silica at an acceleration voltage of 1.5 MV. It is noted that the major part of the energy carried by the implanted borons is consumed by electronic excitations, which are most intense at the surface and decrease almost linearly up to a depth of 2.8  $\mu\text{m}$ . On the other hand the nuclear energy loss increases gradually from zero at the surface to a rather sharp peak at around 2.3  $\mu\text{m}$  and falls steeply to zero at 2.7  $\mu\text{m}$ . It should be noted that the about 99% of the kinetic energy is dissipated through electronic excitations.

In the upper part of the figure the concentration profile of the implanted borons is shown. It has fairly sharp peak around 2.5  $\mu\text{m}$ .

### 3.2. Induced Optical Absorptions

Figure 2 shows the optical absorption spectra in the vuv-uv region induced in the silica glass by boron implantation. The spectra were obtained on the same sample which was subjected to a stepwise etching of the surface implanted layer. The thickness of the etched-off layer is given in the figure. It is easily recognized that at least three distinct optical absorption bands were induced by the implantation at around 5.1 eV, 5.9 eV and 7.6 eV. The assignment of the 5.8-5.9 eV band to the E' center [6,7] is well established, but that for the other two has been controversial. Unrelaxed Si-Si bonding[8], divalent silicon [9], and small sized silicon clusters [10] were proposed as the defect species responsible for 5.1 eV. An accidental coincidence in the absorption energies is a possible solution of the problem. As for the 7.6 eV band, there seems to be a widely accepted recognition that the Si-Si bond in  $\text{SiO}_2$  has an absorption band at 7.6 eV [11]. The following discussions will be made on the basis of this assignment.

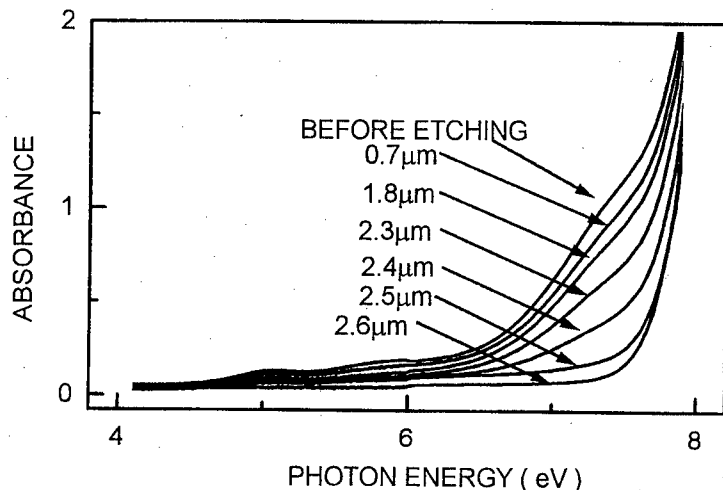


Fig. 2. Boron-implanted induced optical absorption spectra of silica glass.  
A thin layer of the implanted surface was stepwisely etched off.  
The thickness of the etched off layer is given in the figure.

The most pronounced observation in the figure is that the induced absorption bands diminish with decreasing thickness of the implanted layer and became negligible at about  $2.6 \mu\text{m}$ , which is very close to the energy dissipation thickness estimated by the TRIM code [5].

### 3.3 Concentration Profile of Si-Si Bond

The concentration profile of the respective defects is in principle obtained by calculating a difference spectrum. The difference spectra were obtained by subtracting the spectrum of the sample after etching from that before etching. Before discussing the results, the reason why only the Si-Si homobond is considered is outlined. The oscillator strength of the  $7.6 \text{ eV}$  band due to the Si-Si bond is  $0.5$  [11], which is approximately three times larger than that of the  $5.8 \text{ eV}$  [6,7] band due to the  $E'$  center. There are two possibilities for the defect responsible for the  $5 \text{ eV}$  band, i.e. an unrelaxed Si-Si bond [12] and a POR [13]. No ESR signal due to a POR was observed. Therefore, we assumed that the present  $5 \text{ eV}$  band is due primarily to unrelaxed Si-Si bonds. The oscillator strength of this defect is approximately the same as that of a Si-Si homobond. The apparent intensity ratio for the  $7.6 \text{ eV}$  band,  $5.8 \text{ eV}$  band and  $5 \text{ eV}$  band is  $6:1:0.5$ . Taking the oscillator strength (the width of these three bands does not differ significantly into consideration, the concentration ratio is calculated as  $6:3:0.5$ . Furthermore, since the  $5.8 \text{ eV}$  band is located at the tail of the intense  $7.6 \text{ eV}$  band, the concentration ratio for the  $E'$  center, estimated from the resolved spectra, is smaller than this ratio. Therefore, we consider the Si-Si homobonds as the primary defects created by implantation of boron.

Figure 4 shows the concentration of the Si-Si bond as a function of the depth

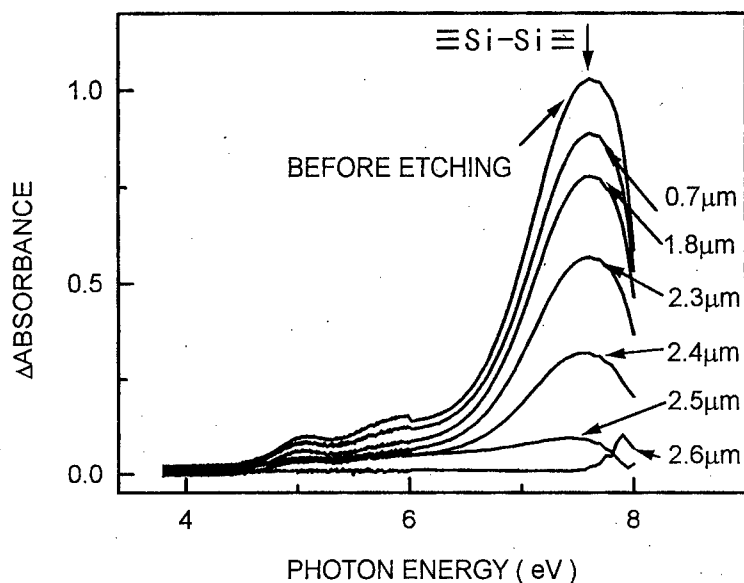


Fig. 3. Difference spectra for the thin layers of which depth is given in the figure. These were obtained from the spectra shown in Fig. 2.

from the surface. It may be noted that the concentration of the vacancy at depths smaller than  $0.7 \mu\text{m}$  is negligible. It starts to increase gradually from  $0.7 \mu\text{m}$  to  $2.3 \mu\text{m}$ . A sharp peak appears at around  $2.4\text{--}2.5 \mu\text{m}$ , followed by a steep decay to zero at around  $2.7 \mu\text{m}$ . The concentration profile is very similar to that of the implanted borons estimated by the TRIM Code (Fig. 1). In addition, the con-

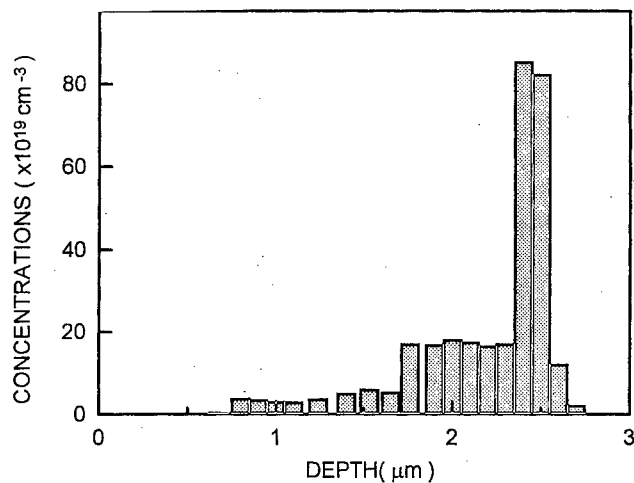


Fig. 4. The concentration profile of Si-Si bonding, estimated from the optical absorption intensities at  $7.6 \text{ eV}$  of the sample which was subjected to a stepwise chemical etching.

centration ration  $[\text{Si-Si}]/[\text{implanted boron}]$  was found to be close to 1. A similar 1:1 relation has also been for 150 kV acceleration [14]. These observation suggest that the presence of boron is one of the necessary conditions for the formation of a Si-Si bond under the present experimental conditions.

## 4. DISCUSSION

### 4.1. Possible Chemical Reactions

The defect species detected by optical absorption measurements are of oxygen deficient type, although only Si-Si bonding has been discussed so far. No defect species associated directly with the implanted boron was detected. Formation of oxygen deficient in  $\text{SiO}_2$  is an indication that reduction of the silica glass occurred:  $\text{SiO}_2 \rightarrow \text{SiO}_{2-x} + x\text{O}$ . Here, Si-Si bonding, the small sized silicon cluster, divalent silicon and the unrelaxed oxygen vacancy belong to the family of defects " $\text{SiO}_{2-x}$ ". A characteristic in the above reducing reaction induced by the boron implantations is the fact that the ration  $[\text{Si-Si}]/[\text{B}]$  was almost 1 at any depth throughout the implanted layer. We may speculate from the observation that the generated oxygens were used for oxidization of the implanted borons, or in other words oxygens in the silica network were extracted by the implanted borons. No direct information was obtained on the structure of boron associated species.

### 4.2. Changes in Network Structure

As mentioned in Section 2, a difference in the etching rate was detected between the implanted and unimplanted surfaces, and densification of the implanted layer was apparent in optical measurements and direct measurements of surface roughness. It seems that the changes in macroscopic properties cannot be attributed to the presence or formation of the defects previously discussed. In fact it seems possible that structural modification including bond switching occurred throughout the implanted layer during the ion implantation process, whereas the concentration of defects, which were detected long after the implantation, was of order  $10^{19} \text{ cm}^{-3}$ .

Raman scattering spectra of the implanted and unimplanted surfaces measured by the same optical system are displayed in Fig. 5. The spectrum of silica or quartz which was neutron irradiated up to a total dose of  $2 \times 10^{20} / \text{cm}^2$  is also shown for comparison [15]. It is clearly noted that the intensities of the defect lines at  $494 \text{ cm}^{-1}$  and  $606 \text{ cm}^{-1}$  increased upon boron implantation, although the signal to noise ratio was not high. The defect lines are assigned to the six membered ring and the eight membered ring, respectively [16]. The change in the fractions of these structural units in the silica network is direct evidence of the fact that bond switching in unit time and in unit volume. As far as we are aware, no direct information on bond switching was higher than the concentration of Si-Si bonding, which was close to  $10^{20} \text{ cm}^{-3}$ . In rough estimation the average energy transferred to a single atom constituting the silica glass amounts to  $10^3$ - $10^4 \text{ eV}$ . Therefore, the drastic situation that almost all of the Si-O binding in the layer was broken at least once seems likely.

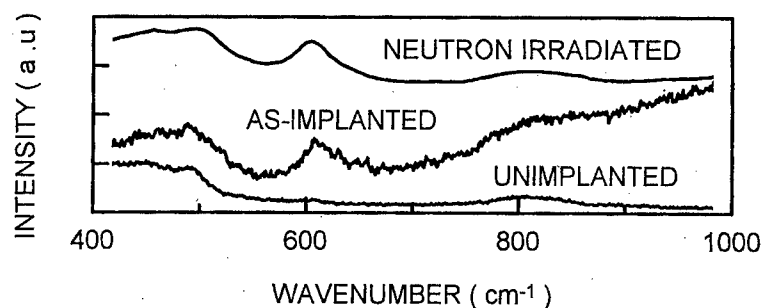


**Fig. 5.** Raman spectra of the implanted and unimplanted surfaces if the boron implanted silica glass were measured on the same optical system.  
The spectrum obtained for neutron irradiated silica is shown for comparison.

## 5. CONCLUSION

Implantation of boron into wet synthetic silica glasses was carried out, and the formation of defects and changes in network structure were examined optically.

Si-Si direct bonding and oxygen deficient defects were induced throughout the implanted layer. The concentration profile of the Si-Si bonding was close to as that of the implanted boron atoms, and the concentration ratio between the Si-Si bond and implanted boron was found to be close to 1.

Defect lines attributable to certain ring structures in silica were found to grow during the ion implantation. This is an indication of bond switching during the implantation.

## Acknowledgments

This work was in part supported by a Grant-in-Aid for Scientific Research from the Japanese Ministry of Education, Science, and Culture.

## REFERENCES

- [1] U. Osterberg & W. Margulis, *Opt. Lett.* **115** (1986), 516.
- [2] K.O. Hill, Y. Fujii, D.C. Johnson & B.S. Kawasaki, *Appl. Phys. Lett.* **32** (1978), 647.
- [3] H. Hosono & N. Matsunami, *Phys. Rev.* **B48** (1993), 13469.
- [4] I.K. Naik, *Appl. Phys. Lett.* **43** (1983), 519.
- [5] J.F. Ziegler, J.P. Biersack & U. Littmark, *The Stopping and Range of Ions in Solids* (Pergamon Press, New York, 1985).
- [6] R.A. Weeks, *J. Appl. Phys.* **27** (1956), 1376.
- [7] R.A. Weeks & E. Sonder, In: *Paramagnetic Resonance* Ed. V.V. Low (Academic, New York, 1963), p 869.
- [8] G. Arnold, *IEEE Trans. Nucl. Sci.* **NS-2** (1978), 220.
- [9] E.P. O'Reilly & J. Robertson, *Phys. Rev.* **B27** (1983), 3780.
- [10] M. Kohketsu, K. Awazu, H. Kawazoe & M. Yamane, *Jpn. J. Appl. Phys.* **28**(1989), 615.
- [11] H. Hosono, Y. Abe, H. Imai & K. Arai, *Phys. Rev.* **B44** (1991), 12043.
- [12] H. Hosono & R.A. Weeks, *J. Non-Cryst. Solids* **116** (1990), 289.
- [13] K. Arai, H. Imai, H. Hosono, Y. Abe & H. Imagawa, *Appl. Phys. Lett.* **53** (1988), 1891.
- [14] H. Hosono, *J. Non-Cryst. Solids* **187** (1995), 457.
- [15] J.B. Bates, R.W. Hendricks & L.B. Shaffer, *J. Chem. Phys.* **61** (1978), 4163.
- [16] F.L. Galeener, *J. Non-Cryst. Solids* **49** (1982), 53, *ibid* 71 (1985), 373.

## EFFECT OF THE COMPOSITION OF SOME LEAD BORATE GLASSES CONTAINING URANIUM AND TIN IONS ON THEIR OPTICAL ABSORPTION CHARACTERISTICS

Morsi M. MORSI & Nabil ABD-ELSHAFI  
*Glass Research Department, National Research Centre,  
Dokki, Cairo, Egypt*

The optical absorption curves of lead borate glasses of the nominal compositions (in mol%)  $(100-x)\text{B}_2\text{O}_3 \cdot x\text{PbO}$ , containing  $y$  and  $z$  gram atoms of uranium and tin, respectively per 100 gram glass, were studied in the range 300-900 nm (where  $x=40, 52, 56$ , and  $60$ ,  $y=0.0.1$ , and  $z=0, 0.05, 0.1$  or  $0.2$ ). The U-Sn-free glass samples appeared colorless or with a yellow tint depending on the amount of PbO. These glass samples show no absorption characteristics in the visible region. However, their UV cut off shifts towards longer wavelengths with increasing PbO content. U-doping causes a further shift of the UV cut off towards longer wavelengths, in addition to the development of two absorption bands at 410-440 and 480-495 nm due to  $\text{U}^{6+}$  ions in uranyl groups. The simultaneous presence of Sn-ions with U-ions in glass samples with more than 40 mol% PbO causes the development of two other absorption bands at 625-650 and 820-840 nm due to  $\text{U}^{4+}$  and  $\text{U}^{5+}$ , respectively. The results are discussed on the bases of redox reactions between  $\text{Sn}^{2+}$  and  $\text{U}^{6+}$ , and of the stability of  $\text{U}^{6+}$  in the glass samples with the lowest PbO content.

### 1. INTRODUCTION

Uranium forms different compounds in which it acts as a cation of different oxidation states or partially as an anion. Under oxidizing conditions  $\text{U}^{6+}$  is the stable form. The uranyl and uranate groups are derivatives of this state [1]. It was reported [2] that the general appearance of the spectra of the uranium complexes is almost identical but the overall intensities vary in different complexes. Four different states of uranium ions can be detected in glass, viz.,  $\text{U}^{6+}$  (in uranyl  $\text{UO}_2^{2+}$  or uranate  $\text{UO}_4^{2-}$  groups),  $\text{U}^{5+}$ ,  $\text{U}^{4+}$  and  $\text{U}^{3+}$ . The  $\text{U}^{2+}$  ions are very rarely formed in glasses, but may be formed in some borosilicate glasses in the presence of strong reducing agents [3]. The absorption spectra of  $\text{U}^{6+}$  in borate glasses have been found [4] to be similar to those in aqueous solution, especially in those glasses of low alkali content. The colors produced by uranium in silicate and borosilicate glasses have been extensively discussed [1].

Changes of the spectroscopic features in some borate glasses have been investigated as a function of the uranium content [5]. The absorption and luminescence-characteristics of uranium activated boron oxide glasses were also

studied [6]. The effect of gamma irradiation on the absorption characteristics [7] and the oxidation states of uranium [8] in aluminoborate glasses have been investigated. In the present work the absorption characteristics of uranium-ions in lead borate glasses with different PbO content is investigated partly in combination with tin ions.

## 2. EXPERIMENTAL

### 2.1. Uranium-free Specimens

A series of lead borate glasses (Table 1), containing 40-60 mol% PbO, were prepared. The glass with the least PbO content visually appeared colorless while other glasses appeared yellowish. The materials used for the preparation used were analytical-grade chemicals. Glass batches were melted in platinum crucibles at 900-1050°C, according to the glass composition, in an electrically heated furnace. After melting for two hours, part of the melt was poured in a clean dish and quenched in air; this part will be referred to as the parent glass. The other part of the melt (which remained in the crucible) was cast onto a preheated clean rectangular iron plate, which was immediately transferred to an annealing muffle furnace at 400°C.

**Table 1**  
Positions and Possible Assignments of the Observed Bands in the Spectra of the Binary Lead Borate Glasses Investigated.

Possible Assignment				U <sup>6+</sup>	U <sup>6+</sup>	U <sup>4+</sup>	U <sup>5+</sup>	
Glass No.	x PbO	y U	z Sn	Band Position B	Position C	G	M	Colour
1	40	-	-	-	-	-	-	Colourless
1U	40	0.1	-	410	480	-	-	Yellow
1a	40	0.1	0.05	430	495	-	-	Yellow
1b	40	0.1	0.1	430	480	-	-	Golden-yellow
1c	40	0.1	0.2	430	480	-	-	Yellow
2	52	-	-	-	-	-	-	Yellowish tint
2U	52	0.1	-	435	490	-	-	Brownish-yellow
2a	52	0.1	0.05	*	485	650	825	Yellowish-green
2b	52	0.1	0.1	*	490	650	820	Greenish-yellow
2c	52	0.1	0.2	*	490	650	830	Pale green
3	56	-	-	-	-	-	-	Pale yellow
3U	56	0.1	-	435	495	-	-	Brownish-yellow
3a	56	0.1	0.05	435	490	635	840	Yellowish-green
3b	56	0.1	0.1	435	460	645	840	Green
3c	56	0.1	0.2	*	450	650	840	Greenish-yellow
4	60	-	-	-	-	-	-	Yellow
4U	60	0.1	-	440	495	-	-	Brownish-yellow
4a	60	0.1	0.05	435	490	625	820	Yellowish-green
4b	60	0.1	0.1	*	*	635	820	Olive (deep green)
4c	60	0.1	0.2	*	*	635	825	Green

\*The position is not clearly identified; x in mol%; y and z in gram atoms per 100 gram glass



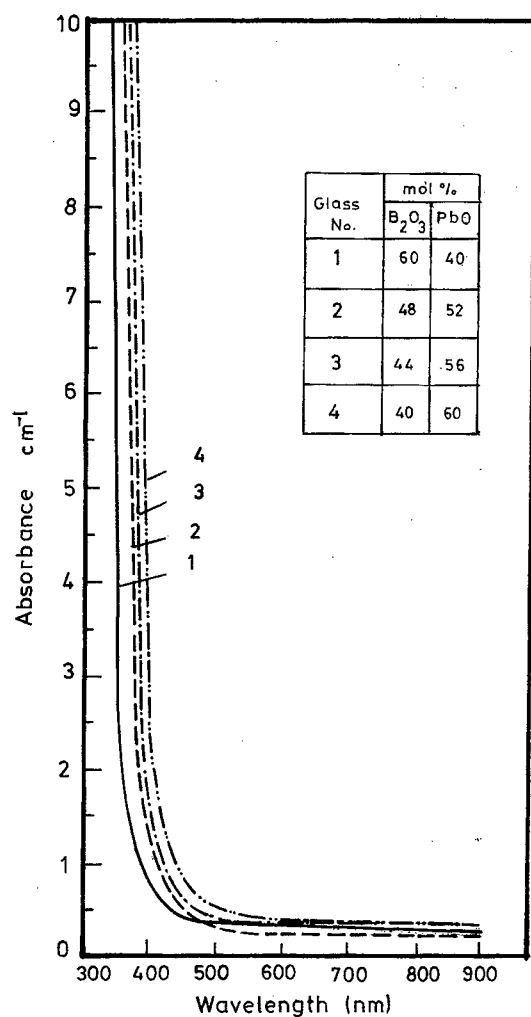


Fig. 1. The effect of base glass composition on the optical absorption spectra of U- and Sn-free glasses.

## 2.2. Uranium and Tin-Containing Specimens

The quenched parent glass was crushed and used as a synthetic model glass for incorporation of uranium and tin ions.  $\text{UO}_2(\text{CH}_3\text{COO})_2 \cdot 2\text{H}_2\text{O}$  was used to incorporate 0.1 g atom of uranium per 100 g glass. The added ingredients were thoroughly mixed, then the batches were melted, cast, and annealed as previously described. SnO was used to incorporate 0.05, 0.1 and 0.2 g of Sn atom per 100 g glass.

## 2.3. Optical Absorption Measurements

The optical absorption in the region 300-900 nm was measured using a re-

cording Uvicon 860 Spectrophotometer (Kontron Swiss Company). The spectra are presented in terms of absorbance per cm versus wavelength (nm) to facilitate comparison of samples with different thickness.

### 3. RESULTS AND DISCUSSION

#### 3.1. The Optical Absorption of U-Free Glasses

Figure 1 shows no absorption bands in the visible region. However, as the PbO content increases the UV-absorption edge of the glass shifts towards longer wavelengths. It shifts from 345 to 375 nm in glasses containing 40 and 60 mol% PbO, respectively. This shift explains the change of the visual colors of the glasses from colorless (glass no. 1) to yellow (glasses nos. 2-4). This shift can be considered as evidence for the existence of  $Pb^{4+}$ , since this would give rise to the electron-transfer absorption which has its maximum at longer wavelength than that of  $Pb^{2+}$  [9,10]. The probability of formation of the dipole  $[Pb^{4+}(2e^-)]^{2+}$  [11], represents an alternative explanation for the yellow and colorless appearance of lead borate glasses. This dipole is responsible for the asymmetric environment of  $Pb^{2+}$  ions by oxygen ions in these yellowish glasses. If these ions ( $Pb^{2+}$ ) are moved into a symmetric environment, the color is destroyed and the glass appears less colored or colorless. Consequently, the  $Pb^{2+}$  ions in glass no. 1, with the least PbO-content, are present in symmetrical sites and in high proportions.

#### 3.2. The Optical Absorption of Uranium-Doped Glasses

The absorption spectra of uranium-containing glasses in Fig. 2 show two absorption bands B and C, at about 410-440 and 480-495 nm, respectively. When the positions of these bands are compared with those recorded by other workers [12-16] the bands B and C can be attributed to the optical absorption of  $U^{6+}$  associated with uranyl groups. It has been suggested that  $U^{6+}$  is present in uranyl or in uranate groups depending upon the basicity of the glass and that the colour change from pale greenish to deeper yellow is due to the shift of the uranyl-uranate equilibrium towards uranate groups [1].

Comparison of the absorption spectra of solutions containing uranium ions has led to the conclusion [17] that it is unlikely for  $U^{6+}$  to occur as the uranate group  $UO_4^{2-}$  in basic glasses and that it is present in uranyl groups for all alkali contents. This uranyl group is probably present in glasses no. 1U-4U as  $[UO_2(O_2)]^{2-}$  with considerable increase in structural asymmetry which may explain the high increase in the intensities of the two bands B and C as the PbO content is increased.

From Figs 1 and 2, it can be noticed that the addition of uranium ions to lead borate glasses causes the UV absorption edge to shift further towards longer wavelengths. It shifts from 345-375 to 355-415 nm. This shift may suggest either a weakening of the bonding in the glass structure or the formation of  $Pb^{4+}$  ions coordinated by four oxygens in the glass structure, with higher proportions as the PbO content is increased. Durability studies indicated [18] that doping of lead borate glasses with uranium ions retards the dissolution

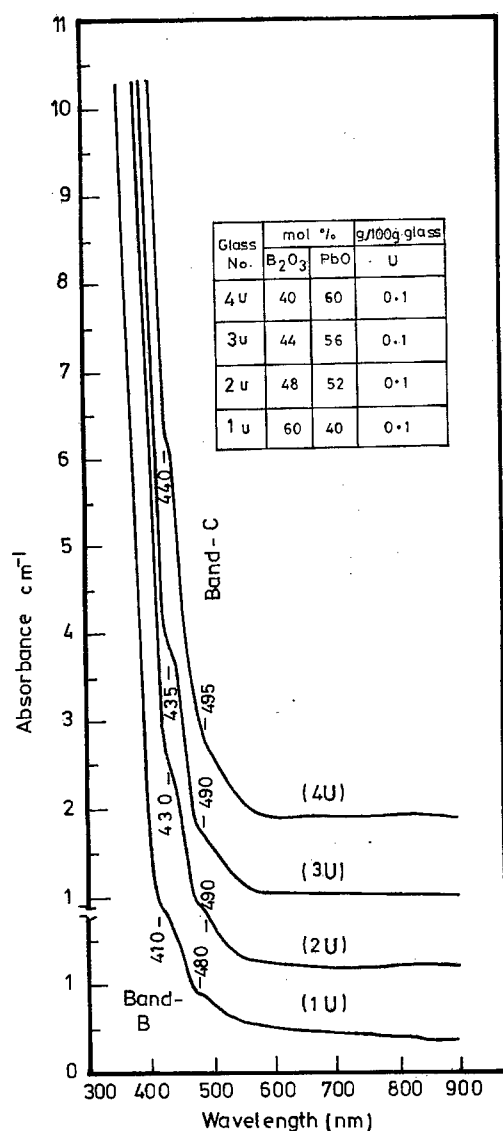


Fig. 2. The effect of base glass composition on the optical absorption spectra of U-containing glasses.

rate, which suggests that the first suggestion is unlikely.

### 3.3. Effect of Sn<sup>2+</sup> Ions on Uranium Oxidation States

The addition of Sn<sup>2+</sup> to uranium-containing glasses (1U, 2U, 3U and 4U) induces visual colour changes (Table 1) from yellow (for the glass with the least PbO content) to yellowish-green and even green colors (for glasses with 52, 56 and 60% PbO). This change in coloration indicates the formation of lower

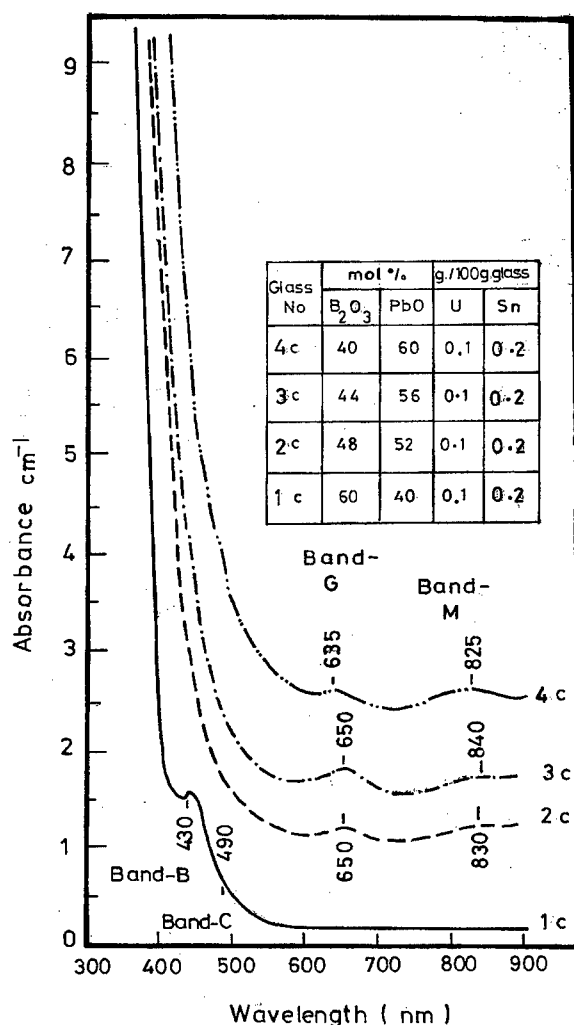
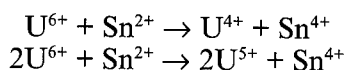


Fig. 3. The effect of base glass composition on the optical absorption spectra of U- and Sn-containing glasses.

oxidation states of uranium in appreciable amounts in those glasses with more green coloration. Figure 3 shows the development of bands G, M, B and C in glasses with the highest tin content at varying PbO content. Table 1 illustrates the positions of these bands. The bands G (at 625-650 nm), and M (at 820-840 nm) can be attributed to  $U^{4+}$  and  $U^{5+}$ , respectively. The formation of lower oxidation states of uranium suggests the occurrence of the redox reactions:



The acidity and basicity of the glasses seem to be connected with the reduc-

tion susceptibility, but may be not the only factors which affect the reducibility of uranium ions in the glasses studied. The above reactions seem more likely to occur in borate glasses with 52-60 mol% PbO than in the glass with 40 mol% PbO. It can be seen that the uranium ions in the latter glass are difficult to interact with  $\text{Sn}^{2+}$ . These results may indicate that increasing PbO-content decreases the stability of the  $\text{U}^{6+}$  oxidation state, thus rendering it more susceptible for reduction by tin ions as revealed by the more intense and well developed bands due to  $\text{U}^{5+}$  and  $\text{U}^{4+}$  states. A field stabilization may be brought into the glass by the presence of dominant adequate coordination sites for  $\text{U}^{6+}$  (uranyl ions) in the glass matrix [3].

#### 4. REFERENCES

- [1] W.A. Weyl, *Colored Glasses* (Soc. Glass Technol., Sheffield, 1959), pp 204-211.
- [2] J.L. Rayan & W.E. Keder, *Adv. Chem. Ser.*, **71** (1967), 335.
- [3] H.D. Schreiber & G.B. Balazs, *Phys. Chem. Glasses* **23** (1982), 193.
- [4] A. Paul, *Chemistry of Glass* (Chapman and Hall, London, 1982), pp188-191.
- [5] E. Culoa, I. Milea & T. Iliescu, *J. Non-Cryst. Solids* **175** (1994), 98.
- [6] N.G. Lohani, G.C. Joshi & J.C. Joshi, *Indian J. Phys.* **58B** (1984), 512.
- [7] S. El-Kansol, M.M. Morsi & M.A. Adawi, *Egypt J. Phys.* **14** (1983), 209.
- [8] M.M. Morsi, S. El-Kansol & M.A. Adawi, *J. Am. Ceram. Soc.* **66** (1983), 41-c.
- [9] H. Bach & J.A. Duffy, *Phys. Chem. Glasses* **22** (1981), 86.
- [10] A. Paul, *Phys. Chem. Glasses* **11** (1970), 46.
- [11] W.A. Weyl & E.C. Marboe, *The Constitution of Glasses - A dynamic Interpretation* Vol. 1: *Fundamentals of the Structure of Inorganic Liquids and Solids* (Interscience, N.Y. London, 1964), p 25.
- [12] H.D. Schreiber, *J. Non-Cryst. Solids* **49** (1982), 189.
- [13] C.B. Greenberg & P.W. French, *J. Optical Soc. America* **58** (1968), 475.
- [14] M.R. Chakrabarty, *Glass Ceram. Bull.* **48** (1969), 1076.
- [15] D.J. Mackay, N.A. Runciman & E.R. Vance, *Phys. Rev.* **B11** (1975), 211.
- [16] M.A. Carrell & D.R. Wilder, *J. Nucl. Mater.* **13** (1964), 142.
- [17] A. Paul, *Trans. Indian Ceram. Soc.* **28** (1969), 63.
- [18] N. Abd-El Shafi, Ph.D. Thesis (Cairo University, 1992).

# HYPERSENSITIVITY OF NEODYMIUM IONS IN SODIUM BORATE, SODIUM SILICATE, AND SODIUM BOROSILICATE GLASSES

Karl GATTERER

*Institut für Physikalische und Theoretische Chemie,  
Graz University of Technology, A-8010 Graz, Austria*

The optical absorption spectra of sodium borate, sodium silicate, and sodium borosilicate glasses containing different amounts of the network modifier and 1 mol%  $\text{Nd}_2\text{O}_3$  are compared. Special emphasis is laid on the shape of the hypersensitive transition  $^4\text{I}_{9/2} \rightarrow ^4\text{G}_{5/2}$  of the  $\text{Nd}^{3+}$  ions which changes significantly with the composition in sodium borate and sodium borosilicate glasses, but is remarkably constant in sodium silicate glasses. The shape of this transition strongly depends on the symmetry and strength of the crystalline field acting on the  $\text{Nd}^{3+}$  ions. Generally, a difference in its shape demonstrates a difference in the environment, or conversely, similar environments will produce similar shapes. The constancy of the shape in sodium silicate glasses provides an easy method for estimating the partitioning of the  $\text{Nd}^{3+}$  ions between boron and silicon rich portions in sodium borosilicate glasses. A correlation of these results with the structural model of Bray and co-workers on sodium borosilicate glasses is attempted.

## 1. INTRODUCTION

The continuing interest in glasses doped with lanthanide ions is based on their potential application as laser materials, amplifiers, and up-converting phosphors. Extensive investigations of the absorption and luminescence properties of these ions in different glass types as well as in glasses of the same type but with different compositions have indicated significant and characteristic effects of the glass host on the ions optical spectra [1-6]. In oxide glasses the addition of a network modifier leads to the creation or annihilation of structural groups differing in their space requirements and in the relative number of bridging oxygens (BO) and non-bridging oxygens (NBO). Hence continuous changes of the molar volumes, densities, packing ratios, etc., result. On the microscopic scale lanthanide-oxygen distances, partial oxygen charges and rare-earth coordination numbers are affected. These properties, however, are relevant for the optical spectra because positions, shapes and intensities of electronic  $f-f$  transitions depend to some extent on the distribution of charges in the first coordination shell. The continuous changes of the above mentioned bulk properties are thus reflected in continuous changes of the optical spectra. There are some  $f-f$  transi-

tions in lanthanides which are exceptionally sensitive to changes in the ions environment. They are called hypersensitive transitions (h.s.t.) and conform to the free-ion quadrupole selection rules  $\Delta S=0$ ,  $\Delta L \leq 2$ ,  $\Delta J \leq 2$  [7,8]. Here S, L, and J are the spin, orbital, and total angular momentum quantum numbers of the  $^{2S+1}L_J$  states involved in the transition. While several different mechanisms have been proposed which lead towards a quantitative understanding of the phenomenon of hypersensitivity in rare-earth ions [9-14], only in very few single crystals with well defined rare-earth environment is a semi-quantitative agreement between observed and calculated h.s.t. intensities obtained [15].  $\text{Nd}^{3+}$  has a h.s.t. which is conveniently placed in the visible range. The shape of the h.s.t. depends on the symmetry and strength of the crystalline field acting on the  $\text{Nd}^{3+}$  ions [16-19]. In the present contribution  $\text{Nd}^{3+}$  is used as a probe demonstrating to what extent the structural changes in sodium borate, sodium silicate, and sodium borosilicate glasses with increasing modifier content are reflected in the changes of the h.s.t. shape. The chosen glass systems have the advantage of being well characterised by different experimental methods as well as by structure simulations. For all three glass types structural models derived from the experimental data do exist. This is mainly due to the outstanding contribution of P.J. Bray and co-workers to this field [20-24].

## 2. EXPERIMENTAL

Glasses with the composition  $x\text{Na}_2\text{O} \cdot y\text{B}_2\text{O}_3 \cdot z\text{SiO}_2$  (x, y, z are mol %) to which was added 1 mol %  $\text{Nd}_2\text{O}_3$  were prepared (Table 1). The glasses were obtained by melting appropriate amounts of analytical grade  $\text{Na}_2\text{CO}_3$ ,  $\text{SiO}_2$ ,  $\text{H}_3\text{BO}_3$ , and  $\text{Nd}_2\text{O}_3$  (99.99%) in platinum crucibles for 1.5 to 2 h at temperatures between 850-1000°C for sodium borates, 900-1050°C for sodium borosilicates and 1600°C for sodium silicates. The melts were quenched between metal plates. The flat samples were ground and carefully polished for the optical measurements.

The optical spectra in the visible range (12 000-30 000  $\text{cm}^{-1}$ ) were recorded with a spectrophotometer equipped with a  $f=0.25$  m Czerny-Turner double monochromator and photomultiplier. For low temperature measurements (20 K) the same spectrometer was used in combination with a closed cycle helium cryostat. The density was determined using the pycnometer method.  $\text{Nd}^{3+}$  concentrations were calculated from the densities. Table 1 contains the corresponding compositions, densities, and  $\text{Nd}^{3+}$  concentrations. The fraction of  $\text{Nd}^{3+}$  in the silicate portion of the ternary glasses, which is also included in Table 1, was determined by the method explained in the text.

## 3. RESULTS AND DISCUSSION

### 3.1. Absorption Spectra

The absorption spectra of  $\text{Nd}^{3+}$  ions doped into oxide glasses consist of transitions from the ground state,  $^4I_{9/2}$ , to a number of excited  $^{2S+1}L_J$  states. All states are crystal-field-split by the influence of the immediate environment (i.e. the first coordination shell) which consists of oxygens from the glass host.

**Table 1**  
Composition\*, Density, Nd<sup>3+</sup> Concentration and Fraction of Nd<sup>3+</sup> in the Sodium Silicate Portion of the Glass Samples

Composition (mol %)			R=	K=	Density	Nd <sup>3+</sup> Conc.	Fract. of Nd <sup>3+</sup>
xNa <sub>2</sub> O	yB <sub>2</sub> O <sub>3</sub>	zSiO <sub>2</sub>	Na <sub>2</sub> O/B <sub>2</sub> O <sub>3</sub>	SiO <sub>2</sub> /B <sub>2</sub> O <sub>3</sub>	(g/cm <sup>3</sup> )	(mol/dm <sup>3</sup> )	in SiO <sub>2</sub> (%)
<b>Sodium Borate Glasses</b>							
10	90	-	0.111	-	2.099	0.5869	-
12.5	87.5	-	0.143	-	2.147	0.6019	-
15	85	-	0.176	-	2.194	0.6167	-
17.5	82.5	-	0.212	-	2.237	0.6305	-
20	80	-	0.250	-	2.282	0.6449	-
27.5	72.5	-	0.379	-	2.373	0.6760	-
30	70	-	0.429	-	2.377	0.6790	-
33.3	66.7	-	0.499	-	2.427	0.6957	-
35	65	-	0.538	-	2.430	0.6979	-
37.5	62.5	-	0.600	-	2.444	0.7038	-
<b>Sodium Silicate Glasses</b>							
28	-	72	-	-	2.573	0.8120	100
30	-	70	-	-	2.581	0.8141	100
33.3	-	66.7	-	-	2.596	0.8180	100
35	-	65	-	-	2.600	0.8188	100
37.5	-	62.5	-	-	2.615	0.8230	100
40	-	60	-	-	2.630	0.8271	100
42.5	-	57.5	-	-	2.635	0.8189	100
45	-	55	-	-	2.646	0.8309	100
47.5	-	52.5	-	-	2.674	0.8390	100
50	-	50	-	-	2.740	0.8591	100
<b>Sodium Borosilicate Glasses</b>							
16	64	20	0.250	0.313	2.290	0.6620	0.5
20	60	20	0.333	0.333	2.390	0.6939	1.5
22.9	57.1	20	0.401	0.350	2.448	0.7130	2.0
24.8	55.2	20	0.449	0.362	2.446	0.7139	2.5
26.7	53.3	20	0.500	0.375	2.478	0.7248	4.0
28.4	51.6	20	0.550	0.387	2.533	0.7423	6.5
30	50	20	0.600	0.400	2.538	0.7250	10.0
33	47	20	0.702	0.426	2.533	0.7461	26.5
17.1	42.9	40	0.399	0.932	2.450	0.7290	2.5
18.6	41.4	40	0.449	0.966	2.485	0.7406	3.0
20	40	40	0.500	1.000	2.499	0.7460	3.5
21.3	38.7	40	0.550	1.034	2.533	0.7572	4.0
22.5	37.5	40	0.600	1.067	2.541	0.7607	7.0
25	35	40	0.714	1.143	2.558	0.7679	15.5
28	32	40	0.875	1.250	2.576	0.7760	32.0
30	30	40	1.000	1.333	2.590	0.7820	21.0
10	30	60	0.333	2.000	2.371	0.7199	2.0
13.3	26.7	60	0.498	2.247	2.488	0.7583	5.0
16	24	60	0.667	2.500	2.538	0.7760	6.0
20	20	60	1.000	3.000	2.549	0.7829	22.0
25	15	60	1.667	4.000	2.587	0.7993	47.0
30	10	60	3.000	6.000	2.581	0.8021	21.0

\* ... 1 mole Nd<sub>2</sub>O<sub>3</sub> was added per 100 mole glass



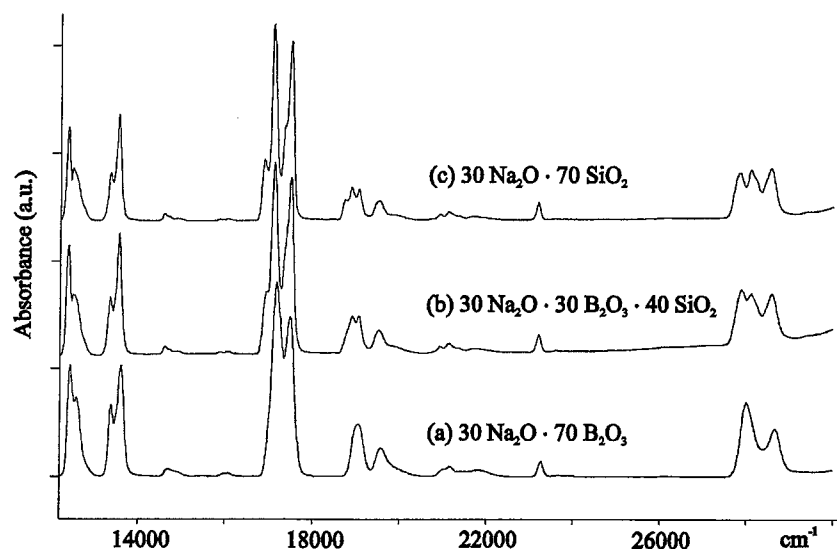


Fig.1. Optical absorption spectra recorded at 20 K of sodium borate (a), sodium borosilicate (b) and sodium silicate glasses (c) containing 1 mol %  $\text{Nd}_2\text{O}_3$ .

Due to the absence of long range order in the glass the microsymmetry around the  $\text{Nd}^{3+}$  ions differs slightly from site to site and therefore the transitions are inhomogeneously broadened with typical halfwidths of ca.  $200\text{ cm}^{-1}$  for isolated bands. Figure 1 shows exemplary spectra of a sodium borate (bottom), a sodium borosilicate (middle) and a sodium silicate glass (top). The most pronounced differences in these spectra appear in the intense absorption band centred at  $17200\text{ cm}^{-1}$  which consists of transitions to the two excited states  $^4\text{G}_{5/2}$  and  $^2\text{G}_{7/2}$ . These two states are already close in energy in the free ion and therefore usually not resolved in glasses and solutions due to the inhomogeneous broadening of the absorption bands. The  $^4\text{I}_{9/2} \rightarrow ^4\text{G}_{5/2}$  transition of  $\text{Nd}^{3+}$  is hypersensitive. The region of the h.s.t. is shown in the expanded scale view of Fig. 2(a) for all sodium borate glasses and in Fig. 2(b) for the sodium silicate glasses investigated. The traces are offset against each other with increasing modifier content on the absorbance axis. For later reference the four distinct features of the h.s.t. shape are labelled with letters A-D. In Fig. 3 the same spectral region is displayed for the sodium borosilicate glasses with 20, 40, and 60 mol%  $\text{SiO}_2$ .

### 3.2. Shape of the Hypersensitive Transition

From Fig. 2 it is evident that the h.s.t. shape of  $\text{Nd}^{3+}$  in sodium silicate glasses is almost independent of the modifier content. It shows two main peaks located at  $17090\text{ cm}^{-1}$  (B) and  $17490\text{ cm}^{-1}$  (D) with shoulders (A and C) towards their low energy sides. On the other hand the h.s.t. shape in sodium borate glasses shows a continuous change with the modifier content. A shift of band B is observed and the shoulders are developed only for modifier con-

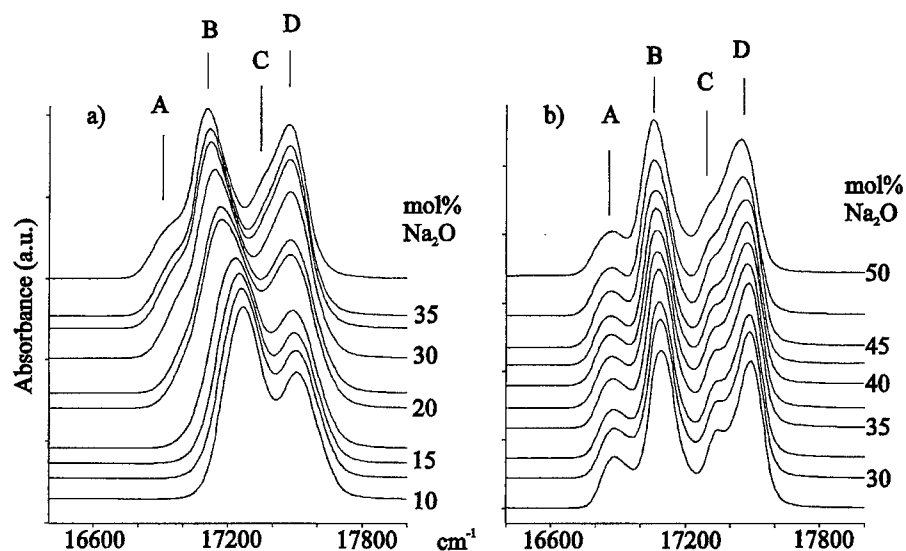


Fig.2. The hypersensitive  $^4I_{9/2} \rightarrow ^4G_{5/2}, ^2G_{7/2}$  transitions of  $Nd^{3+}$  in sodium borate glasses (a) and in sodium silicate glasses (b).

tents starting with 33.3 mol%. Generally, a difference in the shape of a h.s.t. demonstrates a difference in the environment of the rare-earth ion, or conversely, similar environments will produce similar shapes.

In solutions the shape of the h.s.t. of  $Nd^{3+}$  has already successfully been used to monitor changes of the coordination number of the rare-earth ion in differ-

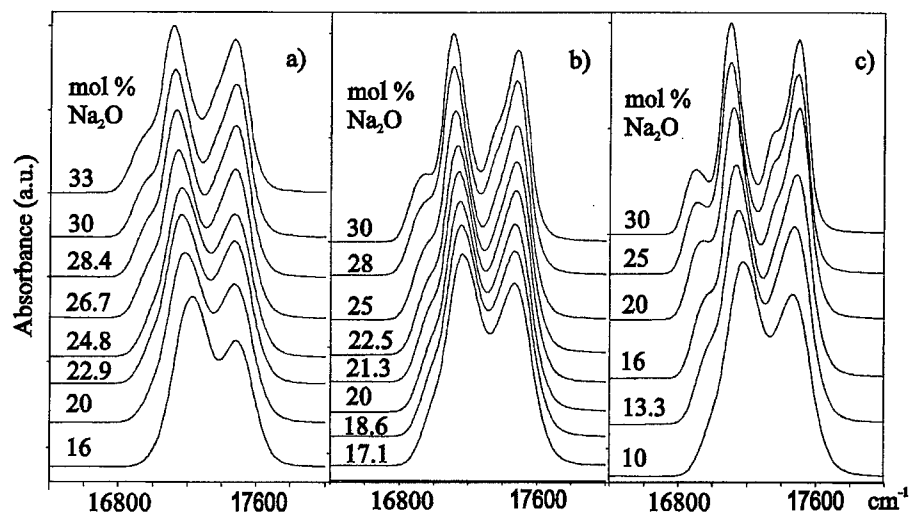


Fig.3. The hypersensitive  $^4I_{9/2} \rightarrow ^4G_{5/2}, ^2G_{7/2}$  transitions of  $Nd^{3+}$  in sodium borosilicate glasses with 20 (a), 40 (b), and 60 (c) mol%  $SiO_2$ .

ent solvents [17]. For oxide glasses, where the rare-earth ion is surrounded by oxygens, the type (BO or NBO), the number, and the arrangement of these oxygens are the determining factors for the h.s.t. shape. From the near constancy of this shape in sodium silicate glasses one must therefore conclude, that the environment around the  $\text{Nd}^{3+}$  ions is established in these glasses already at low modifier contents and remains fairly constant in terms of symmetry and coordination numbers, while it undergoes an evolution with increasing modifier content in the sodium borate glasses. Since the h.s.t. in sodium borate glasses with modifier contents of 33.3 mol% or more develops the four distinct features (A-D) and begin to resemble more and more closely the sodium silicate h.s.t. shape it must further be concluded that both in the high modifier content sodium borate glasses and the sodium silicate glasses the environment of the  $\text{Nd}^{3+}$  ions are very similar.

In oxide glasses the surrounding oxygens are either BO or NBO where the latter are the preferred neighbours of the  $\text{Nd}^{3+}$  ions. This is due to their stronger electrostatic interaction and to the fact that NBO can be more readily controlled to satisfy the rare-earth ions bonding requirements since they are attached at only one end to the glass network. For oxide glasses rare-earth coordination environments consisting of eight or nine NBO have been proposed [25-27]. In sodium silicate glasses the creation of NBO starts immediately with the addition of the modifier and according to the  $Q^n$  distribution determined by MAS-NMR [28] the glasses used for the present investigation (28-50 mol%  $\text{Na}_2\text{O}$ ) contain ample amounts of  $Q^3$  with one and  $Q^2$  with two NBO per  $\text{SiO}_4$  unit. In sodium borate glasses on the other hand the situation is quite different. Up to about 30 mol%  $\text{Na}_2\text{O}$  the modifier is consumed to convert trigonal  $\text{B}_3$  into tetrahedral  $\text{B}_4$  units with all BO and the creation of NBO only starts at higher  $\text{Na}_2\text{O}$  contents [23,24]. The change of the h.s.t. shape (development of the shoulders A and C) starting at about 33.3 mol% modifier content indicates that as soon as NBO are available the  $\text{Nd}^{3+}$  ions are attracted by them and an NBO coordination environment similar to that in sodium silicate glasses is established [4].

### 3.3. Partitioning of the $\text{Nd}^{3+}$ Ions in Sodium Borosilicate Glasses

For the description of the structural changes in the ternary sodium borosilicate glasses the two compositional parameters  $R=\text{Na}_2\text{O}/\text{B}_2\text{O}_3$  and  $K=\text{B}_2\text{O}_3/\text{SiO}_2$  are commonly used. According to the Bray model [22-24] glasses with  $R<0.5$  consist of a boron-rich and a silicon-rich portion which do not mix. All the  $\text{Na}_2\text{O}$  is included in the boron-rich phase of the glass and consumed to create  $\text{B}_4$  units. Thus, the glass may be considered as a sodium borate glass diluted with pure silica. The maximum sodium content in the boron-rich portion is reached with the diborate composition at  $R=0.5$ . At higher modifier contents sodium ions and tetrahedral  $\text{B}_4$  groups enter the silicate portion of the glass to form reedmergnerite groups. The sodium ions are used for charge compensation in these groups. Only when all the  $\text{SiO}_2$  is used up at  $R>0.5+K/16$  does the creation of NBO in the silicate portion of the glass start. A recent investigation on sodium borosilicate glasses in this compositional range indicated that all the NBO are located in  $Q^3$  or  $Q^2$  groups

which are not connected to  $B_4$  units. This could be rendered possible by danburite groups [29]. At  $R > 0.5 + K/4$  the additional  $Na_2O$  is shared for the formation of NBO in the boron-rich portion and the creation of  $Q^2$ . From this structural model the following predictions concerning the optical spectra of  $Nd^{3+}$  in sodium borosilicate glasses can be made. In glasses with  $R < 0.5 + K/16$  the ions are expected to be found in the sodium borate portion of the glasses only. It is well known that it is almost impossible to dope  $Nd_2O_3$  into pure silica phases without the presence of a modifier [30]. In glasses with  $R > 0.5 + K/16$   $Nd^{3+}$  ions may enter the silicate portion as well. Given the affinity of  $Nd^{3+}$  to NBO the optical spectra would then consist of a convolution of sodium borate and sodium silicate shapes where the weight of the sodium silicate shape corresponds to the fraction of  $Nd^{3+}$  ions in the silicate portion of the glass. The near-constancy of the h.s.t. shape in sodium silicate glasses then provides an easy method for estimating the amount of  $Nd^{3+}$  ions in the silicate portion of the glass. From the h.s.t. shape of a sodium borosilicate glass the constant h.s.t. sodium silicate shape weighted by a factor  $c$  ( $0 \leq c \leq 1$ ) is subtracted. Since the h.s.t. shapes of  $Nd^{3+}$  in sodium silicate and sodium borate glasses differ most on the low energy side of the band a factor  $c$  which is too large will produce a negative absorbance on the low energy side of the difference spectrum. The largest  $c$ -values which do not produce this negative absorbance hence serve as estimates for the upper limit of the fraction of  $Nd^{3+}$  ions in the silicate portion of the glass. The fraction of  $Nd^{3+}$  ions in the sodium silicate portion of the ternary glasses determined with this weighted difference method are included in Table 1.

Even for  $R < 0.5$  a small but continuous increase of the  $Nd^{3+}$  concentration for all three sodium borosilicate systems is found. With increasing modifier content a much sharper increase is observed between  $R = 0.55$  and  $0.60$  for the 20 mol%  $SiO_2$  glasses, between  $R = 0.60$  and  $0.714$  for the 40 mol%  $SiO_2$  glasses, and between  $R = 0.667$  and  $1.0$  for the 60 mol%  $SiO_2$  glasses. The ternary glasses used for the present investigation were not prepared with constant  $K$ -values, however the  $K$ -values of the sodium borosilicate families (20, 40, and 60 mol%  $SiO_2$ ) are sufficiently different and do not overlap. In order to correlate the results of the partitioning of the  $Nd^{3+}$  ions with the Bray model averaged  $K$ -values for each family were taken (20 mol%  $SiO_2$ :  $K_{av} = 0.37$ , 40 mol%  $SiO_2$ :  $K_{av} = 1.09$ , 60 mol%  $SiO_2$ :  $K_{av} = 3.30$ ). With these  $K$ -values the sharp increase of the  $Nd^{3+}$  concentration in the silicate portion of the glasses is found to take place just in the compositional range where according to the Bray model the creation of silicate NBO commences. However, the small continuous increase of the  $Nd^{3+}$  concentration at much smaller  $R$ -values, however, indicates that a small amount of the modifier enters the silicate phase at a much earlier stage. This behaviour was also suspected before [29]. The drop of the  $Nd^{3+}$  concentration in the silicate portion which is observed for the two glasses  $30Na_2O.30B_2O_3.40SiO_2$  and  $30Na_2O.10B_2O_3.60SiO_2$  occurs in the range  $R > 0.5 + K/4$  where additional NBO are created in the boron-rich portion and indicates a stronger affinity of the  $Nd^{3+}$  ions for this phase. A similar conclusion was drawn from an investigation of  $Mn^{2+}$  in sodium borosilicate glasses [31].

#### 4. CONCLUSIONS

None of the proposed theoretical mechanisms of the hypersensitivity in rare-earth ions lends itself easily for adaptation to glasses because all of them require a very accurate knowledge of bond angles and rare-earth oxygen distances. However, in the present contribution it has been shown that the shape of the h.s.t. of  $\text{Nd}^{3+}$  ions in some oxide glasses can be used to monitor the changes in the rare-earth environment due to the creation and annihilation of BO and NBO induced by the addition of the network modifier. An estimate for the partitioning of the  $\text{Nd}^{3+}$  ions into borate and silicate portions of sodium borosilicate glasses was obtained by making use of the near-constancy of the h.s.t. shape in sodium silicate glasses.

#### Acknowledgements

The author gratefully thanks Prof. Salah Arafa from the American University in Cairo for helpful discussions. The work was supported by the Austrian Science Foundation, project no. P10713-CHE.

#### REFERENCES

- [1] R. Reisfeld, *Structure and Bonding* **22** (1975), 123.
- [2] M.J. Weber, *J. Non-Cryst. Solids* **123** (1990), 208.
- [3] Y. Nageno, H. Takebe & K. Morinaga, *J. Am. Ceram. Soc.* **76** (1993), 3081.
- [4] K. Gatterer, G. Pucker, H.P. Fritzer & S. Arafa, *J. Non-Cryst. Solids* **176** (1994), 237.
- [5] M.B. Saisudha & J. Ramakrishna, *Phys. Rev. B* **53** (1996) 6186.
- [6] G. Pucker, K. Gatterer, H.P. Fritzer, M. Bettinelli & M. Ferrari, *Phys. Rev. B* **53** (1996) 6225.
- [7] B.R. Judd, *Phys. Rev.* **127** (1962), 750.
- [8] C.K. Jørgensen & B.R. Judd, *Mol. Phys.* **8** (1964), 281.
- [9] B.R. Judd, *J. Chem. Phys.* **44** (1966), 839.
- [10] S.F. Mason, R.D. Peacock & B. Stewart, *Chem. Phys. Lett.* **29** (1974), 149.
- [11] S.F. Mason, R.D. Peacock & B. Stewart, *Mol. Phys.* **30** (1975), 1829.
- [12] R.D. Peacock, *Structure and Bonding* **22** (1975), 83.
- [13] D.E. Henrie, R.L. Fellows & G.R. Choppin, *Coord. Chem. Rev.* **18** (1976), 199.
- [14] B.R. Judd, *J. Chem. Phys.* **70** (1979), 4830.
- [15] F.S. Richardson, J.D. Saxe, S.A. Davis & T.R. Falkner, *Mol. Phys.* **42** (1981), 1401.
- [16] G.R. Choppin, D.E. Henrie & K. Buijs, *Inorg. Chem.* **5** (1966), 1743.
- [17] D.G. Karraker, *Inorg. Chem.* **6** (1967), 1863.
- [18] D.G. Karraker, *Inorg. Chem.* **7** (1968), 473.
- [19] D.E. Henrie & G.R. Choppin, *J. Chem. Phys.* **49** (1968), 477.
- [20] Y.H. Yun & P.J. Bray, *J. Non-Cryst. Solids* **27** (1978), 363.
- [21] S.Z. Xiao, *J. Non-Cryst. Solids* **45** (1981), 29.
- [22] W.J. Dell, P.J. Bray & S.Z. Xiao, *J. Non-Cryst. Solids* **58** (1983), 1.
- [23] P.J. Bray, *J. Non-Cryst. Solids* **75** (1985), 29.
- [24] J. Zhong & P.J. Bray, *J. Non-Cryst. Solids* **111** (1989), 67.
- [25] R. Reisfeld & N. Lieblich, *J. Phys. Chem. Solids* **34** (1973), 1467.
- [26] R. Reisfeld & Y. Eckstein, *J. Non-Cryst. Solids* **11** (1973), 261.
- [27] C. Brecher & L.A. Riseberg, *Phys. Rev. B* **13** (1973), 271.
- [28] H. Maekawa, T. Maekawa, K. Kawamura & T. Yokokawa, *J. Non-Cryst. Solids* **127** (1991), 53.
- [29] B.C. Bunker, D.R. Tallant, J.R. Kirkpatrick & G.L. Turner, *Phys. Chem. Glasses* **31** (1990), 30.
- [30] E.M. Levin, *Phys. Chem. Glasses* **7** (1966), 90.
- [31] P.E. Menassa, D.J. Simkin & P. Taylor, *J. Lumin.* **35** (1980), 223.

# LUMINESCENCE QUENCHING MECHANISMS FOR $\gamma$ -IRRADIATED BARIUM ALUMINOBORATE GLASSES DOPED WITH Fe

Walter M. PONTUSCHKA, Maria I.T. OLIVEIRA  
*Instituto de Física da Universidade de São Paulo,  
Caixa Postal 66318, 05315-970 São Paulo, Brazil.*

and

Sheila M. DEL NERY  
*Faculdade de Engenharia de Guaratinguetá,  
Universidade Estadual Paulista "Júlio Mesquita Filho",  
12500 - Guaratinguetá, SP, Brazil.*

A thermoluminescence (TL) study of barium aluminoborate glasses doped with Fe has been carried out in the temperature range 320 to 780 K. The origin of the TL is attributed to  $h^+$ - $Fe^{2+}$  recombinations between holes released from the remaining boron-oxygen hole centers (which survived after the complete elimination of boron electron centers), by heating to about 500 K, and the  $Fe^{2+}$  produced by the reduction of a small fraction of the  $Fe^{3+}$  ions during the ionizing irradiation. It is proposed that the recombination occurs inside the radius of interaction of about 15 Å of the delocalized antibonding state of a neighbouring substitutional  $Fe^{3+}$  (or  $Fe^{2+}$ ). Bypassing conditions are then created involving the simultaneous annihilation of the electron and hole.

## 1. INTRODUCTION

Iron ions, irrespective of their oxidation state, as well as cobalt and nickel [1] are found to be among the most efficient luminescence quenching agents when introduced as impurities, both in crystalline and amorphous systems. Previous work [2] has shown that not only  $Fe^{3+}$ , but also the  $Fe^{2+}$  is an efficient quenching agent of the blue thermoluminescence (TL) from the  $e^-h^+$  recombinations in aluminoborate glasses X-irradiated at 77 K. The complete quenching of the TL was achieved with the addition of 0.4 at.% of  $Fe^{3+}$  to the base glass.

The intention of the present work is to study the processes involved in the red TL emissions between 320 and 780 K. The possible recombination mechanisms are discussed on the basis of a theory proposed by Sumi [3,4], where the excited electron is trapped by a deep level releasing a multiphonon emission known as a "phonon-kick", followed by a coherent trapping of the hole and a subsequent non-radiative recombination.

## 2. EXPERIMENTAL

### 2.1. Sample Preparation

Barium aluminoborate glasses containing different concentrations of iron were prepared from E. Merck (Darmstadt) reagent grade raw materials ( $\text{Al}_2\text{O}_3$ ,  $\text{H}_3\text{BO}_3$  and  $\text{Ba}(\text{OH})_2 \cdot 8\text{H}_2\text{O}$ ), weighed to obtain samples of  $30\text{BaO} \cdot 50\text{B}_2\text{O}_3 \cdot 20\text{Al}_2\text{O}_3$  (mol%) base glass, with added amounts of  $\text{Fe}_2\text{O}_3$  and  $\text{FeSO}_4$ , as shown in Table 1. Most of the batches were melted in a platinum crucible at  $1300^\circ\text{C}$  for 2 h, annealed at  $500^\circ\text{C}$  and cooled to room temperature over 24 h. The  $\text{Fe}^{3+}$  concentration for each sample was evaluated from a calibration straight line drawn from the origin of a graph of the  $g=4.3$  EPR line [5] intensity plotted versus the nominal  $\text{Fe}^{3+}$  concentration, using the points for the samples having more than 0.1 at.% Fe. For lower dopant concentrations, it is difficult to introduce exactly the desired amount of dopant, due to the increased relative error in weighing, and hence it is essential for the purpose of the present TL study to determine the correct amount of  $\text{Fe}^{3+}$  in each sample.

As the EPR spectrum of the sample  $\text{B}_2$  (0.8 at.% Fe) has shown a negligible intensity for the signal of  $g=2.0$ , it was assumed that no clustering is present among the Fe ions, as it is expected for concentrations not greater than about 3 mol%  $\text{Fe}_2\text{O}_3$  [6]. On the other hand, the  $\text{Fe}^{2+}$  relative concentration in barium borate glasses is of about 4%, so that most of the iron is in the trivalent state [7]. Additional details of the method are found in reference [2].

### 2.2. TL Measurements

The measurements were carried out in the temperature range 320 to 780 K, with a commercial TL detector from Harshaw Nuclear Systems (model 2000A) and a pico-ammeter with integrator (model 2000B), an electrometer and plotter

**Table 1**  
Glass samples of  $30\text{Ba} \cdot 50\text{B}_2\text{O}_3 \cdot 20\text{Al}_2\text{O}_3$  (mol%) doped with  $\text{Fe}_2\text{O}_3$

Sample	Nominal doping Fe (at.%)	Measured by EPR Fe (at.%)	$\text{Fe}^{3+}$ spin density ( $10^{18}$ spins/ $\text{cm}^3$ )
$\text{E}_0$	-	$(5.9 \pm 0.4) \times 10^{-3}$	$1.13 \pm 0.08$
$\text{A}_3$	$1 \times 10^{-3}$	$(1.1 \pm 0.1) \times 10^{-2}$	$2.1 \pm 0.2$
$\text{D}_3$	$2 \times 10^{-3}$	$(1.5 \pm 0.1) \times 10^{-2}$	$2.9 \pm 0.2$
$\text{A}_2$	$1 \times 10^{-2}$	$(2.5 \pm 0.2) \times 10^{-2}$	$4.8 \pm 0.3$
$\text{D}_2$	$2 \times 10^{-2}$	$(3.2 \pm 0.3) \times 10^{-2}$	$6.1 \pm 0.6$
$\text{G}_2^{(a)}$	$2 \times 10^{-2}$	$(2.2 \pm 0.2) \times 10^{-2}$	$4.3 \pm 0.3$
$\text{F}_2$	$4 \times 10^{-2}$	$(5.7 \pm 0.5) \times 10^{-2}$	$11 \pm 1$
$\text{A}_1$	$1 \times 10^{-1}$	$(7.8 \pm 0.5) \times 10^{-2}$	$15 \pm 1$
$\text{C}_1^{(b)}$	$2 \times 10^{-1}$	$(2.2 \pm 0.2) \times 10^{-1}$	$42 \pm 4$
$\text{C}_2^{(b)}$	$3.5 \times 10^{-1}$	$(2.9 \pm 0.3) \times 10^{-1}$	$55 \pm 5$
$\text{B}_1$	0.5	$0.60 \pm 0.05$	$112 \pm 9$
$\text{B}_2$	0.8	$0.78 \pm 0.05$	$150 \pm 9$

<sup>(a)</sup> Sample doped with  $\text{FeSO}_4$ .

<sup>(b)</sup> Melted in an alumina crucible.

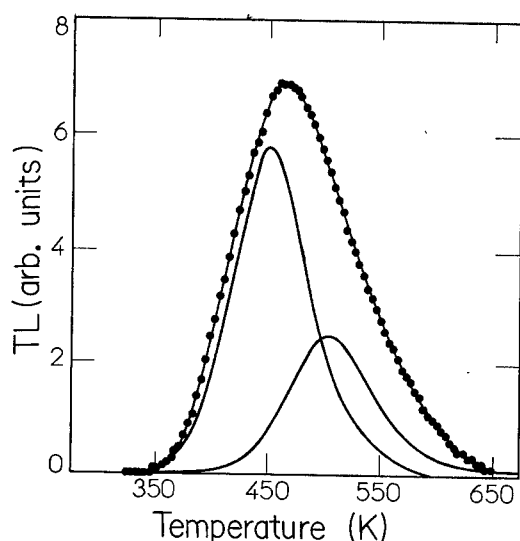


**Fig. 1.** A typical TL curve for the base glass sample  $E_0$ , fitted with two curves centered respectively at 440 and 504 K. The experimental curve is represented by the data points and curve fit by solid lines.

(model RB102) and an automatically controlled heater. Each run was performed for 90s with a  $5^\circ\text{C/s}$  linear temperature slope. The intensity calibration adjustments were made by comparing with the fluorescent light from an internal standard lamp and an internal circuit corrected for the effects of spurious dark currents. The glass samples were powdered and measured in a nitrogen atmosphere. A filter was used to avoid the interference from infrared radiation. The excitation was provided by a  $^{60}\text{Co}$  source ( $6.14 \text{ R/min}$ ) and preceded by thermal bleaching at  $400^\circ\text{C}$  for 30 min, in order to empty the traps contained in the sample.

### 3. RESULTS

A typical TL curve for the base glass sample,  $E_0$ ,  $\gamma$ -irradiated with  $10^6 \text{ Rad}$  for 10 min, is shown in Fig. 1, where a broad emission peaked at 463 K is observed, which was fitted with two peaks centered respectively at 440 and 504

**Table 2**

TL emission quenching effect, in the range between 320 and 670 K, produced by  $\text{Fe}^{3+}$  doping

Sample	$\text{Fe}^{3+}$ (at.%)	TL (arb. units)	$T_m$ (K)
$E_0$	$(5.9 \pm 0.4) \times 10^{-3}$	$(11 \pm 2)$	463
$A_2$	$(2.5 \pm 0.2) \times 10^{-2}$	$(8.30 \pm 0.05)$	449
$A_1$	$(7.8 \pm 0.5) \times 10^{-2}$	$(2.30 \pm 0.05)$	470
$C_1$	$(2.2 \pm 0.2) \times 10^{-1}$	$(8 \pm 2) \times 10^{-1}$	468
$C_2$	$(2.9 \pm 0.3) \times 10^{-1}$	$(7 \pm 1) \times 10^{-2}$	-
$B_1$	$0.50 \pm 0.05$	$(3 \pm 1) \times 10^{-3}$	-
$B_2$	$0.78 \pm 0.05$	-	-



K. The TL intensities for samples E<sub>0</sub>, A<sub>2</sub>, A<sub>1</sub>, C<sub>1</sub>, C<sub>2</sub>, B<sub>1</sub> and B<sub>2</sub>,  $\gamma$ -irradiated with a dose of 10<sup>3</sup> Rad and measured over the range 320 to 670 K, are shown in Table 2. An exponential decay of the TL, as a function of the Fe<sup>3+</sup> concentration, was found as shown in Fig. 2, which was fitted by the formula

$$A = 9.7 \exp\{-7.55 \times 10^{-20} (\text{cm}^3/\text{ion})[\text{Fe}^{3+}]\} \quad (1)$$

Using the initial rise method, the activation energies were evaluated for the samples E<sub>0</sub>, A<sub>2</sub> and C<sub>1</sub> and yielded values of 0.9±0.1, 1.2±0.1 and 1.1±0.1 eV, respectively.

## 4. DISCUSSION AND CONCLUSIONS

### 4.1. General outline

For the barium aluminoborate glasses doped with Fe<sub>2</sub>O<sub>3</sub>, when prepared under normal melting conditions in air, most of the iron impurity appears as Fe<sup>3+</sup>, the remainder (about 5 at.%) being Fe<sup>2+</sup> [7,8]. In the absence of impurities such as iron, it is expected that only boron-oxygen hole centers (BOHC) [9] and boron electron centers (BEC) [10] will be present among the possible radiation-induced metastable centers. However, since Fe is an ever present impurity, it was observed by EPR that, after the complete elimination of BEC, there remains a fraction of the BOHC which survived after heating to about room temperature [11]. A further heating to about 450 K produces the complete bleaching of the BOHC, coincident with the appearance of the red TL emission.

### 4.2. Quenching mechanisms

**4.2.1. Low temperature TL** - Del Nery et al. [2] studied the quenching effect of the Fe impurity on the blue radiative e<sup>-</sup>-h<sup>+</sup> recombination, in the range 80 to 320 K, produced by the untrapping of electrons from BEC with an activation energy of 0.21 eV. This was expressed by the exponential law

$$A = 46.3 \exp\{-2.604 \times 10^{-19} [\text{Fe}^{3+}] - 6.211 \times 10^{-19} [\text{Fe}^{2+}]\} \quad (2)$$

where A is the calculated area under the TL curve.

**4.2.2. High temperature TL** - In order to better analyse the possible TL mechanisms involved in the e<sup>-</sup>-h<sup>+</sup> recombination processes occurring in  $\gamma$ -irradiated barium aluminoborate glasses, some experimental evidences should be considered:

- (a) the [Fe<sup>3+</sup>] of a barium aluminoborate glass decreases monotonically with increasing dose of ionizing irradiation;
- (b) the self-trapped hole concentration [BOHC] is equal to [BEC] plus the extra [Fe<sup>3+</sup>] produced under irradiation;
- (c) as the complete TL quenching occurs at Fe concentrations of the order of 0.4 at.% Fe, all the Fe can be considered as isolated ions, since its clustering effects start to appear at about 5 at.% Fe [6];
- (d) most of Fe ions contained in barium borate glasses are of Fe<sup>3+</sup> as a result

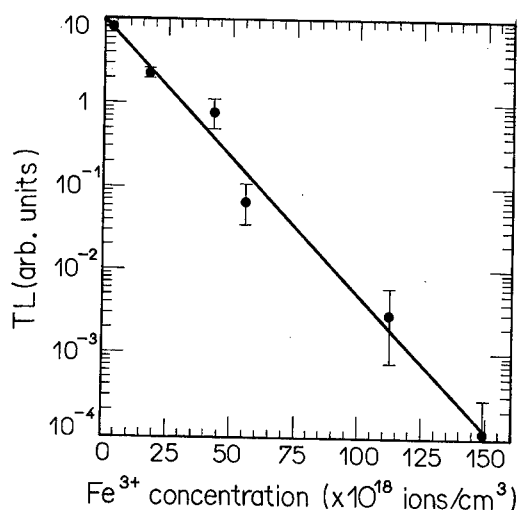


Fig. 2. TL intensity extinction as a function of the  $\text{Fe}^{3+}$  concentration.

of the redox equilibrium for the peculiar basicity of these glasses.

After the BEC's ( $E_a=0.21$  eV) are completely bleached by heating to 320 K [11], the excess holes in the BOHC's remain trapped due to their higher activation energy ( $E_a=1.0$  eV) and acquire their mobility, at temperatures not less than 320 K. Their motion is essential for the occurrence of collisions with the excess  $\text{Fe}^{2+}$ , produced by the reducing reactions of  $\text{Fe}^{3+}$  with the photoelectrons from the initial X- or  $\gamma$ -irradiation. The red TL emission is then observed in the range 320 to 780 K, and is also quenched by the addition of an increasing amount of Fe, following the exponential law of Eq. (1). A complete quenching is obtained with the addition of 0.35 at.% Fe impurity to the base glass, so that the radius of interaction surrounding an Fe ion ( $\text{Fe}^{3+}$  and also  $\text{Fe}^{2+}$ ) is about 15 Å.

The TL extinction curve plotted in Fig. 2 shows that the neighbouring Fe ions are efficient quenching agents also for the  $\text{h}^+-\text{Fe}^{2+}$  radiative recombination, in a similar way as it occurred for the  $\text{e}^-\text{h}^+$  recombinations of the low temperature TL [2].

According to some possible mechanisms reported for semiconductors [12-14], a qualitative configurational sketch of the radiative  $\text{h}^+-\text{Fe}^{2+}$  recombination, shown in Fig. 3a is suggested where the hole of the BOHC is displaced on heating from A to the activated position B, where a direct radiative transition occurs. Fig. 3b illustrates the displacement of the hole in the real space from A to B, assuming that the  $\text{Fe}^{2+}$  ion is substitutionally occupying a tetrahedral or octahedral site.

If the  $\text{h}^+-\text{Fe}^{2+}$  recombination occurs inside the radius of interaction of the delocalized antibonding state of a neighbouring substitutional  $\text{Fe}^{3+}$  (or  $\text{Fe}^{2+}$ ) in a tetrahedral or octahedral site (see Fig. 4), bypassing or resonance energy con-

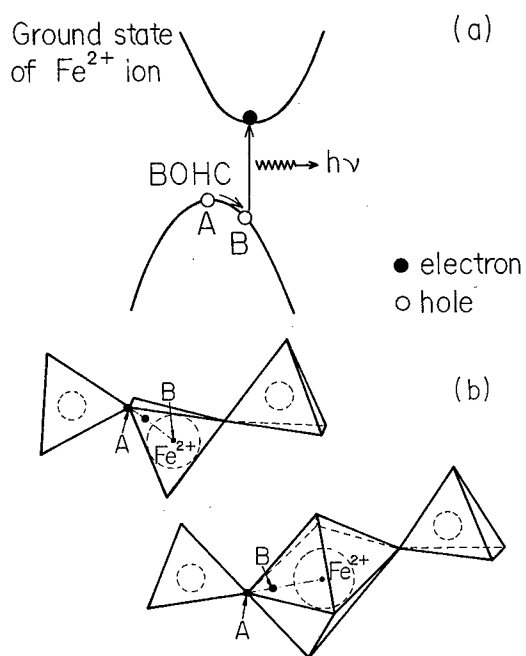


**Fig. 3.** Model of the red TL emission in aluminoborate glasses. The hole of the BOHC is untrapped from site A by heating and a radiative transition occurs at B.  
(a), Configurational sketch and (b), real space diagram.

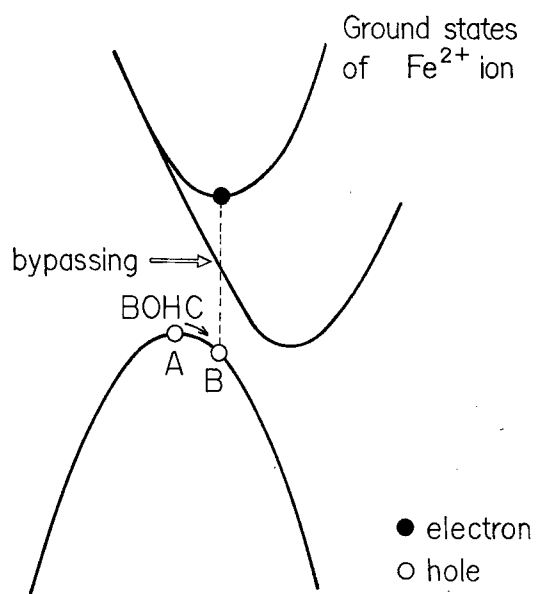


**Fig. 4.** Configurational sketch of the red TL emission quenching in aluminoborate glasses doped with iron.

ditions [15] are created involving the simultaneous annihilation of the electron and hole. Thus, the radiative transition occurring at site B is no longer possible, since it is now performed in two steps, involving the emission either of photons with longer wavelengths or phonons, so that the iron ions are effective in the quenching of the red TL emission attributed to the  $h^+$ -Fe<sup>2+</sup> recombination.

### Acknowledgments

The authors wish to acknowledge C.G. Rouse by the enlightening discussions.

This work was supported by the Conselho Nacional de Desenvolvimento Científico (CNPq), the Fundação de Amparo à Pesquisa do Estado de São Paulo (FAPESP) and the Financiadora de Estudos e Projetos (FINEP).

### REFERENCES

- [1] R.H. Bube, S. Larach & R.E. Shrader, *Phys. Rev.* **92** (1953), 1135.
- [2] S.M. Del Nery, W.M. Pontuschka, S. Isotani & C.G. Rouse, *Phys. Rev.* **B49** (1994), 3760.
- [3] H. Sumi, *Phys. Rev.* **B27** (1983), 2374.
- [4] H. Sumi, *J. Lumin.* **40&41** (1988), 76.
- [5] T. Castner, Jr., G.S. Newell, W.C. Holton & C.P. Slichter, *J. Chem. Phys.* **32** (1960), 668.
- [6] D.W. Moon, J.M. Aitken & R.K. MacCrone, *Phys. Chem. Glasses* **16** (1975), 91.
- [7] T.K. Bansal & R.G. Mendiratta, *J. Non-Cryst. Solids* **86** (1986), 13.
- [8] A.K. Bandyopadhyay, M. Ribes, F. Pernot & J. Zarzycki, *Phys. Chem. Glasses* **23** (1982), 31.
- [9] D.L. Griscom, P.C. Taylor, D.A. Ware & P.J. Bray, *J. Chem. Phys.* **48** (1968), 5158.
- [10] D.L. Griscom, *J. Chem. Phys.* **55** (1971), 1113.
- [11] W.M. Pontuschka, S. Isotani & A. Piccini, *J. Am. Ceram. Soc.* **70** (1987), 59.
- [12] S.G. Bishop & P.C. Taylor, *Phil. Mag.* **B40** (1979), 483.
- [13] J. Jortner, *Phil. Mag.* **B40** (1979), 317.
- [14] D.J. Robins & P.J. Dean *Adv. Phys.* **27** (1978), 499.
- [15] M. Tabei, S. Shionoya & H. Ohmatsu, *Jpn. J. Appl. Phys.* **14** (1975), 240.

## PHOTOSTIMULATED LUMINESCENCE OF BORATE GLASSES DOPED WITH $\text{Ce}^{3+}$ AND $\text{Sm}^{3+}$ IONS

Jianrong QIU, Y. SHIMIZUGAWA, N. SUGIMOTO  
*Hirao Active Glass Project, ERATO, Keihanna Plaza,  
Kyoto 619-02, Japan*

and

K. HIRAO  
*Faculty of Engineering, Kyoto University, Sakyo-ku,  
Kyoto 606-01, Japan*

We report on photostimulated luminescence in sodium borate glasses doped with  $\text{Ce}^{3+}$  and  $\text{Sm}^{3+}$ . When X-ray irradiated glasses were excited by a He-Ne laser (633 nm), photostimulated luminescence at 360 nm due to the 4f-5d transition of  $\text{Ce}^{3+}$  was observed. The intensity of the photostimulated luminescence of  $\text{Ce}^{3+}$ - $\text{Sm}^{3+}$  co-doped glass was weaker than that of  $\text{Ce}^{3+}$ -doped glass. X-ray absorption spectra of glasses X-ray irradiated for various durations were measured. By comparing with the mechanism of photostimulated luminescence in  $\text{BaFBr:Eu}^{2+}$ , the luminescence is proposed to result from the photostimulated recombination of holes and electrons at traps which leave electrons in a long-lived excited state. These glasses may be promising materials for two-dimensional imaging sensors of X-ray.

### 1. INTRODUCTION

Photostimulated luminescence, a phenomenon due to the photostimulated recombination of holes and electrons at traps which leave the electrons in a metastable state, has attracted considerable attention in recent years [1]. In photostimulated luminescence, a material excited by a light 1 after irradiation by X-rays for example, emits light 2 whose wavelength is usually shorter than that of the excitation light 1, and the intensity of light 2 is dependent on the X-ray exposure. Photostimulable luminescence dosimeters, using photostimulable luminescence phosphor are considered to have advantages over thermoluminescence dosimeters, since they can be stimulated by photons without thermal stress and are able to be read out faster.

A "computed radiography system" has been widely used in the medical, biological and physical fields in the last decade in which an imaging plate made of a photostimulable luminescence phosphor  $\text{BaFX:Eu}^{2+}$  ( $\text{X}=\text{Br}, \text{I}$ ) is used as a two-dimensional imaging sensor of X-rays.

However, it is difficult to fabricate a photostimulable luminescence phosphor in the single crystal state of a large enough size. In fact, the fabricated photostimulable luminescence phosphors are usually powders having non-uniform particle shapes, comprising polyhedra whose average size ranges from 1 to 100  $\mu\text{m}$ . They are mixed with an organic binder and coated on a flexible plastic plate and, therefore, scatter the excitation light as well as the fluorescence light. Additionally, it is very difficult to fabricate a flat imaging plate using these phosphor powders together with an organic binder. The sensitivity and resolution of the imaging plate is largely restricted by these factors.

If the photostimulated luminescence sensor is made of a glass, we think that these faults may be overcome since a glass is homogeneous and can be easily fabricated into various forms, such as a large flat plate, a fiber and a microchannel plate made by a large number of fibers. As far as we know, however, there is no report on photostimulated luminescence in glass.

In the present study, we report the phenomenon of photostimulated luminescence in  $\text{Ce}^{3+}$ -doped sodium borate glasses. The mechanism of the photostimulated luminescence of these glasses is also discussed.

## 2. EXPERIMENTAL

The compositions of the glass prepared were  $25\text{Na}_2\text{O} \cdot 75\text{B}_2\text{O}_3 \cdot 0.50\text{CeO}_2$  and  $25\text{Na}_2\text{O} \cdot 75\text{B}_2\text{O}_3 \cdot 0.50\text{CeO}_2 \cdot 0.50\text{Sm}_2\text{O}_3$  (mol%). High purity  $\text{B}_2\text{O}_3$ ,  $\text{Na}_2\text{CO}_3$ ,  $\text{CeO}_2$  and  $\text{Sm}_2\text{O}_3$  were used as starting materials. Approximately 10 g batches were mixed and then melted in Pt crucibles at  $1200^\circ\text{C}$  for 30 min under an ambient atmosphere. The melts were then poured on a stainless plate and cooled to room temperature. The yellowish glasses obtained were then put into a vitreous carbon crucible and treated under a  $\text{N}_2 + \text{H}_2$  (5 vol%) atmosphere at  $1250^\circ\text{C}$  for 60 min in a horizontal carbon furnace. The melts were then quenched to room temperature. Transparent and colorless glasses were obtained. The glass specimen was cut, polished and subjected to the optical measurements.

Absorption spectrum measurements were carried out using a JASCO V-570 spectrophotometer. Normal fluorescence spectra were measured by a Hitachi 850 fluorescence spectrophotometer using 300 nm UV light from a xenon lamp as the excitation source. For the measurement of the photostimulated luminescence decay curve, the glass specimens were first irradiated with 40 KV/30 mA X-rays from a W target for 600 s and a He-Ne laser (633 nm) with a power of  $170 \mu\text{W}/\text{cm}^2$  was used as the source of excitation light. One piece of U360 filter was used to cut off the background light. A photomultiplier tube was used as the detector. The X-ray absorption spectra of  $\text{Ce}^{3+}$ - $\text{Sm}^{3+}$  co-doped glass X-irradiated (wavelength: 0.2 nm) for various durations were measured. All measurements were carried out at room temperature.

## 3. RESULTS

Figures 1(a) and (b) show the absorption spectra of  $\text{Ce}^{3+}$ - $\text{Sm}^{3+}$  co-doped glasses prepared under an ambient and a reducing atmosphere. For compari-

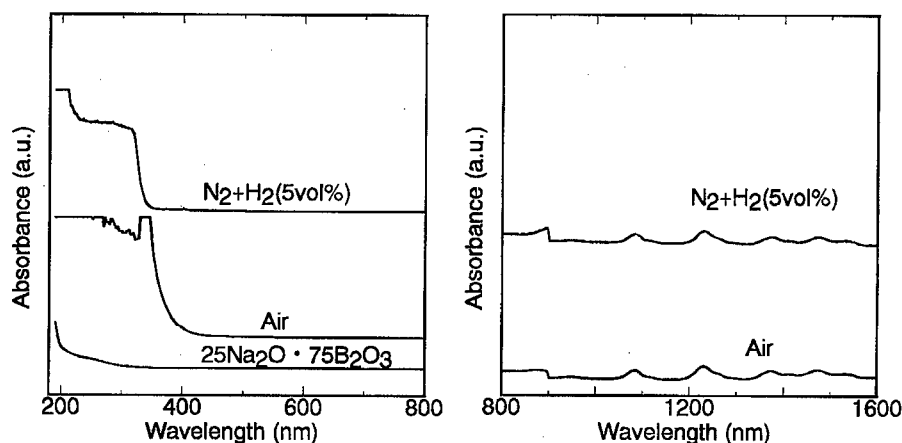


Fig. 1. Absorption spectra of the  $\text{Ce}^{3+}$ - $\text{Sm}^{3+}$  co-doped glasses fabricated under different atmospheres.

son, the absorption spectrum of  $25\text{Na}_2\text{O} \cdot 75\text{B}_2\text{O}_3$  (mol%) glass is also shown. The absorption bands in the 200-400 nm wavelength region in Fig. 1 (a) can be ascribed to the transitions of Ce ions. The strong absorption at 220~300 nm in the spectrum of the glass prepared under the ambient atmosphere is attributed to a charge transfer effect for  $\text{Ce}^{4+}$  ions [2]. Since  $\text{Ce}^{4+}$  ions absorb visible light with a short wavelength, the glass prepared under the ambient atmosphere appears yellowish in color. On the other hand, little absorption in the visible wavelength region is found in the absorption spectrum of the glass prepared under a reducing atmosphere and, therefore, the Ce ions exist in the trivalent state. This was also confirmed by the X-ray absorption spectrum. Additionally, little difference is observed between the absorption spectra of the glasses prepared under different atmospheres due to the 4f-4f transitions of  $\text{Sm}^{3+}$  in the 800-1600 nm wavelength region [3]. Therefore, Sm ions still exist in the trivalent state in the glass prepared under the reducing atmosphere. We only discuss the results for glasses fabricated under the reductive atmosphere below.

Figure 2 shows the normal fluorescence spectra of the glasses when excited by the 300 nm UV light. Both the glass doped with  $\text{Ce}^{3+}$  and the glass co-doped with  $\text{Ce}^{3+}$ - $\text{Sm}^{3+}$  show a broad emission band from 300 to 450 nm with a maximum at 360 nm due to the 4f-5d transition of  $\text{Ce}^{3+}$ . The emissions at 560, 600 and 650 nm are caused by the transitions  $^4\text{G}_{5/2} \rightarrow ^6\text{H}_{n/2}$  ( $n=5, 7$  and  $9$ ) of  $\text{Sm}^{3+}$ .

When X-irradiated glasses were excited by a He-Ne laser, the glasses emitted light at 360 nm, and the intensity of the luminescence decreased quickly. Figure 3 shows the decay curves of the luminescence at 360 nm for the X-irradiated glasses when they were continuously excited by the He-Ne laser. It is clear that the emission at 360 nm for the  $\text{Ce}^{3+}$ -doped glass decays slowly, while that of the glass co-doped with  $\text{Ce}^{3+}$ - $\text{Sm}^{3+}$  decays quickly. Moreover, the intensity of the luminescence of the  $\text{Ce}^{3+}$ - $\text{Sm}^{3+}$  co-doped glass is weaker than that of the  $\text{Ce}^{3+}$  doped glass.

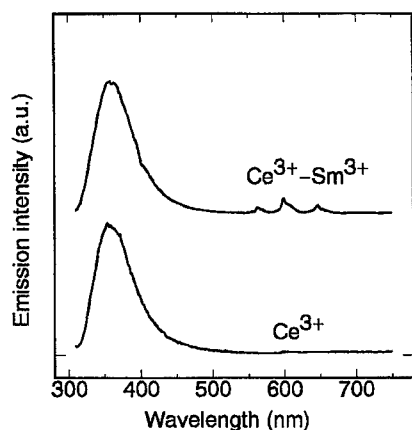


Fig. 2. Normal fluorescence spectra of the  $\text{Ce}^{3+}$  doped and  $\text{Ce}^{3+}\text{-Sm}^{3+}$  co-doped glasses. The wavelength of the excitation light is 300 nm.

Figure 4 shows the X-ray absorption spectra due to the absorption of the Sm ions in the  $\text{Ce}^{3+}\text{-Sm}^{3+}$  co-doped glass X-irradiated for various times together with the spectrum of a  $\text{Sm}^{2+}\text{-Sm}^{3+}$  co-doped glass. Little difference can be found between the absorption spectra of the glasses before and after X-ray irradiation.

#### 4. DISCUSSION

The possible causes of the occurrence of the 360 nm emission, when excited at 633 nm, may be upconversion or multiphonon absorption as well as photo-stimulated luminescence processes.

If the emission at 360 nm is caused by excited absorption (i.e. upconversion) or multiphonon-absorption as shown in Fig. 5, the emission intensity should remain constant when glass is constantly excited by the 633 nm light. There-

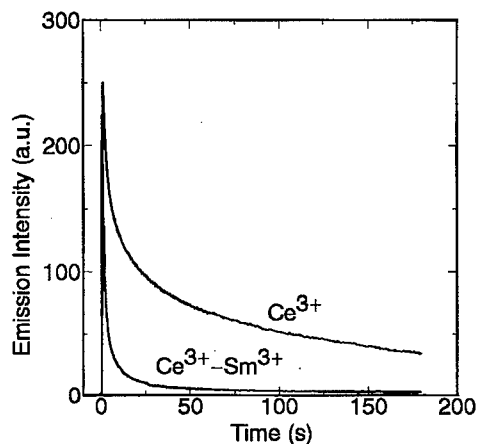


Fig. 3. Decay curves for the photostimulated luminescence at 360 nm for the  $\text{Ce}^{3+}$  doped and the  $\text{Ce}^{3+}\text{-Sm}^{3+}$  co-doped glasses. The excitation light is from a He-Ne laser (633 nm).



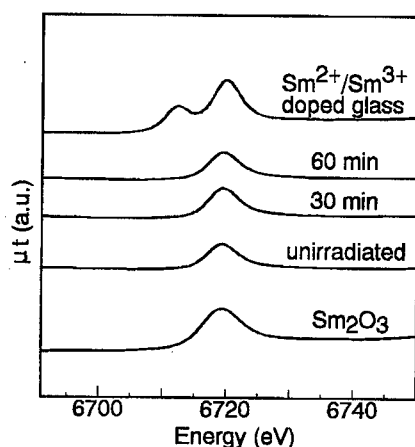


Fig. 4. X-ray absorption spectra for the Sm ions of the  $\text{Ce}^{3+}$ - $\text{Sm}^{3+}$  co-doped glass X-irradiated for various durations.

fore, the emission at 360 nm is not due to upconversion or two-photon absorption process. It is a typical phenomenon of photostimulated luminescence as observed in the  $\text{BaFBr:Eu}^{2+}$  [4-5].

The intensity of photostimulated luminescence in the glasses is weaker than that of crystalline  $\text{BaFBr:Eu}^{2+}$ , and the lifetime of the photostimulated luminescence in the glass was not evaluated exactly. However, the lifetimes of the photostimulated luminescence for various photostimulable phosphors are always equal to the lifetimes of the excited states of the active ions [5]. The lifetime of photostimulated luminescence seems to be mainly determined by the lifetime of the excited active ions, e.g.  $\text{Ce}^{3+}$ , and the other related processes are considered to be very fast during the optical stimulation [5]. The lifetimes of excited  $\text{Ce}^{3+}$  ions have been investigated intensively [6], therefore, the lifetime of the photostimulated luminescence in the present borate glasses doped with  $\text{Ce}^{3+}$  is estimated to be several tens of nanoseconds.

The mechanisms of the photostimulated luminescence in various photostimulable phosphors have been investigated intensively. However, they remain unclear, even for the well known  $\text{BaFBr:Eu}^{2+}$  photostimulable phosphor. More than three models have been proposed to explain the photostimu-

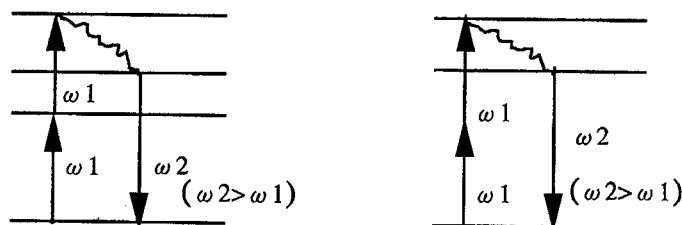


Fig. 5. Mechanism of luminescence with higher frequency ( $\omega_2$ ) than that of the excitation light ( $\omega_1$ ) due to excited state absorption (a) and multiphonon-absorption (b) processes.

lated luminescence processes in  $\text{BaFBr:Eu}^{2+}$ . They differ from each other in (1) the way in which an electron trap is formed; (2) the way in which the electron is transferred from the electron trap to the trapped hole, and (3) the nature of the hole traps [4-5].

Iwabuchi et al. have performed several experiments to confirm the mechanism of the photostimulated luminescence in  $\text{BaFBr:Eu}^{2+}$  [4] and propose that  $\text{Eu}^{2+}$  ions are ionized by X-ray irradiation and converted to  $\text{Eu}^{3+}$  ions either directly or by trapping holes, and that electrons excited to the conduction band are captured by  $\text{F}^+$  centers (halogen ion vacancies) to form F centers. Then, by green to red light irradiation to cause photostimulated luminescence, trapped electrons are liberated into the conduction band and return to  $\text{Eu}^{3+}$  ions, converting them into excited  $\text{Eu}^{2+}$  ions, thus the  $\text{Eu}^{2+}$  luminescence occurs. However, an ESR study by Hangleiter et al. showed that no  $\text{Eu}^{3+}$  was formed on X-irradiation [7]. Moreover, the model proposed by Iwabuchi et al. does not specify how charge compensation is achieved when the negative ion vacancies ( $\text{F}^+$  center) are present during crystal growth. On the other hand, Seggern et al. suggested that photostimulated luminescence occurs by a recombination of an F-center and hole center in close proximity. Charge transfer after photostimulation occurs through tunneling and not through the conduction band [8]. Other models have also been proposed to explain the photostimulated luminescence in the  $\text{BaFBr:Eu}^{2+}$  phosphor [9,10]. However, none of these models fully explain all of the observed experimental phenomena.

Nevertheless, all of the models assume that F centers act as the electron traps and that the photostimulated luminescence is caused by electronic transfer from the  $4f^65d$  level to the  $4f^7$  ground state of  $\text{Eu}^{2+}$  when electrons are released by photostimulation and recombine with trapped holes.

On the other hand, ESR and absorption spectra of undoped and  $\text{Ce}^{3+}$ -doped alkali borate glasses, before and after X-irradiation, have been investigated extensively [11].  $\text{Ce}^{3+}$  is considered to act as a strong hole trap. Additionally, X-irradiated glasses in the sodium borate system exhibited a broad absorption band from 400 to 800 nm with a maximum at about 600 nm. The band is assigned to the absorption of electron traps, i.e. the quasi-F-centers.

Therefore, by comparison with the mechanism of the photostimulated luminescence of  $\text{BaFBr:Eu}^{2+}$ , the mechanism of photostimulated luminescence in the present glasses may be proposed as shown in Fig. 6. After X-irradiation, the electron and hole pairs are formed in the glasses, some of electrons are trapped by electron trap centers, and quasi-F-centers are formed in the glasses. On the other hand, some of the holes were caught by hole traps, e.g.  $\text{Ce}^{3+}$  ions. The wavelength of the He-Ne laser (633 nm) is just in the region of the absorption due to the quasi-F-center. When excited by the He-Ne laser, electrons which are trapped by the quasi-F $^+$ -centers are liberated, and combine with the holes, thus leading to the characteristic  $\text{Ce}^{3+}$  emission.

$\text{Sm}^{3+}$  ions are considered to act as hole traps in  $\text{Ce}^{3+}$ - $\text{Sm}^{3+}$  co-doped sulfide crystals [12]. However, no variation in the valence state and the local structure

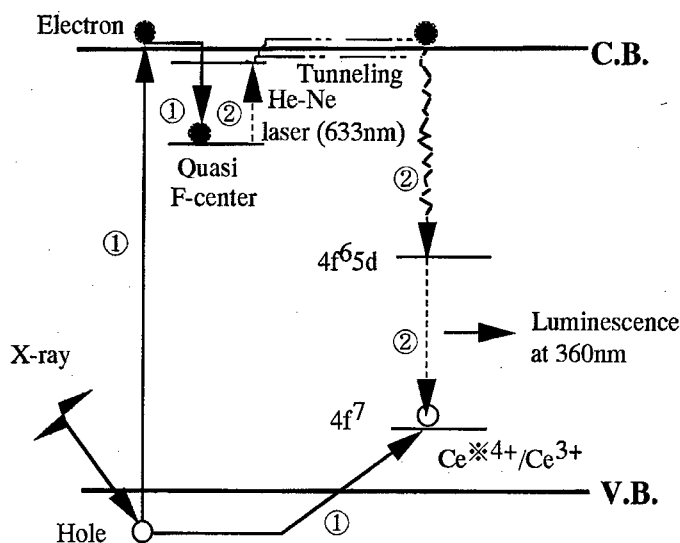


Fig. 6. The rudimentary mechanism of photostimulated luminescence in the present glass.  
 ①: X-ray Irradiated process. ②: Laser stimulated process. - - - - - unclear.

of the Sm ions before and after X-ray irradiation has been observed from the X-ray absorption spectra. Therefore, as opposed to their behavior in sulfide crystals,  $\text{Sm}^{3+}$  ions probably do not act as hole traps in the present glass. The fast decay of the photostimulated luminescence for  $\text{Ce}^{3+}$ - $\text{Sm}^{3+}$  co-doped glass may be attributed to the energy transfer from  $\text{Ce}^{3+}$  to  $\text{Sm}^{3+}$ .

## 5. CONCLUSIONS

The photostimulated luminescence phenomenon is reported in sodium borate glasses doped with  $\text{Ce}^{3+}$  and  $\text{Sm}^{3+}$  ions. When X-irradiated glasses were excited by a He-Ne laser (633 nm), photostimulated luminescence was observed at 360 nm due to the 4f-5d transition of  $\text{Ce}^{3+}$  ions. The intensity of the photostimulated luminescence for a  $\text{Ce}^{3+}$ - $\text{Sm}^{3+}$  co-doped glass is weaker than that of the  $\text{Ce}^{3+}$ -doped glass. The X-ray absorption spectra of glasses X-irradiated for various durations show that the valence state and the local structure surrounding the  $\text{Sm}^{3+}$  ions remain unchanged.  $\text{Ce}^{3+}$  ions and quasi- $\text{F}^+$ -centers in the glasses act as hole and electron traps, respectively. These glasses may be promising materials for two-dimensional imaging sensors of X-rays.

## REFERENCES

- [1] Y. Amemiya & J. Miyahara, *Nature*, **336** (1988), 89.
- [2] P. Paul, M. Mulholland & M. S. Zaman, *J. Mater. Sci.*, **11** (1976), 2082.
- [3] T. Izumitani & K. Nakagawa, In: *Glass Handbook*, Eds. S. Sakka, T. Sakaino and K. Takahashi (Asakura Press, Tokyo, 1975), pp. 163.
- [4] Y. Iwabuchi, N. Mori, K. Takahashi, T. Matsuda & S. Shionoya, *Jpn. J. Appl. Phys.*, **33** (1994), 178.

- [5] A. R. Lakshamanan, *Phys. Stat. Sol. (a)*, **3** (1996), 153.
- [6] T. Kanou, *Phosphors Handbook*, (Ohm Press, Tokyo, 1987), pp. 120.
- [7] T. Hangleiter, F. K. Koschnick, J. M. Spaeth & R. S. Eachus, *Radiat. Eff.*, **119** (1991), 615.
- [8] H. V. Seggern, T. Voigt, W. Knupfer & G. Lange, *J. Appl. Phys.*, **64** (1988), 1405.
- [9] M. Thoms, H. V. Seggern & A. Winnacker, *J. Appl. Phys.*, **76** (1994), 1800.
- [10] F. K. Koschnick, J. M. Spaeth, R. S. Eachus, W. G. McDugle & R. H. D. Nuttal, *Phys. Rev. Lett.*, **67** (1991), 3571.
- [11] R. Yokota, In: *Glass Handbook*, Eds. S. Sakka, T. Sakaino and K. Takahashi (Asakura Press, Tokyo, 1975), pp. 826.
- [12] K. Chakrabarti, V. Mathur, L. Thomas & R. Abbundi, *J. Appl. Phys.*, **65** (1989), 2021.

## **AB INITIO BASED STUDIES OF BORATE GLASSES**

Michael TETER

*Corning Inc., Corning, New York 14831, USA*

*Ab initio* calculations of boric oxide are used to parameterize a classical model of the interactions between boron and oxygen. This model yields a structure that agrees extremely well with all known measurements of the properties of vitreous boric oxide, but the concentration of boroxol rings is nearly an order of magnitude less than commonly accepted. Quantitative Raman measurements using calibrated samples of boroxol ring concentrations yield a quantitative measurement of the ring concentration in vitreous boric oxide in close agreement with the simulation.

### **1. INTRODUCTION**

From the time of Zachariasen [1], we have had reasonable ideas about glass structure. According to Zachariasen, first neighbor environments look almost exactly the same as they do in crystals, but these building blocks are put together in a continuous random network. Electro-neutrality is preserved in the smallest possible volume consistent with ion sizes. Unfortunately, the bonding differences between a glass and a crystal of the same composition are reasonably subtle. We can determine the structure of the crystal through the analysis of x-ray and neutron diffraction experiments due to the crystal's repeating nature. The glass has no exact repeating units, and so the diffraction patterns are blurred. They still tell us a great deal about the first and second neighbor environments, and usually blur significantly around third neighbors. Most other probes, when used to study an amorphous structure, give strong information about first neighbors, weak results about second and are washed out by third neighbors. Thus we are not absolutely certain about the structure of even the most prototypical of all glasses, fused silica, which serves as a backbone for most of the silicate glasses.

It was to fill the need for better pictures of amorphous structures, that molecular modeling in glass began over twenty years ago. The success of Born-Meyer-Huggins potentials in describing alkali-halides led to their use by Woodcock, Angell & Cheeseman [2] to describe fused silica as an ionic substance and their reproduction of the details of x-ray diffraction was really quite amazing given the simple nature of the interactions.

A study of the potentials used in this modeling showed that they could not reproduce as stable structures the crystalline polymorphs of silica, and it was not until the recent work of van Beest et al. [3] that pairwise potentials could

be found that did a reasonable job of predicting crystalline silica structure.

The theory which should work properly is quantum mechanics. Gaussian based *ab initio* studies of clusters of silicon and oxygen have been made for many years, but, until 1987, there were no infinite periodic calculations for oxides. The reason for this lack was due to the difficulty of the calculation. A typical condensed matter calculation for a semiconductor such as silicon usually consisted of a few atoms in a periodic cell. Planewaves and pseudopotentials were used, and to model silicon required approximately fifty planewaves per atom. The diagonalization of matrices a few hundred square was not a demanding task, but since diagonalization grew as the number of planewaves cubed, much bigger problems were computationally intractable. Because of the deep nonlocal pseudopotentials required to accurately model oxygen, oxygen needs ten times as many planewaves per atom as silicon. To simulate quartz would require the diagonalization of 10000 by 10000 matrices. These diagonalizations would have to be done many times to reach self-consistency, and then many times more to relax the structure. In 1985, Car & Parrinello [4] wrote a paper on quantum mechanical molecular dynamics which emphasized the iterative approach to matrix diagonalization and showed how to derive an eigenvector by a method which scaled nearly linearly with the number of planewaves instead of cubically. The new method required local pseudopotentials which would not work for oxygen and was still too slow. Allan & Teter [5] showed how oxides could be modeled successfully, and Teter, Payne & Allan [6] showed how eigenvectors could be extracted much more efficiently than the Car & Parrinello method. The details of the resulting iterative diagonalization along with a review of the planewave pseudopotential method may be found in the review article by Payne et al. [7]. For the first time, the planewave pseudopotential treatment of oxides was viable.

Much subsequent work has shown that, using the Local Density Approximation (LDA) for exchange and correlation in an *ab initio* calculation, the structural, vibrational and optical properties of oxide crystals are accurately reproduced [8,9]. Unfortunately, this theory is much too computationally intensive to be used in modeling glass structures which require hundreds to thousands of atoms. Consequently, the following strategy has been adopted: (1) Study the crystalline forms of oxides whose composition is near that of the glass in question, (2) Parameterize the interactions so that the quantum mechanical results are reproduced for both relaxed and distorted crystals, and (3) Use the much faster classical interactions to predict the glass behavior.

Ionic simulations of fused silica have shown good agreement structurally with experiment, and as mentioned previously, if the potentials of van Beest et al. [3] are used, the crystal structures of quartz, cristobalite and stishovite are reasonably reproduced. To show the improvements which accrue from the use of data from quantum mechanical calculations, it would be best to use as a prototype a glass for which ionic simulation does not agree with experimental determination of its structure. A glass which shows significant disparity between the predictions of ionic models and experimental measurements is vit-

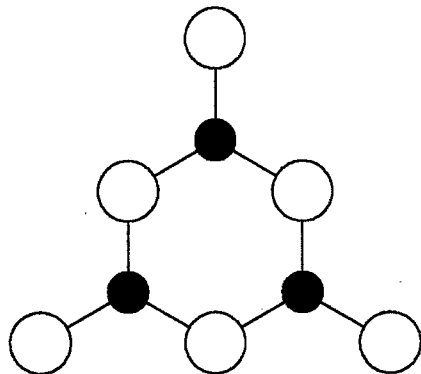


Fig. 1. The Boroxol group

reous boric oxide. The fundamental building unit in boric oxide is the  $\text{BO}_3$  triangle. The basic issue of the structure of  $\text{B}_2\text{O}_3$  glass is how these triangles are bonded together. The prevailing idea suggested by Goubeau & Keller [10], strengthened by the infra-red work of Krogh-Moe and further developed by the x-ray diffraction analysis of Mozzi & Warren [11] is that the structure of boric oxide glass is one in which three  $\text{BO}_3$  triangles, bonded in a planar boroxol ring, with a BOB bonding angle of  $120^\circ$  plays a strong role.

The first molecular dynamics study of vitreous  $\text{B}_2\text{O}_3$  was done by Soules [12]. Independent work by Amini, Mitra & Hockney [13] verified Soules' results. The conclusion was that the BOB bonding angle averaged about  $154^\circ$ , and the B-B separation was too large to close boroxol rings. Their ionic potentials would not reproduce the low pressure crystal structure of  $\text{B}_2\text{O}_3$ , and their B-B separations and bonding angles were refuted effectively by the neutron-diffraction studies of Johnson, Wright & Sinclair [14], who concluded that about 75 of the borons were in boroxol rings. This conclusion was strengthened by the work of Windisch & Risen [15] who measured the Raman spectra of  $\text{B}_2\text{O}_3$  glass and found by isotopic substitution that the single large peak at  $808\text{ cm}^{-1}$  was a breathing mode of the boroxol ring.

The NMR spectra and the infrared spectra also are compatible with the boroxol ring being a major part of the vitreous  $\text{B}_2\text{O}_3$  structure. The only data which seems inconsistent with this interpretation is the inelastic neutron scattering data [16] which shows no strong peak in the vibrational density of states at  $808\text{ cm}^{-1}$ . This is shown in Fig. 2.

Given the narrow nature of the peak in the Raman spectrum, and the supposed dominant nature of the boroxol ring in the structure, the weakness of the peak in this measurement is difficult to understand if the model which has 70-80 of the borons in boroxol rings is correct. Since there is one symmetric breathing mode per boroxol ring, and the total number of vibrational modes is three times the number of atoms, it is trivial to show that these Raman-active boroxol modes must constitute a fraction  $0.0444f_b$  of the total number

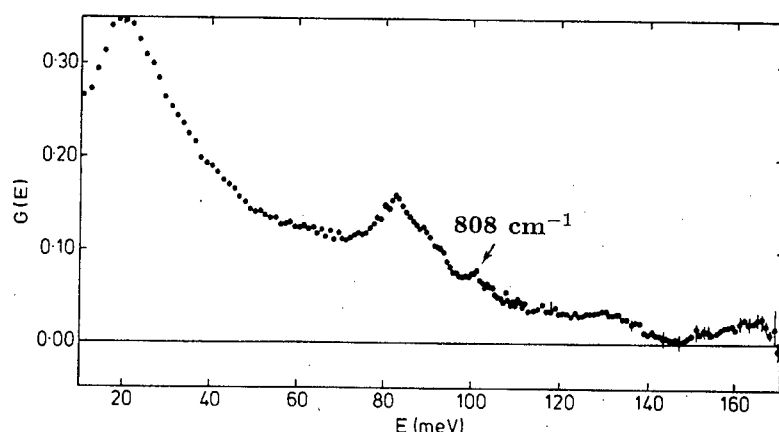


Fig. 2. Uncorrected vibrational density of states from Ref. [16].

of vibrational degrees of freedom. Here  $f_b$  is the fraction of borons in boroxol rings. If  $f_b$  is 0.75, then the symmetric breathing modes *must* be one part in 30 of the total vibrational degrees of freedom. More recent work by Hannon et al. [19] has better resolved the peak at  $808\text{ cm}^{-1}$ , but the area under the peak is much too small, even after corrections for multiple scattering and multiphonon events, to be compatible with 75 of the borons being in boroxol rings.

Hand built models display the prejudices of the builder, and what is needed is either a super microscope which will allow us to view the actual structure, or the ability to construct a model using only the laws of nature. Since *ab initio* quantum mechanics using density functional theory has shown the ability to accurately reproduce the structures and dynamics of all oxide crystals which

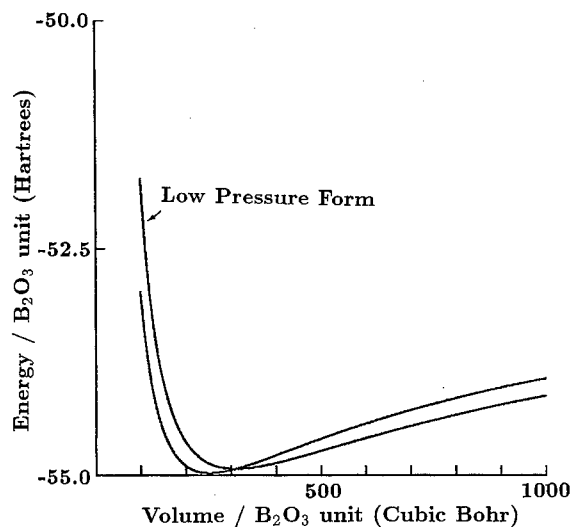


Fig. 3. *Ab initio* energy of crystalline boric oxide versus volume.



have been modeled, it seems a natural reference point from which to build our models of interactions in borate glasses. If we could perform molecular dynamics for glass models with 1000 atoms for a million time steps using LDA, our methods search would be over. A single time step, however, would involve the iterative diagonalization of a 300 000 by 300 000 matrix for each time step. The process on a gigaflop computer would take a few days per time step using current methods. Consequently, there is no recourse other than developing classical potentials which reproduce the quantum mechanical results for smaller systems.

## 2. MODELING OF VITREOUS BORIC OXIDE

There are two well known crystal structures of boric oxide. The low pressure structure [17] which consists of ribbons of  $\text{BO}_3$  triangles and the high pressure structure [18] which consists of  $\text{BO}_4$  edge-shared tetrahedra. These two structures were simulated using ab initio quantum mechanics, and the following figure shows the total energy/ $\text{B}_2\text{O}_3$  versus the volume/ $\text{B}_2\text{O}_3$  for both the low and high pressure structures.

The atomic coordinates were not relaxed, but simply scaled, and at each new lattice constant, the new wavefunction, forces on the atoms and the total energy were calculated.

The energy of the low pressure form per  $\text{B}_2\text{O}_3$  unit as a function of the volume per  $\text{B}_2\text{O}_3$  unit is well described by the following form.

$$E_{\text{low}} = -50.577 + 9869.011/v^{5/3} + 1102.539/v^{4/3} - 37.976/v^{1/3}$$

The high pressure form is similarly described.

$$E_{\text{high}} = -50.548 + 9652.772/v^{5/3} + 320.498/v^{4/3} - 35.270/v^{1/3}$$

One important result of this calculation is that the  $1/r$  tail of the curve in both cases is 70% of the Ewald sum for each of the structures, strongly implying that partial charges should be 85% of the real ones.

Any potentials between atoms must satisfy these total energy curves for the two structures. Many much smaller crystals, not occurring in nature were modeled as well, and the results for these were combined into a data base used to design potentials. When ionic models were compared with the quantum mechanical results, something else very important was discovered. The boron-boron repulsive interaction due to ionic forces was much too strong. It was found that in the vicinity of an oxygen ion, the ion polarized and screened the borons from one another. Consequently, it was found necessary to construct a model of an oxygen ion which was polarizable. The polarizability in the presence of multiple charges was also directionally dependent, and showed tetrahedral symmetry. A simple model of the oxygen ion was then constructed which had a central charge, and four auxiliary charges in a tetrahedron around the center. These auxiliary charges had one set of springs attaching them to each other and another set attaching them to the nucleus.

Thus the parameters in the model were the size of the auxiliary charges, their equilibrium distance from the oxygen nucleus, their spring constants and their repul-

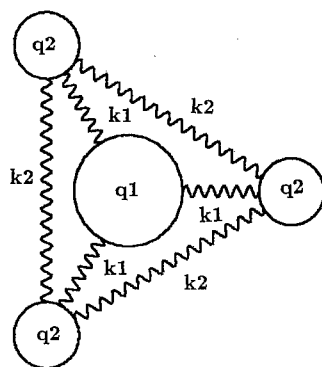


Fig. 4. A triangular schematic of the tetrahedral model.

sive coefficients for external interactions. If the charges were zero, one had the simple ionic model for the oxygen ion. The range explored for the charges was from zero to  $-2$  for the four auxiliary charges, and the central charge was correspondingly changed from  $-2$  to  $+6$  to make the sum of the five charges be  $-2$ . The details of this fitting procedure will be explained in a more comprehensive paper to follow.

Over the range of parameters explored, vitreous boric oxide was modeled. In every case, the predominant structural feature to emerge was the  $\text{BO}_3$  triangle. Over the full range of parameters, the numbers of boroxol rings varied from 1 in the simple ionic structure to 40 in the upper limit of parameters explored. Since each ring contains three borons, and there are 400 borons in the simulation, each ring corresponds to  $3/4\%$  of the borons in boroxol rings. Thus the range observed over the full parameter set was from less than  $1\%$  to  $30\%$  of the borons in boroxol rings. When the requirement was added that the parameters reproduce the crystal structures as stable structures was added, the number of boroxol rings in the structures ranged from 5 to 20. When the last requirement was added that the potentials reproduce the crystalline energy curves as a function of cell size, as well as the data base for smaller crystals which do not occur in nature because their energies are too high, the complete parameter set was determined. The final model was generated by a Monte Carlo study in which the temperature was set very high and cooled by five parts per million after adjusting each of the degrees of freedom in the problem, and each degree of freedom had an adjustable step size which was slowly changed to keep the success rate of the steps slightly under  $50\%$ . Under this cooling schedule, the rate of cooling was proportional to the temperature, and the lower the temperature, the slower the cooling. The degrees of freedom were accessed in random order to avoid correlation between neighboring adjustments.

The polarizable model has the correct density, consists primarily of  $\text{BO}_3$  triangles with some bonding defects, and contains 16 boroxol rings corresponding to  $12$  of the borons in boroxol rings.

One feature of the more complex model is that the B-B first peak and the O-O first peak occur at the same separation. In the ionic model, this is not true. The two models give BOB bonding angles of  $120^\circ$  and  $154^\circ$  respectively

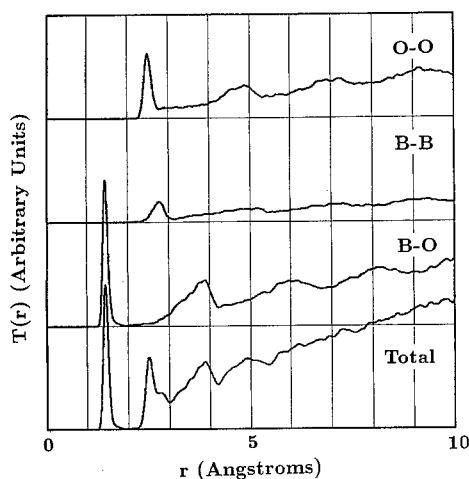


Fig. 5. Correlation function of simple ionic model.

with a width of a few degrees. The next two figures compare the correlation functions of the simple ionic model and the oxygen model and are followed by the neutron correlation function of Johnson et al. [17].

### 3. RAMAN SPECTRA OF BORATES

To quantitatively check this prediction, it would be necessary to compare the Raman spectrum of the boric oxide glass with a sample in which the concentration of boroxol rings is known. Fortunately, it is possible to prepare such a sample. When boric acid is neutralized with sodium hydroxide, sodium metaborate is formed, and as long as there is a slight excess of sodium hydroxide, the conversion

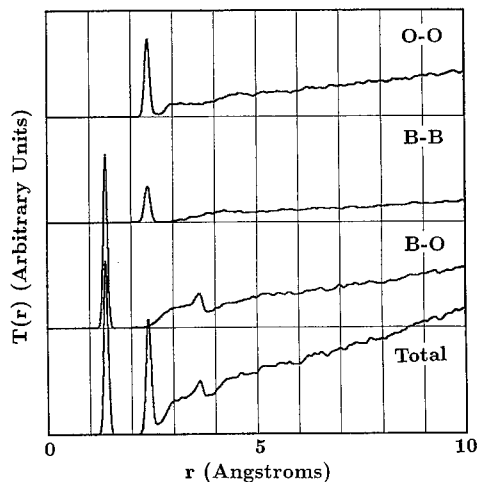


Fig. 6. Correlation functions of polarizable oxygen model.

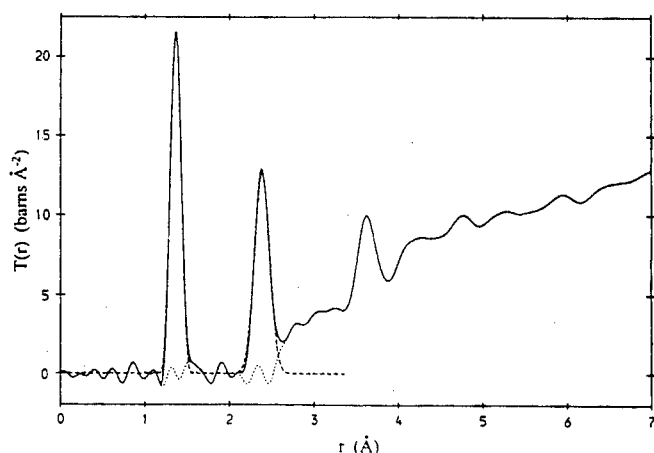


Fig. 7. Correlation functions of neutron diffraction [17].

is complete. Therefore a sample was prepared by dissolving 7.73 g of boric acid with 5.03 g sodium hydroxide in 100 ml of water. The Raman spectrum of this sample was taken on the high resolution Raman spectrometer at Cornell University along with the sample diluted by a factor of two and by two again. A sample of anhydrous vitreous boric oxide pure to a part per million was purchased from a semiconductor supply house. This sample was ground under oil to just fit in the same spectrophotometer bottle as the liquid samples. A thin film of index oil was used to index match the interface between the boric oxide and silica surfaces. The Raman spectrum of the sample was taken along with that of a bottle of the index oil. No index oil peaks were found in the Raman spectrum of the glass.

The peak of the sodium metaborate rings was at  $795\text{ cm}^{-1}$ , and its area was proportional to the concentration. The Raman peak of the boric oxide glass was at  $808\text{ cm}^{-1}$ , and the area under the peak was 4.07 times the area of the most concentrated sodium metaborate sample. This corresponds to 10.7% of the borons in the vitreous boric oxide in boroxol rings.

The errors in the Raman determination have to do with changes in transition matrix elements, a tumbling versus static environment, the fraction of the metaborate actually in rings and differences in the electric field intensities due to differences in the index of refraction. The oxygen ions in the ring are moving in this mode, and the bonding environment of these ions does not differ from those in the glass until third neighbors, and the estimated effect on the matrix element is of the order of a few percent. Estimates of the moment of inertia of the boroxol group also indicate that the tumbling time is long compared to the vibration time and consequently no effect should be expected, and the liquid and vitreous samples can both be considered stationary. If some of the metaborate is not in rings, which the excess of sodium hydroxide is supposed to prevent, the above estimate will be an *over* estimate of the ring concentration in the glass. Worst case analysis of these errors leads one to an upper bound of 20% in the error of the determination, or 2% in the fraction of borons in boroxol rings.

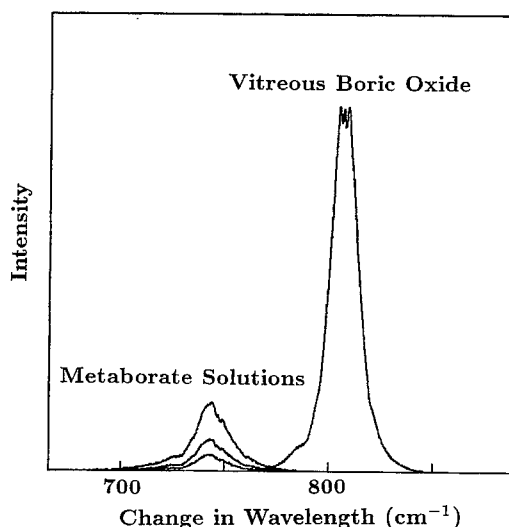


Fig. 8. Raman spectra of vitreous boric oxide and sodium metaborate solutions.

#### 4. REVERSE MONTE CARLO

Reverse Monte Carlo simulations by Swenson & Börjesson [20] put an upper limit of 30% of the borons being in boroxol rings in the following manner. One can construct a model with large numbers of boroxol rings, but above 30% it is impossible to achieve both a good fit to the diffraction pattern and a good density. Their best fit was with a fraction of boron in boroxol rings of around 10%. The primary criticism of Reverse Monte Carlo is that it can fit far too much since its only constraints are bonding topology and fitting the diffraction results. When Reverse Monte Carlo is unable to construct a viable model, it argues strongly that such a model is topologically infeasible under the constraints of fitting the density and the diffraction results.

As an exercise, the neutron diffraction results were fitted using as a starting point the final relaxed results of the polarizable oxygen model, and perfect agreement was reached with an root-mean-square displacement of only one-tenth Angstrom per atom. Although the density and diffraction results were very good for the original model, the exact density, and a perfect fit to the diffraction results are achieved with an essentially infinitesimal perturbation of the model.

#### 5. CONCLUSIONS

By making advances in the calculation methods for solutions to Schroedinger's equation, we have been able to bring quantum mechanical methods indirectly to glass chemistry. We now have a simple way to summarize these results and are able, for the first time, to derive structures for simple glasses which show correct covalent effects in the bonding. The results are sometimes surprising as in the case of the boroxol rings in boric oxide. This simulation predicts that while all BOB bonding angles are near  $120^\circ$ , only 12% of the

borons in boric oxide glass are in boroxol rings.

An independent quantitative Raman measurement places the number at 11%. It is estimated that the error on each of these determinations is in the neighborhood of 2-3%.

Thus, both the simulation and the direct determination of ring concentration find the fraction of borons in boroxol rings lies between 9-15%. A crude integration under the peak of vibrational density of states measured in [19] is completely compatible with this result as is the result from Reverse Monte Carlo [20].

In conclusion, potentials which reproduce *ab initio* interactions between arbitrary combinations of boron and oxygen ions lead to a model which also reproduces structural and property determinations of vitreous boric oxide. This model predicts a concentration of boroxol rings nearly an order of magnitude lower than other interpretations of the known data.

The simulations may perhaps be controversial, but the direct measurement of concentration of boroxol rings cannot be in error enough to make up the factor of seven difference between what is observed and what is commonly believed.

### Acknowledgements

I would like to thank the Materials Science Center of Cornell University for the use of the Raman spectrometer, Jiu Feng Tu for taking the spectra, the Cornell Theory Center for computational resources, The Laboratory of Atomic and Solid State Physics and Corning, Inc. This work was supported by the National Science Foundation under grant number DMR-9520315.

### REFERENCES

- [1] W.H. Zachariasen, *J. Am. Chem. Soc.* **54** (1932), 3841.
- [2] L.V. Woodcock, C.A. Angell & P. Cheeseman, *J. Chem. Phys.* **65** (1976), 1565.
- [3] B.W.H. van Beest, G.J. Kramer & R.A. van Santen, *Phys. Rev. Lett.* **64** (1990), 1955.
- [4] R. Car & M. Parrinello, *Phys. Rev. Lett.* **55** (1985), 2471.
- [5] D.C. Allan & M.P. Teter, *Phys. Rev. Lett.* **59** (1987), 1136.
- [6] M.P. Teter, M.C. Payne & D.C. Allan, *Phys. Rev. B* **40** (1989), 12255.
- [7] M.C. Payne, M.P. Teter, D.C. Allan, T.A. Arias & J.D. Joannopoulos, *Rev. Mod. Phys.* **64** (1992), 1045.
- [8] D.C. Allan & M. P. Teter, *J. Am. Ceram. Soc.* **73** (1990), 3309.
- [9] X. Gonze, D.C. Allan & M.P. Teter, *Phys. Rev. Lett.* **68** (1992), 3603.
- [10] J. Goubeau & H. Keller, *Z. Anorg. Chem.* **272** (1953), 303.
- [11] R.L. Mozzi & B.E. Warren, *J. Appl. Crystallogr.* **3** (1970), 251.
- [12] T.F. Soules, *J. Chem. Phys.* **73** (1980), 4032.
- [13] M. Amini, S.K. Mitra & R.W. Hockney, *J. Phys. C: Solid State Phys.* **14** (1981), 3689.
- [14] P.A.V. Johnson, A.C. Wright & R.N. Sinclair, *J. Non-Cryst. Solids* **50** (1982), 281.
- [15] C.F. Windisch, Jr. & W.M. Reisen, Jr., *J. Non-Cryst. Solids* **48** (1982), 307.
- [16] R.N. Sinclair, *J. Non-Cryst. Solids* **76** (1985), 61.
- [17] G.E. Gurr, P.W. Montgomery, C.D. Knutson & B.T. Gorres, *Acta Cryst.* **B26** (1970), 906.
- [18] C.T. Prewitt & R.D. Shannon, *Acta Cryst.* **B24** (1968), 869.
- [19] A.C. Hannon, D.I. Grimley, R.A. Hulme, A.C. Wright & R.N. Sinclair, *J. Non-Cryst. Solids* **177** (1994), 299.
- [20] J. Swenson & L. Börjesson submitted to *Phys. Rev. B*.

# **AB INITIO MOLECULAR ORBITAL CALCULATIONS ON THE STRUCTURE AND THE LOW-FREQUENCY VIBRATIONAL MODES IN $B_2O_3$ AND ALKALI BORATE GLASSES**

Takashi UCHINO & Toshinobu YOKO  
*Institute for Chemical Research, Kyoto University,  
Uji, Kyoto 611, Japan*

We have performed *ab initio* molecular orbital calculations on the clusters modeling the medium-range structures in  $B_2O_3$  and alkali borate glasses at the Hartree-Fock/6-31G\* level. It has been shown that the optimized structural parameters are in good agreement with the observed ones. The calculations yield Na-O distances ranging from 2.17 to 2.42 Å. Using the optimized clusters, we have carried out a vibrational analysis to interpret low-frequency vibrational modes observed for the glasses. The frequency calculations of the clusters having pentaborate and diborate units have successfully reproduced the observed far infrared asymmetric absorption profiles which can be deconvoluted into two broad bands. According to the normal coordinates calculated, the two absorption bands are attributed to two different types of vibrations of alkali cations in a specific network environment. Furthermore, the calculations have reproduced the low-frequency (20–100  $cm^{-1}$ ) Raman scattering peak or the so-called “boson peak” observed for  $B_2O_3$  and alkali borate glasses. We have found that these low-frequency vibrational modes result from the collective or wavelike motions localized in the medium-range order in the glasses.

## **1. INTRODUCTION**

Borate glasses are technologically interesting materials since they have found use in various commercial applications such as fast ionic conductors and microelectronic devices. In addition to the practical importance, they are of considerable interest from a structural point of view. NMR [1,2], Raman [3,4], X-ray [5] and neutron scattering [6,7], and infrared [8] studies have demonstrated that borate glasses consist mainly of relatively large structural units such as boroxol, pentaborate, triborate, diborate, and metaborate groups. Thus, borate glasses cannot be viewed as a simple three-dimensional continuous random network constructed from  $BO_3$  triangles and/or  $BO_4$  tetrahedra.

Although such structural units in borate glasses have been well documented, a complete knowledge about the coordination environments of the so-called network modifier cations is still lacking. It is generally accepted that vibrations of alkali cations in oxide glasses give rise to far infrared absorption bands

below  $\sim 500\text{ cm}^{-1}$  [9,10]. The far-infrared spectra hence yield information about the nature of the bond between the alkali cation and its surrounding glass network; such information will be necessary for a better understanding of the conduction mechanism, which is most likely related to jump motions of the mobile cations. The cation-network interactions in alkali borate glasses have been extensively studied by Kamitsos and his coworkers [10,11]. They have found that the far-infrared spectra of alkali borate glasses yield the asymmetric profile that can be deconvoluted into two Gaussian type bands. Kamitsos et al. [10] then proposed that these two far-infrared bands are assigned to cation vibrations in two different distributions of anionic site environments. However, this hypothesis has not been proved directly yet, and no previous model calculations have reproduced these two component bands in alkali borate glasses.

On the other hand, much interest has recently been devoted to the study of the low-frequency ( $< \sim 100\text{ cm}^{-1}$ ) Raman spectra of borate glasses [12,13].  $\text{B}_2\text{O}_3$  glass yields a broad low-frequency peak at  $\sim 25\text{ cm}^{-1}$ , and the peak shifts to higher frequencies with increasing alkali-oxide content [12,13]. The presence of the low-frequency peak, which is often called the "boson peak," is a property common to other glass-forming systems but is absent in the corresponding crystalline solids. The origin of the boson peak, however, has not been fully understood yet and is still a subject of discussion.

Recently, *ab initio* molecular orbital (MO) methods have achieved great successes in calculating electronic, geometrical, and vibrational structures of oxide and molecular glasses [14–16], indicating the principal importance of the local and medium-range geometries in establishing real non-crystalline solids. In this study, we carry out *ab initio* MO calculations on several model clusters having boroxol, pentaborate, and diborate groups to interpret low-frequency vibrational properties of  $\text{B}_2\text{O}_3$  and sodium borate glasses. On the basis of the calculated results, a new model of the two component bands of alkali borate glasses in the far-infrared region is presented. Furthermore, we calculate Raman scattering intensities for the low-frequency vibrational modes of these model clusters and show that the boson peak results from the collective motions localized in the medium-range structure in the glasses.

## 2. MODELS AND CALCULATIONAL PROCEDURE

In this work, we use some small "optimized" clusters as models of the medium-range structure of the corresponding glass systems. This is based on the concept that in glasses the medium-range structure is determined not by the long-range potential surface that can be found in crystals but by the relatively localized potential surface that might be found in melts. This concept is in line with the suggested idea that the tendency to form a glass rather than a crystal may be, in general, due to the elements of medium-range order in the melt which do not exist topologically in any of crystalline polymorphs [17].

As for the structure of  $\text{B}_2\text{O}_3$  glass, a wide variety of experimental data sup-



port the boroxol ring ( $B_3O_6$ ) model; that is,  $B_2O_3$  glass consists of a random three-dimensional network of  $BO_3$  triangles with a large fraction of almost planar boroxol rings [2–6]. We hence employed the  $H_4B_6O_{11}$  cluster, which is composed of two boroxol rings interconnected by one extra-annular oxygen, as a model of the medium-range structural unit in  $B_2O_3$  glass. The hydrogen atoms in the cluster are used to saturate the dangling bonds of “surface” oxygen atoms. It should be mentioned that previous *ab initio* MO calculations on the vibrational spectra of  $B_3O_3(OH)_3$  modeling one boroxol ring did not yield frequencies lower than  $100\text{ cm}^{-1}$  [18,19], indicating that the  $B_3O_3(OH)_3$  cluster is too small to reproduce the observed boson peak frequencies at  $\sim 25\text{ cm}^{-1}$ . The geometry of the  $H_4B_6O_{11}$  cluster was completely optimized at the Hartree-Fock (HF) level with the 6-31G\* basis set [20] and the frequency calculations were carried using the HF/6-31G\* geometry. Force constants were obtained by the gradient method [21], and Raman scattering intensities were calculated according to the procedure of Frisch and coworkers [22].

The  $H_4B_5O_{10}Na$  and  $H_4B_4O_9Na_2$  clusters, which represent the pentaborate and diborate groups, respectively, were used to model the medium-range structures of sodium borate glasses. The geometries of these clusters were also completely optimized, and frequency calculations were performed at the HF/6-31G\* level.

All *ab initio* MO calculations in this work were carried out using the GAUSSIAN94 computer program [23] on the CRAY Y-MP2E/264 supercomputer.

### 3. RESULTS

#### 3.1. Optimized Structure

Principal optimized bond distances of the  $H_4B_6O_{11}$  cluster calculated at the HF/6-31G\* level are shown in Fig. 1. We see from Fig. 1 that the almost plane boroxol rings were obtained and that the average B–O bond distance of model I at the HF/6-31G\* level is  $1.359\text{ \AA}$ , which is reasonably in accordance with the observed B–O distance for vitreous  $B_2O_3$  ( $1.367\text{ \AA}$ , Ref. 7).

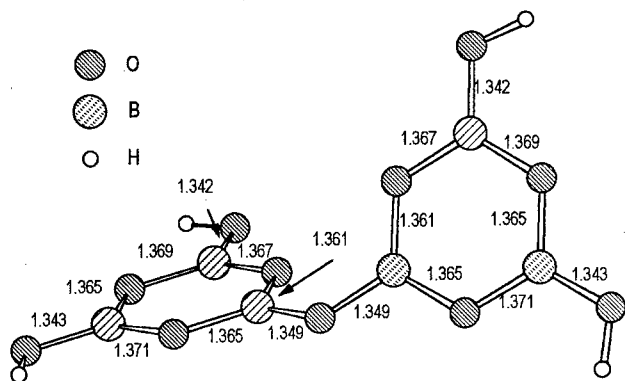
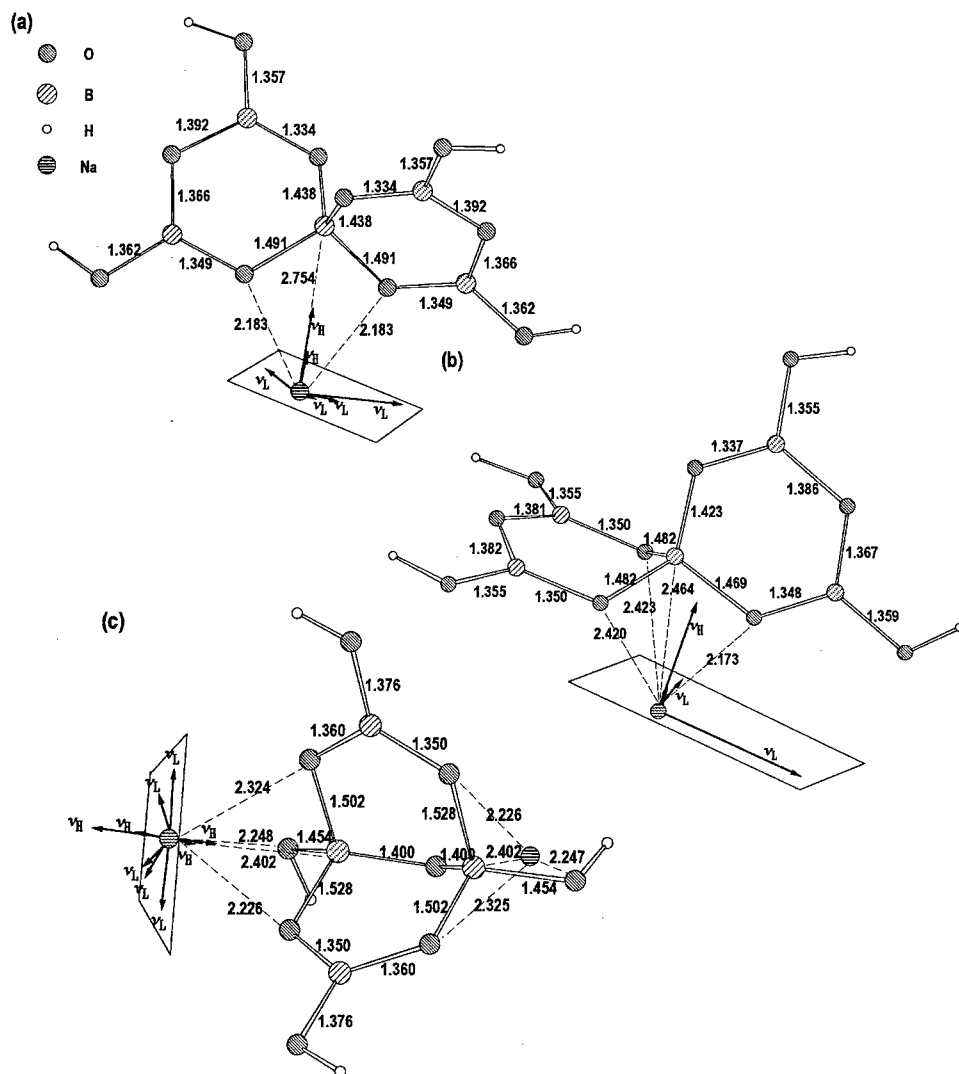


Fig.1. The optimized geometry of the  $H_4B_6O_{11}$  cluster calculated at the HF/6-31G\* level. Principal bond distances are shown in Å.

As for the  $\text{H}_4\text{B}_5\text{O}_{10}\text{Na}$  cluster, we obtained the two optimized geometries whose total energies  $E$  slightly differ from each other ( $\Delta E = 10.1 \text{ kJ/mol}$ ). We refer to the lower and higher energy forms of the clusters as types I (Fig. 2(a)) and II (Fig. 2(b)), respectively.

One notices from Fig. 2 that the coordination environment of Na in type I is considerably different from that in type II. That is, the Na atom in type I is



**Fig.2** The optimized geometry of the alkali borate clusters at the HF/6-31G\* level: (a) a lower (type I) and (b) a higher (type II) energy forms of  $\text{H}_4\text{B}_5\text{O}_{10}\text{Na}$ , (c)  $\text{H}_4\text{B}_4\text{O}_9\text{Na}_2$ . Principal bond distances are shown in Å. Arrows indicate the vector displacements of each Na atom for the  $v_H$  and  $v_L$  modes.

**Table 1**  
Vibrational Frequencies  $\nu$ , Infrared  $I_{\text{IR}}$  and Raman scattering  $I_{\text{R}}$  intensities of the modes less than  $200 \text{ cm}^{-1}$  calculated for the  $\text{H}_4\text{B}_6\text{O}_{11}$  cluster at the HF/6-31G\* level.

	Mode No.								
	1	2	3	4	5	6	7	8	9
$\nu (\text{cm}^{-1})$	23.9	25.4	36.8	121.1	125.1	128.9	129.0	133.8	138.71
$I_{\text{IR}} (\text{km/mol})$	0.13	0.48	0.19	0.19	0.22	0.04	0.78	1.63	0.36
$I_{\text{R}} (\text{\AA}^4/\text{AMU})$	0.84	0.24	0.32	0.13	0.08	0.04	0.01	0.02	0.08

two-coordinated to the oxygens in the  $\text{BO}_4$  tetrahedron (the average Na–O distance  $R_{\text{Na-O(av)}}$  is  $2.183 \text{ \AA}$ ), whereas the Na in type II is three-coordinated to the oxygens in the  $\text{BO}_4$  tetrahedron ( $R_{\text{Na-O(av)}} = 2.339 \text{ \AA}$ ). X-ray [24] and neutron [7] diffraction and EXAFS [25] experiments on alkali borate glasses have reported different values of the nearest-neighbor Na–O distance, namely,  $\sim 2.4$ ,  $\sim 2.3$ , and  $\sim 2.2 \text{ \AA}$ , respectively. Thus, we cannot tell which type of the Na coordination environment would be more realistic in the actual glass network. It should also be noted that the nearest-neighbor Na–B distances in types I and II are calculated to be  $2.754 \text{ \AA}$  and  $2.464 \text{ \AA}$ , respectively. The radial distribution functions (RDFs) obtained from X-ray diffraction measurements [24] indeed have shown that the Na atoms in borate glasses have coordination environments at  $\sim 2.7 \text{ \AA}$ , suggesting that the Na–B correlations should not be neglected in analyzing the Na–O peak in the RDFs.

On the other hand, the geometry optimization of the  $\text{H}_4\text{B}_4\text{O}_9\text{Na}_2$  cluster yielded one stable structure shown in Fig. 2 (c), in which each Na atom is three-coordinated to the oxygens in the nearest  $\text{BO}_4$  tetrahedron. The optimized values of  $R_{\text{Na-O(av)}}$  and  $R_{\text{B-O(av)}}$  were calculated to be  $2.266$  and  $2.402 \text{ \AA}$ , respectively.

**Table 2**  
Vibrational Frequencies  $\nu$ , Infrared  $I_{\text{IR}}$  and Raman scattering  $I_{\text{R}}$  intensities of the modes less than  $350 \text{ cm}^{-1}$  calculated for the alkali borate cluster at the HF/6-31G\* level.

	Mode No.											
	1	2	3	4	5	6	7	8	9	10	11	12
<b><math>\text{H}_4\text{B}_5\text{O}_{10}\text{Na}</math> type I</b>												
$\nu (\text{cm}^{-1})$	34.3	49.4	49.9	70.6	110.2	138.1	140.0	189.0	257.2	264.0	318.8	333.0
$I_{\text{IR}} (\text{km/mol})$	0.96	0.86	0.35	27.21	3.05	1.27	6.35	28.11	14.67	34.07	19.82	3.85
$I_{\text{R}} (\text{\AA}^4/\text{AMU})$	0.18	0.51	0.86	0.24	0.03	0.01	0.06	0.01	0.40	0.33	0.33	0.30
<b><math>\text{H}_4\text{B}_5\text{O}_{10}\text{Na}</math> type II</b>												
$\nu (\text{cm}^{-1})$	31.9	52.7	55.1	73.7	118.2	135.6	138.6	143.2	265.1	281.4	301.6	320.8
$I_{\text{IR}} (\text{km/mol})$	2.19	4.48	20.53	1.83	0.01	2.78	3.17	31.37	4.38	56.80	1.95	13.89
$I_{\text{R}} (\text{\AA}^4/\text{AMU})$	0.63	0.34	0.32	0.54	0.00	0.05	0.00	0.07	0.6	0.27	0.02	0.39
<b><math>\text{H}_4\text{B}_4\text{O}_9\text{Na}_2</math></b>												
$\nu (\text{cm}^{-1})$	69.6	89.3	98.0	120.3	135.5	148.5	165.1	270.4	288.2	303.4	316.8	329.8
$I_{\text{IR}} (\text{km/mol})$	2.36	0.00	18.19	23.68	11.87	4.66	26.36	46.54	4.62	26.13	36.77	57.15
$I_{\text{R}} (\text{\AA}^4/\text{AMU})$	0.69	0.17	0.12	0.09	0.04	0.12	0.00	1.10	0.89	0.28	0.36	0.04

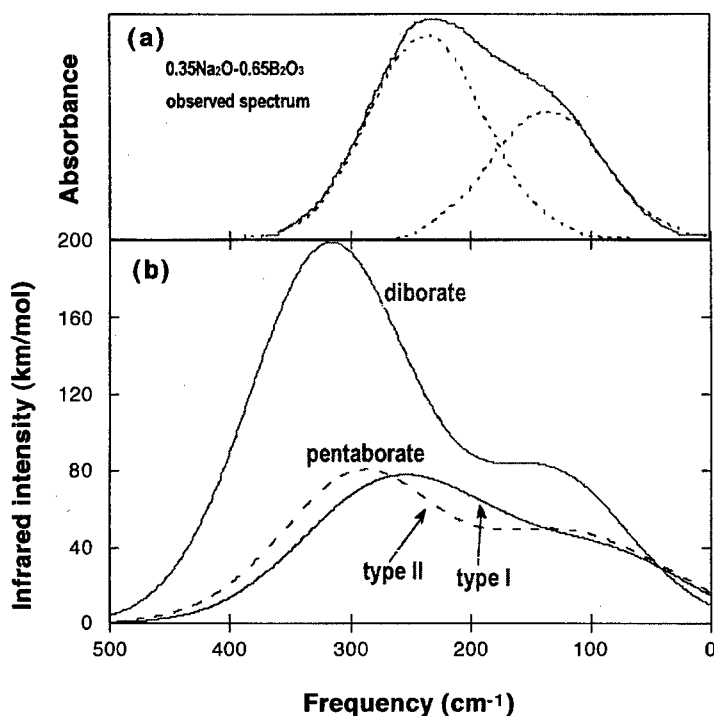


Fig.3. (a) Experimental (Ref. [11]) and (b) calculated far-infrared spectra of sodium borate glasses.

### 3.2. Frequency Calculations

The calculated low-frequency ( $< 400 \text{ cm}^{-1}$ ) harmonic frequencies and their infrared and Raman scattering intensities are listed in Tables 1 and 2. Figures 3 and 4 show the calculated far-infrared and Raman spectra. The effects of broadening were included by introducing a Gaussian-like (Fig. 3) and a Lorentzian-like (Fig. 4) distributions for each vibrational mode with full widths at half maximum of 120 and  $50 \text{ cm}^{-1}$ , respectively, to reproduce the observed spectra.

## 4. DISCUSSION

### 4.1. Far-Infrared Spectra

As mentioned in the Introduction, Kamitsos et al. [10] showed that the observed far-infrared absorption spectra of alkali borate glasses, especially those of Li, Na, and K glasses, can be deconvoluted into two Gaussian component bands; the frequencies at peak maxima have been designated by  $\nu_H$  and  $\nu_L$ , for the high- (H) and low- (L) frequency components, respectively. Both  $\nu_H$  and  $\nu_L$  increase with increasing alkali-oxide content. For sodium borate glasses,  $\nu_H$  ranges from 150 to  $250 \text{ cm}^{-1}$ , and  $\nu_L$  from 100 to  $150 \text{ cm}^{-1}$ . As shown in Fig. 3, the observed far-infrared envelopes have been reasonably reproduced by the present cluster model calculations.\* As a result of the normal mode analysis,

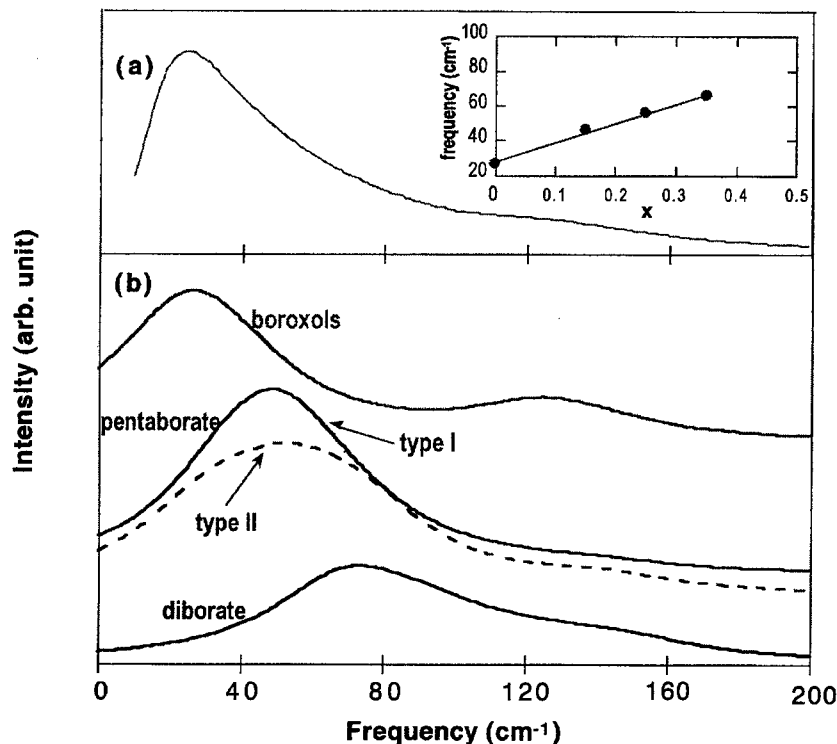


Fig.4. (a) Experimental (Ref. [13]) and (b) calculated Raman spectra of  $B_2O_3$  and sodium borate glasses. Inset shows the observed changes in the boson peak frequencies of  $B_2O_3-xNa_2O$  glasses (Ref. [13]).

we have found that these far-infrared bands are mainly due to the motions of the Na atom and that two types of nuclear motion in each Na coordination environment produce the H and L components (see Figs. 2 and 3); each Na atom is oscillating in one virtual plane to yield the L components, and the other motions perpendicular to the plane give rise to the H components. These calculated results strongly suggest that the origin of the two component bands in the far-infrared spectra of alkali borate glasses should be attributed to the two types of vibrational motions in a specific Na coordination environment.

#### 4.2. Low-Frequency Raman Spectra

We see from Fig. 4 that the calculated low-frequency Raman scattering peak shifts to higher frequencies in the order  $H_4B_6O_{11}$  ( $\sim 30\text{ cm}^{-1}$ ),  $H_4B_5O_{10}Na$  ( $\sim 50\text{ cm}^{-1}$  for both types I and II),  $H_4B_4O_9Na_2$  ( $\sim 75\text{ cm}^{-1}$ ). The tendency is quantita-

\*It appears that the calculated frequencies are slightly higher than the observed ones. This is a common feature of the HF frequencies. It has been demonstrated that the harmonic frequencies calculated at the HF level are consistently larger than the experimental values by 10–15 % [26].

tively in agreement with the experimental results [13]. A normal-mode analysis has revealed that these low-frequency vibrational modes result from a sort of out-of-plane bending motions of the whole skeleton of the respective clusters. We have recently been shown that the cyclic glycerol trimer, which represents the region of medium-range ordering in liquid and supercooled glycerol, gives rise to the low-frequency vibrational modes at  $\sim 50 \text{ cm}^{-1}$  in good accord with experiments and that these modes result from the localized collective motions of the cooperatively hydrogen-bonded hydroxyl groups [27]. These calculated results on borate glasses and glycerol allow us to propose a microscopic origin of the boson peak; that is, the boson peak most likely originates from the localized collective motions of the medium-range structure in glasses.

### Acknowledgment

We would like to thank the Supercomputer Laboratory, Institute for Chemical Research, Kyoto University, for providing the computer time and for permission to use the CRAY Y-MP2E/264 supercomputer.

### REFERENCES

- [1] P.E. Stallworth & P.J. Bray, In: *Glass Science and Technology, Vol. 4B*, Eds. D.R. Uhlmann and N.J. Kreidl (Academic Press, San Diego, 1990), Chap. 2.
- [2] R.E. Youngmann, S.T. Haubrich, J.W. Zwanziger, M.T. Janicke & B.F. Chmelka, *Science* **269** (1995), 1416.
- [3] F.L. Galeener, G. Lucovsky & J.C. Mikkelsen, Jr., *Phys. Rev. B* **22** (1980), 3983.
- [4] B.N. Meera & J. Ramakrishna, *J. Non-Cryst. Solids* **159** (1993), 1.
- [5] R.L. Mozzi & B.E. Warren, *J. Appl. Cryst.* **3** (1970), 251.
- [6] A.C. Hannon, D.I. Grimley, R.A. Hulme, A.C. Wright & R.N. Sinclair, *J. Non-Cryst. Solids* **177** (1994), 299.
- [7] J. Swenson, L. Börjesson & W.S. Howells, *Phys. Rev. B* **52** (1995), 9310.
- [8] E.I. Kamitsos, M.A. Karakassides & G.D. Chryssikos, *J. Phys. Chem.* **91** (1987), 1073.
- [9] G.J. Exarhos, P.J. Miller & W.M. Risen Jr., *J. Chem. Phys.* **60** (1974), 4145.
- [10] E.I. Kamitsos, M.A. Karakassides & G.D. Chryssikos, *J. Phys. Chem.* **91** (1987), 5807.
- [11] E.I. Kamitsos, G.D. Chryssikos & M.A. Karakassides, *Phys. Chem. Glasses* **29** (1988), 121.
- [12] S. Guha & G.E. Walrafen, *J. Chem. Phys.* **80** (1984), 3807.
- [13] A.K. Hassan, L. Börjesson & L.M. Torell, *J. Non-Cryst. Solids* **172-174** (1994), 154.
- [14] J.A. Tossell & P. Lazzeretti, *J. Phys. Chem.* **94** (1990), 1732.
- [15] T. Uchino, M. Iwasaki, T. Sakka & Y. Ogata, *J. Phys. Chem.* **95** (1991), 5455.
- [16] T. Uchino & Y. Ogata, *J. Non-Cryst. Solids* **181** (1995), 175.
- [17] R. A. Barrio, F.L. Galeener, E. Martinez & R.J. Elliott, *Phys. Rev. B* **48** (1993), 15672.
- [18] J.A. Tossell, *J. Non-Cryst. Solids* **183** (1995), 307.
- [19] H.Z. Zhuang, X.W. Zou, Z.Z. Jin & D.C. Tian, *Phys. Rev. B* **52** (1995), 829.
- [20] M.S. Gordon, *Chem. Phys. Lett.* **76** (1980), 163 and references therein.
- [21] P. Pulay, G. Fogarasi, F. Pang, & J.E. Boggs, *J. Am. Chem. Soc.* **101** (1979), 2550.
- [22] M.J. Frisch, Y. Yamaguchi, J.F. Gaw, H.F. Schaefer III & J. S. Binkley, *J. Chem. Phys.* **84** (1986), 531.
- [23] M.J. Frisch et al. *Gaussian 94, Revision B.3* (Gaussian, Inc., Pittsburgh PA, 1995).
- [24] G. Paschina, G. Piccaluga & M. Magini, *J. Phys. Chem.* **81** (1984), 6201.
- [25] G.N. Greaves, In: Ref.1, Chap. 1.
- [26] D.J. DeFrees & A.D. McLean, *J. Chem. Phys.* **82** (1985), 333.
- [27] T. Uchino & T. Yoko, *Science* **273** (1996), 480.

# AN INVESTIGATION OF THE STRUCTURE OF VITREOUS BORON TRIOXIDE BY REVERSE MONTE CARLO SIMULATIONS

Jan SWENSON & Lars BÖRJESSON

*Department of Applied Physics, Chalmers University of Technology,  
S-412 96 Göteborg, Sweden*

The structure of vitreous boron trioxide has been investigated by the Reverse Monte Carlo (RMC) method using reported neutron and X-ray data. The aim was twofold; to test structural models with and without boroxol rings and to estimate the extent of intermediate range structural ordering. For the first purpose we created structural configurations with a variable fraction of boron atoms in boroxol rings. The models containing large amounts of boroxol rings show significantly larger deviations from the experimental diffraction results than those with small fractions. Furthermore, features of the bond angle and dihedral angle distributions as well as visual inspection of the boroxol rich models show that most of the rings in these models are seriously distorted from planarity. It is evident that it is not possible to reproduce the experimental neutron structure factor with a high fraction (>30%) of borons in planar boroxol rings. For the second purpose we have created RMC models of vitreous  $B_2O_3$  with various number of atoms (100-5000 atoms). The comparison with experimental neutron diffraction results shows that the shape of the first sharp diffraction peak (FSDP) is determined by intermediate range correlations extending out to about 15 Å for vitreous  $B_2O_3$ .

## 1. INTRODUCTION

The structure of network glasses in general and vitreous boron trioxide ( $B_2O_3$ ) in particular has been a much debated issue for many years. Two of the most controversial issues have been the structural origin of the first sharp diffraction peak (FSDP) and the possible presence of well-defined rings in the structure. The phenomenon of the FSDP in network glasses is still not well understood [1-16] and there is not even any consensus on the spatial extent of the ordering associated with it. A number of models based on different structural assumptions have been proposed with the aim of explaining the structural origin of the FSDP. Most models explain the FSDP in terms of various specific characteristic structural features such as ordering between layers [1], correlations of randomly close-packed short range structural units [5-6], correlations between cation centered clusters and voids in the network structure [7-9], repeated and well correlated density fluctuations or clusters [2-4], the

presence of quasi-lattice Bragg planes [13] etc. The universality of the phenomenon for network glasses may, however, indicate some kind of general explanation.

In several of the models the FSDP is associated with a (quasi-)periodicity in real space characteristic of the intermediate range order in the material. The position,  $Q_1$ , of the FSDP is then usually assumed to be related to a real space periodic distance,  $d \approx 2\pi/Q_1$ , and the width of the peak is interpreted to arise from a damping in amplitude of the real space oscillations. For most network glasses the FSDP is located at around  $1.1\text{--}1.7 \text{ \AA}^{-1}$  and the width,  $\Delta Q_1$ , is about  $0.3Q_1$ . This corresponds then to a characteristic distance of about  $3\text{--}6 \text{ \AA}$  and a correlation length,  $l \approx 2\pi/\Delta Q_1$ , of  $10\text{--}20 \text{ \AA}$ . Recently it has been indicated that there is a further extended range ordering, which extends well beyond  $35 \text{ \AA}$ , on the basis of an analysis of large molecular dynamics simulations of a-Si [3]. This distance is considerably longer than the width of the FSDP would indicate. Whether this is a general phenomenon for network glasses remains to be investigated.

The question about the presence of well-defined rings in the structure of network glasses is particularly debated for  $B_2O_3$ . Krogh-Moe suggested that the majority of the  $BO_3$  triangles form planar six-fold ( $B_3O_3$ ) boroxol rings [17]. According to the Krogh-Moe model, the glass structure consists of randomly connected boroxol rings rather than a random network of corner linked triangles as was formerly suggested by Zachariasen [18]. Other experimental observations, such as the sharp Raman vibrational mode at  $808 \text{ cm}^{-1}$  [19], and specific features in the nuclear magnetic resonance (NMR) [20] and nuclear quadrupole resonance (NQR) [21] spectra, have given strong indications of the presence of well defined molecular entities in the structure which are suggested to be boroxol rings. Furthermore, local structural models, containing a mixture of boroxol rings and  $BO_3$  triangles with a variable fraction of boron atoms in boroxol rings, have been compared with neutron diffraction data [22,23] and the results indicated that the structure of  $B_2O_3$  consists of a relatively high fraction of boroxol rings. The models were compared with the experimental real space correlation function  $T(r)$  [22] and the structure factor [23] obtained from neutron diffraction and the best agreement was obtained for models containing 60% and 80% of the boron atoms in boroxol rings, respectively. The comparisons were, however, only made in the  $r$ -range  $0\text{--}2.7 \text{ \AA}$  and the  $Q$ -range  $5\text{--}24 \text{ \AA}^{-1}$ , respectively, and no density constraint was applied. Thus, the investigations in references 22 and 23 have considered mainly the short range order of  $B_2O_3$ , which largely is insensitive to the fraction of boroxol rings.

The aim of this study is to test the boroxol ring model on a structural basis, considering both the short and intermediate range order, and to investigate the extent of the intermediate range order associated with the FSDP of vitreous  $B_2O_3$ . It is evident that both these investigations are difficult to perform using only experimental techniques. Computer simulations of model structures of-



fer the possibility to investigate intermediate range correlations more easily, provided that the atomic configurations are large enough. However, it seems to be difficult to estimate the fraction of boroxol rings by using conventional simulation techniques such as molecular dynamics (MD) and Monte Carlo (MC), since it has, so far, not been possible to find interatomic potentials which produce structural models with a large fraction of boroxol rings and which simultaneously can reproduce the experimental data and the correct density. Therefore, we take a new approach and apply the Reverse Monte Carlo (RMC) simulation technique [24,25] to the reported experimental neutron and X-ray data [26]. Models with the correct density and with varying number of atoms (100-5000) and fractions (9-50%) of boroxol rings are created, which all are in better or equal agreement with the experimental  $S(Q)$  than the simple models in [22,23].

## 2. COMPUTATIONAL PROCEDURE

The Reverse Monte Carlo method [24,25] has been shown to be an excellent tool to investigate various structural aspects of disordered materials. It is particularly useful for investigations of intermediate range structures (4-20 Å) represented by the FSDP [27-29] and to test the relevance of different structural assumptions such as the boroxol ring model. In the RMC simulation technique the atoms of an initial configuration are moved so as to minimize the deviation from experimental structural data, e.g. X-ray and neutron diffraction or EXAFS or combinations of them, using a standard Metropolis Monte Carlo algorithm [30]. Note that the RMC technique then uses an approach completely different from other common simulation techniques such as molecular dynamics (MD) and Monte Carlo (MC) which instead minimize the potential energy using model potentials of the interparticle interaction. The latter techniques therefore require detailed knowledge of all relevant interatomic potentials to be able to reproduce glass structures reasonably well.

The starting configurations for the RMC simulations were created using hard sphere Monte Carlo (HSMC) simulations with constraints applied to avoid physically unrealistic structures, in the sense that there is no overlap of atoms and that a proper B-O network is formed. The constraints were of three kinds; closest atom-atom approach, connectivity and fraction of six membered rings. The closest distances that two atoms were allowed to approach were determined from experimental results, such as the radial distribution function. The constraints on the B-O network connectivity were that all the oxygens were coordinated to two borons and that all the borons were coordinated to three oxygens. The B-O distance was allowed to vary between 1.32 and 1.42 Å, which is consistent with the first peak in the experimental pair correlation function,  $G(r)$ , deconvoluted with the resolution function. The fraction of boron atoms in boroxol rings was chosen to be either unconstrained or constrained to 30% and 50%, respectively. Unconstrained simulations were performed for systems of six different sizes containing 100, 200, 400, 800, 2160

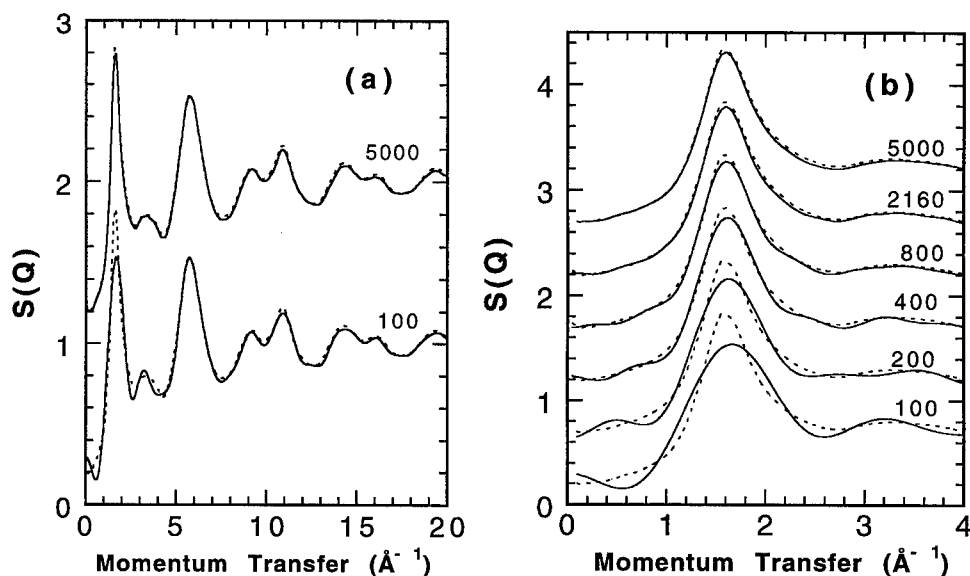


**Fig. 1.** Computed neutron weighted total structure factors,  $S(Q)$ , for different RMC configurations (full lines) in comparison with the experimental structure factor from Ref. [22] (dashed). (a)  $S(Q)$  in the range  $0-20 \text{ \AA}^{-1}$  for configurations containing 100 and 5000 atoms, respectively, and (b)  $S(Q)$  in the range  $0-4 \text{ \AA}^{-1}$  for configurations containing 100, 200, 400, 800, 2160 and 5000 atoms, respectively. The upper curves have been shifted to higher values for clarity.

and 5000 atoms, respectively. The unconstrained configurations had 8-10% of their boron atoms in boroxol rings, which is the statistical number of six membered rings in a HSMC produced structure with no special preference of rings. In both the ring constrained simulations, the total number of atoms was 2160. Periodic boundary conditions were used in all the simulations and box lengths were chosen to correspond to the experimentally measured density ( $1.88 \text{ g/cm}^3$ ).

### 3. RESULTS AND DISCUSSION

#### 3.1. Extent of Intermediate Range Order

Let us begin with the investigation of the extent of the intermediate range order associated with the FSDP of vitreous  $\text{B}_2\text{O}_3$ . The neutron weighted total structure factor,  $S(Q)$  [31], and the corresponding pair correlation function,  $G(r)$  [31], have been computed for the RMC produced structures without ring constraints and compared with the experimental neutron diffraction results (from Ref. [22]), see Fig. 1. Excellent agreement with the experimental data in the high  $Q$ -region above  $5 \text{ \AA}^{-1}$  (i.e. within the experimental errors) is obtained for all the RMC structure factors, (see Fig. 1.(a) for the smallest and largest system) indicating that the short range order is well reproduced for all configurations.

In the low  $Q$ -region, however, there are large deviations from the experimental data for the small systems (see Fig. 1(b)); the peak amplitude of the

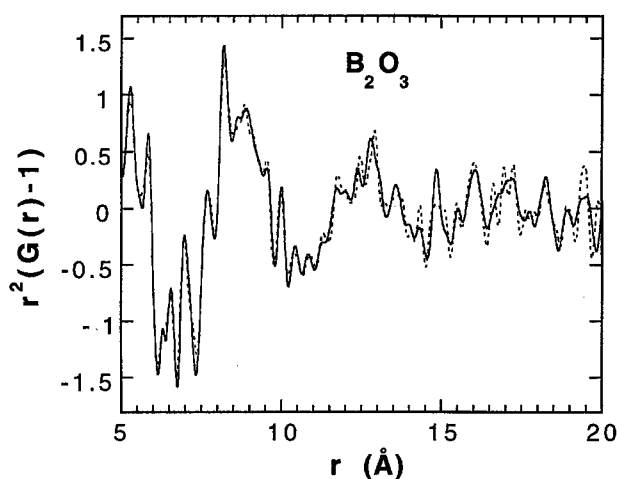
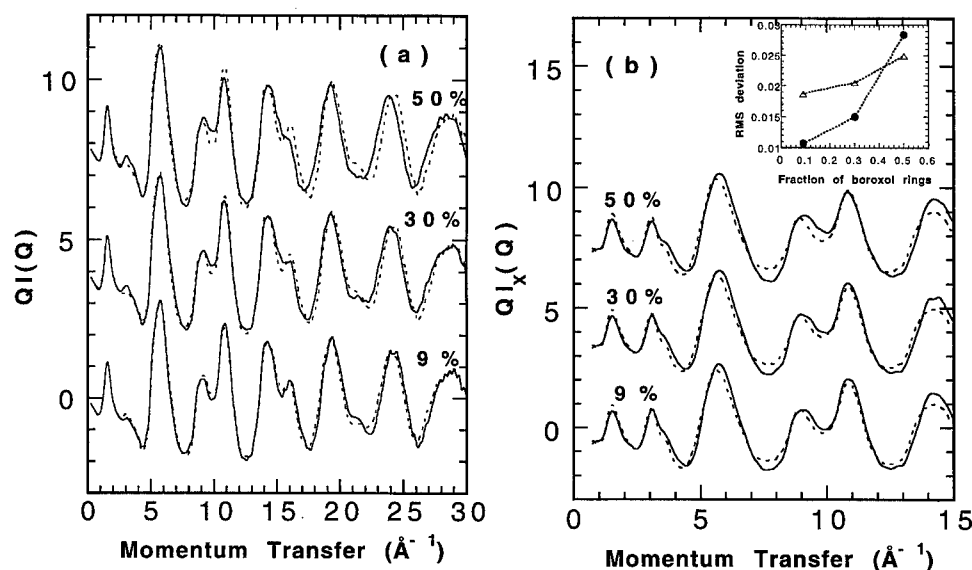


Fig. 2. Reduced radial distribution function,  $r^2(G(r)-1)$ , calculated from the largest model containing 5000 atoms (dashed) in comparison with the corresponding experimental correlation function (full line).

FSDP is too low and the width is too large. The agreement with the experimental FSDP becomes better with increasing size of the system and is almost perfect for the two largest systems with half box-lengths of 14.93 and 19.75 Å, respectively. This shows that the smaller configurations with half box-lengths of 10.72 Å or shorter contain too few atoms to be able to correctly reproduce the intermediate range structures of the glass that produces the FSDP in the data, i.e. the half box-lengths of the configurations are shorter than the longest length-scale characteristic of the FSDP of the glass. A similar intermediate range length scale of about 10 Å was also concluded from a recent molecular dynamics (MD) simulation of  $\text{SiO}_2$  [12].

Next we turn to the real space correlations. In Fig. 2 we compare the reduced radial distribution function,  $r^2(G(r)-1)$ , of the Fourier transformed experimental  $S(Q)$  data [22] with that calculated for the largest RMC model of 5000 atoms. To ensure a proper comparison, the reduced radial distribution function for the RMC configuration was obtained by Fourier transformation of the calculated structure factor using the same cut-off at high  $Q$  as that used for the experimental determination, rather than a direct calculation from the configuration.

It is evident from Fig. 2 that the agreement with the experimental result is excellent for all  $r$ -values out to the edge of the box, which again shows that the size of the system, i.e. half the box-length, does not need to be larger than the longest structural correlation length in the material. It is worth noting that an oscillatory behaviour with a period of about 4 Å is observed that extends out to about 15 Å, i.e. the period is approximately  $2\pi/Q_1$ , where  $Q_1$  is the position of the FSDP for  $\text{B}_2\text{O}_3$ . Thus, the FSDP seems to arise mainly from a damped periodic oscillation in real space. We note that several of the structural models mentioned earlier produce such a quasi-



**Fig. 3.** Computed neutron weighted (a) and X-ray weighted (b) total interference functions (full lines) for the RMC configurations with constrained boroxol ring fractions 9%, 30% and 50% in comparison with the experimental neutron interference function from Ref. [23] (dashed) and the experimental X-ray interference function from Ref. [26] (dashed), respectively. The curves have been shifted vertically, in steps of 4, for clarity. The inset shows the root mean square (RMS) deviations from the experimental neutron (●) and X-ray (Δ) structure factors for the same RMC configurations.

periodic oscillation [1-4,7-9,13]. We have found on close inspection of the computer configurations that the origin of the FSDP is a weak correlation between neighbouring segments of  $\text{BO}_3$  triangles separated by voids in the structure.

### 3.2. A Test of the Boroxol Ring Model

Let us now turn to the investigation of the fraction of boroxol rings in vitreous boron trioxide. Figure 3(a) shows the computed neutron weighted total interference functions,  $QI(Q)$ , for the RMC configurations with constrained boroxol ring fractions 9%, 30% and 50% in comparison with the experimental interference function (from Ref. [23]). All the interference functions are in good agreement with the experimental interference function, indicating that the neutron data are not particularly sensitive to the ring constraint. However, it is obvious that the agreement improves for a decreasing fraction of boroxol rings. This is seen in the inset of Fig. 3(b), which shows the root mean square (RMS) deviations from the experimental structure factor,  $S(Q)$  (equivalent to  $I(Q)+1$ ), for the three RMC produced models. The most serious difference is that the oscillation becomes out of phase for the highest  $Q$ -values and that a peak at about  $16 \text{ \AA}^{-1}$  in the experimental  $QI(Q)$  is only reproduced as a shoulder in the RMC simulation.

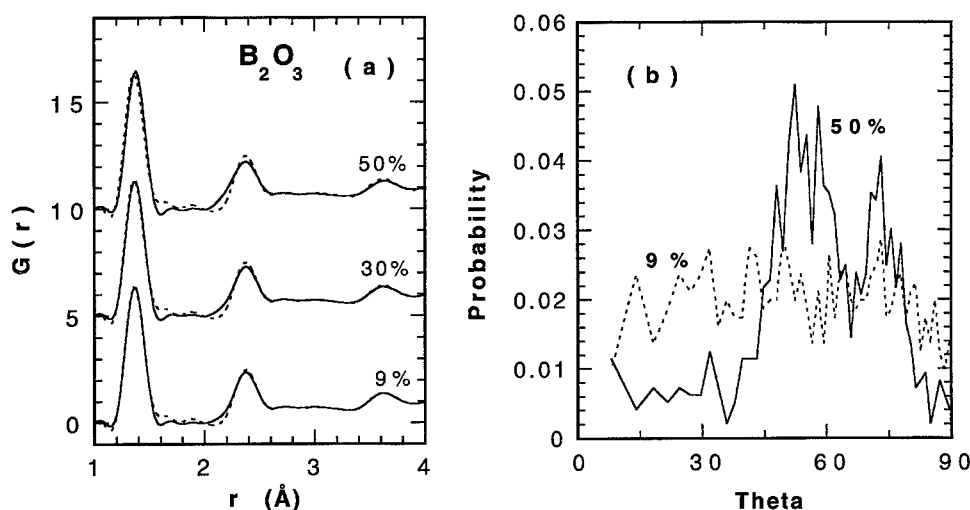


Fig. 4. (a) shows computed neutron weighted atomic pair correlation functions for the RMC models containing 9%, 30% and 50% boroxol rings (full lines) compared with the experimental neutron weighted atomic pair correlation function (dashed). The curves have been shifted vertically, in steps of 5, for clarity. In (b) the dihedral angle distributions between interconnected  $\text{BO}_3$  triangles are shown for the models containing 9% (dashed) and 50% (full line) boroxol rings, respectively.

Figure 3(b) shows the computed X-ray weighted total interference functions,  $Q_x I(Q)$ , in comparison with the experimental interference function (from Ref. [26]), for the same RMC configurations. All the calculated interference functions show some deviations from the experimental interference function. However, it should be noted that the experimental errors in the X-ray data are probably relatively large, indicated by the significant differences between different investigations [26,32,33]. As for the neutron weighted  $S(Q)$  the agreement improves slightly for a decreasing fraction of boroxol rings (see inset of Fig. 3(b)). However, the significance of this decrease is considerably less than for the neutron case, because of the limited accuracy of the experimental X-ray data.

Next we turn to the implications of boroxol models for the real space correlations. In Fig. 4(a) we compare the neutron weighted atomic pair correlation function,  $G(r)$ , of the Fourier transformed experimental  $S(Q)$  data [23] with those calculated for the RMC models containing 9%, 30% and 50% boroxol rings. It is evident from the models containing boroxol rings that a large fraction of boroxol rings gives a slight shift of both the first and second peak. The first peak shifts to a higher  $r$ -value while the second shifts to a lower  $r$ -value. This indicates that the average B–O–B and/or O–B–O bond angles are too low. It is also interesting to note that the relatively sharp peak at about 3.6 Å is perfectly reproduced in the model containing 9% boroxol rings, while it is slightly too low in the model containing 50% boroxol rings. In Ref. [23] it was proposed that this peak is due to the second B–O distance between an oxygen

outside a boroxol ring and a boron within the boroxol ring. It was assumed that the well defined planar boroxol ring was the reason for the sharpness of the peak. Thus, the present results show that no boroxol rings are required to reproduce the peak.

The reason why a wrong bond angle distribution is produced in the boroxol rich model is evident in Fig. 4(b), where the dihedral angle distributions between interconnected  $\text{BO}_3$  triangles are shown for the models containing 9% and 50% boroxol rings, respectively. The figure shows that the dihedral angle distribution for the model containing 9% boroxol rings is almost flat, i.e. the distribution is effectively random. This is, however, not the case for the boroxol rich model, which shows two clearly pronounced peaks at about  $53^\circ$  and  $72^\circ$ , respectively. This is surprising since for a high fraction of planar boroxol rings a significant peak at  $0^\circ$  is expected. It was found that the origin of the peak at  $53^\circ$  is due to 'bent' boroxol groups, i.e. the three oxygens connecting a boroxol ring to the rest of the network are considerably out of the plane of the ring. In addition, the inner rings of bonds of the boroxol groups are often significantly distorted. The peak at  $72^\circ$  cannot be due to two interconnected  $\text{BO}_3$  triangles within the same boroxol group, since the closest allowed B-B and O-O distances would not allow such a heavily 'bent' boroxol group.

The question is why the 'strange' dihedral angle distribution shown in Fig. 4(b) is produced in the model containing 50% boroxol rings? There is no obvious reason for it, because the calculated nearest interatomic distances would agree better with the experimental values if the average O-B-O bond angle was  $120^\circ$  and if boroxol rings were perfectly planar. Thus, the features in the dihedral angle distribution and the shifted peaks in  $G(r)$  are all due to 'compensation effects'. The reason for these 'compensation effects' is the constraints that the RMC configurations have to reproduce the short range order including the connectivity, the intermediate range order (the low-Q part of the structure factor), and simultaneously have the experimentally measured density of  $\text{B}_2\text{O}_3$ . Thus, it is the combination of correct density, connectivity and/or the intermediate range order that cannot be reproduced in the boroxol rich model. The structural models in Refs. [22,23] do not include the constraints of correct density and reproduced intermediate range order and can therefore reproduce the short range order with a high fraction of boroxol rings.

#### 4. SUMMARY

The present results show that for a typical network glass, such as  $\text{B}_2\text{O}_3$ , the FSDP gives rise to a damped quasi-periodic structural correlation with a characteristic length of about  $2\pi/Q_1$  extending out to about 15 Å. The quasi-periodicity arises from a weak ordering between locally aligned segments of  $\text{BO}_3$  triangles separated by voids in the structure. Thus, for this type of oxide glass there is no need to involve any extended range ordering out to 35-50 Å as was done for a-Si [3].

It has also been shown that RMC produced boroxol rich models exhibit

certain features that are not compatible with the experimental data. In particular the average bond angle is shifted to a lower value due to shifts of the first and second peak in  $G(r)$  to higher and lower  $r$ -values respectively. These shifted peaks in  $G(r)$  and the wrong bond angle distribution are produced in the RMC simulation to 'compensate' other more serious errors in the boroxol ring model. In order for the boroxol ring rich models to satisfy the experimental density and the structure factor the  $B_3O_6$  groups have to distort seriously giving a dihedral angle distribution between  $BO_3$  triangles in the group which is incompatible with the definition of planar boroxol rings. To conclude, the results indicate that the structure of vitreous boron trioxide contains less than 30% of boron atoms in boroxol rings.

#### Acknowledgements

We are grateful to Dr Robert McGreevy for stimulating discussions and for providing the RMC simulation program. This work was financially supported by the Swedish Natural Science Research Council.

#### REFERENCES

- [1] L. E. Busse, *Phys. Rev.* **B29** (1984), 3639.
- [2] M. F. David & A. J. Leadbetter, *Phil. Mag.* **B44** (1981), 509.
- [3] A. Uhlherr & S.R. Elliott, *J. Phys.: Condens. Matter* **6** (1994), L99; *Phil. Mag.* **B71** (1995), 611.
- [4] P. S. Salmon, *Proc. R. Soc. Lond.* **A445** (1994), 351.
- [5] S. C. Moss & D. L. Price, *Physics of Disordered Materials* ed. D. Adler, H. Fritzsch and S. R. Ovshinsky (Plenum Press, New York, 1985).
- [6] D.L. Price, S.C. Moss, R. Reijers, M-L. Saboungi & S. Susman, *J. Phys. Condens. Matter* **1** (1989), 1005.
- [7] S. R. Elliott, *Phys. Rev. Lett.* **67** (1991), 711.
- [8] S. R. Elliott, *J. Phys.: Condensed Matter* **4** (1992), 7661.
- [9] J. H. Lee & S.R. Elliott, *Phys. Rev. B* **50** (1994), 5981.
- [10] T. G. Fowler & S. R. Elliott, *J. Non-Cryst. Solids* **92** (1987), 31.
- [11] H. Iyetomi & P. Vashishta, *Phys. Rev. B* **47** (1993), 3063.
- [12] A. Nakano, R. K. Kalia & P. Vashishta, *J. Non-Cryst. Solids* **171** (1994), 157.
- [13] P.H. Gaskell & D.J. Wallis, *Phys. Rev. Lett.* **76** (1996), 66.
- [14] A.P. Sokolov, A. Kisliuk, M. Soltwisch & D. Quitmann, *Phys. Rev. Lett.* **69** (1992), 1640.
- [15] L. Börjesson, A.K. Hassan, J. Swenson, A. Fontana & L.M. Torell, *Phys. Rev. Lett.* **70** (1993) 1275; *Phys. Rev. Lett.* **70** (1993), 4027.
- [16] L. Börjesson, L. M. Torell, U. Dahlborg & W. S. Howells, *Phys. Rev. B* **39** (1989), 3404.
- [17] J. Krogh-Moe, *J. Non-Cryst. Solids* **1** (1969), 269.
- [18] W. H. Zachariasen, *J. Am. Chem. Soc.* **54** (1932), 3841.
- [19] F. Galeener, G. Lucovsky & J. C. Mikkelsen, Jr., *Phys. Rev. B* **22** (1980), 3983.
- [20] G. E. Jellison, Jr., L. W. Panek, P. J. Bray & G. B. Rouse, Jr., *J. Chem. Phys.* **66** (1977), 802.
- [21] S. Garvina, P. J. Bray & G. L. Petersen, *J. Non-Cryst. Solids* **123** (1990), 165.
- [22] P. A. V Johnson, A. C. Wright & R. N. Sinclair, *J. Non-Cryst. Solids* **50** (1982), 281.
- [23] A. C. Hannon, D. I. Grimley, R. A. Hulme, A. C. Wright & R. N. Sinclair, *J. Non-Cryst. Solids* **77** (1994), 299.
- [24] R. L. McGreevy & L. Pusztai, *Mol. Simul.* **1** (1988), 359.
- [25] D. A. Keen & R. L. McGreevy, *Nature* **344** (1990), 423.
- [26] E. Chason & F. Spaepen, *J. Appl. Phys.* **64** (1988), 4435.

- 
- [27] J.D. Wicks, L. Börjesson, G. Bushnell-Wye, W.S. Howells & R.L. McGreevy, *Phys. Rev. Lett.* **74** (1995), 726.
  - [28] J. Swenson, R. L. McGreevy, L. Börjesson, J. D. Wicks & W. S. Howells, *J. Phys.: Condens. Matter* **8** (1996), 3545.
  - [29] J. Swenson, L. Börjesson, R. L. McGreevy & W. S. Howells, *Phys. Rev. B* **55** (1997), 11236.
  - [30] N. Metropolis, A. W. Rosenbluth, M. N. Rosenbluth, A. H. Teller & E. Teller, *J. Phys. Chem.* **21** (1953), 1087.
  - [31] J. Swenson, L. Börjesson & W. S. Howells, *Phys. Rev. B* **52** (1995), 9310.
  - [32] R. L. Mozzi & B. E. Warren, *J. Appl. Cryst.* **3** (1970), 251.
  - [33] G. Paschina & G. Piccaluga, *J. Chem. Phys.* **81** (1984), 6201.



## MOLECULAR DYNAMICS SIMULATION OF $\text{PbO-xB}_2\text{O}_3$ GLASSES WITH BOND ANGLE CONTROL

Youichi AKASAKA

*Opto-Technology Laboratory, The Furukawa Electric Co.,  
LTD., 6, Yawata-Kaigandori, Ichihara, Chiba 290, Japan*

and

Itaru YASUI

*Institute of Industrial Science, University of Tokyo, Roppongi,  
Minato-ku, Tokyo 106, Japan*

The structures of  $\text{PbO-xB}_2\text{O}_3$  glasses have been studied using molecular dynamics (MD) simulations. A three body potential, which controls O-B-O and B-O-B bond angles, estimated by *ab initio* molecular orbital calculations was introduced into the MD simulations. Six-membered rings, such as boroxol, tri-borate, di-pentaborate and di-triborate, whose existence has been demonstrated by spectroscopic studies, were successfully reproduced in the structural models obtained from the present MD simulations. On the basis of calculation results and calculation parameters, it was supposed that the nonlinear dependences of properties on composition are caused by changes of bonding character and network dimension.

### 1. INTRODUCTION

In recent years, molecular dynamics (MD) simulation has been used to investigate the structure and properties of many glasses [1,2]. In spite of many efforts, characteristic structural units of borate glasses (e.g. the boroxol ring) were not reproduced by MD simulations with pair wise type potentials [3], due to inadequate bond angles, especially B-O-B angles. Six membered rings which characteristically exist in borate glasses have a high local structure order compared with a random network structure like silicate glasses. Therefore the method of arranging atoms at random in space, which is used for pair wise type potentials, is not suitable for borate glasses. It is thus interesting whether MD simulation which includes some control of bond angles can reproduce six membered rings or not.

The properties of borate glasses change nonlinearly with change in composition. It was originally believed that this phenomenon is caused by the change of oxygen coordination number of boron from three to four. However, Bray's NMR data subsequently revealed that this coordination change does not provide a direct explanation [4]. In this study, we have tried to reconstruct six membered rings and

investigate the structures of  $\text{PbO-xB}_2\text{O}_3$  glasses ( $x=4,2,1,1/2$ ) with improved MD simulations, which can control bond angles, and have considered the non-linear change of properties (e.g. thermal expansion coefficient) with composition.

## 2. CALCULATION

The structural models were calculated by MD simulation including network bond angle (B-O-B, O-B-O) control forces which were evaluated by *ab initio* molecular orbital (MO) calculation. Total forces used in this MD simulation are the summation of an interatomic interaction and a bond angle one. The former is a Born-Mayer type force described in Eq. (1),

$$F_{ij} = -\frac{e^2}{4\pi\epsilon_0} \frac{Z_i Z_j}{r_{ij}^2} - \frac{B}{\rho} \exp\left(-\frac{r_{ij}}{\rho}\right) \quad (1)$$

where  $e^2/4\pi\epsilon_0$  is a constant term ( $230.717 \times 10^{-30} \text{ Jm}$ ),  $r_{ij}$  is an interatomic distance,  $Z$  is an ionic charge,  $B$  is a repulsive constant, and  $\rho$  is an empirical constant.

### 2.1. The Introduction of Bonding Angle Control

The bond angle interactions introduced in this simulation were determined as follows:

- (1). The decision of force direction.
- (2). The estimation of energy changes when the bond angle is away from the ideal angle.
- (3). The removal of the contribution due to the repulsive interaction between like atoms.
- (4). Fitting the force function to the bond angle interaction described in Eq.(2).

$$F_{ijk} = k(\theta_{ijk} - \theta_{ideal})^\lambda \quad (2)$$

where  $k$  and  $\lambda$  are constant terms given for each species of bond angle.

**2.1.1. Direction of bond angle force** - When the bond angle is away from the ideal angle in borate glasses, it may be corrected by rotating around the center atom as shown in Fig. 1(a).

However, in this MD simulation the three-body force works in the direction of the summation of vectors of two B-O atom pairs, shown in Fig. 1(b), in order to ignore the repulsive interatomic interaction between two atoms around a center atom. The force to correct a bond angle is designed not to cause rotations or the movement of the center of gravity of the three atoms.

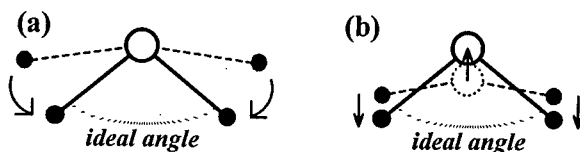


Fig. 1. Direction of bonding angle force. (a) in nature (b) in this MD calculation.

**2.1.2. The estimation of energy changes by MO calculations** - Energy gaps between arbitrary angles and ideal bond angles were estimated by MO methods. The clusters used in MO calculations were built up with the atomic arrangement of boric acid crystal [5] ( $\text{H}_3\text{BO}_3$  cluster and  $\text{H}_4\text{B}_2\text{O}_5$  cluster) and were optimized with a LCAO-SCF calculation (Gaussian 82) by using a 3-21G basis function [6]. Ideal angles for B-O-B, O-B<sup>3</sup>-O (oxygen, three oxygen coordinated boron and oxygen) and O-B<sup>4</sup>-O (oxygen, four oxygen coordinated boron and oxygen) were 131°, 120° and 109·46°, respectively. Energy gaps for smaller angles increased more steeply than those of larger angles because of repulsive interatomic interactions.

**2.1.3. The removal of the repulsive interatomic interaction** - The repulsive energy of neighboring like atoms (in the case of B-O-B, B-B repulsive energy) was subtracted from the energy gaps obtained by the MO calculations. Fig. 2 shows the three body potentials for B-O-B and O-B<sup>3</sup>-O angles. In the case of the B-O-B angle, the ideal angle for the three body potential shifts to 120° from 131° in total energy.

**2.1.4. Fitting the force function to the bond angle interaction** - The Constant terms  $k$  and  $\lambda$  of Eq. 2 were determined to be divided between the interatomic distance changes and bonding angle changes. In the case of the B-O-B angle,  $k$  was  $15 \times 10^{-10} \text{ J m}^{-1}$  and in the case of the O-B-O angle,  $k$  was  $11 \times 10^{-10} \text{ J m}^{-1}$ . In both cases  $\lambda$  was 0·5. Fig. 3 shows the total potential of B-O-B, including the stable potential minimum (hatched area), which is located in the direction of ideal B-O-B bond angle.

## 2.2. Conditions of Simulation

MD calculations were performed with 6000 steps at each temperature 6000 K, 3000 K and 300 K, and the time step was  $3 \times 10^{-15} \text{ s}$ . Cell sizes, whose shape was cubic, were determined by the measured densities. Unit cells were piled up three-dimensionally and atoms in the central cell were affected by several ten thousand atoms.

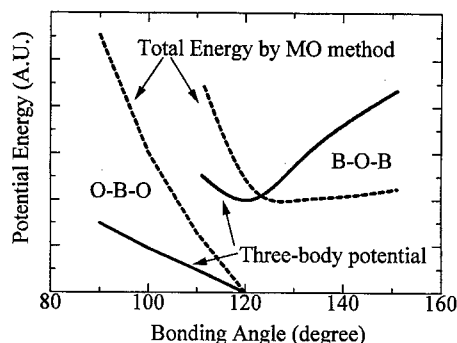


Fig. 2. Potentials estimated by calculation of B-O-B and O-B-O angles.

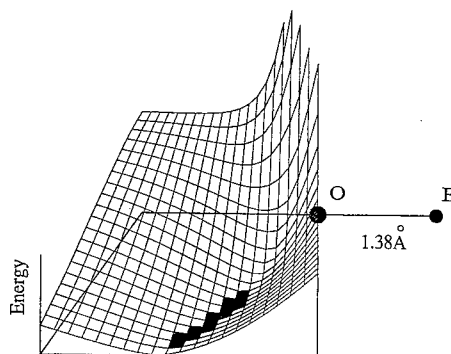


Fig. 3. Total potential distribution including the B-O-B angle potential.

### 3. DIFFRACTION DATA

Mixtures of reagent grade  $\text{H}_3\text{BO}_3$  and  $\text{PbO}$  were melted at  $800^\circ\text{C}$  for 15 min in an Au-Pd crucible and poured onto a steel plate. Polished block samples were used for X-ray diffraction measurements whilst crushed samples were used for neutron diffraction measurements. 99.64%  $^{11}\text{B}$  enriched  $\text{H}_3\text{BO}_3$  was used to produce the samples for the neutron measurements, because the thermal neutron capture cross-section of  $^{10}\text{B}$  is very large. The measured densities of  $\text{PbO}-x\text{B}_2\text{O}_3$  glasses ( $x=4, 2, 1$  and  $1/2$ ) were  $3.23, 4.42, 5.71$  and  $6.83 \text{ g cm}^{-3}$ , respectively. The X-ray diffraction patterns were measured with Mo  $\text{K}\alpha$  radiation monochromatized with balanced filters (Zr-Y) and a graphite monochromator in the diffracted beam using a Rigaku Denki RU-200 diffractometer. Neutron diffraction measurements were carried out using the time of flight (TOF) technique with pulsed neutrons at the HIT facility at the National Institute of High-Energy Physics, Tsukuba.  $Q_{\text{max}}$  values for X-ray and neutron were  $16.8$  and  $30 \text{ \AA}^{-1}$ , respectively. After standard normalization and correction procedures, the radial distribution functions (RDFs) were calculated by Fourier transformation.

### 4. RESULTS

Parameters used in the MD simulations were determined by trial and error to satisfy the information obtained from the X-ray and neutron RDFs, as discussed below, of  $\text{PbO}-x\text{B}_2\text{O}_3$  glasses ( $x=4, 2, 1$  and  $1/2$ ), shown in Fig. 4 [7].

In the observed RDFs, the first peak at about  $1.3 \text{ \AA}$  is attributed to nearest neighbor B-O pairs, and the second large peak at around  $2.4 \text{ \AA}$  consists of the nearest Pb-O and O-O pairs. These results revealed that the B-O-B angles are around  $135^\circ$  on average. Appropriateness of the structure models was judged by whether the interatomic distance, bonding angles and coordination num-

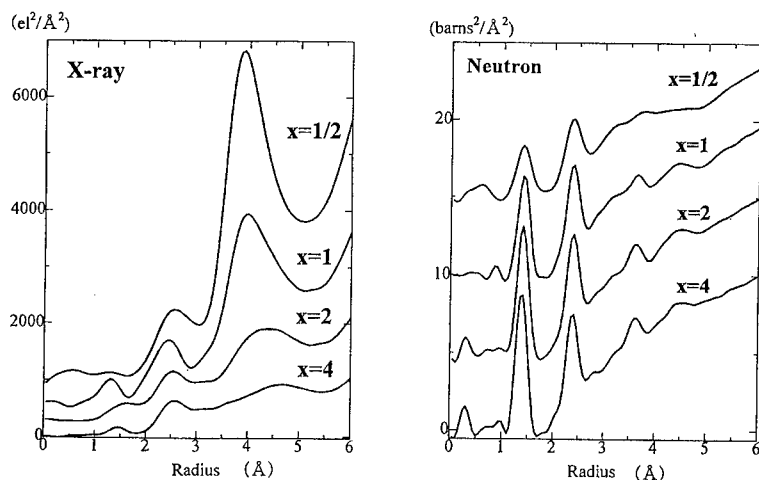


Fig. 4. X-ray and neutron RDFs of  $\text{PbO}-x\text{B}_2\text{O}_3$  glasses ( $x=4, 2, 1, 1/2$ ).

bers were adequate and six membered rings were reconstructed in the structural models, or not. Mainly interatomic distances were controlled by  $B_{ij}$  and intermediate range order was arranged by  $Z_i$ . Calculation parameters were shown in Table 1.

The effect of changing these parameters was severe, and a very slight change gave non-coordination oxygen, three coordination one and/or four membered rings. The structural models obtained by the MD simulation are shown in Fig. 5(a)-(d). In the cases of  $x=4, 2$  and  $1$ , six membered rings, boroxol and triborate ( $x=4$ ), di-pentaborate and di-triborate ( $x=2$ ) and di-triborate ( $x=1$ ), were reproduced. In the case of  $x=1/2$ , six membered rings did not exist. Structural parameters obtained from the models are listed in Table 2.

Each bond angle for each glass was distributed around the ideal angle. For instance, the bond angle distributions of  $\text{PbO}-4\text{B}_2\text{O}_3$  glass are shown in Fig. 6. The average angle for  $\text{B}-\text{O}-\text{B}$  was  $135.57^\circ$ , which is a little bigger than the ideal bond angle obtained by MO method ( $131^\circ$ ). The average angle for  $\text{O}-\text{B}^3-\text{O}$  was  $118.46^\circ$  and that of  $\text{O}-\text{B}^4-\text{O}$  was  $109.43^\circ$ , which shows good agreement with the ideal angles which are  $120.0^\circ$  and  $109.46^\circ$ , respectively. The accumulated coordination numbers for oxygen around boron were 3.27, 3.50, 3.53 and 3.39, respectively. These numbers agree with the values obtained by Bray with NMR [4]. The fraction of the boron atoms which are in six membered rings in the structural models ( $x=4, 2, 1, 1/2$ ) are 22.5, 42.5, 18.8 and 0%, respectively.

**Table 1**  
Conditions and Parameters used in the MD Calculations.

Conditions		Cell Size Å	Density g/cm <sup>3</sup>	Atom number				
				Pb	B	O		
PbO-4B <sub>2</sub> O <sub>3</sub>		10.885	3.23	5	40	65		
PbO-2B <sub>2</sub> O <sub>3</sub>		11.084	4.42	10	40	70		
PbO-1B <sub>2</sub> O <sub>3</sub>		11.087	5.71	16	32	64		
PbO-1/2B <sub>2</sub> O <sub>3</sub>		11.133	6.83	22	22	55		
Parameters		Charge $Z_i$	Pb $B_{ij}$	B $\rho$	O $B_{ij}$	$\rho$	$B_{ij}$	$\rho$
PbO-4B <sub>2</sub> O <sub>3</sub>	Pb	+2.0	1635.64	0.29	4.96	0.29	14.12	0.25
	B	+2.42			2.50		4.08	
	O	-1.643					13.08	
PbO-2B <sub>2</sub> O <sub>3</sub>	Pb	+2.0	785.87	0.29	22.95	0.29	16.85	0.25
	B	+2.45			8.79		4.38	
	O	-1.686					10.52	
PbO-1B <sub>2</sub> O <sub>3</sub>	Pb	+2.0	439.99	0.29	24.36	0.29	13.33	0.25
	B	+2.60			9.90		4.97	
	O	-1.800					12.00	
PbO-1/2B <sub>2</sub> O <sub>3</sub>	Pb	+2.0	439.99	0.29	24.82	0.29	18.23	0.25
	B	+2.65			10.28		5.13	
	O	-1.824					12.32	

B:  $\text{B} \times 10^{16}$  J;  $\rho$ : in Å.

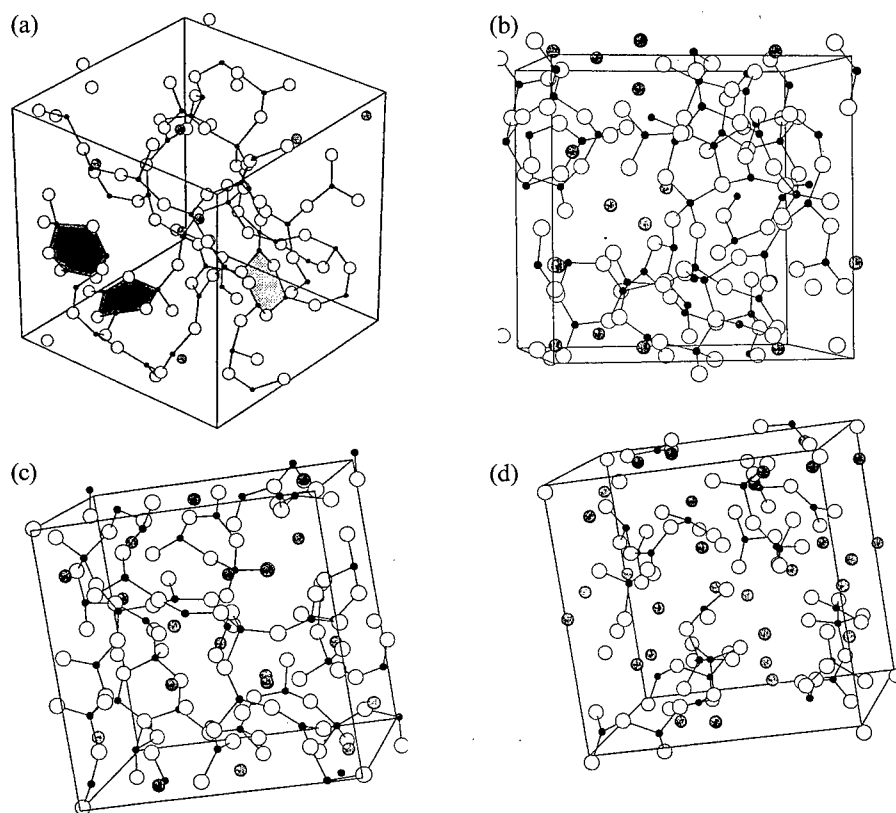


Fig. 5. Structural models.(a) $\text{PbO-4B}_2\text{O}_3$  (b) $\text{PbO-2B}_2\text{O}_3$  (c) $\text{PbO-1B}_2\text{O}_3$  (d) $\text{PbO-1/2B}_2\text{O}_3$ .

**Table 2**  
Structural Parameters of the MD Simulations

	$\text{PbO-4B}_2\text{O}_3$	$\text{PbO-2B}_2\text{O}_3$	$\text{PbO-1B}_2\text{O}_3$	$\text{PbO-1/2B}_2\text{O}_3$
Bond angle	Average (Std Deviation) degree			
B-O-B	135.57(12.08)	130.15(10.78)	131.50(7.95)	129.53(8.81)
O-B <sup>3</sup> -O	118.46(7.37)	118.04(9.22)	117.76(6.83)	118.01(6.82)
O-B <sup>4</sup> -O	109.43(6.90)	109.25(8.87)	109.20(7.42)	109.38(6.25)
Coordination	Number			
Boron	3.27	3.50	3.53	3.39
Oxygen	2.0	2.0	1.70	1.47
Six membered rings	boroxol triborate	di-pentaborate di-triborate	di-triborate	None
Ring rate* (%)	22.5	42.5	18.8	0.0

\* The fraction of the boron atoms which are in six membered rings.

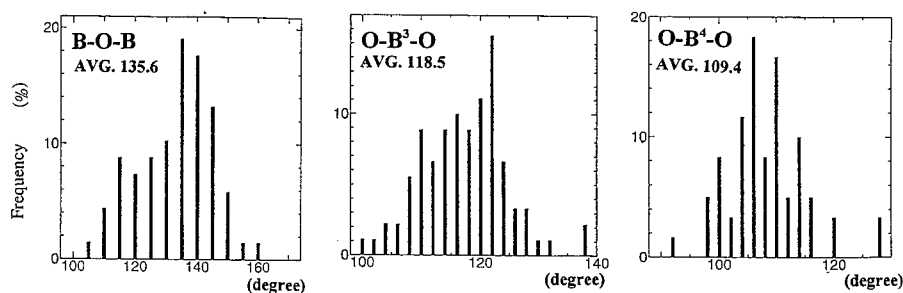


Fig. 6. Bond angle distribution for PbO-4B<sub>2</sub>O<sub>3</sub> glass  
(a) B-O-B angle (b) O-B<sup>3</sup>-O angle (c) O-B<sup>4</sup>-O angle.

## 5. DISCUSSION

The B-O-B and O-B-O bond angles, for the network structure of PbO-xB<sub>2</sub>O<sub>3</sub> glasses, were distributed around the ideal angles in these MD simulations. Six membered rings were reproduced in the structural models. Not all boron atoms form six membered rings ( $x=4, 2, 1$ ), which is different from PbO-xB<sub>2</sub>O<sub>3</sub> crystals. It is supposed that the difference was caused by the rapid quenching rate in the MD calculations and by insufficient calculation time to give a more accurate structure filled with six membered rings. Konijnendijk et al [8] have assigned the peaks of the Raman spectra of alkali and alkaline-earth borate glasses to structural units. They explained that adding metal oxide causes four coordinated boron to occur in six membered rings, adding more metal oxide causes two borons in a ring to be four coordinated and still more metal oxide causes six membered rings not to occur. Our structural models show the same tendency from boroxol ( $x=4$ ) to tri-borate ( $x=4$ ), di-pentaborate ( $x=2$ ), di-triborate ( $x=2,1$ ), and no six membered rings ( $x=1/2$ ). The thermal expansion coefficient of PbO-xB<sub>2</sub>O<sub>3</sub> glasses decreases as PbO content goes from 0% to 25 or 30% and then increases as PbO content goes from 30% to 80%.

Atomic electrical charges for the simulations in Table 1 and structural information in Table 2 supported this nonlinear property change. An ionic charge of bonding should change linearly (when PbO content increases, an ionic charge must increase linearly). However, in our calculation, the proper model for each composition was given only by a non-linear change in the ionic charge of the boron atoms. When  $x$  is 4 or 2, the boron charge has a small value (2.42 or 2.45) and when  $x$  values is 1 or 1/2 it has large values (2.60 and 2.65). This suggests that the covalence of the B-O bond is high when  $x$  is over 2 but is low when  $x$  is under 1. Since PbO-2B<sub>2</sub>O<sub>3</sub> glass has more 4 coordinated boron compared to PbO-4B<sub>2</sub>O<sub>3</sub> glass and has high covalency, it is hard to activate thermally because of the higher network dimension. On the other hand, since PbO-1/2B<sub>2</sub>O<sub>3</sub> glass has less 4 coordinated boron compared to PbO-1B<sub>2</sub>O<sub>3</sub> glass and resembles an ionic state, it is easy to activate thermally.

## 6. CONCLUSION

The structures of  $\text{PbO-xB}_2\text{O}_3$  glasses have been studied by using molecular dynamics (MD) simulations. A three body potential, which controls O-B-O and B-O-B bond angles, estimated by the *ab initio* molecular orbital method was introduced into the MD simulation. Six-membered rings, boroxol, tri-borate, di-pentaborate and di-triborate, whose existence has been demonstrated by spectroscopic studies were successfully reproduced in the structural models obtained from the present MD simulation. On the basis of the calculation results and parameters, it is indicated that the nonlinear changes of properties with composition are caused by changes in bonding character and network dimension.

## Acknowledgments

The authors wish to thank Professor M. Misawa of KEK and Professor T. Fukunaga of Nagoya University who have given much help in the neutron diffraction measurements and in the treatment of data.

## REFERENCES

- [1] L.V. Woodcock, C.A. Angell & P. Cheeseman, *J. Chem. Phys.* **65** (1976), 1565.
- [2] T.F. Souls & R.F. Busbey, *J. Chem. Phys.* **75** (1981), 969.
- [3] Q. Xu, K. Kawamura & T. Yokokawa, *J. Non-Cryst. Solids* **104** (1988), 261.
- [4] P.J. Bray, M. Leventhal & H.O. Hopper, *Phys. Chem. Glasses* **4** (1963), 47.
- [5] R. Wyckoff, *Crystal structures* (Interscience, New York, 1964) **2**, 513.
- [6] A. Pople, M. Head-Gordon, D.J. Fox, K. Raghavachari & L. Crutiss, *J. Chem. Phys.* **90** (1989), 5622.
- [7] Y. Akasaka, I. Yasui & T. Nanba, *Phys. Chem. Glasses* **34** (1993), 232.
- [8] W.L. Konijendijk & J.M. Stevels, *J. Non-Cryst. Solids* **18** (1975), 307.



# MOLECULAR DYNAMICS SIMULATION OF $B_2O_3$ GLASS USING A COORDINATION DEPENDENT POTENTIAL

Byeongwon PARK & Alastair N. CORMACK  
*New York State College of Ceramics at Alfred University,  
Alfred, NY 14802, USA*

The structure of pure  $B_2O_3$  glass was simulated by molecular dynamics using a coordination dependent potential. Pair correlation functions and bond angle distributions were well matched to experimental results. Boroxol rings were found to be present and have a planar structure.

## 1. INTRODUCTION

Knowledge about the atomic structure of a given substance is a prerequisite to understanding its physical or chemical properties. Whilst the determination of the structure of a crystalline solid is relatively easy because of its periodicity, in glasses there is no straightforward way to determine the structure, because of the lack of translational periodicity. Another approach to analyzing glass structures, from an atomistic viewpoint, uses molecular dynamic (MD) computer simulation. In MD computer simulations, which have become one of the more powerful tools with which to investigate materials having a random structure, such as liquids and glasses, information about individual ion configurations may be analyzed and various properties of the materials may be predicted. The principal limitation of the technique is the need for a viable interatomic potential model. The technique has seen a widespread successful application to silica based glasses [1-3]. This paper describes the development of a suitable model for vitreous  $B_2O_3$ .

## 2. BORON OXIDE GLASS

### 2.1. Vitreous Boron Oxide Structure

The structure of borate glasses has been studied using various methods such as NMR [4], Raman spectroscopy [5], x-ray diffraction [6] and neutron diffraction [7,8]. Zachariasen [9] proposed a simple random network model for vitreous boron oxide glass, consisting of planar  $BO_3$  triangles, as found in crystalline  $B_2O_3$ , with the boron being in three-fold coordination. However, the intermediate range structure, that is, how the  $BO_3$  units are connected together, remains controversial.

According to Krogh-Moe [10], the glass network is made up of a randomly connected arrangement of  $BO_3$  triangles with a comparatively high fraction

of six membered boroxol rings. Many experimental results are apparently in agreement with Krogh-Moe's model, especially the extremely intense, narrow and highly polarized peak at  $808\text{ cm}^{-1}$  in the Raman spectrum, which is assigned to a symmetric breathing motion mainly involving the three oxygens of the highly planar boroxol ring [10]. When Mozzi & Warren [6] compared their real space correlation function with a model made up of boroxol rings with external B-O-B angles of  $130^\circ$ , they found that the model was well matched up to  $6\text{ \AA}$ . Interpretation of neutron diffraction experiments by Johnson et al. [7] and Hannon et al. [8] led to conclusion that vitreous  $\text{B}_2\text{O}_3$  should consist largely of boroxol rings, with a fraction of 0.6-0.8 of the boron atoms in boroxol rings, in order to explain fully the vitreous structure.

However, Elliott [13] has claimed that the continuous random network model without boroxol rings can explain most, if not all, of the experimental results and that it is not necessary to invoke the presence of boroxol rings.

## 2.2. MD Simulations of Borate Glass Systems

Recently, there have been several studies using MD calculations of systems containing  $\text{B}_2\text{O}_3$  [16-26]. In contrast to the success of MD simulations in silicate systems, most MD simulations of borate systems show some discrepancies with experimental data. Pair potential models can reproduce the RDFs derived from x-ray and neutron scattering data at short distance. However, there still remain discrepancies in the intermediate region structure, including B-O-B angles which are often far from the average of the estimated values of around  $130^\circ$ . Pair potential models always generate continuous random networks without any boroxol rings, even when a three body potential was included for some simulations. In their MD simulation studies, Verhoef & den Hartog [23,24] argued that an assumption of a large fraction of boroxol rings in the glass network is not necessary to explain the experimental properties.

Since the vitreous state is an extension state of the crystalline phase, the potential model should be transferable to some degree. However, when Takada et al. [25] used Verhoef & den Hartog potential parameters, they failed to reproduce the  $\text{B}_2\text{O}_3$  crystal structure. Therefore, Verhoef's potential parameters may not be adequate to reproduce the true vitreous  $\text{B}_2\text{O}_3$  structure.

These discrepancies may come from inadequate potential parameters and hence force calculation between atoms. The development of adequate theoretical models for borates is much more difficult than for silicates due to the complexity of boron-oxygen bonding, which is not only partially covalent, but also exhibits a change in boron coordination depending on its environment [25]. Therefore it is necessary to improve the interatomic potential model in order to get more reliable simulation results. Recently, Takada et al. [25] developed a new interatomic potential model for the two crystalline phases of boron oxide, which depends on the coordination number of oxygen atoms and applied it to vitreous  $\text{B}_2\text{O}_3$  using a molecular dynamics simulation [26]. They suggested that the use of partial charges, and the inclusion of a B-O-B bond

bending, three body term, are necessary to reproduce the boroxol rings in B<sub>2</sub>O<sub>3</sub> glass. This scheme has been implemented in a conventional MD simulation .

### 2.3. New Improved Interatomic Potential Model

As indicated above, Takada et al. [27,28] reported two improved interatomic potential models. These were obtained by fitting to ab initio quantum mechanical data. One is a transferable potential, which reproduces both the crystalline B<sub>2</sub>O<sub>3</sub>-I and B<sub>2</sub>O<sub>3</sub>-II structures. B<sub>2</sub>O<sub>3</sub>-I has three-fold boron whereas B<sub>2</sub>O<sub>3</sub>-II has four fold boron. A Buckingham potential is used for O-O and B-B short range interactions;

$$V(r_{ij}) = A \exp\left(-\frac{r_{ij}}{\rho_{ij}}\right) - \frac{C}{r^6} \quad (1)$$

and a Morse potential is used for the B-O interaction;

$$V(r_{ij}) = D_{ij} \left\{ 1 - \exp[-\beta_{ij}(r_{ij} - r_0)] \right\}^2 \quad (2)$$

In order to include more covalent effects, a three-body term, as a simple harmonic bond-bending form, is added;

$$V(\theta) = \frac{1}{2} K_B (\theta - \theta_0)^2 \quad (3)$$

The second model is a coordination dependent potential model. Experimental data show that bond lengths are strongly dependent on the coordination number, so the potential may be explicitly formulated to depend on it. Although coordination dependent potential models have been used before [28], standard MD codes do not incorporate them. The conventional MD code does not allow a continuous variation of potential with respect to coordination number change because atom labels are not usually allowed to change during the course of a simulation. For example, there is no way to differentiate between a three-fold oxygen and a two-fold oxygen because the code just picks up the species name within cutoff distance to calculate the force. Tersoff [28] discussed a new empirical approach for the structure and energy of covalent systems in which environmental dependent bond order is explicitly implemented into the interatomic potential model. Some basic steps to derive these coordination dependent potential parameters can be found in the papers of Takada et al. [25, 26] and Tersoff [28].

## 3. EXPERIMENTAL PROCEDURES

### 3.1. Potential Parameters

Potential models were implemented based on those of Takada et al. [25,26]. The MD program used is FUNGUS [29]. The original source code, and especially the force calculation subroutine, had to be heavily modified to imple-

**Table 1**  
Potential Parameters Based On Takada's [25]

Parameter	Value
<u>Charge</u>	
q(B)	+1.2
q(O)	-0.8
<u>Morse potential for B-O</u>	
for two fold Oxygen atom :O2	
D[eV]	1.84
$\beta$ [1/Å]	2.7
$r_0$ [Å]	1.35
for three fold Oxygen atom: O3	
D[eV]	0.98
$\beta$ [1/Å]	2.7
$r_0$ [Å]	1.475
<u>Buckingham potential for O-O</u>	
A[eV] for O2-O2	1990.8
A[eV] for O2-O3	1650.9
A[eV] for O3-O3	692.3
$\rho$ [Å]	0.30
C[eV Å <sup>6</sup> ]	0.0
<u>Buckingham potential for B-B</u>	
A[eV]	323.1
$\rho$ [Å]	0.30
C[eV Å <sup>6</sup> ]	0.0
<u>Three body term for O-B-O (<math>\theta_0=120^\circ</math> for three fold)</u>	
for three fold Boron atom	
k[eV/rad <sup>2</sup> ]	0.0
for three fold Boron atom	
k[eV/rad <sup>2</sup> ]	1.66
<u>Three body term for B-O-B (<math>\theta_0=120^\circ</math>)</u>	
for two fold Oxygen atom	
k[eV/rad <sup>2</sup> ]	6.38
for three fold Oxygen atom	
k[eV/rad <sup>2</sup> ]	4.22
R=1.8 Å D=0.2 Å	

ment the coordination dependent potential model.

The distances between atoms are evaluated at every time step and the coordination state for each atom within a cutoff distance is calculated. Then the appropriate label for each atom is assigned, e.g. three fold, two fold or intermediate coordination, and the proper interatomic potential is chosen according to the new label. The long range Coulombic interaction is calculated using the usual Ewald method, and the potential parameters are given in Table 1. A larger transition range, 0.4 Å, was used than Takada's 0.2 Å.

### 3.2. Simulation Procedure for B<sub>2</sub>O<sub>3</sub> Glass

The MD simulations were run on Silicon Graphics workstations. A total of 405 (162 B, 243 O) atoms was used in the simulation. The starting structure

was based on  $B_2O_3$ -I, which consists of  $BO_3$  triangles only without boroxol rings. Though the initial coordinates are randomly given, the final structure is similar. The simulation box size was adjusted to give the experimental density ( $1.83 \text{ g/cm}^3$ ), under constant volume conditions. At high temperatures, the box size was enlarged to account for thermal expansion of the material. Initially, the atoms were heated and equilibrated to a target temperature of 5000 K for 10,000 time steps (each timestep=1 fs). This process destroyed the crystallinity of the starting structure and gave a random, disordered structure. After melting, the system was cooled to room temperature through several steps: 3000 K, 1500 K, 600 K and finally 300 K with 10,000 timesteps at each temperature. The positions of the atoms, averaged over the last 1000 timesteps, were used to obtain the radial distribution function, bond angle distribution, and coordination number. Graphical visualization was achieved using commercial software: Cerius<sup>2</sup> and InsightII from Molecular Simulation Incorporated.

## 4. RESULTS AND DISCUSSIONS

### 4.1. Typical Structure of Simulated Pure $B_2O_3$ Glass

The typical structure of simulated  $B_2O_3$  glass is illustrated in Fig. 1. The basic structural unit of the glass is the  $BO_3$  triangle, and no  $BO_4$  tetrahedra are seen. The  $BO_3$  units are randomly connected together. Boroxol rings are also seen in the simulated glass, with 13% of the B atoms in these rings.

Note that this fraction of B atoms in boroxol rings is far below the estimated values of 40% (Takada et al. [26]), 60% (Johnson et al. [7]) and 80% (Hannon et al. [8]). There are two possibilities for the low fraction of B atoms in boroxol rings seen in our simulation, apart from the obvious one that it

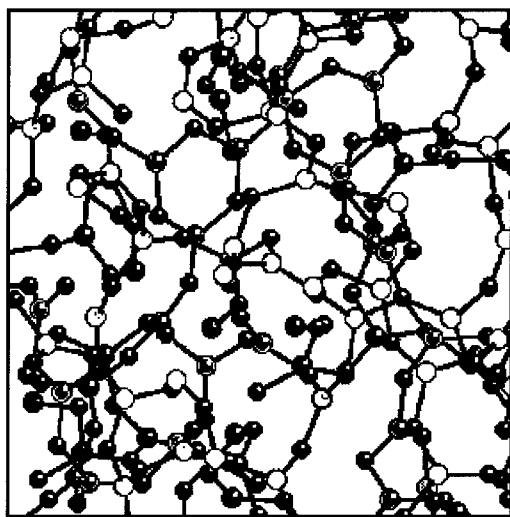


Fig. 1. The typical structure of simulated  $B_2O_3$  glass. The boroxol ring can be found.  
(● = O, ○ = B)

might be correct. In Walrafen's spectroscopy data [27], the integrated intensity of the polarized  $808\text{ cm}^{-1}$  line, ascribed to the boroxol ring breathing mode, decreases with increasing temperature yielding a  $\Delta H$  value of  $5.0\text{ kcal/mol}$ , which has been ascribed to ring rupture [27]. In molecular dynamics, the nominal cooling rate may be too fast compared with that of the real glass. Therefore, the simulated glass may retain a higher temperature structure, and so the fraction of B atoms in boroxol rings could be lower in the MD simulated glass than that estimated from the real glass. Secondly, the parameters for interatomic potential may not be fully optimized and so our simulation could underestimate the number of boroxol rings.

There is, however, an opposite argument, that the enhancement of the  $\text{B}_3\text{O}_6$  breathing mode in the Raman spectrum may be due to a matrix effect and not necessarily to a high fraction of boroxol rings. Elsewhere in these proceedings, there are reports of other simulation studies using different methods. These studies also come to the conclusion that the number of boroxol rings is much lower than previously argued from the earlier data. We remark that  $5\text{ kcal/mol}$  is somewhat on the small side of bond breaking energy values.

#### 4.2. Pair Correlation Function and Coordination Number

The calculated neutron correlation function and coordination number distribution are given in Fig. 2 along with experimental data [8] for comparison. The simulation is folded with correct real space peak function,  $P(r)$ , to provide the peak broadening due to finite measured  $Q_{\text{max}}$ .

The positions of peaks agree with experiment. The first three peaks (B-O, O-O, B-B), which come from the nearest neighbors of each atom, are quite well matched to the experimental data. However, in the intermediate region, there is some discrepancy with the experimental data. The peak at  $2.74\text{ \AA}$  in Fig. 2(b), which comes from the second nearest oxygen neighbors around boron (2-6 in Fig. 3) is a small peak in our calculated PDF for B-O. This may be due to too small number of the boroxol rings in the simulated glass. The coordination number of O around B is 3 and that of B around O is 2, as expected.

#### 4.3. B-O-B and O-B-O Bond Angle Distribution

Figure 4 shows the O-B-O and B-O-B bond angle distribution. These bond angle distributions provide information about how the  $\text{BO}_3$  triangles units are connected. The O-B-O bond angle is distributed around  $120^\circ$ , consistent with boron having three oxygen neighbors, forming a  $\text{BO}_3$  triangles. The B-O-B angle is distributed around  $128^\circ$ , which corresponds to the angle outside the boroxol rings. All of the previous MD simulations, except that of Takada et al. [26], give angles of  $160^\circ$  and fail to reproduce the boroxol ring structure. According to the NMR experiments of Jellison et al. [12], there are two types of oxygen environment in vitreous boron oxide, one of which is ascribed to oxygen atoms in boroxol rings and the other to oxygen atoms outside boroxol rings. Johnson et al. [7] compared their neutron diffraction data with a model

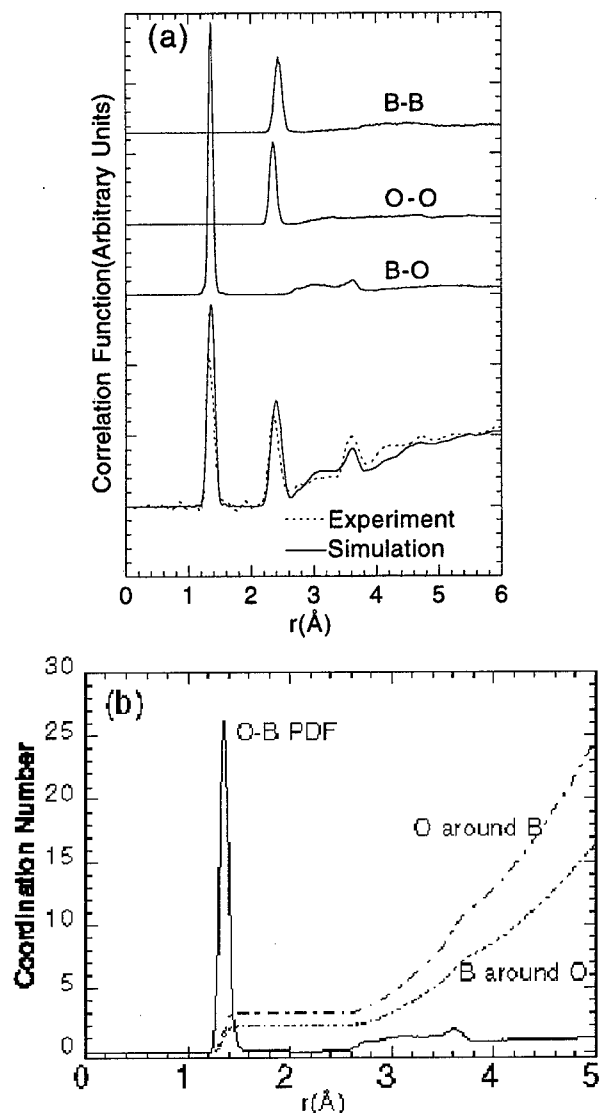
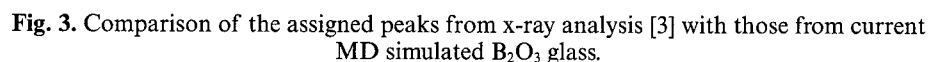


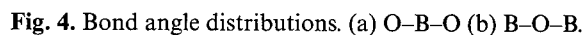
Fig. 2. (a) Calculated neutron correlation function for simulated  $B_2O_3$  glass and (b) coordination numbers of O around B and B around O.

which includes all of the fixed distances occurring in a continuous random network composed of both boroxol groups and  $BO_3$  triangles, together with the first non-bonding B-B distance assuming a bond angle on the bridging oxygen atoms of  $130^\circ$ . This model correctly predicts all of the experimental peaks out to 6 Å. The present simulated glass is also well matched to the experimental data and successfully reproduces the boroxol ring group.



Kind of atoms	Designation on Figure 3	Interatomic distance(Å)	Calculated distance from simulated glass (Å)
B-O	1-2	1.37	1.37
O-O	1-3	2.37	2.37
B-B	2-4,2-5	2.43	2.47
B-O	2-6	2.74	2.72
B-O	2-7	variable	small hump
B-O	2-8	3.63	3.62
O-O	3-8	4.10	4.07
O-O	3-7	variable	4.55
O-O	1-8	4.75	4.62
B-O	4-6	5.25	cannot assign

The key geometrical factor of the boroxol ring is its planarity. The presence of boroxol groups is indicated in Fig. 5(a) with a detailed configuration given in Fig. 5(b). Larger rings, with more than six atoms are also detected. To explain the sharp Raman spectroscopy peak at  $808\text{ cm}^{-1}$ , which is ascribed to the breathing mode of the boroxol ring and mainly involves three oxygen atoms,



— Current simulation; ■■■ Takada et al. [26]; ■■■ Soppe et al. [17]; ■■■ Xu et al. [20]; ■■■ Amini et al. [15]; ■■■ Soules et al. [14].



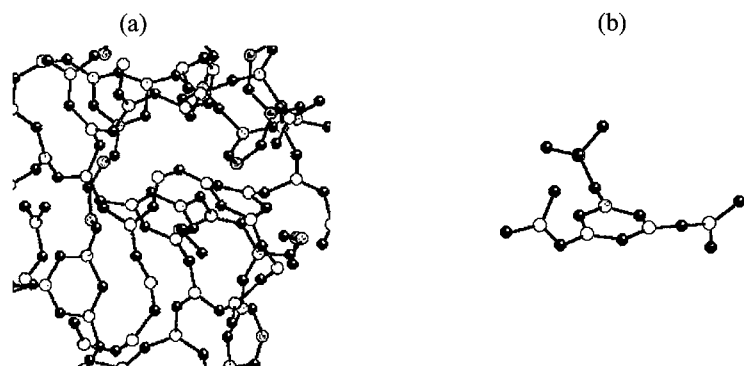


Fig. 5. (a) Boroxol groups in simulated  $B_2O_3$  glass (shaded area denotes 6 membered boroxol ring) and (b) linkage of  $BO_3$  triangles around a boroxol ring.

the boroxol ring should be planar. However, in the instantaneous view from the simulation, the boroxol ring appears not to be perfectly planar (Figs 1 and 5). When the calculated distribution of distances within the boroxol rings is averaged over a number of timesteps and compared with the theoretical distances, assuming a perfectly planar boroxol ring, it is seen that our simulated rings are indeed planar. The results are given in Fig. 6.

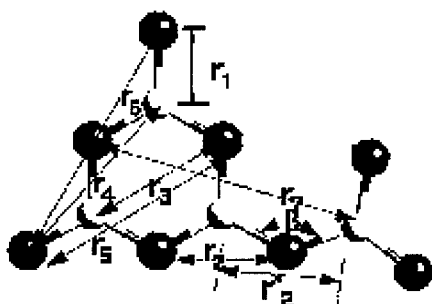


Fig. 6. Comparison with theoretical distance ratio for perfect planar boroxol ring and for simulated glass.

Distance	Type	$r_i/r_1$ theoretical ratio for perfect planar $B_3O_6$	$r_i$ by calculation	$r_i^*$ simulated glass	$\Delta r$ $ r_i - r_i^* $	$\sigma$ standard deviation of $r_i^*$
$r_1$	B-O	1	1.368	1.368	0.000	0.050
$r_2$	B-B	$\sqrt{3}$	2.369	2.367	0.002	0.074
	O-O					
$r_2'$	B-B	$2\sin(b/2)$	2.459	2.383	0.076	0.070
$r_3$	B-O	2	2.736	2.670	0.066	0.146
$r_4$	B-O	$\sqrt{7}$	3.619	3.629	0.010	0.081
$r_5$	O-O	3	4.104	4.040	0.064	0.055
$r_6$	O-O	$2\sqrt{3}$	4.739	4.718	0.021	0.136
$r_7$	B-O	$\sqrt{(10-6\cos\beta)}$	5.062	4.929	0.133	0.206

The difference in the interatomic distance between a perfectly planar ring and those in the simulated glass, is given in column 6. Although this difference increases in the second and third coordination shells, the standard deviation of the distances in the simulated glass is much larger than the actual differences. Therefore, it is concluded that the boroxol ring in the simulated glass is planar and that the deformed boroxol ring in the Fig. 5(b) is due to fact that this is an instantaneous snapshot of the vibrating network.

## 5. SUMMARY

A pure boron oxide glass containing boroxol rings has been successfully generated, using MD simulation, by adopting a coordination dependent potential. The pair distribution functions are well matched to experimental data. The fraction of the boron atoms in boroxol rings in the simulated glass is 13%, which is somewhat lower than experimental results where values up to 80% are claimed.

## REFERENCES

- [1] C. Huang & A.N. Cormack, *J. Chem. Phys.* **93** (1990), 8180.
- [2] C. Huang & A.N. Cormack, *J. Chem. Phys.* **95** (1991), 3634.
- [3] C. Huang & A.N. Cormack, *J. Mater. Chem.* **2** (1992), 281.
- [4] H. Maekawa, Y. Inagaki, S. Shiakawa & T. Yokogawa, *J. Chem. Phys.* **103** (1995), 371.
- [5] B.N. Meera & J. Ramakrishna, *J. Non-Cryst. Solids* **159** (1993), 1.
- [6] R.L. Mozzi & B.E. Warren, *J. Appl. Crystallogr.* **3** (1970), 251.
- [7] P.A.V. Johnson, A.C. Wright & R.N. Sinclair, *J. Non-Cryst. Solids* **50** (1982), 281.
- [8] A.C. Hannon, D.I. Grimley, R.A. Hulme, A.C. Wright & R.N. Sinclair, *J. Non-Cryst. Solids* **177** (1994), 299.
- [9] W.H. Zachariasen, *J. Am. Chem. Soc.* **54** (1932), 3841.
- [10] J. Krogh-Moe, *J. Non-Cryst. Solids* **1** (1969), 269.
- [11] J. Goubeau & H. Keller, *Z. Anorg. Chem.* **272** (1953), 303.
- [12] G.E. Jellison, Jr., L.W. Panek, P.J. Bray & G.B. Rouse, Jr, *J. Chem. Phys.* **66** (1977), 802.
- [13] S.R. Elliot, *Phil. Mag.* **B37** (1978), 435.
- [14] T.F. Soules, *J. Chem. Phys.* **73** (1980), 4032.
- [15] M. Amini, S.K. Mitra & R.W. Hockney, *J. Phys. C: Solid State Phys.* **14** (1981), 3689.
- [16] M.C. Abramo, G. Pizzimenti & G. Carini, *J. Non-Cryst. Solids* **85** (1986), 233.
- [17] W. Soppe, C. van der Marel & H.W. den Hartog, *J. Non-Cryst. Solids* **101** (1988), 101.
- [18] H. Inoue, N. Aoki & I. Yasui, *J. Am. Ceram. Soc.* **70** (1987), 622.
- [19] W. Soppe, C. van der Marel, W.F. van Gunsteren & H.W. den Hartog, *J. Non-Cryst. Solids* **103** (1988), 201.
- [20] Q. Xu, K. Kawamura & T. Tokokawa, *J. Non-Cryst. Solids* **104** (1988), 261.
- [21] W. Soppe & H.W. den Hartog, *J. Non-Cryst. Solids* **108** (1989), 260.
- [22] M.C. Abramo & G. Pizzimenti, *Phil. Mag.* **B64** (1991), 495.
- [23] A.H. Verhoef & H.W. den Hartog, *J. Non-Cryst. Solids* **146** (1992), 267.
- [24] A.H. Verhoef & H.W. den Hartog, *J. Non-Cryst. Solids* **182** (1995), 235.
- [25] A. Takada, C.R.A. Catlow & G.D. Price, *J. Phys: Condens. Matter* **7** (1995), 8659.
- [26] A. Takada, C.R.A. Catlow & G.D. Price, *J. Phys: Condens. Matter* **7** (1995), 8693.
- [27] G.E. Walrafen, M.S. Hokmabadi, P.N. Krishnan, S. Gupta & R.G. Munro, *J. Chem. Phys.* **79** (1983), 3609.
- [28] J. Tersoff, *Phys. Rev.* **B37** (1988), 6991.
- [29] J.R. Walker, In: *Computer Simulation of Solids*, Eds. C.R.A. Catlow and W.C. Mackrodt (Springer-Verlag, Berlin 1982), Chap. 5.

## SURFACE CRYSTALLIZATION OF CsLiB<sub>6</sub>O<sub>10</sub> GLASS

Yong DING, Yoshinari MIURA, Shinji NAKAOKA,  
Tokuro NANBA

*Department of Environmental Chemistry and Materials,  
Okayama University, Okayama-shi 700, Japan*

and

Akiyoshi OSAKA

*Department of Bioengineering Science, Okayama University,  
Okayama-shi 700, Japan*

The surface crystallization of CsLiB<sub>6</sub>O<sub>10</sub> (CLBO) on a glass with the same composition as the crystal was stimulated by ultrasonic surface treatment (UST) with ethanol suspensions containing crystalline CLBO particles and subsequent heat treatment. The effects of UST parameters, including ultrasonic frequency, treating period, suspending medium and concentration of suspended CLBO, were investigated in detail. Glass surfaces doped with CLBO microcrystallites with a narrow size distribution and thin CLBO films on glass were prepared.

### 1. INTRODUCTION

Some of the borate crystals have excellent nonlinear optical properties in the ultraviolet range, such as  $\beta$ -BaB<sub>2</sub>O<sub>4</sub> (BBO) and LiB<sub>3</sub>O<sub>5</sub> (LBO), due to their B<sub>3</sub>O<sub>6</sub> and B<sub>3</sub>O<sub>7</sub> structural groups [1-3]. Recently it was found that CsLiB<sub>6</sub>O<sub>10</sub> (CLBO) crystal which contains the B<sub>3</sub>O<sub>7</sub> structural group could also have a large second-order optical nonlinearity  $d_{36}=0.95$  pm/V and a short absorption edge near 180 nm as well as good phase matching ability in the ultraviolet region [4]. However, it is difficult to grow these borate single crystals, and especially to prepare them in some special forms such as fibers. In contrast, borate glass can easily be prepared in large sizes and various forms. Glasses can easily be formed with the same compositions as LBO and CLBO crystals, and it would thus be worthwhile if the advantages of glass and nonlinear optical crystal could be combined. Recently, we have developed a novel technique for growing various microcrystallites or thin films on glass by controlled surface crystallization of glass. This is realized by an ultrasonic surface treatment (UST) with suspensions for implanting nuclei on glass and subsequent heat treatment [5-7].

A preliminary investigation has been made of the crystallization character of a glass with LBO composition [8]. The glass showed partial crystallization

in limited locations or foamy crystallization. No UST effect has so far been observed on the crystallization of the glass. The conventional crystallization characteristics of a glass of CLBO was similar to that of the glass of LBO. However, it was found that our UST technique is able to stimulate the uniform surface crystallization of CLBO. This paper reports the crystallization characteristics of the glass of CLBO and the effects of various UST parameters. The kinetics of the stimulated surface crystallization are also discussed.

## 2. EXPERIMENTAL PROCEDURES

The glass with CLBO composition was prepared by melting a batch of reagent grade  $\text{Cs}_2\text{CO}_3$ ,  $\text{Li}_2\text{CO}_3$  and  $\text{B}_2\text{O}_3$  in a platinum crucible at 1150°C for about 2 h in an electric furnace and then quenching, followed by annealing at 430°C for 1 h. The samples were mirror-polished with an aqueous suspension of alumina particles ( $\sim 1\ \mu\text{m}$  average diameter) before UST or heat treatment. The UST technique was similar to that reported in Refs [5-7]. During the UST, the samples were placed in a plastic bottle ( $\sim \text{D}40 \times \text{H}100\ (\text{mm}^2)$ ) containing aqueous (distilled  $\text{H}_2\text{O}$ ) or ethanol ( $\sim 95\ \text{wt}\%$  EtOH, composed of  $\sim 5\ \text{wt}\%$   $\text{H}_2\text{O}$ ) suspensions of CLBO crystalline particles ( $\sim 4\ \mu\text{m}$  average diameter). An ultrasonic bath (VS-100III SUNPAR, 100 W, Velvo-Clear Co.) was used with three changeable frequencies, 28, 45, 100 kHz, and the capability to alternate the three frequencies for a predetermined period (1 min was used here) for each frequency. The effect on the surface crystallization of CLBO due to ultrasonic frequency or alternating treatment, UST period and the concentration of CLBO particles in suspension was investigated. Here the CLBO powder was obtained by annealing the glass at 700°C for 1 h and subsequent pulverizing.  $\text{CuK}\alpha$  X-ray diffraction (XRD) confirmed the crystallized phase was only CLBO crystal [9]. After UST, the samples were heat treated at predetermined temperatures for various periods with a heating and cooling rate of 30°C/min.

The crystallized phase was determined by XRD. The microstructure of the crystallized upper surface and cross section (fracture surfaces) were examined under a scanning electron microscope (SEM), from which estimates were made of the particle density and size distribution (maximum diameter) of the surface crystallites and thickness of the crystallized layer.

## 3. RESULTS

### 3.1. Some Physical Properties of the Glass and Crystallization Without UST

The glass transition temperature  $T_g$  and crystallization temperature  $T_x$  were 431°C and 534°C, respectively, due to differential thermal analysis with a heating rate of 10°C/min. The optical absorption edge of the glass was  $\sim 217\ \text{nm}$ , which was 37 nm longer than that reported for CLBO single crystal (180 nm) [4]. The glass has a density of 2.363 g/cm<sup>3</sup>.

The onset temperature of the crystallization of the as-polished glass was at 490°C when 6 h heating was applied. However, the glass showed only partial crystallization in limited locations at this temperature or crystallized into cracked or

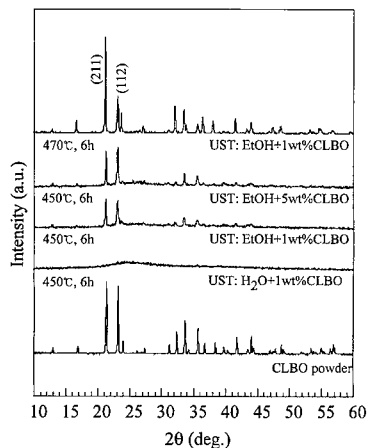


**Fig. 1.** Surface XRD patterns of the samples after UST (28 kHz, 30 min) and heat treatment with the experimental conditions indicated in the figure. The XRD pattern of the CLBO powder is shown as a reference.

foamy states at higher temperature. The crystallized phase was CLBO confirmed by XRD. It is impossible to prepare thin films of CLBO or uniform microcrystallite-doped glass by means of surface crystallization of the as-polished glass.

### 3.2. Effects of UST Parameters on the Stimulated Surface Crystallization of CLBO

**3.2.1. The effect of suspension media** - Figure 1 shows the surface XRD patterns of the samples heated at 450°C for 6 h after UST with an aqueous suspension or an ethanol suspension of CLBO (~1 wt% crystalline powder) for 30 min using an ultrasonic frequency of 28 kHz. No crystallization was detected for the sample after UST with the aqueous suspension. Partial dissolution of the CLBO powder in water was observed. Thus, when an aqueous suspension was used, UST could not seed the CLBO particles on the glass for surface crystallization due to the simultaneous dissolution. Surface crystallization of CLBO was stimulated by UST with the ethanol suspension. No significant preferred orientation was

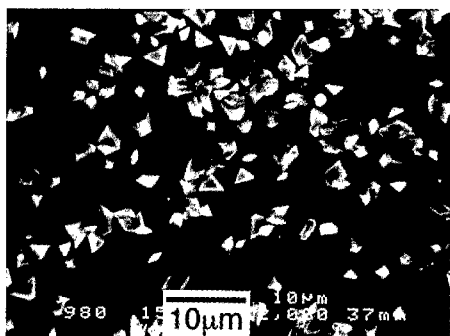


**Fig. 2.** SEM photograph of crystallized surface of the sample heated at 450°C for 6 h after UST: 28 kHz, EtOH + 1 wt% CLBO, 30 min.

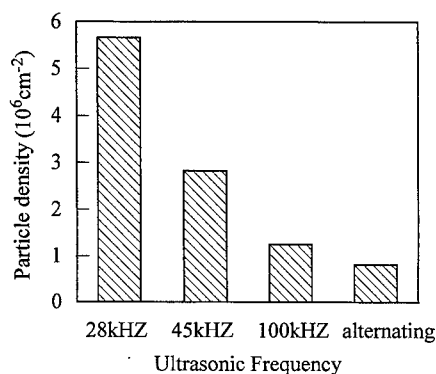


**Fig. 3.** The particle density of the surface crystallites as a function of ultrasonic frequency for the samples heated at  $450^\circ\text{C}$  for 6 h after UST: EtOH+1 wt% CLBO, 30 min.

observed for the surface crystallized CLBO, as shown by a comparison with the XRD pattern from CLBO powder also indicated in Fig. 1 as a reference. The SEM photograph in Fig. 2 of a crystallized surface shows that the surface microcrystallites were randomly or uniformly distributed on the glass surface, with a particle density of  $\sim 5.66 \times 10^6 \text{ cm}^{-2}$ . The size distribution analysis from the SEM photograph indicated that most of the particles were smaller than  $6 \mu\text{m}$  and the sizes were symmetrically distributed with the most probable diameter near  $2\text{--}3 \mu\text{m}$ . The surface CLBO microcrystallites seem to float on the glass, with poor wetting between the crystallites and glass substrate.

**3.2.2. The effect of ultrasonic frequency -** The surface particle density determined by SEM of the microcrystallites on glass as a function of ultrasonic frequency is shown in Fig. 3 for the samples heated at  $450^\circ\text{C}$  for 6 h after UST: EtOH+1 wt% CLBO, 30 min. It is clear that an ultrasonic frequency of 28 kHz gives the highest surface crystallite density among the frequencies indicated

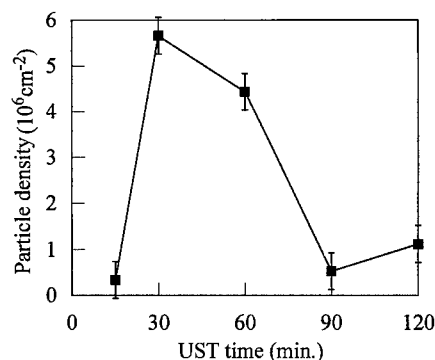


**Fig. 4.** The particle density of surface crystallites as a function of UST period for the samples heated at  $450^\circ\text{C}$  for 6 h after UST: 28 kHz, EtOH+1 wt% CLBO). The lines are drawn as a guide the eye.

in the figure. The result shows that ultrasonic frequency is also a very important parameter for efficiently stimulating the surface crystallization of CLBO.

**3.2.3. The effect of UST period** - The observed surface particle density as a function of UST period was plotted in Fig. 4, where UST: 28 kHz, EtOH+1 wt% CLBO, and heat treatment: 450°C, 6 h, were applied. With increasing UST period, there is an initial increase in surface particle density followed by a decrease for UST periods longer than 60 min. It was found the temperature of the suspension was increased significantly after long UST (~50°C) and some of the CLBO particles in the suspension were dissolved (the transparency of the suspension became higher after longer UST). It is thus expected that there is a competition between ultrasonic seeding and dissolution of CLBO during UST, even when ethanol is used as the medium. Longer UST increased the temperature, which increased the possibility for the dissolution of the seeds on surface.

**3.2.4. The effect of the content of the suspended CLBO particles** - The concentration of CLBO in the suspension is also important for effectively stimulating the surface crystallization of CLBO. CLBO crystalline films were deposited for all of the samples after UST (28 kHz) for 30 min with ethanol suspensions containing 2, 3, 5 or 7 wt% CLBO and heated at 450°C for 6 h. Fig. 5a and 5b are typical SEM photographs for the samples treated with suspensions containing 2 and 5 wt% CLBO, respectively. Their morphologies are different, even though no significant difference was observed for the thickness of the films (~2.7 µm). The surface crystallites became larger and denser in distribution initially with increasing CLBO content, but became smaller and looser after a further increase to 7 wt% CLBO, giving a similar morphology to that in Fig. 5a. Significant precipitation of CLBO on the glass surface after UST was observed when a higher content of CLBO such as 7 wt% was used. The precipitation may hinder the ultrasonic bombardment of the particles in suspension on the glass surface, and reduce the possibility of seeding the glass surface with CLBO fragments for dense surface crystallization. There is no significant preferred orientation for the crystalline films, as indicated in Fig. 1 for the sample after UST with a suspension of 5 wt% CLBO.

### **3.3. Kinetics of the Stimulated Surface Crystallization of CLBO by UST**

According to the above results, UST with ethanol suspensions of CLBO can efficiently stimulate the surface crystallization of CLBO on glass. However, the stimulation is very sensitive to the UST parameters. Here, the kinetics of the stimulated surface crystallization were investigated using samples heated for 6 h at various temperature after the UST: 28 kHz, EtOH+1 or 3 wt% CLBO, 30 min.

**3.3.1. UST with EtOH + 1 wt% CLBO suspensions** - The onset temperature for the stimulated surface crystallization of CLBO was 440°C. Figs. 6a and 6b show typical SEM photographs of the samples heated at 460°C and 470°C, respectively. The SEM analysis shows that the surface-crystallite particle density decreases as

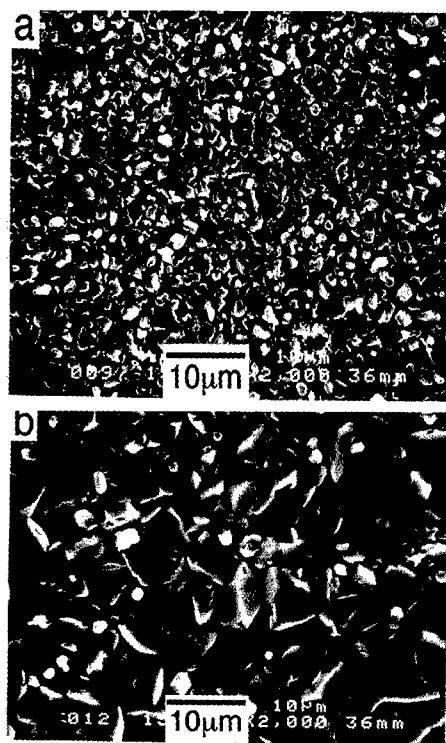


**Fig. 5.** SEM photographs of the crystallized surfaces of the samples heated at 450°C for 6 h after UST (28 kHz, 30 min) with a: EtOH+2 wt% CLBO; b: EtOH+5 wt% CLBO.

the heating temperature increases up to 470°C. What happened in this temperature range was mainly growth along the glass surface and coarsening in the surface layer by integrating a few particles, but not growth into the glass substrate (the depth direction). Due to the coarsening, the sample heated at 470°C gave two kinds of crystallite size distribution ranges (maximum diameter) with most probable sizes near 1~2 µm and 7~8 µm. Above 480°C, the introduced nuclei could grow into the glass substrate and form CLBO films, with a morphology similar to that shown in Fig. 5b. A very weak orientation tendency along the (211) plane of the surface crystallized CLBO was observed for the samples heated at higher temperature, as can be seen in Fig. 1 by comparing the XRD pattern of the sample heated at 470°C with the XRD pattern from CLBO powder.

**3.3.2. UST with EtOH + 3 wt% CLBO suspensions** - CLBO film was not formed for the sample heated at 440°C for 6 h, whilst above this temperature films were precipitated. The relationship between the average thickening rate in 6 h,  $U$  (cm/s), and the heating temperature,  $T$  (in Kelvin), can be described by an Arrhenius equation:  $U = U_0 \exp(-E_D/RT)$ , with an apparent activation energy  $E_D = 444$  kJ/mol. That is to say, the thickness of the surface crystallized CLBO



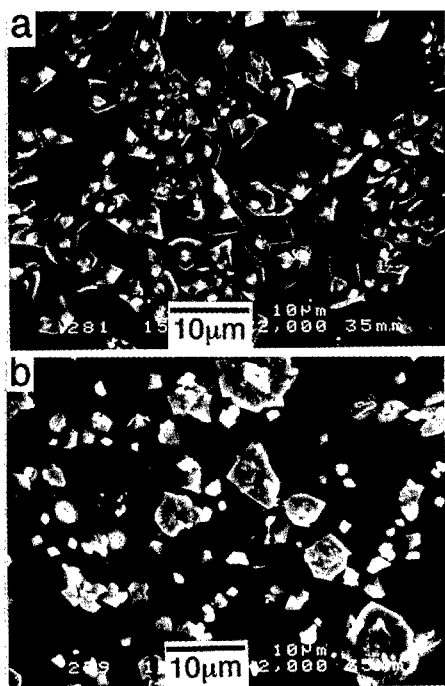


**Fig. 6.** SEM photographs of crystallized surfaces of the samples heated for 6 h at a: 460°C; b: 470°C after UST: 28 kHz, EtOH+1 wt% CLBO, 30 min.

film on the glass can be controlled by heat treatment subsequent to UST with ethanol suspensions containing suitable concentration of CLBO particles.

#### 4. DISCUSSION

The mechanism for the stimulated surface crystallization of CLBO by UST is considered to be as reported previously [5-7], i.e. the ultrasonic bombardment with a suspension of CLBO causes many very fine CLBO fragments to be deposited on the glass surface, and these fine particles act as the nuclei or seeds for epitaxial growth of CLBO. The present study shows that the efficiency for seeding the glass surface strongly depends on the UST parameters, such as the suspending medium, UST period, ultrasonic frequency and the concentration of the suspended CLBO. Since CLBO is hygroscopic [4], the use of water as a suspending solution or the increased suspension temperature after long UST, even with an ethanol suspension (containing ~5 wt% H<sub>2</sub>O), will dissolve the suspended CLBO particles or the seeds on the glass surface significantly, thus reducing the seeding efficiency of UST. On the other hand, there is a competition between the cleaning and seeding by UST. With the changeable frequency of the present ultrasonic cleaning bath [10], a higher ultrasonic frequency is found to give higher efficiency for cleaning, whilst ultrasonic treatment with alternating frequency has the best cleaning effect. As a result, the seeding effect may be reduced when

higher or alternating frequency is used, thus reducing the UST effect on the stimulated surface crystallization. Also, the cleaning effect may be the main factor when low concentrations of CLBO (<2 wt%) in the suspension were used. However, when high concentrations of CLBO (>5 wt%) were used in the suspensions, the precipitation of CLBO particles covered the glass and hindered the ultrasonic bombardment for seeding the glass surface.

The results of the kinetic study of the stimulated surface crystallization of CLBO by UST for the present glass indicate that the nuclei are introduced by UST. If a small amount of nuclei is seeded, the growth at lower temperatures than 480°C was mainly directed along the glass surface and coarsening, not inside the glass substrate. In this way CLBO microcrystallite surface-doped glass with changeable particle size, distribution and density can be prepared. If a large amount of nuclei is seeded, CLBO films are easily prepared with a controllable thickness depending on subsequent heat treatment. Their properties (such as nonlinear optical properties) depend on the texture, and are under investigation.

## 5. CONCLUSIONS

The uniform surface crystallization of CLBO was stimulated by ultrasonic surface treatment (UST) with ethanol suspensions containing CLBO particles and subsequent heat treatment. The selection of the UST parameters is important for effective stimulation of crystallization. Under the experimental conditions in the present research, UST with an ultrasonic frequency of 28 kHz for about 30 min using an ethanol suspension of CLBO particles gave better efficiency. The texture of the crystallized surface can be controlled by the concentration of suspended CLBO and by heat treatment. Glass surfaces doped with CLBO microcrystallites with a narrow size distribution and thin CLBO films on glass were prepared.

## Acknowledgments

This work was supported by the Proposal-Based Advanced Industrial Technology R&D Program awarded by NEDO of Japan, and by the Grant-in-Aid for Scientific Research from the Ministry of Education, Science, Sports and Culture.

## REFERENCES

- [1] C.T. Chen, B.C. Wu, A.D. Jiang & G.M. You, *Sci. Sin. Ser. B (Engl. ed)* **28** (1985), 235.
- [2] D. Eimerl, L. Davis, S. Velsko, E.K. Velsko, E.K. Graham & A. Zalkin, *J. Appl. Phys.* **62** (1987), 1968.
- [3] C.T. Chen, Y.C. Wu, A.D. Jiang, B.C. Wu, G.M. You, R.K. Li & S.J. Lin, *J. Opt. Soc. Am.* **B6** (1989), 616.
- [4] Y. Mori, I. Kuroda, S. Nakajima, T. Sasaki & S. Nakai, *Appl. Phys. Lett.* **67** (1995), 1818.
- [5] Y. Ding, A. Osaka & Y. Miura, *J. Am. Ceram. Soc.* **77** (1994), 749.
- [6] Y. Ding, A. Osaka & Y. Miura, *J. Non-Cryst. Solids* **178** (1994), 103.
- [7] Y. Ding, A. Osaka, Y. Miura, H. Toratani & Y. Matsuoka, *J. Appl. Phys.* **77** (1995), 2208.
- [8] Y. Ding, Y. Miura & A. Osaka, Unpublished results.
- [9] T. Sasaki, Y. Mori, I. Kuroda, S. Nakajima, K. Yamaguchi, S. Watanabe & S. Nakai, *Acta Cryst.* **C51** (1995), 2222.
- [10] *Data of the ultrasonic cleaning bath VS-100III SUNPAR*, Velvo-Clear Co., 1995, (in Japanese).

## MICROSTRUCTURE OF LOW-MELTING $B_2O_3$ -CONTAINING GLASSY COATINGS FOR TRADITIONAL CERAMICS

Stoyan P. DJAMBAZOV, Yordanka Y. IVANOVA,  
Elena P. KASHCHIEVA & Alben P. YOLEVA  
*University of Chemical Technology and Metallurgy,  
Blvd. Kl. Ohridski 8, Sofia-1756, Bulgaria*

Investigations are carried out on multicomponent glassy coatings in the which  $B_2O_3$  and  $Bi_2O_3$  content is varied. The substitution of  $B_2O_3$  for  $Bi_2O_3$  influences the development of different microheterogeneous structures due to liquid phase separation or to increasing tendency for crystallization. It is established that the changes in the microstructure are responsible for the surface properties of the coatings obtained in a narrow temperature range between 500 and 800°C. The coatings, based on  $B_2O_3$ -containing multicomponent glasses, possess good adhesion with the ceramic body and high microhardness for compositions with high  $B_2O_3$  content.

### 1. INTRODUCTION

Multicomponent borate glasses find wide application in contemporary high-temperature technology. One of their applications is the use of  $B_2O_3$  in frits, glasses and coatings for the traditional ceramic industry. These materials use around 11-13% of the total  $B_2O_3$  consumed by the glass industry. The other applications of borate containing glasses are in fibers, heat resisting glasses (Pyrex), sealing, Vycor glass and optical glasses [1]. In the glazes,  $B_2O_3$  reduces the softening and melting temperatures, lower the surface tension and improves their mechanical and thermal properties [2,3]. On the other hand,  $B_2O_3$  influences considerably the aesthetic characteristics of the coating, because of the special optical effects created by its inclusion. In previous investigations, the authors have obtained new multicomponent glassy coatings with non-traditional decorative effects which we found to be connected with the formation of a complex microheterogeneous structure due to the existence of liquid-phase separation and crystallization. It is established that the co-participation of  $TeO_2$  and  $B_2O_3$  leads to a wide liquid-phase separation range and the presence of different microheterogeneous structures [4-8]. New results have been published for the  $B_2O_3$ - $Bi_2O_3$ - $TeO_2$ - $PbO$  system which show that transparent glasses with high refractive index and also opaque glasses and glass-ceramic materials can be obtained [8].

The aim of this study is to follow the change in microstructure as a function of the proportion of  $B_2O_3$  and  $Bi_2O_3$  in multicomponent compositions con-

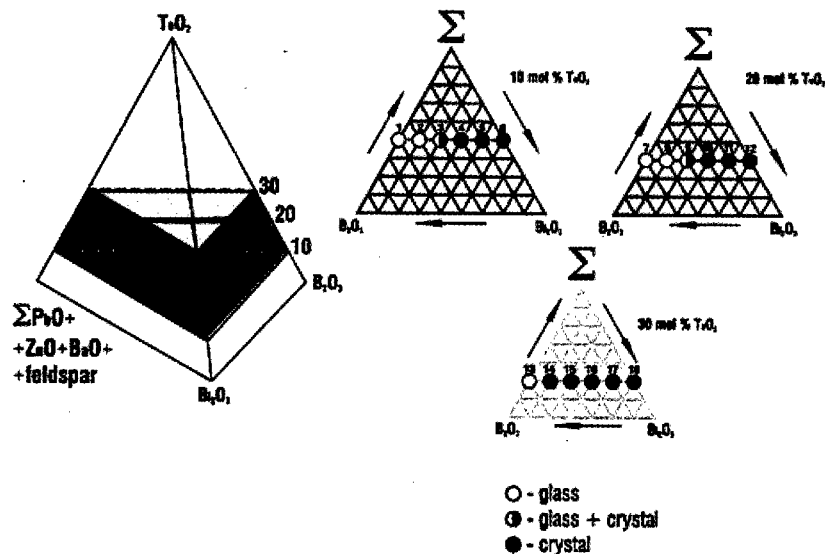


Fig. 1. Spatial presentation of glass compositions and tendency for crystallization after additional thermal treatment at 600°C.

taining  $B_2O_3$ ,  $TeO_2$ ,  $Bi_2O_3$ ,  $SiO_2$ ,  $ZnO$ ,  $BaO$  and  $PbO$  and its influence on the production of new non-traditional decorative effects.

## 2. EXPERIMENTAL

The selection of the glaze components was made according to published data relating to special compositions for frits and glazes [2,3]. The choice of the above combination of non-traditional components- $Bi_2O_3$  and  $TeO_2$ , together with  $B_2O_3$  for the multicomponent compositions results from the conclusions of previous investigations [4-8]. The compositions studied are presented in Fig. 1 in the form of a tetrahedron on the first three vertices which there are  $TeO_2$ ,  $B_2O_3$  and  $Bi_2O_3$ , while the fourth has the other components: feldspar,  $PbO$ ,  $BaO$  and  $ZnO$ . Sections with 10, 20 and 30 mol%  $TeO_2$  are shown, in which the content of  $B_2O_3$  is varied from 0 to 50 mol%. The batches were prepared by mixing elemental  $Te$ ,  $H_3BO_3$ ,  $Bi_2O_3$ ,  $Pb_3O_4$ , feldspar,  $BaCO_3$  and  $ZnO$  in the appropriate amounts 200 g. Batches were homogenized in an rotating mill and melted in a laboratory electric furnace in alumina crucibles at temperatures in the range 1000-1300°C, depending on the composition. The obtained glass-like melts were cooled in water to obtain frits, which were then crushed to grains size 1-1.5 mm and applied to white zirconium glazed tiles. These were subject to thermal treatment in the temperature range 500-800°C for periods of 15 min. to 3 h.

The phases formed, crystallization processes and the microstructure of glassy coatings synthesized were studied by X-ray diffraction (DRON-UN diffractometer,  $Cu K\alpha$  radiation), infrared spectroscopy SPECORD M 80 spectrophotometer, DTA (Hench apparatus) and TEM (Philips 400 electron mi-

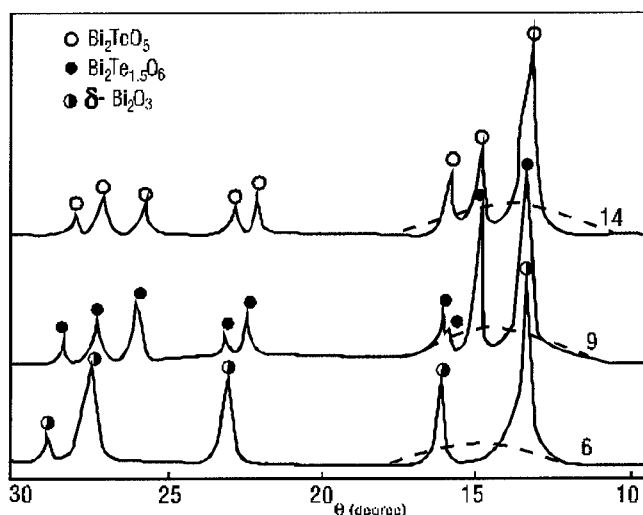


Fig. 2. X-ray diffraction patterns for glass compositions 6, 9 and 14: --- after melting and — after thermal treatment at 600°C for 3 h.

croscope). The Vickers hardness of the glassy coatings was determined using a Nu (Carl Zeiss-Jena) hardness testing microscope with a loading of 30 g for a duration of 30 s.

### 3. RESULTS AND DISCUSSION

All compositions after melting and cooling are amorphous. The colour of the glasses changes depending on the composition, from yellow through yellow-brown to black-brown depending on the degree of oxidation of Te to  $\text{TeO}_2$ . Following additional thermal treatment, samples with a high content of  $\text{B}_2\text{O}_3$

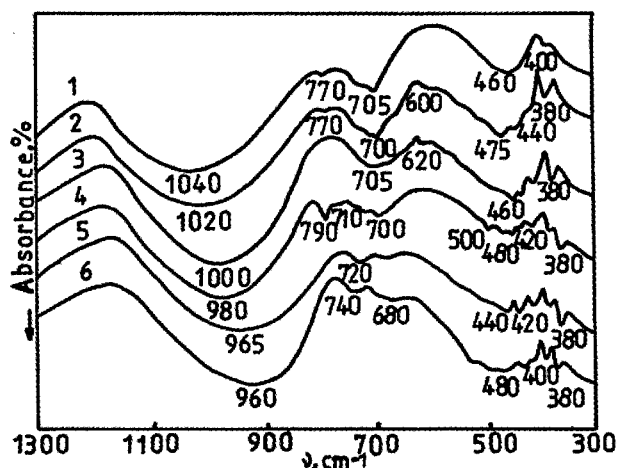


Fig. 3. IR spectrum for glass compositions 1 to 6, in which the  $\text{B}_2\text{O}_3$  and  $\text{Bi}_2\text{O}_3$  contents vary from 0 to 50 mol%.

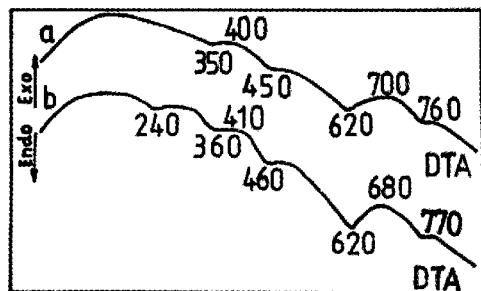


Fig. 4. DTA of composition 3.a, after melting and b, after thermal treatment at 600°C.

are amorphous, while the increasing content of  $\text{Bi}_2\text{O}_3$  stimulates crystallization. The introduction of  $\text{TeO}_2$ , above 30 mol%, also increases the tendency for crystallization (Fig. 1). The main crystalline phases, which appear may be connected with the formation of a solid solution with the common formula  $\text{Bi}_{1-x}\text{Te}_x\text{O}_{(3+x)/2}$  [9]. With increasing  $\text{Bi}_2\text{O}_3$  content the boundary phases,  $\text{Bi}_2\text{TeO}_5$ ,  $\text{Bi}_2\text{Te}_{1.5}\text{O}_6$  and  $\delta\text{-Bi}_2\text{O}_3$  are formed (Fig. 2). A glassy phase also remains at most compositions (the diffraction patterns exhibit a residual amorphous halo) and may include all of  $\text{B}_2\text{O}_3$ . This is confirmed by the IR spectra of the glasses (Fig. 3). The band around  $1040\text{-}1020\text{ cm}^{-1}$  may be interpreted with formation of polymerized  $\text{SiO}_4$  tetrahedra in the network which are depolymerized with increasing  $\text{Bi}_2\text{O}_3$  content, as confirmed by the is shifting of the band to  $960\text{-}940\text{ cm}^{-1}$ . The spectra in Fig. 3 indicate the presence of three-membered borate rings containing a  $\text{BO}_4$  tetrahedron (small peak at about  $770\text{ cm}^{-1}$ ) [10]. According to the DTA curves, the compositions are melting around  $620\text{-}680^\circ\text{C}$  (Fig. 4). The endothermal effect to the non-thermal treated samples is smaller, because the samples do not crystallize during the time of heating. Non-thermal treated samples with high  $\text{B}_2\text{O}_3$  content are amorphous, according to TEM observations (Fig. 5). The electron microscope study of the thermal treated samples confirm X-ray diffraction data. In Fig. 6 is shown the microstructure of composition 3, con-

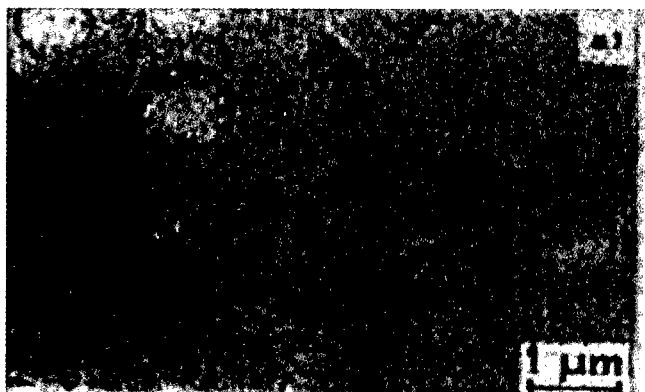


Fig. 5. TEM micrograph of glass 1, containing 50 mol%  $\text{B}_2\text{O}_3$ .



Fig. 6. TEM micrograph of glass 3, containing 30 mol%  $B_2O_3$ , after thermal treatment at 600°C.

taining 30 mol%  $B_2O_3$ , after thermal treatment at 600°C. An amorphous matrix is seen in which separate crystals are formed with size of 1-3  $\mu m$ .

The composition containing only 10 mol%  $B_2O_3$  is crystalline after thermal treatment at 600°C with coarse-grained crystals of size 10-20  $\mu m$  (Fig. 7). X-ray analysis shows that these correspond to the phase  $Bi_2TeO_5$  which is also confirmed by IR spectroscopy (Fig. 8). The IR bands may be assigned to the characteristic frequencies of the building units of the compound  $Bi_2TeO_5$ : 425, 465, 540, 570 and 610  $cm^{-1}$  corresponding to the vibrations of  $BO_n$  polyhedra and 705, 670 and 380  $cm^{-1}$  corresponding to  $TeO_n$  polyhedra [11].

The coatings exhibit high thermal stability and there is no appearance of cracks up to 150°C when performing a standard test. All of the coatings are characterized by very good adhesion to the ceramic body. The compositions with high  $B_2O_3$  content are characterized by good microhardness, which decreases with increasing  $B_2O_3$  content (Fig. 9). The coatings possess Mohs' hardness of 5-6, which is com-



Fig. 7. TEM micrograph of glass 11, containing 10 mol%  $B_2O_3$ , after thermal treatment at 600°C.

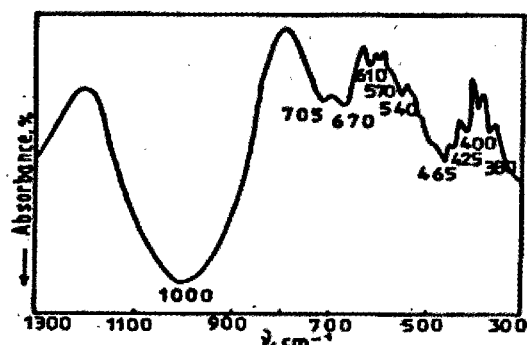


Fig. 8. IR spectrum for glass 11, after thermal treatment at 600°C.

parable to that for other traditional glazes [12]. A low melting  $B_2O_3$ -containing glassy coating of composition 6, obtained at 600°C, is shown in Fig. 10.

#### 4. CONCLUSION

A thermal regime for controlling the microheterogeneous structure of coatings containing crystalline phases and liquid immisibility regions has been developed. It has been established that multicomponent low-melting  $B_2O_3$ -containing compositions, after thermal treatment, are appropriate for applications in the tile industry and lead to non-traditional decorative effects.

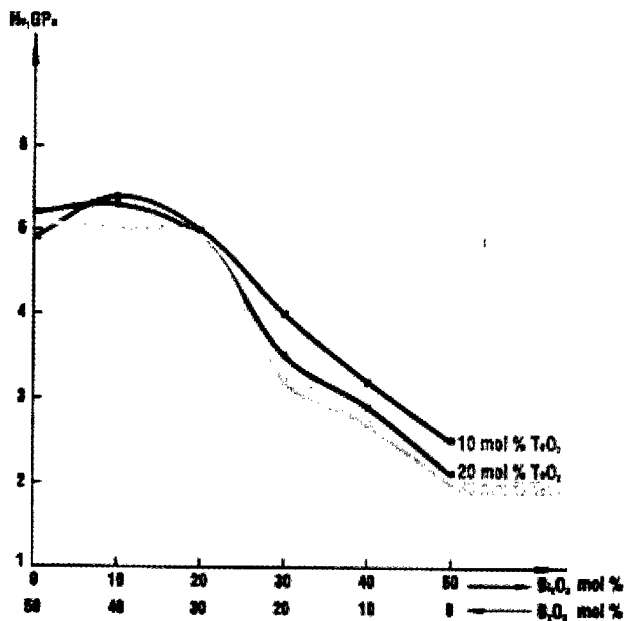


Fig. 9. Variation of the Vickers hardness of the glassy coatings as a function of the  $B_2O_3$  content.





Fig. 10. Photograph of a low melting  $B_2O_3$ -containing glassy coating of composition 6, obtained after thermal treatment at  $600^\circ C$ .

## ACKNOWLEDGEMENTS

This investigation is financially supported by the Bulgarian National Foundation for Science under Contract No. X-308/1993.

## REFERENCES

- [1] R.A. Smith, *J. Non-Cryst. Solids* **84** (1986), 421.
- [2] S. Stefanov & S. Batchvarov, *Smalti Ceramici* (Gruppo Editore Faenza Editrice, 1994).
- [3] N. Tozzi, *Smalti Ceramici Consideration Teoriche e Pratiche* (Gruppo Editore Faenza Editrice, 1992).
- [4] Y.B. Dimitriev & E.P. Kashchieva, *J. Mater. Sci.* **10** (1975) 1419.
- [5] S.P. Djambazov, N. Nedelchev, Y.B. Dimitriev, Y.Y. Ivanova & A.P. Yoleva, In: *Proc. Int. Ceramics Congress*, Istanbul, Turkey, Oct. 24-28, 1994, p. 216.
- [6] S.P. Djambazov, Y.Y. Ivanova, A.P. Yoleva, E.P. Kashchieva, Y.B. Dimitriev & N. Nedelchev In: *Proc. IV World Congress on Ceramic Tile and Quality, Qualicer '96*, Castellon, Spain, March 15-17, 1996, vol. 2, p. 445.
- [7] S.P. Djambazov, Y.B. Dimitriev, E.P. Kashchieva, A.P. Yoleva & N. Nedelchev, In: *XXXV Congreso Anual Sociedad Espanola De Ceramica Y Vidrio*, May, 17-20, Seville, Spain, 1995.
- [8] Y.B. Dimitriev, E.P. Kashchieva & S.P. Djambazov, In: *Proc. 4th European Conf. on Advanced Materials and Processes*, Sept. 25-28, Padua, Italy, 1995, p.613.
- [9] M. Farissi, D. Mercurio & B. Frit, *Mater. Chem. Phys.*, **16** (1987) 144.
- [10] W.L. Koonijnendijk, *Glastechn. Ber.* **48** (1975) 216.
- [11] V. Kucha, V.V. Chomich, V. Kravchenko & P. Perov, *Neorg. Mater.*, **20** (1984) 314.
- [12] A. Moreno, J. Toledo, M. Gazulla & R. Garrote, In: *Proc. IV World Congress on Ceramic Tile and Quality, Qualicer '96*, Marc 15-17, Castellon, Spain, 1996, p.731.

## XAFS STUDIES OF THE LOCAL STRUCTURE OF CaO-K<sub>2</sub>O-B<sub>2</sub>O<sub>3</sub> AND K<sub>2</sub>O-B<sub>2</sub>O<sub>3</sub> GLASSES

Katsumi HANDA

*Department of Physics, Ritsumeikan University,  
1916, Noji-cho, Kusatsu, Siga 525-77, Japan*

Norimasa UMESAKI, Derek A.H.CUNNINGHAM,  
Nagao KAMIJO

*Osaka National Research Institute (ONRI), AIST,  
1-8-31, Midoriga-oka, Ikeda, Osaka 563, Japan*

and

Yasuhiko IWADATE

*Department of Materials Science, Chiba University,  
1-33, Yayo-cho, Inage-ku, Chiba 263, Japan*

We have studied the glass structure of K<sub>2</sub>O-xB<sub>2</sub>O<sub>3</sub> (x=2~5) and CaO-K<sub>2</sub>O-yB<sub>2</sub>O<sub>3</sub> (y=4,6,8,10) glasses by using laboratory XAFS facilities. The average coordination numbers are 6 oxygen atoms around Ca and K, and the mean distances are 2.37~2.45 Å for Ca-O and 2.77~2.83 Å for K-O, respectively. The XAFS results are in good agreement with our MD simulation and X-ray diffraction results.

### 1. INTRODUCTION

The Structures of pure B<sub>2</sub>O<sub>3</sub> and alkali borate glasses have been examined by various investigators from different points of view: Raman scattering [1], X-ray diffraction, Neutron diffraction [2-5] and NMR [6]. However, ternary glass systems containing alkaline earth oxides have been studied to a lesser extent than the binary borate glasses.

X-ray absorption fine structure (XAFS) spectroscopy has been used extensively as an aid to understanding local coordination characteristics [7-9]. In this study, the major purposes are to determine the calcium and potassium coordination environments for K<sub>2</sub>O-B<sub>2</sub>O<sub>3</sub> and CaO-K<sub>2</sub>O-B<sub>2</sub>O<sub>3</sub> glasses, mainly based on experiments on Ca and K K-edges using a laboratory XAFS facility. The Measurements are compared with Molecular Dynamics (MD) simulations and X-ray diffraction results.

## 2. EXPERIMENT

### 2.1 Sample Preparation

Samples were prepared as follows:  $K_2O-xB_2O_3$  ( $x=2\sim5$ ),  $CaO-K_2O-yB_2O_3$  ( $y=4,6,8,10$ ) glasses,  $K_2CO_3$  crystal,  $CaO$  crystal, and Calcium meta-borate ( $Ca(BO_2)_2$ ) crystal. All glass samples of  $K_2O-xB_2O_3$  and  $CaO-K_2O-yB_2O_3$  were prepared from analytical reagent grade powders:  $H_3BO_3$ ,  $K_2CO_3$ ,  $CaCO_3$ . Batches of about 10 g were mixed and then melted at 1273K for  $K_2O-xB_2O_3$ , and 1473K for  $CaO-K_2O-yB_2O_3$ , in Pt crucibles inside an electrical furnace, until the melt was free of  $CO_2$  and  $H_2O$  bubbles. After melting, the liquids were cooled down to room temperature rapidly on a stainless steel plate to obtain the glass samples [10].

The glass powders were obtained by crushing the bulks in a mortar, and were intermingled in thin films of polymethylpentene.

### 2.2 XAFS Measurement

K and Ca  $K$ -edge XAFS spectra of  $CaO-K_2O-B_2O_3$  glasses were obtained with laboratory XAFS facilities, Technos EXAC 800, in transmission mode. This facility consists of a rotating anode X-ray generator having thin Be windows (25 mm), curved-crystal monochromator, Si(Li) solid state detector (SSD) and evacuated path. In the present study, the Mo rotating anode X-ray source was operated at 12.5 kV and 70 mA, and the X-ray source current could be controlled in order to be almost constant in light source emission. A Johantype LiF(200) ( $2d=4.026 \text{ \AA}$ ) monochromator was used, supplied by Quartz and Silice Co., France.

The K and Ca  $K$ -edge absorption spectra of the samples have been collected up to about 500 eV above the absorption edge for extended X-ray absorption fine structure (EXAFS) studies.

The EXAFS data were analyzed using a standard procedure [11]. The threshold energy  $E_0$  was taken as the photon energy at the inflection point of the absorption edge. After the subtraction of a McMaster-type background in the pre-edge region and a polynomial-type baseline in the XAFS region, the EXAFS signal  $k^3\chi(k)$  gives the radial structure function (RSF) in  $R$  space

$$\phi(R_j) = \frac{1}{\sqrt{\pi}} \int_{K_{min}}^{K_{max}} W(k) k^3 \chi(k) e^{-2ikR} dk, \quad (1)$$

where the Hanning window function  $W(k)$  reduces the effect of restricting the Fourier transform within the range of  $k$  ( $k_{min}=2.0 \text{ \AA}^{-1}$  and  $k_{max}=10.0 \text{ \AA}^{-1}$ ). In order to obtain the local structure around potassium and calcium atoms, non-linear least-square fitting, given by

$$\chi(k) = \sum_j N_j F_j(k, \pi) e^{-2\sigma_j^2 k^2} e^{-2r_j/\lambda(k)} \frac{\sin(2kr + \delta(k))}{kr_j^2} \quad (2)$$

was carried out in the filtered  $k$ -space, utilizing the theoretical phase and amplitude functions of Rehr et al. [12]. Here  $r_j$  is the interatomic distance between

the absorber and the  $j$ th neighboring atom,  $N_j$  is the coordination number and  $s_j$  is the Debye-Waller factor resulting from thermal vibration and static disorder. The phaseshift and amplitude parameters for Ca-O and K-O were extracted by best-fitting the EXAFS of reference samples (CaO, Ca(BO<sub>2</sub>)<sub>2</sub>, K<sub>2</sub>CO<sub>3</sub>).

### 2.3 Molecular Dynamics Simulation

The Molecular Dynamics (MD) calculations were performed in a similar way to that described previously by one of the authors [5]. The simulation has been carried out on CaO-K<sub>2</sub>O-4B<sub>2</sub>O<sub>3</sub> and CaO-K<sub>2</sub>O-8B<sub>2</sub>O<sub>3</sub> glasses at room temperature.

The pair potential function is assumed to consist of simplified Coulombic, repulsive and van der Waals attraction terms:

$$U_{ij}(r_{ij}) = \frac{z_i z_j e^2}{r_{ij}} + f_0(b_i + b_j) \exp\left(\frac{a_i + a_j - r_{ij}}{b_i + b_j}\right) - \frac{c_i c_j}{r_{ij}^6}, \quad (3)$$

where  $z_i$  is the formal charge number of ion  $i$ ,  $e$  is the unit charge,  $r_{ij}$  is the distance between ions  $i$  and  $j$ ,  $f_0$  is a force constant arbitrarily taken here to be 1 kcal/molÅ (=6.948×10<sup>-6</sup> dyne) and  $a_i$  and  $b_i$  are the crystal radius and  $c_i$  is compressibility of ion  $i$ . All the parameters are shown in Table 1.

**Table 1**  
Parameters of Interatomic Potential Models.

Ion	w	z	a (Å)	b(Å)	c(kJ <sup>1/2</sup> Å <sup>3</sup> mol <sup>-1/2</sup> )
B	10.81	+3	0.720	0.080	0.0
O	16.00	-2	1.626	0.085	20.0
K	39.10	+1	1.595	0.080	15.0
Ca	40.08	+2	1.414	0.080	10.0

A cubic basic cell was assumed for all the MD simulations. The number of atoms within the basic cell was 750 (B:240, O:420, K:60, Ca:30) for CaO-K<sub>2</sub>O-4B<sub>2</sub>O<sub>3</sub> and 810 (B:288, O:468, K:36, Ca:18) for CaO-K<sub>2</sub>O-8B<sub>2</sub>O<sub>3</sub>. The time increment  $\Delta t$  was chosen as 2.5×10<sup>-15</sup> s, and was sufficiently short to satisfy the conditions of energy conservation. In evaluating the potential energy and force, the Coulombic term was calculated at each time step by application of the Ewald method.

### 3. RESULTS AND DISCUSSION

Figure 1 shows the XAFS spectra at the Ca and K  $K$ -edges for CaO-K<sub>2</sub>O-B<sub>2</sub>O<sub>3</sub> glass system and CaO, Ca(BO<sub>2</sub>)<sub>2</sub> or K<sub>2</sub>CO<sub>3</sub> crystals. These spectra have few distinct EXAFS features because of the random structure of glass similar to that of silicate glass [11]. However, XAFS spectra obtained in this study show enough quality to determine the structure around Ca<sup>2+</sup> and K<sup>+</sup>

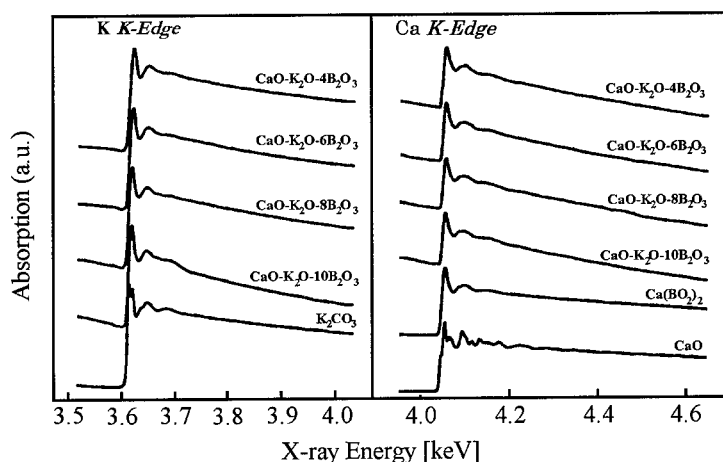


Fig. 1. K and Ca K-edge XAFS spectra of CaO-K<sub>2</sub>O-B<sub>2</sub>O<sub>3</sub> glass systems.

environment.

Figure 2 shows  $k^3\chi(k)$  functions extracted from Ca XAFS spectra and Fig. 3 shows radial structure functions obtained from fourier transformation of Ca  $k^3\chi(k)$ . FEFF is a  $\chi(k)$  simulation program, starting from atomic positions [12,13]. These spectra suggest that the structures around Ca for the CaO-K<sub>2</sub>O-B<sub>2</sub>O<sub>3</sub> glasses are very similar to each other. As shown in Fig. 3, we could not observe a notable feature due to the next nearest-neighbour correlation. This result suggests that Ca<sup>2+</sup> cations are homogeneously distributed in the B-O network. Radial structure functions about K atoms are shown in Fig. 4.

The  $k^3\chi(k)$  spectra and radial structure functions about K for the glasses are also very similar to each other. The results of a curve-fitting analysis are listed

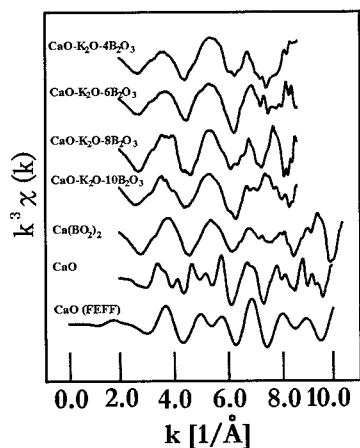


Fig. 2.  $k^3\chi(k)$  spectra about Ca of CaO-K<sub>2</sub>O-B<sub>2</sub>O<sub>3</sub> glass systems.

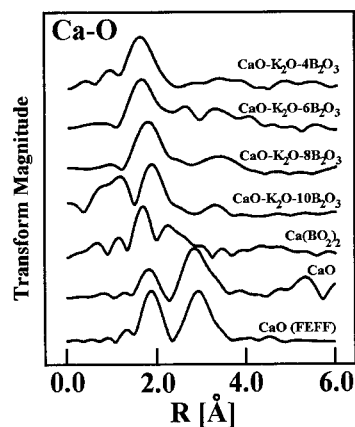


Fig. 3. Radial structure functions about Ca of CaO-K<sub>2</sub>O-B<sub>2</sub>O<sub>3</sub> glass systems.

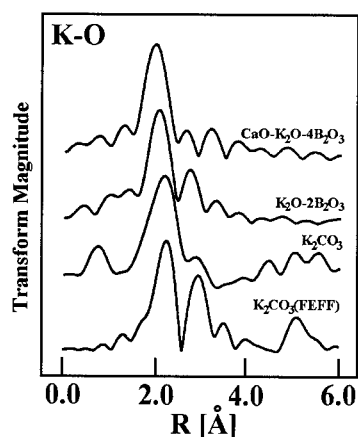


Fig. 4. Radial structure functions about K of CaO-K<sub>2</sub>O-B<sub>2</sub>O<sub>3</sub> glass systems.

in Table 2. Our experimental XAFS results agree approximately with the MD simulations and X-ray diffraction, and the structure of CaO-K<sub>2</sub>O-8B<sub>2</sub>O<sub>3</sub> glass obtained by the simulation is shown in Fig. 5.

Table 2

Structure Parameters for the Short Range Order; Mean Distances,  $r_{ij}$  (Å), Coordination Numbers,  $N_{ij}$  (atoms), and Debye-Waller Factor,  $\sigma_{ij}$  (Å), for CaO-K<sub>2</sub>O-B<sub>2</sub>O<sub>3</sub> Glasses

Glass	$R_{ij}$ (Å)	$N_{ij}$ (atoms)	$\sigma_{ij}$ (Å)	
(CaO-K <sub>2</sub> O-4B <sub>2</sub> O <sub>3</sub> )				
B-O	1.38	3.3	-	MD
O-O	2.38	4.6	-	MD
K-O	2.82	6.6	0.130	XAFS
K-O	2.72	7.0	-	MD
Ca-O	2.37	7.1	0.112	XAFS
Ca-O	2.34	5.8	-	MD
(CaO-K <sub>2</sub> O-6B <sub>2</sub> O <sub>3</sub> )				
B-O	1.37	3.0	0.134	XRD
B-O	1.48	4.0	0.134	XRD
O-O	2.40	4.0	0.148	XRD
K-O	2.83	5.9	0.082	XAFS
Ca-O	2.38	7.3	0.113	XAFS
Ca-O	2.42	-	0.152	XRD
(CaO-K <sub>2</sub> O-8B <sub>2</sub> O <sub>3</sub> )				
B-O	1.38	3.2	-	MD
O-O	2.40	4.5	-	MD
K-O	2.82	5.2	0.171	XAFS
K-O	2.74	6.5	-	MD
Ca-O	2.45	6.5	0.108	XAFS
Ca-O	2.36	6.4	-	MD
(CaO-K <sub>2</sub> O-10B <sub>2</sub> O <sub>3</sub> )				
K-O	2.77	6.0	0.106	XAFS
Ca-O	2.45	5.9	0.071	XAFS

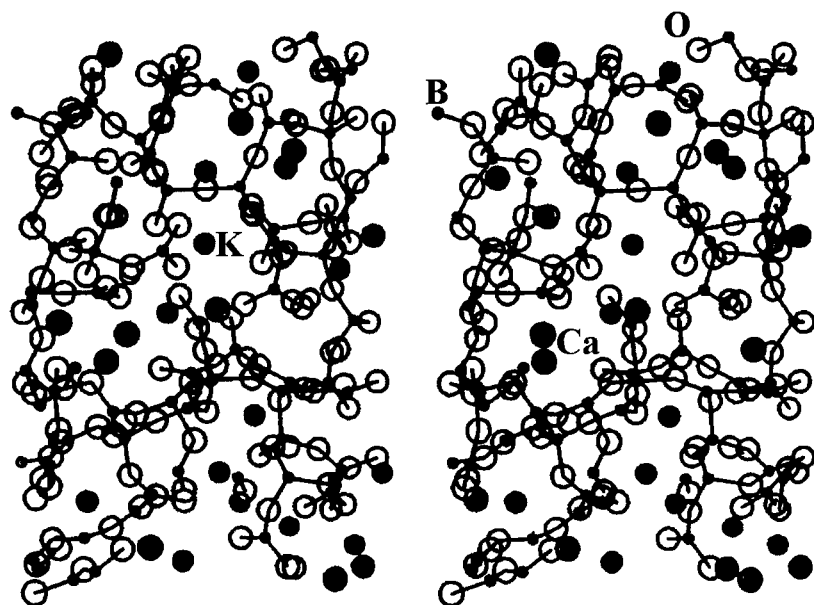


Fig. 5. Structure of  $\text{CaO-K}_2\text{O-8B}_2\text{O}_3$  glass obtained from MD simulation.

#### 4. CONCLUSIONS

We conclude from the experiments described above that the structures around Ca and K for  $\text{CaO-K}_2\text{O-yB}_2\text{O}_3$  glasses are very similar to each other. The mean Ca-O and K-O distances are about  $2.37\sim 2.45$  and  $2.77\sim 2.83$  Å, and the average coordination numbers of oxygens for Ca or K are about 6, respectively. The XAFS results are in good agreement with our MD simulation and X-ray diffraction results.

#### REFERENCES

- [1] B.N. Meera & J. Ramakrishna, *J. Non-Cryst. Solids* **159** (1993), 1.
- [2] G. Paschina, G. Piccaluga & M. Magini, *J. Chem. Phys.* **81** (1984), 6201.
- [3] M.P. Medda, A. Musinu, G. Paschina & G. Piccaluga, *J. Non-Cryst. Solids* **150** (1992), 76.
- [4] Y. Iwadate, K. Igarashi, T. Hattori, S. Nishiyama, K. Fukushima, J. Mochinaga, N. Igawa & H. Ohno, *J. Chem. Phys.* **99** (1993), 6890.
- [5] N. Umesaki, Y. Kita, T. Kirihaara, T. Iida, T. Fukunaga & M. Misawa, *J. Non-Cryst. Solids* **177** (1994), 200.
- [6] P.J. Bray, *J. Non-Cryst. Solids* **95&96** (1987), 45.
- [7] G.N. Greaves, In: *Glass Science and Technology, Vol. 4B*, Eds. D.R. Uhlmann and J. Kreidl (Academic Press, Boston, 1990), Chap. 1.
- [8] G.N. Greaves, *J. Non-Cryst. Solids* **71** (1985), 203.
- [9] D.A. McKeown, G.A. Waychunas & G.E. Brown Jr, *J. Non-Cryst. Solids* **74** (1985), 325.
- [10] W. Soppe, C. van der Marel, W.F. van Gunsteren & H.W. den Hartog, *J. Non-Cryst. Solids* **103** (1988), 201.
- [11] N. Kamijo, K. Handa & N. Umesaki, *Mat. Trans. JIM* **37** (1996), 927.
- [12] J.J. Rehr, J. Mustre de Leon, S.I. Zabinsky & R.C. Albers, *J. Am. Chem. Soc.* **113** (1991), 5136.
- [13] W. Primak, H. Kaufman & R. Ward, *JACSA* **70** (1948), 2043.

## CRYSTALLIZATION BEHAVIOUR OF SOME GLASSES IN THE SYSTEMS $\text{Li}_2\text{O}-\text{B}_2\text{O}_3$ AND $\text{Li}_2\text{O}-\text{B}_2\text{O}_3-\text{Al}_2\text{O}_3$

Farouk A. KHALIFA & Hatem A. EL BATAL  
*Glass Research Department, National Research Centre,  
Dokki, Cairo, Egypt*

Vibrational and crystallization techniques are employed to investigate the structure and sequence of crystallization of glasses in the systems  $\text{Li}_2\text{O}-\text{B}_2\text{O}_3$  and  $\text{Li}_2\text{O}-\text{B}_2\text{O}_3-\text{Al}_2\text{O}_3$ . Infrared spectra have been measured and analyzed in order to elucidate the role of  $\text{Al}_2\text{O}_3$  in such glasses. A correlation between vibrational groups and variation in glass composition is made. X-ray diffraction analysis was done to investigate the crystalline phases formed during thermal treatment conversion of the glasses to their corresponding glass-ceramics.

### 1. INTRODUCTION

The ability to control crystallization allows one to utilise glasses for high technology applications such as advanced ceramics for high temperature aerospace and automotive uses [1], and for optical data storage systems [2,3]. Of particular importance in many applications is the high uniformity of the microstructure of glass ceramics, the absence of porosity and the minor changes in volume during the conversion of glass into ceramic [4].

The key to understanding glass-ceramic formation is the knowledge of the kinetics of crystallization [5]. This type of knowledge will enable the glass scientist to make better glass ceramics, design glasses to meet specific needs, and to make novel glasses. The detailed processes involved in the formation of crystal nuclei and their subsequent growth are not clearly understood, even in the simpler composition. For the simpler composition it is often not clear if the nucleation is truly homogeneous or involves some form of heterogeneous process. It is the objective of this work to investigate the crystallization behaviour of some glasses of the binary  $\text{Li}_2\text{O}-\text{B}_2\text{O}_3$  system and the ternary  $\text{Li}_2\text{O}-\text{B}_2\text{O}_3-\text{Al}_2\text{O}_3$  system, and to reveal the crystal phase formed and the variation of crystallization with glass composition. In the course of this investigation, DTA, vibrational spectroscopy and controlled crystallization techniques are employed to investigate the crystallization behaviour of this glass system and also to find out the role of  $\text{Al}_2\text{O}_3$ .

### 2. EXPERIMENTAL

#### 2.1. Glass Preparation and Infrared Investigation

The binary and ternary glasses investigated (Table 1) were prepared by conventional glass making methods using chemically pure  $\text{Li}_2\text{CO}_3$ ,  $\text{H}_2\text{BO}_3$  and  $\text{Al}_2\text{O}_3$ . The



molten masses were subjected to normal annealing in a muffle furnace set at  $\approx 400^\circ\text{C}$  which was then left to cool to room temperature at a rate of  $30^\circ\text{C/h}$ . Infrared spectrophotometry was carried out on glass powder by the KBr technique using a JASKO (JAPAN) FT/IR-300E recording spectrophotometer in the range  $200\text{--}4000\text{ cm}^{-1}$ . The ratio of the glass powder to KBr in the measured discs was 2:200.

## 2.2. X-ray Investigations

Identification of crystalline phases was carried out by x-ray diffraction using a Philips powder camera (type CPM 9920/05) by examining a fine powder of the glasses before and after thermal treatment and conversion to the corresponding glass-ceramic or crystalline derivatives. Cu  $K\alpha$  radiation was used with a Ni filter.

## 2.3. Differential Thermal Analysis

Finely powdered glass samples were examined up to  $\approx 800^\circ\text{C}$  in a standard Perkin-Elmer 7 series Thermal Analysis System Instrument using powdered alumina as a reference with a heating rate of  $10^\circ\text{C/min}$ . The results are illustrated in Fig. 1. The data from these exothermic peaks were used for further heat-treatment regimes.

## 2.4. Heat Treatment

The main objective in heat treatment is to achieve many nuclei growing to small crystals. It is accepted that the investigated glass system can exhibit internal nucleation without the addition of any nucleating agents. Inspection of Fig. 1 showing the DTA thermogram, led us to thermally heat-treat the glass sample at  $490^\circ\text{C}$  for 2 h followed by raising the temperature to  $700^\circ\text{C}$  and holding the samples for another 2 h after which the muffle furnace was switched off to cool to room temperature at a rate of  $30^\circ\text{C/h}$ . This procedure is believed to give satisfactory glass-ceramic products.

# 3. RESULTS AND DISCUSSION

## 3.1. Infrared Spectra of The Glasses

Figure 2 depicts the infrared spectra of obtained from the  $\text{Li}_2\text{O--B}_2\text{O}_3$  glasses. The spectra of the glasses are generally characterized by the familiar three

Table 1  
Composition of Glasses Studies

Glass No.	Glass Composition (wt %)		
	$\text{Li}_2\text{O}$	$\text{B}_2\text{O}_3$	$\text{Al}_2\text{O}_3$
1	5	95	
2	7.5	92.5	
3	10	90	
4	12.5	87.5	
5	15	85	
6	13	85	2
7	11	85	4
8	9	85	6

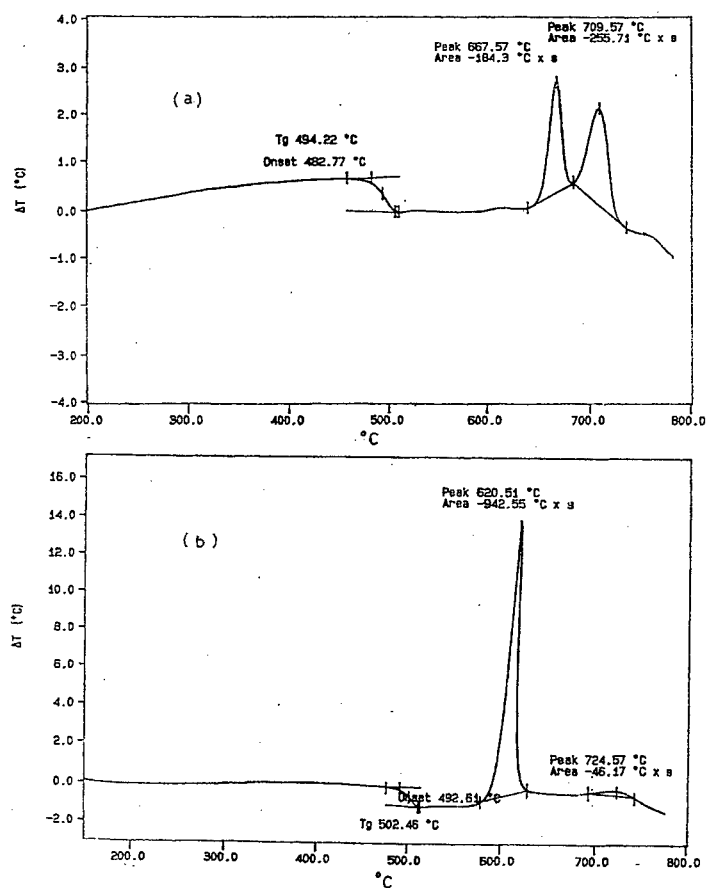


Fig. 1. DTA thermogram of (a) Li<sub>2</sub>O-B<sub>2</sub>O<sub>3</sub> glass, and (b) Li<sub>2</sub>O-B<sub>2</sub>O<sub>3</sub>-Al<sub>2</sub>O<sub>3</sub> glass.

absorption regions observed and distinguished in various publications on borate glasses [6,7]. The first region is extending from 1200 to 1600 cm<sup>-1</sup> (due to B-O stretching of BO<sub>3</sub> units), the second region extends from 800 to 1200 cm<sup>-1</sup> (due to B-O stretching of BO<sub>4</sub> units), the third region lies around 700 cm<sup>-1</sup> (due to bending of B-O-B linkages in the borate network). Also one can observe the far-infrared spectra extending from 200 to approximately 500 cm<sup>-1</sup>. These far infrared bands are assigned to the vibration of metal cations in their oxygen sites [8,9]. The broad composite bands extending from 3200 to 3600 cm<sup>-1</sup> are attributed with hydroxyl or water groups [10,11]. However, Doremus et al [12,13] have divided the broad water bands to:

- (a) Peak at 2700-3000 cm<sup>-1</sup> originating from hydrogen bonding,
- (b) Peak at 3200-3500 cm<sup>-1</sup> originating from molecular water, and
- (c) Peak at 3600-3750 cm<sup>-1</sup> originating from SiOH group.

It is evident from numerous authors [6,14,15] that the alkali oxide/B<sub>2</sub>O<sub>3</sub> ratio is

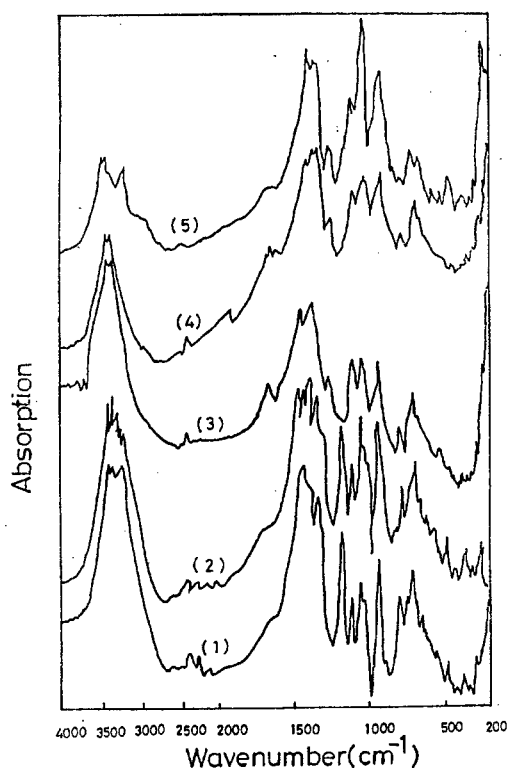


Fig. 2. Infrared spectra of binary  $\text{Li}_2\text{O}-\text{B}_2\text{O}_3$  glasses.

an important determinant of the borate glass structure, since both the relative number of 3- and 4-coordinated borons and the type of groups present in binary borates depend strongly on this ratio. The lithium borate glasses studied were previously assumed to contain tetraborate units, close to their maximum concentration at higher  $\text{Li}_2\text{O}$  content, as well as boroxol and diborate groups [16]. Krogh-Moe and coworkers [6,17] demonstrated that remarkable similarities exist between the spectra of glassy and crystalline borates, and this was taken to indicate the presence of the same type of borate group in the glassy state as in the corresponding crystals.

Figure 2 further illustrates that increasing the  $\text{Li}_2\text{O}$  content causes a growth in intensity in the  $805\text{-}1100\text{ cm}^{-1}$  region and also the far infrared bands become quite identifiable. In addition, changes of the relative intensities of the bands at about  $1250\text{-}1600\text{ cm}^{-1}$  are observed. Figure (2) reveals that the progressive intensity increase of the mid-infrared envelope in the region  $850\text{-}1200\text{ cm}^{-1}$  is accompanied by the simultaneous decrease of the envelope absorption intensity around  $1150\text{-}1600\text{ cm}^{-1}$  with increasing  $\text{Li}_2\text{O}$  content. This behaviour is expected as it indicates the progressive formation of  $\text{BO}_4$  units as it is known that the first region of the spectrum comprises both diborate groups (causing absorption around  $950\text{-}1000$

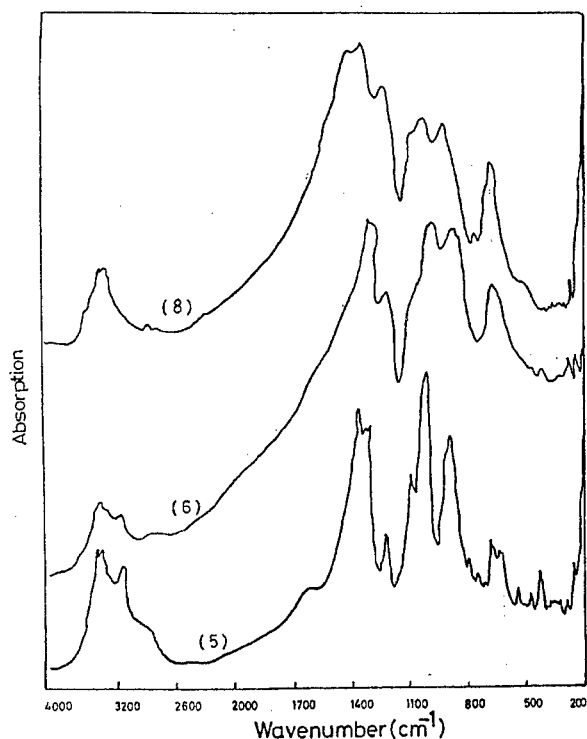


Fig. 3. Infrared spectra of some ternary  $\text{Li}_2\text{O}-\text{B}_2\text{O}_3-\text{Al}_2\text{O}_3$  glasses.

$\text{cm}^{-1}$  and tetraborate (triborate, pentaborate) groups (exhibiting absorption at 880 and  $1050 \text{ cm}^{-1}$ ) [18]. The band at  $\sim 1250 \text{ cm}^{-1}$  is observed in pure  $\text{B}_2\text{O}_3$  glass and still persists even with high alkali content where no boroxol rings are assumed to be present. This indicates that the tetraborate groups should also contribute to this band as well as  $\text{BO}_3$  units [6]. The downshift and decrease in intensity of the band at about  $1400 \text{ cm}^{-1}$ , which is assigned to a ring stretching vibration [18,19], is indicative that the ratio  $\text{B}^{3+}/\text{B}^{4+}$  progressively decreases with alkali content until a certain alkali oxide content is reached. Also the peak at  $1120 \text{ cm}^{-1}$  is assumed [18] to be related to the formation of pyroborate  $(\text{B}_2\text{O}_5)^+$  units.

Although Tarte [20] and Kamitsos et al [18] suspected that  $\text{Li}_2\text{O}$  can act as a network former in certain glass compositions with high  $\text{Li}_2\text{O}$  content, it was found impossible to detect the presence of  $\text{LiO}_4$  tetrahedra from the infrared spectra.

Figure 3 illustrates the infrared spectra of glasses in the system  $\text{Li}_2\text{O}-\text{B}_2\text{O}_3-\text{Al}_2\text{O}_3$ . It is obvious that the progressive introduction of  $\text{Al}_2\text{O}_3$  results in a systematic variation of the infrared spectra revealing broad bands which lose their sharpness especially in the mid region of the spectra studied. The envelope absorption at  $850-1250 \text{ cm}^{-1}$  becomes the second in intensity. The band at about  $700 \text{ cm}^{-1}$  evidently becomes more prominent with  $\text{Al}_2\text{O}_3$  content while the far-infrared at  $450-500 \text{ cm}^{-1}$  is hardly identified. The near-infrared absorp-

tion at  $3200\text{--}3600\text{ cm}^{-1}$  is still retained but with less intensity. The effect of  $\text{Al}_2\text{O}_3$  on the absorption spectra can be explained by considering the role of alumina in glasses.  $\text{Al}_2\text{O}_3$  by itself cannot form a glass. However, it is known that the replacement of a silicon by an aluminium ion in a silicate glass structure allows the network to maintain its stable polymerized 3-dimensional structure while accommodating one singly charged cation [21]. The radius ratio for aluminium and oxygen is 0.43, a value that permits aluminium to assume either a 4- or 6-coordinated state [22]. A single positive charge is required to maintain electrical neutrality each time a  $(\text{AlO}_4)^{5-}$  tetrahedron is formed. In boroaluminate glasses containing alkali or alkaline earth modifier ions,  $\text{B}^{3+}$  and  $\text{Al}^{3+}$  compete for tetrahedral sites, with most going to  $\text{Al}^{3+}$  [23].

Therefore, it is expected that introducing  $\text{Al}_2\text{O}_3$  into the lithium borate glass studied will initiate the presence of  $\text{BO}_3$  groups since  $\text{Al}_2\text{O}_3$  needs the oxygen ions available from  $\text{Li}_2\text{O}$  to share as  $(\text{AlO}_4)^{5-}$  groups in the glass network, with  $\text{Li}^+$  in neighbourhood positions to maintain electrical neutrality. This explains the observed increase of the absorption bands related to  $\text{BO}_3$  units. Also, the observed diminution of the far infrared bands can be related to vibrations of  $\text{Li}^+$  cations due to the tightening of the alkali cations in positions close to the  $(\text{AlO}_4)^{5-}$  groups formed. It appears possible that some of the absorption bands are explained by the presence of mixed B–O–Al bridges or Al–O–Al bridges or the aluminium–oxygen stretching vibration of  $\text{AlO}_4$  tetrahedra. These groupings are responsible for the Raman bands at about 500, 500 and  $710\text{ cm}^{-1}$  as observed by McMillan et al [24,25].

### 3.2. Vibrational Spectra of Crystalline Glass-Ceramics

Figure 4 illustrates the infrared spectra of the fully crystallized glass-ceramic products. It is observed that the mid and far-infrared absorption bands are highly resolved with sharp peaks with increasing  $\text{Al}_2\text{O}_3$  content. The near-infrared bands at  $3200\text{--}3600\text{ cm}^{-1}$  are highly diminished and are replaced by a low-intense extended broad band. The envelope extending from  $1250\text{--}1600\text{ cm}^{-1}$  assumes the high prominent peaks. Also one can observe the reappearance of a near-infrared band at about  $460\text{ cm}^{-1}$ .

Almost all of the same absorption bands were detected in the crystalline glass-ceramic of the previously studied glasses. It is interesting to note that no new bands, other than those attributable to borate species and the possible presence of Al-bearing phases are present. For convenience, the IR assignments have been collected in Table 2.

The reason for the reappearance of the near-infrared bands due to  $\text{Li}^+$  cations at  $\sim 460\text{ cm}^{-1}$  with high-alumina glass-ceramics (Fig. 4) is that it can be assumed that the crystallization process might result in separate crystalline phases including different lithium metaborate polymorphs and possibly other separate Al-containing phases. These Li-containing phases might have the freedom to vibrate independently thus exhibiting the far-infrared band again after crystallization.

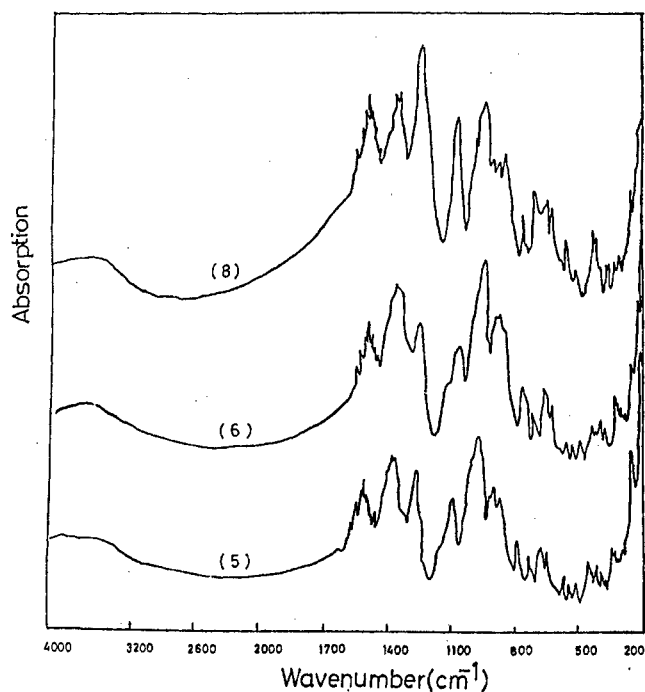


Fig. 4. Infrared spectra of heat treated glass-ceramics of the  $\text{Li}_2\text{O}-\text{B}_2\text{O}_3-\text{Al}_2\text{O}_3$  system.

Tarte [26] believed that the complexity of the structure of lithium aluminate might be due to the possibility of vibrational interaction and the occurrence of both cations (Li and Al) on both types of crystallographic sites (tetrahedral and

**Table 2**  
Assignment of the Infrared Bands Present in the Spectra of  $\text{Li}_2\text{O}-\text{B}_2\text{O}_3-\text{Al}_2\text{O}_3$  Glasses

Peak Position ( $\text{cm}^{-1}$ )	Assignment
1420-1550	$\text{BO}_3$ Stretching
1350-1400	B-O-bonds
1250	B-O vibration of various borate rings
1225-1270	boroxol rings, tri-, tetra- and pentaborate groups
1050	pyro - and orthoborate units
	$\text{BO}_4$ stretching
	tri-, tetra- and pentaborate groups
900-1000	diborate groups
880	tri-, tetra- and pentaborate groups
	B-O-B bending
760-770	oxygen bridges between one tetrahedral and one trigonal boron atom
690-730	oxygen bridges between two trigonal boron atoms

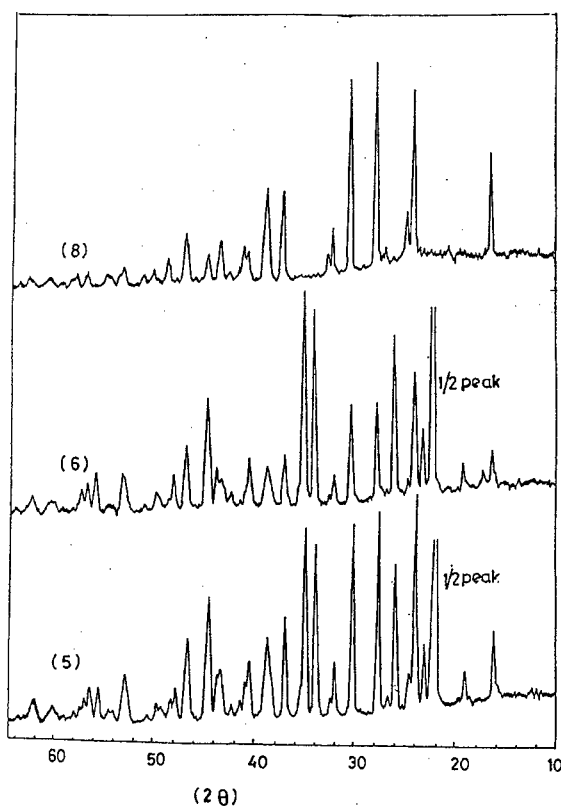


Fig. 4. X-ray diffraction patterns of glass-ceramics of the  $\text{Li}_2\text{O}-\text{B}_2\text{O}_3-\text{Al}_2\text{O}_3$  system.

octahedral). He further added the following assignments for the observed bands:

Position ( $\text{cm}^{-1}$ )	Assignment
396 $\rightarrow$ 496	$\text{AlO}_4$ - $\text{LiO}_4$ lattice mixed frequencies
520, 656 $\rightarrow$ 884	$\text{AlO}_4$ stretching

All previous studies have assumed that aluminium can exist solely as  $\text{AlO}_4$  tetrahedra and  $\text{AlO}_6$  octahedra. However, recent Magic Angle Spinning NMR Studies [27] indicate that 5-fold coordinated aluminium could exist in  $\text{CaO}-\text{B}_2\text{O}_3-\text{Al}_2\text{O}_3$  glasses. Highly polarising cations (e.g. Mg) initiate the presence of  $\text{Al}(5)$  and, in our opinion, further work is needed to include the possibility of the presence of 5-fold coordinated Al and its possible effect on the infrared absorption spectrum.

The infrared absorption spectra of lithium borate glasses appear more complex due to their extensively overlapping bands [28]. Recent Studies [29-31] have shown that some glasses reveal structural characteristics that are very

different from their corresponding crystals. Specifically, the discrepancy of the results obtained from the infrared spectra of lithium borate glasses comes from the presence of lithium metaborate in three possible polymorphs ( $\alpha$ -,  $\beta$ - and  $\gamma$ -LiBO<sub>2</sub>) which undergo isomerization, transformation and bond rearrangements depending on thermal history and the nature of the charge-balancing cation [31,32].

Recent crystallization studies of lithium borate glasses were performed by Aydin et al [33]. Their results indicate that, in the high temperature regime, only the diborate and metaborate phases formed for all isothermal heating times investigated. For the diborate phase, the measured intensity ratio (I) and d values were always found in acceptable agreement with the reported XRD file data for lithium diborate phases. However, the measured d values for the metaborate phase were close to the reported values, but the I ratios varied. It was concluded by the same authors [33] that, when the glasses were heated, crystallites of both metaborate and diborate were observed. The metaborate phase was suggested to nucleate at the air-glass interface away from the container with a possibility that at least a small amount of diborate phase formed first when the glass was heated at high temperature.

Our diffraction studies (Fig. 5) indicate that the main phases in the glass-ceramics studied are tetraborate Li<sub>2</sub>B<sub>8</sub>O<sub>13</sub> (Li<sub>2</sub>O.4B<sub>2</sub>O<sub>3</sub>) card index 16-200, lithium metaborate of two polymorphs card index 20-619 and Li-537 and traces of triborate. Increasing the Al<sub>2</sub>O<sub>3</sub> content, initiates the formation of more of the tetraborate phase.

## CONCLUSIONS

Phases crystallized from Li<sub>2</sub>O.B<sub>2</sub>O<sub>3</sub> and Li<sub>2</sub>O.B<sub>2</sub>O<sub>3</sub>.Al<sub>2</sub>O<sub>3</sub> glass systems are identified by X-ray diffraction and infrared techniques

## REFERENCES

- [1] P.W. McMillan, *Glass-Ceramics* 2nd Edn., Academic Press, London (1979).
- [2] D. Strand, *Opt. Eng.*, **20** (1981), 379.
- [3] S.R. Ovshinsky & P.H. Klose, *J. Non-Cryst. Solids* **8-10** (1972), 892.
- [4] P.F. James, *J. Non-Cryst. Solids* **181** (1995), 1.
- [5] D.R. Uhlmann, *J. Am. Ceram. Soc.* **66** (1983), 95.
- [6] For a review of the absorption spectra of borate glasses, see : J. Krogh-Moe, *Phys. Chem. Glasses* **6** (1965), 46; *J. Non-Cryst. Solids* **1** (1969), 269.
- [7] J. Wong & C.A. Angell, *Glass Structure by Spectroscopy*, (Dekker, New York, 1976).
- [8] G.J. Exarhos & W.M. Risen, Jr., *Chem. Phys. Lett.* **10** (1971), 484.
- [9] B.N. Nelson & G.J. Exarhos, *Chem. Phys.* **71** (1979), 2739.
- [10] R.V. Adams & R.W. Douglas, *J. Soc. Glass Technol.* **43** (1959), 147.
- [11] H. Scholze, *Glass, Nature, Structure and Properties*, (Springer-Verlag, New York, 1991).
- [12] H. Dunker & R.H. Doremus, *J. Non-Cryst. Solids* **92** (1987), 61.
- [13] R.H. Husung & R.H. Doremus, *J. Mater. Res.* **5** (1990), 2209.
- [14] D.L. Griscom, in: *Borate Glass Structure, Properties, Applications*, Eds. L.D. Pye, V.D. Frechette and N.J. Kreidl, (Plenum Press, New York, 1978), 11.
- [15] P.E. Stallworth & P.J. Bray, in: *Glass Science and Technology* Vol 4 B, Eds by D.R. Uhlmann and N.J. Kreidl (Academic Press, San Diego, 1990).



- [16] E. Kamitsos, M.A. Karakassides & G.D. Chryssikos, *J. Phys. Chem.* **90** (1986), 4528.
- [17] L.A. Kristiansen & J. Krogh-Moe, *Phys. Chem. Glasses* **9** (1968), 96.
- [18] E. Kamitsos, M.A. Karakassides & G.D. Chryssikos, *Phys. Chem. Glasses* **28** (1987), 203.
- [19] E. Kamitsos, M.A. Karakassides & G.D. Chryssikos, *J. Phys. Chem.* **91** (1987), 1073
- [20] P. Tarte, *Spectrochim. Acta* **20** (1964), 238.
- [21] W.H. Zachariasen, *J. Am. Chem. Soc.* **54** (1932), 3841.
- [22] J.F. MacDowell, in: *Alumina Chemicals Science and Technol. Handbook*, (The American Ceramic Society, 1990) 365.
- [23] P.J. Bray, *The Structure of Glass* Vol. 7, Ed. E. Porai-Koshits, (Consultants Bureau, New York, 1966).
- [24] P. McMillan, B. Piriou & A. Navrotsky, *Geochim. Cosmochim. Acta* **46** (1982), 2021.
- [25] P. McMillan & B. Piriou, *J. Non-Cryst. Solids* **53** (1982), 277; *Ibid*, **55** (1983), 221.
- [26] P. Tarte, *Spectrochim. Acta* **23A** (1967) 2127.
- [27] B.C. Bunker, R.J. Kirpatrick & R.K. Brow, *J. Am. Ceram. Soc.* **74** (1991), 1425.
- [28] E.I. Kamitsos, A.P. Patsis, M.A. Karakassides & G. D. Chryssikos, *J. Non-Cryst. Solids* **126** (1990), 52.
- [29] P. Tarte, A. Robinson & M. Almou, *Phys. Chem. Glasses* **28** (1987), 136.
- [30] M. Tatsumisago, Y. Komada & M. Minami, *Phys. Chem. Glasses* **29** (1988), 256.
- [31] G.D. Chryssikos, E.I. Kamitsos, A.P. Patsis, M.S. Bitsis & M.A. Karakssides, *J. Non-Cryst. Solids* **126** (1990), 42.
- [32] G.D. Chryssikos, J.A. Kapoutsis, A.P. Patsis & E.I. Kamitsos, *Spectrochim. Acta* **47A** (1994), 1117.
- [33] A. Aydin Goktas, G.F. Neilson & M.C. Weinberg, *J. Mater. Sci.* **27** (1992), 24.

## EFFECT OF $B_2O_3$ ON BORON-CONTAINING METALLIC GLASSES BASED ON COBALT

Mikhail A. KHUSAINOV

*Novgorod State University, Bolshaya St. Peterburgskaya 41,  
Novgorod, 173003, Russia*

and

Adrian C. WRIGHT

*J.J. Thomson Physical Laboratory, University of Reading,  
Whiteknights, Reading, RG6 6AF, UK*

New data are reported on the formation, structure and properties of binary CoB and multicomponent CoFeNiCrMbSiB amorphous alloys. Their structural peculiarities and the problems associated with the melting of the initial cobalt-based alloy ingots in an air atmosphere are discussed. It is pointed out that cobalt metaborate,  $CoB_2O_4$ , and glassy  $B_2O_3$  have an harmful influence on the quality of the rapidly quenched ribbon.

### 1. INTRODUCTION

The distinguishing features of amorphous metallic alloys having a high content of cobalt are almost zero magnetostriction, high magnetic penetrability and low coercive force. As a result, magnetically soft alloys based on cobalt are of great interest for producing transformers of various types [1].

To convert a high cobalt alloy into a glass-like state, it is necessary to make additions in the form of metalloids. One of the most widely used metalloids, added to the metallic base of an alloy, is boron. When the content of boron is between 13 and 25 at.%, there is an anomalous improvement in the mechanical properties and magnetic characteristics of the alloy.

An important method of obtaining glassy alloys (metal glasses) is by rapid melt quenching ( $\geq 10^6$  K/s) on to a rapidly rotating drum (melt spinning). In the course of this process a fine tape (20-25 mm) is formed. The stability of the amorphous structure of the tapes obtained greatly depends on the structural state of the ingots and on the method of production. The most economical method of ingot production is by melting the mixture in the open air. Experiments have shown that, in this case, oxides, such as  $B_2O_3$ ,  $CoB_2O_4$  and  $Co_3O_4$  are sure to appear in the form of crystalline inclusions and coatings. The method of producing  $Co_{1-x}B_x$  metallic glasses and phases of the  $Co_{58}Fe_5Ni_{10}Mo_{20}Si_{13}B_{12}$

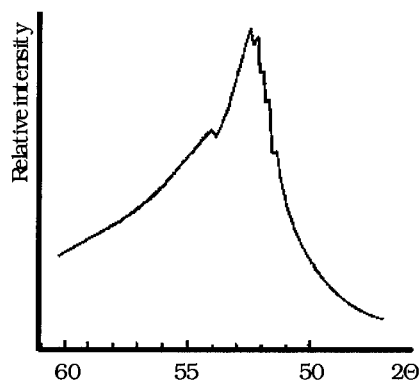


Fig. 1. Diffraction pattern for a rapidly quenched tape of  $\text{Co}_{80}\text{B}_{20}$  alloy ( $\text{Co K}\alpha$  radiation).

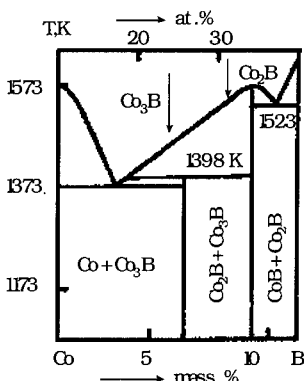


Fig. 2. Phase diagram for the Co-B system.

type is by superheating of the melt up to 400-450 K, holding at this temperature for 5 min, reducing the temperature to the point characterised by a sharp change of the melt viscosity and then finally spinning. Superheating causes the disintegration of crystal-like clusters and a more homogeneous state of the liquid metal. With the usual method of the melt spinning on to a rotating disc (superheating 140-160 K), the tape of  $\text{Co}_{80}\text{B}_{20}$  alloy obtained is characterised by the presence of a micro-crystalline phase, close to cobalt with a face-centered lattice (Fig. 1).

## 2. EXPERIMENTAL RESULTS AND DISCUSSION

Ingots were obtained with three compositions:  $\text{Co}_{84}\text{B}_{16}$  (eutectic composition – cf. Fig. 2),  $\text{Co}_{80}\text{B}_{20}$  and  $\text{Co}_{77}\text{B}_{23}$ . Typical diffraction patterns for  $\text{Co}_{77}\text{B}_{23}$  and  $\text{Co}_{80}\text{B}_{20}$  are given in Figs. 3 and 4. It is clear that the compositions of the melts discussed differ in the type of oxide phases. In the alloy  $\text{Co}_{77}\text{B}_{23}$ , boron oxide,  $\text{B}_2\text{O}_3$ , and  $\text{CoB}_2\text{O}_4$  are macroscopic glass-like inclusions of high hardness ( $H\mu \geq 25000$  MPa) while, in ingots of  $\text{Co}_{83}\text{B}_{17}$  and  $\text{Co}_{80}\text{B}_{20}$ , there appear easily subliming fine oxide coatings of compositions  $\text{B}_7\text{O}$  and  $\text{B}_2\text{O}_3$  (Fig. 4).

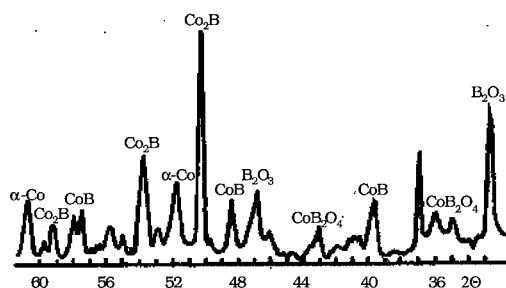


Fig. 3. Diffraction pattern for a  $\text{Co}_{77}\text{B}_{23}$  alloy ingot.

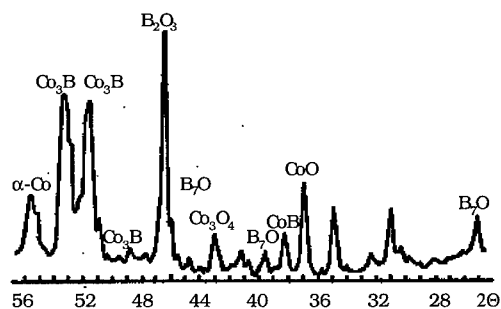


Fig. 4. Diffraction pattern for a  $\text{Co}_{80}\text{B}_{20}$  alloy ingot.

This is why the final tape from these ingots does not contain boron oxide. To all appearances, highly defective crystalline  $\text{B}_2\text{O}_3$  [2] forms a thin coating on the ingot surface. Such conditions are more often realised in an oxygen deficient atmosphere, e.g. in a weak argon/air current.

Attention is drawn to the fact that it was impossible to obtain tapes from the ingots with inclusions of  $\text{B}_2\text{O}_3$  and  $\text{CoB}_2\text{O}_4$ . The reason is believed to be high ingot inhomogeneity, due to the formation of boron oxide particles in the melt. In the case of the replacement of part of the boron atoms by silicon atoms, and of the cobalt atoms by Fe, Ni and Mo atoms, a considerable change in the phase composition of the ingot and the magnetic properties takes place.

In Figs. 5,6 the results of Curie temperature ( $T_c$ ) and differential thermal analysis (DTA) measurements are given for the magnetically soft alloy tapes. It is seen that  $T_c$  for the cobalt-based alloys noticeably increases with increasing boron concentration. The  $\text{Co}_{80}\text{B}_{20}$  alloy has the highest Curie temperature. The crystallisation of the  $\text{Co}_{66}\text{Fe}_5\text{Ni}_4\text{Cr}_{1.5}\text{Mo}_{0.5}\text{Si}_{13}\text{B}_{10}$  alloy, according to the DTA data, has two stages, while for the other alloys (Fig. 6) there is one exothermic minimum marking the beginning of the disintegration of the amorphous struc-

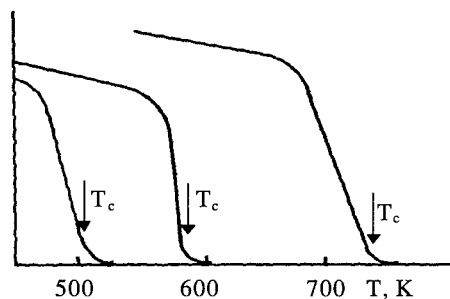


Fig. 5. Dependence of magnetization on temperature for amorphous tapes of the following alloys:

- (1)  $\text{Co}_{66}\text{Fe}_5\text{Ni}_4\text{Cr}_{1.5}\text{Mo}_{0.5}\text{Si}_{13}\text{B}_{10}$ ; (2)  $\text{Co}_{64}\text{Fe}_5\text{Ni}_4\text{Cr}_{1.5}\text{Mo}_{0.5}\text{Si}_{13}\text{B}_{12}$ ; and (3)  $\text{Co}_{80}\text{B}_{20}$ .

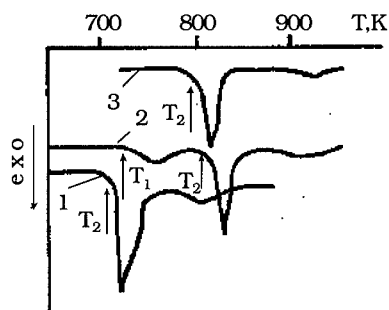


Fig. 6. DTA curves for amorphous tapes of the following alloys:

- (1)  $\text{Co}_{80}\text{B}_{20}$ ; (2)  $\text{Co}_{66}\text{Fe}_5\text{Ni}_4\text{Cr}_{1.5}\text{Mo}_{0.5}\text{Si}_{13}\text{B}_{10}$ ; and (3)  $\text{Co}_{64}\text{Fe}_5\text{Ni}_4\text{Cr}_{1.5}\text{Mo}_{0.5}\text{Si}_{13}\text{B}_{12}$ .

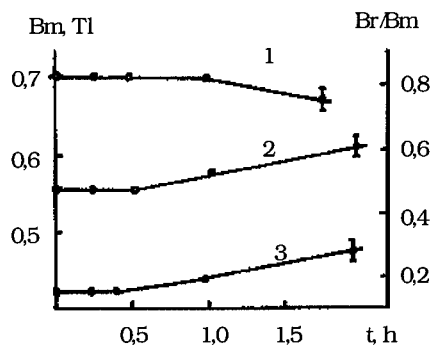


Fig. 7. Characteristics of the hysteresis loop for a rapidly quenched  $\text{Co}_{64}\text{Fe}_5\text{Ni}_4\text{Cr}_{1.5}\text{Mo}_{0.5}\text{Si}_{13}\text{B}_{12}$  alloy as a function of the annealing time,  $t$ , at a temperature of 690 K: (1) maximum induction in a field 2300 A/m; (2) the same in a field 230 A/m; and (3) the ratio  $B_r/B_m$  in a field of 2300 A/m.

ture. X-ray analysis of the phase composition at the temperature  $T_1$  showed the emergence of cobalt crystals having a face-centered cubic lattice, while at  $T_2$  there was also the formation of crystalline phases such as  $\text{Co}_2\text{Si}$  and Co with a hexagonal lattice structure.

The magnetic properties were studied, using samples of the amorphous tapes of dimension  $15 \times 2.5$  mm, in magnetic fields of 230 and 2300 A/m at a frequency of 1400 Hz. The thermomagnetic treatment of the alloys under study took place in a vacuum furnace with a residual pressure of 0.1 kPa. The data

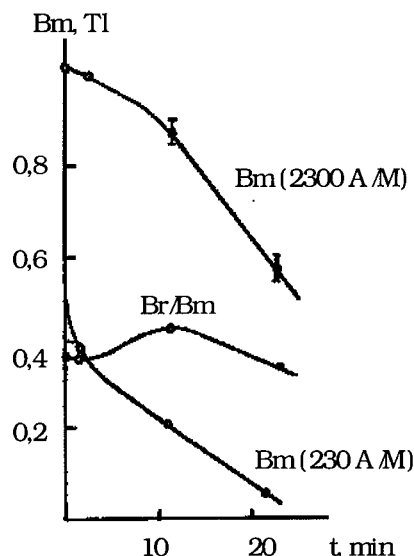


Fig. 8. Magnetic properties for rapidly quenched  $\text{Co}_{66}\text{Fe}_5\text{Ni}_4\text{Cr}_{1.5}\text{Mo}_{0.5}\text{Si}_{13}\text{B}_{10}$  alloy.

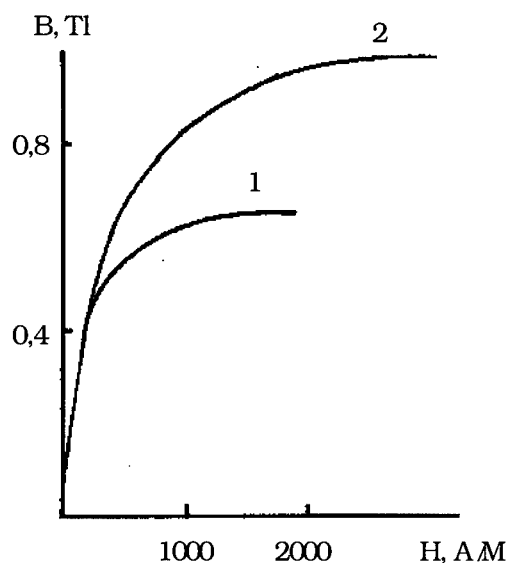


Fig. 9. Magnetization curves for rapidly quenched alloys: (1)  $\text{Co}_{64}\text{Fe}_5\text{Ni}_4\text{Cr}_{1.5}\text{Mo}_{0.5}\text{Si}_{13}\text{B}_{12}$  and (2)  $\text{Co}_{66}\text{Fe}_5\text{Ni}_4\text{Cr}_{1.5}\text{Mo}_{0.5}\text{Si}_{13}\text{B}_{10}$ .

obtained are shown in Figs. 8 and 9.

From the results given, it follows that the alloy  $\text{Co}_{66}\text{Fe}_5\text{Ni}_4\text{Cr}_{1.5}\text{Mo}_{0.5}\text{Si}_{13}\text{B}_{10}$  has a high maximum induction in large fields (2300 A/m). However, while on annealing at the relevant temperature  $B_m$  sharply decreases, the magnetic characteristics of the  $\text{Co}_{64}\text{Fe}_5\text{Ni}_{10}\text{Mo}_2\text{Si}_{13}\text{B}_{12}$  alloy are the most stable. Specifically, the ratio  $B_r/B_m$  for the hysteresis loop in this alloy grows monotonically up to value of 0.6. The maximum induction in a field of 230 A/m also increases compared to the  $\text{Co}_{66}\text{Fe}_5\text{Ni}_4\text{Cr}_{1.5}\text{Mo}_{0.5}\text{Si}_{13}\text{B}_{10}$  alloy (see Figs. 8 and 9).

### 3. CONCLUSIONS

On the basis of the present research, the following conclusions can be drawn:

1. While melting in a highly oxidising atmosphere crystalline phases of  $\text{B}_2\text{O}_3$  and  $\text{CoB}_2\text{O}_4$  appear in  $\text{Co}_{77}\text{B}_{23}$ , reducing the viscosity of the melt. A reduction of the boron content to 17 at.% excludes the formation of  $\text{B}_2\text{O}_3$ , owing to the primary formation of boron oxides such as  $\text{B}_7\text{O}$  which do not prevent the process of melt spinning.
2. It is shown that, at the first stage of the structural relaxation of the amorphous alloy the emergence of a dispersible crystalline phase occurs in the form of cobalt with a face-centered cubic lattice. During the second stage, crystals emerge from the remaining amorphous matrix, which contain metalloids, e.g.  $\text{Co}_2\text{Si}$  and Co having a hexagonal lattice structure.
3. The Curie temperature of the boron-containing alloy ( $\geq 20$  at.%) is high ( $\sim 750$  K), while  $T_c$  for the multicomponent alloys containing boron (10 and

12 at.%) is lower (525 K and 575 K). The temperature for the beginning of the alloy crystallisation,  $T_1$ , is 250 K higher than the Curie temperature. This effect does not occur with the other alloys.

4. The high magnetic induction of the  $\text{Co}_{66}\text{Fe}_5\text{Ni}_4\text{Cr}_{1.5}\text{Mo}_{0.5}\text{Si}_{13}\text{B}_{10}$  rapidly quenched alloy ribbon is characterised by a low stability to thermal annealing. This is shown by a sharp fall of  $B_m$  with increasing annealing time.

## REFERENCES

- [1] Sudzuki, H. Futzimori & K. Hashimoto, *Amorphous Metals*. Tr. (Russian) by E.I. Polyak. ("Metallurgy", Moscow, 1987), P. 328).
- [2] A. Feltz, *Amorphous and Glassy Inorganic Solids*. Tr. (Russian) I.V. Janaev (Moscow, 1986), p 271.

## BIOACTIVITY OF ALKALI AND ALKALINE EARTH BOROSILICATE GLASSES

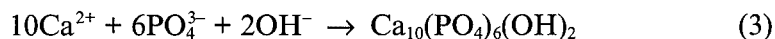
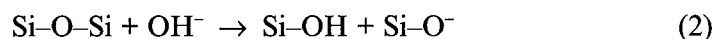
Akiyoshi OSAKA, Satoshi HAYAKAWA, Kanji TSURU  
& Chikara OHTSUKI

*Biomaterials Laboratory, Faculty of Engineering,  
Okayama University, Tsushima, Okayama-shi 700 Japan*

The ability to form apatite was examined under *in vitro* conditions for calcium and sodium borosilicate glasses by the use of a simulated body fluid, Kokubo solution. 50CaO.5B<sub>2</sub>O<sub>3</sub>.45SiO<sub>2</sub> glass was found to be most bioactive, depositing apatite for less than one day soaking in the fluid. This was attributed to the substitution of B–O bonds susceptible to water corrosion for Si–O bonds in 50CaO.50SiO<sub>2</sub> glass. The superior bioactivity of the calcium glasses to the sodium glasses was attributed to the existence of calcium ions in the vicinity of silanol groups in hydrated silica gel formed on the surface in the fluid. From <sup>29</sup>Si MAS NMR analysis the best bioactivity of 30Na<sub>2</sub>O.20B<sub>2</sub>O<sub>3</sub>.50SiO<sub>2</sub> in the sodium glasses examined was attributed to the presence of the largest fraction of Si atoms bonding to two bridging oxygen atoms.

### 1. INTRODUCTION

Bone-bonding ability is characteristic of bioactive glasses and glass ceramics. The first bioactive glass, Bioglass<sup>®</sup>, was announced by Hench *et al.* [1, 2] in the system Na<sub>2</sub>O–CaO–P<sub>2</sub>O<sub>5</sub>–SiO<sub>2</sub> on which an apatite layer was deposited when implanted in a mammal body. Kokubo, Ohtsuki and coworkers pointed out [3, 4] that the ability of apatite layer deposition on the surface was essential for the bone-bonding behavior. They also showed [5] that: (1) the apatite was formed on binary calcium silicate glasses free of phosphorus pentoxide; (2) the hydrated silica gel layer induced apatite nucleation; and (3) the calcium ions released out of the glasses enhanced the degree of supersaturation for apatite. Those surface reactions may be expressed by eqs. (1) through (3).



Recently Ohtsuki *et al.* [6] indicated that as little as 1 or 2 mol% of alumina or titanium oxide added to a binary calcium silicate glass of composition 50CaO.50SiO<sub>2</sub> suppressed the bioactivity of the mother glass. One can account for the results as showing that those oxides prohibit the surface reactions (eqs.



(1) and (2)). Thus, one may consider that if they are the first steps toward the bioactivity, then the introduction of a network former that is susceptible to attack by water molecules leads to better bioactivity. Boron oxide is an important ingredient in glass and may reduce chemical durability depending on the constitution of the glass.

In the present experiment we examined the effect of boron oxide on the ability of apatite formation, i.e. bioactivity, of the glasses in the ternary system  $\text{Na}_2\text{O}-\text{B}_2\text{O}_3-\text{SiO}_2$  and  $\text{CaO}-\text{B}_2\text{O}_3-\text{SiO}_2$ . The difference in bioactivity between those two systems is compared and correlated to the borosilicate network structure.

## 2. EXPERIMENTAL

Glasses in the sodium and calcium borosilicate systems were prepared by the melt-quench process, with batches of the appropriate mixtures of  $\text{Na}_2\text{CO}_3$ ,  $\text{CaCO}_3$ ,  $\text{B}_2\text{O}_3$  and  $\text{SiO}_2$ , by the use of an electric furnace and a platinum crucible. They were annealed for 30 min near  $T_g$  derived from thermal expansion diagrams. A simulated body fluid (Kokubo solution) was prepared as described in the literature [3-6] that with an inorganic ion composition ( $\text{Na}^+$ : 142.0,  $\text{K}^+$ : 5.0,  $\text{Mg}^{2+}$ : 1.5,  $\text{Ca}^{2+}$ : 2.5,  $\text{Cl}^-$ : 147.8,  $\text{HCO}_3^-$ : 4.2,  $\text{HPO}_4^{2-}$ : 1.0,  $\text{SO}_4^{2-}$ : 0.5 (in  $10^{-3}$  mol/l)) similar to that of human blood plasma. The solution was kept at 7.2 in pH with HCl and trishydroxymethylaminomethane. It well reproduces *in vivo* reactions of materials under *in vitro* conditions [7]. Mirror polished glass plates of  $15 \times 10 \times 1 \text{ mm}^3$  in size were soaked in the Kokubo solution at  $36.5^\circ\text{C}$  for up to 30 days. Surface reactions were monitored by thin-film X-ray diffraction (TF-XRD, Cu-K $\alpha$ ), Fourier transform infrared (FT-IR) reflection spectroscopy, and scanning electron micrograph (SEM). The concentration of inorganic ions in the Kokubo solution was measured by inductively coupled plasma spectrophotometry (ICP).  $^{29}\text{Si}$  MAS NMR spectra were measured of a series of glasses  $x\text{Na}_2\text{O} \cdot (50-x)\text{B}_2\text{O}_3 \cdot 50\text{SiO}_2$ ; we employed a JEOL JNM-GX400 FT-NMR spectrometer (9.4 T) with a 6 kHz sample spinning; 5  $\mu\text{s}$  pulses of the resonance frequency 79.3 MHz were irradiated with 2.5 s recycle delays and 17.4  $\mu\text{s}$  dead time. The signals of 360 pulses were accumulated. Polydimethyl silane ( $\delta = -34.0$  ppm against TMS:  $\delta = 0.0$  ppm) was used as the secondary external reference to obtain the  $^{29}\text{Si}$  chemical shifts where  $\delta$  denotes the isotropic chemical shift.

## 3. RESULTS AND DISCUSSION

### 3.1. Bioactivity of Glasses in the System $\text{Na}_2\text{O}-$ and $\text{CaO}-\text{B}_2\text{O}_3-\text{SiO}_2$

Figure 1 shows the TF-XRD patterns of selected glasses in the sodium borosilicate systems after the soaking in the Kokubo solution for various periods. Here, the glass composition is presented in a form like 20Na30B50Si for  $20\text{Na}_2\text{O} \cdot 30\text{B}_2\text{O}_3 \cdot 50\text{SiO}_2$ . The diffraction patterns for a specimen without soaking are denoted as "0d". The diffraction peaks at about  $26^\circ$  and  $32^\circ$  in  $2\theta$  are due respectively to (002) and an envelope of (211), (112) and (300) of apatite (JCPDS 9-432). Introduction of 20 mol%  $\text{B}_2\text{O}_3$  caused the glass most bioactive

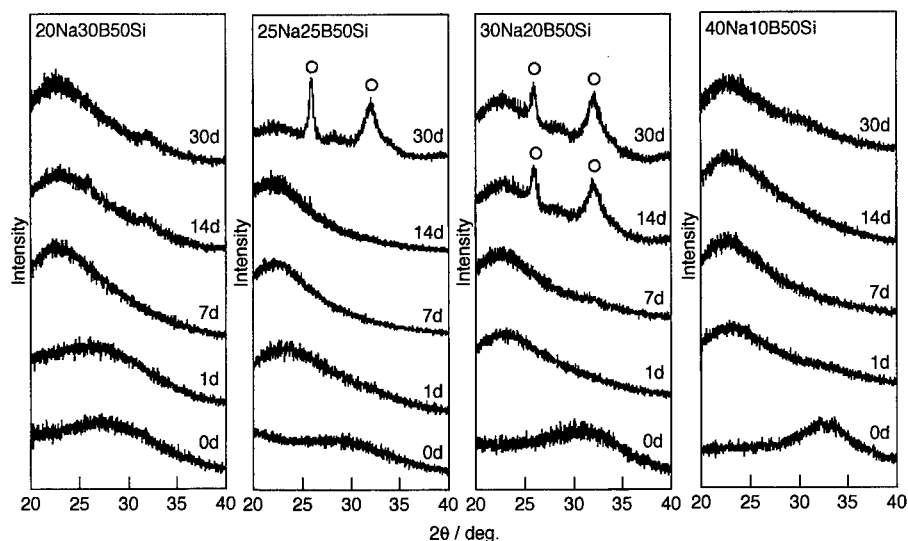


Fig. 1. Thin-film X-ray diffraction patterns of the surfaces of some of the  $\text{Na}_2\text{O}-\text{B}_2\text{O}_3-\text{SiO}_2$  glasses soaked in the Kokubo solution for various periods. O: Apatite

among the series indicated, and apatite was deposited in 14 days of soaking (induction period). 25Na25B50Si glass needed 30 days, and the other two glasses did not deposit apatite in 30 days. Figure 2 shows the FT-IR reflection spectra for the same series of glasses. The  $500\text{ cm}^{-1}$  peak is due to a  $\delta(\text{Si}-\text{O})$  mode,

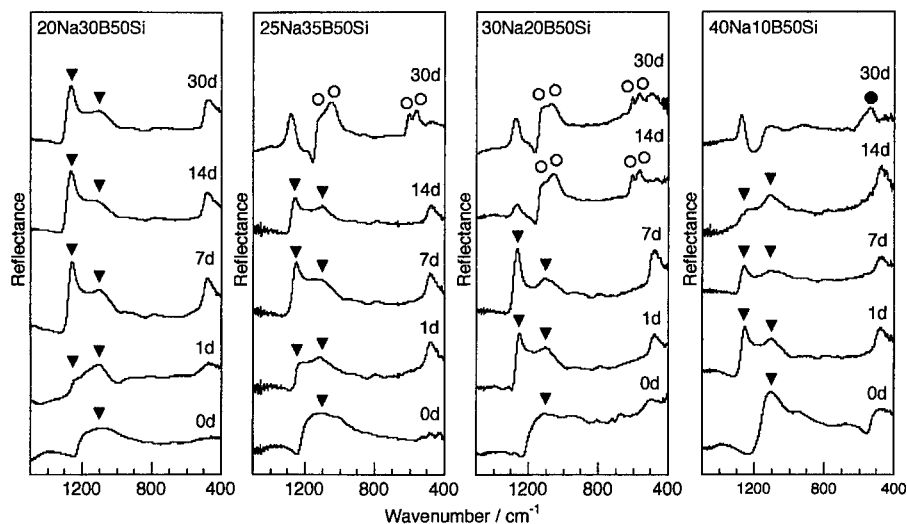
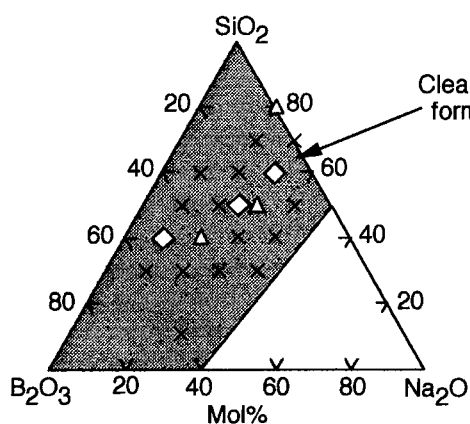
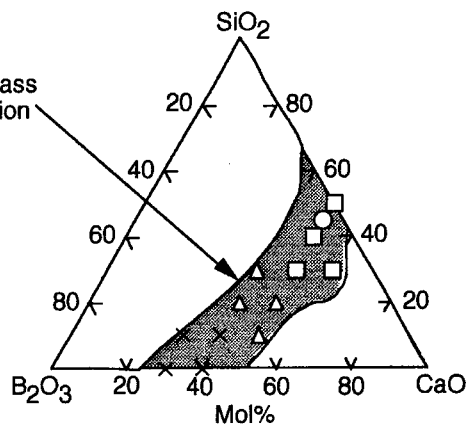


Fig. 2. Fourier transform infrared reflection spectra of the surfaces of some of the  $\text{Na}_2\text{O}-\text{B}_2\text{O}_3-\text{SiO}_2$  glasses soaked in the Kokubo solution for various periods. O: Apatite, ▽: Si-O stretching vibration, ■: P-O bending vibration.



**Fig. 3.** Compositional dependence of apatite formation on the surface of glasses in the system  $\text{Na}_2\text{O}-\text{B}_2\text{O}_3-\text{SiO}_2$  in the Kokubo solution.  
Induction periods ;  $\Delta$ : 14 days,  $\diamond$ : 30 days,  $\times$ : no formation



**Fig. 4.** Compositional dependence of apatite formation on the surface of glasses in the system  $\text{CaO}-\text{B}_2\text{O}_3-\text{SiO}_2$  in the Kokubo solution.  
Induction periods ;  $\circ$ : 6 h,  $\square$ : 1 day,  $\Delta$ : 14 days,  $\times$ : no formation

while those at  $1100$  and  $1250\text{ cm}^{-1}$  are attributed to optical  $\nu(\text{Si}-\text{O})$  modes [2,5,8]. The IR peaks due to P-O appeared at about  $560$  and  $610\text{ cm}^{-1}$  ( $\delta(\text{P}-\text{O})$  modes) and at about  $1060$  and  $1130\text{ cm}^{-1}$  ( $\nu(\text{P}-\text{O})$  modes). The increase in intensities of these peaks corresponds to apatite formation. In the IR spectra for the glasses irrespective of apatite forming ability the  $\nu(\text{Si}-\text{O})$  peak at  $1250\text{ cm}^{-1}$  appeared in 1 day. This is accounted for by formation of a hydrated silica gel layer on the glasses before the apatite formation. It is noted that the silica gel layer formed in 1 day for all the glasses, as found for  $50\text{CaO}.50\text{SiO}_2$  [5,6], but it took a much longer time (longer induction period) for apatite to appear. Similar examinations were carried out for all the glasses prepared and the induction period of the apatite formation is plotted in Fig. 3. Here it was confirmed that only a limited number of glasses were bioactive and the induction period depended on composition.

The calcium borosilicate glasses were different from the sodium borosilicate glasses in bioactivity. The apatite formation ability was examined by the same techniques, and the induction periods are summarized in Fig. 4. It is noted that: (1) most calcium borosilicate glasses were bioactive except those of lesser  $\text{SiO}_2$  content, and (2) they had shorter induction period than the sodium glasses, even shorter ( $\sim 6\text{ h}$ ) for a glass  $50\text{Ca}5\text{B}45\text{Si}$  than that (1 day) for  $50\text{Ca}50\text{Si}$  glass.

### 3.2. The Effects of Calcium Ions Dissolved into the Kokubo Solution

The shorter induction period for  $50\text{Ca}5\text{B}45\text{Si}$  than for  $50\text{Ca}50\text{Si}$  suggests that substitution of water-corrosive B-O bonds for Si-O bonds stimulates the dissolution of glass and release of  $\text{Ca}^{2+}$  ions into the Kokubo solution and hence favours the apatite deposition by increasing the degree of supersatura-

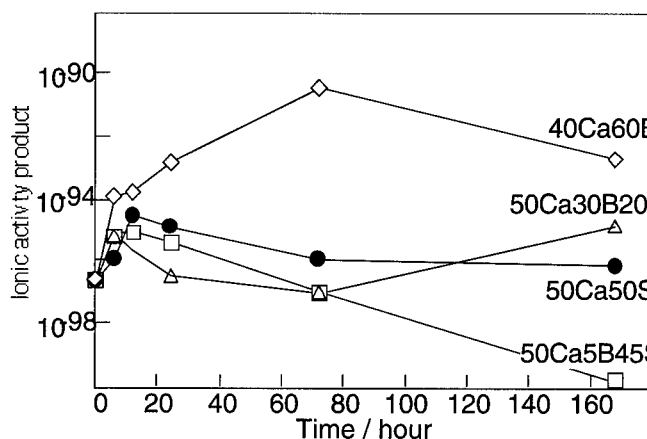


Fig. 5. Changes in ionic activity product of the apatite in the Kokubo solution with immersion of  $\text{CaO-B}_2\text{O}_3\text{-SiO}_2$  glasses.

tion against apatite. The ionic activity product was calculated according to eq. (3) for the Kokubo solution as used to soak a series of calcium borosilicate glasses,  $50\text{CaO} \cdot x\text{B}_2\text{O}_3 \cdot (50-x)\text{SiO}_2$ , and a borate glass  $40\text{CaO} \cdot 60\text{B}_2\text{O}_3$  [5]. It is plotted in Fig. 5 as a function of the soaking period where the glass composition is denoted in the abbreviated form. Since the solubility product of apatite according to eq. (3) is  $5.5 \times 10^{-118}$  for an aqueous solution at  $37^\circ\text{C}$  the Kokubo solution is already under supersaturation [5].  $50\text{Ca}5\text{B}45\text{Si}$  glass has a greater ionic activity product than  $50\text{Ca}50\text{Si}$  when compared at 6 h. The increased reactivity on the glass surface due to the introduction of boron oxide is consistent with the results of Hench & Wilson [9] derived for boron oxide substitution in Bioglass®. The silica free  $40\text{Ca}60\text{B}$  glass showing the greatest product forms no apatite because the glass cannot provide the silica gel layer essential for the apatite nucleation. It follows that boron oxide substitution for silica increases the bioactivity as long as the mother glass contains enough  $\text{SiO}_2$  for the corroded surface to provide the hydrated silica gel required for nucleation. Thus one can interpret the reduced bioactivity of  $50\text{Ca}30\text{B}20\text{Si}$  glass as being due to the reduced nucleation ability of the surface silica gel layer.

### 3.3. The Origin of the Bioactivity of the Sodium borosilicate Glasses

Figure 6 shows the ionic activity product for selected sodium borosilicate glasses,  $x\text{Na}_2\text{O} \cdot (50-x)\text{B}_2\text{O}_3 \cdot 50\text{SiO}_2$  where the glasses are denoted like  $40\text{Na}10\text{B}50\text{Si}$  for  $x=40$ . The increases in ionic activity product with immersion of the sodium glasses reached a similar magnitude as for the calcium glasses. It should be noted, however, that sodium borosilicate glasses required relatively long induction periods for apatite formation. The effect due to the released  $\text{Ca}^{2+}$  ions does not occur in the sodium borosilicate glasses and therefore, it is considered that the superior ability of apatite formation of the calcium borosilicate glasses is attributable to the existence of calcium ions in the vicinity of silanol

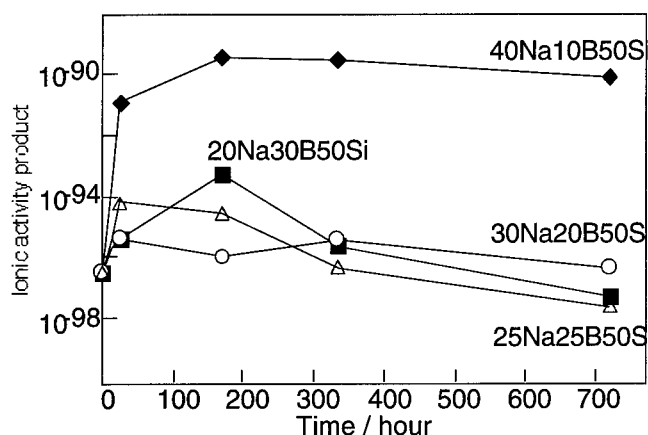


Fig. 6. Changes in ionic activity product of the apatite in the Kokubo solution with immersion of  $\text{Na}_2\text{O}-\text{B}_2\text{O}_3-\text{SiO}_2$  glasses.

groups in the hydrated silica gel formed on the surface in the fluid.

It is also apparent from Fig. 6 that the ionic activity product is very similar among the glasses with  $x=20, 25$  and  $30$ , but that for  $x=40$  is quite different to the others. Nevertheless, we have found in Figs. 1 and 2, a greater difference in their bioactivity, i.e. apatite formation ability;  $30\text{Na}20\text{B}50\text{Si}$  was most bioactive followed by  $25\text{Na}25\text{B}50\text{Si}$ , whilst the others were barren within 30 days. The ionic activity product of the sodium borosilicate glasses shows an inverse in degree of supersaturation with respect to apatite due to inversed pH caused by surface dissolution after the immersion of the glasses. However, this inverse in ionic activity product does not seem to influence the difference in the induction periods for apatite formation. Thus the difference in bioactivity among the sodium glasses should be attributed to their composition: if the network of a glass favours the production of a hydrated silica gel layer appropriate for apatite nucleation then the glass exhibits superior bioactivity. Since  $50\text{Ca}50\text{Si}$  glass and Bioglass<sup>®</sup> which contains about 50 mol% silica are typical glasses exhibiting the best bioactivity one may suppose that the metasilicate type network is appropriate for producing the hydrated silica gel layer which has apatite nucleating ability. The chemical states of  $\text{SiO}_4$  tetrahedra have thus been examined by the  $^{29}\text{Si}$  MAS NMR technique for the glasses of compositions  $x\text{Na}_2\text{O} \cdot (50-x)\text{B}_2\text{O}_3 \cdot 50\text{SiO}_2$ . Let  $Q^n$  denote an Si atom with  $n$  bridging oxygen neighbours; a metasilicate unit has two bridging oxygen atoms and is denoted as a  $Q^2$  group. The  $^{29}\text{Si}$  MAS NMR spectrum of each glass shows an asymmetric peak whose position shifts toward more positive  $\delta$  (a high frequency or low field shift) with increase in  $x$  (sodium oxide content). Each peak is deconvoluted into two components. The component peaks are located at the isotropic chemical shift  $\delta \approx -105, -94, -85$ , and  $-75$  in ppm. Each of them can be assigned to  $Q^4, Q^3, Q^2$ , and  $Q^1$ , respectively, after Maekawa *et al.* [10] who assigned the signals with  $\delta = -105.1 \sim -96.0$  ppm to  $Q^4$ ,  $\delta = -94.3 \sim -85$  ppm to

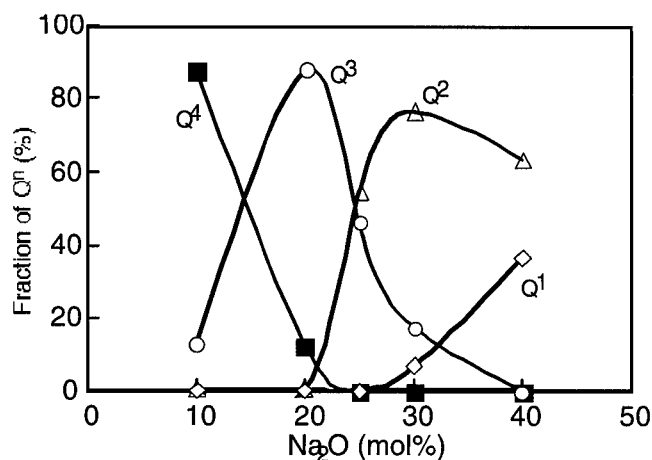


Fig. 7. NMR determined fractions of  $Q^n$  for glasses in the system  $x\text{Na}_2\text{O}-(50-x)\text{B}_2\text{O}_3-50\text{SiO}_2$ .

$Q^3$ ,  $-82.9 \sim -75.5$  ppm to  $Q^2$ , and  $> -75$  ppm to  $Q^1$ . We have then assumed the area of the component peaks is proportional to the fraction of each  $Q^n$  unit, and have evaluated the fractions to plot in Fig. 7 as a function of the  $\text{Na}_2\text{O}$  content. The fraction of  $Q^2$  shows a sudden increase at 25 mol% and reaches a maximum at 30 mol%. The change in  $Q^2$  is in good agreement with the change in bioactivity of the series of sodium borosilicate glasses described above. The fact that 40Na10B50Si is barren though rich in  $Q^2$  is interpreted by the greater fraction of  $Q^1$  which favours vigorous corrosion indicated by the largest ionic activity product in Fig. 6.

#### 4. CONCLUSIONS

The ability to form apatite was examined under *in vitro* conditions for calcium and sodium borosilicate glasses by the use of a simulated body fluid, Kokubo solution, that was kept at  $36.5^\circ\text{C}$  and 7.2 in pH. Almost all the calcium borosilicate in the vitrifying range deposited apatite on the surface though the period of soaking leading to the deposition changed from less than one day for  $50\text{CaO}.5\text{B}_2\text{O}_3.45\text{SiO}_2$  glass, one day for  $\text{B}_2\text{O}_3$  free  $50\text{CaO}.50\text{SiO}_2$ , to 7 days for  $50\text{CaO}.30\text{B}_2\text{O}_3.20\text{SiO}_2$ . From the ionic activity product for apatite precipitation (eq. (3)), the better apatite forming ability achieved by substitution of appropriate amounts of  $\text{B}_2\text{O}_3$  for  $\text{SiO}_2$  was attributed to a greater susceptibility of B-O bonds to water corrosion. However, the bioactive sodium borosilicate glasses required a longer period of soaking in the Kokubo solution for apatite formation to occur. The superior bioactivity of the calcium glasses compared to the sodium glasses was attributed to the existence of calcium ions in the vicinity of silanol groups in the hydrated silica gel formed on the glass surface in the fluid.  $^{29}\text{Si}$  MAS NMR analysis indicated that the best sodium glass bioactivity for  $30\text{Na}_2\text{O}.20\text{B}_2\text{O}_3.50\text{SiO}_2$  resulted from the largest fraction of Si atoms bonding to two bridging oxygen atoms.

### Acknowledgments

Financial support by the Asahi Foundation (1995) to C.O. is gratefully acknowledged. The authors are indebted to Professors T. Kokubo and T. Yoko at Kyoto University for kindly arranging the use of ICP, TF-XRD and NMR facilities

### REFERENCES

- [1] L.L. Hench, R. J. Splinter, W. C. Allen & T. K. Greenlee, Jr., *J. Biomed. Mater. Res. Symp.* **2** (1972), 117.
- [2] L.L. Hench, *J. Am. Ceram. Soc.* **74** (1991), 1487.
- [3] T. Kokubo, *J. Ceram. Soc. Japan* **99** (1991), 965.
- [4] C. Ohtsuki, H. Kushitani, T. Kokubo, S. Kotani & T. Yamamuro, *J. Biomed. Mat. Res.* **25** (1991), 191.
- [5] C. Ohtsuki, T. Kokubo & T. Yamamuro, *J. Non-Cryst. Solids* **143** (1992), 84.
- [6] C. Ohtsuki, A. Osaka & T. Kokubo, In: *Bioceramics*, Vol. 7, Eds. O.H. Andersson and A. Yli-Urpo (Butterworth-Heinemann, Oxford, 1994), pp. 73-78.
- [7] T. Kokubo, H. Kushitani, S. Sakka, T. Kitsugi & T. Yamamuro, *J. Biomed. Mater. Res.* **24** (1990), 721.
- [8] R. M. Almeida, T. A. Guiton & C. G. Pantano, *J. Non-Cryst. Solids* **119** (1990), 238.
- [9] L. L. Hench & J. Wilson, *Science* **226** (1984), 630.
- [10] H. Maekawa, T. Maekawa, K. Kawamura & T. Yokokawa, *J. Non-Cryst. Solids* **127** (1991), 53.

# A COMPARISON OF THE DENSITIES OF LITHIUM AND SODIUM BORATE AND SILICATE GLASSES WITH VERY HIGH ALKALI CONTENTS

Paul VENHUIZEN, A. Michael PETERS,  
Faisal ALAMGIR, Kong LOH,  
Richard B. WILLIAMS & Steven A. FELLER  
*Physics Department, Coe College,  
Cedar Rapids, IA 52402 USA*

The densities of alkali borate and alkali silicate glasses as a function of composition show similar trends. The origins of the respective density trends are distinct in each family. In the alkali borates the density changes are initially controlled by the fraction of fourfold coordinated borons. This structural unit is extremely dense in comparison with the trigonal boron groups. In the alkali silicates the density is a strong function of the numbers of non-bridging oxygens on the silica tetrahedra. A useful way to plot the borate data is to compare the volume per mole  $B_2O_3$  with the ratio of alkali to boron, denoted as  $R$ . In both lithium and sodium borates this volume initially decreases due to the coordination change of boron. At higher alkali concentrations non-bridging oxygens are formed on trigonal borons at the expense of tetrahedral borons and the modified molar volume increases linearly. In silicate glasses the volume per mole  $SiO_2$  increases with an increasing ratio of alkali oxide to silica,  $J$ . As  $J$  is increased, in either the lithium or sodium case, the modified molar volume increases linearly. This is indicative of the conversion of bridging oxygens into non-bridging oxygens through the addition of alkali oxide.

## 1. INTRODUCTION

Density has been shown to be a sensitive parameter to structural changes occurring in various glass systems and including, specifically, the alkali borates and silicates [1-4]. For example, in the lithium borates it is possible to follow the well-known coordination change as trigonal borons are transformed into tetrahedra [1]. In this paper comparison of the densities of lithium and sodium borates and silicates over an extraordinarily wide range of alkali concentrations are reported. It will be shown that the microscopic origin of the density trends are different in the borates and silicates.

## 2. EXPERIMENTAL PROCEDURES

### 2.1 Glassmaking

Glass batches were prepared from reagent grade or better silica, boric acid, and alkali carbonates or alkali oxides. The glasses were made either in plati-



num or vitreous carbon crucibles (for glasses prepared from alkali oxides). The glasses displayed increasing hygroscopicity with increasing alkali content and water-sensitive glasses were melted and subsequently handled in glove boxes under a dry nitrogen atmosphere.

The fusion took place at 1000°C for periods of about twenty minutes. The samples were weighed five minutes before the end of fusion to verify sample composition as reported previously [1-4]. Evidence for carbon dioxide retention is noted for the sodium borates and silicates of high alkali concentration ( $R > 2$  in the borates,  $J > 1.4$  in the silicates) prepared from carbonates—none was observed in the lithium cases. This phenomenon was also observed previously [5]; however no consequent effects on the physical properties were found. The crucible was reheated and the glass was formed either through roller or plate quenching, or the outside bottom of the crucible was briefly dipped in ice-water.

## 2.2 Density measurements

Density was measured either by a modified sink-float method employing acetone and diiodomethane or through the use of a micropycnometer which used helium as the working gas. The experimental uncertainties are estimated to be:  $\pm 0.02$  and  $\pm 0.03$  g/cc for the lithium and sodium borates, respectively, and  $\pm 0.01$  g/cc for the lithium silicates, and  $\pm 0.02$  g/cc for the sodium silicates. With such an uncertainty small differences in density due to the variation in glass formation cooling rates used in this study fall within the experimental error.

## 2.3 $T_g$ Measurements

The glass transition temperature was measured on a Perkin-Elmer DSC-2 (lithium borates, sodium borates, and lithium silicates) and a Perkin-Elmer DSC-7 (sodium silicates) each operating at a scan rate of 40 K/min. Runs were duplicated and the estimated experimental uncertainty is  $\pm 7$  K.  $T_g$  was taken as the onset temperature.

## 3. EXPERIMENTAL RESULTS

Table 1 lists the densities measured in this laboratory for the four systems:  $RLi_2O.B_2O_3$ ,  $RNa_2O.B_2O_3$ ,  $JLi_2O.SiO_2$ , and  $JNa_2O.SiO_2$  over the ranges  $0.0 < R < 3.0$  and  $0.0 < J < 2.2$ . Figures 1 and 2 depict the alkali borate densities as a function of  $R$  and the alkali silicate densities as a function of  $J$ , respectively. Included in the silicate figure are composite results reported by Bansaal & Doremus [6] for comparison and extension of the data to the more usual low alkali regime ( $J < 1.0$ ).

## 4. DISCUSSION OF THE RESULTS

### 4.1 Review of the Density Trends

Figure 1 displays the density trends of the lithium and sodium borates over the range  $R = 0.0$  to 3.0. There is, in both systems, a rapid increase in density as alkali is initially added to the glass. This is attributed to, primarily, the well-

known coordination change in borates as added alkali oxide causes trigonally coordinated borons to be converted into tetrahedra [7]. In the lithium borates the density reaches a maximum in the range  $R=0.5$  to  $0.8$  and declines for further addition of alkali. This additional trend is indicative of the glass undergoing a secondary coordination change as the boron tetrahedra reconvert to trigonal borons with the addition of one, two, and ultimately three non-bridging oxygens per boron as the glass forming range (employing rapid cool-

**Table 1**  
Densities of  $RLi_2O.B_2O_3$ ,  $RNa_2O.B_2O_3$ ,  $JLi_2O.SiO_2$ , and  $JNa_2O.SiO_2$  Glasses  
Measured in this Laboratory

R	Lithium Borate Density (g/cc) ( $\pm 0.02$ g/cc)	Sodium Borate Density (g/cc) ( $\pm 0.03$ g/cc)	J	Lithium Silicate Density (g/cc) ( $\pm 0.01$ g/cc)	Sodium Silicate Density (g/cc) ( $\pm 0.02$ g/cc)
0.00	1.81	1.81			
0.05	1.88	1.92	0.20	2.274	
0.07		2.00, 2.03	0.30	2.297	
0.10	1.96	2.04	0.40	2.340	2.46
0.15	2.00	2.11, 2.13	0.50	2.355	
0.20	2.11	2.14	0.60	2.352	
0.25	2.10	2.19	0.75	2.346, 2.358	
0.30	2.18	2.25	0.80		2.54
0.40	2.22	2.32	0.90	2.350	
0.50	2.27	2.37	1.00	2.344, 2.331	2.56
0.60	2.28	2.37	1.10	2.349, 2.343	
0.70	2.28	2.37, 2.38	1.20	2.322	2.56
0.80	2.28	2.39	1.25	2.322	
0.85		2.37	1.30	2.319	
0.90	2.24		1.40		2.50, 2.55
1.00	2.23		1.50	2.307	
1.10	2.24		1.60	2.299	2.47, 2.51
1.20	2.19		1.75	2.296	
1.30	2.18	2.36	1.80	2.291	2.53
1.40	2.18		2.00		2.49
1.50	2.16		2.20		2.49
1.60	2.14				
1.70	2.15	2.39			
1.80	2.11				
1.90	2.09				
2.00	2.11	2.39			
2.10	2.09				
2.20	2.09	2.39			
2.30	2.08				
2.40	2.08				
2.50	2.07	2.38			
2.60	2.10				
2.70	2.10	2.39			
2.75	2.10				
3.00		2.39			

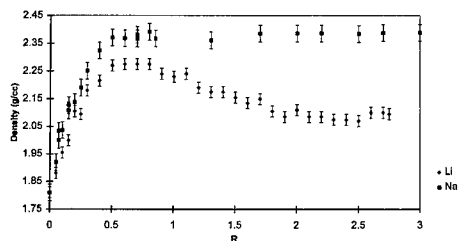


Fig. 1. The density of lithium and sodium borate glasses as a function of R.

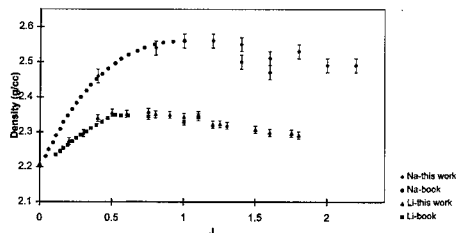


Fig. 2. The density of lithium and sodium silicate glasses as a function of J.

ing) terminates near  $R=3.0$ . In the sodium borate system, the density levels out near  $R=0.5$  and remains at a constant value near  $2.39 \text{ g/cc}$  for all subsequent alkali additions. It is believed that the origin of this trend is similar to that for the lithium borates with the complicating factor that the sodium ion is of comparable size to the oxygen; this was not the case for the lithium borates where the lithium ion is much smaller than oxygen and so contributes little to volume changes in the glass. Evidence that there is a common structural origin in the lithium and sodium borate density trends can be seen by examination of Fig. 3. This figure shows the volume per mole boron oxide,  $V_b$ , plotted for both systems as a function of R. As can be seen in the figure upon initial addition of alkali oxide,  $0.0 < R < 0.4$ , this volume becomes smaller. The change is attributed to network contraction due to the three-fold to four-fold coordination change. For larger additions of alkali oxide the volume increases linearly in both systems, this is thought to be due to the formation of non-bridging oxygens and the reverse coordination change back to trigonal borons.

Figure 2 presents the density of lithium and sodium silicates for the compositional range  $J=0.0$  to  $2.2$ . As in the borates there is an initial rapid increase in density in both systems. This is thought to be due to the incorporation of interstitial alkali and the formation of non-bridging oxygens on the silica tetrahedra ( $Q_4 \rightarrow Q_3 \rightarrow Q_2 \rightarrow Q_1 \rightarrow Q_0$ ) [8]. In both of the silicate systems studied the density reaches a maximum, in the lithium case near  $J=0.5$  and in the sodium case at  $J \approx 1.0$ . The density declines in each system upon further addition of

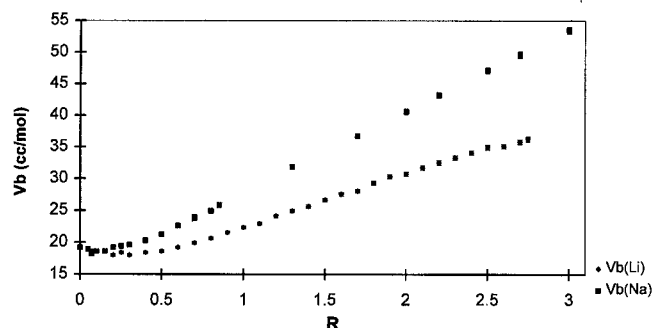


Fig. 3. The volume per mole of boron as a function of R.

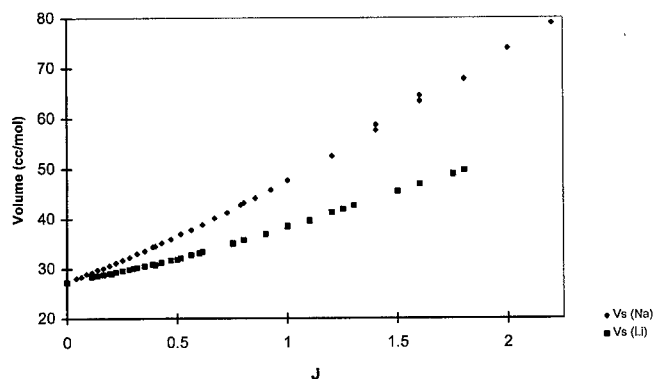


Fig 4. The volume per mole of silicon as a function of J.

alkali oxide. This change in trend is hypothesized to be the result of the addition of increasing numbers of non-bridging oxygens to the silica tetrahedra. As can be seen in Fig. 4, which is a plot of the volume per mole silica ( $V_s$ ) as a function of J, there is an enlargement at an increasing rate in the volume of the silica tetrahedra, with the slope reaching a maximum as J nears 2. This is consistent with the structural model associated with the alkali silicates. Note that there is not an initial contraction of the network as is evidenced in the plot of  $V_b$  versus R (compare Figs 3 and 4).

#### 4.2 Determination of Structural Volumes

The work of Phil Bray and others has led to a series of NMR-determined quantitative structural models in the alkali borates [7,9-11]. By associating the density trends with the changes in structure as R is varied it has been shown possible to determine the volumes associated with each of five fundamental borate groups [1,2] (See Table 2). It is also possible to determine volumes for the silica tetrahedra in both the lithium and sodium silicate systems through a non-linear least squares analysis of the data [4]. This was done by minimizing the sum of the differences squared between model and experiment by employing the solver routine in Microsoft Excel and allowing all volumes to vary throughout the glass forming range. The standard measure of error which estimates deviation between calculated and measured density was deter-

Table 2  
Borate Structural Groups and Their volumes

Unit	Composition	Boron Coordination	(NBO)/Boron	Volume (in terms of $f_i$ at $R=0$ )	
				Li	Na
$f_1$	$\text{BO}_{1.5}$	3	0	0.98	0.96
$f_2$	$\text{BO}_2$	4	0	0.91	1.19
$f_3$	$\text{BO}_2$	3	1	1.32	1.65
$f_4$	$\text{BO}_{2.5}$	3	2	1.69	2.15
$f_5$	$\text{BO}_3$	3	3	1.95	2.80

**Table 3**  
Silicate Structural Groups and Their Volumes

Unit	Composition	(NBO)/Silicon	Volume (in terms of $Q_4$ at $J = 0$ )	
			Li	Na
$Q_4$	$SiO_2$	0	1.00	1.00
$Q_3$	$SiO_{2.5}$	1	1.17	1.34
$Q_2$	$SiO_3$	2	1.41	1.74
$Q_1$	$SiO_{3.5}$	3	1.67	2.24
$Q_0$	$SiO_4$	4	1.93	2.70

mined to be 0.005 g/cc for the lithium silicates and 0.012 g/cc for the sodium silicates using the volumes presented in Table 3. By comparison with ionic radii [2,3,12-14] it is possible to calculate packing fractions (filled space ratios) for each of the borate and silicate units and these are displayed in Table 4. It is instructive to note the high packing fraction of the tetrahedral boron unit,  $f_2$ .

**Table 4**  
Packing Fractions for Borate and Silicate Groups

Borate unit	Packing fraction		Silicate unit	Packing fraction	
	Li	Na		Li	Na
$f_1$	0.34	0.35	$Q_4$	0.32	0.32
$f_2$	0.68	0.65	$Q_3$	0.38	0.42
$f_3$	0.38	0.41	$Q_2$	0.40	0.46
$f_4$	0.40	0.47	$Q_1$	0.41	0.46
$f_5$	0.44	0.48	$Q_0$	0.42	0.47

#### 4.3 Further Discussion of Structure and Property

It also is useful to plot the modified molar volumes  $V_b$  and  $V_s$  as a function of the total oxygen to anion ratio, see Fig. 5. The varying trends of  $V_b$  and  $V_s$  make clear the structural differences between the borates and the silicates. For example, the contrast at low  $R$  versus low  $J$  is seen. In the borates there is a coordination change whereas in the silicates there is not. Comparison of the

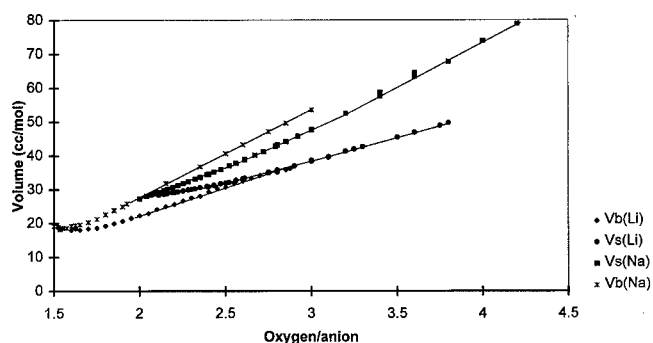


**Fig. 5.**  $V_b$  and  $V_s$  as a function of total oxygen per anion. The solid lines are guides to the eye.

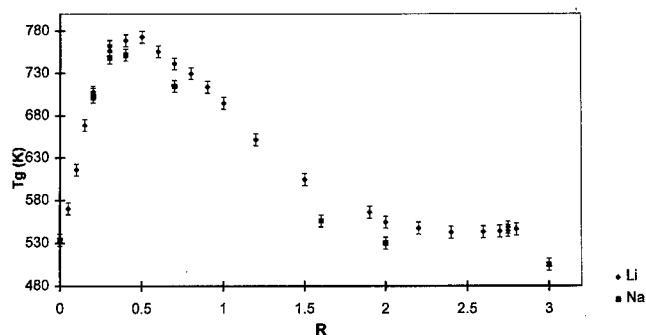


Fig. 6.  $T_g$  glass transition temperature of lithium and sodium borate glasses as a function of  $R$ .

trend between the two sodium systems shows that at high alkali content the volume per mole of boron rises above the volume per mole silicon. This is perhaps due to the volume enlargement associated with borate triangles versus that of silica tetrahedra. The fact that both borate and silicate volumes,  $V_b$  and  $V_s$ , increase linearly in the high alkali regime is supporting evidence for the conversion of bridging oxygens into non-bridging oxygens.

Figures 6 and 7 present  $T_g$  as a function of the respective alkali concentration parameters  $R$  and  $J$  in the borates and silicates. These data support the fundamental difference in short range structure as alkali is dissolved in a borate versus a silicate matrix. In the borates the  $T_g$  trend clearly reflects the rise and decline of the fraction of tetrahedral borons (See Fig. 6). The mostly monotonic decrease in  $T_g$  for the alkali silicates is indicative of the lever-rule type conversion of the silica tetrahedra from  $Q_4$  through  $Q_0$  as  $J$  is varied from 0.0 through 2.4 (See Fig. 7).

## 5. CONCLUSIONS

The densities of glassy borates and silicates containing lithium and sodium have been measured over the widest compositional range reported to date in the literature. These data have been compared with structural models deter-

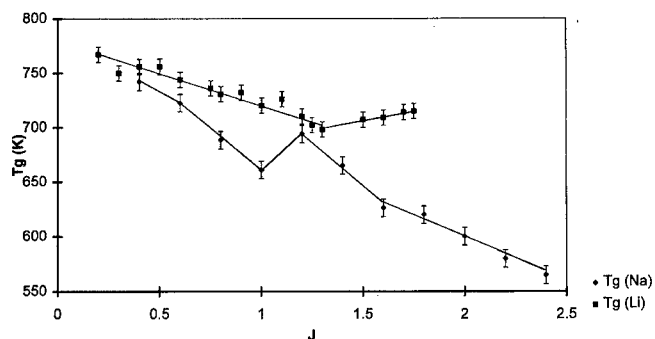


Fig. 7. The glass transition temperature of lithium and sodium silicate glasses as a function of  $J$ . The solid lines are guides to the eye.

mined principally from NMR. It is shown that the microscopic origins of the density trends differ for the silicates and the borates. In the borates the well-known coordination change of the borons from three-fold to four-fold and back to three-fold bonding with oxygen is responsible for the density trends observed whereas in the silicates there is a more straightforward conversion of bridging oxygens on the silica tetrahedra to non-bridging oxygens.

## 6. ACKNOWLEDGMENTS

The authors wish to gratefully acknowledge the support by the National Science Foundation under grants DMR 93-01247 and DMR 96-23681. Coe College is thanked for providing housing and other support for this project. Dr Adrian Wright of Reading University (UK) is thanked for useful discussions and his kind hospitality during S. Feller's recent sabbatical. The US/UK Fulbright Commission is also acknowledged for their support of S. Feller.

## REFERENCES

- [1] M. Shibata, C. Sanchez, H. Patel, S. Feller, J. Stark, G. Sumcad & J. Kasper, *J. Non-Cryst. Solids* **85** (1986), 29.
- [2] B.C.L. Chong, S.H. Choo, S. Feller, B. Teoh, O. Mathews, E. J. Khaw, D. Feil, K. Chong, M. Affatigato, D. Bain, K. Hazen & K. Farooqui, *J. Non-Cryst. Solids* **109** (1989), 105.
- [3] M. Royle, M. Sharma, S. Feller, J. MacKenzie & S. Nijhawan, *Phys. Chem. Glasses* **34** (1993), 149.
- [4] A.M. Peters, F.M. Alamgir, S.W. Messer, S.A. Feller & K.L. Loh, *Phys. Chem. Glasses* **35** (1994), 212.
- [5] H. Zhang, S. Koritala, K. Farooqui, R. Boekenhauer, D. Bain, S. Kambeyanda & S. Feller, *Phys. Chem. Glasses* **32** (1991), 185.
- [6] N.P. Bansaal & R.H. Doremus, *Handbook of Glass Properties* (Academic Press, Orlando, 1986), p. 54.
- [7] P.J. Bray & J.G. O'Keefe, *Phys. Chem. Glasses* **4** (1963), 37.
- [8] H. Maekawa, T. Maekawa, K. Maekawa & T. Yokokawa, *J. Non-Cryst. Solids* **127** (1991), 53.
- [9] S. Feller, W. Dell & P.J. Bray, *J. Non-Cryst. Solids* **51** (1982), 21.
- [10] G.E. Jellison, Jr. & P.J. Bray, *J. Non-Cryst. Solids* **29** (1978), 187.
- [11] J. Zhong & P.J. Bray, *J. Non-Cryst. Solids* **111** (1989), 67.
- [12] R.D. Shannon, *Acta Crystallogr. A*, **32** (1976), 751.
- [13] R.L. Warren & B.E. Warren, *J. Appl. Crystallogr.* **3** (1970), 251.
- [14] W.H. Zachariasen, *Acta Crystallogr.* **17** (1963), 749.

**A PROPOSED RELATIONSHIP BETWEEN THE  
POSITION OF THE FIRST NEUTRON DIFFRACTION  
PEAK FOR ALKALI BORATE GLASSES AND THE  
SEPARATION BETWEEN THE MODIFYING CATIONS  
AS FOUND FROM DENSITY MEASUREMENTS**

Andrew J. WANLESS, Adrian C. WRIGHT, Roger N. SINCLAIR  
*J.J. Thomson Physical Laboratory, University of Reading,  
Whiteknights, Reading, RG6 6AF, UK*

and

Steven A. FELLER, Richard B. WILLIAMS,  
Bruce C. JOHANSON, Mark T. MAYHEW  
*Physics Department, Coe College, Cedar Rapids, IA 52402, USA*

A close correspondence has been found between  $D_1=2\pi/Q_1$ , where  $Q_1$  is the position of the first diffraction peak observed from neutron scattering, and  $D_d$  the average distance between alkali ions calculated from the density in a series of alkali borate glasses. The separation between pairs of alkali ions was found by assuming a random distribution of alkali cages. The glasses studied include a series of alkali borates at  $R=0.4$ , where  $R$  is the molar ratio of the alkali oxide to boron oxide, and rubidium and cesium borates with increasing alkali concentrations covering the range  $0.51 \leq R \leq 0.11$ . For the glasses with a constant alkali concentration with  $R=0.4$ , a nearly linear relationship was found between  $D_d$  and  $D_1$ . For the alkali dependent rubidium and cesium borate glasses, it was found that, at high modifier content, the density determined distances are less than the neutron distances. This is interpreted as an indication of a tendency for the alkali ions to cluster. For low alkali concentrations this trend is reversed.

## 1. INTRODUCTION

In the course of performing neutron diffraction studies of alkali borate glasses it has been observed that the first diffraction peak appears to correlate well with the alkali incorporation into the glass. It is thought that the first diffraction peak arises due to neutron diffraction from alkali ions incorporated into adjacent network cages. If this is the case then the neutron determined separation distance between pairs of alkali ions,  $D_1$ , would be described by

$$D_1=2\pi/Q_1 \quad (1)$$

where  $Q_1$  is the position of the first diffraction peak.

In this paper the neutron determined alkali separation distances have been



obtained for a number of alkali borate glasses. In addition, these distances have been compared with average separation lengths found from density data, determined on the basis of a random distribution of the alkali ions.

## 2. EXPERIMENTAL PROCEDURES

### 2.1 Glassmaking

Glass batches were prepared from boric acid and alkali carbonates or alkali oxides. The compositions are described by R which is the molar ratio of alkali oxide to boron oxide. Samples for neutron diffraction experiments require boric acid enriched in  $^{11}\text{B}$  [1] to reduce the effects of the large neutron absorption cross section for  $^{10}\text{B}$ . Similarly, the lithium borate sample required and was prepared from  $^7\text{Li}$  enriched [2] lithium carbonate. In order to minimize the concentration of water in the resulting glass, the boric acid was initially heated for periods of several hours at  $1000^\circ\text{C}$  to produce dry boron oxide glass and the desired alkali borate glasses were then prepared using this dry boron oxide glass. The glasses were made in platinum crucibles and were melted and subsequently handled in glove boxes under a dry nitrogen atmosphere.

The fusion took place at  $1000^\circ\text{C}$  for periods of about twenty minutes. The samples were weighed five minutes before the end of heating to verify sample composition as reported previously [3-5], and then reheated and plate-quenched. The glasses were crushed to a powder and sealed under nitrogen in vanadium cans for the neutron diffraction experiments.

### 2.2 Neutron diffraction measurements

The neutron diffraction experiments were performed on the Liquid and Amorphous Detector (LAD) at the Rutherford-Appleton Laboratory as described previously [6]. The position of the first diffraction peak was found by peak fitting.

### 2.3 Density measurements

Density was measured either by a modified sink-float method, which used acetone and diiodomethane, or through the use of a micropycnometer with helium as the working gas [3,5,7]. The experimental uncertainty is  $\pm 0.03$  g/cc.

**Table 1**  
 $Q_1$  and  $D_1$  for Alkali Borate Glasses

Alkali	R	$Q_1$ ( $\text{\AA}^{-1}$ )	$D_1$ ( $\text{\AA}$ )
Li	0.40	$1.496 \pm 0.003$	$4.20 \pm 0.01$
Na	0.40	$1.352 \pm 0.003$	$4.65 \pm 0.01$
K	0.40	$1.224 \pm 0.003$	$5.13 \pm 0.01$
Rb	0.17	$1.112 \pm 0.004$	$5.65 \pm 0.02$
Rb	0.34	$1.164 \pm 0.006$	$5.40 \pm 0.03$
Rb	0.51	$1.177 \pm 0.005$	$5.34 \pm 0.02$
Cs	0.11	$1.016 \pm 0.004$	$6.19 \pm 0.03$
Cs	0.20	$1.083 \pm 0.004$	$5.80 \pm 0.02$
Cs	0.40	$1.117 \pm 0.003$	$5.62 \pm 0.02$

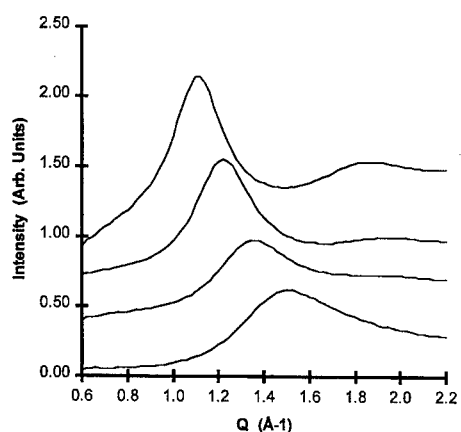


Fig. 1. The first peak in the neutron diffraction patterns from a series of alkali borate glasses with  $R=0.4$ . From top to bottom the spectra are from cesium, potassium, sodium, and lithium borate glasses, respectively.

### 3. EXPERIMENTAL RESULTS

#### 3.1 Neutron diffraction

Figure 1 displays several representative first peaks in the neutron diffraction patterns from the alkali borate glasses with  $R=0.40$ , whereas Fig. 2 depicts neutron diffraction data from cesium borate glasses with variable  $R$ . Table 1 is a compilation of  $Q_1$  and  $D_1$  from the series of alkali borate glasses studied.

#### 3.2 Density

Assuming that the alkali ions fill space in random spherical cages of oxygen atoms then the following is a straightforward procedure for determining the ionic separation distance,  $D_d$ , from the density. Denoting the composition unit of the

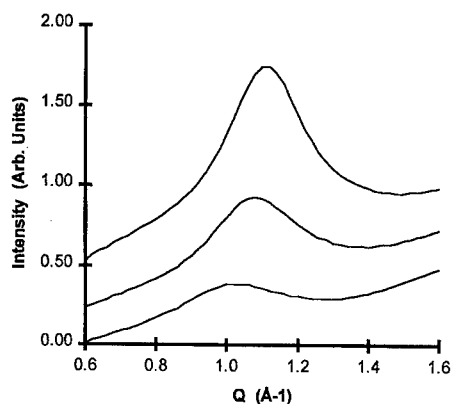


Fig. 2. First peak in the neutron diffraction patterns from cesium borate glasses with  $R=0.11$  (bottom),  $R=0.20$  (middle), and  $R=0.40$  (top).

**Table 2**

Density and Separation Distances,  $D_d$ , for Alkali Borate Glasses Studied by Neutron Diffraction

Alkali	R	Density (g/cc) ( $\pm 0.03$ g/cc)	$D_d$ (Å) ( $\pm 0.03$ Å)
Li	0.40	2.23	4.52
Na	0.40	2.33	4.68
K	0.40	2.29	4.91
Rb	0.17	2.34	6.37
Rb	0.34	2.69	5.28
Rb	0.51	2.94	4.81
Cs	0.11	2.43	7.24
Cs	0.20	2.72	6.17
Cs	0.40	3.21	5.23

glass by  $RM_2O \cdot B_2O_3$ , where M is the alkali ion under consideration, the molar volume per alkali ion (including empty space), V, can be determined from

$$V = m / (2Rd) \quad (2)$$

where m is the mass of one composition unit and d the bulk density. Assuming that the  $M^+$  ions are situated at the centers of the spheres of a random close packing, a similar derivation to that for the molecular model in Section 7.6 of Ref. [6] can be employed to relate  $D_d$  to V, via the packing density,  $\eta$ , which for a random close packing is 0.6366, viz.

$$\eta = (4/3)\pi(D_d/2)^3/V \quad (3)$$

Rearranging Eq. (3) gives

$$D_d^3 = 6\eta V / \pi \quad (4)$$

and the working relationship between  $D_d$  and V becomes

$$D_d = (1.2638)(3\sqrt{V}) \text{ (Å)} \quad (5)$$

where  $D_d$  is given in Ångstrom units. Table 2 records the densities and values for  $D_d$  from the alkali borate glasses used in the neutron diffraction experiments.

#### 4. DISCUSSION OF THE RESULTS

Evidence that the first diffraction peak is directly related to the incorporation of alkali into the glass is provided by Fig. 2 which shows the systematic growth of the first diffraction peak (with normalized intensity) as the  $Cs_2O$  concentration increases from  $R=0.11$  to 0.40.

Figure 3 presents a plot of  $D_d$  as a function of  $D_1$  for the alkali borate glasses with  $R=0.4$ . The straight line represents equality of the two distances. There is a close correspondence between the experimental values for the two distances with a nearly linear relationship observed for which slope is less than unity. Figure 4 depicts  $D_d$  plotted against  $D_1$  for the series of rubidium and cesium borate glasses with variable alkali concentration. In this figure, a

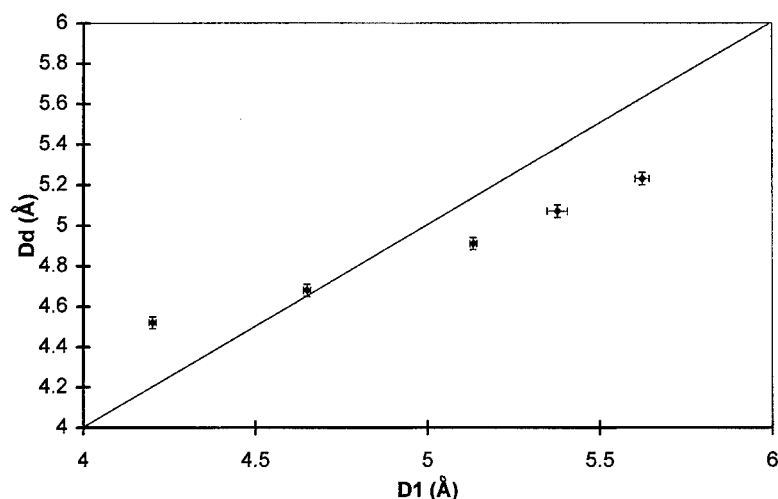


Fig. 3.  $D_d$  as a function of  $D_1$  for alkali borate glasses with a constant alkali concentration of  $R=0.4$ . The straight line denotes  $D_d=D_1$ .

monotonic relationship between the two distances can be seen for each alkali (lack of data precludes further elucidation of the precise quantitative relationship). As  $R$  increases,  $D_d$  becomes smaller than  $D_1$ , this is evidence for clustering of the alkali cations at high concentration. Also, the trends which describe the rubidium data are similar for the cesium  $D_1$  data except they are displaced towards smaller distances for equivalent values of  $R$ . This is likely to be due to the smaller diameter of the rubidium compared to the cesium ion.

A hypothetical first-order model for the incorporation of the alkali oxide has the cations surrounded by oxygen to form cages. The ion separation,  $D_i$ ,

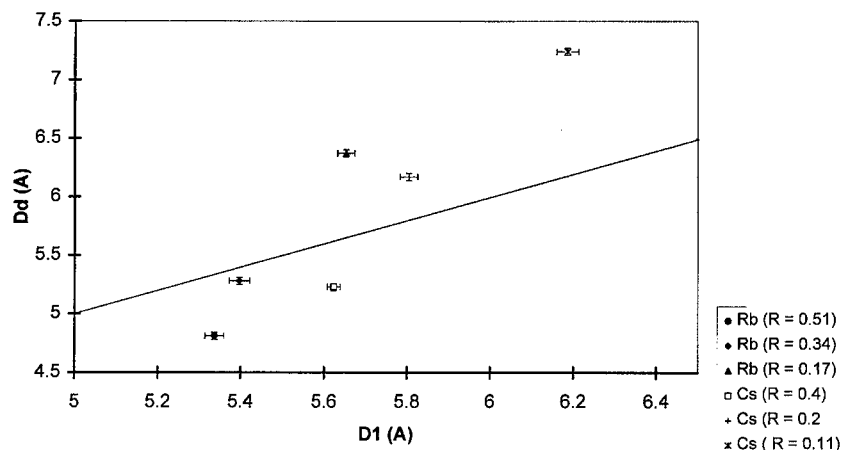


Fig. 4.  $D_d$  as a function of  $D_1$  for rubidium and cesium borate glasses with variable alkali concentration. The straight line denotes  $D_d=D_1$ .

**Table 3**  
Estimates of Ion Cage Dimensions for Alkali Borate Glasses

Alkali	$r_{M^+}$	R (Å)	$D_i=D_1$ (Å)	$2r_{M^+}$ (Å)	$t=D_i-2r_{M^+}$ (Å)
Li	0.78	0.40	4.20	1.56	2.64
Na	1.20	0.40	4.65	2.40	2.25
K	1.65	0.40	5.13	3.30	1.83
Rb	1.77	0.17	5.65	3.54	2.11
Rb	1.77	0.34	5.40	3.54	1.86
Rb	1.77	0.51	5.34	3.54	1.80
Cs	1.95	0.11	6.19	3.90	2.29
Cs	1.95	0.20	5.80	3.90	1.90
Cs	1.95	0.40	5.62	3.90	1.72

for this model is given by:

$$D_i = 2r_{M^+} + t \quad (6)$$

where  $r_{M^+}$  is the alkali ion radius, and  $t$  is the wall thickness. Knowledge of the ionic radii [8-10], and setting  $D_i$  equal to  $D_1$  allows estimates of  $t$  to be made. These values can be found in Table 3.

A comparison between  $t$  and the oxygen diameter, 2.54 Å [3,11], is illustrative. Here the diameter was chosen to be that appropriate to oxygen associated with tetrahedrally coordinated boron since this is the likely oxygen environment for use with the alkali ions [12,13]. For the lithium borate glass the agreement is good. For the other alkali ions the calculated wall thickness is less than the oxygen diameter. In the rubidium and cesium cases the wall thickness approaches the oxygen diameter, as  $R$  becomes small, which implies that the alkali cage enlarges as the alkali becomes more dilute. This is a reasonable result. It is also interesting to note the similarity of the wall thicknesses for the large ions at  $R = 0.4$ . The potassium borate glass yields 1.83 Å, the rubidium borate glass (extrapolated) is 1.84 Å, and the cesium borate glass is 1.72 Å. This suggests an isostructural environment for the large alkali ions.

## 5. CONCLUSIONS

The positions of the first diffraction peak from neutron diffraction measurements for a number of alkali borate glasses are reported. The resulting interionic distances are then compared with average distances determined from density measurements under the assumption of a random distribution of alkali ions. A strong correlation is found between the two sets of length measures implying that the origin of the first diffraction peak in alkali borate glasses is diffraction by alkali ions housed in the network cages.

## 6. ACKNOWLEDGMENTS

Work supported by the National Science Foundation under grants DMR 93-01247 and DMR 96-23681. The neutron diffraction studies were performed

at the Rutherford Appleton Laboratory, supported by the EPSRC. The UK/US Fulbright Commission is thanked for supporting S.A. Feller at the Rutherford Appleton Laboratory and at Reading University during the course of these experiments and for the period when the paper was written. Coe College is acknowledged for their support of students.

## REFERENCES

- [1]  $^{11}\text{B}$  enriched boric acid (99.98 atomic%  $^{11}\text{B}$ ), Eagle-Picher, Quapaw, Oklahoma, 74363, USA.
- [2]  $^7\text{Li}$  enriched lithium carbonate (99.94 atomic%  $^7\text{Li}$ ), Euriso-Top (France).
- [3] B.C.L. Chong, S.H. Choo, S. Feller, B. Teoh, O. Mathews, E. J. Khaw, D. Feil, K. Chong, M. Affatigato, D. Bain, K. Hazen & K. Farooqui, *J. Non-Cryst. Solids* **109** (1989), 105.
- [4] H. Zhang, S. Koritala, K. Farooqui, R. Boekenhauer, D. Bain, S. Kambeyanda & S. Feller, *Phys. Chem. Glasses* **32** (1991), 185.
- [5] M. Shibata, C. Sanchez, H. Patel, S. Feller, J. Stark, G. Sumcad & J. Kasper, *J. Non-Cryst. Solids* **85** (1986), 29.
- [6] A.C. Wright, Chapter 8 in: *Experimental Techniques of Glass Science* edited by C.J. Simmons and O.H. El-Bayoumi (Am. Ceram. Soc., Westerville, OH) (1993), p. 205.
- [7] M. Royle, M. Sharma, S. Feller, J. MacKenzie & S. Nijhawan, *Phys. Chem. Glasses* **34** (1993), 149.
- [8] R.D. Shannon, *Acta Crystallogr. A* **32** (1976), 751.
- [9] R.L. Mozzi & B.E. Warren, *J. Appl. Crystallogr.* **3** (1970), 251.
- [10] W.H. Zachariasen, *Acta Crystallogr.* **17** (1963), 749.
- [11] N.M. Vedishcheva, B.A. Shakhmatkin, A.C. Wright, D.I. Grimley, G. Etherington & R.N. Sinclair, *Rivista della Stazione Sperimentale del Vetro* **XXIII** (1993) p.459.
- [12] P.J. Bray & J.G. O'Keefe, *Phys. Chem. Glasses* **4** (1963), 37.
- [13] J. Zhong & P.J. Bray, *J. Non-Cryst. Solids* **111** (1989), 67.

## THE ABNORMAL PROPERTIES OF BORON OXIDE IN GLASS

Jay J. L. Yi

*Circon ACMI, 300 Stillwater Avenue, Stamford,  
Connecticut, 06904, USA*

The abrupt change in the property versus composition curves for simple borate glasses can be considered as the result of changing from one type of boron structural group to another. In addition to the Raman spectra, etc. which indicate the existence of such structural groups, the author has found that the shift of the ESR peaks for  $Mn^{2+}$  doped alkali borate glasses confirms such abrupt changes in the property-composition curves. By carefully studying the contribution of boron to the specific volume of simple borate glasses, the author has found that the partial volume data for boron (as the boron oxide component) show stable values at the compositions corresponding to  $XY_4$ ,  $XY_2$  and  $X_2Y_2$  structural groups (X is a 4-coordinated  $BO_4$  tetrahedron, and Y is a 3-coordinated  $BO_3$  triangle). A third component, such as  $BeO$ ,  $Al_2O_3$ ,  $SiO_2$  etc., was added to binary borate glasses, and their effects on the formation of boron structural groups were studied. The property data for  $Na_2O-B_2O_3-SiO_2$  and  $BaO-B_2O_3-SiO_2$  glasses were used as examples to investigate the formation of  $BO_4$  tetrahedra, as well as the existence of various structural groups in borosilicate glasses. Based on the  $B_2O_3$  and  $SiO_2$  components in these glasses, a general model has been established, describing the property-structure-composition relationships for borate and borosilicate glasses.

## A VIBRATIONAL SPECTROSCOPIC STUDY OF ALKALINE EARTH BORATE GLASSES

Yiagos D. YIANNPOULOS, Efstratios I. KAMITSOS,  
Georgios D. CHRYSSIKOS & John A. KAPOUTSIS  
*Theoretical and Physical Chemistry Institute, NHRF, 48, Vass.  
Constantinou Ave., 116 35 Athens, GREECE*

The study of the mid infrared and Raman spectra of Ca-, Sr- and Ba-borate glasses has shown that their network is composed of borate arrangements containing  $B\emptyset_4^-$  tetrahedra ( $\emptyset$ =bridging oxygen atom) and metaborate,  $B\emptyset_2O^-$ , triangular units. The fraction of four-coordinated boron atoms,  $N_4$ , was obtained and found to exhibit a maximum at compositions depending on the type of alkaline earth cation. For fixed metal oxide contents,  $N_4$  increases with increasing metal ion size, a trend opposite to that exhibited by alkali borate glasses. Mg-borates were found to have the lowest  $N_4$  values, and this was shown to originate from the disproportionation of the borate network to boroxol rings and pyroborate species. The analysis of the far infrared profiles suggests the presence of two types of sites hosting alkaline earth cations, i.e. sites which are well organised, or 'crystal-like', and sites which are less organised.

### 1. INTRODUCTION

The structure and properties of oxide glasses depend strongly on the nature and concentration of the constituent oxides. The effect of alkaline earth cations on the structure of borate glasses,  $xMO \cdot (1-x)B_2O_3$ , has been studied extensively by Bray and co-workers using  $^{11}B$  NMR spectroscopy [1-5]. It was shown that at low MO contents the alkaline earth cations behave like alkali modifier ions and the fraction of four-coordinated boron atoms,  $N_4$ , follows the  $N_4 = x/(1-x)$  law. At higher MO contents the  $M^{2+}$  ions start gaining network forming ability, and this is manifested by lowering their coordination number with oxygen atoms. As an effect the conversion rate of boron coordination from three to four is reduced, this phenomenon being particularly strong in Mg-containing borate glasses [4]. Besides their glass modifying/forming properties, MO oxides can induce also a change of oxygen coordination number from two to three. This was reported to be the case of  $SrO-B_2O_3$  glasses with compositions in the range  $0.33 < x \leq 0.41$  [3].

As shown for alkali borate glasses, Raman and mid infrared spectroscopies are very sensitive probes of the structures assumed by the borate network [6-9], while far infrared spectroscopy can reveal the nature of interactions between the alkali metal ions and their sites [10-13]. It is the strength of such interactions



that determines the nature of M–O bonding and thus the glass-modifying/forming properties of metal oxide.

In comparison to alkali borates, a limited number of vibrational studies has been published for alkaline earth borate glasses [7,14-17]. In this work we report some characteristic results of a systematic Raman and infrared reflectance study of glasses in the systems  $x\text{MO} \cdot (1-x)\text{B}_2\text{O}_3$ ,  $\text{M}=\text{Mg}$ ,  $\text{Ca}$ ,  $\text{Sr}$  and  $\text{Ba}$ , in an attempt to quantify the effect of  $\text{M}^{2+}$  on glass structure and to investigate the nature of M–O bonding as a function of metal oxide content.

## 2. EXPERIMENTAL

Alkaline earth borate glasses were prepared from stoichiometric mixtures of anhydrous  $\text{B}_2\text{O}_3$  and metal carbonates ( $\text{M}=\text{Sr}$ ,  $\text{Ba}$ ), or metal oxides ( $\text{M}=\text{Mg}$ ,  $\text{Ca}$ ). The thoroughly mixed batches were melted in platinum crucibles for about half an hour in the temperature range 1100–1300°C. Glasses were obtained by quenching the melt between two polished copper blocks. The glass forming regions found in this work are given in Table 1, where they are compared with those determined for alkali borate glasses [18].

It is evident that the glass forming region becomes wider as the cation size increases. The lower MO content for glass formation is set by the onset of phase separation, while crystallization processes determine the upper MO limit. The difference in glass forming ability between alkaline earth and alkali metal oxides can be understood in terms of the field strength of the metal cations. Because of their higher field strengths,  $\text{M}^{2+}$  cations require sites of higher anionic charge density, which can exist only in glasses of relatively high MO contents.

Infrared spectra were recorded in the reflectance mode on a Fourier-transform spectrometer (Bruker IFS 113v), and were analyzed by the Kramers–Kronig technique [19] to calculate the absorption coefficient spectra reported here. Raman spectra were measured on a Jobin-Yvon spectrometer (Ramanor HG 2S) at a 90° scattering geometry, using for excitation the 488 nm line of an argon ion laser (Spectra Physics 165).

**Table 1**  
Glass Forming Regions of Alkaline Earth and Alkali Borate Glasses

Cation	Glass Forming Region
$x\text{MO} \cdot (1-x)\text{B}_2\text{O}_3$	
Mg	$0.45 \leq x \leq 0.55$
Ca	$0.33 \leq x \leq 0.50$
Sr	$0.20 \leq x \leq 0.47$
Ba	$0.20 \leq x \leq 0.47$
$x\text{M}_2\text{O} \cdot (1-x)\text{B}_2\text{O}_3$	
Li	$0 \leq x \leq 0.75$
Na	$0 \leq x \leq 0.45$ and $0.55 \leq x \leq 0.75$
K	$0 \leq x \leq 0.45$ and $0.60 \leq x \leq 0.70$
Rb	$0 \leq x \leq 0.45$ and $0.65 \leq x \leq 0.70$
Cs	$0 \leq x \leq 0.75$

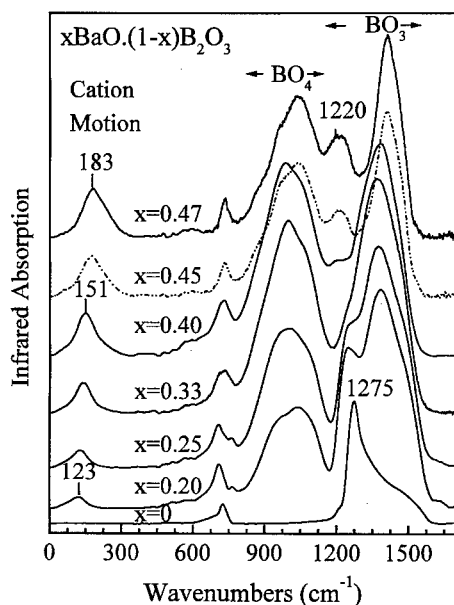


Fig. 1. Infrared Absorption Spectra of  $x\text{BaO} \cdot (1-x)\text{B}_2\text{O}_3$  glasses.

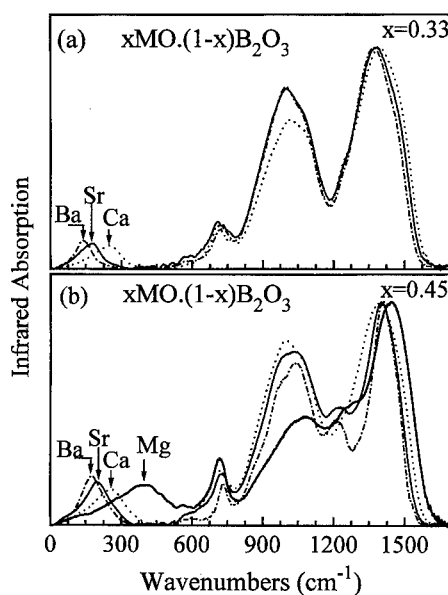


Fig. 2. Infrared Absorption Spectra of  $x\text{MO} \cdot (1-x)\text{B}_2\text{O}_3$  glasses with  $x=0.33$  (a) and  $x=0.45$  (b).

### 3. RESULTS AND DISCUSSION

#### 3.1. Effect of Alkaline Earth Oxide on the Structure of the Borate Network

Infrared absorption spectra of glasses in the barium borate system are shown in Fig. 1. The corresponding reflectivity spectra are in good agreement with those published recently by Kim et al [20]. In order to understand the effect of BaO addition on the structure of the borate network we consider the mid-infrared region ( $500\text{--}1600\text{ cm}^{-1}$ ), where the vibrations of the boron-oxygen arrangements are active. In particular, absorption in the  $800\text{--}1150\text{ cm}^{-1}$  range can be attributed to the B-O asymmetric stretching vibration of  $\text{BO}_4$  tetrahedra, and the high frequency absorption profile ( $1150\text{--}1550\text{ cm}^{-1}$ ) to the corresponding vibration of  $\text{BO}_3$  triangles [19]. Therefore, the evolution of the  $800\text{--}1150\text{ cm}^{-1}$  envelope with  $x$  in the range  $0 < x \leq 0.40$  (Fig. 1) shows the progressive change of boron coordination number from three to four. For higher BaO contents a decrease of the relative intensity of the  $\text{BO}_4$  absorption band is observed, signaling the formation of non-bridging oxygen (NBO) containing triangles. Indeed, the band developing at  $1220\text{ cm}^{-1}$  can be assigned to the B-O asymmetric stretching vibration of  $\text{B}\text{O}_2\text{O}^-$  triangles in metaborate rings [19,21].

The dependence of the glass structure on the type of alkaline earth cation is illustrated in Fig. 2, where the spectra of glasses with fixed MO content ( $x=0.33$ ,  $0.45$ ) are compared. To facilitate comparison, all spectra have been scaled at the high frequency absorption envelope. It is clear from Fig. 2 that absorption in the

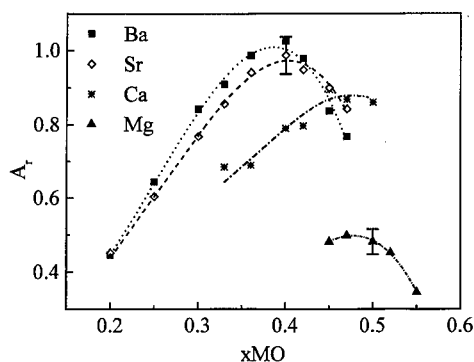


**Fig.3.** Relative integrated intensity  $A_r = A_4/A_3$  for  $x\text{MO} \cdot (1-x)\text{B}_2\text{O}_3$  glasses. Lines through data points are drawn to guide the eye.

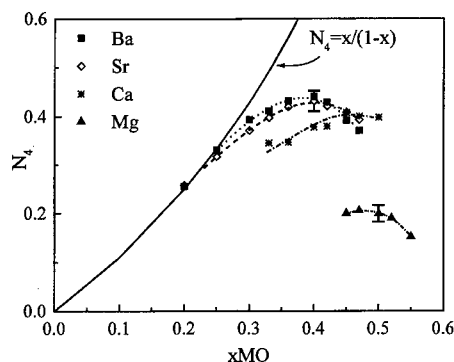


**Fig.4.** The fraction of four-coordinated boron atoms,  $N_4$ , in  $x\text{MO} \cdot (1-x)\text{B}_2\text{O}_3$  glasses calculated using Eq. (1). Comparison is made with the theoretical,  $x/(1-x)$ , values. Lines through data points are drawn to guide the eye.

range characteristic of  $\text{BO}_4$  tetrahedra depends on type of alkaline earth cation. To quantify the effect of alkaline earth oxide on the short-range structure of the borate network we have calculated the integrated intensity of the absorption envelopes  $800\text{--}1150\text{ cm}^{-1}$  and  $1150\text{--}1550\text{ cm}^{-1}$ , denoted by  $A_4$  and  $A_3$ , respectively. The relative integrated intensity,  $A_r = A_4/A_3$ , is plotted in Fig. 3 versus MO content. The change of boron coordination from three to four with increasing MO content towards the metaborate composition ( $x=0.50$ ) is illustrated very clearly in this figure. It is observed also that the MO content at which  $A_r$  exhibits its maximum value is a function of the type of alkaline earth oxide.

The relative integrated intensity,  $A_r$ , can be employed to calculate the fraction of boron atoms with fourfold coordination,  $N_4$ , by using the expression,

$$N_4 = A_r / (\alpha + A_r) \quad (1)$$

where  $\alpha$  is the relative absorption coefficient of boron tetrahedra versus boron triangles [22,23]. The value of  $\alpha$  can be obtained by comparing infrared data of this work (Fig. 3) with recently published NMR results by Huebert et al [15]. Using these NMR data it can be shown that the  $N_4$  values for binary Sr-borate glasses with  $x=0.40$  and  $x=0.47$  are  $N_4=0.44$  and  $N_4=0.39$ , respectively [15]. These values and Eq. (1) give an average value of  $\alpha=1.3$ . Although  $\alpha$  is expected to show a cation dependence, the lack of recent NMR data for binary Ba- and Ca-borate glasses leads us to employ the value  $\alpha=1.3$  to calculate  $N_4$  for the three Ba-, Sr- and Ca-borate glass systems. As shown in Fig. 3 Mg-borate glasses exhibit distinctly lower values of  $A_r$ , indicating that the value of  $\alpha$  for these glasses should be calculated separately. According to Dell & Bray,  $N_4=0.20$  for the  $0.45\text{MgO} \cdot 0.55\text{B}_2\text{O}_3$  glass [5], giving the value  $\alpha=1.9$  for Mg-borate glasses.

Using the infrared data ( $A_r$ ) and the values of  $\alpha$  obtained above,  $N_4$  was

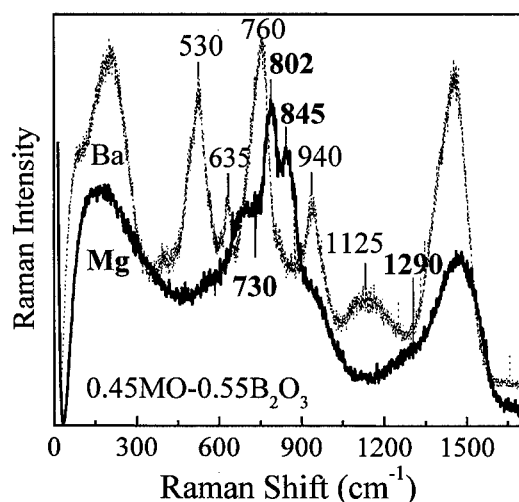


Fig. 5. Raman spectra of Ba- and Mg-borate glasses with  $x=0.45$ .

calculated through Eq. (1). The results are shown in Fig. 4 versus MO content and compared with the theoretical values,  $x/(1-x)$ . The following observations can be made; (a) for Ba- and Sr-glasses of low MO contents (up to  $ca\ x=0.25$ )  $N_4$  follows the theoretical value, (b) the MO content at which  $N_4$  attains its maximum value shifts to higher  $x$  values as the field strength of  $M^{2+}$  increases, and (c) for glasses of the same MO content  $N_4$  decreases with increasing field strength of  $M^{2+}$  cation. It is worth noting that this trend is opposite to that found in alkali borate glasses, i.e. a decrease of  $N_4$  from Li to Cs [21, 24].

To understand the origin of the distinctly lower  $N_4$  values exhibited by Mg-borate glasses we compare in Fig. 5 the Raman spectra of Mg- and Ba-borate glasses with  $x=0.45$ .

The spectrum of the barium-borate glass shows features characteristic of borate arrangements containing  $B\text{O}_4^-$  tetrahedra (bands at 530, 760 and 940  $\text{cm}^{-1}$ ) and metaborate rings,  $(B_3O_6^{3-})$ , (635  $\text{cm}^{-1}$ ) [25,26]. Therefore, the structure of the Ba-borate glass is consistent with the metaborate stoichiometry and can be described in terms of the isomerisation process:  $B\text{O}_4^- \leftrightarrow B\text{O}_2\text{O}^-$ . On the contrary, the spectrum of the Mg-borate glass reveals the presence of boroxol rings,  $B_3O_{4.5}$ , (802  $\text{cm}^{-1}$ ) and pyroborate species,  $B_2O_5^{4-}$ , (845  $\text{cm}^{-1}$ ) [16]. The coexistence of undermodified (boroxol rings) and overmodified (pyroborate dimers) species at the metaborate composition can be understood in terms of the following disproportionation reaction:  $4B\text{O}_2^- \rightarrow (2/3)B_3O_{4.5} + B_2O_5^{4-}$ , where  $B\text{O}_2^- = B\text{O}_4^-$  and/or  $B\text{O}_2\text{O}^-$ . This behavior of Mg-borate glasses is attributed to the largest field strength of  $Mg^{2+}$  ions, and is consistent with the fact that they exhibit the smallest value of  $N_4$  and the smallest glass forming region among the rest of alkaline earth borates. This justifies also the different value of the relative absorption coefficient,  $\alpha$ , of the Mg-borate glasses.

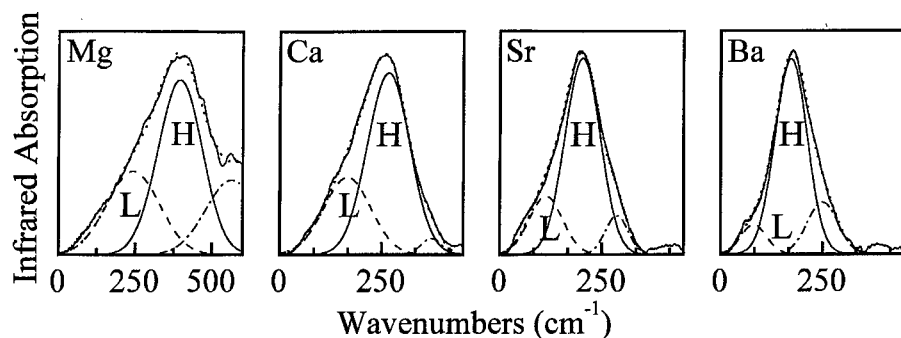


Fig. 6. Deconvoluted far infrared profiles of 0.45MO.0.55B<sub>2</sub>O<sub>3</sub> glasses (M=Mg, Ca, Sr, Ba).

### 3.2. Far Infrared Spectra and Metal Ion / Site Interactions

As shown in Fig. 1, addition of BaO to B<sub>2</sub>O<sub>3</sub> causes the appearance of a new band in the far infrared whose frequency and intensity are increasing with  $x$ . For glasses of the same MO content, the frequency of the far infrared band increases upon decreasing the mass of the alkaline earth cation (Fig. 2). Similar bands in the spectra of alkali borate glasses have been assigned to vibrations of metal ions in their equilibrium sites [10-13].

When the far infrared spectra are shown in an expanded frequency scale becomes obvious that the description of their asymmetric profiles requires deconvolution into component bands. A typical example of such spectral deconvolution into Gaussian components is shown in Fig. 6 for the 0.45MO.0.55B<sub>2</sub>O<sub>3</sub> glasses. The frequencies of the two lower-frequency bands (designated by  $\nu_L$  and  $\nu_H$ ) are plotted versus the inverse square root of the alkaline earth cation mass in Fig. 7. The linear dependence of  $\nu_H$  and  $\nu_L$  on  $m_c^{-1/2}$  suggests that the H and L bands could be attributed to vibrations of M<sup>2+</sup> cations in two types of anionic site environments in the glass (sites H and L) [21]. Besides the L and H bands, Fig. 6 shows the existence of a third band at the high frequency side. This component can be attributed to borate network modes, like the libration mode of metaborate rings [21,27].

To investigate the nature of L and H glass sites hosting M<sup>2+</sup> ions, we compare in Fig. 8 the far infrared spectrum of the 0.50CaO.0.50B<sub>2</sub>O<sub>3</sub> glass with that of a corresponding crystalline compound. It is observed that the H glass band forms the envelope of the infrared bands of the crystal in the range 100-350 cm<sup>-1</sup>. According to Rulmont & Almou [28], the intense bands of Ca-metaborate crystal in this frequency range arise from the translational modes of Ca<sup>2+</sup> cations in their sites. On these grounds we suggest that the H glass band can be attributed to vibrations of metal cations in well organized, or 'crystal-like', sites in the glass. Metal cations that do not succeed to establish such environments occupy less organized sites and may give rise to the L-type band. It is of interest to note that a similar picture was established recently from the consideration of the far infrared spectra of glassy and crystalline alkali-germanates [29].

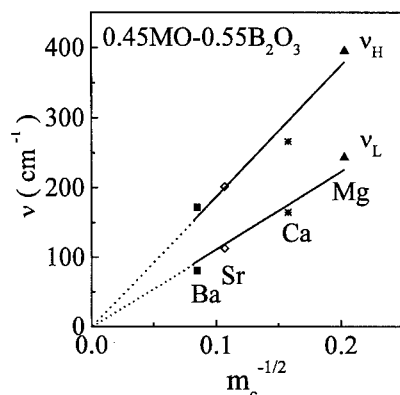


Fig. 7. Cation motion frequencies versus  $m_c^{-1/2}$ , where  $m_c$  is the metal ion mass. Error bars are of the size of symbols. Lines are least square fittings.

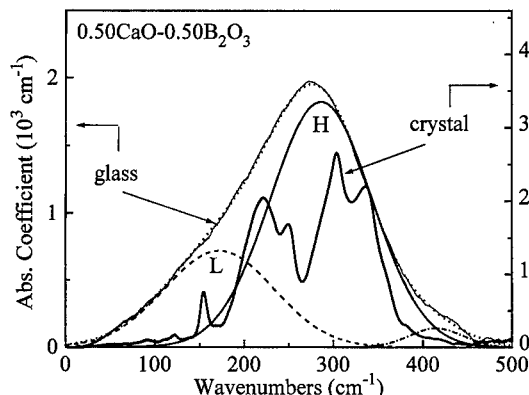


Fig. 8. Comparison of the far-infrared spectra of crystalline and glassy  $0.50\text{CaO} \cdot 0.50\text{B}_2\text{O}_3$ . Dashed and dotted component bands resulted from the deconvolution of the glass spectrum.

#### 4. CONCLUSIONS

The glass-forming regions of alkaline earth borate glasses were determined and found to become wider with increasing cation size. The analysis of the infrared reflectance spectra, and comparison with recent NMR results, allowed the quantification of network structure in terms of the fraction of four-coordinated boron atoms,  $N_4$ . It was found that  $N_4$  increases with alkaline earth oxide content, MO, and attains maximum values at compositions depending on  $M^{2+}$  type. For glasses of the same MO content,  $N_4$  decreases from Ba to Mg, a trend opposite to that exhibited by alkali borate glasses. The Raman spectra have shown that this effect is due to the high field strength of the  $\text{Mg}^{2+}$  cations which induce a structural disproportionation into neutral (boroxol rings) and highly charged (pyroborates) borate units. Alkaline earth cations occupy two types of site (H and L), where they vibrate with characteristic frequencies  $\nu_H$  and  $\nu_L$ , respectively. Comparison of the far infrared spectra of glasses and crystals of the same metal oxide content has indicated that the H-type sites are better organized than the L-type sites.

#### REFERENCES

- [1] S.G. Bishop & P.J. Bray, *Phys. Chem. Glasses* **7** (1966), 73.
- [2] S. Greenblatt & P.J. Bray, *Phys. Chem. Glasses* **8** (1967), 190.
- [3] M.J. Park & P.J. Bray, *Phys. Chem. Glasses* **13** (1972), 50.
- [4] K.S. Kim & P.J. Bray, *Phys. Chem. Glasses* **15** (1974), 47.
- [5] W.J. Dell & P.J. Bray, *Phys. Chem. Glasses* **23** (1982), 98.
- [6] J. Krogh-Moe, *Phys. Chem. Glasses* **6** (1965), 46.
- [7] W.L. Konijnendijk & J.M. Stevels, *J. Non-Cryst. Solids* **18** (1975) 331.
- [8] J. Lörosch, M. Couzi, J. Pelous, R. Vasher & A. Levasseur, *J. Non-Cryst. Solids* **69** (1984), 1.
- [9] E.I. Kamitsos, M.A. Karakassides & G.D. Chryssikos, *Phys. Chem. Glasses* **28** (1987), 203.

- [10] G.I. Exarhos P.J. Miller & W.M. Risen, *J. Chem. Phys.* **60** (1974), 4145.
- [11] E.I. Kamitsos, M.A. Karakassides & G.D. Chryssikos, *J. Phys. Chem.* **91** (1987), 5807.
- [12] E.I. Kamitsos, *J. Phys. Chem.* **93** (1989), 1604.
- [13] E.I. Kamitsos, G.D. Chryssikos, A.P. Patsis & J.A. Duffy, *J. Non-Cryst. Solids* **196** (1996), 249.
- [14] V.O. Kabanov, G.P. Sedmale & O.V. Yanush, *Fiz. Khim. Stekla* **16** (1990), 83.
- [15] T. Huebert, U. Banach, K. Witke & P. Reich, *Phys. Chem. Glasses* **32** (1991), 58.
- [16] E.I. Kamitsos, G.D. Chryssikos & M.A. Karakassides, *J. Phys. Chem.* **91** (1987), 1067; **91** (1987), 1073.
- [17] B.N. Meera & J. Ramakrishna, *J. Non-Cryst. Solids* **159** (1993), 1.
- [18] M. Karakassides, *Ph.D. Thesis* (Athens University, 1990).
- [19] E.I. Kamitsos, A.P. Patsis, M.A. Karakassides & G.D. Chryssikos, *J. Non-Cryst. Solids* **126** (1990), 52.
- [20] Y.J. Kim, S.H. Lee, T.W. Noh & J. Kim, *J. Non-Cryst. Solids* **170** (1994), 190.
- [21] E.I. Kamitsos, A.P. Patsis & G.D. Chryssikos, *J. Non-Cryst. Solids* **152** (1993), 246.
- [22] G. D. Chryssikos, J. A. Kapoutsis, E. I. Kamitsos, A. P. Patsis & A. J. Pappin, *J. Non-Cryst. Solids* **167** (1994), 92.
- [23] J.A. Kapoutsis, E.I. Kamitsos & G.D. Chryssikos, *Proc. Second Int. Conf. on Borates Glasses, Crystals and Melts*, 303.
- [24] J. Zhong & P.J. Bray, *J. Non-Cryst. Solids* **111** (1989), 67.
- [25] E.I. Kamitsos, M.A. Karakassides & G.D. Chryssikos, *Phys. Chem. Glasses* **30** (1989), 229.
- [26] G.D. Chryssikos, J.A. Kapoutsis, A.P. Patsis & E.I. Kamitsos, *Spectrochimica Acta* **47A** (1991), 1117.
- [27] T. Bogang, W. Guozhen & X. Ruiya, *Spectrochimica Acta* **43A** (1987), 65.
- [28] A. Rulmont & M. Almou, *Spectrochimica Acta* **45A** (1989), 603.
- [29] E.I. Kamitsos, Y.D. Yiannopoulos, H. Jain & W.C. Huang, *Phys. Rev.* **B54** (1996), 9775.





---

## Author Index

	Page
<b>A</b>	
N. Abd-Elshafi	377
M. Affatigato	246
Y. Akasaka	435
F. Alamgir	498
N.S. Andreev	107
<b>B</b>	
J.D. Bass	349
J.F. Bauer	324
D.M. Beall	239
G. Bhasin	246
A. Bhatnagar	246
S. Bhowmik	246
R. Boekenhauer	246
N.A. Bokov	107
L. Börjesson	348, 425
M. Braun	21
P.J. Bray	1
R.S. Bubnova	120
K. Budhwani	246
M.A. Bursukova	231
<b>C</b>	
W. Cermignani	239
J. Cho	279
G.D. Chryssikos	128, 303, 514
S.-J. Chung	42
R.A. Condrate, Sr.	164
A.N. Cormack	443
D.A.H. Cunningham	99, 468
<b>D</b>	
G. Dalba	295
S.M. Del Nery	392
Y.B. Dimitriev	112, 231
V.V. Dimitrov	112
Y. Ding	453
S.P. Djambazov	461

	<b>E</b>	
H.A. El Batal		474
	<b>F</b>	
D. Feil		246
S.A. Feller		140, 246, 498, 506
J.F. Fernandez		207
S.K. Filatov		120
P. Fornasini		295
M. Frank		332
S. Fujitsu		370
J. Fukunaga		199
	<b>G</b>	
P.H. Gaskell		71
E.M. Gattef		112
K. Gatterer		384
V.V. Golubkov		88
	<b>H</b>	
K. Handa		99, 468
A.C. Hannon		140
U. Harder		156
F.L. Harding		324
S. Hayakawa		263, 490
P.D. Hinkov		231
K. Hirao		399
W. Höland		332
H. Hosono		370
T. Hübert		156
	<b>I</b>	
Y.Y. Ivanova		461
Y. Iwadate		99, 468
	<b>J</b>	
H. Jain		287
A.K. Jilavenkatesa		164
B.C. Johanson		140, 506
	<b>K</b>	
S. Kambeyanda		246
N. Kamijo		99, 468
E.I. Kamitsos		128, 287, 303, 514

J.A. Kapoutsis	287, 303, 514
E.P. Kashchieva	231, 461
K. Kawamura	370
H. Kawazoe	370
P. Keller	323
F.A. Khalifa	474
M.A. Khusainov	484
J. Kieffer	349
H.-T. Kim	42
T. Kimura	323
M.I. Klinger	357
T. Kloss	323
M. Kodama	181
S. Kojima	181
G. Kordas	148
J. Kottke	246
M.G. Krzhizhanovskaya	120

## L

K.A. Landa	364
L.M. Landa	364
G. Lautenschläger	323
W. Linz	323
K. Loh	498

## M

J. Mackenzie	246
S.W. Martin	262, 279
J.E. Masnik	349
S. Matsumoto	173
M.T. Mayhew	140, 506
B.M. Meyer	140
A.C. Miller	287
Y. Miura	173, 453
F. Monti	295
M.M. Morsi	377
G. Mosel	156
C. Murakami	173

## N

T. Nagase	271
S. Nakaoka	453
T. Nanba	173, 453
S. Nijhawan	246

	<b>O</b>	
C. Ohtsuki		490
M.I.T. Oliveira		392
A. Osaka		263, 453, 490
R. Ota		199
	<b>P</b>	
P. Pandikuthira		246
C.G. Pantano		239
K. Papadopoulos		340
C. Parameswar		246
B. Park		443
M.-J. Park		42
A.M. Peters		498
H. Poisl		63
I.G. Polyakova		120, 223
W.M. Pontuschka		392
E.A. Porai-Koshits		51
C. Prieto		207
	<b>Q</b>	
J. Qiu		399
	<b>R</b>	
M.A. Ramos		207
B.J. Reardon		349
C. Rhee		33
V. Rheinberger		332
F. Rocca		295
M.L. Royle		140, 246, 279
H.H. Russell, III		324
	<b>S</b>	
K. Sakane		271
K. Schneider		323
S. Sen		34
M. Seto		370
B.A. Shakhmatkin		80, 189, 215
M. Sharma		246
Y. Shimizugawa		399
M.M. Shultz		215
K. Sieber		340
V.N. Sigaev		254
R.N. Sinclair		140, 506

R.A. Smith	313
J.F. Stebbins	34
N. Sugimoto	399
J. Swenson	425
G.A. Sycheva	254

## T

Y. Takahashi	323
S.N. Taraskin	357
M. Teter	407
E.V. Tokareva	223
K. Tsuru	490

## U

T. Uchino	417
D.R. Uhlmann	63
N. Umesaki	99, 468

## V

N.M. Vedishcheva	80, 189, 215
P. Venhuizen	498
S. Vieira	207

## W

H. Wada	271
T. Wakasugi	199
A.J. Wanless	140, 506
M.C. Weinberg	63
J. Welter	246
D.L. Wilkerson	140
R.B. Williams	140, 498, 506
K. Witke	156
A.C. Wright	51, 80, 112, 140, 189, 215, 484, 506

## X

X. Xu	324
-------	-----

## Y

I. Yasui	435
J.J.L. Yi	513
Y.D. Yiannopoulos	514
T. Yoko	417
A.P. Yoleva	461
R.E. Youngman	21

H. Zhang  
J.W. Zwanziger

**Z**

246  
21

## Subject Index

	Page
<b>A</b>	
Absorption	
Spectroscopy	384, 399
Spectrum	384
Acoustic Properties	181
Activity Coefficient, Sodium Oxide	199
Ag <sup>+</sup> Ion	295
Distribution	303
AgI	287, 295
Ag-O Bonding	303
Ag <sub>2</sub> O.4B <sub>2</sub> O <sub>3</sub>	71
Alkali	
Borate	
Crystal	1, 80, 88
Glass	1, 21, 51, 80, 173, 181, 295, 417, 453, 506
Melt	51
Borosilicate	
Crystal	223
Glass	
Mechanical Properties	246
Structure	246
System	223
Oxyfluoroborate Glass	263
Thioborate Glass	262, 279
Alkaline Earth	
Borate	
Crystal	80
Glass	80, 173
Structure	514
Borophosphate Glass	254
AlO <sub>4</sub> Vibration	474
α-RbB <sub>3</sub> O <sub>5</sub>	120
AlPO <sub>4</sub>	239
Aluminoborate Glass	239, 392
Amorphous Metallic Alloy	484
Apatite	490
Associated Solutions Model	189, 215
Asymmetry Parameter (NMR)	1

## B

B <sub>2</sub> O <sub>3</sub>	1, 88, 107, 164, 207, 239, 417, 425, 443
Effect on Metallic Glass	484
B <sub>2</sub> O <sub>3</sub> -GeO <sub>2</sub> Glass	164
B <sub>2</sub> O <sub>3</sub> -SiO <sub>2</sub> Glass	164
Barium	
Aluminoborate Glass	392
Borate Glass	173, 514
Borophosphate Glass	254
Borosilicate Glass	513
Haloborate Glass	340
β-RbB <sub>3</sub> O <sub>5</sub>	120
Bi <sub>2</sub> O <sub>3</sub>	461
-B <sub>2</sub> O <sub>3</sub> Glass	112
Bioactivity	490
Biosolubility	324
Bond Angle	425, 435, 443
Borate	
Containing Glass	164
Crystal	
Structure	71, 128
Glass	33
Anomaly	1, 63
Structure	71, 128, 303, 498, 506
Melt	349
Structural Groupings	1, 42, 128, 156, 435, 474
Boroleucite	
Anomaly	223
Crystal	223
Boron	
Co-ordination Number	21
Electron Centre	392
Implantation	370
Oxide	164
Anomaly	63, 513
Crystal	1, 148, 407, 443
Crystallisation (from Melt)	80
Glass	1, 80, 107, 140, 207, 443
Density	80
Structure	88, 407, 417, 425
Water Content	207
Liquid-Glass Transition	348
Melt	349
Boron-Oxygen Hole Centre	392



Boron Sulphide	279
Borosilicate	
Fibreglass	313, 324
Glass	33, 34, 231, 246, 323, 324, 364, 514
Fibre	324
History	313
Mechanical Properties	246
Structure	246
Boroxol	
Group	80, 140, 231, 407
Ring	21, 156, 199, 425, 443
Bray Model	80, 364
Bridging Oxygen Atom	287
Brillouin Scattering	207, 349

## C

Ca <sup>2+</sup> Ion Environment	468
Calcium	
Borate Glass	514
Borophosphate Glass	254
Metaborate	1
CaO.B <sub>2</sub> O <sub>3</sub>	1
CaO-K <sub>2</sub> O-B <sub>2</sub> O <sub>3</sub> Glass	468
Catalysed Crystallisation	254
Cation Environment	514
Ce <sup>3+</sup> Ion	399
Ceramic Tile	461
Cesium	
Borate	
Glass	173, 181
Structure	71, 506
Borosilicate Glass	
Mechanical Properties	246
Structure	246
Thioborate Glass	279
Triborate	71
Chain	128
Chemical	
Inhomogeneity	88
Structure	287
Chlorine Evaporation	271
Cluster Calculation	417
Clustering	506
Coating	461

Cobalt Metaborate	484
$\text{CoB}_2\text{O}_4$	484
Compressibility	107
Computer Simulation	231, 407, 443
Reverse Monte Carlo	425
Co-ordination	
Dependent Potential	443
Number	99, 156, 199, 443
Correlation Function (Real Space)	112
Coupling Constant (NMR)	1
Crystal Structure	80, 120
Crystallisation	254, 340, 474
Catalysed	254
Kinetics	254
$\text{Cs}_2\text{O} \cdot 3\text{B}_2\text{O}_3$	71
$\text{CsLiB}_6\text{O}_{10}$	453

## D

Debye Temperature	207
Decoration	461
Defect	399
Degenerate Excited State Model	107
Degree of Crystallinity	254
Density	199, 246, 262, 279, 498, 506
Fluctuations	51
Structural Model	279
Dental Glass Ceramic	332
Diborate	
Crystal Structures	80
Group	42
Modified (by Al)	42
Differential	
Scanning Calorimetry	See DSC
Thermal Analysis	See DTA
Diffusion	34
Distribution, Sodium Oxide	199
Doped Glass	384
DSC	207, 364
DTA	254, 271, 461, 474, 484
DV-Xa Cluster Method	173
Dynamic Angle Spinning (NMR)	21
Dynamical Properties	348, 357, 407

## E

Elastic	
Constants	181, 207
Properties	207, 357
Electric Field Gradient	1
Electrical Conductivity	189
Electron	
Diffraction	231
Paramagnetic Resonance	See EPR
Spin Echo Envelope Modulation Spectroscopy	148
Spin Resonance	See ESR
Electronegativity	239
Electronic	
Excitation	370
Properties	357
Structure	173
Enamel	313
EPR	148, 392
ESR	513
Europium Doped Glass	340
EXAFS	99, 156, 295, 468
Extended X-Ray Absorption Fine Structure	See EXAFS

## F

F <sup>-</sup> Ion	263
Far Infrared Spectrum	303, 417
Fast Ion Conductor	287, 295
Fatigue Resistance Parameter	324
Fe <sup>3+</sup> Ion	392
Fibreglass	313, 324
Borosilicate	313, 324
History	313
Insulation	324
Fictive Temperature	34
First (Sharp) Diffraction Peak	71, 425, 506
Flat Glass	323
Float Process	323
Fluorescence	399
Spectroscopy	399
Four-Fold Co-ordinated Boron Atoms	21, 34, 215
Fourier Transform EPR Spectroscopy	148
Frit	461

## G

$\gamma$ -Irradiation	148
Gibbs Free Energy	263
Mixing	189
Glass	
Ceramic	332, 340, 474
Density	189
Fibre	324
Formation	340, 349
Forming	
Region	80, 262
Systems	120, 223
Science, History	313
Structure	63, 128, 215, 223
Synthesis	254
Transition	107
Order Parameter	364
Temperature	34, 207, 223, 254, 262, 498
Effect of Water Content	207
Glaze	313, 461

## H

Hägg Model	1
Halide-Oxide Glass	340
Haloborate Glass	340
Hardness	461
Heat	
of Mixing	263
Treatment	474
Heterogeneity	231
High	
Alkali Glass	498
Pressure	357
Temperature	
Crystal Chemistry	120
NMR	34
Raman Spectroscopy	164
SAXS	88
Viscosity	324
History	313
Borate Glass	313
Borosilicate Glass	313
Fibreglass	313, 324
Hydrated Silica Gel	490

Hypersensitive Transition	384
Hysteresis Loop	484

## I

Inductively Coupled Plasma Spectrophotometry	514
Ideal Solution	189
Immiscibility	51
Infrared	See IR
Inhomogeneity	51, 88
Interatomic Potential	99, 435, 468, 443
3-Body	435
Intermediate	
Angle X-Ray Scattering	51
Range Order	21, 295, 425
Iodoborate	287
Ion	
Implantation	370
Scattering Spectroscopy (ISS)	239
Ionic	
Activity Product	490
Conductivity	295
IR	
Reflection Spectrum	303, 490, 514
Spectroscopy	112, 128, 156, 303, 461, 474, 514
Spectrum	417
Iron Doped Glass	392
Isothermal Compressibility	51, 107

## J

## K

K <sup>+</sup> Ion Environment	99, 468
K <sub>2</sub> O-Al <sub>2</sub> O <sub>3</sub> -SiO <sub>2</sub> System	332
Kokubo Solution	490
Krogh-Moe Model	1

## L

Landa-Patashinskii Model	364
Lead	
Borate Glass	156, 377, 435
Diborate	1
Leucite	223, 332
LiBO <sub>2</sub>	474
Li <sub>2</sub> B <sub>8</sub> O <sub>13</sub>	474

Li <sub>4</sub> B <sub>7</sub> O <sub>12</sub> Cl	271
Li <sub>2</sub> O.B <sub>2</sub> O <sub>3</sub>	1
Li <sub>2</sub> O.2B <sub>2</sub> O <sub>3</sub>	1, 71
Li <sub>2</sub> O-B <sub>2</sub> O <sub>3</sub> -Al <sub>2</sub> O <sub>3</sub> Glass	42
Light Scattering	107, 349
Lineshape (NMR)	1
Dependence on Quadrupolar Parameters	1
Liquid Phase Separation	223
Liquidus Temperature	51, 324
Lithium	
Aluminoborate Glass	474
Boracite	271
Borate	
Crystal	1
Glass	128, 148, 173, 181, 474
Structure	71, 498, 506
Melt	189
Borosilicate Glass	
Structure	246
Mechanical Properties	246
Chloroboracite	271
Preparation	271
Powder	271
Film	271
Diborate	1, 71
Metaborate	1, 474
Silicate Glass Structure	498
Tetraborate	474
Vibration	474
Low	
Charge Density Oxygen Atom	287
Frequency	
Raman Spectrum	417
Vibrational Modes	417
Luminescence	340, 399
Quenching	392
<b>M</b>	
Magic Angle Spinning (MAS) NMR	34, 263, 514
Magnesium Borate Glass	514
Magnetic Properties	484
Magnetically Soft Alloy	484
Magnetisation	484
MD Simulation	99, 435, 468, 443

Mechanical Properties	246
Medium Range Order	21, 71, 215, 295, 417
Melt	189
Quenching	231
Spinning	484
Structure	34, 215
Metaborate Structure	128
Metallic Glass	484
Microfloat Process	323
Microheterogeneous Structure	88
Mixed Alkali Effect	128
Mn <sup>2+</sup> Ion	513
Mode Coupling Theory	348
Model of Associated Solutions	189, 215
Molar Volume	199, 498
Molecular	
Dynamics	See MD
Orbital Calculation	148, 173, 263, 417
Ab Initio	435
MNDO	148
MOPAC	263
N	
N <sub>4</sub>	1, 34, 42, 63, 80, 181, 215, 303, 514
Model	42
Na <sub>2</sub> O-B <sub>2</sub> O <sub>3</sub> -GeO <sub>2</sub> System	199
Na <sub>2</sub> O-B <sub>2</sub> O <sub>3</sub> -SiO <sub>2</sub>	164
Nd <sup>3+</sup> Ions	384
Negative	
Pressure Glass	364
-U Centre	357
Neodymium Ions	384
Network Structure	303, 514
Neutron	
Diffraction	71, 295, 425, 435, 506
Inelastic Scattering	140
Scattering Law	140
NMR	1, 33, 42
Boron Isotopes	1
Double Rotation	21
Dynamic Angle Spinning	21
Magic Angle Spinning (MAS)	34, 263, 514
Spectroscopy	21, 34, 263
Spectrum	

Computer Simulation	1
Lineshape	1, 34
Quadrupolar Effects	1
Spin Lattice Relaxation Time	34
Non	
-Bridging Oxygen Atom	1, 239, 287, 384
Alkali Ion Dependence	1
-Stationary Nucleation	254
Nonlinear Optical Glass	453
NQR	1
High Resolution/Precision Spectroscopy	1
Nuclear	
Collision	370
Magnetic Resonance	See NMR
Quadrupole Resonance	See NQR
Nucleation	332
Non-Stationary	254
Stationary	254
	<b>O</b>
Opalescence	332
Optical	
Microscopy	254
Properties	332
Spectroscopy	377, 384, 399
Oxidation State	377
Oxyfluoroborate Glass	263
	<b>P</b>
Pair Correlation Function	425, 443
Paramagnetic Centres	148
Partial Entropy	189
Pauling Charge	239
Pb <sup>2+</sup> Ion Environment	156
PbO-B <sub>2</sub> O <sub>3</sub> System	80
PbO.2B <sub>2</sub> O <sub>3</sub>	1
Phase	
Diagram	120, 223
Separation	332
Transition on Relaxation	364
Photostimulated Luminescence	340, 399
Physical Properties	189
Poisson Ratio	349
Polymorphic Transitions	80



Polymorphism	128
Glass	364
Melt	364
Potassium	
Borate	
Glass	173, 468
Structure	21, 99, 506
Melt	189
Boroleucite	223
Borosilicate	
Glass	
Mechanical Properties	246
Structure	246
System	223
Metaborate	21
Thioborate Glass	279
Potential Parameters	443
Pressure-Induced Phenomena	357
Pseudophases	51

## Q

Q <sup>n</sup> Species	514
Quasi-Bragg Scattering	71
Quadrupolar Parameters (NMR)	1

## R

Radial	
Distribution Function	See RDF
Structure Function (XAFS)	468
Radiation Stimulation	340
Raman	
Spectroscopy	21, 99, 128, 140, 156, 164, 199, 303, 323, 514
Spectrum	370, 407, 417
RbB <sub>3</sub> O <sub>5</sub>	120
RbB <sub>5</sub> O <sub>8</sub>	120
Rb <sub>2</sub> B <sub>4</sub> O <sub>7</sub>	120
Rb <sub>3</sub> BO <sub>3</sub>	120
Rb <sub>3</sub> B <sub>7</sub> O <sub>12</sub>	120
RDF	231, 425, 435
Real Space Correlation Function	112
Redox Reaction	377
Refractive Index	120, 189
Regions of Inhomogeneity	88
Relaxation	349

Glass-Forming Melts	364
Spin Lattice (NMR)	34
Time (NMR)	34
Reverse Monte Carlo Simulation	407, 425
Rings	128, 164
Rubidium	
Borate	
Crystal Structure	120
Glass	140, 173
Structure	506
Melt	189
Borosilicate	
Glass	
Mechanical Properties	246
Structure	246
System	223
Diborate	120
Pentaborate	120
Orthoborate	120
Thioborate Glass	279

## S

SAXS	51, 88
Scanning Electron Microscopy	See SEM
SEM	271, 332, 490
Semiconducting Glass	357
Short Range Order	21, 215, 231, 295
<sup>29</sup> Si MAS NMR	490
Silanol Group	490
Silica	
Gel, Hydrated	490
Glass	370
Silicate Glass, Structure	498
Silver	
Borate	287
Crystal Structure	295
Glass Structure	71, 295, 303
Iodide	287, 295
Ion	295
Tetraborate	71
SiO <sub>2</sub> Glass	370
Si-Si Bonding	370
Six-Membered Rings	435
Sm <sup>3+</sup> Ion	399

Small Angle X-Ray Scattering	See SAXS
Sodium	
Borate	
Crystalline Polymorphs	80
Glass	173, 215, 384, 399
SAXS	88
Structure	1, 34, 88, 498, 506
Melt	189, 215, 349
System	199, 215
Borogermanate System	199
Borosilicate	
Glass	1, 164, 384, 513
Mechanical Properties	246
Structure	246
System	223
Germanate System	199
Oxide	
Activity	199
Affinity	199
Oxyfluoroborate Glass	263
Silicate	
Glass	189, 384
Structure	34, 498
Thioborate Glass	279
Soft Configuration Model	357
Sol-Gel	
Glass	231
Technique	271
Sound Velocity	181, 207
Spin-Lattice Relaxation Time (NMR)	34
Sr <sup>2+</sup> Ion Environment	156
Stationary Nucleation	254
Strontium	
Borate Glass	156, 514
Borophosphate Glass	254
Structural	
Changes, Temperature Dependent	164
Grouping	1, 128, 513
Model	435
Relaxation	34
Reorganisation	349
Unit	128, 181
Structure	34, 88, 112, 156, 231, 262, 295
Chemical	287

Superstructural Units	51, 80, 140, 215
Surface	
Composition	239
Crystallisation	332, 453
Nucleation	453
Structure	239

## T

Tellurium Oxide	231, 461
TEM	231, 461
TeO <sub>2</sub>	231, 461
Thermal	
Density Fluctuations	51, 88
Expansion	63, 120, 324
$\alpha$ -RbB <sub>3</sub> O <sub>5</sub>	120
RbB <sub>5</sub> O <sub>8</sub>	120
Rb <sub>2</sub> B <sub>4</sub> O <sub>7</sub>	120
Rubidium	
Diborate	120
Pentaborate	120
Triborate	120
Thermodynamic	
Model	189, 215
Potential	189
Properties	263
Thermoluminescence	392
Thin Film	
Lithium Chloroboracite	271
X-Ray Diffraction	271, 514
Thioborate Glass	262, 279
TiB <sub>2</sub>	1
Tile	461
Tin Ion	377
Titanium Boride	1
Topology	407
Transmission Electron Microscopy	See TEM
Transport Properties	189

## U

Ultrasonic	
Surface Treatment	453
Velocity	181
Ultraviolet	See UV
Unpaired Electron Centre	148

Uranium Ion	377
UV Absorption	
Edge	377
Spectrum	370

## V

Vacuum UV Absorption Spectrum	370
Velocity of Sound	181, 207
Vibrational	
Density of States	140, 407
Spectroscopy	128, 474
Spectrum	417
Vickers Hardness	461
Visco-Elastic Properties	349
Viscosity	34, 349
Visible Light Scattering	107
Vitreous Boron Oxide	See Boron Oxide Glass

## W

Water Content	207, 254
Effect on Nucleation Rate	254

## X

XAFS	99, 468
XANES	99, 295
XAS	295, 399
XPS	173, 239, 263, 287
X-Ray	
Absorption	
Fine Structure	See XAFS
Near Edge Structure	See XANES
Spectroscopy	See XAS
Analysis	254
Correlation Function	112
Diffraction	120
Glass	71, 99, 112, 295, 425, 435
Polycrystalline	120, 223, 254, 271, 461, 474, 484
Single Crystal	120
Surface	453
Irradiation	399
Phosphor	340
Photoelectron Spectroscopy	See XPS
Sensor	399

**Y**

**Z**

Zinc Phosphate Glass

Zirconium Boride

ZrB<sub>2</sub>

189

1

1

## Appendix 1

### Conference Participants

**Professor M. Affatigato**

*Department of Physics, Coe College, Cedar Rapids, IA 52402, USA.*  
Tel: +1 319 399 8483. Fax: +1 319 399 8748. E-mail: maffatig@coe.edu

**Dr. Y. Akasaka**

*Opto-Technology Laboratory, Furukawa Electric Co. Ltd., 6 Yawata Kaigan  
Dori, Ichihara 290, Japan.*  
Tel: +81 436 42 1772. Fax: +81 436 42 9340. E-mail: akasaka@optec.ch.furukawa.co.jp

**Dr. R.J. Araujo**

*Corning Incorporated, Research, Development & Engineering Divisions,  
SP FR 03 01, Corning, NY 14831, USA.*  
Tel: +1 607 974 3432. Fax: +1 607 974 3675. E-mail: araujo-rj@corning.com

**Dr. M. Austerberry**

*Borax Europe Ltd., 170 Priestley Road, Guildford, GU2 5RQ, UK.*  
Tel: +44 1483 734000. Fax: +44 1483 457676. E-mail: 100145,104@compuserve

**Mrs. B. Berger**

*Johann Wolfgang Goethe-Universität, Institut für Phys Theoretische Chemie,  
Marie-Curie Strasse 11, D-60439 Frankfurt am Main, Germany.*  
Tel: +49 69 798 29453. Fax: +49 69 798 29445

**Dr. N.A. Bokov**

*Institute of Silicate Chemistry, Russian Academy of Sciences, Ul Odoevskogo 24  
Korp 2, Sankt Petersburg 199155, Russia.*  
Tel: +7 812 351 0805. Fax: +7 812 351 0813. E-mail: vir@ihs.lspb.su

**Dr. L. Börjesson**

*Department of Applied Physics, Chalmers University of Technology, Goteborg  
S-412 96, Sweden.*  
Tel: +46 31 772 3307. Fax: +46 31 7 722090. E-mail: borje@fychalmers.se

**Professor P.J. Bray**

*Department of Physics, Box 1843, Brown University, Providence, RI 02912, USA.*  
Tel: +1 401 863 2587. Fax: +1 401 863 2024. E-mail: bray@physics.brown.edu

**Mrs. H.C. Brook**

*Department of Chemistry, University of Kent, Canterbury, CT2 7NH, UK.*  
Tel: +44 1233 740978. Fax: +44 1233 740978. E-mail: challock@dial.pipex.com

**Dr. P. Chrysicopoulou**

*Materials Science, National Centre NSCR Demokritos, Agia Pavaskavi Attica,  
Athens 15310, Greece.  
Tel: +30 1 957 7051. Fax: +30 1 957 7050. E-mail: mousdis@cycladesmatersci.ariadne-t.gr*

**Dr. G.D. Chryssikos**

*Theoretical & Physical Chemistry Institute, National Hellenic Research Foundation,  
48 Vass Constantinou Ave., Athens 11635, Greece.  
Tel: +30 1 724 9483. Fax: +30 1 724 9104.  
E-mail: chryss@apollo.servicenet.ariadne-t.gr*

**Professor Dr. H.-U. Chun**

*Johann Wolfgang Goethe-Universität, Institut für Phys Theoretische Chemie,  
Marie-Curie Strasse 11, D-60439 Frankfurt am Main, Germany.  
Tel: +49 69 798 29453. Fax: +49 69 798 29445.*

**Professor S.-J. Chung**

*Department of Physics, Chonnam National University, 300 Yongbong-Dong,  
Buk-ku Kwangju, 500 575 Korea.  
Tel: +82 62 520 6833. Fax: +82 62 521 6562.*

**Professor R.A. Condrate, Sr.**

*Ceramic Engineering and Science, New York State College of Ceramics, Alfred  
University, Alfred, NY 14802, USA.  
Tel: +1 607 871 2446. Fax: +1 607 871 2392. E-mail: fcondrate@bigvax.alfred.edu*

**Professor A.N. Cormack**

*New York State College of Ceramics, Alfred University, Alfred, NY 14802-1296, USA.  
Tel: +1 607 871 2448. Fax: +1 607 871 2354*

**Dr. A. Dean-Wray**

*Borax Europe Ltd, 170 Priestley Road, Guildford, GU2 5RQ, UK.  
Tel: +44 1483 734000. Fax: +44 1483 457676. E-mail: 100145,104@compuserve*

**Professor Y.B. Dimitriev**

*University of Chemical Technology and Metallurgy, 8 Boulevard Kliment  
Ohridski, 1756 Sofia, Bulgaria.  
Tel: +359 262 54234. Fax: +359 268 5488. E-mail: ybd%hti@bgcict.acad.bg*

**Dr. Y. Ding**

*Faculty of Environmental Science & Technology, Department of Environmental  
Chemistry, & Materials, Okayama University, 2-1-1 Tsushima-naka, Okayama  
Shi 700 Japan.  
Tel: +81 86 251 8102. Fax: +81 86 253 5755. E-mail: ding@cc.okayama-u.ac.jp*



**Dr. S. Djambazov**

*University of Chemical Technology and Metallurgy, 8 Boulevard Kliment Ohridski,  
1756 Sofia, Bulgaria.  
Tel: +359 262 54214. Fax: +359 268 5488.*

**Dr. O. El Bayoumi**

*US Air Force, ESC/1A, 50 Griffiss Street, Hanscom AFB, MA 10731-1618, USA.  
Tel: +1 617 271 7341. Fax: +1 617 271 8663. E-mail: elbayounio@escia.hanscom.af.mil*

**Professor S.A. Feller**

*Coe College, Department of Physics, 1220 First Ave N.E., Cedar Rapids, IA 52402, USA.  
Tel: +1 319 399 8633. Fax: +1 319 399 8748. E-mail: sfeller@coe.edu*

**Professor S.K. Filatov**

*Department of Crystallography, St. Petersburg University, University Emb 719,  
St. Petersburg 199 034, Russia.  
Tel: +7 812 218 9577. Fax: +7 812 218 0792. E-mail: flt@cryst.geol.pu.ru*

**Dr. P.H. Gaskell**

*Cavendish Laboratory, University of Cambridge, Madingley Road, Cambridge,  
CB3 7HB, UK.  
Tel: +44 1223 337290. Fax: +44 1223 363263. E-mail: phg1@cam.ac.uk*

**Dr. E.M. Gattef**

*University of Chemical Technology and Metallurgy, 8 Boulevard Kliment Ohridski,  
1756 Sofia, Bulgaria.  
Tel: +359 262 54411. Fax: +359 268 5488. E-mail: emg%hti@bgcict.acad.bg*

**Dr. K. Gatterer**

*Institut für Phys & Theor Chem, Technische Universität Graz, A-8010 Graz,  
Rechbauerstrasse 12, Austria.  
Tel: +43 316 873 8239. Fax: +43 316 873 8225. E-mail: gatterer@ptc.tu-graz.ac.at*

**Dr. V.V. Golubkov**

*Institute of Silicate Chemistry, Odoevskogo 24, St. Petersburg 199 155, Russia.  
Tel: +7 812 351 0805. Fax: +7 812 351 0813. E-mail: vir@ihsl.spb.su*

**Ms. E. Graznak**

*Coe College, Department of Physics, 1220 First Ave N.E., Cedar Rapids, IA 52402, USA.  
Tel: +1 319 399 8483. Fax: +1 319 399 8748*

**Mr. K. Handa**

*Department of Physics, Ritsumeikan University, 1916 Noji-cho, Kusatsu, Siga 525-77, Japan.  
Tel: +81 775 66 1111. Fax: +81 775 61 2657. E-mail: qzt02057@niftyserve.or.jp*

**Dr. A.C. Hannon**

*ISIS Facility, Rutherford Appleton Laboratory, Chilton, Didcot, Oxon, OX11 0RX, UK  
Tel: +44 1235 445358. Fax: +44 1235 445720. E-mail: ach@rl.ac.uk*

**Dr. F.L. Harding**

*Mountain Technical Centre, Schuller International, P.O. Box 625005, Littleton,  
CO 80162-5005, USA.  
Tel: +1 303 978 3269. Fax: +1 303 978 3123. E-mail: hardingf@schuller.com*

**Dr. S. Hayakawa**

*Biomaterials Laboratory, Faculty of Engineering, Okayama University, Tsushima,  
Okayama-shi 700, Japan.  
Tel: +81 86 251 8214. Fax: +81 86 252 7889. E-mail: satochi@cc.okayama-u.ac.jp*

**Ms. D. Hogan**

*Coe College, Department of Physics, 1220 First Ave N.E., Cedar Rapids, IA 52402, USA.  
Tel: +1 319 399 8483. Fax: +1 319 399 8748.*

**Dr. W. Höland**

*Research & Development, IVOCAR AG, Bendererstrasse 2, Schaan FL 9494,  
Lichtenstein.  
Tel: +41 75 235 3535. Fax: +41 75 233 1279. E-mail: ivoclar.ea@dm.rs.ch*

**Dr. T. Hübner**

*Bundesanstalt für Materialforschung & Prüfung (BAM), Unter den Eichen 44-46,  
D-12203 Berlin, Germany.  
Tel: +49 30 81 04 18 24. Fax: +49 30 81 04 18 27. E-mail: hubert@ah.bam.berlin.de*

**Professor H. Jain**

*Department of Materials Science & Engineering, Lehigh University, Whitaker  
Laboratory, 5 East Packer Avenue, Bethlehem, PA 18015-3195, USA.  
Tel: +1 610 758 4217. Fax: +1 610 758 4244. E-mail: hj00@lehigh.edu*

**Dr. E.I. Kamitsos**

*Theoretical & Physical Chemistry Institute, National Hellenic Research Foundation,  
48 Vass Constantinou Ave., Athens 11635, Greece.  
Tel: +30 1 724 9483. Fax: +30 1 724 9104.  
E-mail: eik@apollon.servicenet.ariadne-t.gr*

**Mr. J.A. Kapoutsis**

*Theoretical & Physical Chemistry Institute, National Hellenic Research Foundation,  
48 Vass Constantinou Ave., Athens 11635, Greece.  
Tel: +30 1 724 7973. Fax: +30 1 724 9104.  
E-mail: jkap@apollon.servicenet.ariadne-t.gr*

**Professor H. Kawazoe**

*Materials & Structure Laboratory, Tokyo Institute of Technology, Nagatsuta  
Midori-ku, Yokohama 226, Japan.  
Tel: +81 45 924 5357. Fax: +81 45 922 5169.  
E-mail: kawazoe1@rlem.titech.ac.jp*

**Professor F.A. Khalifa**

*National Research Centre, Tahrir Street, Dokki, Cairo, Egypt.  
Tel: +20 2 701 211. Fax: +20 2 337 0931.*

**Professor M.A. Khusainov**

*Mech/Phys of Strength Mater & Constr, State University, 41 Bolshaya Sankt-  
Peterburgskaya, 173 003 Novgorod, Russia.  
Tel: +7 816 222 9962. Fax: +7 816 222 4110. E-mail: nic@lannovsu.ac.ru*

**Dr. J. Kieffer**

*Department of Materials Science & Engineering, 105 South Goodwin Avenue,  
University of Illinois, Urbana, IL 61801, USA.  
Tel: +1 217 244 0189. Fax: +1 217 244 6917. E-mail: breardon@aiac.edu*

**Professor H.-T. Kim**

*Department of Physics Education, Chonnam National University, 300 Yongbong-  
Dong, Buk-ku Kwangju, 500 575 Korea.  
Tel: +82 62 520 6593. Fax: +82 62 521 6562.*

**Professor M.I. Klinger**

*Bar-Ilan University, Department of Physics, 52900 Ramat Gan, Tel Aviv, Israel.  
Tel: +972 3 531 8726. Fax: +972 3 535 3298. E-mail: klinger@physnet.ph.biu.ac.il*

**Dr. T. Kloss**

*Flat Glass Division, JENA Glaswerk GmbH, Otto-Schott-Str. 13, D-07745 Jena,  
Thuringia, Germany.  
Tel: +49 3641 681 602. Fax: +49 3641 681 709.*

**Professor M. Kodama**

*Department of Industrial Chemistry, Kumamoto Institute of Technology, Ikeda  
4-22-1, Kumamoto shi, Kumamoto 860, Japan.  
Tel: +81 96 326 3111. Fax: +81 96 326 3000.  
E-mail: kodama@chem.kumamoto-it.ac.jp*

**Mr. P. Koopman**

*Coe College, Department of Physics, 1220 First Ave N.E., Cedar Rapids, IA 52402,  
USA.  
Tel: +1 319 399 8483. Fax: +1 319 399 8748. E-mail: pkoopman@coe.edu*

**Professor G. Kordas**

*Materials Science, National Centre NSCR "Demokritos", Agia Paraskevi Attikis, Athens 15310, Greece.*

*Tel: +30 1 654 7690. Fax: +30 1 651 9430. E-mail: kordas@cyclades.nrcps.ariadne-t.gr*

**Professor L. Landa**

*Glass R&D, Lancer Tech Inc., 218 South 5th, Jeannette, PA 15644, USA.*

*Tel: +1 412 523 8097. Fax: +1 412 523 4327.*

**Professor A.J. Leadbetter**

*Institut Laue-Langevin, Avenue des Martyrs, B.P. 156, F-39042 Grenoble Cedex 9, France.*

*Tel: +33 76 20 71 00. Fax: +33 76 96 11 95. E-mail: Leadbetter@ill.fr*

**Professor S.W. Martin**

*Iowa State University, Department Materials Science & Engineering, 110 Engineering Annex, Ames, IL 50011, USA.*

*Tel: +1 515 294 5606. Fax: +1 515 294 5444.*

**Mr. S. Matsumoto**

*Department Environmental Chemistry & Materials, Okayama University, 2-1-1 Tsushima-Naka, Okayama-shi, 700 Japan.*

*Tel: +81 86 251 8102. Fax: +81 86 253 5755. E-mail: syuji@cc.okayama-u.ac.jp*

**Mr. M. Mayhew**

*Coe College, Department of Physics, 1220 First Ave N.E., Cedar Rapids, IA 52402, USA.*

*Tel: +1 319 399 8483. Fax: +1 319 399 8748.*

**Mr. B. Meyer**

*Coe College, Department of Physics, 1220 First Ave N.E., Cedar Rapids, IA 52402, USA.*

*Tel: +1 319 399 8483. Fax: +1 319 399 8748. E-mail: bmeyer@coe.edu*

**Professor Y. Miura**

*Faculty of Environmental Science & Technology, Department of Environmental Chemistry & Materials, Okayama University, 2-1-1 Tsushima-naka, Okayama Shi 700, Japan.*

*Tel: +81 86 251 8100. Fax: +81 86 253 5755. E-mail: miuray@cc.okayama-u.ac.jp*

**Dr. M.M. Morsi**

*National Research Centre, Tahrir Street, Dokki, Cairo, Egypt.*

*Tel: +20 2 33 701211. Fax: +20 2 33 70 931.*

**Ms. T. Nagase**

*Shikoku National Industrial Research Institute, 2217-14 Hayashi, Takamatsu 761-03, Japan.*

*Tel: +81 878 69 3526. Fax: +81 878 69 3551. E-mail: nagase@sniri.go.jp*

**Mr. N. Nelson**

*Coe College, Department of Physics, 1220 First Ave N.E., Cedar Rapids, IA 52402, USA.  
Tel: +1 319 399 8483. Fax: +1 319 399 8748.*

**Dr. M. D. Noirot**

*U.S. Borax Inc., 26877 Tourney Road, Valencia, CA 91355, USA.  
Tel: +1 805 287 5072. Fax: +1 805 287 6014.*

**Mr. R. O'Connor**

*Borax Europe Ltd., 170 Priestley Road, Guildford, GU2 5RQ, UK.  
Tel: +44 1483 734000. Fax: +44 1483 457676. E-mail: 100145,104@compuserve*

**Dr. C. Ohtsuki**

*IRC in Biomedical Materials, Queen Mary & Westfield College, Mile End Road,  
London E1 4NS, UK.  
Tel: +44 171 975 5285. Fax: +44 181 983 1799. E-mail: gfa03557@niftyserve.or.jp*

**Professor R. Ota**

*Department of Chemistry & Materials Technology, Kyoto Institute of Technology,  
Matsugasaki Sakyo-ku, Kyoto 606, Japan.  
Tel: +81 75 724 7565. Fax: +81 75 724 7580.*

**Dr. B. Ozaslan**

*Kalefrit Co., Can-Canakkale 17430, Turkey.  
Tel: +90 286 426 5124. Fax: +90 286 416 5840.*

**Professor C.G. Pantano**

*Pennsylvania State University, Materials Science and Engineering, 123 Steidle  
Building, University Park, PA 16802, USA.  
Tel: +1 814 863 2071. Fax: +1 814 865 0016.  
E-mail: pantano@ems.psu.edu*

**Dr. K. Papadopoulos**

*Eastman Kodak Co., Research Laboratories, Rochester, NY 14650-2022, USA.  
Tel: +1 716 477 9821. Fax: +1 716 722 3925. E-mail: kr25.lwb700@kodako.kodak.com*

**Dr. I.G. Polyakova**

*Institute of Silicate Chemistry, Odoevskogo 24-2, St. Petersburg 199 155, Russia.  
Tel: +7 812 351 0829. Fax: +7 812 218 5401. E-mail: vlad@ihs2.spb.su*

**Dr. W.M. Pontuschka**

*Universidade de Sao Paulo, Instituto de Fisica, Caixa Postal 66318, Sao Paulo  
05389-970, Brazil.  
Tel: +55 11 818 7073. Fax: +55 11 813 4334. E-mail: pontuschka@if.usp.br*

**Mr. D. Popowski**

*Coe College, Department of Physics, 1220 First Ave N.E., Cedar Rapids, IA 52402, USA.  
Tel: +1 319 399 8483. Fax: +1 319 399 8748. E-mail: dpopowsk@coe.edu*

**Professor E.A. Porai-Koshits**

*Institute of Silica Chemistry, Russian Academy of Sciences, Ul Odoevskogo 24  
Korp 2, Sankt Petersburg 199 155, Russia.  
Tel: +7 812 351 0805. Fax: +7 812 350 4816. E-mail: mazurin@termex.spb.su*

**Dr. J. Qiu**

*Hirao Active Glass Project, ERATO R&D Corporation of Japan, Keihanna Plaza  
1-7, Hikaridai, Seika-cho, Kyoto 619-02, Japan.  
Tel: +81 774 95 5205. Fax: +81 774 95 5206. E-mail: jrq@hap.jrdc.go.jp*

**Dr. M.A. Ramos**

*Departamento de Fisica de Materiales, Condensada C-III, Universidad Autónoma  
de Madrid, Cantoblanco, E-28049 Madrid, Spain.  
Tel: +34 1 397 5551. Fax: +34 1 397 3961. E-mail: mramos@vm1.sdi.uam.es*

**Dr. C. Rhee**

*Korea Research Institute of Standards and Science, PO Box 102, Yusong, Taejon  
305 600, Republic of Korea.  
Tel: +82 42 868 5008. Fax: +82 42 868 5022. E-mail: crhee@krissol.re.kr*

**Dr. F. Rocca**

*Centro CNR-ITC di Fisica, degli Stati Aggregati, I-38050 Povo (TN), Italy.  
Tel: +39 461 881 685. Fax: +39 461 881 680. E-mail: rocca@science.unitn.it*

**Mr. M. Royle**

*Materials Science & Engineering, Iowa State University, 3053 Gilman Hall, Ames,  
IA 50011, USA.  
Tel: +1 515 294 9345. Fax: +1 515 294 5444. E-mail: mroyle@iastate.edu*

**Dr. B.A. Shakhmatkin**

*Institute of Silicate Chemistry, Odoevskogo 24-2, St. Petersburg 199 155, Russia.  
Tel: +7 812 351 0810. Fax: +7 812 218 5401. E-mail: natalia@termex.spb.su*

**Mr. J. Simon**

*Borax Europe Ltd., 170 Priestley Road, Guildford, GU2 5RQ, UK.  
Tel: +44 1483 734000. Fax: +44 1483 457676. E-mail: 100145,104@compuserve*

**Professor R.N. Sinclair**

*J.J. Thomson Physical Laboratory, University of Reading, Reading RG6 6AF, UK.  
Tel: +44 1734 318543. Fax: +44 1734 750203. E-mail: r.n.sinclair@reading.ac.uk*

---

**Dr. R.A. Smith**

*U.S. Borax Inc., Technology Department, 26877 Tourney Road, Valencia, CA 91355, USA.  
Tel: +1 805 287 6070. Fax: +1 805 287 6014.*

**Professor J.F. Stebbins**

*Stanford University, Department of Geology, Stanford, CA 94305-2115, USA.  
Tel: +1 415 723 1140. Fax: +1 415 725 2199. E-mail: [stebbins@pangea.stanford.edu](mailto:stebbins@pangea.stanford.edu)*

**Mr. C. Stehle**

*Coe College, Department of Physics, 1220 First Ave N.E., Cedar Rapids, IA 52402, USA.  
Tel: +1 319 399 8483. Fax: +1 319 399 8748. E-mail: [cstehle@coe.edu](mailto:cstehle@coe.edu)*

**Dr. J. Swenson**

*Physics Department, Chalmers University of Technology, Fysikgrand 3, Gothenburg  
S-41296, Sweden.  
Tel: +46 31 772 3427. Fax: +46 31 772 3177. E-mail: [f5xjs@fy.chalmers.se](mailto:f5xjs@fy.chalmers.se)*

**Dr. G.A. Sycheva**

*Institute of Silicate Chemistry, Odoevskogo 24-2, St. Petersburg 199 155, Russia.  
Tel: +7 812 351 0829. Fax: +7 812 218 5401. E-mail: [vlad@isa2.spb.su](mailto:vlad@isa2.spb.su)*

**Dr. M.P. Teter**

*Department of Glass & Glass Ceramic Research, Corning Inc., FR-5 Sullivan Park,  
Corning, NY 14831, USA.  
Tel: +1 607 974 3457. Fax: +1 607 974 2410. E-mail: [teter\\_mp@corning.com](mailto:teter_mp@corning.com)*

**Professor L.M. Torell**

*Chalmers University of Technology, University of Gothenburg, Department of  
Physics, S-412 96 Gothenburg, Sweden.  
Tel: +46 31 772 3335. Fax: +46 31 7723 177. E-mail: [torrell@fychalmers.se](mailto:torrell@fychalmers.se)*

**Instructor T. Uchino**

*Institute for Chemical Research, Kyoto University, Gokasho, Uji Kyoto 611, Japan.  
Tel: +81 774 323 111. Fax: +81 774 335 212. E-mail: [uchino@scl.kyoto-u.ac.jp](mailto:uchino@scl.kyoto-u.ac.jp)*

**Professor D.R. Uhlmann**

*Materials Science & Engineering, A.M.L., University of Arizona, 4715 E. Fort  
Lowell Road, Tucson, AZ 85712, USA.  
Tel: +1 520 322 2965. Fax: +1 520 322 2993.*

**Dr. N. Umesaki**

*Department of Optical Materials, National Research Institute (ONRI), A.I.S.T.,  
1-8-31 Midorigaoka, Ikeda City, Osaka 563, Japan.  
Tel: +81 727 51 9536. Fax: +81 727 51 9631. E-mail: [umesaki@onri.go.jp](mailto:umesaki@onri.go.jp)*

**Dr. N.M. Vedishcheva**

*Institute of Silicate Chemistry, Russian Academy of Sciences, Ul Odoevskogo  
24, Korp 2, Sankt Petersburg, 199 155, Russia.  
Tel: +7 812 351 0810. Fax: +7 812 218 5401. E-mail: natalia@termex.spb.su*

**Mr. P. Venhuizen**

*Coe College, Department of Physics, 1220 First Ave N.E., Cedar Rapids, IA 52402, USA.  
Tel: +1 319 399 8483. Fax: +1 319 399 8748.*

**Ms. C. Vira**

*Coe College, Department of Physics, 1220 First Ave N.E., Cedar Rapids, IA 52402, USA.  
Tel: +1 319 399 8483. Fax: +1 319 399 8748.*

**Professor R.A. Weeks**

*Vanderbilt University, Box 6007-B, Nashville, TN 37235, USA.  
Tel: +1 615 322 2923. Fax: +1 615 343 8645. E-mail: raw@vuse.vanderbilt.edu*

**Mr. D. Wilkerson**

*Coe College, Department of Physics, 1220 First Ave N.E., Cedar Rapids, IA 52402, USA.  
Tel: +1 319 399 8483. Fax: +1 319 399 8748.*

**Mr. R. Williams**

*Coe College, Department of Physics, 1220 First Ave N.E., Cedar Rapids, IA 52402, USA.  
Tel: +1 319 399 8483. Fax: +1 319 399 8748. E-mail: mouser@topaz.coe.edu*

**Dr. A.C. Wright**

*J.J. Thomson Physical Laboratory, University of Reading, Whiteknights, Reading  
RG6 6AF, UK.  
Tel: +44 118 931 8555. Fax: +44 118 975 0203. E-mail: a.c.wright@reading.ac.uk*

**Dr. J. Yi**

*Circon ACMI, 300 Stillwater Avenue, Stamford, Connecticut, 06904-1971, USA.  
Tel: +1 203 328 8670. Fax: +1 203 328 8789.*

**Mr. Y. Yiannopoulos**

*Theoretical & Physical Chemistry Institute, National Hellenic Research Foundation,  
48 Vass Constantinou Ave., Athens 11635, Greece.  
Tel: +30 1 724 7973. Fax: +30 1 724 9104. E-mail: yiagos@apollon.servicenet.ariadne-t.gr*

**Professor J.W. Zwanziger**

*Department of Chemistry, Indiana University, Bloomington, IN 47405, USA.  
Tel: +1 812 855 3994 Fax: +1 812 855 8300 E-mail: jzwanzig@indiana.edu*